# An Open Microcavity for Diamond-based Photonics

## Inauguraldissertation

zur
Erlangung der Würde eines Doktors der Philosophie
vorgelegt der
Philosophisch-Naturwissenschaftlichen Fakultät
der Universität Basel

von

**Sigurd Flågan**

Basel, 2022

Genehmigt von der Philosophisch-Naturwissenschaftlichen Fakultät auf Antrag von

Prof. Dr. Richard J. Warburton

Prof. Dr. Patrick Maletinsky

Prof. Dr. Stephan Götzinger

Basel, den 22. Juni 2021

Prof. Dr. Marcel Mayor
Dekan

**Abstract**

In recent years, tunable Fabry-Perot microcavities have emerged as a compelling platform for enhancing the flux of coherent photons from single colour centres in solid-state hosts. A prominent example of one such colour centre is the nitrogen-vacancy (NV) centre in diamond. The NV centre has a highly coherent, optically addressable electron spin. Furthermore, the NV centre is a source of single photons. Advances in the creation of entangled spin-photon pairs allow for establishing remote spin-spin entanglement – a key building block in a quantum network. However, the scalability past a few network nodes is limited by modest entanglement rates, in turn limited by the detection efficiency of coherent photons. Limiting factors include the long radiative lifetime and the small branching ratio of "useful" photons into the zero-phonon line (ZPL). However, neither the radiative lifetime nor the branching ratio are rigid features of the NV centre – the flux of ZPL photons can be greatly accelerated in a resonant microcavity.

This thesis reports on the realisation of a high-quality tunable Fabry-Perot microcavity embedded with a diamond membrane. However, the diamond alters the cavity performance, rendering the cavity sensitive to surface related losses. Despite operating in a geometry where the standing wave inside the cavity possesses an anti-node at the diamond surface, quality ($\mathcal{Q}$) factors exceeding 100 000 were realised. The benefit of this geometry is the strong confinement of the vacuum electric-field to the diamond – the current cavity design allows for the realisation of Purcell factors exceeding 300, thus increasing the fraction of photons emitted into the ZPL from 3 % to 89 %.

The versatile design of the microcavity was demonstrated further by enhancing the Raman transition from the single crystalline diamond. Compared to free-space measurements under likewise identical conditions, a 59-fold intensity enhancement was demonstrated. This enhancement factor encompasses the Purcell effect and the improved detection efficiency provided by the cavity. The Raman transition couples to all cavity modes, allowing for in situ optimising and benchmarking the cavity performance. Additionally, it facilitates coupling to the external single-mode detection optics. Further enhancement of the Raman intensity can be achieved by establishing a double resonant condition, with both the pump laser and the Raman transition being resonant. Resonant recirculation of the pump laser increases the power density inside the cavity, providing a platform with prospects of realising a Raman laser with sub-mW threshold pump power. Exploiting a small thickness gradient in the diamond enabled continuous tuning of the double resonance condition across a spectral window of $\sim 1\,\mathrm{THz}$. The tuning range is only limited by the travel range of the piezo – with an adequate travel range, continuous tuning is, at least in principle, possible across the entire reflective stopband.


BEER
HIGH A
CAVITY

# Contents


**1 Introduction** **1**

1.1 The Scope and Structure of the Thesis . . . . . 4

**2 Background Theory** **8**

2.1 Cavity Quantum Electrodynamics . . . . . 8

2.1.1 Plano-Concave Fabry-Perot Cavity . . . . . 9

2.1.2 Jaynes-Cummings Model . . . . . 15

2.1.3 Emitter-Cavity Coupling in the Presence of Damping . . . . . 17

2.1.4 The Weak Coupling Regime – The Purcell Effect . . . . . 19

2.2 The Nitrogen-Vacancy Centre in Diamond . . . . . 23

2.2.1 Formation of NV Centres . . . . . 24

2.2.2 Electronic Level Structure . . . . . 27

2.2.3 Phonon Assisted Optical Transitions . . . . . 29

2.2.4 Resonant Excitation and the Associated Dynamics . . . . . 31

2.2.5 Optical Spin Initialisation, Manipulation and Readout . . . . . 34

2.2.6 Optically Detected Magnetic Resonance and Magnetic Field Sensing 36

2.3 Other Colour Centres . . . . . 37

2.3.1 Group-IV Split-Vacancies in Diamond . . . . . 38

2.3.2 Defects in Silicon Carbide . . . . . 42

2.3.3 Rare-Earth Ions in Crystalline . . . . . 43

2.4 Raman Scattering . . . . . 44

2.4.1 Phonons in Diamond . . . . . 46

2.4.2 Quantum Memory using Phonons in Diamond . . . . . 47

2.4.3 Cavity-Enhanced Raman Scattering and Raman Lasing . . . . . 48

**3 Hybrid Diamond-Air Cavity - the Coupled Cavity Model** **50**

3.1 The Hard-Mirror Model - Analytic Solution . . . . . 50

3.2 Effective Cavity Length . . . . . 51

3.3 Air-Confined vs. Diamond-Confined Cavity Modes – a Comparative Illustration . . . 53
3.3.1 The Hybridised Mode-structure . . . 54
3.3.2 Vacuum Electric Field Profile . . . 54
3.3.3 Introducing Losses . . . 57
3.3.4 Purcell Enhancement . . . 60
3.3.5 Condition for Maximal Photon Collection Efficiency . . . 62
3.3.6 Dependency on $R_{cav}$ . . . 66

**4 A Diamond-Confined Open Microcavity Featuring a High Quality-Factor and a Small Mode-Volume 69**
4.1 Introduction . . . 70
4.2 Methods . . . 72
4.2.1 The Cavity Mode-Structure . . . 76
4.2.2 The Finesse and the Quality-Factor . . . 80
4.2.3 Extracting the Cavity Linewidth . . . 80
4.3 Results on $\mathcal{Q}$-Factor . . . 82
4.3.1 Bare Cavity . . . 82
4.3.2 Diamond Membrane in the Cavity . . . 84
4.4 Prediction on the Purcell Factor . . . 89
4.4.1 Applying the Purcell Factor on an NV Centre . . . 91
4.4.2 Purcell Factor for Air- and Diamond-Confined Cavity Modes . . . 93
4.4.3 Estimating the Cavity Outcoupling Efficiency . . . 94
4.5 Conclusions and Outlook . . . 95

**5 Cavity-Enhanced Raman Scattering for in Situ Alignment and Characterisation of Solid-State Microcavities 97**
5.1 Introduction . . . 98
5.2 Methodology . . . 100
5.2.1 The Fabry-Perot Microcavity . . . 102
5.2.2 Experimental Setup . . . 103
5.3 Cavity-Enhanced Raman Scattering . . . 105
5.3.1 Probing the Cavity Mode Structure . . . 107
5.3.2 Quantitative Analysis of the Enhancement Factor . . . 112
5.4 Outlook and Conclusion . . . 114

**6 Widely-tunable, Doubly-Resonant Raman Scattering on Diamond in an Open Microcavity** **117**
6.1 Introduction . . . 118
6.2 Open Microcavity as a Platform for Nonlinear Optics . . . 119
6.2.1 Establishing the Double-Resonance Condition . . . 122
6.2.2 The $\mathcal{Q}$-Factor . . . 124
6.3 Doubly-Resonant Raman Scattering . . . 125
6.3.1 Estimating the Lasing Threshold . . . 127
6.3.2 Tuning the Double-Resonance Condition . . . 128
6.4 Discussions . . . 130
6.4.1 Cavity Mode Structure . . . 130
6.4.2 Tuning of the Double Resonance Condition . . . 131
6.4.3 Calculation of the Effective Raman Mode Volume . . . 133
6.5 Future Directions . . . 134
6.5.1 Minimising $V_{\mathrm{R}}$ . . . 136
6.6 Conclusion . . . 138
6.7 Appendix - Extended Methods . . . 140

**7 Photoluminescence Excitation Spectroscopy of NV centres in Microstructured Diamond** **142**
7.1 Measurement Methodology . . . 143
7.2 The effect of Microfabrication on the Optical Linewidth . . . 148
7.3 Reversed Fabrication Order . . . 150
7.3.1 Sample Preparation . . . 150
7.3.2 Pre-Characterisation of NV Centres in Bulk Diamond . . . 151
7.3.3 Microstructuring . . . 152
7.3.4 The Effect of Microstructuring . . . 154
7.3.5 Deep Etching . . . 158
7.3.6 Optical Linewidths After Deep Etching . . . 159
7.4 Optical Linewidths in Postimplanted Microstructures . . . 163
7.4.1 Sample Preparation . . . 163
7.4.2 Characterisation of the Optical Linewidths . . . 164
7.4.3 Spectral Stability . . . 168
7.4.4 Disentangling Inhomogeneous Broadening from Power Broadening 171
7.4.5 Statistical Modelling of the Optical Linewidths . . . 175
7.5 Overgrown NV Centres in a $\langle 111 \rangle$-oriented Diamond . . . 178

7.6 Conclusion and Further Improvements . . . . . 180

**8 Summary and Future Directions** **183**

8.1 Towards an Efficient Spin-Photon Interface . . . . . 186

8.1.1 The LaserOptik Mirrors . . . . . 189

8.1.2 Low-index Terminated Top-Mirror . . . . . 193

8.1.3 Depositing a $\lambda/4$-layer of Oxide on the Diamond . . . . . 196

8.1.4 The ECI Mirrors . . . . . 199

8.1.5 Comparison of the Mirrors . . . . . 201

8.2 Concluding Remarks . . . . . 205

**Appendices** **207**

**A Introducing the Transfer-Matrix Formalism** **207**

**B Modelling Clipping Losses** **211**

**C Incorporate Clipping Losses** **215**

**D A Toy Model Describing $\Delta\mathcal{Q}_0$** **218**

**E Piezo-Calibration Using the Cavity Mode-Structure** **221**

**F Cavity-Enhanced Detection Efficiency** **225**

**G A Note on $\mathcal{Q}$-Factor and Mirror Parallelity** **228**

**H Calculation of the Raman Lasing Threshold** **231**

**I Inhomogeneous Broadening of NV Centres under Resonant Drive** **234**

**J PLE Spectroscopy of NV Centres under Blue Illumination** **240**

**K Spin-Photon Entanglement** **246**

**References** **300**

**Acknowledgements** **301**

**Curriculum Vitae** **303**

**List of Publications** **304**

CHAPTER 1

# Introduction

The field of quantum mechanics was born at the turn of the 19th century, when classical physics failed to explain new and emerging physical phenomena [1]. Max Planck, regarded by many as the founding father of the field, proposed the idea of *quantised* energy levels in his attempt to explain the radiation spectrum of a black-body [2]. Planck was awarded the 1918 Nobel Prize in Physics "in recognition of the services he rendered to the advancement of Physics by his discovery of energy quanta" [3]. The idea of energy quantisation was developed one step further by Albert Einstein in his explanation of the photoelectric effect. Einstein proposed that light itself was quantised [4], leading to the birth of the photon [5]. Like Planck, Einstein was awarded the 1921 Nobel Prize in physics "for his services to Theoretical Physics, and especially for his discovery of the law of the photoelectric effect" [6].

The early discoveries of the "*first quantum revolution*" provide the foundation for much of the technology of the present everyday life [1]. Two prominent examples; the understanding of how light interacts with matter lead to the development of the laser and solar cells. Second, understanding how electrons behave in a solid paved the way for the creation of the transistor, a key component in the computer industry [7]. While the first quantum revolution could explain the world around us, the control and manipulation of single atoms and electrons was out of reach [1]. However, we are now at the doorstep of the "*second quantum revolution*", where our increasing understanding of quantum mechanics alongside technological development pushed by the likes of the semiconductor industry, allows for engineering and controlling the behaviour of single electrons and photons at our own will for our own benefit [1, 8]. The second quantum revolution promises new technologies such as, but not limited to, quantum sensors [9–11], quantum computers [12, 13], secure communication [14] and the quantum internet [15–17].

The field of quantum information [18] lies at the crossroad between quantum mechanics and information science, and concerns the use of quantum mechanics to store, manipulate

and transfer the information associated with individual quantum states. In the subfield of quantum computing, quantum bits (qubits) are used to solve computational tasks. As a direct consequence of the unique nature of quantum mechanics, quantum computers offer an exponential speed-up of the computational time compared to its classical counterpart [19, 20]. Contrary to classical bits, which can only assume the value 0 or 1, a qubit can take the values $|0\rangle$, $|1\rangle$ or a linear superposition of both $|0\rangle$ and $|1\rangle$, i.e. $|\psi\rangle = \alpha|0\rangle + \beta|1\rangle$ [21]. In simplified terms, the superposition state allows for parallel calculations, offering the aforementioned exponential speed-up [19, 20]. Quantum computers are expected to outperform their classical counterparts in tasks such as factorising large numbers [22, 23], searching through large unsorted databases [24] and hopefully in predicting when the next pandemic will hit [25]. Quantum advantage, or more famously "quantum supremacy", has been experimentally demonstrated using photons [26] and superconducting resonators [27].

The development of real-world applications requires the interconnection of many qubits in a robust, scalable manner. Trapped atoms and ions have been used in various proof-of-principle experiments [28–31]. However, the scalability of these experiments remain a great challenge due to the complex laser cooling and trapping techniques required. Qubits embedded in solid-state host materials, on the other hand, offer a viable route to scalability on the account of the possibility of integration into pre-existing microelectronic technologies [32].

Optically active defect centres in wide bandgap semiconductors have attracted significant attention over the course of the years [33, 34]. These defect centres often combine atom-like optical properties with a long-lived electron spin [35, 36]. A qubit can be formed by coherent manipulation of the electron spin between two discrete energy levels, for example spin up $|\uparrow\rangle$ and spin down $|\downarrow\rangle$ [7]. Arguably the most prominent example of such a defect centre is the nitrogen-vacancy (NV) centre in diamond [37], where the long-lived electron spin can be initialised, manipulated and readout all optically [38, 39], even at room-temperature [40]. Quantum entanglement between the electron spin and an emitted photon [41] paved the way for entanglement of well-separated electron spins [42, 43]; a key requirement for remote quantum information processing protocols [44].

The fields of quantum communication [45] and quantum cryptography [14] concerns the transfer of quantum information from one place to another in a secure, unhackable manner [46, 47]. Single optical-photons are widely used to transmit quantum information over long distances owing to the small interaction cross-section with each other and the environment [48], combined with the direct comparability with pre-existing classical fibre

networks [49–51]. However, residual absorption losses in the fibre links require the use of repeaters. Contrary to classical bits, exact copying of a quantum state is forbidden by the no-cloning theorem [14, 52, 53]. The development of quantum repeaters provides a means to overcome the propagation loss [54]. In a simplified picture, quantum repeaters work by establishing pair-wise entanglement between neighbouring network nodes, where each network link covers a subsection of the total distance [55, 56]. Quantum information can be transferred via entanglement swapping of the neighbouring network nodes. The distance between each node needs to be smaller than the distance light can propagate during the coherence time of the qubit [57]. The development of an efficient interface between the travelling photon and the stationary spin qubits is limited by the inherently weak interaction cross-section between light and matter [30, 58]. However, this interaction cross-section can be greatly enhanced by embedding the spins inside high-quality photonic resonators [59–61].

The realisation of a large-scale distributed quantum network requires the interconnection of remote network nodes [15, 16]. A key criterion for these quantum nodes is the ability to store- and process quantum information with high fidelity [17]. As previously mentioned, the NV centre in diamond possesses a highly-coherent, optically addressable electron spin [38, 62], and has thus been proposed as a node-candidate in a near-term quantum network [63–66]. Furthermore, weak coupling between the NV centre electron spin and nearby $^{13}$C nuclear spins [67], allow for the realisation of a long-lived multi-qubit quantum register [68–71], without compromising the coherence of the electron spin [72]. Furthermore, the presence of the $^{13}$C nuclear spins play a crucial role in achieving high fidelity remote spin-spin entanglement via entanglement distillation [73]. In this protocol, entanglement is swapped from the electron spin onto the $^{13}$C memory qubit [74], and thus freeing the electron spin for another round of entanglement [73]. For a fibre-based quantum network, frequency conversion to telecommunication wavelengths [75, 76] is required to mitigate photon loss in the network links [14, 48]. All these criteria have been demonstrated in proof-of-principle experiments using the NV centre.

However, scalability to more than a few network nodes is limited by the modest entanglement rates owing to the low flux of coherent photons. The rate of indistinguishable photons from NV centres are limited by (at least) four factors [77]. First, the NV centre possesses a long radiative lifetime of $\sim 12\,\mathrm{ns}$. Second, only $\sim 3\,\%$ of these photos are emitted along the zero-phonon line (ZPL) [78], while the remaining $97\,\%$ are emitted accompanied by a rapidly dephasing phonon. Third, the large contrast in refractive index across the diamond-air interface ($n_\mathrm{d} = 2.41$) leads to total internal reflection, consequently compromising the photon extraction efficiency. Finally,

random spectral fluctuations of the exact transition frequency render two ZPL photons distinguishable [79, 80]. However, at least in principle, the first three problems can be addressed by coupling the ZPL emission to a resonant photonic cavity [81–84].

## 1.1 The Scope and Structure of the Thesis

The overarching goal of this project is to enhance the flux of coherent photons from NV centres in diamond. The approach pursued here consists of enhancing the ZPL transition by resonant coupling to a single optical-mode in a Fabry-Perot microcavity. This thesis builds on the work performed by Ref. [77, 85], where the excited state lifetime was reduced from 12.6 ns in bulk to 7.06 ns in the cavity. More importantly, the fraction of light emitted into the ZPL was increased from $\sim 3\,\%$ to $46\,\%$ [77]. However, the experiment suffered from a modest $\mathcal{Q}$-factor of 58 500 limiting the cavity finesse to $\mathcal{F} = 5260$. Furthermore, the Purcell factor did not result in a significant increase in the photon countrate; the photons were lost before they could reach the detectors. Finally, the optical linewidth of the NV centres was found to increase from $\sim 100\,\mathrm{MHz}$ in bulk diamond to $\sim 1\,\mathrm{GHz}$ in thinned ($\sim 1\,\mu\mathrm{m}$) diamond membranes, presumably as a result of fabrication induced surface damage. This thesis aims at addressing the Q-nundrum of the low $\mathcal{Q}$-factor and the origin of the broadening of the optical linewidth.

The remainder of this thesis is divided into 7 chapters, organised in the following way. Chapter 2 presents the theoretical framework, from which the subsequent experimental chapters are built upon. The chapter is divided into four main sections, starting with an overview of the field of cavity quantum electrodynamics. First, the plano-concave Fabry-Perot cavity will be presented from a classical optics point of view. Key concepts, like the resonant condition, the mode-structure and the quality factor ($\mathcal{Q}$-factor) will be introduced. Moving on from the classical description, the Jaynes-Cummings model, describing the quantum mechanical nature of the interaction between a two-level emitter and a quantised cavity mode, will be introduced next. Here, the presence of the cavity significantly alters the optical properties of the emitter; on-resonance, the rate of spontaneous emission is greatly enhanced via the Purcell effect [86]. Up until this point, the theory discussed is completely generic: no assumptions will be made on the type of emitter. Therefore, the emitter of choice in this project, the NV centre in diamond, will be introduced in Section 2.2. Starting from a discussion of different methods of creating NV centres, the key electronic, optical and to some extent the spin properties of the

NV centre will be presented. The aim of this section is to give the reader an overview of the NV centre, and to point out key references along the way. The third part, Section 2.3 discusses the drawbacks and limitations of the NV centre, followed by a short introduction to new and emerging colour centres. The final section of Chapter 2 introduces Raman scattering, the inelastic scattering of photons via the creation of optical phonons. Raman scattering will first be discussed from a generic point of view, before introducing the diamond lattice and phonons in diamond. The chapter culminates in a short discussion concerning the use of phonons in diamond as a quantum memory and the use of diamond as the gain medium in a low-threshold Raman laser. Note that the theory presented in this chapter is by no means a complete review of everything there is to know about anything; the readers are kindly referred to the indicated references.

The presence of a diamond membrane inside the Fabry-Perot microcavity significantly alters the cavity mode-structure compared to a conventional, empty cavity. The finite contrast in refractive index across the diamond-air interface leads to hybridisation of the cavity mode [61]. In Chapter 3, one-dimensional transfer-matrix simulations will be used to quantitatively describe the resulting mode structure. Depending on the exact diamond thickness, two different regimes emerge: the so-called air- and diamond-confined geometries. For the air-confined geometry, the electric field is mostly confined to the air-gap, while in the diamond-confined geometry the field is more strongly confined to the diamond, leading to an enhanced coupling strength to emitters [87]. The two geometries also exhibit different sensitivity to surface losses and to length fluctuations.

Chapter 4 is the first experimental chapter of this thesis. This chapter presents the experimental realisation of a $\mathcal{Q}$-factor exceeding 120 000 and a finesse $\mathcal{F} \simeq 11\,000$ on a diamond membrane embedded in a Fabry-Perot microcavity. In this work, the diamond thickness ($\sim 0.73\,\mu\text{m}$) leads to the formation of a diamond-confined geometry, where the electric field possesses a field anti-node across the diamond-air interface. The maxima of the electric field render the cavity sensitive to scattering losses. Based on the aforementioned one-dimensional transfer-matrix calculations introduced in Chapter 3, a model capturing the cavity losses will be developed. This model reproduces the cavity finesse to within 10 %. The strong confinement of the electric field to the diamond leads to a theoretical Purcell factor of $F_\text{P} \simeq 170$. A Purcell factor on this order corresponds to $\sim 80\,\%$ of the photons being emitted into the ZPL. Note that the Purcell factor depends solely on the cavity parameters. Furthermore, the generic design of the microcavity platform allows for the incorporation of other colour centres in diamond, or in wide bandgap materials.

Chapter 5 demonstrates that the Raman transition in diamond provides a way to

fully characterise the Fabry-Perot microcavity. The Raman transition acts as a narrow-band internal lighthouse, providing an efficient method for *in situ* mode-matching to external detection optics on two grounds. First, the Raman transition is bright, offering $\sim 2\,\mathrm{Mcounts/s}$ on a standard silicon avalanche photodiode (APD). More importantly, the Raman scattering is an inherent property of the diamond and is largely independent on the xy-alignment of the cavity mode. Furthermore, the Raman transition couples to all Gaussian cavity modes, including higher-order transverse modes. Analysing the spacing of the cavity modes allows for the extraction of all the geometrical parameters of the cavity, such as the radius of curvature of the top mirror and the thickness of the diamond membrane. A comparison between the signal intensity of the cavity-enhanced Raman signal to the free-space Raman signal puts a number on the single-particle Purcell factor and the enhanced detection efficiency provided by the cavity. All the techniques developed in this chapter are directly transferable to measurements where single emitters are used [77].

Chapter 6 is a direct continuation of Chapter 5. Here, the cavity length was carefully tuned to establish a double resonance condition, where both the pump laser and the Raman transition were resonant for the same cavity length. In this configuration, the Raman transition is enhanced on two grounds. First, as in Chapter 5 the Raman transition experiences Purcell enhancement. Second, the resonant recirculation of the pump laser increases the power density inside the cavity. The motivation behind this chapter was the possibility of establishing a low-threshold tunable diamond Raman laser in the visible regime. The current geometry predicts a theoretical lasing threshold for continuous wave (CW) pump-power $P_{\mathrm{th}} = 187.50\,\mathrm{mW}$. However, with realistic changes to the geometry, sub mW threshold pump powers can be reached for CW operation. Furthermore, utilising a slight thickness gradient, $\sim$ THz tuneability of the double-resonance condition was demonstrated, only limited by the size of the diamond membrane and the travel-range of the piezo-electric nanopositioners. With an adequate travel-range and suitable sized diamond, continuous tuning across the entire reflective stopband is possible, amounting to several tens of THz.

While the first two experimental chapters aim at characterising the cavity, Chapter 7 aims at addressing the final issue listed above, namely the broadening of the optical linewidth induced during the fabrication of the diamond membranes. The optical coherence of NV centres was investigated on three different samples. In the first sample, the NV centres were formed by nitrogen ion implantation prior to fabrication. By measuring the optical linewidths before and after fabrication, it is evident that even exposing the diamond to a slight etching step has a devastating effect on the optical coherence. For

the the second sample, the NV centres were created by ion implantation after the fabrication of diamond membranes. In this sample, the measured linewidths were found to fall within two distinct populations, with narrow and broad linewidths, respectively. The two populations were attributed to NV centres created from native and implanted nitrogen ions. The narrow population routinely revealed linewidths $\lesssim 100\,\mathrm{MH}$ in $\sim 3\,\mu\mathrm{m}$ thick diamond. For both the samples, a statistical model was used to quantify the difference in the observed linewidths. In the final sample, the NV centres were introduced during the growth of an isotopically purified diamond film. The combination of controlled growth and isotopically purification offers an ideal condition for long spin coherence times at a depth desired for cavity coupling. Unfortunately, no narrow linewidths were observed in this sample.

The final chapter of this thesis, Chapter 8, takes a look back and summarises the work presented, followed by a look towards the future. In this chapter, the pros and cons of different, realistic mirror configurations will be discussed in terms of the achievable Purcell factor and photon extraction efficiency. As for Chapter 3, the analysis presented is largely based on one-dimensional transfer-matrix simulations, where the thickness of the diamond corresponds to the diamond thickness used in the second part of Chapter 7.

Finally, experimental techniques and mathematical derivations deemed too technical for the main text are bundled up in the appendices found at the end of this document.

CHAPTER 2

# Background Theory

The realisation of a large scale quantum network relies on the development of an efficient interface between stationary and flying qubits. For flying qubits, weakly interacting photons are the obvious choice [48]. However, deterministic interaction between stationary qubits and single photons is intrinsically weak. For an emitter placed in a tightly focused light beam with area $A = \frac{\pi}{4} w_0^2$, the absorption cross-section is on the order of $\sigma_{\text{abs}} = \frac{3\lambda^2}{2\pi}$. Deterministic light-matter coupling is possible, provided $\sigma_{\text{abs}} \gg A$. Due to the diffraction limit, this condition cannot be met in free space [30]. However, the interaction between light and matter can be greatly enhanced by placing the emitter inside a resonant cavity.

This chapter aims to provide the theoretical framework upon which the experiments presented in the subsequent chapters are built upon. This chapter is organised as follows. The first section discusses the interaction between light and matter. The second part of the chapter introduces our qubit of choice; the NV centre in diamond. Finally, the last section concerns Raman scattering and optical phonons in diamond.

## 2.1 Cavity Quantum Electrodynamics

Cavity quantum electrodynamics (cQED) describes the interaction between matter and light confined to a small volume. The presence of the cavity significantly alters the optical properties of an emitter. For example, in the so-called weak coupling regime of cavity QED, the radiative emission rate of single photons is greatly enhanced via the Purcell effect [86]. Starting from the classical description of a Fabry-Perot cavity, this section will discuss the quantum mechanical nature of the interaction between light and matter confined to small volumes.

### 2.1.1 Plano-Concave Fabry-Perot Cavity

The Fabry-Perot cavity consists of two high reflectivity mirrors separated by a distance $L_{\text{cav}}$, in such a way that light travelling back and forth between the two mirrors undergoes constructive interference, thus forming a standing wave. The optical field $|\Psi\rangle$ inside the cavity can be described as a linear superposition of the cavity modes $|\psi_i\rangle$ [88–90]:

$$|\Psi\rangle = \sum_i C_i \, |\psi_i\rangle \ . \tag{2.1}$$

The eigenmodes of the cavity can then be found from

$$\gamma_i \, |\Psi_i\rangle = \mathbb{M} \, |\Psi_i\rangle \ , \tag{2.2}$$

where the mode-mixing matrix $\mathbb{M}$ describes the change of the optical field after one roundtrip and $\gamma_i$ determines the amplitude of the corresponding eigenmode $|\Psi_i\rangle$. For a non-perfect cavity, the loss per round trip $\mathcal{L}_i$ for mode $|\Psi_i\rangle$ can be extracted from [88, 89]

$$\mathcal{L}_i = 1 - |\gamma_i|^2 \, . \tag{2.3}$$

The mode mixing matrix $\mathbb{M}$ is given by

$$\mathbb{M} = e^{2ikL_{\text{cav}}} \, \mathbb{B}^+ \times \mathbb{B}^- \, , \tag{2.4}$$

where $\mathbb{B}^{\pm}$ is the mode overlap integral over the finite extent of the mirrors located at distance $z = \pm \frac{L_{\text{cav}}}{2}$, respectively:

$$\mathbb{B}^{\pm}_{n,m} = \int_{-y_0}^{y_0} \int_{-x_0}^{x_0} \psi_n^{\mp} \psi_m^{\pm *} e^{-2ik\Delta(x,y)} dx dy \Big|_{z=\pm\frac{L_{\text{cav}}}{2}} \, . \tag{2.5}$$

The term $\Delta(x, y)$ describes the deviation of the mirror profile from a planar surface. For a spherical mirror with radius of curvature $R$, this deviation can be approximated by [88]

$$\Delta(x, y) \approx \frac{r^2}{2R} \, , \tag{2.6}$$

where $r = \sqrt{x^2 + y^2}$.

Up until this point, no assumption has been made on the form of $\psi_i$. In Cartesian coordinates, the general solution to the paraxial wave equation is the set of Hermite-

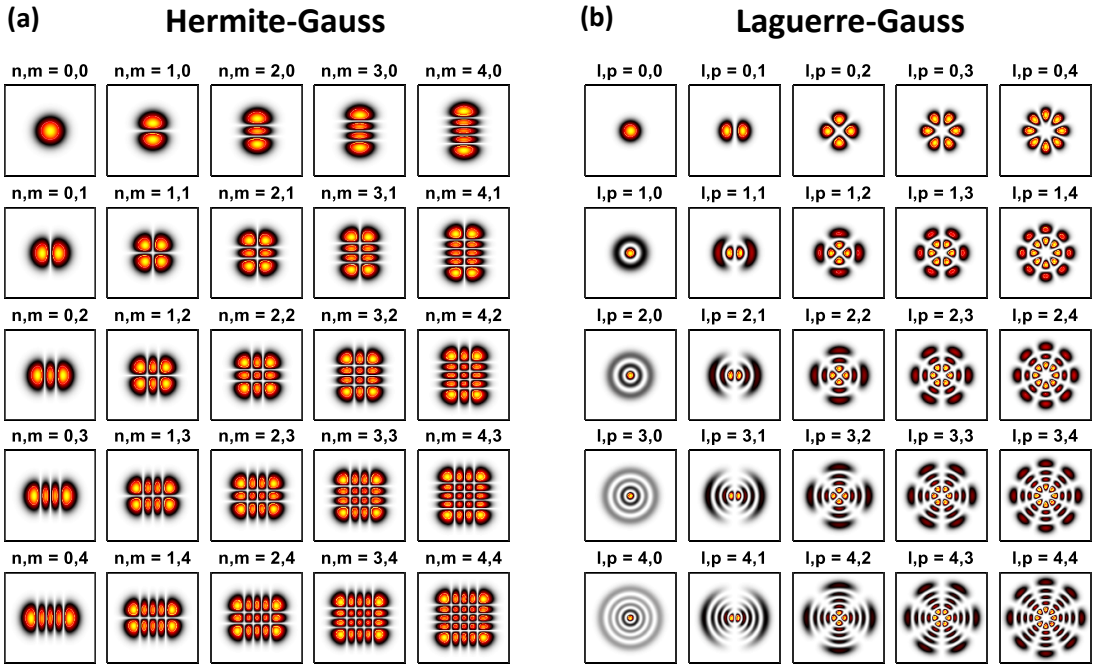


Fig. 2.1. **(a)** The spatial extent of the first 25 Hermite-Gauss modes calculated from Eq. 2.7. **(b)** The spatial extent of the first 25 Laguerre-Gauss modes for comparison.

Gauss modes* [91, 93]:

$$\psi_{nm}(x,y,z) = \frac{w_0}{w(z)} \cdot H_n\left(\sqrt{2}\frac{x}{w}\right) \cdot H_m\left(\sqrt{2}\frac{y}{w}\right) e^{-i\left(kz-\Phi_{mn}(z)\right)-i\frac{k}{2q(z)}(x^2+y^2)}, \qquad (2.7)$$

where $w(z)$ and $w_0$ are the beam radius at distance $z$ and $z = 0$ from the waist respectively, $\Phi_{mn}$ is the Gouy phase, $k = \frac{2\pi}{\lambda}$ is the wave vector and $q$ is complex beam parameter given by $\frac{1}{q(z)} = \frac{1}{R(z)} - i\frac{\lambda}{\pi w^2(z)}$. The terms $H_n$ and $H_m$ are Hermite polynomials of order $n$ and $m$ describing *higher-order transverse modes*. The Gouy phase, $\Phi = (n+m+1)\tan^{-1}(z/z_R)$, with $z_R$ being the Rayleigh length, describes the additional phase shift picked up by a Gaussian beam a distance $z$ away from the waist compared to a plane wave [93]. The first few Hermite-Gauss and Laguerre-Gauss modes are shown in Fig. 2.1 (a) and (b), respectively.

To achieve constructive interference, the optical field must replicate itself after one round trip. This is only possible provided the round trip phase change $\phi_{nm} = q \cdot 2\pi$,

*For a system with radial symmetry, the corresponding solution will be expressed by the Laguerre-Gauss modes [91, 92].

where $q$ is the longitudinal mode number* [93, 94]. If $L_{\text{cav}}$ is the separation of the two mirrors, the cavity is resonant provided [95]

$$\phi_{nm} = 2kL_{\text{cav}} - 2 \cdot (n + m + 1) \cdot \left[ \tan^{-1}\left(\frac{z_2}{z_R}\right) - \tan^{-1}\left(\frac{z_1}{z_R}\right) \right] = q \cdot 2\pi \,, \tag{2.8}$$

where $z_1$ and $z_2$ are the positions of the two mirrors with respect to the beam waist at $z = 0$ [93]. Introducing the dimensionless parameters $g_{1(2)} = 1 - \frac{L_{\text{cav}}}{R_{1(2)}}$, where $R_{1(2)}$ is the radius of curvature for the respective mirror, the resonance frequencies of the cavity can be derived from Eq. 2.8 for $g_1, g_2 > 0$ [93]

$$\nu_{nm} = \left( q + \frac{n + m + 1}{\pi} \cdot \cos^{-1}(\sqrt{g_1 g_2}) \right) \cdot \frac{c}{2L_{\text{cav}}} \,. \tag{2.9}$$

Here, $0 \leq g_1 g_2 \leq 1$ set the constrain for possible stable cavity geometries. In the experimental work presented in Chapter 4, Chapter 5 and Chapter 6, a planar-concave mirror configuration was used. For a planar mirror, $R_2 \to \infty$, hence $g_2 = 1$ and the stability criterion reduces to $0 \leq g_1 \leq 1$, in other words, $R > L_{\text{cav}}$ [93]. From a simple rearrangement of Eq. 2.9 one finds that the spacing of the cavity modes is given by

$$L_{\text{cav}}(q, n, m) = \left( q + \frac{n + m + 1}{\pi} \cdot \cos^{-1}(\sqrt{g_1}) \right) \cdot \frac{c}{2\nu_{nm}} \,. \tag{2.10}$$

The free spectral range, $\Delta\nu_{\text{FSR}} = \frac{c}{2L_{\text{cav}}}$, is defined as the frequency separation between two sequential (fundamental) longitudinal modes, i.e. $q_i$ and $q_{i+1}$. The frequency spacing between two adjacent transverse (higher-order) modes, $q_m$ and $q_{m+1}$, can be derived from Eq. 2.9:

$$\Delta\nu_{\text{trans}} = \frac{\Delta\nu_{\text{FSR}}}{\pi} \cdot \cos^{-1}\left( \sqrt{1 - \frac{L_{\text{cav}}}{R}} \right) \,. \tag{2.11}$$

From a simple rearranging, it follows that the radius of curvature of the curved mirror is given by

$$R = L_{\text{cav}} \cdot \left[ 1 - \cos^2\left( \frac{\Delta\nu_{\text{trans}}}{\Delta\nu_{\text{FSR}}} \pi \right) \right]^{-1} \,. \tag{2.12}$$

In other words, from Eq. 2.12 it is apparent that all the geometrical parameters of the optical cavity can be derived by analysing the frequency spacing of the fundamental and higher-order modes. This was experimentally demonstrated in Chapter 5.

For a stable Fabry-Perot cavity with arbitrary mirror geometry, the spot-size at the

*Not to be confused with the complex beam parameter $q(z)$ introduced in Eq. 2.7 [93].

mirror $w$ and beam waist $w_0$ can be calculated according to* [91, 93]

$$w^2 = \frac{\lambda L_{\text{cav}}}{n\pi} \cdot \sqrt{\frac{g_2}{g_1(1-g_1g_2)}} \tag{2.13a}$$

$$w_0^2 = \frac{\lambda L_{\text{cav}}}{n\pi} \cdot \frac{\sqrt{g_1g_2(1-g_1g_2)}}{g_1+g_2-2g_1g_2} \,. \tag{2.13b}$$

For a plano-concave cavity, i.e. $g_2 = 1$, Eq. 2.13 reduces to

$$w^2 = \frac{\lambda R}{n\pi} \cdot \left(\frac{L_{\text{cav}}}{R} - 1\right)^{-\frac{1}{2}} \tag{2.14}$$

$$w_0^2 = \frac{\lambda}{n\pi} \cdot \left(L_{\text{cav}}R - L_{\text{cav}}^2\right)^{\frac{1}{2}} \,. \tag{2.15}$$

A smaller beam waist implies tighter confinement of the optical field. The value of $w_0^2$ can be minimised by two means: minimising $L_{\text{cav}}$, with a suitable geometry for coupling to emitters close to the planar mirror [77, 96–103] or by working in the concentric geometry where $L_{\text{cav}} \to R$. However, in the second case, as $w^2 \to \infty$ the cavity is prone to diffraction loss at the finite extent of the mirror [88, 104, 105]. Diffraction losses will be further discussed in Chapter 4.

### Energy Stored in an Optical Cavity

So far, the geometrical parameters of the Fabry-Perot cavity have been outlined. In the following section, the energy associated with the standing wave inside the cavity will be described. In the following analysis, the two mirrors forming the Fabry-Perot cavity have reflection- and transmission coefficients $r_{1(2)}$ and $t_{1(2)}$, respectively where the subscript indicates mirror 1 or 2. Consider an electromagnetic wave with amplitude $E_0$ incident from the left (mirror 1). The corresponding electric field inside the cavity can be calculated from the infinite geometric series [93]

$$E_{\text{cav}} = E_0t_1 \cdot \sum_{j=0}^{\infty} \left(r_1r_2e^{-i\phi}\right) = \frac{E_0t_1}{1-r_1r_2e^{-i\phi}} \,, \tag{2.16}$$

*More potentially confusing notation. Here, and whenever $n$ appears in connection with $\lambda$ or $\nu$, i.e. $\frac{\lambda}{n}$ and $\frac{\nu}{n}$, $n$ is the refractive index, not to be confused with the mode index.

where the round trip phase delay $\phi$ is given by Eq. 2.8. The circulating intensity can then be calculated from [4, 93]

$$I_{\text{cav}} = |E_{\text{cav}}|^2 = I_0 \frac{t_1^2}{(1 - r_1 r_2)^2 + 2 r_1 r_2 \sin^2\left(\phi/2\right)}, \tag{2.17}$$

which can be approximated with a Lorentzian centred around $\phi = q \cdot 2\pi$, where $\Delta\phi_{\text{FSR}} = 2\pi$ is the free spectral range of the cavity. The full width at half max (FWHM) of Eq. 2.17 is equal to

$$\text{FWHM} = 2\phi_{1/2} = \frac{2\left(1 - r_1 r_2\right)}{\sqrt{r_1 r_2}}, \tag{2.18}$$

where $\phi_{1/2}$ is the phase at half the maximum of $I_{\text{cav}}$. The finesse, $\mathcal{F}$, of the cavity is defined as the ratio of the free spectral range of the cavity, $\Delta\phi_{\text{FSR}}$, to the FWHM of the resonance, i.e. [93]

$$\mathcal{F} = \frac{\Delta\phi_{\text{FSR}}}{2\phi_{1/2}} = \frac{\pi\sqrt{r_1 r_2}}{1 - r_1 r_2}. \tag{2.19}$$

Alternatively, the finesse can be defined in terms of the cavity length $L_{\text{cav}}$ and the frequency $\nu$ of the electromagnetic field,

$$\mathcal{F} = \frac{\Delta L_{\text{FSR}}}{\delta L_{\text{cav}}} = \frac{\lambda/n}{2\delta L_{\text{cav}}} \tag{2.20}$$

$$\mathcal{F} = \frac{\Delta\nu_{\text{FSR}}}{\delta\nu} = \frac{c/n}{2L_{\text{cav}}\delta\nu}, \tag{2.21}$$

where $\delta L_{\text{cav}}$ and $\delta\nu$ is the linewidth of the resonance in length and frequency, respectively.

The finesse is a measure of the total round-trip losses in the cavity $\mathcal{L}_{\text{tot}}$. By defining the mirror transmission, $\mathcal{T}_1 = |t_1|^2$ and $\mathcal{T}_2 = |t_2|^2$, where $t_i = 1 - |r_i|^2$, and the round-trip loss of the cavity $\mathcal{L}_{\text{cav}}$, the finesse can be approximated by: [93, 106]

$$\mathcal{F} = \frac{2\pi}{\mathcal{L}_{\text{tot}}}, \tag{2.22}$$

where $\mathcal{L}_{\text{tot}} = \mathcal{T}_1 + \mathcal{T}_2 + \mathcal{L}_{\text{cav}}$. In Chapter 4 the interplay between different loss-mechanisms, such as scattering and absorption, were experimentally studied.

For a general resonator, the quality-factor ($\mathcal{Q}$-factor) is defined as the ratio of the energy stored to the rate of energy loss [93]

$$\mathcal{Q} \mathrel{\widehat{=}} \frac{\omega\mathcal{E}}{d\mathcal{E}/dt} = \omega t_{\text{cav}}, \tag{2.23}$$

where $t_{\text{cav}} = \frac{2L_{\text{cav}}}{c\mathcal{L}_{\text{tot}}}$ is the photon lifetime inside the cavity. Using Eq. 2.22, the $\mathcal{Q}$-factor

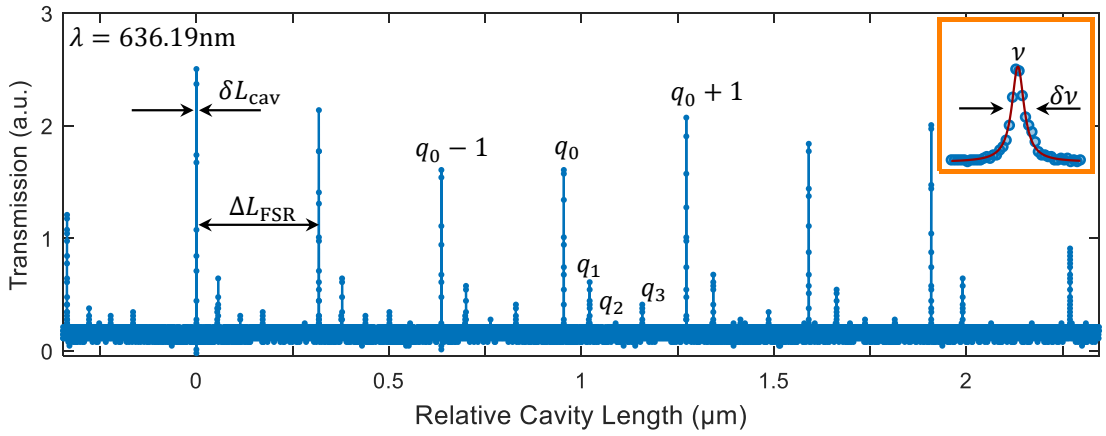


Fig. 2.2. Transmission as a function of cavity length for fixed $\lambda = 636.2\,\mathrm{nm}$. Several fundamental- and higher-order cavity modes are resolved. The cavity modes are labelled according to $q_{n+m}$, where $n + m = 0$ for the fundamental modes. The spacing of the fundamental modes is given by $\Delta L_{\mathrm{FSR}} = \frac{\lambda}{2}$. The inset shows a zoom of the fundamental cavity mode $q_0 + 3$.

can be expressed as

$$\mathcal{Q} = \omega \cdot \frac{2L_{\mathrm{cav}}}{c/n \cdot \mathcal{L}_{\mathrm{tot}}} = \frac{2L_{\mathrm{cav}}\nu}{c/n} \cdot \mathcal{F} = \frac{2L_{\mathrm{cav}}}{\lambda/n} \cdot \mathcal{F}. \tag{2.24}$$

From the last equality, the $\mathcal{Q}$-factor can be interpreted as the finesse times the number of half-waves between the two mirrors [85, 93]. Introducing $\tau = \frac{2L_{\mathrm{cav}}}{c}$ as the cavity round-trip time combined with $\omega = 2\pi\nu$ and Eq. 2.22, leads to

$$\mathcal{Q} = 2\pi\nu t_{\mathrm{cav}} = \frac{2L_{\mathrm{cav}}\nu}{c} \cdot \mathcal{F} = \nu\tau\mathcal{F}, \tag{2.25}$$

from which the finesse can be interpreted as the relative energy loss per round-trip [85]. From Eq. 2.22 and Eq. 2.24, one obtains the relation between the $\mathcal{Q}$-factor and the total round-trip loss

$$\mathcal{Q} = \frac{4\pi L_{\mathrm{cav}}}{\lambda\mathcal{L}_{\mathrm{tot}}}. \tag{2.26}$$

Finally, combining Eq. 2.21 and Eq. 2.25 defines the $\mathcal{Q}$-factor as the frequency resolution of the cavity [93]

$$\mathcal{Q} = \frac{\nu}{\delta\nu} = \frac{\omega}{\delta\omega} = \frac{\omega}{\kappa}, \tag{2.27}$$

where $\kappa = \frac{2\pi}{\tau\mathcal{F}}$ is the photon loss-rate from the cavity.

To conclude this section, Fig. 2.2 shows the transmission of the cavity as a function of increasing cavity length $L_{\mathrm{cav}}$ for fixed $\lambda = 636.2\,\mathrm{nm}$. Several fundamental and higher-

order cavity modes are resolved. The cavity modes are labelled according to $q_{n+m}$, where $q_{n+m=0}$ are the fundamental modes. The spacing of the cavity modes is given by Eq. 2.10. The inset shows a zoom of the mode $q_0 + 3$, illustrating how the $\mathcal{Q}$ is defined*.

### 2.1.2 Jaynes-Cummings Model

The Jaynes-Cummings model [107] describes the interaction between a single two-level emitter and a quantised cavity mode of frequency $\omega_c$. The cavity is (close to) resonance with the energy spacing $\hbar\omega_a$ between the ground- and excited-state of the emitter, denoted by $|g\rangle$ and $|e\rangle$, respectively [30, 108]. The Hamiltonian $\hat{\mathcal{H}}$ describing the dynamics can be broken down into three components, the emitter $\hat{H}_a$, the cavity $\hat{H}_c$ and the interaction $\hat{H}_I$, i.e. [109]

$$\hat{\mathcal{H}} = \hat{H}_a + \hat{H}_c + \hat{H}_I \,, \tag{2.28}$$

where the bare emitter- and cavity terms are given by [110]

$$\hat{H}_a = \frac{1}{2} \cdot \hbar\omega_a \hat{\sigma}_z \tag{2.29}$$

$$\hat{H}_c = \hbar\omega_c \hat{a}^\dagger \hat{a} \,, \tag{2.30}$$

where $\hat{a}^\dagger$ and $\hat{a}$ are the creation and annihilation operators of a cavity photon, respectively, and $\hat{\sigma}_z = |e\rangle\langle e| - |g\rangle\langle g|$. Note that in this definition of the atomic term, the level of zero energy is defined as halfway between the ground and excited state, i.e. $E_e = -E_g = \frac{1}{2}\hbar\omega_a$, consistent with Ref. [110]

In the dipole approximation, where the electric field is assumed to be spatially uniform, on the grounds that the typical dimensions of the emitter being much smaller than the wavelength of light, the interaction term is given by [110]

$$\hat{H}_I = -\underline{\hat{d}} \cdot \underline{\hat{E}} = \hbar g \left(\hat{\sigma} + \hat{\sigma}^\dagger\right) \cdot \left(\hat{a} + \hat{a}^\dagger\right), \tag{2.31}$$

where $\hat{d} = \underline{d}_{eg}\hat{\sigma}^\dagger + \underline{d}_{ge}\hat{\sigma}$, $\underline{\hat{E}}$ and $g$ are the electric dipole operator, the electric field operator and the coupling constant, respectively. Here $\hat{\sigma} = |g\rangle\langle e|$ and $\hat{\sigma}^\dagger = |e\rangle\langle g|$ are the atomic lowering- and raising operators. From this, the emitter-cavity coupling strength can be defined as $g = \frac{d \cdot E}{\hbar}$ [30]. In the interaction picture, the time dependence of Eq. 2.31

*Careful here, the $\mathcal{Q}$-factor is more commonly defined in terms of frequency, i.e. $\mathcal{Q} = \frac{\nu}{\delta\nu}$, rather than $\mathcal{Q} = \frac{L_{cav}}{\delta L_{cav}}$. The former definition will be used throughout this thesis.

becomes [30]

$$\hat{H}_I(t) = \hbar g \left(\hat{\sigma}^\dagger e^{i\omega_\mathrm{a} t} + \hat{\sigma} e^{-i\omega_\mathrm{a} t}\right) \cdot \left(\hat{a} e^{-i\omega_\mathrm{c} t} + \hat{a}^\dagger e^{i\omega_\mathrm{c} t}\right) \tag{2.32}$$

$$= \hbar g \left(\hat{\sigma}^\dagger \hat{a} e^{i(\omega_\mathrm{a}-\omega_\mathrm{c})t} + \hat{\sigma}^\dagger \hat{a}^\dagger e^{i(\omega_\mathrm{a}+\omega_\mathrm{c})t} + \hat{\sigma}\hat{a} e^{-i(\omega_\mathrm{a}+\omega_\mathrm{c})t} + \hat{\sigma}\hat{a}^\dagger e^{-i(\omega_\mathrm{a}-\omega_\mathrm{c})t}\right). \tag{2.33}$$

Provided $g \ll \omega_\mathrm{a}, \omega_\mathrm{c}$, the rotating wave approximation (RWA) can be applied. In this approximation, the rapidly varying, energy non-conserving terms $\hat{\sigma}^\dagger \hat{a}^\dagger$ and $\hat{\sigma}\hat{a}$ can be neglected compared to the slowly varying, resonant $\hat{\sigma}^\dagger \hat{a}$ and $\hat{\sigma}\hat{a}^\dagger$ terms, on the grounds that they average out over the relevant timescales [111]. Consequently, Eq. 2.33 reduces to [110]

$$\hat{H}_I = \hbar g \left(\hat{\sigma}^\dagger \hat{a} + \hat{\sigma}\hat{a}^\dagger\right). \tag{2.34}$$

Finally, combining Eq. 2.34 with Eq. 2.29 and Eq. 2.30 yields the Jaynes-Cummings Hamiltonian [30]

$$\hat{\mathcal{H}}_{JC} = \hbar\omega_a \hat{\sigma}^\dagger \hat{\sigma} + \hbar\omega_c \hat{a}^\dagger \hat{a} + \hbar g \left(\hat{\sigma}^\dagger \hat{a} + \hat{\sigma}\hat{a}^\dagger\right). \tag{2.35}$$

In the Jaynes-Cummings model, for photon number $|n\rangle$, the dynamics can be described by considering separate two-level systems with basis vectors [110]

$$|\psi_1\rangle = |e, n\rangle \tag{2.36}$$

$$|\psi_2\rangle = |g, n+1\rangle. \tag{2.37}$$

The Jaynes-Cummings Hamiltonian can only couple the pair of states $|g, n+1\rangle$ and $|e, n\rangle$ [109]. In other words, the emitter is excited from the ground-state $|g\rangle$ to excited-state $|e\rangle$ by absorbing a cavity photon. Relaxation from state $|e\rangle$ to state $|g\rangle$ occurs by emitting a cavity photon, i.e. [85, 110]

$$|e, n\rangle \leftrightarrow |g, n+1\rangle. \tag{2.38}$$

In matrix form, the Jaynes-Cummings Hamiltonian can be expressed as [110]

$$\hat{H} = \hbar \cdot \begin{pmatrix} n\omega_\mathrm{c} + \frac{\omega_\mathrm{a}}{2} & g\sqrt{n+1} \\ g\sqrt{n+1} & (n+1)\omega_\mathrm{c} - \frac{\omega_\mathrm{a}}{2} \end{pmatrix} \tag{2.39}$$

with eigenvalues

$$E_{n,\pm} = \left(n + \frac{1}{2}\right)\hbar\omega_\mathrm{c} \pm \frac{1}{2}\hbar\sqrt{\Delta_\mathrm{ac}^2 + 4g^2(n+1)}, \tag{2.40}$$

and corresponding eigenvectors

$$|\pm, n\rangle = \frac{1}{\sqrt{2}} \left( |e, n\rangle \pm |g, n+1\rangle \right) . \tag{2.41}$$

Here, $\Delta_{\mathrm{ac}} = \omega_{\mathrm{a}} - \omega_{\mathrm{c}}$ is the emitter-cavity detuning and $\Omega_n = 2g\sqrt{(n+1)}$ is the corresponding Rabi frequency [30]. The eigenvalues of the Jaynes-Cummings Hamiltonian are the so-called dressed states, where the energy spectrum resulting from Eq. 2.40 is referred to as the Jaynes-Cummings ladder. Each step in the ladder consists of the doublet $|\pm, n\rangle$ with energy spacing $\Delta E_n = 2\hbar g\sqrt{n+1}$, which increases non-linearly with the number of excitations $n$ [30, 112].

To conclude this section, consider an emitter initially in the excited-state $|e\rangle$ resonantly coupled to a cavity (i.e. $\Delta_{\mathrm{ac}} = 0$) containing $n$ photons. The initial state $|i\rangle = |e, n\rangle = (1, 0)^T$ can only couple to the final state $|f\rangle = |g, n+1\rangle = (0, 1)^T$. For zero detuning, $E_i = \frac{1}{2}\hbar\omega_{\mathrm{c}} + n\hbar\omega_{\mathrm{c}}$ and $E_f = -\frac{1}{2}\hbar\omega_{\mathrm{c}} + (n+1)\,\omega_{\mathrm{c}}$ *. The state vectors can be expressed as

$$|\Psi\rangle = C_i(t)\,|i\rangle + C_f(t)\,|f\rangle\,, \tag{2.42}$$

with $C_i(0) = 1$ and $C_f(0) = 0$ [110]. Solving the Schrödinger equation gives the probability of finding the system in state $|i\rangle$ (or $|f\rangle$) after a time $t$

$$P_i(t) = \left|C_i(t)\right|^2 = \cos^2(g\sqrt{n+1}\cdot t) \tag{2.43}$$

$$P_f(t) = \left|C_f(t)\right|^2 = \sin^2(g\sqrt{n+1}\cdot t)\,. \tag{2.44}$$

In other words, the system undergoes Rabi oscillations between the state $|e, n\rangle$ and $|g, n+1\rangle$ at frequency $\Omega_n = 2g \cdot \sqrt{n+1}$. For the case $n = 0$ the emitter undergoes vacuum Rabi oscillations with frequency $\Omega_0 = 2g$. In this picture, the emitter undergoes "oscillatory spontaneous emission" where a photon is being spontaneously emitted before being reabsorbed [109].

### 2.1.3 Emitter-Cavity Coupling in the Presence of Damping

In the above section, the emitter-cavity dynamics were described in the absence of any loss mechanism: a photon emitted into the cavity mode will undergo oscillatory spontaneous emission for all eternity. However, in a real-life experiment, photons leak out of

*Recall that here, the zero energy level is defined halfway between the ground and excited-state of the emitter [110]. By defining the emitter ground-state as the zero energy level allows the initial and final energy to be expressed as $E_i = \hbar\omega_{\mathrm{a}} + n\hbar\omega_{\mathrm{c}}$ and $E_f = (n+1)\,\omega_{\mathrm{c}}$ [30]. For zero detuning, $\omega_{\mathrm{a}} = \omega_{\mathrm{c}}$ and consequently $E_i = E_f$.

the cavity at a rate $\kappa$ due to the finite transmission of the end mirrors, in addition to scattering and absorption from the mirrors. Furthermore, excitations can be lost at a rate $\gamma$ due to decay into all other channels than the cavity mode [30].

In the presence of losses, the emitter-cavity dynamics can be described by introducing the density matrix $\hat{\rho} = |\psi\rangle\langle\psi|$ and the Lindblad Master equation

$$\frac{d\hat{\rho}}{dt} = \frac{1}{i\hbar}\left[\hat{\mathcal{H}}_{\mathrm{JC}}, \hat{\rho}\right] + \sum_i \left(\hat{L}_i\hat{\rho}\hat{L}_i^\dagger - \frac{1}{2}(\hat{L}_i\hat{L}_i^\dagger\hat{\rho} + \hat{\rho}\hat{L}_i^\dagger\hat{L}_i)\right), \tag{2.45}$$

where $\hat{L}_1 = \sqrt{2\gamma}\hat{\sigma}$ and $\hat{L}_2 = \sqrt{2\kappa}\hat{a}$ are the emitter- and cavity jump operators, respectively [30, 109]. The dynamics are now determined by the relative ratio of $g$, $\kappa$ and $\gamma$. A key figure of merit is the cooperativity:* [58]

$$\mathcal{C} \mathrel{\widehat{=}} \frac{4g^2}{\kappa\gamma}\,. \tag{2.46}$$

In simple words, the cooperativity gives the ratio of the desired coupling to the undesired coupling. Broadly speaking, the value of $\mathcal{C}$ give rise to the two different regimes of cavity QED: the strong coupling regime where $g \gg \kappa, \gamma$ and the weak coupling regime where $\kappa > g, \gamma$. For $\mathcal{C} \gg 1$, the emitter-cavity coupling is stronger than decoherence mechanisms, paving the way for deterministic emitter-photon interactions [30, 58, 61].

In the strong coupling regime, the coupling between the cavity and the emitter is faster than the loss-rates. Therefore, a photon emitted can be re-absorbed by the emitter before being lost from the cavity, leading to the observation of vacuum-Rabi oscillations as described in Section 2.1.2 [30, 99]. Strong coupling, and the resulting Jaynes-Cummings ladder, has been experimentally demonstrated on various platforms, including but not limited to, superconducting resonators [111, 116, 117], atoms [118], molecules [103] and self-assembled quantum dots coupled to a Fabry-Perot microcavity [99].

In the weak coupling regime, the loss-rates are greater than the emitter-cavity coupling. Therefore, a photon emitted in the cavity will be lost before being re-absorbed, and no vacuum-Rabi oscillations can take place. However, the presence of the cavity alters the photonic density of states, rendering spontaneous emission in the weak coupling regime different from free-space spontaneous emission. The experiments presented in this thesis were conducted in the weak coupling regime.

*The exact definition of the cooperativity differ between different sources. The definition used here follows from Ref. [58, 61, 113, 114]. The alternative definition, $\mathcal{C} = \frac{2g^2}{\kappa\gamma}$, is also commonly found in literature, such as Ref. [99, 115].

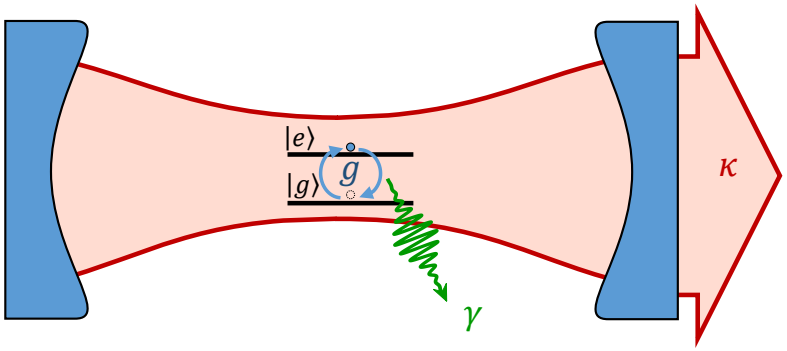


Fig. 2.3. Schematic of a two-level emitter coupled to a single-mode of an optical cavity with coupling rate $g$. Photons are lost from the cavity at rate $\kappa$ due to scattering, absorption or transmission through the end mirrors. Photon decay to non-cavity modes occurs at rate $\gamma$.

### 2.1.4 The Weak Coupling Regime – The Purcell Effect

An emitter coupled to a cavity will experience a different photonic environment compared to an emitter in free-space. On resonance, the photonic density of states are greatly enhanced, leading to enhanced emission rates and consequently a reduction in the exited state lifetime [86]. This effect was first characterised by E. M Purcell in 1946, for which the effect now carries his name. For this work, Purcell was jointly awarded the 1952 Nobel Prize in physics together with Felix Bloch "*for their development of new methods for nuclear magnetic precision measurements and discoveries in connection therewith*" [119]. For the far off-resonant case, however, the photonic density of states is suppressed compared to free-space, leading to reduced emission rates [120].

In the weak coupling regime, the light-matter interaction can be calculated using perturbation theory; the emitter is perturbed by the *vacuum electric-field* $E_{\text{vac}}$ confined by the cavity. For an emitter in free-space, the transition rate from excited-state $|e\rangle$ to ground-state $|g\rangle$ is governed by Fermi's golden rule:

$$\Gamma_{\text{e}\to\text{g}} = \frac{2\pi}{\hbar^2} \cdot \left|\mathcal{M}_{\text{e}\to\text{g}}\right|^2 \cdot \rho(\omega)\,, \tag{2.47}$$

where $\mathcal{M}_{\text{e}\to\text{g}} = \langle g|\,\hat{H}_P\,|e\rangle$ is the transition matrix element for perturbation Hamiltonian $\hat{H}_P$ and $\rho(\omega)$ is the density of final states [112]. Using $\hat{H}_{\text{P}} = -\vec{d}\cdot\vec{E}_{\text{vac}}$ (Eq. 2.31), the transition matrix element becomes

$$\mathcal{M}_{\text{e}\to\text{g}} = -\vec{\mu}_{\text{eg}}\cdot\vec{E}_{\text{vac}}, \tag{2.48}$$

where $\vec{\mu}_{\mathrm{eg}} = q \langle g | \vec{d} | e \rangle$ is the electric dipole moment for electric charge $q^*$. The magnitude of the vacuum electric field confined to volume $V$ can be calculated from [112]

$$\left|\vec{E}_{\mathrm{vac}}\right| = \sqrt{\frac{\hbar\omega}{2\epsilon_0\epsilon_R V}}\,. \tag{2.49}$$

In vacuum, the photonic density of states is given by [112]

$$\rho(\omega) = \frac{\omega^2 V}{\pi^2} \cdot \left(\frac{c}{n}\right)^{-3}. \tag{2.50}$$

Combining the above, the free-space spontaneous emission rate is given by

$$\Gamma_0 = \frac{1}{3} \cdot \frac{\mu_{\mathrm{eg}}^2 \omega^3}{\pi\hbar\epsilon_0\epsilon_R} \cdot \left(\frac{c}{n}\right)^{-3}, \tag{2.51}$$

where the factor of $\frac{1}{3}$ arises by averaging over all possible dipole orientations with respect to the vacuum field [112].

Introducing a cavity with quality factor $\mathcal{Q} = \frac{\omega_{\mathrm{c}}}{\delta\omega_{\mathrm{c}}}$ (Eq. 2.27) confines the vacuum fluctuations to volume $V$. For a single cavity mode, the density of states have to fulfil

$$\int_0^\infty \rho(\omega) d\omega \stackrel{!}{=} 1\,, \tag{2.52}$$

which is satisfied by a normalised Lorentzian of the form [112]

$$\rho(\omega) = \frac{2}{\pi\delta\omega_{\mathrm{c}}} \cdot \frac{\delta\omega_{\mathrm{c}}^2}{4(\omega-\omega_{\mathrm{c}})^2 + \delta\omega_{\mathrm{c}}^2} = \frac{2\mathcal{Q}}{\pi\omega_{\mathrm{c}}} \cdot \frac{\delta\omega_{\mathrm{c}}^2}{4(\omega-\omega_{\mathrm{c}})^2 + \delta\omega_{\mathrm{c}}^2}\,. \tag{2.53}$$

For the emitter in the cavity, the transition matrix element becomes

$$\mathcal{M}_{\mathrm{e}\to\mathrm{g}}^2 = \xi^2 \mu_{\mathrm{eg}}^2 E_{\mathrm{vac}}^2, \tag{2.54}$$

where

$$\xi = \frac{\left|\vec{d}\cdot\vec{E}_{\mathrm{vac}}\right|}{\left|\vec{d}\right| \cdot \left|\vec{E}_{\mathrm{vac}}\right|} = \cos(\theta)\,, \tag{2.55}$$

is the vacuum field component along the electric dipole moment of the emitter [112]. As for free-space, the spontaneous emission into the cavity mode can be calculated from

*The dipole moment is related to the *oscillator strength* $f_{ij} = \frac{2m\omega_{ji}}{3\hbar}|\mu_{ij}|^2$ [112, 121].

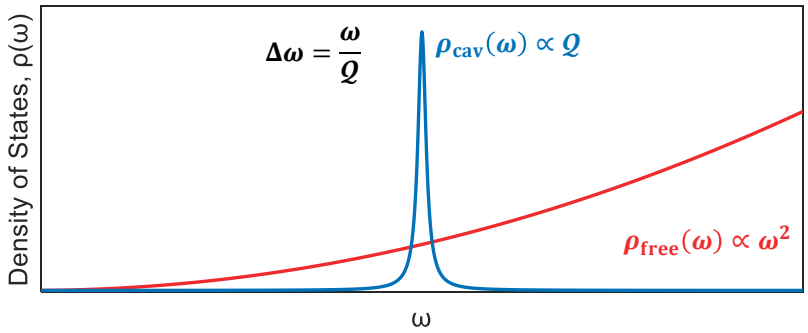


Fig. 2.4. Schematic comparing the density of states in free-space to that of an optical cavity. For an optical emitter in free-space, the density of states scales with $\omega^2$ (red curve), while in the cavity the density of states scales as a Lorentzian parametrised by the $\mathcal{Q}$-factor of the resonator (blue curve). Adapted and modified from Ref. [122].

Fermi's golden rule (Eq. 2.47)

$$\Gamma_{\text{cav}} = \frac{2\mathcal{Q}\mu_{\text{eq}}^2}{\hbar\epsilon_0\epsilon_R V} \cdot \xi^2 \cdot \frac{\delta\omega_{\text{c}}^2}{4(\omega-\omega_{\text{c}})^2 + \delta\omega_{\text{c}}^2} \,. \tag{2.56}$$

For an emitter in the excited-state, a photon can be emitted either into the cavity mode or to any free-space modes, with rates $\Gamma_{\text{cav}}$ and $\Gamma_0$, respectively. Thus, the total emission rate $\Gamma_{\text{tot}}$ is obtained from Eq. 2.51 and Eq. 2.56: [85]

$$\Gamma_{\text{tot}} = \Gamma_0 + \Gamma_{\text{cav}} = \left(1 + \frac{\Gamma_{\text{cav}}}{\Gamma_0}\right)\Gamma_0 = F_{\text{P}}\Gamma_0 \,, \tag{2.57}$$

where $F_{\text{P}}$ is the Purcell factor. Intuitively, the value of the Purcell factor captures the effect of the cavity: the transition rate is enhanced for $F_{\text{P}} > 1$. Using $\omega_{\text{c}} = \frac{2\pi c}{\lambda_{\text{c}}}$, the Purcell factor can be calculated from Eq. 2.51 and Eq. 2.56

$$F_{\text{P}} = 1 + \frac{3}{4\pi^2} \cdot \frac{\mathcal{Q}}{V}\left(\frac{\lambda_{\text{c}}}{n}\right)^3 \cdot \xi^2 \cdot \frac{\delta\omega_{\text{c}}^2}{4(\omega-\omega_{\text{c}})^2 + \delta\omega_{\text{c}}^2} \,. \tag{2.58}$$

For an emitter perfectly aligned with the cavity field on resonance (i.e $\xi = 1$ and $\omega = \omega_{\text{c}}$), the Purcell factor reduces to [85, 112]

$$F_{\text{P}} = 1 + \frac{3}{4\pi^2} \cdot \frac{\mathcal{Q}}{V} \cdot \left(\frac{\lambda_{\text{c}}}{n}\right)^3 \,. \tag{2.59}$$

For an emitter located at position $\vec{r} = \vec{r}_0$, the effective mode volume $V$ can be calculated

according to [81, 85, 123, 124]

$$V = \frac{\int_V \epsilon_0 \epsilon_{\mathrm{R}}(\vec{r}) \left|\vec{E}_{\mathrm{vac}}(\vec{r})\right|^2 \mathrm{d}^3\vec{r}}{\epsilon_0 \epsilon_{\mathrm{R}}(\vec{r}_0) \left|\vec{E}_{\mathrm{vac}}(\vec{r}_0)\right|^2} . \tag{2.60}$$

In section 2.1.3 the emitter-cavity coupling strength $g$ and the decay rates $\kappa$ and $\gamma$ were introduced. Using the definitions [30, 112]

$$g = \frac{\mu_{\mathrm{eg}} E_{\mathrm{vac}}}{\hbar} = \sqrt{\frac{\mu_{\mathrm{eg}}^2 \omega}{2\hbar\epsilon_o \epsilon_{\mathrm{R}} V}} \tag{2.61}$$

$$\kappa = \delta\omega_{\mathrm{c}} = \frac{\omega_{\mathrm{c}}}{\mathcal{Q}} = \frac{\pi c}{L\mathcal{F}} \tag{2.62}$$

$$\gamma = \Gamma_0 = \frac{\mu_{\mathrm{eg}}^2 \omega^3}{3\pi\hbar\epsilon_0\epsilon_{\mathrm{R}}} \cdot \left(\frac{c}{n}\right)^{-3} , \tag{2.63}$$

the Purcell factor can be expressed as

$$F_{\mathrm{P}} = 1 + \frac{4g^2\kappa}{\left(\kappa^2 + 4(\omega - \omega_c^2)\right)\gamma} , \tag{2.64}$$

which, for zero detuning, reduces to

$$F_{\mathrm{P}} = 1 + \frac{4g^2}{\kappa\gamma} . \tag{2.65}$$

From Eq. 2.46, the Purcell factor can be expressed in terms of the cooperativity parameter [*]: $F_{\mathrm{P}} = 1 + \mathcal{C}$ [125].

The Purcell effect depends solely on the cavity parameters, not on the properties of the emitter itself. From Eq. 2.59, it is evident that a cavity with a high $\mathcal{Q}$-factor and a small mode volume is essential in order to achieve a high Purcell factor. For short cavities, $w \approx w_0$ (Eq. 2.14 and Eq. 2.15) the mode volume can be approximated by [85, 126]

$$V = \frac{\pi w_0^2 L_{\mathrm{cav}}}{4} . \tag{2.66}$$

[*] Using the alternative definition of the cooperativity, $\mathcal{C} = \frac{2g^2}{\kappa\gamma}$, one find $F_{\mathrm{P}} = 1 + 2\mathcal{C}$.

Using this expression for $V$ and $\mathcal{Q} = \frac{2L_{\text{cav}}\mathcal{F}}{\lambda/n}$ (Eq. 2.24), Eq. 2.59 can be written as

$$F_{\text{P}} = 1 + \underbrace{\frac{3}{2\pi}\frac{\lambda^2}{n}}_{\sigma_{\text{abs}}} \cdot \underbrace{\frac{\mathcal{F}}{\pi}}_{\substack{\#\text{ of} \\ \text{roundtrips}}} \cdot \underbrace{\frac{1}{\pi w_0^2/4}}_{\text{beam area}} , \tag{2.67}$$

where $\sigma_{\text{abs}}$ is the absorption cross-section of the emitter [30, 85]. Intuitively, the cavity increases the effective absorption cross-section of the emitter, consequently increasing the light-matter interaction [30].

Finally, the ratio of photons emitted into the cavity mode to the number of photons emitted into all modes, the so-called $\beta$-factor, is given by

$$\beta = \frac{\Gamma_{\text{cav}}}{\Gamma_{\text{cav}} + \Gamma_0} . \tag{2.68}$$

From the cavity QED parameters $g, \kappa, \gamma$, $\Gamma_{\text{cav}}$ can be written as

$$\Gamma_{\text{cav}} = \frac{4g^2}{\kappa} , \tag{2.69}$$

from which the $\beta$-factor becomes

$$\beta = \frac{4g^2/\kappa\gamma}{4g^2/\kappa\gamma + 1} . \tag{2.70}$$

Using Eq. 2.65 as the definition for the Purcell factor*, the $\beta$-factor can be expressed as

$$\beta = \frac{F_{\text{P}} - 1}{F_{\text{P}}} . \tag{2.71}$$

For large values of $F_{\text{P}}$, $\beta \to 1$, meaning that photons are preferentially emitted into the cavity mode, coining the term "*one-dimensional atoms*" [127].

## 2.2 The Nitrogen-Vacancy Centre in Diamond

Diamond is a wide-bandgap semiconductor with a range of interesting physical properties. The high thermal conductivity and extreme hardness make diamond an attractive material for industrial applications, ranging from heat management in high-power electronics to drill bits for the petroleum industry. Furthermore, diamond is also an at-

*Using the alternative definition for the Purcell factor, $F_{\text{P}} = \frac{4g^2}{\kappa\gamma}$, the $\beta$-factor reduces to the perhaps more familiar $\beta = \frac{F_{\text{P}}}{F_{\text{P}}+1}$ [102].

tractive material for applications in quantum technology [128, 129]. The wide bandgap of 5.5 eV renders diamond transparent from infrared to the ultraviolet part of the spectrum [130–132]. The wide transparency window combined with the possibility of chemical synthesis of a near spin-free lattice [133] makes diamond a prominent solid-state host material for optically active qubits [134–136]. In other words, diamond has more interesting properties than its use in engagement rings.

The diamond lattice hosts a variety of optically active defect centres [130, 137, 138]. Arguably the most prominent and most studied defect centre is the nitrogen-vacancy (NV) centre. As the name suggests, the NV centre consists of a substitutional nitrogen atom and an adjacent vacant lattice site (see Fig. 2.5). The five unpaired electrons associated with the surrounding atoms (three from carbon and two from nitrogen) form the neutrally charged NV centre, $NV^0$ [130]. A sixth electron can be captured from a nearby donor, leading to the formation of the negatively charged NV centre, $NV^-$ [139–142]. Of the two charge states*, $NV^-$ has the more interesting physical properties [36], and has thus become the victim of extensive research, while $NV^0$ on the other hand, have largely been left alone [37, 145]. However, during optical pumping, undesirable charge conversion from $NV^-$ to $NV^0$ may occur, resulting in a "dark" state [146, 147], thereby (potentially) requiring the use of charge state initialisation protocols [148]. Therefore, an understanding of the spin- and orbital dynamics of the neutral charge state may provide physical insight into this undesired charge conversion [145, 149]. In this work, the $NV^-$ was the main focus. Therefore, for the remainder of this thesis, the phrase "NV centre" will be referring to the negative charge state ($NV^-$), unless explicitly stated otherwise.

Owing to its highly coherent electron spin, the NV centre has attracted attention as a promising workhorse in emerging quantum technologies, such as quantum sensing [11, 150–154], quantum computation [129] and quantum communication [73]. In the following sections, the key physical properties of the NV centre will be introduced.

### 2.2.1 Formation of NV Centres

Two ingredients are needed to form an NV centre; a nitrogen atom and a lattice vacancy. In general, diamonds are classified by the concentration of residual nitrogen. For diamonds with a high concentration of nitrogen, vacancies can be introduced into the diamond by irradiation with high energy particles such as electrons, neutrons or ions [155–158]. During a thermal annealing process ($T \gtrsim 800°C$), these vacancies be-

*By careful surface treatment, the stabilisation of a positive charge state, $NV^+$, has been demonstrated [143]. Hydrogen termination of the surface creates a two-dimensional hole gas at the surface, thus changing the Fermi level inside the diamond, consequently favouring the positive charge state [144].

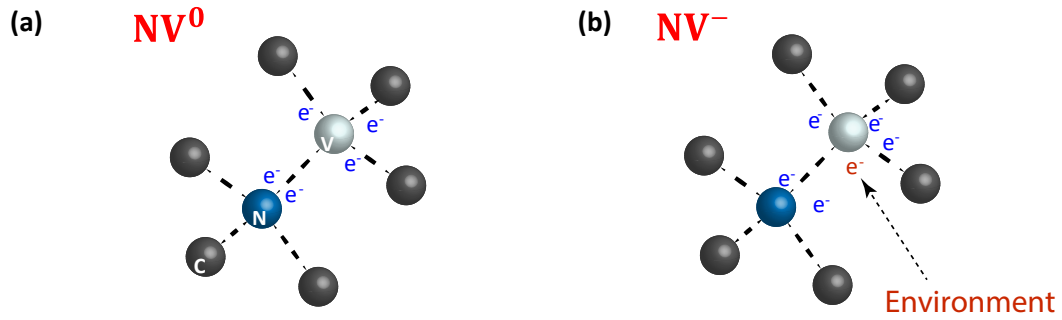


Fig. 2.5. Electron configuration for the two charge states of the NV centre. **(a)** The neutral charge state $NV^0$ consists of 5 electrons: the substitutional nitrogen atom contributes with two unpaired electrons while the three carbon atoms surrounding the vacancy each contribute with one electron. **(b)** Capturing one electron from the environment leads to the formation of the negatively charged NV centre, $NV^-$.

come mobile and diffuse around inside the crystal [159]. During this diffusion process, the vacancy can combine with a native nitrogen atom, forming an NV centre. However, electric and magnetic noise from impurity atoms (mainly nitrogen) limits the spin- and optical properties of the NV centre [133]. Therefore, a high-quality diamond with a low concentration of native nitrogen is favourable for many quantum applications.

The growth of artificial diamonds using plasma-enhanced chemical vapour deposition (PE-CVD) allows for precise control over the dopant concentration. In CVD grown diamond, increased spin coherence times [160] and lifetime-limited optical linewidth [161] have been observed. In ultra-pure diamond, the spin coherence time is now limited by the nuclear spins of surrounding $^{13}C$ isotopes (natural abundance of $\sim 1.1\%$). Using isotropically enriched starting material, the abundance of $^{13}C$ can be reduced, further increasing the spin coherence times [134]. However, $^{13}C$ is not only a source of noise, the nuclear spin can also be harnessed as a quantum memory with storage time close to a minute [68, 69].

In application, such as photonic cavities [77, 81] or in all-diamond scanning probes [152], precise control over the lateral- and vertical positions of the NV centres are required [162]. In a high-purity diamond, the nitrogen concentration is low and hence deterministic fabrication is challenging. A way to remedy this problem is to introduce nitrogen via $\delta$-doping, where nitrogen is introduced during the growth process [132]. The depth of the NV centres is then controlled by the duration of the subsequent overgrowth. After growth, vacancies can be introduced via irradiation, where the use of a transmission electron microscope offers high spatial resolution [163].

Alternatively, nitrogen can be introduced into the diamond post-growth via nitrogen ion implantation [164]. In this process, the implanted ions serve both as a source of

nitrogen and as a means to create vacancies. During the subsequent annealing process, the vacancies become mobile and can form NV centres with either implanted- or the native nitrogen ions. In principle, spatial resolution can be achieved by masking and using focused ion-beam with implantation energy appropriate for the target depth [165, 166]. However, the implanted ions lose energy in collisions with electrons and atomic nuclei inside the lattice [167], potentially leaving a trail of damage along the trajectory [168], where the biggest damage is done around the stopping point of the ion [169]. Furthermore, collisions with nuclei lead to deviations from the designed path, reducing the spatial accuracy. This effect, known as "straggling", depends on the kinetic energy of the implanted ions, where higher energy leads to a larger statistical deviation [129, 164, 167].

By only implanting $^{15}$N ions (natural abundance of 0.37 % [170]), two recent studies correlated the optical coherence of the NV centre with the nitrogen isotope [168, 171]. The different nuclear spin of $^{14}$N ($I = 1$) and $^{15}$N ($I = \frac{1}{2}$) leads to NV centres formed by $^{14}$N and $^{15}$N experiencing different hyperfine interaction. Therefore, optically detected magnetic resonance can be used to distinguish $^{14}$NV from $^{15}$NV [170]. In the aforementioned studies, it was found that NV centres created from the implanted $^{15}$N showed much worse optical coherence compared to NV centres created from the native $^{14}$N. These results indicate that ion implantation does leave a trail of hard-to-anneal lattice damage, causing devastating effects on the NV centres. Therefore, a less invasive technique to create deep NV centres is desirable.

Finally, recent experiments have demonstrated the possibility to create vacancies using tightly focused, ultrafast laser pulses [172–179]. The mechanism behind the vacancy creation is not yet crystal clear [180], but the highly non-linear nature of the process confines the lattice damage to within the focal volume of the laser. Laser writing relies on the native nitrogen present in the diamond. By using diamond with a high nitrogen concentration, vacancy creation with a near-unity yield have been demonstrated [173]. In the latter experiment, the thermal anneal was performed using the same pulsed laser and the formation of NV centres was observed by real-time monitoring the fluorescence [173]. Laser writing constitutes a promising method for the deterministic creation of NV centres deep in the diamond, while preserving a pristine crystalline environment [178]. However, the energy required to form vacancies typically exceeds the energy threshold for surface damage [181, 182]. Therefore, at the time of writing, the possibility of creating NV centres directly in thin structures remains a challenge.

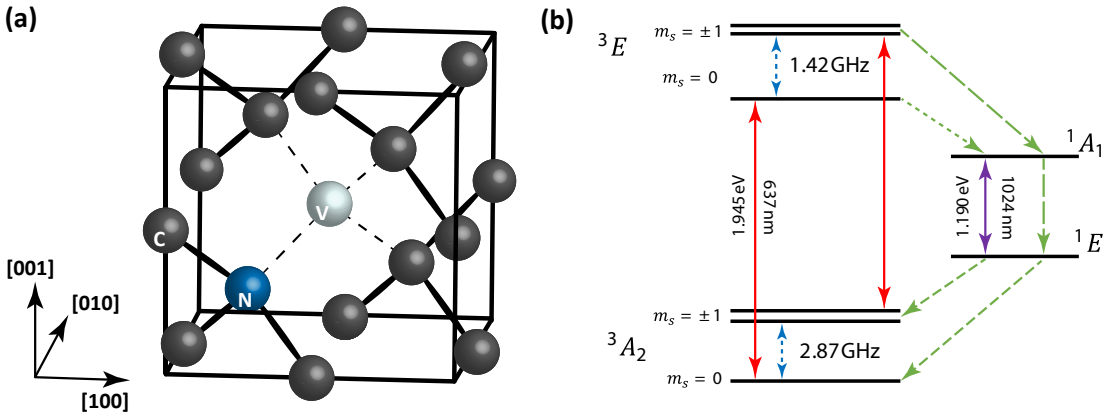


Fig. 2.6. **(a)** Schematic of the nitrogen-vacancy (NV) centre in diamond. The defect centre is formed by replacing two carbon atoms (black) by one substitutional nitrogen atom (blue) and an adjacent lattice vacancy (white). The NV centre possesses $C_{3v}$ symmetry, with symmetry axis along the $\langle 111 \rangle$ crystal axes. **(b)** The (room temperature) electronic structure of the NV centre consists of a spin-triplet ground-state, $^3A_2$, where the $m_s = 0$ and $m_s = \pm 1$ sub-levels are split by 2.87 GHz. The spin-triplet exited state manifold, $^3E$, lies 1.945 eV higher in energy, and is connected to the ground-states via optical transitions with a zero-phonon line at $\lambda_{ZPL} \simeq 637$ nm. There exist two spin-singlet states between the two spin-triplet states. The highest energy singlet state, $^1A_1$, can be populated via an inter-system crossing, predominantly from the $m_s = \pm 1$ sub-level of the $^3E$ state. Decay from the $^1A_1$ to the lower-lying $^1E$ state occurs either optically with a zero-phonon line at 1024 nm (1.190 eV) or via non-radiative transitions. From the long-lived spin-singlet state $^1E_1$ the population decays equally to the $m_s = 0$ and $m_s \pm 1$ sub-levels of $^3A_2$.

### 2.2.2 Electronic Level Structure

The NV centre is a point defect with $C_{3v}$ symmetry, with the symmetry axis lying along the $\langle 111 \rangle$ crystal axes [37], as depicted schematically in Fig. 2.6 (a). In principle, the electronic level structure can be calculated using first principle numerical calculations [183–185]. However, the symmetry of the NV centre enables an accurate description of the electronic level structure based on group theory [186]. The full group theoretic calculations are beyond the scope of this thesis; only the main results are outlined below. For more details, the reader is guided to Ref. [37, 41, 139, 142, 185–190] and references therein.

The (room-temperature) electronic level structure of the NV centre is depicted in Fig. 2.6 (b). From the aforementioned symmetry arguments, one finds that the NV centre ground-state is an orbital singlet state denoted by $^3A_2$. Here, $A_2$ describe the orbital symmetry of the wave function, while the superscript indicates a spin-triplet (S=1), where the sub-levels are labelled $m_s = 0, \pm 1$ [140, 191]. At zero magnetic field, the sub-level $m_s = 0$ and the degenerate states $m_s = \pm 1$ are split by the zero-field

splitting $D = 2.88\,\mathrm{GHz}$, owing to spin-spin interactions [37, 192–194].

The ground-states are connections to the excited-state manifold via optical transitions with an energy difference of $1.945\,\mathrm{eV}$ ($\sim 637\,\mathrm{nm}$) [37]. Based on symmetry arguments one finds that the excited-state is an orbital-doublet spin-triplet state denoted by $^3E$ [37]. Here, the states $E_\mathrm{x}$ and $E_\mathrm{y}$ correspond to $m_\mathrm{s} = 0$, while the states $A_{1,2}$ and $E_{1,2}$ correspond to $m_\mathrm{s} = \pm 1$ [188]. The presence of local strain affects the excited-states more strongly than the ground-states [142, 195]. Strain parallel to the NV axis causes a shift of all energy levels, and thus does not change the wave functions or the corresponding dynamics. On the other hand, strain perpendicular to the NV axis lifts the degeneracy of the orbital states $E_\mathrm{x}$ and $E_\mathrm{y}$ [124, 142, 192, 196]. Turning the argument around, measuring the relative energy spacing between the $E_\mathrm{x}$ and $E_\mathrm{y}$ transitions yield a measurement on the local strain environment. This will be discussed further in Chapter 7.

In addition, there exist two singlet states, $^1A_1$ and $^1E_1$, located between the two spin-triplet states [197, 198]. These singlet states are separated by $1.190\,\mathrm{eV}$ ($1024\,\mathrm{nm}$), with the state $^1E_1$ being the lowest in energy [37]. From the exited state $^3E$, the system can undergo a spin-state dependent inter-system crossing to the singlet state $^1A_1$ [199, 200]. The probability to undergo this inter-system crossing is significantly greater for the $m_\mathrm{s} = \pm 1$ spin state compared to $m_\mathrm{s} = 0$ [198, 201, 202]. Relaxation from $^1A_1$ to $^1E_1$ can occur optically with a zero-phonon line at $1024\,\mathrm{nm}$ or via non-radiative decay channels [197, 198]. From the long-lived $^1E_1$, another inter-system crossing brings the system back to the $^3A_2$ ground-state, with similar decay rates into the $m_\mathrm{s} = 0$ and $m_\mathrm{s} = \pm 1$ spin sub-levels [199]. The presence of the spin-state dependent decay into the meta-stable shelving states plays a crucial role for optical spin-initialisation and spin-readout, as will be discussed further in Section 2.2.5.

At cryogenic temperatures, the fine structure components of the $^3E$ excited-state can be resolved. As shown in Fig. 2.7 (a), each of the excited-state sub-levels can be addressed from the ground-states via spin-conserving optical transitions* [37, 38]. However, at elevated temperatures, phonon transitions between the fine structure sub-levels lead to a rapid averaging over the orbital components, without inducing a spin-flip [32, 202, 203]. As a consequence, the room temperature fine structure of the $^3E$ excited-state exhibit spin-singlet orbital properties (Fig. 2.6 (b)) [32, 37, 203].

As illustrated in Fig. 2.7 (b), the ground- and exited energy levels of the NV centre lies deep inside the bandgap of the diamond [36]. Therefore, the NV centre can be illustrated as a trapped-ion in a crystalline matrix [129, 204]. The NV centre exhibit

*The selection rules can be derived based on group theory. For more details, the reader is directed to Ref. [186] and the supplementary information for Ref. [41].

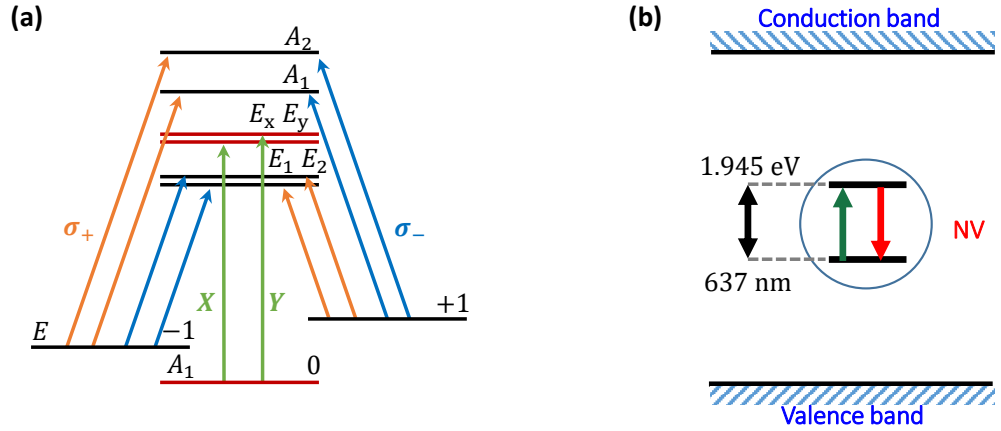


Fig. 2.7. **(a)** Low-temperature electronic level structure of the NV centre, where the spin-conserving optical transitions are indicated. Linearly polarised optical transitions connect the $m_s = 0$ ground-state to the $E_x$, $E_y$ excited-states, while the $m_s = \pm 1$ ground-states are connected to the $E_1$, $E_2$, $A_1$, $A_2$ excited-states via circularly polarised light. **(b)** The ground- and exited state of the NV centre lies deep inside the bandgap of the diamond, allowing the NV centre to be depicted as a single trapped ion.

atom-like properties, including an optically addressable electron spin, which will be discussed further in Section. 2.2.5. However, as will be discussed in Section 2.2.3 and Section 2.2.4, the properties of the host crystal strongly influence the optical properties of the NV centre.

### 2.2.3 Phonon Assisted Optical Transitions

The optical spectrum of the NV centre consists of a sharp zero-phonon line (ZPL) located at $\lambda_{ZPL} \simeq 637\,\text{nm}$ accompanied by a broad phonon sideband (PSB) stretching up to $\lambda \sim 800\,\text{nm}$. The ZPL corresponds to the direct electronic transitions between the $^3E$ excited- and $^3A_2$ ground-state, whereas the PSB originates due to electron-phonon interactions (Fig. 2.8 (a)).

In a simplified model, the electron-phonon interaction can be described by the Huang-Rhys model [205], where the quasi-continuum of vibrational modes are replaced by single vibrational modes [37]. The coordinates of these modes $Q$ are given with the respect to the equilibrium coordinates of the nucleus, where $Q_0 = 0$ is the equilibrium coordinates of the nuclei in the electronic ground-state [187, 206, 207]. In Fig. 2.8 (b), the vibrational modes are described by a quantum harmonic oscillator, where the energy of the vibrational mode $\nu$ is given by $E_\nu = \hbar\omega\left(\nu + \frac{1}{2}\right)$ [37, 187]. The Huang-Rhys theory assumes the two parabolas to be identical apart from a linear shift $\delta Q$ in the minimum of the parabola [185, 187].

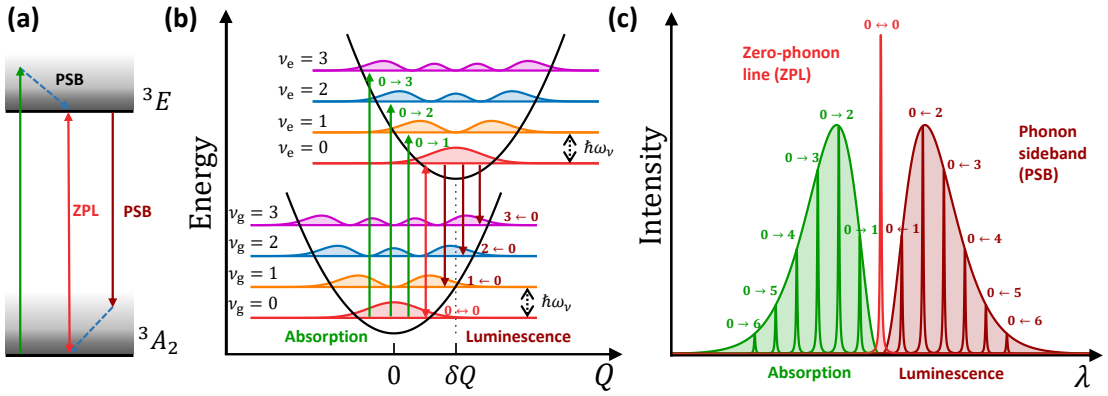


Fig. 2.8. Phonon-assisted optical transitions. **(a)** Energy level scheme including phonon sidebands (PSBs). The zero-phonon line arises from direct transitions between the electronic states $^3A_2$ and $^3E$. Off-resonant excitations of the NV centre are possible via the creations of phonons. Similarly, phonon-assisted emission results in a red-shifted phonon sideband. **(b)** Huang-Rhys model describing the transition probabilities between ground- and excited-states via phonons for a single vibrational mode. The nuclear equilibrium configuration in the excited-state is displaced by $\delta Q$ compared to the ground-state equilibrium configuration. **(c)** The single peaks correspond to optical transitions between the vibronic modes $\nu_g \rightleftharpoons \nu_e$ for a single vibrational mode. The zero-phonon line corresponds to the coupling between the $\nu_e = 0$ and $\nu_g = 0$ states. The envelopes depicting the PSBs arise due to the integration over all possible vibrational modes. Adapted and modified from Ref. [85].

Exciting the NV centre from the $^3A_2$ ground-state to the $^3E$ the excited-stated changes the symmetry of the electronic orbitals. This change in electron orbitals shuffles the charge environment, altering the equilibrium position of the nuclei by $\delta Q$ [37, 208, 209] (Fig. 2.8 (b)). In the Born-Oppenheimer approximation, the dynamics governing electrons and the nuclei can be treated separately, owing to the much larger nuclear mass. Following this approximation, the Franck-Condon principle states that the electronic transitions occur on a time scale much faster than the movement of the surrounding lattice [187, 206].

At room temperature, the thermal phonon population in diamond is low, owing to a high Debye temperature $\Theta_D \simeq 2200\,\mathrm{K}$ [196, 210]. Therefore, an incident photon promotes the NV centre from the vibrational ground-state ($\nu_g = 0$) of the state $^3A_2$ to a vibrationally excited-state $\nu_e$ of $^3E$ with the same relative coordinates (i.e $Q_0$). From there, rapid non-radiative relaxation brings the NV centre to the $^3E$ vibrational ground-state ($\nu_e = 0$), which displaces the nuclei to the new equilibrium coordinates $\delta Q$ [37]. This relaxation occurs via the emission of phonons [207], leading to a blue-shifted phonon sideband in absorption [37].

Due to the difference in equilibrium coordinates ($\delta Q$), the overlap between the vi-

brational occupancies of the two electronic states are non-zero. Therefore, radiative transitions from $\nu_e = 0$ to any of the $\nu_g$ states are allowed, from where phonon emission leads to a rapid relaxation to the $\nu_g = 0$ vibrational state of $^3A_2$. The zero-phonon line arrise from coupling between $\nu_e = 0$ and $\nu_g = 0$ states, while transitions between vibrational states with different occupancy result in red-shited photon emission [37].

In the Huang-Rhys model outlined so far, the vibrational spectrum is described by single vibrational modes. In reality, to accurately describe the transition spectrum, the superposition of all vibrational modes must be considered [32]. Coupling of modes with different occupancy now results in a red-shifted (blue-shifted) continuous phonon sideband in emission (absorption) (Fig. 2.8 (c)). The zero-phonon line is the result of transitions between the $\nu_e = 0$ and $\nu_g = 0$ state for each mode.

The presence of the phonon-sideband carries certain advantages. Efficient off-resonant excitation allows for optical spin initialisation and spin readout. Furthermore, the broad extent of the PSB allows for spectral filtering of the ZPL, while still maintaining an appreciable countrate. Therefore, during resonant excitation of the NV centre, the laser can be suppressed using a narrow-band filter, mitigating the need for dark-field microscopy [211, 212]. On the downside, the Debye-Waller factor $\xi_{\mathrm{ZPL}}$ describing the fraction of photon emitted into the ZPL accounts for only $\sim 3\,\%$ of the total photon emission [81]. Since the photons emitted into the PSB are accompanied by a rapidly dephasing phonon, only the photons emitted into the ZPL are useful for entanglement protocols relying on the quantum interference of indistinguishable photons [79, 213]. However, $\xi_{\mathrm{ZPL}}$ can be enhanced by coupling the ZPL emission to a resonant cavity [77, 81, 214].

### 2.2.4 Resonant Excitation and the Associated Dynamics

Entanglement protocols relying on two-photon quantum interference requires a high degree of single-photon indistinguishability, quantified by the dip in a Hong-Ou-Mandel (HOM) interference experiment [215]. Contrary to trapped atoms or ions, emitters embedded in solid-state materials are strongly influenced by their local environment [216]. In the excited-state, the electron configuration of the NV centre is significantly shifted towards the nitrogen atom, resulting in a permanent electric dipole moment [184, 217–219]. Consequently, the NV centre is highly sensitive to local variations in the strain or charge environment, manifested by inhomogeneous broadening of the ZPL linewidth [188], compromising the observable two-photon interference [79, 80, 213]. The NV centre exhibits an exited state lifetime of $\tau \simeq 12\,\mathrm{ns}$, which translates to a transform-limited linewidth of $\Delta\nu \simeq 13\,\mathrm{MHz}$. However, the measured linewidths are typically an order of magnitude

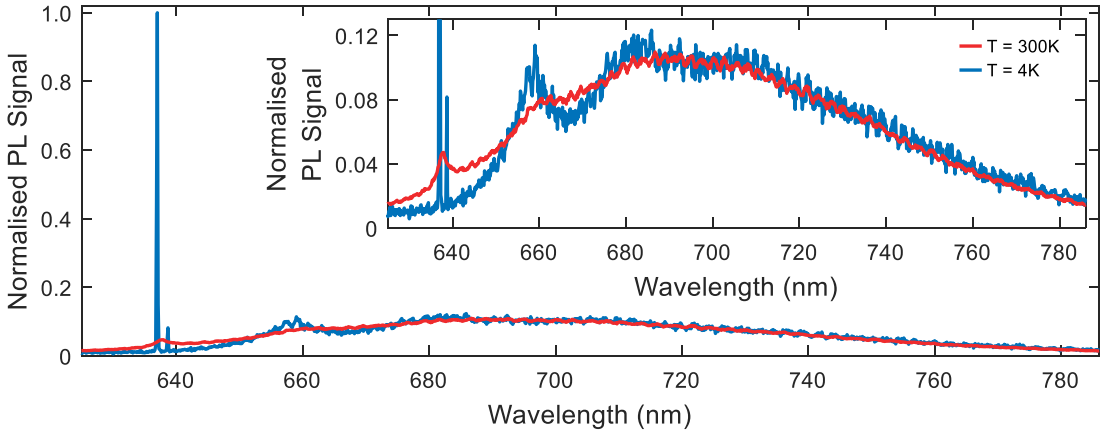


Fig. 2.9. Comparison between photoluminescence spectrum of an NV centre recorded at room temperature (red) and at cryogenic temperature (blue). At 4 K, the PL spectra exhibit a sharp ZPL. The two spectra are normalised by integrating the intensity of the PSB ($\lambda = 680 \cdots 785$ nm).

larger, owing to the mentioned sensitivity to the crystalline environment. Measuring the optical linewidth will be discussed at length in Chapter 7.

At room temperature, the zero-phonon line is broadened to several nanometers due to interactions with thermal phonons [124]. However, at cryogenic temperatures ($T < 10$ K), the width of the zero-phonon line approaches the natural linewidth of 13 MHz [220]. The ZPL linewidth increases rapidly with temperature, following a $T^5$ dependence [221]. This temperature dependence can be explained by phonon induced population transfer between the $E_x$ and $E_y$ transitions (Jahn-Teller effect) [124, 221]. Furthermore, at elevated temperature, the well-defined selection rules for the linearly polarised $E_x$ and $E_y$ breaks down due to phonon interactions [221]. As a consequence, cryogenic temperatures are a requirement for quantum protocols relying on single-photon indistinguishably from NV centres. Fig. 2.9 shows the comparison of the PL spectrum of a single NV centre acquired at room temperature (red) and cryogenic temperature (blue). A significant reduction in the ZPL linewidth is observed at cryogenic temperature.

At cryogenic temperature, the NV centre can be resonantly excited using a laser frequency matching the ZPL transition frequency (Fig. 2.10 (a)). However, the energy splitting between the $^3A_2$ ground-state and the $^3E$ exited state is larger than the energy spacing between the $^3E$ exited state and the conduction band minimum [146]. Therefore, during resonant excitation, there is a probability for an electron to undergo two-photon absorption from $^3A_2$ to the conduction band, where an Auger process further detaches the electron from the defect (Fig. 2.10 (b)) [222]. This ionisation process corresponds to the charge-state conversion from $NV^-$ to $NV^0$ [147, 223].

A similar mechanism can restore the charge-state from $NV^0$ back to $NV^-$. After exciting an electron from the ground- to the exited state of $NV^0$, a second excitation can promote an electron from the valence band into the now vacant $NV^0$ ground-state (Fig. 2.10 (c) - (d)) [222]. Since the energy splitting between the ground- and exited state are larger for $NV^0$ ($\lambda_{\mathrm{ZPL}}^{\mathrm{NV}^0} = 575\,\mathrm{nm}$, $E_{\mathrm{ZPL}}^{\mathrm{NV}^0} = 2.156\,\mathrm{eV}$) compared to $NV^-$ ($\lambda_{\mathrm{ZPL}}^{\mathrm{NV}^-} = 637\,\mathrm{nm}$, $E_{\mathrm{ZPL}}^{\mathrm{NV}^-} = 1.945\,\mathrm{eV}$), the laser frequency used to excite the $NV^-$ is insufficient to excite $NV^0$ (Fig. 2.10 (c)) [147]. Therefore, green light ($\lambda = 532\,\mathrm{nm}$) is often used to restore the charge-state.

However, green illumination comes at a price: the energy provided by the green laser is sufficiently large to excite impurities in the vicinity of the NV centre [224, 225], thereby altering the local charge environment [226]. For example, the ground-state of substitutional nitrogen impurities is found approximately $1.7 \sim 2.2\,\mathrm{eV}$ below the conduction band edge [227]; in other words comparable to the ${}^3A_2 \rightarrow {}^3E$ energy difference. As a consequence, excitation of the NV centre with green light simultaneously leads to photoionisation of nitrogen impurities inside the focal volume of the excitation laser [161]. During this photoionisation process, the impurity is transferred from a neutral to a positive charge state by giving one electron to the conduction band [228].

As mentioned, the permanent electric dipole moment renders the NV centre transition frequency susceptible to changes in the surrounding charge environment on two grounds. First, reconfiguration of the charge environment caused by photoionisation of nearby charge traps shifts the ZPL frequency via the dc Stark effect, leading to the observation of spectral jumps [229, 230]. Observed over time, the random spectral jumps leads to spectral diffusion and inhomogeneous broadening of the ZPL [130, 194, 226, 230]. This inhomogeneous broadening compromises the spectral stability required for two-photon interference protocols [220]. However, resonantly exciting $NV^0$ has been demonstrated to significantly mitigate spectral fluctuations of $NV^-$ on the grounds that resonant excitation requires lower laser power [220, 222].

Second, the sensitivity of the local environment leads to different NV centres having slightly different ZPL frequencies [162], thereby limiting the achievable two-photon interference from spatially separated NV centres. However, the NV centres sensitivity to electric field allows for controllably tuning of the ZPL frequency via the Stark effect [42, 161, 217, 227]. An externally applied electric field affects the NV centre similar to strain (see Section 2.2.2). A longitudinal applied electric field causes an equal, linear shift of all energy levels, while a transverse electric field split the orbitals into two branches, where the energy difference is proportional to the applied electric field [161, 231]. Stark tuning of the relative ZPL frequency of remote NV centres is a key requirement to achiev-

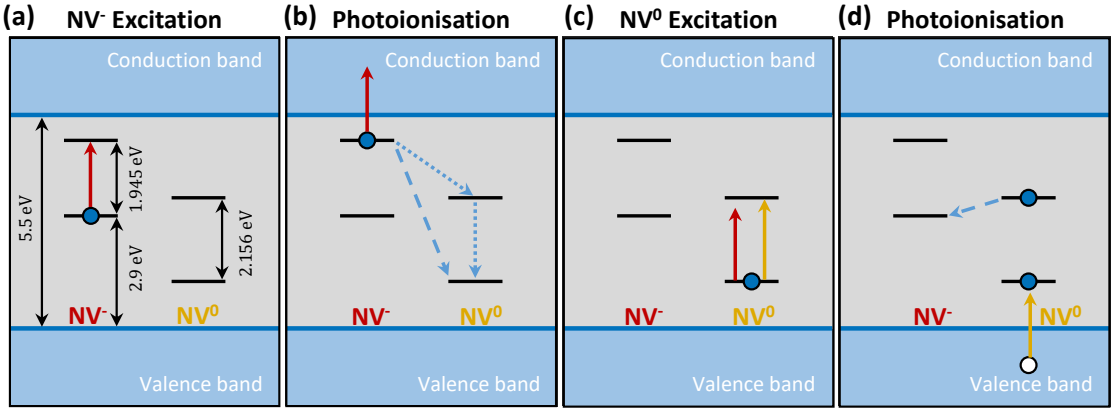


Fig. 2.10. Photoionisation of the NV centre under resonant excitation. **(a)** The $NV^-$ can be excited by the absorption of one red photon. **(b)** When in the excited-state, the absorption of an additional red photon transfers the excited electron to the conduction band, creating $NV^0$. The NV centre ends up in the ground-state of $NV^0$ either directly after the ionisation or via fast decay from the $NV^0$ excited-state. **(c)** Recovery of the negative charge state requires excitation and subsequent ionisation of $NV^0$. A photon resonant with $NV^-$ has insufficient energy to excite $NV^0$. **(d)** A yellow photon resonantly excites $NV^0$. When $NV^0$ is in the excited-state, a second yellow photon can promote an additional electron from the valence band to the ground-state, and thus convert $NV^0$ back to $NV^-$. Photoionisation of $NV^0$ is also possible using off-resonant green light. Adapted and modified from Ref. [147, 235].

able two-photon quantum interference from separated NV centres [80], where electrical contacts on the diamond surface can be used to apply the required electric field [161, 227]. By continuously monitoring the ZPL transition frequency, the spectral fluctuations can be compensated for by the use of a fast feedback loop [217, 231]. Finally, at least in principle, the spectral fluctuations induced by the repump laser can be combated by actively stabilising the charge environment, in a similar fashion to quantum dots [232–234].

### 2.2.5 Optical Spin Initialisation, Manipulation and Readout

Diamond is an excellent host for long-lived spin qubits on at least three grounds. First, the diamond lattice is mostly composed of spinless $^{12}C$ atoms (natural abundance of $\sim 98.9\,\%$) [134], thus suppressing magnetic noise. Furthermore, the concentration of the noisy $^{13}C$ ($I = \frac{1}{2}$) nuclear spins can be further reduced in isotopically purified artificial diamonds, and consequently quenching the hyperfine interaction between the host nuclei and the electron spin [133, 134]. Second, the spin-orbit interaction is weak in diamond [236]. Finally, the strong and short covalent carbon-carbon bonds result in a high Debye temperature ($\Theta_D \simeq 2200\,K$ [196, 210]). As a consequence, the phonon population is low, even at room temperature, thus suppressing spin-lattice relaxation

(long $T_1$) [32, 129].

As mentioned in Section 2.2.2, the NV centre ground-state forms a spin-triplet state ($S = 1$), where the sublevels $m_s = 0$ and $m_s = \pm 1$ can be addressed using microwave fields [36, 162]. Furthermore, fast driving of the electron spin using microwave fields allows for dynamical decoupling sequences, further prolonging the spin coherence time [204]. A detailed discussion of spin control and spin readout techniques is beyond the scope of this thesis; the keen reader is referred to Ref. [62, 129, 162, 191, 204, 237, 238] and references therein. Instead, this section will focus on the possibility of all-optical spin initialisation and readout [38].

The $^3A_2$ ground- and the $^3E$ excited-state manifolds are connected via spin-conserving optical transitions (Fig. 2.7 (a)) [124]. While the two $m_s = 0$ spin-states form excellent cyclic transitions, there is a significant probability to undergo the inter-system crossing (ISC) into the singlet states from the $m_s = \pm 1$ sublevels of $^3E$ (compare Section 2.2.2) [141, 191]. The lifetime of the lowest-lying singlet state ($^1E$) has been experimentally measured to be on the order of several hundred nanoseconds [197, 198]. Therefore, during off-resonant pumping, the ISC leads to shelving of the population, resulting in spin-state dependent rate of photoluminescence [198]. If the initial spin population is in the $m_s = \pm 1$ state, the NV centre will decay into the singlet states after a few optical cycles, and photon emission into the PSB will stop. If however, the initial spin population is in the $m_s = 0$ state, the cycling optical transitions will persist and the photon emission into the PSB will remain constant [238]. To that end, the contrast in photoluminescence constitute a measure on the NV centre spin: bright photoluminescence corresponds to $m_s = 0$ while weak photoluminescence corresponds to $m_s = \pm 1$. Furthermore, continuous off-resonant pumping polarises the spin into the $m_s = 0$ state [195, 239]. The spin-selective ISC depopulates the $m_s = \pm 1$ states and spread the population evenly among all spin states [191, 199].

At room temperature, the spin-state of the NV centre can be read out via spin-to-charge conversion, where the spin-state is mapped onto a charge-state distribution [240, 241]. Illuminating the NV centre with 594 nm will excite $NV^-$, while the neutral charge state remains untouched (compare Section 2.2.4). A second laser pulse at 638 nm can further ionise the excited-state manifold of $NV^-$. If the initial spin state was $m_s = 0$, $NV^-$ will be ionised to $NV^0$ (by the pulse at 594 nm). However, if the initial spin state was $m_s = 1$, the system can decay to the singlet states via the ISC, which is protected from ionisation (by the 638 nm pulse), and the NV centre will remain in the negative charge state. Now the spin-state is mapped onto the charge-state, which can be determined by applying a new 594 nm laser pulse. If photoluminescence is observed,

the charge state must have been $NV^-$ and hence the initial spin-state must have been $m_s = \pm 1$. If no photoluminescence is observed, the charge state must have been $NV^0$ and hence the initial spin-state must have been $m_s = 0$.

At cryogenic temperatures, the individual $E_{x,y}$, $E_{1,2}$ and $A_{1,2}$ transitions can be resolved within the ZPL (Fig. 2.7 (a)) [38, 242]. The $E_{x,y}$ transitions couples the spin-states $m_s = 0$ with orthogonal linearly polarised light, while the $E_{1,2}$ and $A_{1,2}$ transitions connect the $m_s = \pm 1$ spin-states via circularly polarised light [41, 190]. Consequently, a careful choice of polarisation allows for all-optical control of the NV centre spin [38]. Furthermore, spin-selective resonant excitation allows for spin-initialisation and spin-readout with higher fidelity compared to the above-mentioned off-resonant technique [194, 242]. Resonant spin-initialisation is performed by resonantly driving one of the spin transitions continuously. Owing to a slight spin-mixing in the exited state, this driving pumps the spin into the other spin-state [38, 243]. Resonant spin initialisation into the $m_s = 0$ has been demonstrated to reduce the preparation error to 0.3% compared to 11 % for off-resonant initialisation [242]. From the $m_s = 0$ spin state, $\sigma_\pm$ polarised light transfers the spin into the desired $m_s = \pm 1$ state as depicted in Fig. 2.7 (a). The spin state can be read out by resonantly driving the $E_x$, where the presence or absence of photoluminescence corresponds to $m_s = 0$ and $m_s = \pm 1$, respectively [242]. Using the resonant readout scheme, single-shot spin readout with a fidelity of 92.3 % has been experientially demonstrated. Single-shot readout requires sufficiently large countrates to distinguish $m_s = 0$ from the $m_s = \pm 1$ spin projection, requiring the use of solid-immersion lenses [242, 244] or optical cavities [245].

Finally, combining resonant excitation with spin-to-charge conversion allows for high-fidelity ($> 95\,\%$) spin readout [244, 246]. In this scheme, a laser resonant with, say, the $E_x$ transition excites the $m_s = 0$ spin projection, while leaving the $m_s = \pm 1$ projections untouched. A second laser further ionises the exited state, resulting in the conversion to the neutral charge state. The charge state can subsequently be read out using an orange laser ($\lambda = 594\,\text{nm}$), where detected photoluminescence corresponds to $NV^-$, and thus $m_s = \pm 1$ [240]. Alternatively, the charge state can be read out using the resonant red laser, where spin mixing can be combated by continuously applying a microwave field [244].

### 2.2.6 Optically Detected Magnetic Resonance and Magnetic Field Sensing

The NV centre is an excellent magnetic field sensor, offering high spatial resolution even at room temperature [153, 247]. The spin-state dependent optical transitions highlighted in Fig. 2.6 (b) lie at the heart of magnetic field sensing using NV centres. The presence

of an external magnetic field $B$ lifts the degeneracy of the $m_s = \pm 1$ ground-states according to the Zeeman effect [153]. This energy splitting can be calculated according to $\Delta E = 2\gamma_{NV} B_{NV}$, where $\gamma_{NV} = 28\,\mathrm{GHzT}^{-1}$ is the gyromagnetic ratio of the NV centre spin and $B_{NV}$ is the magnetic field projected along the NV axis [153].

Under continuous off-resonant excitation, the NV electron spin will be initialised in the $m_s = 0$ ground-state. From this state, the NV centre undergoes cyclic transitions to the $m_s = 0$ excited-state and back, resulting in a constant rate of photoluminescence predominantly emitted into the PSB (compare Section 2.2.5). Applying an external microwave field can drive the electron spin between the $m_s = 0$ and $m_s = \pm 1$ sub-levels, provided the frequency of the microwave field matches the energy splitting. Under green illumination, the NV can be excited from the $m_s = \pm 1$ ground-state to the excited-state with the same spin projection. From the $m_s = \pm 1$ excited-state, the inter-system crossing brings the NV centre into the singlet state (compare Section 2.2.2), causing a dip in the observed photoluminescence [198]. This technique allows for optically detected magnetic resonance (ODMR) [248].

In the ODMR protocol, continuous green illumination initialises the NV centre spin in the $m_s = 0$ ground-state. Furthermore, an external microwave field with frequency $\omega_{MW}$ can be applied to the NV centre, while continuously recording the photoluminescence. Sweeping the frequency $\omega_{MW}$ into resonance with the $m_s = 0 \rightleftharpoons -1$ will cause a population transfer between these two states. From the aforementioned dynamics, this leads to a dip in the observed photoluminescence [198]. Similarly sweeping $\omega_{MW}$ into resonance with $m_s = 0 \rightleftharpoons +1$ will cause another dip in observed photoluminescence. Analysing the frequency spacing between the dip in photoluminescence caused by the $m_s = 0 \rightleftharpoons -1$ and $m_s = 0 \rightleftharpoons +1$ transitions gives a measure on the magnitude of the magnetic field $B_{NV}$ projected along the NV axis.

In addition to magnetic field sensing, ODMR can be used to resolve the hyperfine interaction between the electron- and nuclear spins. For example, the difference in nuclear spins between $^{14}$N ($I = 1$) and $^{15}$N ($I = \frac{1}{2}$) results in the observation of three and two dips in the ODMR spectra, respectively [170]. Therefore, analysing the ODMR spectra from NV centres allows for distinguishing $^{14}$NV and $^{15}$NV [168, 171] as well as identifying coupling to nearby $^{13}$C nuclei [67, 73, 249] or substitutional nitrogen atoms [250].

## 2.3 Other Colour Centres

The NV centre has attracted attention as a possible qubit in a quantum network, owing to its outstanding spin coherence. However, scalability to more than a few network

nodes is limited by the detection rate of coherent photons [43, 66]. The relatively long radiative lifetime of $\sim 12\,\mathrm{ns}$ combined with a Debye-Waller factor of only $\sim 3\,\%$ limits the achievable flux of coherent photons [77]. In principle, these limitations can be combated by coupling to an optical cavity [81, 84, 251]. However, the fabrication of photonic structures in diamond involves invasive fabrication, prone to deteriorate the optical coherence of the NV centres [81, 82]. As discussed in Section 2.2.4, the permanent electric dipole moment renders the NV centre sensitive to strain- and charge fluctuations in the local environment [216, 217]. A fluctuating charge environment leads to inhomogeneous broadening of the zero-phonon linewidth [188], consequently compromising the achievable two-photon quantum interference [79, 80]. These limitations have motivated the search for new colour centres [32, 219, 252–254]. The following sections will briefly present a selected few of these emerging colour centres. Here, the focus lies on colour centres in diamond and silicon carbide; host materials that are compatible with the Fabry-Perot cavity presented in this thesis [77, 255].

### 2.3.1 Group-IV Split-Vacancies in Diamond

The diamond lattice is known to host a multitude of colour centres [61, 130, 138]. The group-IV split-vacancies in diamond [256–258] have attracted significant attention on the grounds of bright photoluminescence [259, 260], comparatively large Debye-Waller factors [131, 261] and low spectral diffusion [262–264]. Fig. 2.11 shows the different structures of (a) the NV centre and (b) the group-IV defects. Contrary to the nitrogen in the NV centre, the group-IV atoms (Si, Ge, Sn or Pb) are too large to occupy a carbon site [219]. Instead, the defect assumes a split-vacancy configuration along the $\langle 111 \rangle$ crystal direction, where the group-IV atom moves to an interstitial site flanked by a vacancy on either side [265]. The resulting defect possesses $D_{3\mathrm{d}}$ symmetry, where the atom lies at the inversion point [256, 266]. The inversion symmetry of the colour centre carries the important implication that the permanent electric dipole moment is vanishingly small, rendering the defects insensitive to linear Stark shifts [256, 267, 268], thus protecting the ZPL transition frequency against charge fluctuations in the local environment [269].

The electronic configuration of the group-IV split-vacancies consists of 10 electrons: six from the dangling bonds associated with the two vacancies and four electrons associated with the group-IV atom [256]. Similar to the NV centre, the capturing of an electron from the environment leads to the formation of the negatively charged group-IV split-vacancies ($\mathrm{XV}^-$). The resulting electronic level structure is composed of an ${}^2E_{\mathrm{g}}$ ground- and ${}^2E_{\mathrm{u}}$ excited-state [256, 270], as shown schematically in Fig. 2.11 (c). In a low-strain environment, the ground- and excited-states form orbital doublets with degenerate spin

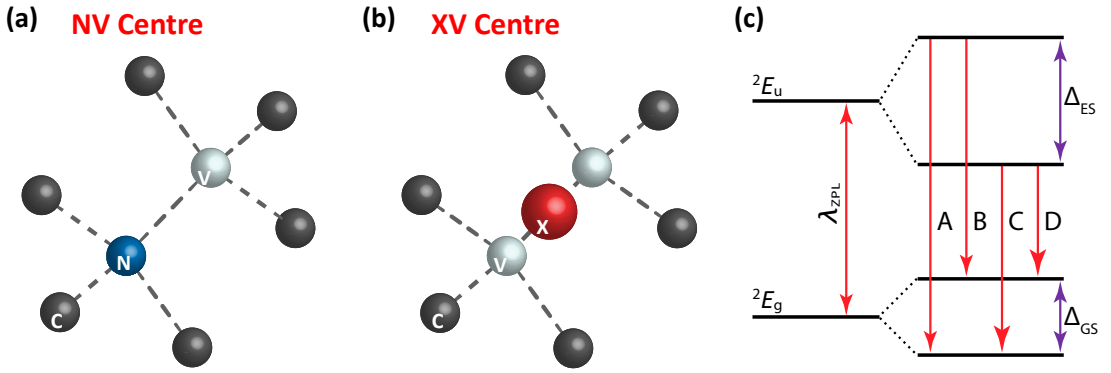


Fig. 2.11. Comparison of the structure of **(a)** the NV centre ($C_{3v}$ symmetry) and **(b)** a group-IV split-vacancy defect, where the atom X is one of the group-IV atoms (Si, Ge, Sn, Pb). The impurity atom is too large to occupy a carbon site, and therefore assumes an interstitial position flanked by two vacancies, resulting in a $D_{3d}$ symmetry. **(c)** The resulting energy structure consists of orbital doublet ground- and excited-states denoted by $^2E_g$ and $^2E_u$, respectively. Spin-orbit interaction and Jahn-Teller effect split the orbital states by $\Delta_{GS}$ and $\Delta_{ES}$, whose magnitude depends on the atomic number of the impurity atom X. Note that the relative spacing of the energy levels is not to scale, $\lambda_{ZPL} \gg \Delta_{GS}, \Delta_{ES}$. Adapted and modified from Ref. [272].

states ($S = \frac{1}{2}$) [194, 271]. A combination of spin-orbit coupling and dynamic Jahn-Teller effect splits the orbital states by $\Delta_{GS}$ and $\Delta_{ES}$ for the ground- and excited-state, respectively [61, 256, 258]. The magnitude of $\Delta_{GS}$ plays a crucial role for the spin-coherence times for the $XV^-$ centres, and is found to increase with the increasing atomic number of the impurity atom [258, 261]. This dependency is attributed to enhanced spin-orbit interaction for the heavier elements [256].

### The Silicon-Vacancy Centre

The silicon-vacancy (SiV) centre is arguably the most studied of the group-IV split-vacancies. Similarly to the NV centre, the SiV centre can be formed during CVD growth [269, 273], by laser writing [274], or by ion implantation [257, 272, 275, 276]. The $SiV^-$ exhibits a sharp ZPL located at $\lambda_{ZPL} = 738\,\text{nm}$ with a radiative lifetime $\tau \simeq 1 - 3\,\text{ns}$, a Debye-Waller factor $\xi_0 \sim 70\,\%$ and a quantum efficiency $\eta_Q \sim 0.1$ [32, 61, 194, 259, 277, 278]. Due to the insensitivity to external fields, SiV centres with narrow optical linewidths have been reported, even in photonic structures [114, 279].

At 4 Kelvin, the spin coherence of the SiV centre is limited to $\sim 100\,\text{ns}$ [280] by the small ground-state splitting of $\Delta_{GS} \sim 48\,\text{GHz}$ [281, 282], caused by phonon scattering between the two orbital branches [258]. Suppression of this phonon interaction is possible

by cooling the sample down to millikelvin temperatures using a dilution refrigerator*, where spin coherence times of $\sim$ 10 ms have been demonstrated [280]. For temperatures $T < 100$ mK, the SiV is polarised into the lowest orbital ground-state. Applying a magnetic field subsequently lifts the degeneracy of the spin-states ($m_s = \pm\frac{1}{2}$), allowing for coherent optical spin control [285–287]. The excellent spin- and optical properties combined with coupling to nearby $^{13}$C memory spins [288, 289] establishes the SiV centre as an unrivalled node-candidate in a quantum network, although only at millikelvin temperatures [114, 286, 290, 291].

For completeness, by careful control of the defect concentration and surface termination of the diamond [270], stabilisation of the neutral charge state, $SiV^0$, has been demonstrated [292]. The neutral SiV possesses a spin $S = 1$ ground-state, with $\lambda_{ZPL} = 946$ nm, a Debye-Waller factor of $\xi_0 \sim 90\,\%$ [269, 293] and lifetime $\tau \simeq 1.3$ ns [292]. Similarly to the NV centre, the ground-state spin $S = 1$ results in a $^3A_{2g}$ ground-state [293]. Contrary to $SiV^-$, the ground-state spin $S = 1$ of $SiV^0$ does not couple strongly to phonons, leading to long spin coherence times ($T_2 \sim 100$ ms) at cryogenic temperatures [32, 257, 292]. Like $SiV^-$, the inversion symmetry renders $SiV^0$ insensitive to charge fluctuations in the environment. The scalability of experiments using $SiV^0$ is limited by the careful Fermi pinning required to stabilise the charge state [292]. For a more extensive review of $SiV^0$, the reader is guided to Ref. [32, 219, 256, 257, 269] and references therein.

### The Germanium-Vacancy Centre in Diamond

The limited spin coherence of the $SiV^-$ motivates the investigation into heavier group-IV vacancy centres. Like the NV and the SiV, germanium-vacancy (GeV) centres can be created either during growth or via ion implantation and subsequent thermal treatment [294, 295]. The GeV exhibits a radiative lifetime of $\tau \simeq 6$ ns, and the PL spectrum shows a ZPL at $\lambda_{ZPL} = 602$ nm accompanied by a phonon sideband [296, 297]. Furthermore, the GeV has a large Debye-Waller factor of $\xi_0 \sim 0.6$ and a quantum efficiency of $\eta_Q \gtrsim 0.4$ [61, 296]. The larger mass of the germanium atom compared to silicon results in an increased ground-state splitting, $\Delta_{GS} = 150 - 172$ GHz, favouring longer spin coherence times [295, 296].

### The Tin-Vacancy Centre in Diamond

The tin-vacancy centre (SnV) can be created by ion implantation, and subsequent thermal treatment [298]. The increasingly large size of the impurity atom leads to more hard-

*Increasing the ground-state splitting $\Delta_{GS}$ is also possible via strain engineering [283, 284].

to-anneal lattice damage, requiring longer annealing steps at higher temperatures [261]. Nevertheless, SnV centres with transform-limited linewidths ($\simeq 30\,\mathrm{MHz}$) have been reported in bulk diamond [260], nanopillars [263] and in waveguides [264]. SnV centres can also be created via shallow ion implantation, and subsequent diamond overgrowth [299]. This latter technique allows for the creation of deep SnV centres, without degradation of the crystalline environment caused by high-energy ion implantation.

The SnV exhibits a radiative lifetime of $\tau \simeq 5 - 6\,\mathrm{ns}$ with a ZPL located at $\lambda_{\mathrm{ZPL}} \simeq 620\,\mathrm{nm}$ [260, 261, 300]. Contrary to SiV and GeV, only the $C$ and $D$ transitions are observable at cryogenic temperatures (see Fig. 2.11 (c)). The thermal population of the upper excited-state increases with temperature, consequently, the A and B transitions can only be observed at elevated temperatures [260]. For SnV, the ground-state splitting, $\Delta_{\mathrm{GS}} \simeq 850\,\mathrm{GHz}$ [263], is a factor of $\sim 17$ larger than for the SiV, potentially allowing for coherent spin control at liquid helium temperatures. The large ground-state splitting, combined with the comparatively large Debye-Waller factor of $\xi_0 \simeq 0.60$ [260] and a large quantum efficiency of $\eta_{\mathrm{Q}} \sim 0.8$ [261], establishes the SnV centre as a promising node candidate in a distributed quantum network [300].

### The Lead-Vacancy Centre in Diamond

Lead is the heaviest stable atom in the periodic table, and the heaviest naturally occurring group-IV element. As for the aforementioned group-IV split-vacancies*, the lead-vacancy (PbV) centres can be formed by ion implantation and subsequent thermal annealing [301, 302]. The large size of the lead ion creates a large number of vacancies, and evidence suggests that large strain is present in the crystal even after thermal treatment [301].

The PbV exhibits an excited-state lifetime of $\tau \gtrsim 3\,\mathrm{ns}$ [302] with a ZPL centred around $\lambda_{\mathrm{ZPL}} \simeq 520\,\mathrm{nm}$ [301]. At the time of writing, the PbV is still in its infancy: the Debye-Waller factor and the quantum efficiency remain to be measured [61]. Similarly to the SnV, only the $C$ and $D$ transitions are observable at cryogenic temperatures. Finally, owing to the large atomic number of lead, the PbV centre exhibits a large ground-state splitting of $\Delta_{\mathrm{GS}} = 4.2 - 5.7\,\mathrm{THz}$, potentially offering ideal conditions for long spin coherence times [301, 302]. With the prospects of long spin coherence combined with the inversion symmetry, the PbV centre has potential as a leading node candidate in a quantum network.

*First-principle calculations predicts a split-vacancy configuration for the PbV [256, 301]. However, at the time of writing, the configuration is yet to be experimentally verified [61].

### Summary and Comparison

To summarise, the group-IV split-vacancies possess mirror symmetry (Fig. 2.11 (b)) and are consequently less susceptible to spectral wandering. Furthermore, the symmetry results in an increased Debye-Waller factor compared to the NV centre. The spin coherence of the group-IV split-vacancies is limited by the ground-state spin splitting $\Delta_{\mathrm{GS}}$. The spin coherence can be extended by either cooling down to millikelvin temperatures in a dilution refrigerator, or by strain engineering [262, 283]. Furthermore, increasing the size of the impurity atom increases $\Delta_{\mathrm{GS}}$ on the ground of a larger spin-orbit interaction [258]. Table. 2.1 summarises and compares the key physical properties of the defect centres discussed above.

Table 2.1. Summary and comparison of the key properties of the NV centre and the group-IV split-vacancies in diamond.

| Colour Centre | $\lambda_{\mathrm{ZPL}}$ | Debye-Waller Factor | Lifetime | Quantum Efficiency | $\Delta_{\mathrm{GS}}$ | $\Theta = \frac{\hbar\Delta_{\mathrm{GS}}}{k_{\mathrm{B}}}$ |
|---|---|---|---|---|---|---|
| $NV^-$ | 637 nm | 0.03 | $\simeq 12$ ns | 0.7 [130] | N/A | N/A |
| $SiV^-$ | 738 nm | 0.7 | $\simeq 1-3$ ns | 0.1 | $\sim 48$ GHz | 2.3 K |
| $SiV^0$ | 946 nm | 0.9 | $\sim 1.3$ ns | – | N/A | N/A |
| $GeV^-$ | 602 nm | 0.6 | $\simeq 6$ ns | $\gtrsim 0.4$ | 150–172 GHz | $7.2-8.3$ K |
| $SnV^-$ | 620 nm | 0.6 | $\simeq 5-6$ ns | $\gtrsim 0.8$ | $\simeq 850$ GHz | $\simeq 41$ K |
| $PbV^-$ | 520 nm | – | $\gtrsim 3$ ns | – | 4.2–5.7 THz | $202-274$ K |

## 2.3.2 Defects in Silicon Carbide

Despite recent advances in synthetic growth of diamond [303–305] and up-scaling of diamond photonics [306], wafer-scale production of artificial diamond remains a great challenge [7, 307, 308]. The limitation in scalability motivates the search for other host materials, exhibiting diamond-like properties such as wide bandgap, low concentration of nuclear spins and a large Debye temperature [32, 140, 309, 310]. All these criteria are satisfied for silicon carbide.

Silicon carbide (SiC) is the offspring of a happy marriage between silicon and diamond*. The SiC structure is composed of silicon and carbon atoms in a hexagonal

*Silicon carbride.

lattice. The different stacking of the hexagons results in numerous polytypes of SiC with different properties and defect centres [32]. SiC, like diamond, is a wide bandgap semiconductor (3-4 eV, depending on the polytype [216, 311]), and the spin-free lattice provides ideal conditions for long-lived spin qubits [311–313]. Furthermore, SiC also inherits important features from silicon [314]: SiC is an established material in the semiconductor industry [39, 315]. The wide bandgap makes SiC attractive for the use in high-power electronics, and wafer-scale growth of SiC is readily available [32]. Controlled doping of SiC allows for the creation of diode structures [311], providing a means to combat spectral diffusion by controlling the charge environment [316].

SiC hosts a variety of optically active defect centres. For an overview, the reader is directed to Ref. [32, 39, 311, 315, 317–319] and references therein. Like in diamond, vacancies in SiC can be created by irradiation of electrons or ions followed by thermal annealing [320], where annealing at different temperatures stabilises different defect centres [316, 318]. Curiously, similarly to the NV centre (compare Section 2.2.1), laser writing of defects in SiC has been demonstrated [321].

One prominent example of a defect centre in SiC is the neutral divacancy, $V_{Si}V_C$, composed of adjacent silicon and carbon vacancies [319]. The $V_{Si}V_C$ is a six electron complex with $C_{3v}$ symmetry and spin $S = 1$, consequently exhibiting similar optical- and electronic properties to the NV centre (compare Section 2.2.2) [311, 322]. The $V_{Si}V_C$ has a comparable excited-state lifetime to the NV centre [323] and a slightly larger Debye-Waller factor of $\xi_0 \sim 0.05 - 0.1$ depending on the polytype of SiC [311, 318, 319]. The key advantage of $V_{Si}V_C$ compared to the NV centre is the ZPL transmission at $\lambda_{ZPL} \sim 1100\,\text{nm}$, significantly suppressing absorption in optical fibres [311]. Despite the long lifetime and low Debye-Waller factor, embedding $V_{Si}V_C$ in an optical cavity constitutes a promising platform for an efficient spin-photon interface at close-to telecom wavelengths [319, 324].

### 2.3.3 Rare-Earth Ions in Crystalline

A final class of emitters to be (very briefly) discussed are rare-earth ions* in crystalline hosts†. For these ions, the optical transitions occur between the partially filled $4f$ shells, shielded from the environment by the outer shells [325–327]. As a consequence, the rare-earth ions exhibit narrow optical transitions and high spectral stability [34] accompanied by long spin-coherence times [328, 329]. In free-space, the $4f$-$4f$ transitions are parity forbidden. However, interactions with the crystal field allow for weak optical transitions

*The lanthanide.
†See Ref. [325] for a review.

with a long radiative lifetime [325]. Due to the long radiative lifetime and subsequent faint PL [330], addressing single ions have proven to be an outstanding challenge [331]. However, with the use of nanophotonic resonators, control and readout of single ions have been demonstrated [331–333]. An added advantage of erbium ions is the emission in the telecom band, potentially enabling long-distance quantum-communication without the need of frequency conversion [101, 330].

## 2.4 Raman Scattering

In 1928, using focused sun rays and colour filters, the Indian physicist Sir Chandrasekhara Venkata Raman investigated the scattering of light from various liquids and vapours [334]. In addition to scattering of light with the same frequency as the incident light (*unmodified scattering*), Raman discovered that a small portion of the scattered light was of a different frequency (*modified scattering*). Contrary to photoluminescence, the frequency of the scattered light $\nu$ was found to be directly related to the frequency of the incident light $\nu_{\mathrm{i}}$, i.e $\nu = \nu_{\mathrm{i}} \pm \nu_{\mathrm{R}}$, where $\nu_{\mathrm{R}}$ is a material-dependent constant [335]. Raman was awarded the 1930 Nobel Prize in Physics "*for his work on the scattering of light and for the discovery of the effect named after him*" [336].

More formally, Raman scattering is the inelastic scattering of light via the creation (Stokes) or annihilation (Anti-Stokes) of an optical phonon [337]. The first-order Raman (Stokes) scattering process can be modelled by a three-level atom-like system (Fig. 2.12 (a)) involving a ground-state $|1\rangle$, a virtual excited state $|2\rangle$ and a meta-stable state $|3\rangle$. In a single particle picture, the ground-state population can be excited to $|2\rangle$ by absorbing an incoming photon with energy $\hbar\omega_1$. The excited-state population can decay either directly down to $|1\rangle$ by emitting a photon with energy $\hbar\omega_1$ (elastic Rayleigh scattering, Fig. 2.12 (b)), or via $|3\rangle$ by emitting a red-shifted photon with energy $\hbar\omega_2$ accompanied by an optical phonon of fixed energy $\hbar\Omega$ (Stokes scattering). Conservation of energy requires $\omega_1 = \omega_2 + \Omega$.

Anti-Stokes scattering is the reverse process, where the ground-state population is excited to state $|2\rangle$ via $|3\rangle$ by the absorption of an optical phonon with energy $\hbar\Omega$ and an incoming photon with energy $\hbar\omega_2$. The population then relaxes down to state $|1\rangle$ by emitting a blue-shifted photon with energy $\hbar\omega_1$ (Fig. 2.12 (c)). However, as anti-Stokes scattering requires the presence of phonons in the material; the anti-Stokes scattering probability is highly temperature dependent, and decreases with decreasing temperature [206]. Consequently, comparing the intensity of the Stokes peak ($I_S$) to that of the anti-Stokes peak ($I_{AS}$) yields a non-contact measurement of the sample temperature

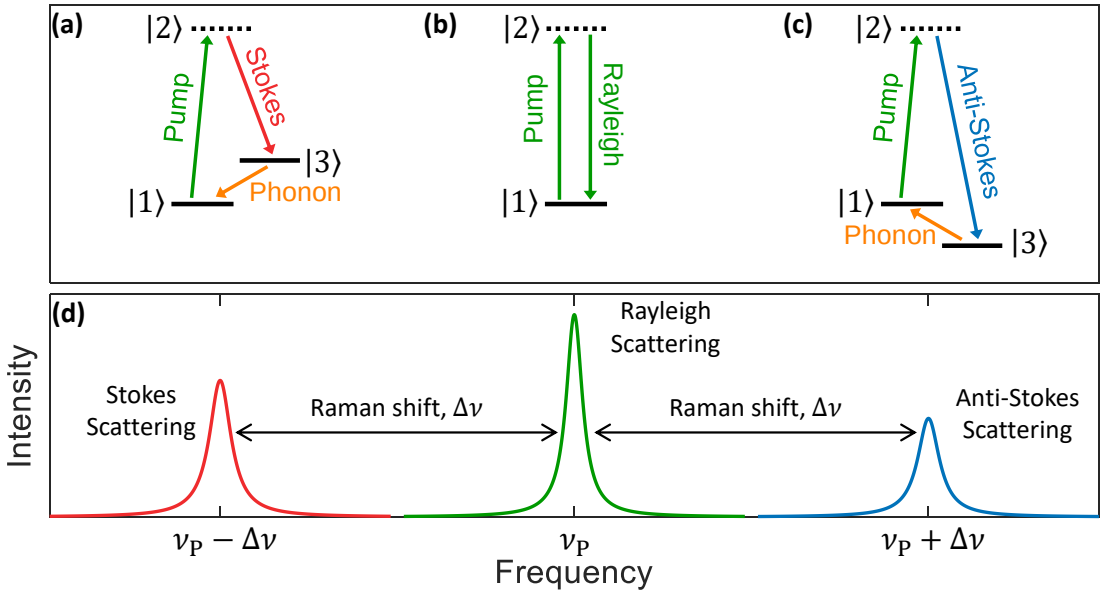


Fig. 2.12. **(a)** Schematic of Stokes scattering, where a pump photon is converted into a red-shifted Stokes photon and a phonon of fixed frequency. **(b)** Schematic of the elastic Rayleigh scattering process. **(c)** Schematic of the anti-Stokes process where a pump photon is converted into a blue-shifted anti-Stokes photon via the absorption of a phonon. **(d)** Idealised spectrum of the Raman process, showing the red- and blue-shifted Stokes and anti-Stokes peaks, respectively. Both peaks are shifted by the amount $\Delta\nu$ compared to the Rayleigh peak at $\nu_{\mathrm{P}}$. The relative intensities are not to scale.

according to [338, 339]

$$\frac{I_{AS}}{I_S} \propto \exp\left(\frac{\hbar\Omega}{k_b T}\right), \tag{2.72}$$

where $\Omega$ is the phonon energy and $k_B$ is the Boltzmann constant.

Another, perhaps, more intuitive picture of Raman scattering can be obtained by considering the effect on the crystal polarisability as a function of vibrational motions caused by the incident light [340]. To first order, the induced polarisation $\vec{P}$ in a material is given by

$$\vec{P} = \bar{\alpha}\vec{E}, \tag{2.73}$$

where $\bar{\alpha}$ is the polarisability tensor and $\vec{E}_i$ is the electric field of the incident light. The incident light can excite vibrational modes in the crystal, causing a time-dependent modulation of the polarisability tensor with the vibrational frequency $\omega_\nu$ [341]. Intuitively, this modulation can be pictured as a change in the local position of the atoms with time.

Including the vibrational modes, the polarisability tensor can be expressed by

$$\bar{\alpha} = \bar{\alpha}_0 + \Delta\bar{\alpha}\cos(\omega_\nu t), \tag{2.74}$$

where $\bar{\alpha}_0$ is the polarisability in the absence of any vibrations and $\Delta\bar{\alpha}$ describes the modification of the polarisability due to the vibrations at frequency $\omega_\nu$. For a monochromatic light source, the electric field is given by

$$\vec{E}_i = \vec{E}_0\cos(\omega t)\,. \tag{2.75}$$

Thus, inserting Eq. 2.75 and Eq. 2.74 in Eq. 2.73 gives

$$\begin{aligned}\vec{P} &= \left[\bar{\alpha}_0 + \Delta\bar{\alpha}\cos(\omega_\nu t)\right]\cdot\vec{E}_0\cos(\omega t)\\ \vec{P} &= \bar{\alpha}_0\vec{E}_0\cos(\omega t) + \frac{\Delta\bar{\alpha}\vec{E}_0}{2}\cdot\left[\cos\left((\omega-\omega_\nu)\cdot t\right) + \cos\left((\omega+\omega_\nu)\cdot t\right)\right],\end{aligned} \tag{2.76}$$

where the term oscillating with $\cos(\omega t)$ corresponds to the Rayleigh (elastic) scattering, while the terms $\cos\left((\omega-\omega_\nu)\cdot t\right)$ and $\cos\left((\omega+\omega_\nu)\cdot t\right)$ correspond to Stokes and anti-Stokes scattering, respectively [342]. A graphical illustration of Eq. 2.76 is shown in Fig. 2.12 (d), where the Stokes (red) and anti-Stokes (blue) components appear as red- and blue-shifted sideband of the Rayleigh peak (green). Note that the relative intensities are not to scale.

### 2.4.1 Phonons in Diamond

The crystal structure of diamond is constructed from two interpenetrating face-centred cubic (FCC) lattices (Fig. 2.13), where the second FCC lattice is shifted by $\frac{a}{4}$ in all directions, and $a = 3.567\,\text{Å}$ is the lattice constant [342, 343]. Visible photons carry only a small wave vector $k$ and can thus only interact with optical phonons with $k \sim 0$ close to the Brillouin zone centre ($\Gamma$ point). In diamond, the dispersion of the longitudinal and the two vibrational modes converge at a frequency of $\sim 40\,\text{THz}$ [344–346]. As a consequence, the resulting Raman spectrum consists of a triply-degenerate vibrational mode along the $\langle 111\rangle$ crystal axes [344, 347, 348]. This vibration corresponds to the relative movement of the two FCC lattices in opposite directions (see Fig. 2.13) [343, 344, 349, 350]. The Raman frequency of $\Omega \sim 40\,\text{THz}$ corresponds to a spectral shift of $\delta\bar{\nu} = 1332\,\text{cm}^{-1}$ [344].

The short carbon-carbon bonds render diamond a hard and stiff material, resulting in the high-frequency phonon mode discussed above [32]. Furthermore, the high Debye

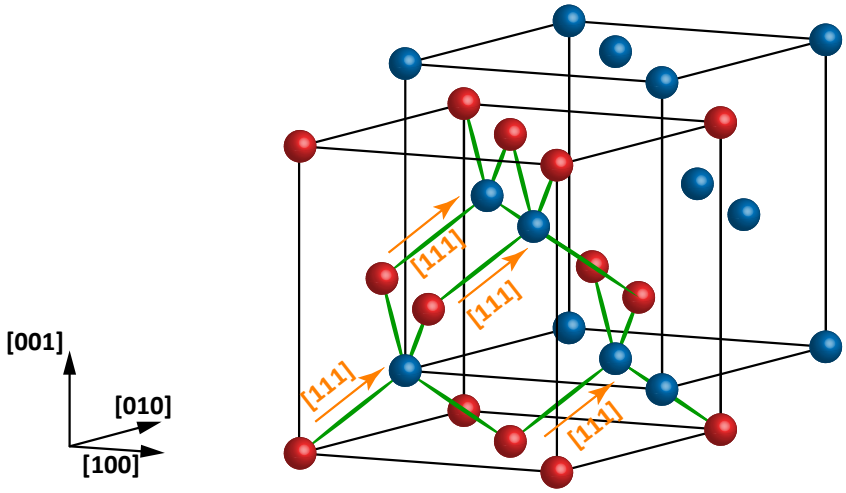


Fig. 2.13. The diamond lattice is constructed from two interpenetrating FCC lattices. In diamond, the Raman vibrational mode occurs along the ⟨111⟩ crystal axes, corresponding to the relative motion of the two FCC lattices in opposite directions. Adapted and modified from Ref. [344].

temperature of diamond ($\Theta_D \simeq 2200\,K$ [196, 210]) translates to a low population of thermal phonons, even at room temperature, making diamond an attractive platform for quantum information processing using phonons. For example, Raman scattering on diamond has used to demonstrate non-classical Stokes–anti-Stokes correlation [351–355], quantum teleportation [356] and entanglement of macroscopic objects [357, 358].

### 2.4.2 Quantum Memory using Phonons in Diamond

In recent years, optical phonons in bulk diamond have emerged as a compelling platform to store and retrieve quantum information [349, 359]. The working principle of a phononic quantum memory is depicted schematically in Fig. 2.14. Here, single photons can be mapped onto phonons via Raman scattering, where the detection of a Stokes photon heralds the creation of an optical phonon, thus confirming the storage of the photon. The quantum information associated with the single photon can subsequently be retrieved via anti-Stokes scattering [350, 360]. The high carrier frequency of the optical phonon ($\Omega \sim 40\,THz$), allows for broadband storage. Furthermore, the high Debye temperature and the wide bandgap allow for room-temperature operation across a broad range of optical frequencies [350, 361].

In high-purity bulk diamond, the dominant decay mechanism of the phonon population is via the Klemens channel [362], where one optical phonon decays into two acoustic phonons with opposite momentum [349, 361]. The lifetime of the optical phonon is

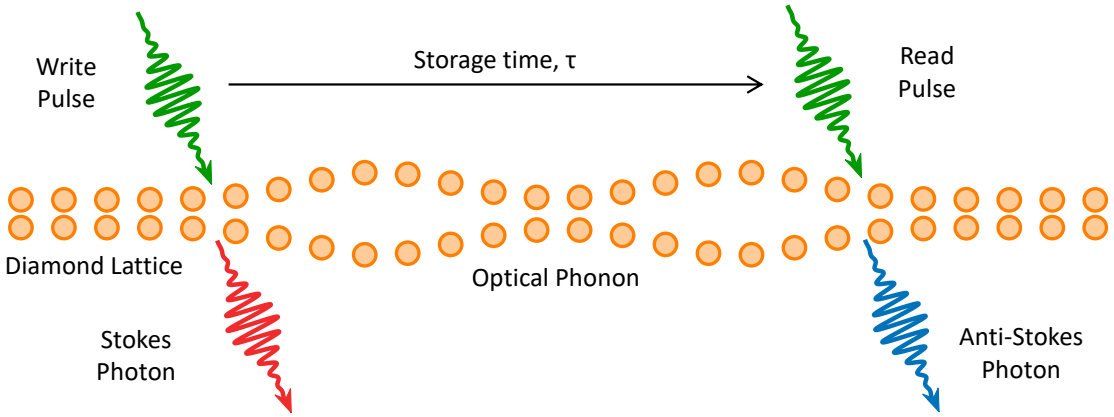


Fig. 2.14. Schematic of a quantum memory based on optical phonons. A photon from the write pulse is mapped onto an optical phonon via Stokes scattering. The stored phonon can subsequently be retrieved using a read via the anti-Stokes process. Adapted and modified from Ref. [349].

$\sim 3.6\,\mathrm{ps}$ [350, 351, 353] which ultimately sets a limit on the achievable storage time [349]. While this storage time is too short for quantum communication protocols connecting remote nodes, the storage time might be sufficient for on-chip processing of quantum information. However, in an engineered diamond lattice constructed from alternating $^{12}$C and $^{13}$C, it is possible, at least in principle, to construct a phononic bandgap to quench the Klemens channel and thus prolonging the lifetime of the optical phonons and extend the storage times [350, 363].

The readout efficiency of the quantum memory hinges on the detection of an anti-Stokes photon. As mention, the anti-Stokes is inherently a weak process. However, the detection efficiency of an anti-Stokes photon can be enhanced by coupling the diamond to waveguides or photonic resonators [355].

### 2.4.3 Cavity-Enhanced Raman Scattering and Raman Lasing

The intrinsically weak nature of the Raman process can be greatly enhanced by coupling to photonic resonators via the Purcell effect (compare Section 2.1.4). Cavity-enhanced Raman scattering has been demonstrated from atmospheric gasses [364, 365] and various solid-state system [366] including, carbon nanotubes [367, 368], silicon [369, 370] and silica [371]. In the previous section, resonant enhancement of the anti-Stokes process was discussed as a potential route towards efficient readout of phononic quantum memories in diamond [355]. This section focuses on resonant enhancement of the Stokes transition to create low-threshold Raman lasers.

A Raman laser works by down-shifting the frequency of a pump laser $\nu_\mathrm{p}$ by an amount

equal to the Raman shift $\delta\bar{\nu}$: the output frequency is given by $\nu_S = \left(\nu_p - c\delta\bar{\nu}\right)$ [337, 344]. The Raman shift is material dependant. Therefore, with a suitable choice of material and pump laser, at least in principle, lasing at any wavelength can be achieved [348, 372]. Contrary to a more conventional laser, where light amplification is established by stimulated emission and population inversion, the amplifier medium of a Raman laser is the material-dependent Raman gain, proportional to the pump intensity $I_P$ and the Raman gain coefficient $g_R$ [348].

Diamond is an attractive material platform for Raman lasers, owing to its unique properties [373]. First, the wide bandgap of diamond ($\sim 5.45\,\mathrm{eV}$) renders the diamond transparent from IR to UV range, allowing for pump wavelengths down to 230 nm [373]. Second, the high thermal conductivity of diamond enabling efficient dissipation of heat, thus allowing for high-power operation [373]. Finally, diamond exhibits a large Raman gain of $\sim 75\,\mathrm{GW}\cdot\mathrm{cm}^{-1}$ for $\lambda = 532\,\mathrm{nm}$. The significance of a large Raman gain is that a relatively small amount of material is required for a low-threshold device [337, 373].

Diamond Raman lasers have been realised across a wide spectrum of wavelengths* [348, 374–378]. A common feature of these lasers is the high pump-powers required. However, the use of resonant microcavities [371, 379–381] constitutes a promising way to reduce the pump threshold drastically [382, 383]. In a microcavity, where both the pump laser and the Raman transition are resonant, the required pump threshold can be reduced on (at least) two ground. First, resonant recirculation of the pump laser increases the Raman gain significantly. Second, the efficiency of stimulated Raman scattering is increased by resonant coupling to the cavity mode. Such a double resonance condition is satisfied provided the Raman shift $\delta\bar{\nu}$ equals an integer $m$ times the free-spectral range of the resonator, i.e.

$$\delta\bar{\nu} = m \cdot \Delta\nu_{\mathrm{FSR}}\,. \tag{2.77}$$

Lasing occurs provided the round-trip gain exceeds the round-trip loss. For a microcavity, the threshold power $P_{\mathrm{th}}$ for bulk Raman gain coefficient $g_R^B$ can be calculated from†

$$P_{\mathrm{th}} = \frac{1}{\eta}\cdot\frac{2n_S n_p \pi^2}{\lambda_S \lambda_p g_R^B}\cdot\frac{V_R\left(\mathcal{Q}_S + \mathcal{Q}_R\right)}{\mathcal{Q}_S^2\mathcal{Q}_P}\,, \tag{2.78}$$

where $\eta$ is the incoupling efficiency, $n_{p(S)}$ is the refractive index at the pump (Stokes) wavelength $\lambda_{p,(S)}$, $\mathcal{Q}_{p,(S)}$ are the cavity $\mathcal{Q}$-factor at the pump (Stokes) wavelength, $\mathcal{Q}_R$ is the quality factor associated with the Raman gain. The Raman mode volume $V_R$ accounts for the spatial and spectral overlap of the pump and Stokes field, and can be

*See Chapter 6.

†The derivation can be found in Appendix H.

calculated according to [370, 384]

$$V_{\mathrm{R}} = \frac{\int_{\mathrm{cav}} n_{\mathrm{p}}^2(\vec{r})|\vec{E}_{\mathrm{p}}(\vec{r})|^2 \mathrm{d}^3 r \cdot \int_{\mathrm{cav}} n_{\mathrm{S}}^2(\vec{r})|\vec{E}_{\mathrm{S}}(\vec{r})|^2 \mathrm{d}^3 r}{\int_{\mathrm{dia}} n_{\mathrm{p}}^2(\vec{r})|\vec{E}_{\mathrm{p}}(\vec{r})|^2 \cdot n_{\mathrm{S}}^2(\vec{r})|\vec{E}_{\mathrm{S}}(\vec{r})|^2 \mathrm{d}^3 r} \,. \tag{2.79}$$

CHAPTER 3

# Hybrid Diamond-Air Cavity - the Coupled Cavity Model

In the experiments performed as part of this thesis, a thin diamond membrane was embedded into a Fabry-Perot microcavity. The presence of the diamond membrane significantly alters the cavity mode structure, leading to the formation of hybridised cavity modes [87]. As a consequence, the theoretical framework presented in Section 2.1.1 is not fully sufficient to capture the full cavity mode-structure. With the aid of one-dimensional transfer-matrix calculations, the physics of the coupled diamond-air cavity will be described in this chapter. Although this chapter uses diamond as an example, the concepts presented here are generic to any solid-state material [61].

## 3.1 The Hard-Mirror Model - Analytic Solution

Before diving into the transfer-matrix simulations, a perfect-world scenario with an analytic solution will be presented. Consider a diamond membrane with thickness $t_\mathrm{d}$ and refractive index $n_\mathrm{d}$ embedded in a Fabry-Perot cavity with perfectly reflecting (i.e hard) mirrors. Let $L$ be the total cavity length, and thus the width of the air-gap is given by $t_\mathrm{a} = L - t_\mathrm{d}$. For this structure, the cavity resonances can be calculated analytically using the transcendental equation [87, 123]

$$(1 + n_\mathrm{d}) \sin\left(\frac{2\pi}{\lambda} \cdot [t_\mathrm{a} + t_\mathrm{d} n_\mathrm{d}]\right) = (1 - n_\mathrm{d}) \sin\left(\frac{2\pi}{\lambda} \cdot [t_\mathrm{a} - t_\mathrm{d} n_\mathrm{d}]\right) , \tag{3.1}$$

where $n_\mathrm{d}$ is the refractive index of diamond.

Fig. 3.1 shows the resulting cavity mode-structure calculated from Eq. 3.1. In an intuitive picture, the mode structure consists of two coupled cavities; one cavity confined to the diamond bounded by the bottom mirror and the diamond-air interface, and one cavity confined to the air-gap bounded by the top mirror and the diamond-air interface. The two cavity modes couple and hybridise, resulting in the emergence of avoided

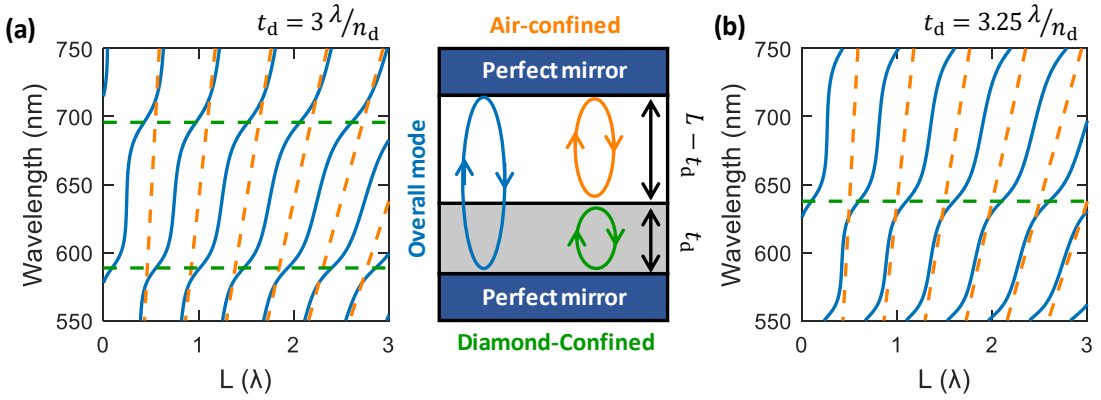


Fig. 3.1. Hard mirror model of the coupled diamond-air cavity. Coupling between the modes confined to air (orange) and diamond (green) results in the emergence of avoided crossings. The mode structure was calculated using Eq. 3.1 with **(a)** $t_d = 3.00 \cdot \frac{\lambda}{n_d}$ and **(b)** $t_d = 3.25 \cdot \frac{\lambda}{n_d}$, where $\lambda = 637.7\,\text{nm}$.

crossings [61]. The location of these avoided crossings depends exclusively on the exact diamond thickness.

A cavity resonance is established provided the overall cavity length is equal to a multiple of $\frac{\lambda}{2}$, i.e $t_d n_d + t_a = j \cdot \frac{\lambda}{2}$. Depending on the diamond thickness, two regimes emerge. If $t_d = (2j-1) \cdot \frac{\lambda}{4}$, the cavity is resonant with the diamond, giving rise to the *diamond-confined* modes [85]. For these modes, a change in $t_a$ will have a relatively small impact on the resonance $\lambda$. In a real-world experiment, the shallow slope, i.e. $\frac{d\lambda}{dt_a}$, renders the cavity "insensitive" to length fluctuations $dt_a$ caused by acoustic vibrations. On the other hand, for $t_d = j \cdot \frac{\lambda}{2}$ the cavity is resonant with the air-gap, thus creating an *air-confined* mode [85]. Contrary to the diamond-confined modes, for the air-confined modes a small change in $t_a$ will have a relatively large impact on the resonant $\lambda$, thus rendering the cavity sensitive to length fluctuations caused by acoustic vibrations [87]. Therefore, in the presence of acoustic vibration, operating in a diamond confined geometry offers higher mechanical stability.

## 3.2 Effective Cavity Length

In the hard-mirror model, perfectly reflecting mirrors were assumed. Although this model gives a good, quantitative explanation of the hybridised mode structure, the model fails to capture the complete picture. Up until this point, the cavity length has been defined as the physical separation between the two end-mirrors. While this is a good approximation for long cavities, for short microcavities the electric field penetration

into the mirror becomes an important effect [94].

Consider a lossless distributed Bragg reflector (DBR) mirror constructed from alternating layers of material with high ($n_{\mathrm{H}}$) and low ($n_{\mathrm{L}}$) index of refraction. The thickness of each layer, $d_{\mathrm{H(L)}}$, is chosen such that $d_{\mathrm{H}} n_{\mathrm{H}} = d_{\mathrm{L}} n_{\mathrm{L}} = \frac{\lambda_{\mathrm{c}}}{4}$, where $\lambda_{\mathrm{c}}$ denotes the centre of the reflective stopband [94]. An incident electromagnetic wave experiences a phase delay $\tau$ upon reflection from the DBR [385]. For a mirror with an infinite amount of layers, the phase delay at the stopband centre $\lambda_{\mathrm{c}}$ can be calculated analytically from [386]

$$\tau = \frac{\lambda_{\mathrm{c}}}{2c} \cdot \frac{1}{n_{\mathrm{H}} - n_{\mathrm{L}}}\,, \tag{3.2}$$

where $c$ is the speed of light. The phase delay can be translated into an effective length, $L_{\mathrm{DBR}} = \frac{c\tau}{2}$, often referred to as the mirror penetration depth: [94].

$$L_{\mathrm{DBR}} = \frac{c\tau}{2} = \frac{\lambda_{\mathrm{c}}}{4} \cdot \frac{1}{n_{\mathrm{H}} - n_{\mathrm{L}}} \tag{3.3}$$

Physically, the penetration depth is the depth inside the mirror at which the optical light seems to be reflected from [386].

The overall effective cavity length is given by the physical separation of the two mirrors, the penetration depth and, for a cavity with curved mirrors, the contributions associated with the Gouy-phase, i.e [85, 94]

$$L_{\mathrm{eff}} = L_{\mathrm{cav}} + L_{\mathrm{Gouy}} + 2L_{\mathrm{DBR}}\,, \tag{3.4}$$

with $L_{\mathrm{cav}} = t_{\mathrm{a}} + \frac{t_{\mathrm{d}}}{n_{\mathrm{d}}}$. Incident light with wavelength detuned from $\lambda_c$ will no longer observe a perfect $\frac{\lambda}{4}$ layer-thickness. As a consequence, light can be reflected back and forth between different layers inside the mirror leading to increased phase delay $\tau$, and thus longer penetration depth and increased mirror transmission. The black lines in Fig. 3.2 show the mirror transmission (a) and the reflected phase delay (b) as a function of excitation frequency *. Note that the reflective stopband appears symmetric in frequency.

Introducing the diamond membrane alters the mirror transmission (Fig. 3.2 (a)) and the phase delay (Fig. 3.2 (b)) differently depending on the exact diamond thickness. If the diamond thickness equals a multiple of $j \cdot \frac{\lambda_{\mathrm{c}}}{n_{\mathrm{d}}}$, constructive interference is maintained for $\lambda = \lambda_{\mathrm{c}}$ rendering the mirror transmission unaltered [85]. From Section 3.1 this corresponds to an air-confined geometry (red lines Fig. 3.2). On the other hand, if the diamond thickness equals a multiple of $(2j-1) \cdot \frac{\lambda_{\mathrm{c}}}{n_{\mathrm{d}}}$, an increase in transmission is ob-

*Motivated by the experiments, high-index terminated DBR mirrors are used here.

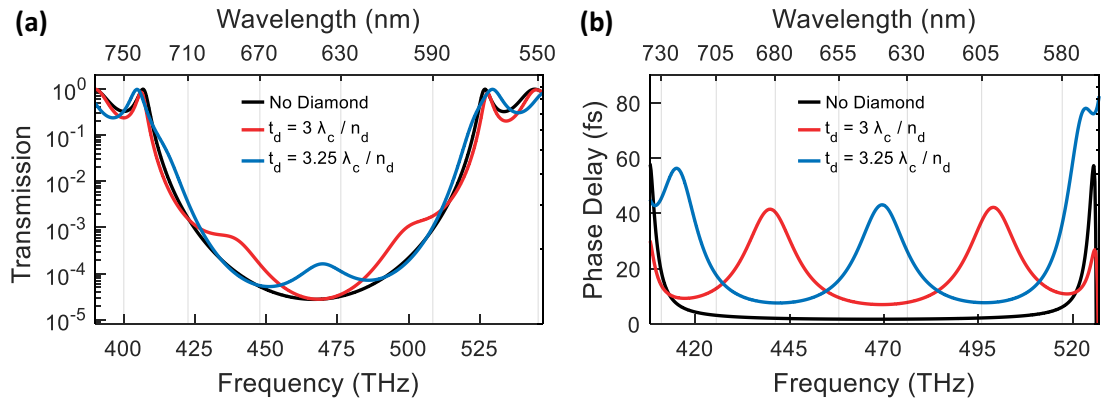


Fig. 3.2. **(a)** The black line shows the mirror transmission across the stopband for a DBR mirror centred at $\lambda_c = 637.7\,\text{nm}$. The presence of the diamond membrane alters the mirror transmission differently depending on the exact diamond thickness. If the diamond thickness equals a multiple of $j \cdot \frac{\lambda_c}{n_d}$, the transmission remains unaltered. On the other hand, if the thickness equals a multiple of $(2j-1) \cdot \frac{\lambda_c}{n_d}$, the effective mirror transmission will increase. To illustrate, the red and blue lines show the transmission with a diamond membrane of thickness $t_d = 3.00 \cdot \frac{\lambda_c}{n_d}$ and $t_d = 3.25 \cdot \frac{\lambda_c}{n_d}$, respectively. **(b)** Reflected phase delay across the reflective stopband. A diamond with thickness $t_d = 3.25 \cdot \frac{\lambda_c}{n_d}$ (blue line) leads to the formation of a weak cavity and thus a larger phase delay at the stopband centre. For wavelengths detuned from $\lambda_c$, the phase delay approaches that of the bare mirror (black line). For the diamond with thickness $t_d = 3.00 \cdot \frac{\lambda_c}{n_d}$ (red line) the phase delay increases with detuning away from the stopband centre.

served. The increased transmission can be explained by the formation of a weak cavity bound by the bottom DBR and the diamond-air interface. Light circulating inside the diamond has an increased probability to be transmitted through the DBR mirror compared to a DBR without a diamond layer [85]. From Section 3.1 this diamond thickness corresponds to a diamond-confined geometry (blue lines Fig. 3.2).

## 3.3 Air-Confined vs. Diamond-Confined Cavity Modes – a Comparative Illustration

This chapter will culminate in a direct comparison between an air-confined and a diamond-confined cavity geometry. All calculations presented in this section were derived from one-dimensional transfer-matrix simulations obtained using Essential Macleod*. Throughout this section, a consistent choice of $t_d = 3.00 \cdot \frac{\lambda}{n_d} = 793.49\,\text{nm}$ and $t_d = 3.25 \cdot \frac{\lambda}{n_d} = 859.61\,\text{nm}$ have been used for the air-confined and diamond-confined

*Essential Macleod, Thin Film Center Inc.

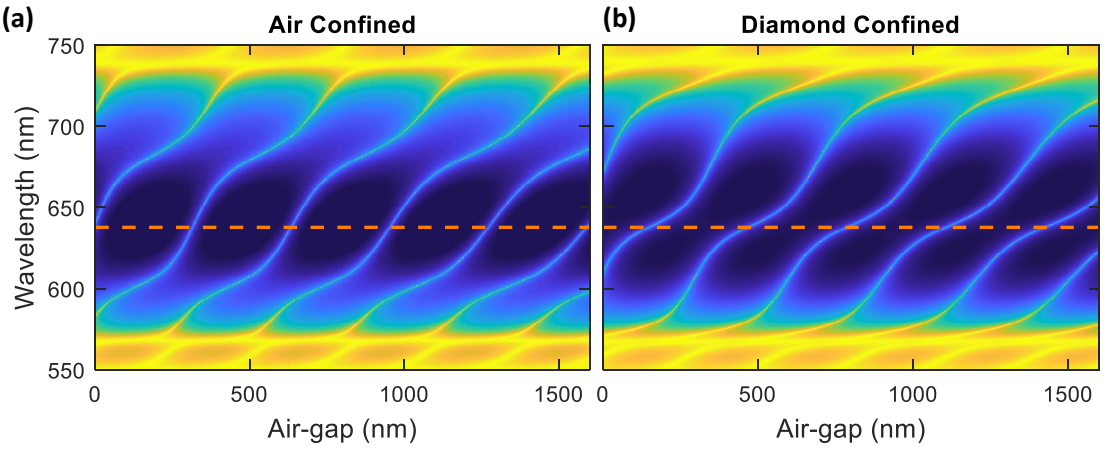


Fig. 3.3. One-dimensional transfer-matrix simulations of the cavity mode structure for **(a)** an air confined cavity ($t_\mathrm{d} = 3.00 \cdot \frac{\lambda}{n_\mathrm{d}}$) and **(b)** a diamond confined cavity ($t_\mathrm{d} = 3.25 \cdot \frac{\lambda}{n_\mathrm{d}}$). The orange dashed line indicates $\lambda = 637.7\,\mathrm{nm}$

geometry respectively, with $\lambda = 637.7\,\mathrm{nm}$ to portray the NV zero-phonon line.

### 3.3.1 The Hybridised Mode-structure

Consider a planar-concave Fabry-Perot cavity formed by two highly-reflected DBR mirrors with asymmetric coating. For the sake of argument, the structure of the top mirror is chosen to be $(n_\mathrm{H} n_\mathrm{L})^{14} n_\mathrm{H}$ and the bottom mirror $(n_\mathrm{H} n_\mathrm{L})^{15} n_\mathrm{H}$ starting from the substrate, with $Ta_2O_5$ and $SiO_2$ as as the high- and low index materials, respectively, i.e. $n_\mathrm{H} = n_{\mathrm{Ta_2O_5}} = 2.12$ and $n_\mathrm{L} = n_{\mathrm{SiO_2}} = 1.46$. The thickness $d$ of each layer is chosen such that $n \cdot d = \frac{\lambda_\mathrm{c}}{4}$, with $\lambda_\mathrm{c} = 637.7\,\mathrm{nm}$.

The resulting cavity mode structure is simulated in Fig. 3.3 for an air-confined (a) and a diamond-confined geometry (b). As expected, the mode structure looks comparatively similar to Fig. 3.1. However, the effect of field penetration into the DBR can be clearly observed close to the stopband edges. The orange line at $\lambda = 637.7\,\mathrm{nm}$ highlights the difference in the slope, $\frac{\mathrm{d}\lambda}{\mathrm{d}t_\mathrm{a}}$ between the two geometries.

### 3.3.2 Vacuum Electric Field Profile

In the above sections, the terms air-confined and diamond-confined geometry have been tossed around without a proper introduction, apart from the cavity being resonant with either the air-gap or the diamond. Therefore, this section will add some meat to the bone.

The profile of the electric field inside the cavity can be calculated using Macleod, from

which, the vacuum electric field, $E_{\mathrm{vac}}$ is quantised according to [255]

$$\begin{aligned}&\int_0^{2\pi} \mathrm{d}\phi \int_0^{\infty} r e^{-r^2/2w_{\mathrm{I}}^2} \mathrm{d}r \int_{\mathrm{cav}} \epsilon_0 \epsilon_{\mathrm{R}}(z) \left|\vec{E}_{\mathrm{vac}}\right|^2 \mathrm{d}z \\ &= 2\pi \cdot \frac{1}{4} w_{0,\mathrm{I}}^2 \cdot \int_{\mathrm{cav}} \epsilon_0 n^2(z) \left|\vec{E}_{\mathrm{vac}}\right|^2 \mathrm{d}z = \frac{\hbar\omega}{2}\,,\end{aligned} \tag{3.5}$$

where $\epsilon_{\mathrm{R}} = n^2$ and $w_{0,\mathrm{I}}$ is the intensity beam waist at the diamond. Eq. 3.5 assumes cylindrical symmetry and a constant beam waist across the length of the cavity.

By substituting $L_{\mathrm{cav}} = t_{\mathrm{a}} + \frac{t_{\mathrm{d}}}{n_{\mathrm{d}}}$ into Eq. 2.14 and assuming a Gaussian cavity mode, the intensity beam waist at the bottom mirror can be calculated from [123]

$$w_{0,\mathrm{I}} = \sqrt{\frac{\lambda}{2}} \left( R_{\mathrm{cav}} \left( t_{\mathrm{a}} + \frac{t_{\mathrm{d}}}{n_{\mathrm{d}}} \right) - \left( t_{\mathrm{a}} + \frac{t_{\mathrm{d}}}{n_{\mathrm{d}}} \right)^2 \right)^{\frac{1}{4}} . \tag{3.6}$$

For a planar-concave cavity, the minimal air-gap achievable is determined by the depth of the fabricated suppression (see Chapter 4). Therefore, the comparison between air-confined and diamond-confined will be carried out at the third cavity resonance (i.e $q_{\mathrm{air}} = 3$), where $q_{\mathrm{air}} = 1$ is defined as the first resonance in the air-gap, i.e. the smallest possible air-gap. By concidering a realistic cavity with $R_{\mathrm{cav}} = 10\,\mu\mathrm{m}$ *, one find $L_{\mathrm{cav}}^{\mathrm{A}} = 1.28\,\mu\mathrm{m}$, $w_{0,\mathrm{I}}^{\mathrm{A}} = 0.82\,\mu\mathrm{m}$ and $L_{\mathrm{cav}}^{\mathrm{D}} = 1.14\,\mu\mathrm{m}$, $w_{0,\mathrm{I}}^{\mathrm{D}} = 0.80\,\mu\mathrm{m}$ for $q_{\mathrm{air}} = 3$. Here, the superscript A (D) refers to the air-confined (diamond-confined) geometry. To illustrate the cavity structure, Fig. 3.4 (a) and (b) display the refractive index as a function of cavity length for the air-confined and diamond-confined geometry, respectively.

The profile of the electromagnetic field across the diamond-air interface, and consequently the relative energy density confined to the air and the diamond, are determined by the thickness of the diamond membrane [61]. At a first glance, there are two striking differences between the air-confined geometry (Fig. 3.4 (c)) and the diamond confined geometry (Fig. 3.4 (d)). First, the air-confined geometry possesses a field node across the diamond-air interface, while the diamond-confined geometry possesses a field anti-node across the said interface. The implications of this will be discussed further in Section 3.3.3.

The second difference lies in the relative intensity of the electric field confined to the air and diamond layer, respectively. For an air-confined cavity mode (Fig. 3.4 (c)), the relative field intensity in the air-gap is larger by a factor $n_{\mathrm{d}}$ compared to that of diamond [61]. On the other hand, for a diamond-confined cavity mode (Fig. 3.4 (d)), the

*Motivated by Fig. 4.3 and Ref. [77, 255, 387].

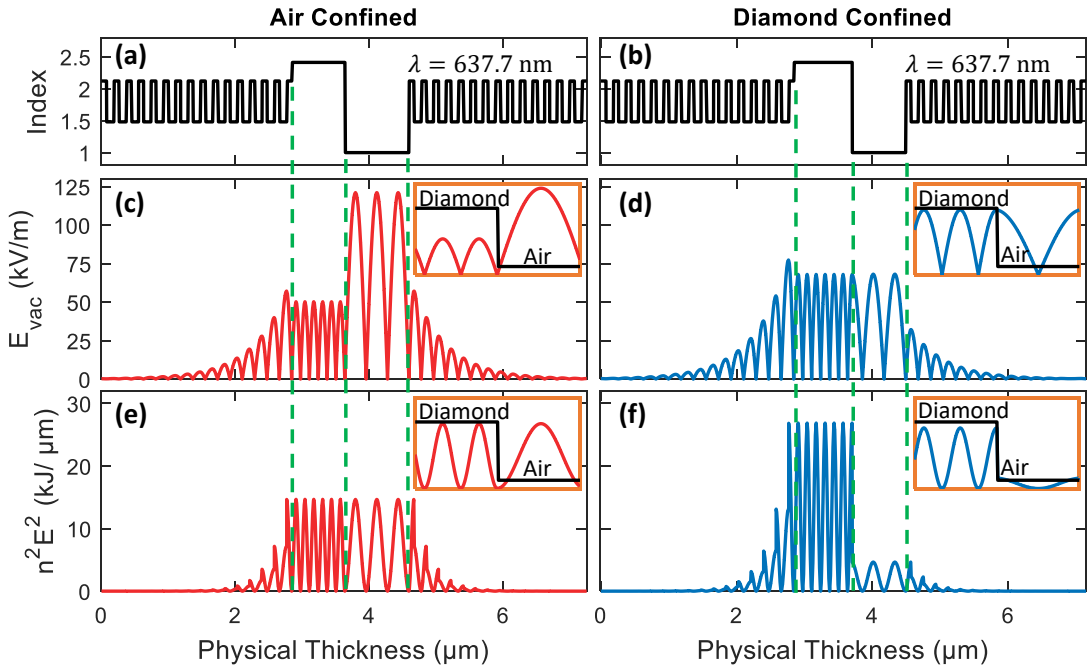


Fig. 3.4. Comparison between an air- and a diamond-confined geometry. **(a)** - **(b)** Refractive index profile of the cavity including a diamond membrane with thickness $t_\mathrm{d} = 3.00 \cdot \frac{\lambda}{n_\mathrm{d}}$ and $t_\mathrm{d} = 3.25 \cdot \frac{\lambda}{n_\mathrm{d}}$, respectively. The green lines indicate the interface between the bottom DBR and the diamond, the diamond-air interface and the interface between air and the top DBR. **(c)** For an air-confined geometry, a larger fraction of the vacuum electric field is confined to the air-gap. Furthermore, the vacuum field possesses a field node across the diamond-air interface (inset). **(d)** In the diamond confined geometry, a relatively larger fraction of the vacuum field is confined to the diamond. The vacuum electric field possesses a field anti-node across the diamond-air interface (inset). **(e)** The energy density stored in the cavity for an air confined geometry. **(f)** For a diamond confined geometry, the energy density is significantly larger in the diamond compared to in the air-gap.

relative field strength in the air-gap and in the diamond remains comparable.

To further emphasise the difference between the two configurations, it is helpful to look at the relative energy density, $n^2E^2$, confined to the air and diamond. Fig. 3.4 (e)-(f) show a plot of $n^2(z)E^2_\mathrm{vac}(z)$ as a function of cavity length for the two geometries. As can be seen in Fig. 3.4 (f), the energy density confined to the diamond is significantly larger for the diamond-confined geometry. The high relative field intensity in the diamond leads to higher coupling strengths to emitters, which will be discussed further in Section 3.3.4.

To summarise, an air-confined cavity mode possesses a field node at the diamond-air interface, while the diamond-confined mode possesses a field anti-node at the said interface. In an air-confined geometry, the relative strength of the electric field is larger

in the air-gap then for the diamond, while the inverse is true for a diamond-confined geometry.

### 3.3.3 Introducing Losses

Up until this point, a perfect-world scenario without any losses has been assumed. An extensive experimental study of the $\mathcal{Q}$-factor as a function of both cavity length and wavelength in the presence of losses will be discussed in Chapter 4 and Ref. [387]. In a Fabry-Perot cavity embedded with a diamond membrane, losses are primarily associated with the diamond surface (here lossless mirrors are assumed, motivated by the results presented in Chapter 4). Losses, such as scattering and absorption depend on the electric field amplitude across the diamond-air interface, and therefore, one would expect a different behaviour between an air-confined and diamond-confined geometry [61].

Eq. 2.25 predicts a linear increase in $\mathcal{Q}$-factor with increased cavity length $L$. For fixed $\lambda$, rewrite $L = L_0 + t_\mathrm{a}$, where $t_\mathrm{a} = q_\mathrm{air} \cdot \frac{\lambda}{2}$. Here, the thickness of the diamond and the field penetration depth into the mirrors are all bundled up in the term $L_0$ [387]. In Fig. 3.5, the $\mathcal{Q}$-factor is simulated as a function of air-gap thickness for (a) an air-confined and (b) a diamond-confined geometry. For short $t_\mathrm{a}$, the $\mathcal{Q}$-factor is larger for the diamond-confined geometry, which can be explained by a longer effective cavity length (Fig. 3.2 (b)). However, for large $t_\mathrm{a}$, the $\mathcal{Q}$-factor becomes larger for the air-confined geometry, owing to a steeper gradient (i.e. a larger finesse, $\mathcal{F} = \frac{\Delta \mathcal{Q}}{\Delta q}$). The larger finesse is reflected by the lower mirror transmission, and thus higher reflectivity, for the air-confined geometry compared to a diamond confined geometry (Fig. 3.2 (a)).

The link between surface roughness $\sigma_\mathrm{q}$ and scattering losses $S$ is established via [104, 388]

$$S \approx \left( \frac{4\pi\sigma_\mathrm{q}}{\lambda} \right)^2 . \tag{3.7}$$

Losses, such as scattering and absorption, can be incorporated into the one-dimensional transfer-matrix simulations following the method reported by Ref. [389]. In this method, scattering at the diamond-air interface can be simulated by adding an additional layer on top of the diamond with thickness $d = 2\sigma_\mathrm{q}$ and complex refractive index $\tilde{n} = n_\mathrm{eff} + i\kappa$. Here, the effective refractive index $n_\mathrm{eff} = \sqrt{\left(n_\mathrm{a}^2 + n_\mathrm{d}^2\right)/2}$ and the extinction coefficient $\kappa$ is given by [389]

$$\kappa = \frac{\pi \left(n_\mathrm{a} - n_\mathrm{d}\right)^2 \left(n_\mathrm{a} + n_\mathrm{d}\right)}{4 n_\mathrm{eff}} \cdot \frac{d}{\lambda} , \tag{3.8}$$

where $\lambda$ is the free-space wavelength and $n_\mathrm{a}$, $n_\mathrm{d}$ are the refractive index of the air and the diamond layer, respectively. The dashed lines in Fig. 3.5 show the $\mathcal{Q}$-factor in the

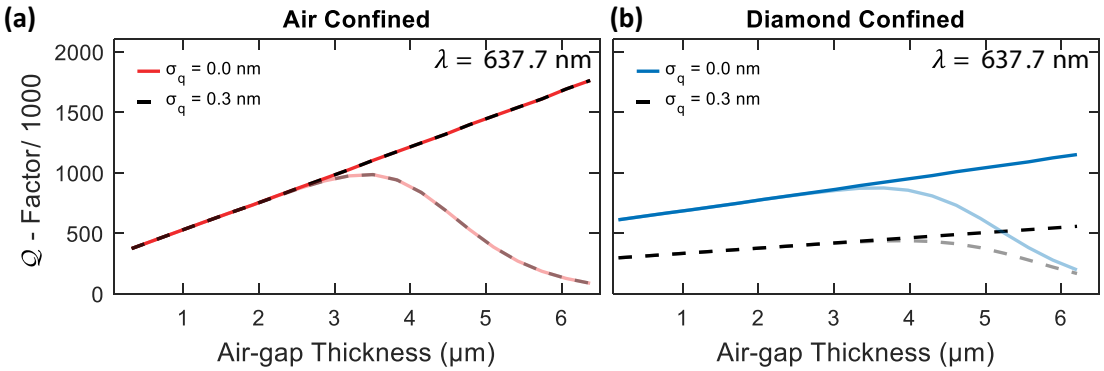


Fig. 3.5. $\mathcal{Q}$-factor as a function of air-gap thickness $t_\mathrm{a}$ for fixed $\lambda = 637.7\,\mathrm{nm}$ for **(a)** an air-confined and **(b)** diamond-confined geometry. As expected, the initial $\mathcal{Q}$-factor is larger for the diamond-confined geometry owing to a larger effective cavity length. In the presence of scattering (dashed lines), the $\mathcal{Q}$-factor for the diamond-confined modes is significantly reduced, owing to the field node across the diamond-air interface. The semi-transparent lines show the $\mathcal{Q}$-factor in the presence of beam clipping, with $R_\mathrm{cav} = 10\,\mu\mathrm{m}$ and $D = 6\,\mu\mathrm{m}$.

presence of a scattering layer with a realistic root-mean-square (RMS) surface roughness $\sigma_\mathrm{q} = 0.3\,\mathrm{nm}$* [159, 387]. Surface scattering affects the air-confined and diamond-confined cavity modes very differently. The electric field node at the diamond-air interface for the air-confined geometry (Fig. 3.4 (c)) minimises surface scattering, and hence the $\mathcal{Q}$-factor is effectively unchanged. On the other hand, for the diamond-confined geometry, the field anti-node maximises the surface scattering resulting in a significant reduction in the $\mathcal{Q}$-factor.

For completeness, the semi-transparent lines in Fig. 3.2 show the dependence on the $\mathcal{Q}$-factor with $t_\mathrm{a}$ in the presence of beam clipping. Clipping losses depends on the geometrical parameters of the curved mirror and occur when the beam waist at the top mirror $w_\mathrm{I}$ extends further than the spherical region $D$ of the said mirror [104]. The beam waist $w_\mathrm{I}$ evolves according to [123, 387]

$$w_\mathrm{I} = \sqrt{\frac{\lambda R_\mathrm{cav}}{\pi}} \cdot \left( \frac{R_\mathrm{cav}}{t_\mathrm{a} + \frac{t_\mathrm{d}}{n_\mathrm{d}}} - 1 \right)^{-\frac{1}{4}}, \tag{3.9}$$

from which the clipping losses are given by [104, 390] *

$$\mathcal{L}_\mathrm{clip} = e^{-\frac{D^2}{2w_\mathrm{I}^2}}. \tag{3.10}$$

*The value of $\sigma_\mathrm{q}$ will be motivated in Chapter 4.

*The readers are referred to Appendix. B for a derivation.

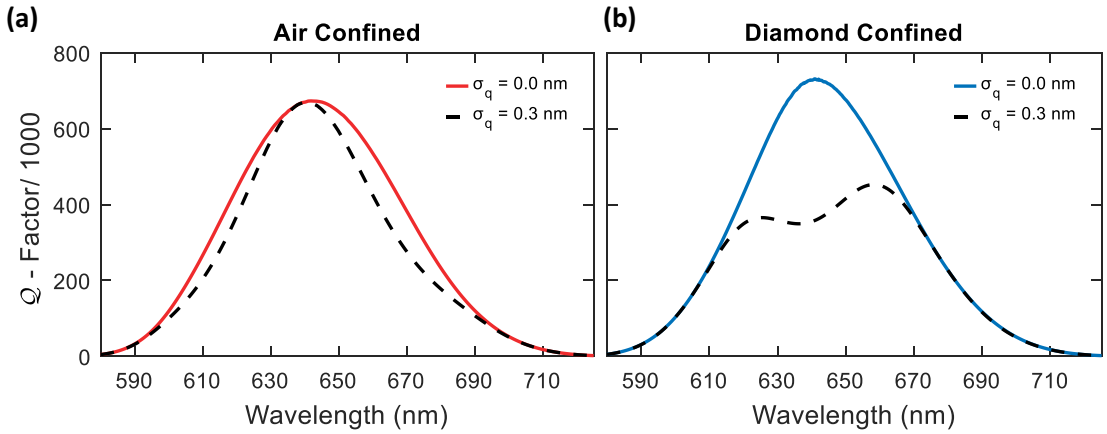


Fig. 3.6. $\mathcal{Q}$-factor across the stopband for **(a)** an air-confined geometry and **(b)** a diamond-confined geometry. The black dashed lines show the simulated $\mathcal{Q}$-factor in the presence of surface scattering with surface roughness $\sigma_q = 0.3\,\text{nm}$. At the stopband centre ($\lambda_c = 637.7\,\text{nm}$), the reduction in $\mathcal{Q}$-factor is significantly larger for the diamond confined geometry owing to the field maxima across the diamond-air interface. Towards the edges of the stopband, the cavity losses are dominated by mirror transmission, and thus the effect of scattering becomes negligible.

Clipping losses were experimentally verified in Chapter 4.

As previously mentioned, scattering (and absorption) losses depend on the amplitude of the electric field at the surface. Tuning the resonant wavelength $\lambda$ alters the standing wave inside the cavity, and subsequently the field intensity across the diamond-air interface. Therefore, a measurement of the $\mathcal{Q}$-factor as a function of $\lambda$ may provide unprecedented insight into the cavity losses [391]. To illustrate, Fig. 3.6 (a) and (b) show the $\mathcal{Q}$-factor as a function of $\lambda$ across the reflective stopband (for short $t_a$) for an air- and diamond-confined geometry, respectively. Here, the solid lines represent a perfect cavity, and the dashed lines represent surface scattering. As before, the presence of surface scattering causes a significant drop in the $\mathcal{Q}$-factor at the stopband centre for the diamond-confined geometry. For $\lambda$ detuned away from the stopband centre, the $\mathcal{Q}$-factor for the diamond-confined geometry quickly converges to the $\mathcal{Q}$-factor expected of a perfect cavity. For the air-confined geometry, scattering losses are negligible at the stopband centre, due to the field minima discussed above. However, for small detuning away from the stopband centre, a drop in $\mathcal{Q}$-factor is observed. This drop can be explained by the now non-zero field amplitude across the diamond-air interface. Furthermore, for a small detuning away from the stopband centre, the mirror transmission increases as can be seen in Fig. 3.2 (a). For wavelengths close to the edges of the stopband, the cavity losses are dominated by mirror transmission, and thus the effect of scattering can be neglected.

### 3.3.4 Purcell Enhancement

The overarching goal of the work presented in this thesis is to enhance the radiative emission rate from single NV centres embedded in a diamond membrane. The coupling strength $g$ between an emitter and a single cavity mode scales with the amplitude of the electric field according to $g = \frac{1}{\hbar} \cdot \mu_{\mathrm{eg}} E_{\mathrm{vac}}$ (Eq. 2.61). Therefore, as the above analysis suggests, the coupling strength differs between an air-confined and a diamond-confined cavity mode.

Consider an optimally aligned NV centre (or any other type of emitter) located at a field-maxima at position $\vec{r} = \vec{r}_0$. The Purcell factor is then given by *

$$F_{\mathrm{P}} = 1 + \frac{3}{4\pi^2} \frac{\mathcal{Q}}{V_{\mathrm{eff}}} \left( \frac{\lambda}{n} \right)^3 , \tag{3.11}$$

where the effective mode volume, $V_{\mathrm{eff}}$, is calculated from [124, 392]

$$V_{\mathrm{eff}} = \frac{\int_{\mathrm{cav}} \epsilon_0 n^2(\vec{r}) |\vec{E}_{\mathrm{vac}}(\vec{r})|^2 \mathrm{d}^3 r}{\epsilon_0 n^2(\vec{r}_0) |\vec{E}_{\mathrm{vac}}(\vec{r}_0)|^2} = \frac{\frac{\hbar\omega}{2}}{\epsilon_0 n^2(\vec{r}_0) |\vec{E}_{\mathrm{vac}}(\vec{r}_0)|^2} . \tag{3.12}$$

In Fig. 3.7 (a) and (b), the amplitude of the vacuum electric field inside the diamond is plotted against the width of the air-gap for an air-confined and diamond-confined geometry, respectively. Here, the amplitude of the vacuum electric field is normalised according to Eq. 3.5. As expected, the field maxima inside the diamond are larger for the diamond-confined geometry. The difference in field intensity is better visualised when the effective mode volume is taken into consideration. Fig. 3.7 (c) shows the drastic increase in $V_{\mathrm{eff}}$ for an air-confined geometry compared to a diamond-confined geometry (d).

Two considerations have to be made when selecting the desired air-gap for a cavity coupling experiment; the increase in both the $\mathcal{Q}$-factor and $V_{\mathrm{eff}}$ with $t_{\mathrm{a}}$. While the $\mathcal{Q}$-factor increases linearly with $t_{\mathrm{a}}$, the non-linear increase in $V_{\mathrm{eff}}$ favours short cavities, thus maximising $\frac{\mathcal{Q}}{V_{\mathrm{eff}}}$. The solid lines in Fig. 3.7 (e) and (f) show $F_{\mathrm{P}}$ as a function of $t_{\mathrm{a}}$. As before, the semi-transparent lines indicate the behaviour of $F_{\mathrm{P}}$ with $t_{\mathrm{a}}$ in the presence of beam clipping. From this, in order to achieve a large Purcell factor, it is clearly beneficial to operate in a diamond-confined regime.

The presence of surface scattering reduces the $\mathcal{Q}$-factor, and hence leads to a reduction in $F_{\mathrm{P}}$. The black dashed lines in Fig. 3.7 (e) and (f) show the dependence of $F_{\mathrm{P}}$ with

*Alternatively, the Purcell factor can be expressed on the form $F_{\mathrm{P}} = 1 + \frac{4g^2}{\kappa\gamma}$ , where the dependency on $E_{\mathrm{vac}}$ perhaps becomes more apparent.

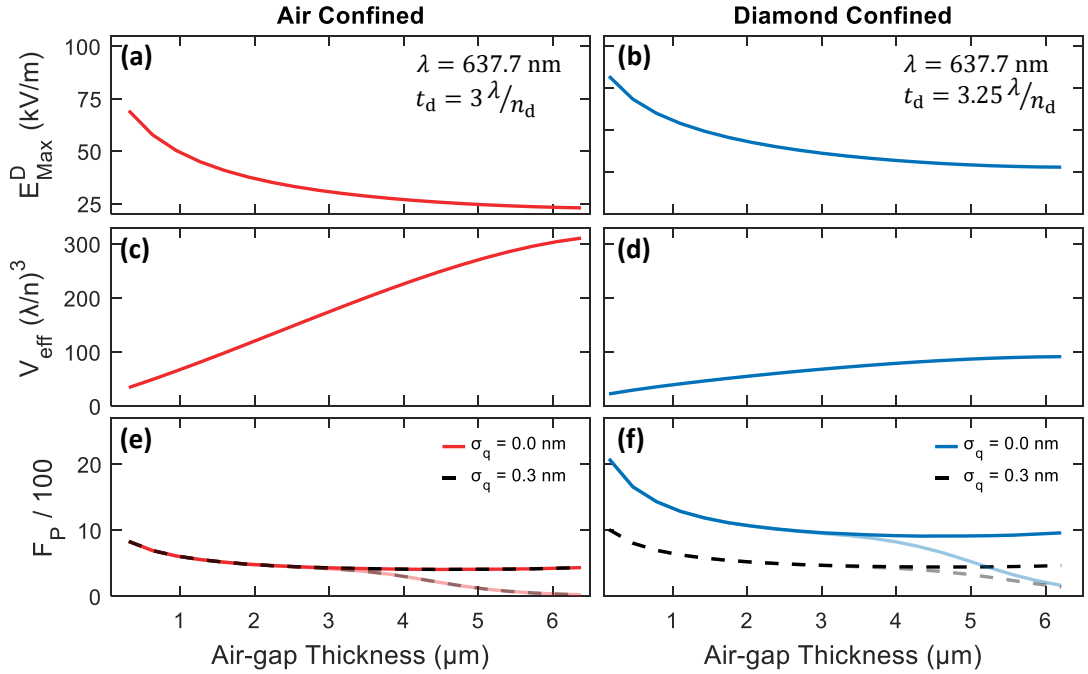


Fig. 3.7. Comparison of the cavity performance between an air-confined and diamond-confined geometry. **(a)** - **(b)** show that the maximum value of the vacuum electric field inside the diamond is larger for the diamond confined geometry. **(c)** - **(d)** with increasing cavity length, the effective mode volume $V_{\text{eff}}$ is significantly larger for the air-confined geometry as the vacuum field is more strongly confined to the air-gap. **(e)** - **(f)** The Purcell factor scales with $\frac{\mathcal{Q}}{V_{\text{eff}}}$. Using the $\mathcal{Q}$-factor from Fig. 3.5, the expected Purcell factor is larger for a diamond confined geometry, even in the presence of surface scattering. The semi-transparent lines indicate the Purcell factor in the presence of beam clipping.

$t_a$ in the presence of surface scattering with $\sigma_q = 0.3\,\text{nm}$. As one would expect from Fig. 3.5, the reduction in $F_P$ is significant for the diamond-confined geometry, while no significant change is observed for the air-confined geometry. Despite the reduction in $\mathcal{Q}$, with a realistic value of $\sigma_q = 0.3\,\text{nm}$, $F_P$ remains marginally larger for the diamond-confined geometry. An added benefit of working in a diamond-confined geometry is the insensitivity of the resonant $\lambda$ with fluctuations in $t_a$ as was discussed in the very first section of this chapter.

### 3.3.5 Condition for Maximal Photon Collection Efficiency

Up until this point, no comments have been made on the ideal combination of top- and bottom mirrors to maximise the detection efficiency of photons from emitters in

diamond. The cavity used for the experiments presented in the subsequent chapters* works in a back-scattering geometry. Therefore, this discussion will consider a highly reflective bottom mirror on the form $(n_{\mathrm{H}}n_{\mathrm{L}})^{20}n_{\mathrm{H}}$, to ensure maximised photon collection through the top mirror. Throughout this subsection, the air-gap for the air-confined case is set to $t_{\mathrm{a}} \simeq 935.6\,\mathrm{nm}$ ($q_{\mathrm{air}} = 4$), and for the diamond-confined geometry $t_{\mathrm{a}} \simeq 1105.9\,\mathrm{nm}$ ($q_{\mathrm{air}} = 3$). To start, Fig. 3.8 (a) and (b) show the dependency of the $\mathcal{Q}$-factor for fixed $\lambda = 637.7\,\mathrm{nm}$ with increasing top-mirror pairs for the air- and diamond-confined geometry, respectively. For few mirror pairs, there is a linear increase in the $\mathcal{Q}$-factor, where the $\mathcal{Q}$-factor is larger for the diamond-confined geometry (consistent with the longer effective cavity length as can be seen in Fig. 3.2 (b)). As expected, introducing surface scattering with $\sigma_{\mathrm{q}} = 0.3\,\mathrm{nm}$ (black dashed line) strongly affects the $\mathcal{Q}$-factor for the diamond-confined geometry, while for the air-confined regime, the $\mathcal{Q}$-factor remains unaltered. Therefore, for the remainder of this subsection, losses will be neglected for the air-confined geometry. In the diamond-confined geometry, for fewer than 8 mirror pairs, the cavity losses are dominated by transmission through the top mirror, and the $\mathcal{Q}$-factor remains relatively unaffected by surface scattering. On the other hand, for more than 12 mirror pairs, the surface scattering starts to dominate. The $\mathcal{Q}$-factor saturates at $\mathcal{Q}_{\mathrm{scat}} = 625\,560$, adding more mirror pairs will not result in a larger $\mathcal{Q}$-factor.

Fig. 3.8 (c) and (d) show the calculated cavity loss-rate $\kappa$ as a function of top-mirror pairs. Here, $\kappa$ is calculated from $\kappa = \frac{2\pi c}{\lambda \mathcal{Q}}$. For a lossless cavity, a photon can only exit the cavity via the two end mirrors, i.e. $\kappa = \kappa_{\mathrm{top}} + \kappa_{\mathrm{bot}}$, where $\kappa_{\mathrm{top}} = \frac{\mathcal{T}_{\mathrm{top}}}{\mathcal{T}_{\mathrm{top}}+\mathcal{T}_{\mathrm{bot}}} \cdot \kappa$ is the loss-rate through the top mirror (and similarly for the bottom mirror). Here, $\mathcal{T}_{\mathrm{top\ (bot)}}$ is the transmission of the top (bottom) mirror. Surface scattering leads to a reduction of the $\mathcal{Q}$-factor ($\mathcal{Q}'$), consequently increasing the cavity loss-rate by amount $\kappa_{\mathrm{loss}}$ according to $\kappa' = \kappa_{\mathrm{top}} + \kappa_{\mathrm{bot}} + \kappa_{\mathrm{loss}}$, where $\kappa' = \frac{2\pi c}{\lambda \mathcal{Q}'}$. From this, the scattering loss-rate is given by $\kappa_{\mathrm{loss}} = \kappa' - \kappa$.

To disentangle further the desired loss-rate through the top mirror $\kappa_{\mathrm{top}}$ to undesired loss-rates $\kappa_{\mathrm{bot}}$ and $\kappa_{\mathrm{loss}}$, Fig. 3.9 evaluates $\frac{\kappa_{\mathrm{top}}}{\kappa_{\mathrm{tot}}}, \frac{\kappa_{\mathrm{bot}}}{\kappa_{\mathrm{tot}}}$ and $\frac{\kappa_{\mathrm{loss}}}{\kappa_{\mathrm{tot}}}$ as a function of mirror pairs. Here, $\kappa_{\mathrm{tot}}$ is the total loss-rate amounting to the aforementioned $\kappa$ ($\kappa'$) in the absence (presence) of surface scattering. For the air-confined geometry (Fig. 3.9 (a)), cavity losses are completely dominated by $\kappa_{\mathrm{top}}$ independently of mirror pairs, provided the number of pairs remains larger for the bottom mirror. On the other hand, for the diamond-confined geometry, $\kappa_{\mathrm{top}}$ is only dominant for less than 8 top-mirror pairs, after which scattering starts to contribute. For 12 top-mirror pairs, $\kappa_{\mathrm{top}} \simeq \kappa_{\mathrm{loss}}$, and for more than 12 top-mirror pairs, $\kappa_{\mathrm{loss}}$ dominates.

*See Fig. 4.1.

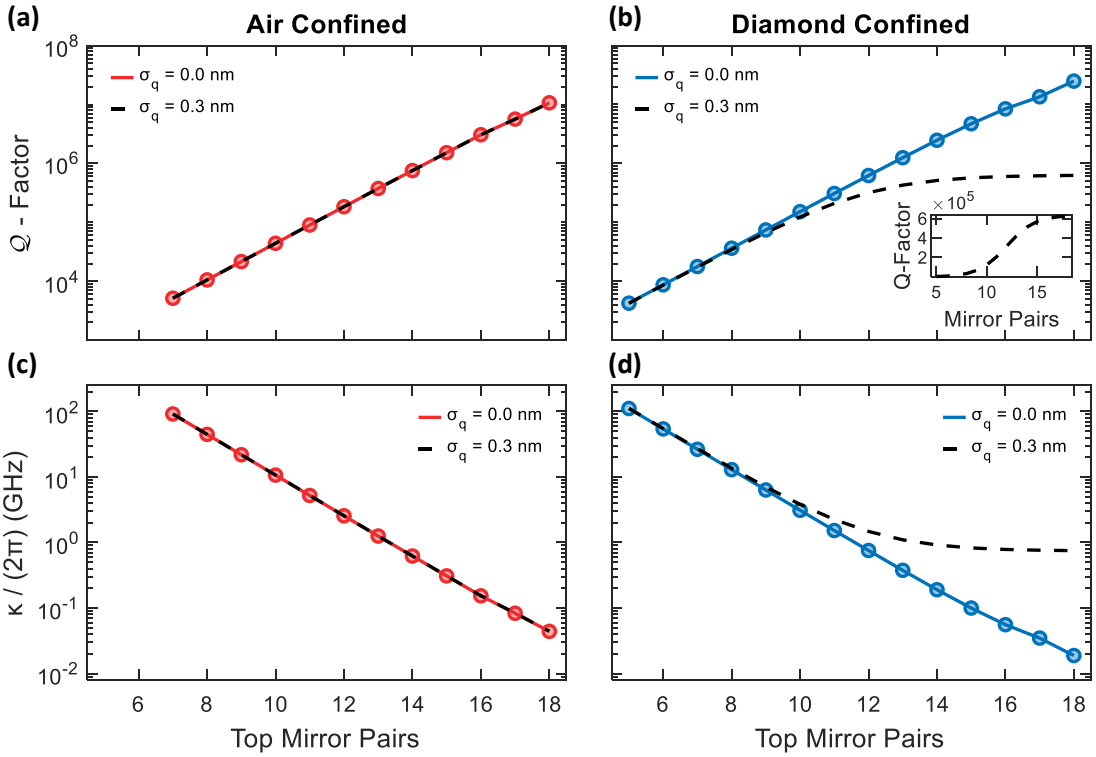


Fig. 3.8. Changing the number of mirrors pairs for the top mirror alters the cavity performance. Here, the structure of the bottom mirror was fixed at $(n_{\mathrm{H}}n_{\mathrm{L}})^{20}n_{\mathrm{H}}$. **(a)** - **(b)** $\mathcal{Q}$-factor as a function of increasing top-mirror pairs for an air- and diamond-confined geometry, respectively. The black dashed lines show the $\mathcal{Q}$-factor in the presence of surface scattering with $\sigma_{\mathrm{q}} = 0.3\,\mathrm{nm}$. As expected, the $\mathcal{Q}$-factor is unaffected by scattering for the air-confined geometry. The diamond-confined geometry is strongly affected by surface scattering. For less than 8 mirror pairs, transmission through the top mirror is the dominant loss channel. For more than 12 mirror pairs, scattering is the dominant loss mechanism; adding more mirror pairs will no longer increase the $\mathcal{Q}$-factor. **(c)** - **(d)** Calculation of the cavity loss-rate $\kappa$ as a function of increasing top-mirror pairs for the two geometries.

Finally, the attention is directed towards the detection efficiency of a single photon from an NV centre. Recall from Section. 2.1.4 that the probability of emission into the cavity mode is given by the $\beta$-factor: $\beta = \frac{F_{\mathrm{P}}-1}{F_{\mathrm{P}}}$*, where $F_{\mathrm{P}} = 1 + \frac{4g^2}{\kappa\gamma}$ as introduced in Section 2.1.4. For an NV centre, the branching into the ZPL is given by the Debye-Waller factor $\xi_0 = 2.55\,\%$ (see Section 2.2.3) [77]. Following the procedure presented in Ref. [387] (see Section 4.4.1), the fraction of ZPL photons emitted into the cavity mode is given by

$$\eta_{\mathrm{ZPL}} = F_{\mathrm{P}} \cdot \frac{\xi_0\gamma_0}{\gamma_{\mathrm{cav}}}\,, \tag{3.13}$$

*Strictly speaking, this is only true for an emitter with 100% internal quantum efficiency.

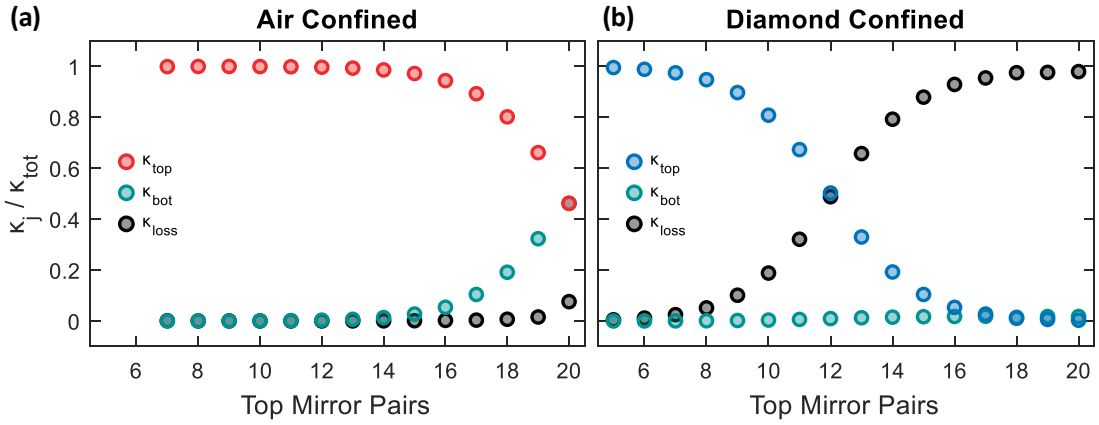


Fig. 3.9. The relative contribution of transmission through the top mirror, $\frac{\kappa_{\text{top}}}{\kappa}$, and scattering, $\frac{\kappa_{\text{loss}}}{\kappa}$, to the total loss-rate $\kappa$ for constant $\lambda = 637.7\,\text{nm}$ and fixed bottom mirror on the form $(n_{\text{H}}n_{\text{L}})^{20}n_{\text{H}}$. **(a)** For the air-confined geometry the loss-rate is dominated by mirror transmission independently of mirror pairs. **(b)** For the diamond-confined geometry, the losses are only dominated by the top mirror for less than 8 top mirror pairs, after which scattering losses start to contribute. For 12 mirror pairs, scattering losses equal transmission losses, and for more than 12 pairs the scattering becomes the dominant loss-channel. Transmission through the bottom mirror remains vanishingly small for all mirror pairs considered here.

where $\gamma_{\text{cav}}$ is the total decay rate in the cavity. The efficiency of transmission through the top mirror is given by

$$\eta_{\text{top}} = \frac{\kappa_{\text{top}}}{\kappa_{\text{tot}} + \gamma_0}\,, \tag{3.14}$$

where $\gamma_0 = \frac{1}{\tau_0}$ and $\tau_0$ is the unperturbed lifetime of the emitter. Combining the above, the conversion efficiency from an NV centre in the excited state to a ZPL photon exciting the cavity through the top mirror is given by [102]

$$\begin{aligned} \eta_{\text{out}} &= \eta_{\text{ZPL}} \cdot \eta_{\text{top}} \\ &= \eta_{\text{ZPL}} \cdot \frac{\kappa_{\text{top}}}{\kappa_{\text{tot}} + \gamma_0}\,. \end{aligned} \tag{3.15}$$

The optimum value for $\kappa_{\text{top}}$ can be calculated from [102]

$$\kappa_{\text{opt}} = \sqrt{\left(1 + \frac{\kappa_{\text{loss}}}{\gamma_0}\right) \cdot \left(4\xi_0 g^2 + \kappa_{\text{loss}}\gamma_0\right)}\,, \tag{3.16}$$

where $g$ is the emitter-cavity coupling rate. For the condition $g \gg \kappa_{\text{loss}}$ and $g \gg \gamma_0$ *,

*For the diamond confined geometry, $\{g, \kappa_{\text{loss}}, \gamma_0\} = 2\pi \times \{1.5\,\text{GHz}, 720\,\text{MHz}, 12.6\,\text{GHz}\}$.

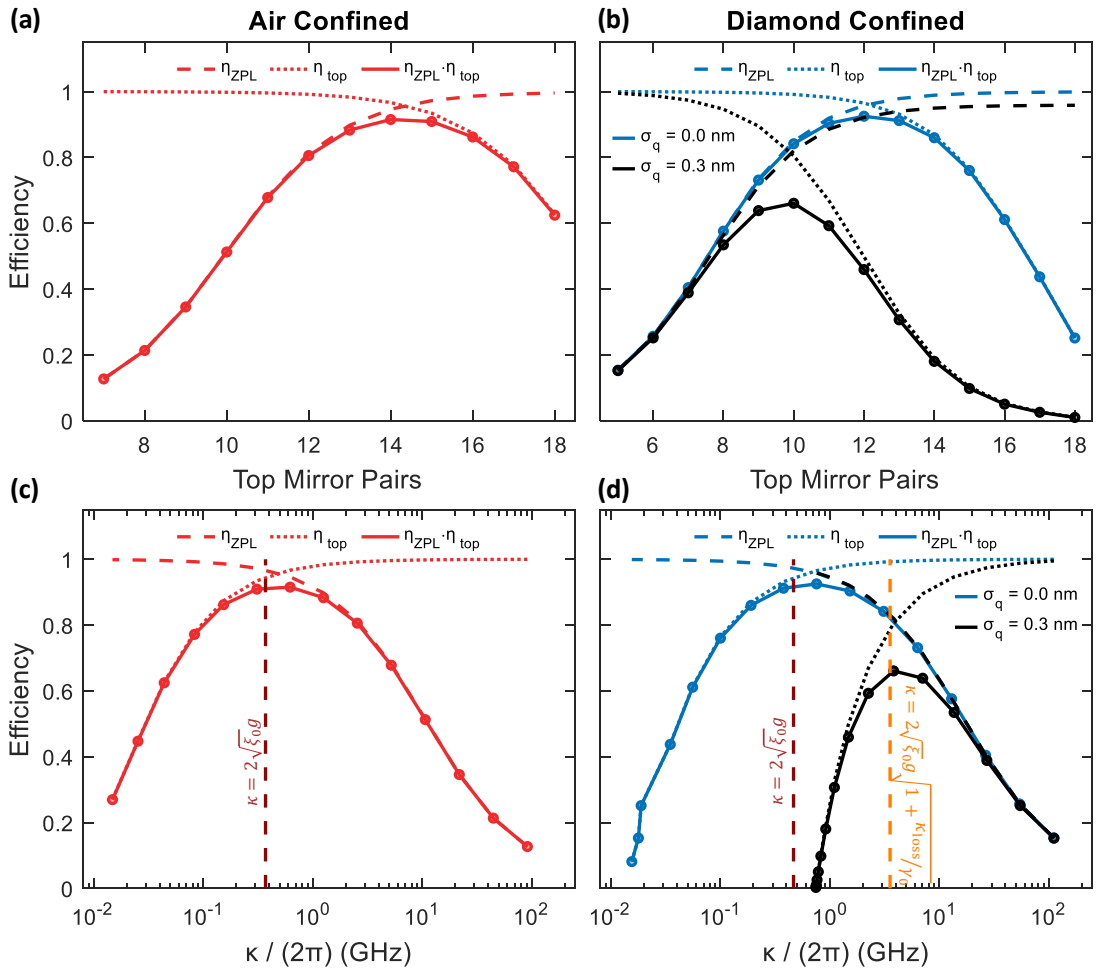


Fig. 3.10. Calculation of the detection efficiency of a ZPL photon through the top mirror. For all panels, the dashed- and dotted lines represent the fraction of emission into the cavity mode, $\beta_{\mathrm{ZPL}}$, and the efficiency of transmission through the top mirror, $\eta_{\mathrm{top}}$, respectively. The total efficiency, $\beta_{\mathrm{ZPL}} \cdot \eta_{\mathrm{top}}$, is represented by the solid line. **(a)** - **(b)** Efficiency as a function of top mirror pairs for an air- and diamond-confined geometry, respectively. Surface roughness, $\sigma_{\mathrm{q}} = 0.3\,\mathrm{nm}$, reduces the optimal number of top-mirror pairs, indicated by the black curves in panel (b). For simplicity, scattering losses are neglected for the air-confined geometry. **(c)** - **(d)** Efficiency as a function of $\kappa$ for the two geometries. The vertical burgundy lines correspond to the ideal condition $\kappa = 2\sqrt{\xi_0}g$. For panel (d), in the presence of losses, the ideal condition is given by $\kappa_{\mathrm{opt}} = 2\sqrt{\xi_0}g \cdot \sqrt{1 + \frac{\kappa_{loss}}{\gamma}}$, indicated by the dashed orange line.

Eq. 3.16 reduces to [102]

$$\kappa_{\mathrm{opt}} = 2\sqrt{\xi_0}g \cdot \sqrt{1 + \frac{\kappa_{\mathrm{loss}}}{\gamma_0}}\,, \tag{3.17}$$

which, for a lossless cavity further reduces to the more familiar

$$\kappa_{\text{opt}} = 2\sqrt{\xi_0}g\,. \tag{3.18}$$

The results are presented graphically in Fig. 3.10. For the air-confined geometry (Fig. 3.10 (a)), the maximum detection efficiency, $\eta_{\text{out}}^{\text{A}} = 0.9152$, is found for 14 top-mirror pairs. For a diamond-confined geometry (Fig. 3.10 (b)), in the absence of losses, $\eta_{\text{out}}$ peaks at 12 top-mirror pairs at $\eta_{\text{out}}^{\text{D}} = 0.9251$. The difference in the number of optimal mirror pairs between the air- and diamond confined geometry can be explained by the effective reduction of the mirror reflectivity for the diamond-confined geometry (Fig 3.2 (a)). In the presence of surface scattering, $\eta_{\text{out}}$ decreases to $\eta_{\text{out}}^{\text{D,scat}} = 0.6607$ for 10 top-mirror pairs.

Fig. 3.10 (c) calculates $\eta_{\text{out}}$ as a function of $\kappa$ for the air-confined geometry. The vertical burgundy line indicates the condition $\kappa = 2\sqrt{\xi_0}g$ (Eq. 3.18). Similarly, Fig. 3.10 (d) show the dependency of $\eta_{\text{out}}$ with $\kappa$ for the diamond confined geometry. Again, the burgundy vertical line corresponds to the $\kappa = 2\sqrt{\xi_0}g$, and coincides with the maximum efficiency for the lossless cavity. The vertical orange line corresponds to $\kappa_{\text{opt}} = 2\sqrt{\xi_0}g \cdot \sqrt{1 + \frac{\kappa_{\text{loss}}}{\gamma_0}}$, and coincides with the maximum efficiency in the presence of surface scattering, as expected from Eq. 3.16.

### 3.3.6 Dependency on $R_{\text{cav}}$

As a final curiosity, Fig. 3.11 calculates the performance of the cavity as a function of the radius of curvature of the top mirror, $R_{\text{cav}}$. For all the sub-figures, the red lines correspond to an air-confined geometry with $t_{\text{a}} = 954\,\text{nm}$ ($q_{\text{air}} = 3$) and $t_{\text{d}} = 3.00 \cdot \frac{\lambda}{n_{\text{d}}}$, while the blue lines correspond to a diamond-confined geometry with $t_{\text{a}} = 787\,\text{nm}$ and $t_{\text{d}} = 3.25 \cdot \frac{\lambda}{n_{\text{d}}}$ extracted from Fig. 3.4.

For increasing $R_{\text{cav}}$ the values of $w_{\text{I}}$ and $w_{0,\text{I}}$ converge, as would be expected since the cavity can be approximated as a planar-planar cavity for large $R_{\text{cav}}$. Minimising the value of $w_{0,\text{I}}$ is important in order to maximise the vacuum field $E_{\text{vac}}$ (Eq. 3.5). Fig. 3.11 (b) evaluates the maxima of the electric field inside the diamond. As expected, with increasing $R_{\text{cav}}$, $w_{0,\text{I}}$ increases, and consequently, the magnitude of the vacuum field decreases. The mode volume $V_{\text{eff}}$ scales inversely with the magnitude of the vacuum field (Eq. 3.12), and consequently increases with $R_{\text{cav}}$ (Fig. 3.11 (c)). Finally, Fig. 3.11 (d) shows the dependency on the Purcell factor with $R_{\text{cav}}$. Increasing the $R_{\text{cav}}$ from 10 µm to 15 µm leads to a 30 % and 20 % reduction of the Purcell factor for the air- and diamond confined geometry, respectively.

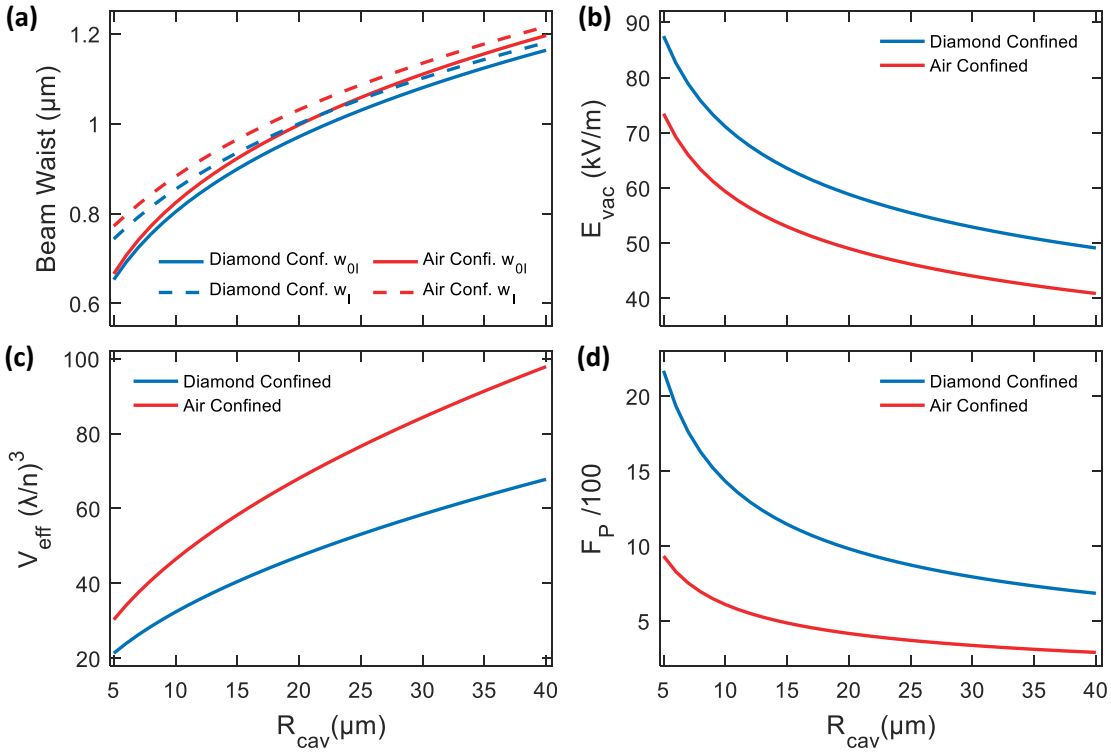


Fig. 3.11. Cavity performance as a function of increasing $R_{\mathrm{cav}}$. For all sub-figures, the red and blue lines correspond to air- and diamond-confined geometries with $t_{\mathrm{d}} = 3.00 \cdot \frac{\lambda}{n_{\mathrm{d}}}$ and $t_{\mathrm{d}} = t_{\mathrm{d}} = 3.25 \cdot \frac{\lambda}{n_{\mathrm{d}}}$, respectively. **(a)** The intensity beam waist $w_{0,\mathrm{I}}$ at the diamond (solid lines) and the beam waist $w_{\mathrm{I}}$ at the top mirror calculated from Eq. 3.6 and Eq. 3.9 respectively. **(b)** Maximum amplitude of the vacuum field inside the diamond calculated from Eq. 3.5. **(c)** Mode volume $V_{\mathrm{eff}}$ calculated according to Eq. 3.12. **(d)** An increase in $V_{\mathrm{eff}}$ leads to a decrease of the Purcell effect.

From the above analysis, it is apparent that in a perfect world scenario minimising $R_{\mathrm{cav}}$ is beneficial. Although it is possible to fabricate mirrors with micron-sized radii of curvature [393], the performance of these small mirrors remains uncertain. From a purely geometrical point of view, the small radii of curvature craters severely limit the cavity stability criterion, $R_{\mathrm{cav}} > L$ (compare Section 2.1.1) [93]. Furthermore, the small dimensions of the indentation may induce strain in the DBR coating during growth. A larger radius of curvature is thus beneficial to ensure a conformal $\frac{\lambda}{4}$ DBR coating. On the other hand, a large radius of curvature extends the beam waist, thus rendering the cavity sensitive to clipping losses. Nevertheless, a $\mathcal{Q}$-factor of $9 \cdot 10^6$ has been experimentally demonstrated in a Fabry-Perot microcavity with $R_{\mathrm{cav}} = 155\,\mu\mathrm{m}$ and $L \simeq 50\,\mu\mathrm{m}$ [101].

CHAPTER 4

# A Diamond-Confined Open Microcavity Featuring a High Quality-Factor and a Small Mode-Volume

**The content of this chapter is partially adapted from:**
Sigurd Flågan, Daniel Riedel, Alisa Javadi, Tomasz Jakubczyk, Patrick Maletinsky and Richard J. Warburton,
**"High quality-factor diamond-confined open microcavity"**, arXiv:2105.08736 (2021)

**Abstract:**
With a highly coherent, optically addressable electron spin, the nitrogen-vacancy (NV) centre in diamond is a promising candidate for a node in a quantum network. A resonant microcavity can boost the flux of coherent photons emerging from single NV centres. Here, we present an open Fabry-Perot microcavity geometry containing a single-crystal diamond membrane, which operates in a regime where the vacuum electric field is strongly confined to the diamond membrane. There is a field anti-node at the diamond-air interface. Despite the presence of surface losses, a finesse of $\mathcal{F} = 11\,500$ was observed. The quality ($\mathcal{Q}$) factor for the lowest mode number is 120 000; the mode volume $V$ is estimated to be $3.9\,\lambda_0^3$ where $\lambda_0$ is the free-space wavelength. We investigate the interplay between different loss mechanisms, and the impact these loss channels have on the performance of the cavity. This analysis suggests that the "waviness" (roughness with a spatial frequency comparable to that of the microcavity mode) is the mechanism preventing the $\mathcal{Q}/V$ ratio from reaching even higher values. Finally, we apply the extracted cavity parameters to the NV centre and calculate a predicted Purcell factor exceeding 150.

## 4.1 Introduction

The development of an efficient interface between stationary and flying qubits [39, 315] is an essential step towards the realisation of large-scale distributed quantum networks [16, 28] and the quantum internet [15, 17]. In such a network, quantum nodes with the ability to store and process quantum information are interconnected via quantum channels in order to distribute quantum information and entanglement across the network [29, 30]. To communicate between remote network nodes, optical photons are a convenient choice owing to low absorption and decoherence [16, 48], alongside compatibility with pre-existing classical fibre-networks [30, 49, 51]. However, the transmission of quantum information over long distances remains a challenge owing to photon propagation-loss in the network links [56, 394].

Quantum-repeater protocols represent a means to compensate for photon-loss [54]. In principle, entanglement can be distributed over long distances by pair-wise entanglement swapping of adjacent nodes, where each network link covers a sub-section of the total distance [55, 56]. These network nodes require high-fidelity processing of quantum information combined with a robust, long-lived quantum memory [30, 57, 291]. Long-lived, optically-addressable spins in the solid-state have emerged as a promising candidate [34, 39, 315]. The development of an efficient spin-photon interface [58] is limited by the weak cross-section between single spins and photons [30]. Crucially, this interaction can be enhanced by embedding the solid-state spins inside optical resonators [30, 59, 61].

Owing to its highly coherent [62, 134], optically addressable electron-spin [38, 242, 244] and the possibility of coherent couplings to nearby nuclear spins [68, 69, 72, 74, 395], the negatively charged nitrogen-vacancy (NV) centre in diamond is a promising candidate as a stationary qubit in a quantum network [63, 64]. Advances in spin-photon [41] and spin-spin entanglement [42] have paved the way for long-distance entanglement [43], quantum teleportation [396], entanglement distillation [73] and on-demand entanglement delivery [397], all key steps towards the realisation of a quantum network [66]. However, the scalability of these experiments is limited by the modest entanglement rates, in turn limited by the small flux of coherent photons [77].

For NV centres in diamond, the generation rate of coherent photons is limited by the long radiative lifetime ($\tau_0 \simeq 12\,\mathrm{ns}$) and the small branching ratio ($\sim 3\%$) of photons into the zero-phonon line (ZPL) [78]. Furthermore, the photon extraction efficiency out of the diamond is poor owing to total internal reflection at the diamond-air interface ($n_\mathrm{d} = 2.41$). In principle, these problems can be addressed by resonant coupling of the ZPL emission to photonic resonators with a high ratio of quality factor ($\mathcal{Q}$) to mode

volume $V$ [60, 77, 214]. The cavity enhances the ZPL emission on two grounds. First, the cavity provides a well-defined output mode, ideally a Gaussian, leading to improved detection efficiency [39, 255]. Secondly, utilising the Purcell effect [86], a cavity resonant with the ZPL enhances the total transition rate and likewise the proportion of the photons emitted into the ZPL [77].

Resonant enhancement of the ZPL has been demonstrated in photonic crystal cavities [82, 83, 398], hybrid- [78, 84, 217] and microring resonators [81]. While these resonators offer a large Purcell factor, the NV centres suffer from poor optical coherence, compromising the photon indistinguishability. This inhomogeneous broadening of the ZPL is a consequence of a fluctuating charge environment presumably caused by fabrication-induced surface damage [77, 214]. Increasing the quality of the crystalline environment has proven to be beneficial [158, 171, 178].

Open Fabry-Perot microcavities offer an alternative to photonic crystal cavities. The required fabrication is relatively modest: only micron-sized single-crystalline membranes of the host material are required. A reasonably small mode-volume and a high $\mathcal{Q}$-factor can be achieved. Furthermore, the Fabry-Perot cavity offers full *in situ* spatial and spectral tunability along with a Gaussian output mode [77, 255, 399]. As a consequence, open Fabry-Perot cavities offer an attractive platform to enhance the emission from various single-photon emitters embedded in solid-state hosts [77, 96, 97, 100–102, 115, 214, 400, 401].

In this work, we present a diamond membrane embedded in a Fabry-Perot microcavity operating in the so-called "diamond-confined" regime [87, 100]. In this regime, there is a vacuum-field anti-node at the diamond-air interface – the design is prone to scattering losses at this interface (Fig. 4.1). Despite this loss channel, $\mathcal{Q}$-factors of more than $10^5$ were observed for short cavity lengths at which the mode volume is $\simeq 3.9\,\lambda_0^3$ ($\lambda_0$ is the NV ZPL free-space wavelength). The high $\mathcal{Q}$-factors render the cavity very sensitive to small losses, allowing the different loss mechanisms to be quantified. The measured $\mathcal{Q}$-factor along with the low scattering-cross-section at the diamond surface lead us to predict a Purcell factor greater than 150 for the ZPL. Although the motivation behind this work is to enhance the flux of coherent photons from NV centres in diamond, the theoretical Purcell factor depends solely on the cavity parameters. Therefore, similar results would be expected for other defect centres in crystalline hosts provided the surface losses are reduced sufficiently.

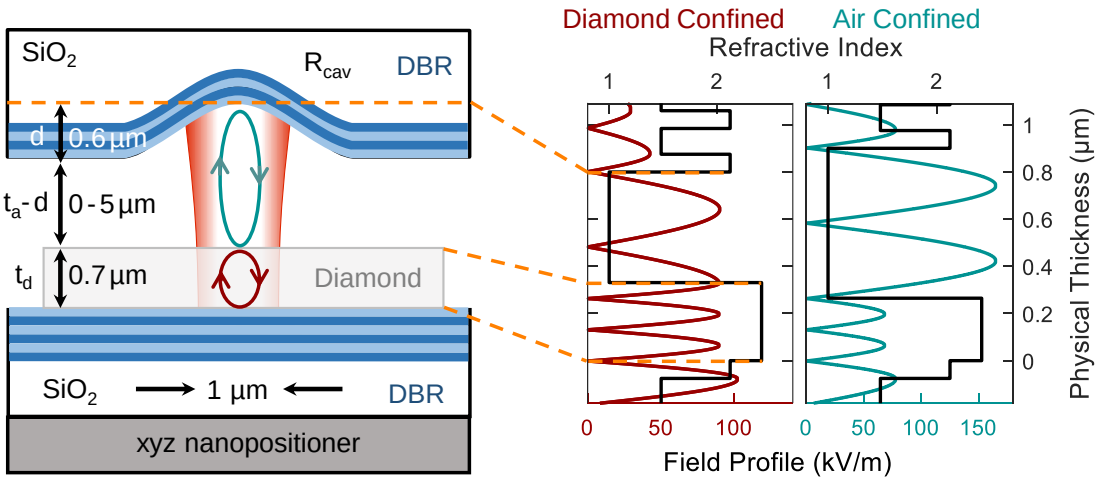


Fig. 4.1. Schematic of the diamond membrane embedded into an open Fabry-Perot cavity. In the diamond-confined regime, the vacuum electric field is strongly confined to the diamond. Furthermore, the field profile possesses an anti-node across the diamond-air interface. In the air-confined regime, there is a field node across the diamond-air interface, and the vacuum electric field is strongly confined to the air-gap.

## 4.2 Methods

At the core of this experiment is the open microcavity, depicted schematically in Fig. 4.1. The device used in this experiment is conceptually the same as the device used in Refs. [77, 255, 381]*, but uses a different combination of top and bottom mirror and a different diamond membrane. The cavity mirrors are created from a $SiO_2$ substrate, where, for the top mirror, a $CO_2$-laser ablation-technique was used to create a matrix of atomically smooth craters with a radius of curvature $R_{\mathrm{cav}} \sim 10 \ldots 30\,\mu\mathrm{m}$ [393, 402]. The profile of the crater was determined using a laser-scanning confocal-microscope image (Keyence Corporation, resolution $\sim 200\,\mathrm{nm}$), as displayed in Fig. 4.2 (a). The surface profile of the radial cross-section of the curved mirror can be described by

$$z(r) = -d \cdot \exp\left(-\frac{r^2}{2R_{\mathrm{cav}} \cdot d}\right) . \tag{4.1}$$

Fitting a truncated Gaussian (Eq. 4.1) to the surface profile yields $R_{\mathrm{cav}} = (19.7 \pm 2.5)\,\mu\mathrm{m}$ and a depth $d = 0.64\,\mu\mathrm{m}$. By comparison, a circular fit to the crater yields $R_{\mathrm{cav}} = 21\,\mu\mathrm{m}$.

After fabrication, the mirror substrates were coated with a high-reflectivity distributed-Bragg-reflector (DBR) coating (ECI evapcoat), consisting of 14 (15) $\lambda/4$

*See Chapter 5 and Chapter 6.

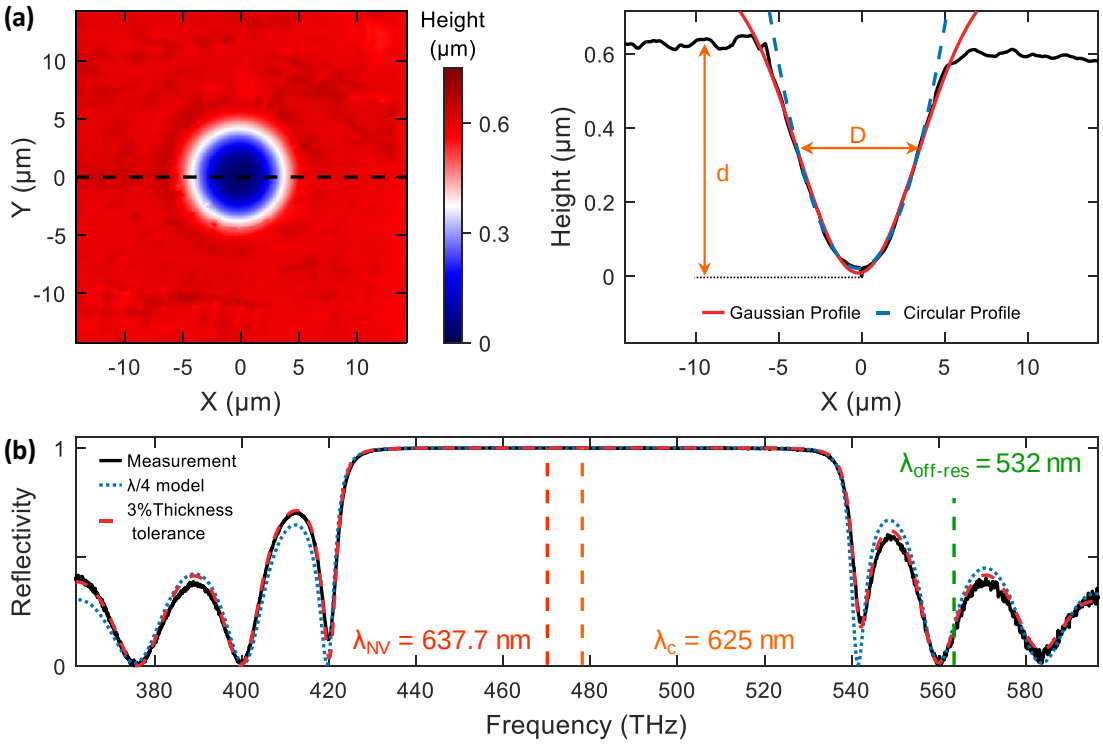


Fig. 4.2. **(a)** The left panel shows a laser-scanning confocal-microscopy image of the crater used in this experiment. The geometrical parameters of the cavity were extracted by analysing the surface profile along the axis of the crater (right panel). The radius $R_{\mathrm{cav}} = (19.7 \pm 2.5)\,\mu\mathrm{m}$ and crater depth $d = 0.64\,\mu\mathrm{m}$ were extracted from a Gaussian fit (Eq. 4.1). A circular fit yields $R_{\mathrm{cav}} = 21.8\,\mu\mathrm{m}$. **(b)** Transmission measurement of the DBR mirror using a white-light source normalised to the transmission through an uncoated $SiO_2$ chip. By fitting the reflectivity spectrum using a transfer-matrix based refinement algorithm, the stopband centre was determined to lie at $\lambda_{\mathrm{c}} = 625\,\mathrm{nm}$.

layers of $SiO_2$ ($n = 1.46$) and $Ta_2O_5$ ($n = 2.11$) for the top (bottom) mirror, respectively, supporting a target finesse $\mathcal{F} \sim 10^4$. The reflective coatings were characterised using the transmission from a white-light source, normalised to the transmission of an uncoated $SiO_2$ substrate (Fig. 4.2 (b)) [255]. Using a transfer-matrix-based calculation (Essential Macleod) we were able to reconstruct the reflective stopband based on a $\frac{\lambda}{4}$ model (blue line Fig. 4.2 (b)). By further allowing for a 3 % tolerance on each individual layer thickness, the exact mirror structure could be reconstructed (red line Fig. 4.2 (b)). From this calculation, we deduce a stopband centre of $\lambda_{\mathrm{c,bot}} = 625\,\mathrm{nm}$ for the bottom mirror. Following the same approach for the top mirror yield a stopband centre at $\lambda_{\mathrm{c,top}} = 629\,\mathrm{nm}$.

Following previously reported fabrication procedures, a diamond micro-membrane

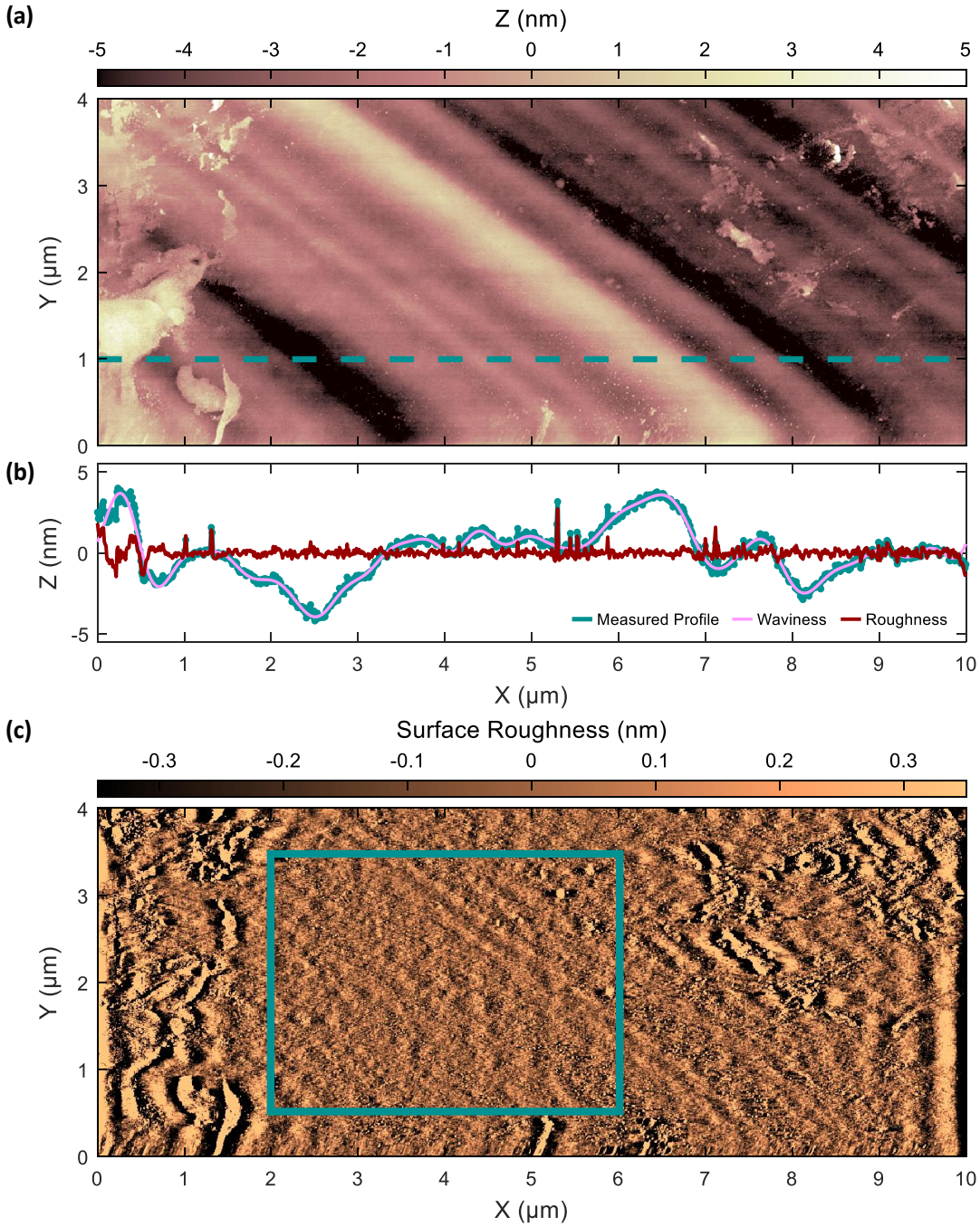


Fig. 4.3. **(a)** AFM measurement of the diamond membrane. Large-range structures attributed to polishing marks are visible. **(b)** Measured surface profile (green line) along the line-cut indicated in (a). Computing the Fourier transform of the surface profile, and removing the high-frequency components ($\xi > 2\,\mu\text{m}^{-1}$), reveals a surface waviness with RMS amplitude $W_\text{q} = 1.64\,\text{nm}$ (pink line). The red line shows the residual short-range ($\xi > 2\,\mu\text{m}^{-1}$) surface-roughness with RMS amplitude of $\sigma_\text{q} = 0.32\,\text{nm}$. **(c)** Residual surface roughness of the image in (a) computed by removing the low-frequency components. The green rectangle indicates a clean area ($4.0 \times 3.5\,\mu\text{m}^2$) with $W_\text{q} = 1.61\,\text{nm}$ and $\sigma_\text{q} = 0.31\,\text{nm}$.

with dimensions $\sim 35 \times 35 \times 0.7\,\mu m^3$ was fabricated from a 50 µm thick commercially available single-crystalline diamond (Element six) using electron-beam lithography and inductively coupled plasma etching [152, 159, 305, 403]. Post fabrication, the diamond membrane was transferred to the bottom DBR using a micro-manipulator. The small contact area, combined with a low surface roughness, facilitates bonding of the diamond membrane to the bottom mirror via van der Waals interactions [77, 255]. After transfer, the surface quality of the top-surface of the diamond membrane was investigated by atomic force microscopy (AFM) (Fig. 4.3 (a)). The surface profile (green line Fig. 4.3 (b)) is composed of large-scale (period $\sim$ µm) surface waviness, which we attribute to polishing marks, superimposed by small-scale surface roughness (period $\sim$ nm). To quantify further the diamond surface, we disentangle the surface waviness from the surface roughness by computing the Fourier transform of the measured surface profile. Here, we attribute surface features with spacial frequency $\xi \leq 2\,\mu m^{-1}$ (spatial wavelength $\lambda \geq 0.5\,\mu m$) to surface waviness, and features with $\xi > 2\,\mu m^{-1}$ to surface roughness. From this analysis, we deduce surface waviness with root-mean-square (RMS) amplitude $W_q = 1.64\,nm$ (pink line Fig. 4.3 (b)) and RMS surface-roughness of $\sigma_q = 0.32\,nm$ (red line Fig. 4.3 (b)). We next extend this analysis to the entire AFM scan. Fig. 4.3 (c) shows the residual surface roughness after removing the low-frequency components ($\xi \leq 2\,\mu m^{-1}$). The green rectangle highlight indicates a relatively large $4.0 \times 3.5\,\mu m^2$ clean area (i.e. free of dust and contaminations) with $W_q = 1.61\,nm$ and $\sigma_q = 0.31\,nm$. For comparison, the typical cavity beam waist at the diamond $w_{0,I}$ amount to $w_{0,I} \simeq (1.02 \ldots 1.22)$ µm*.

After characterisation of the DBRs and the diamond membrane, the bottom mirror was attached to the top-surface of a three-axis piezo-electric nano-positioner (attocube), and the entire piece was then mounted inside a homebuilt titanium cage (Fig. 4.4). The top mirror was glued onto a titanium holder; the holder was attached to the top of the cage with a thin layer of indium between holder and cage. The soft indium acts as an adjustable spacer allowing the relative tilt between the two mirrors to be minimised. The piezo-electric positioners allow the microcavity length and lateral position of the microcavity mode to be adjusted *in situ* [255, 385]. The cage is placed on top of a high-precision mechanical translation stage (Newport, M-562-XYZ), allowing for moving the cavity with respect to the external optics. Although all measurements in this work were carried out at room temperature, the compact design facilitates experiments in a 4 K liquid-helium bath-cryostat [77, 99, 102, 115, 399, 404].

*Calculated according to Eq. 4.10 for modes $q_{air} = 4 \ldots 10$ (Fig. 4.8 (b)).

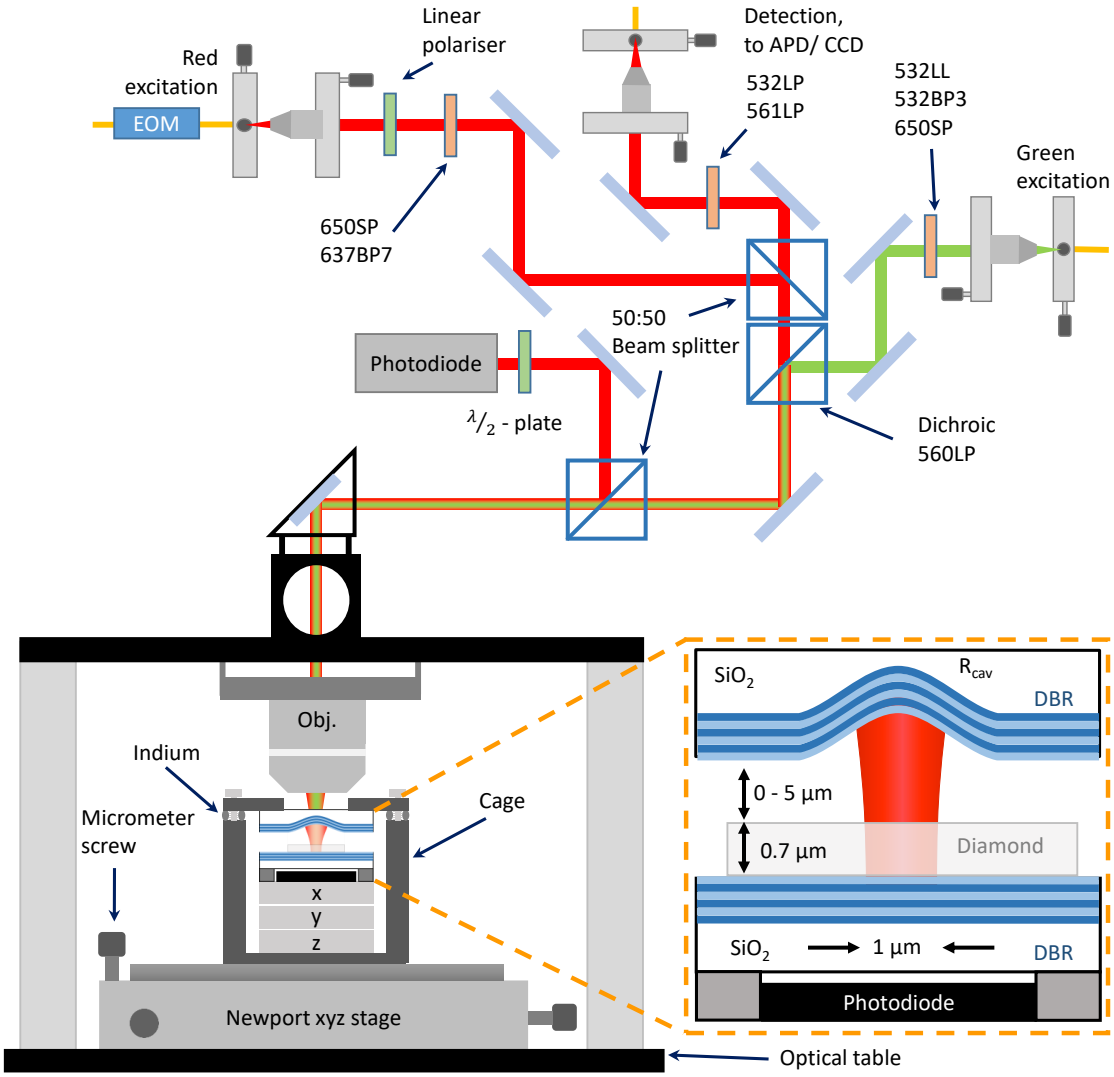


Fig. 4.4. Schematic of the experimental setup. The bottom DBR mirror is mounted on top of a set of three-axis nanopositioners and placed inside a titanium cage. The top mirror is rigidly attached to the cage, whit a thin layer of indium controlling the relative tilt angle between the mirrors. The cavity is placed on a precision mechanical stage. The excitation lasers are fibre coupled and injected via independent arms. An appropriate combination of filters fluorescence from the fibres. PL and reflected light from the cavity collected in a back-scattering geometry.

### 4.2.1 The Cavity Mode-Structure

As a first characterisation, we aim to extract the geometrical parameters of the cavity by using a simple model based on Gaussian optics [385]. The radius of curvature, $R_{\mathrm{cav}}$, of the curved mirror can be extracted by analysing the spacing between the fundamental

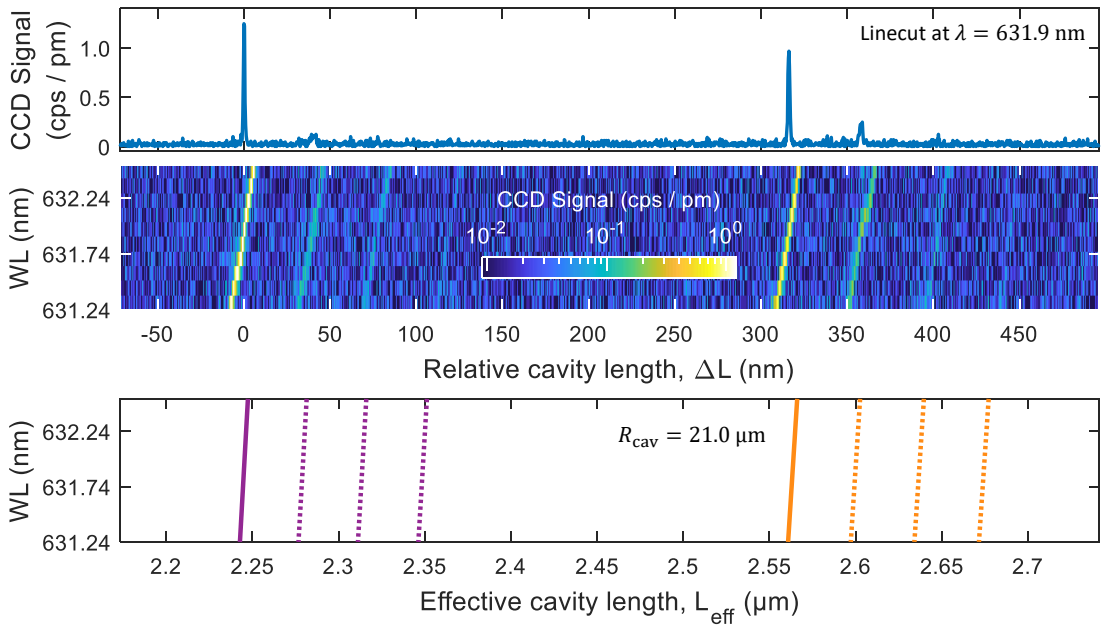


Fig. 4.5. *Centre panel:* Background PL from the diamond as a function of cavity detuning $\Delta L$ under continuous-wave green illumination ($\lambda = 532\,\mathrm{nm}$, $P = 30\,\mathrm{mW}$). The PL couple to fundamental and higher-order cavity modes. *Top panel:* linecut for $\lambda = 631.9\,\mathrm{nm}$. *Bottom panel:* Calculation of the cavity mode structure according to Eq. 4.2. The relative position and spacing of the fundamental (solid lines) and higher-order modes (dotted lines) is well reproduced using $R_{\mathrm{cav}} = 21\,\mu\mathrm{m}$.

$(q, 0, 0)$ and higher-order $(q, n, m)$ modes. The cavity length, $L_{\mathrm{eff}}$, the mode number $(q, n, m)$ and $R_{\mathrm{cav}}$ are linked via [255, 385]

$$L_{\mathrm{eff}}(q, n, m) = \left[q + \frac{n + m + 1}{\pi} \cos^{-1}\left(\sqrt{g}\right)\right] \cdot \frac{\lambda_0}{2}\,, \tag{4.2}$$

where $g = 1 - \frac{L_{\mathrm{eff}}(q,n,m)}{R_{\mathrm{cav}}}$. Here, the effective cavity length $L_{\mathrm{eff}}$ is defined as the physical separation between the two mirrors , the air-gap, plus the field penetration depth into each mirror upon reflection [94, 255].

To put photons into the cavity mode, we rely on the diamond as an internal light source [255]. We pump the diamond with a green continuous-wave laser (Laser Quantum Ventus532, $\lambda = 532\,\mathrm{nm}$, $P = 30\,\mathrm{mW}$) whose wavelength lies on the blue-side of the stopband of the DBRs (Fig. 4.2 (b)). We collect the resulting photoluminescence (PL), here background PL from the diamond, while stepwise reducing the width of the air-gap $t_{\mathrm{a}}$ by applying a positive voltage to the z-piezo (Fig. 4.5). Working in a backscattering geometry, the PL signal is coupled into a single-mode fibre (Thorlabs 630HP) and then

sent to a spectrometer (Princeton Instruments). A long-pass filter (Semrock LP03-532RS-25) and a dichroic mirror (Semrock, FF560-FDi01) are used to filter out the excitation laser from the PL signal [255].

The cavity mode structure exhibits two interesting features: a non-linear dispersion (an obvious feature in Fig. 4.6) and the presence of higher-order transverse modes (weak feature in Fig. 4.5 and Fig. 4.6). By analysing the spacing of the cavity modes according to Eq. 4.2, we extract a radius of curvature $R_{\mathrm{cav}} = 21\,\mu\mathrm{m}$ (Fig. 4.5), in good agreement with the scanning confocal-microscope image shown in Fig. 4.2 (a). We note that the detection optics were deliberately misaligned to facilitate the detection of the higher-order modes (Fig. 4.6).

The non-linear mode dispersion can be understood conceptually with a model consisting of two coupled cavities: one cavity-mode is confined to the diamond by the bottom DBR and the diamond-air interface; the other cavity mode is confined to the air-gap by the diamond-air interface and the top DBR. Across the diamond-air interface, these two cavity modes couple and hybridise, resulting in the avoided crossings depicted in the inset to Fig. 4.6 [87].

In this coupled diamond-air cavity model, the mode structure with changing air-gap $t_{\mathrm{a}}$ and the position of the avoided crossings depends on the exact diamond-thickness $t_{\mathrm{d}}$ [77, 87, 98, 123, 255, 405]. For a cavity of length $L = t_{\mathrm{a}} + t_{\mathrm{d}}$ (Fig. 4.1), fundamental resonances occur provided $t_{\mathrm{d}} n_{\mathrm{d}} + t_{\mathrm{a}} = j \cdot \frac{\lambda_0}{2}\,, j \in \mathbb{N}$. Depending on $t_{\mathrm{a,d}}$, two regimes emerge: the so-called "diamond-confined" and "air-confined" regimes [87]. For the diamond confined modes $t_{\mathrm{d}} = (2i-1) \cdot \frac{\lambda_0}{4}\,, i \in \mathbb{N}$; for the air confined modes $t_{\mathrm{d}} = i \cdot \frac{\lambda_0}{2}\,, i \in \mathbb{N}$ [85]. In the diamond confined geometry, a change in $t_{\mathrm{a}}$ has a relatively small impact on the resonant wavelength, rendering the cavity robust against acoustic vibrations. A feature of the diamond-confined modes is that the vacuum electric-field amplitude is higher in the diamond than in the air-gap (Fig. 4.1), leading to a relatively high coupling strength. However, an inevitable consequence of the diamond-confined modes is that the vacuum electric-field possesses an anti-node at the diamond-air interface [100], thus exacerbating losses associated with scattering or absorption at the diamond-air interface [255]. Conversely, in the air confined geometry, a small change in $t_{\mathrm{a}}$ has a relatively large impact on the resonant wavelength, rendering the cavity sensitive to acoustic vibrations. A feature of the air-confined modes is that the vacuum electric-field is higher in the air-gap than in the diamond, reducing the coupling strength to an NV centre in the diamond [85]. In this case, there is a node in the vacuum electric field at the diamond-air interface such that the design is relatively insensitive to losses at the diamond-air interface [255].

Using a one-dimensional transfer-matrix simulation (Essential Macleod) we simulate

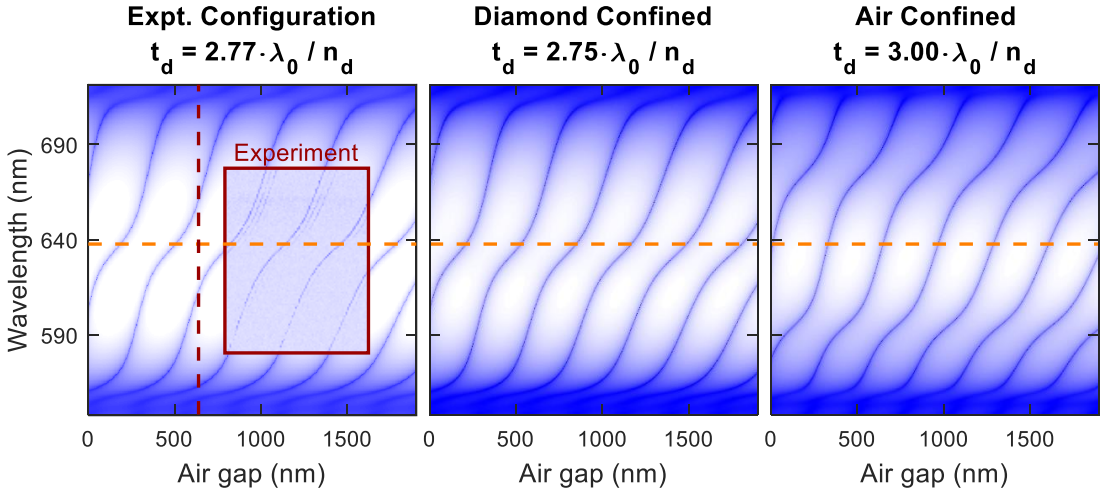


Fig. 4.6. The inset in the leftmost panel shows PL as a function of cavity length under green excitation ($\lambda = 532\,\mathrm{nm}$, $P = 30\,\mathrm{mW}$). The non-linearity of the mode dispersion depends on the exact diamond-thickness. The experimental mode-structure (background) is well reproduced using a one-dimensional transfer-matrix simulation with $t_\mathrm{d} = 733\,\mathrm{nm}$, corresponding to $t_\mathrm{d} = 2.77 \cdot \frac{\lambda_0}{n_\mathrm{d}}$ with $\lambda_0 = 637.7\,\mathrm{nm}$. The vertical red dashed line indicates the depth of the crater. The horizontal orange line indicates $\lambda_0 = 637.7\,\mathrm{nm}$. The middle and rightmost panels show similar simulations for a diamond-confined ($t_\mathrm{d} = 2.75 \cdot \frac{\lambda_0}{n_\mathrm{d}} = 727\,\mathrm{nm}$) and an air-confined ($t_\mathrm{d} = 3.00 \cdot \frac{\lambda_0}{n_\mathrm{d}} = 794\,\mathrm{nm}$) cavity, respectively. By comparison to the simulations, the geometry used in this experiment is clearly diamond-confined at the NV ZPL wavelength (orange dashed line, see main text for details).

the cavity mode-structure for different diamond thicknesses. We find an excellent agreement between the experiment (inset Fig. 4.6) and the simulation (background Fig. 4.6) for $t_\mathrm{d} = 733\,\mathrm{nm}$. In this experiment, the width of the air-gap was made reduced until the two mirrors were in contact (at which point the resonant wavelengths of the cavity no longer depend on the applied piezo voltage). By considering the depth of the crater ($d \sim 0.64\,\mu\mathrm{m}$ from Fig. 4.2 (a)), we extract a minimal mode number $q_\mathrm{air} = 3$ for the mode just out of contact. Here, $q_\mathrm{air}$ is the mode index in air, starting at $q_\mathrm{air} = 1$ for the first resonance, corresponding to $t_\mathrm{a} = 129\,\mathrm{nm}$ for $\lambda_0 = 637.7\,\mathrm{nm}$. Both $q_\mathrm{air} = 1, 2$ are inaccessible in this experiment on account of the depth of the top mirror-crater. The middle and rightmost panel in Fig. 4.6 show simulations for a diamond-confined ($t_\mathrm{d} = 2.75 \cdot \frac{\lambda_0}{n_\mathrm{d}} = 727.4\,\mathrm{nm}$) and for an air-confined ($t_\mathrm{d} = 3.00 \cdot \frac{\lambda_0}{n_\mathrm{d}} = 793.5\,\mathrm{nm}$) geometry, respectively. Here, $\lambda_0 = 637.7\,\mathrm{nm}$ corresponds to the NV ZPL and $n_\mathrm{d} = 2.41$ is the refractive index of diamond. By comparing the experimental and simulated mode-structure it is clear that at the NV ZPL wavelength, the cavity operates in a diamond-confined regime.

### 4.2.2 The Finesse and the Quality-Factor

The round-trip performance of the Fabry-Perot cavity is characterised by the finesse $\mathcal{F}$ defined as [90, 104, 106]

$$\mathcal{F} = \frac{2\pi}{\mathcal{L}_{\text{tot}}}\,, \tag{4.3}$$

where $\mathcal{L}_{\text{tot}} = \mathcal{T}_{\text{t}} + \mathcal{T}_{\text{b}} + \mathcal{L}_{\text{cav}}$ is the fractional energy loss per round-trip. Here, $\mathcal{T}_{\text{t(b)}}$ is the transmission of the top (bottom) mirror and $\mathcal{L}_{\text{cav}}$ is the cavity round-trip-loss caused by additional loss mechanisms such as scattering or absorption. A reliable measurement of the finesse typically requires precise knowledge of the cavity linewidth over several free-spectral ranges (FSR). Such an experiment becomes impractical for high $\mathcal{F}$-values – it requires a high dynamic-range. Conversely, a measurement of the $\mathcal{Q}$-factor, $\mathcal{Q} = \frac{\nu}{\delta\nu}$, requires knowledge of the linewidth $\delta\nu$ for one cavity-mode only, a simpler experiment. For a cavity with perfect mirrors, the $\mathcal{Q}$-factor is linked to the finesse via

$$\mathcal{Q} = \frac{2L_{\text{cav}}}{\lambda} \cdot \mathcal{F}\,. \tag{4.4}$$

In the experiment, we tune the thickness of the air-gap $t_{\text{a}}$; $t_{\text{d}}$ remains constant. For fixed $\lambda$, provided the field penetrations into the mirrors remain constant, we write $L_{\text{cav}} = t_{\text{a}} + L_0$, where $t_{\text{a}} = q_{\text{air}} \cdot \frac{\lambda}{2}$. Here, $t_{\text{d}}$ and the field penetration into the mirrors are included in $L_0$. Thus, Eq. 4.4 reduces to [406]

$$\mathcal{Q} = q_{\text{air}} \cdot \mathcal{F} + \mathcal{Q}_0\,. \tag{4.5}$$

In other words, a measurement of the $\mathcal{Q}$-factor for subsequent modes ($q_{\text{air}}$ and $q_{\text{air}} + 1$) determines the cavity finesse.

### 4.2.3 Extracting the Cavity Linewidth

To determine the cavity linewidth $\delta\nu$, and thus the $\mathcal{Q}$-factor, we couple the output of a tunable diode-laser (Toptica DL Pro 635, $\lambda = 630 \ldots 640\,\text{nm}$ and $\delta\nu \lesssim 500\,\text{kHz}$, $P = 800\,\mu\text{W}$) into the cavity. Keeping the excitation frequency $\nu_{\text{laser}}$ fixed, we tune the cavity length across the cavity resonance while monitoring the reflected signal using a photodiode and a fast oscilloscope (LeCroy WaveRunner 606Zi). To calibrate the displacement of the piezo, and thus extract the cavity linewidth, we use an electro-optic modulator (EOM, Jenoptik PM635) to create laser side-bands at $\nu_{\text{laser}} \pm 5\,\text{GHz}$ [405].

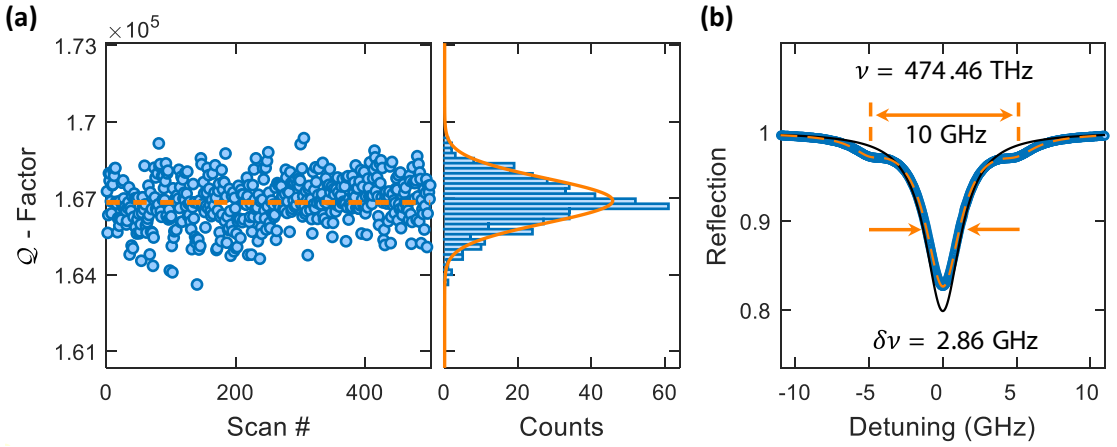


Fig. 4.7. **(a)** Spread of 500 individual $\mathcal{Q}$-factor measurements on the diamond for mode $q_{\text{air}} = 8$. The data follow a Gaussian distribution centred at $\mathcal{Q} = 166\,900$ with a standard deviation $\sigma = 870$. **(b)** Reflection of the cavity as a function of cavity detuning for $\lambda = 631.9\,\text{nm}$. The blue data-points are the average of all the 500 scans displayed in panel (a). The red line shows a triple Lorentzian-fit, where the side-peaks at $\nu_{\text{laser}} \pm 5\,\text{GHz}$ results from a frequency modulation which is employed as a frequency ruler. The black line is the reflected signal without any frequency modulation.

Here, we assume a linear behaviour of cavity length with piezo-voltage across the 10 GHz bandwidth (corresponding to a change in air-gap, $\Delta t_{\text{a}} = 0.056\,\text{nm}$). To extract reliably the cavity linewidth, the cavity is scanned across the resonance 500 times, each scan fitted independently with the sum of three Lorentzians. The $\mathcal{Q}$-factor is defined as the average value of all 500 scans. Fig. 4.7 (a) shows the spread of the individually extracted $\mathcal{Q}$-factors for mode number $q_{\text{air}} = 8$. Using a bin-size of 200 for the values of $\mathcal{Q}$, the data follow a Gaussian centred around $\mathcal{Q} = 166\,900$ with standard deviation $\sigma = 870$. The blue line in Fig. 4.7 (b) shows the average reflectivity data of all the 500 scans. Fitting a triple Lorentzian (orange line) yields an averaged cavity linewidth of $\delta\nu_{\text{avg}} = 2.86\,\text{GHz}$, which gives $\mathcal{Q}_{\text{avg}} = 165\,650$, in good agreement with the average of the individual scans.

We present some details of the experiment – a schematic of the experimental setup is shown in Fig. 4.4. The linearly polarised red excitation-laser was passed through a $\lambda/2$-plate (B. Halle) before entering the cavity. A pellicle beam-splitter (Thorlabs BP145B1) was used to separate the reflected signal from the incident laser-beam. A linear polariser was used to isolate one of the two orthogonally-polarised cavity-modes in the reflected signal. (The mode-splitting arises either from a geometrical asymmetry of the curved mirror [407, 408] or from birefringence in the material comprising the cavity [409, 410]). The cavity was scanned at a typical speed of 8.7 µm/s (1.56 GHz/s). In the bare cavity, i.e. in a cavity without diamond membrane, for slow scanning speeds

($\lesssim$ 3GHz/s) evidence of photothermal bistability [104, 411] was observed. The origin of this effect is likely the weak absorption in the mirror coating on the order of 100 ppb [412]. However, as these losses are negligible compared to the losses introduced by the diamond, the bistability was not investigated further. We note that photothermal bistability was not observed once the diamond membrane was included in the cavity.

## 4.3 Results on $\mathcal{Q}$-Factor

### 4.3.1 Bare Cavity

In order to test our understanding of the mirrors themselves, we characterise initially the $\mathcal{Q}$-factor of the bare cavity, i.e. a cavity without a diamond membrane. Fig. 4.8 (a) shows the behaviour of the $\mathcal{Q}$-factor as a function of increasing mode number $q_{\mathrm{air}}$ for fixed $\lambda = 631.9\,\mathrm{nm}$. We observe a linear increase in $\mathcal{Q}$-factor for $q_{\mathrm{air}} \leq 7$ as predicted by Eq. 4.5. We attribute the drop in $\mathcal{Q}$-factor for $q_{\mathrm{air}} > 8$ to clipping losses at the top mirror [104]. Performing a linear fit for $q_{\mathrm{air}} < 8$ yields a bare-cavity finesse $\mathcal{F}^{\mathrm{exp}}_{\mathrm{bare}} = 42\,500 \pm 4\,200$. The simulations predict $\mathcal{F}^{\mathrm{sim}}_{\mathrm{bare}} = 44\,410$, in agreement with the experimental result to within the measurement uncertainty.

Next, we attempt to describe the dependence of the $\mathcal{Q}$-factor of the bare cavity on mode number $q_{\mathrm{air}}$. Upon changing the cavity length $L$, the intensity beam waist at the curved mirror $w_{\mathrm{I}}$ evolves according to [93]

$$w_{\mathrm{I}} = \sqrt{\frac{\lambda R_{\mathrm{cav}}}{\pi}} \cdot \left(\frac{R_{\mathrm{cav}}}{L} - 1\right)^{-\frac{1}{4}} . \tag{4.6}$$

Clipping losses occur when this beam waist becomes larger than the spherical extent of the curved top-mirror [104, 105, 123]. In principle, a small tilt-angle $\theta$ between the two mirrors will exacerbate clipping [413]. From a Gaussian optics approach [390], we derive a model to estimate the clipping losses*

$$\tilde{\mathcal{L}}_{\mathrm{clip}} = e^{-\frac{D^2}{2w_{\mathrm{I}}^2}} \left[1 + \left(\frac{aD}{w_{\mathrm{I}}^2}\right)^2\right] , \tag{4.7}$$

where $a = R_{\mathrm{cav}}\theta$ and $D$ is the diameter of the spherical extent of the mirror. In this model, the first term accounts for clipping [104, 123, 390] while the second term is a correction factor accounting for the tilt by angle $\theta$. In this model, the tilt results in a

*The full derivation can be found in Appendix B.

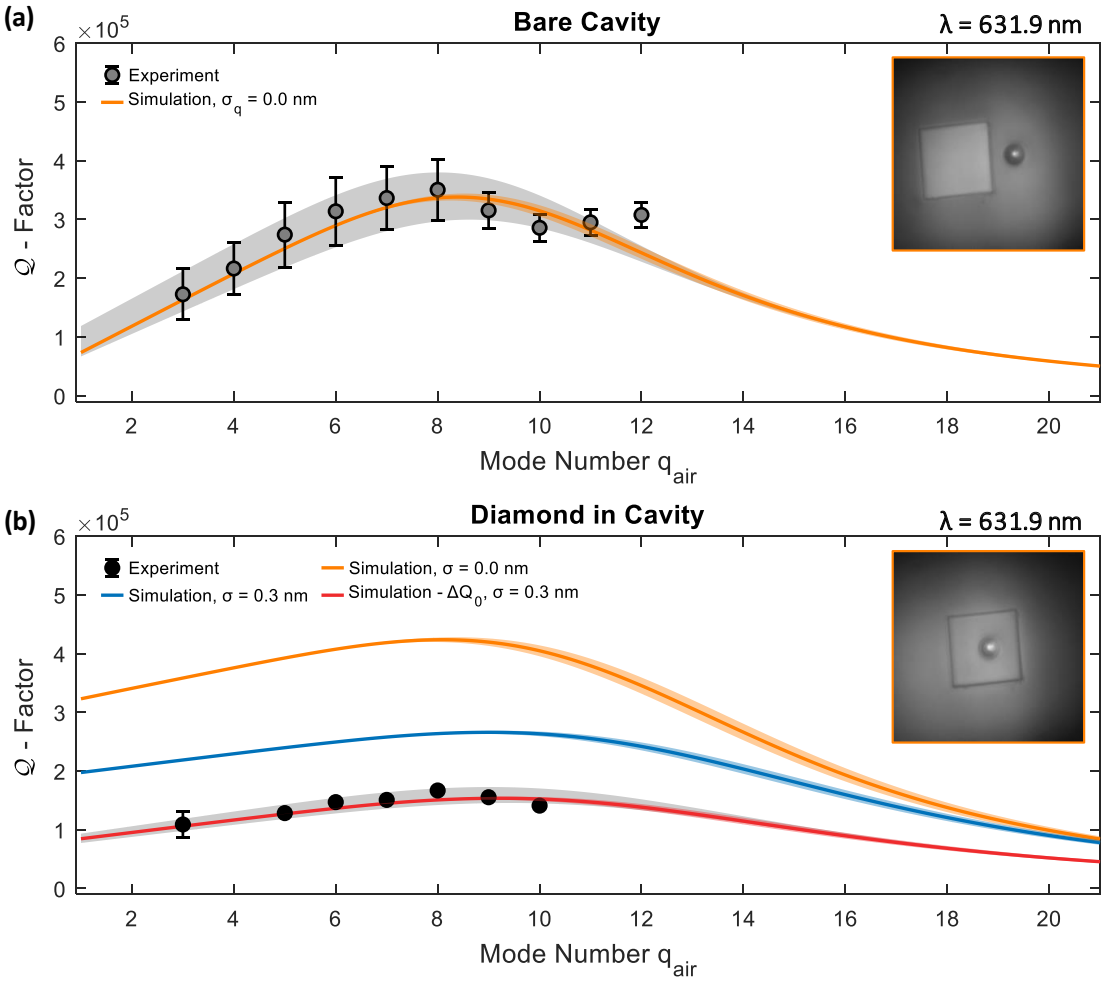


Fig. 4.8. **(a)** In black, the behaviour of the $\mathcal{Q}$-factor with increasing mode number $q_{\mathrm{air}}$ for the bare cavity. The $\mathcal{Q}$-factor increases linearly for $q_{\mathrm{air}} \leq 8$, after which clipping starts to occur. The orange line is the calculated $\mathcal{Q}$-factor using a 1D transfer-matrix model. **(b)** Introducing the diamond into the cavity reduces the $\mathcal{Q}$-factor (black data-points). Calculating the theoretical $\mathcal{Q}$-factor using a lossless model (orange) and scattering with surface roughness $\sigma_{\mathrm{q}} = 0.3\,\mathrm{nm}$ (blue) fail to reproduce the experimental values. The red line represents $\mathcal{Q}^{\mathrm{sim}} - \Delta\mathcal{Q}_0$ with $\Delta\mathcal{Q}_0 = 114\,000$, and describes the experiment well. For both panels, the black shaded regions account for the uncertainty in the fit parameters, while for the simulations, the shaded regions account for the uncertainty in the extracted tilt angle. For details see main text.

small lateral displacement of the cavity mode thereby increasing the clipping loss. Using the exact mirror-design obtained from Fig. 4.2 (b), we simulate the behaviour of the cavity using a lossless 1D transfer-matrix simulation (Essential Macleod). The clipping

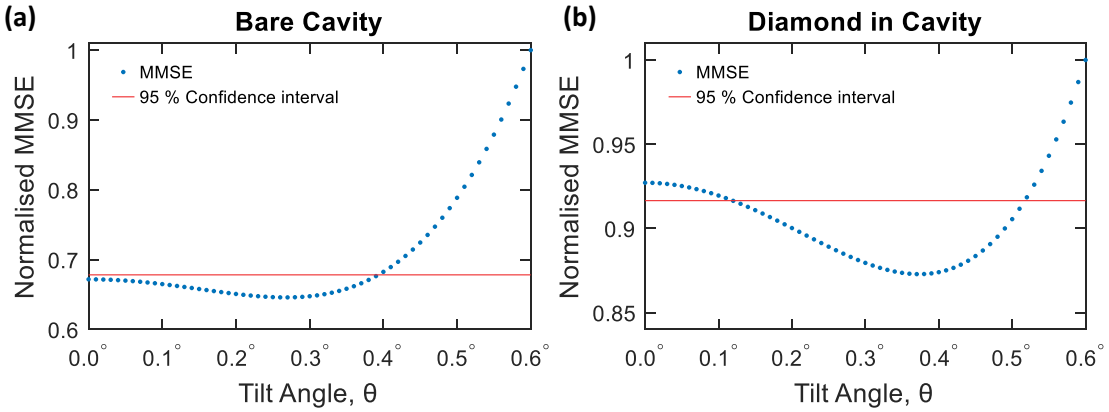


Fig. 4.9. **(a)** Extracting the relative tilt angle $\theta_{\text{bare}} = 0.27$ from a minimum mean-square (MMSE) analysis using Eq. 4.7 for the bare cavity. The red line indicates the 95% confidence interval, and gives a maximum tilt-angle of 0.33°. **(b)** A similar MMSE analysis on the diamond yields $\theta_{\text{d}} = \left(0.37^{+0.15}_{-0.26}\right)^{\circ}$, where the upper and lower limits are calculated from the 95% confidence interval.

losses are incorporated into the model according to*

$$\mathcal{Q}_{\text{sim}} = \frac{4\pi L_{\text{cav}}}{\lambda} \cdot \left( \frac{1}{\mathcal{L}_{\text{sim}} + \mathcal{L}_{\text{clip}}} \right) . \tag{4.8}$$

To quantify the clipping losses, we perform a minimum mean-square error (MMSE) analysis, and find an excellent agreement using $D = 5.9\,\mu\text{m}$ and $\theta_{\text{bare}} = 0 \ldots 0.27^{\circ}$ (Fig. 4.9 (a)). Including a 95% confidence interval yields a maximum tilt-angle of 0.33°. The value of $D$ is in good accordance with the scanning confocal-image displayed in Fig.4.2 (a). The agreement between experiment and simulation indicates that intrinsic losses in the mirrors are negligibly small compared to losses introduced by the diamond, as discussed below.

### 4.3.2 Diamond Membrane in the Cavity

Having established the intrinsic losses in the mirrors themselves, we introduce next the diamond membrane into the cavity by moving the bottom DBR in a lateral direction. Compared to the bare cavity, we observe a reduction in both $\mathcal{Q}$-factor and finesse (smaller $\frac{\Delta \mathcal{Q}}{\Delta q_{\text{air}}}$) with respect to the simulation, (Fig. 4.8 (b)). Conceptually, the diamond effectively reduces the reflectivity of the bottom DBR, thus leading to a drop in the finesse (Eq. 4.3). Performing a linear fit for $q_{\text{air}} < 8$ yields $\mathcal{F}^{\text{exp}}_{\text{diamond}} = 11\,500 \pm 1\,100$. As before, we observe clipping for $q_{\text{air}} > 8$. To quantify the clipping loss, we replace $L$ in Eq. 4.10 by

*This is derived in Appendix C.

$L_{\mathrm{cav}}^{\mathrm{d}} = t_{\mathrm{a}} + \frac{t_{\mathrm{d}}}{n_{\mathrm{d}}}$ [123] and apply Eq. 4.7 with $D = 5.9\,\mu\mathrm{m}$. From a MMSE analysis, we calculate $\theta_{\mathrm{d}} = \left(0.37^{+0.15}_{-0.26}\right)^{\circ}$, where the high- and low limits are calculated from the 95% confidence interval. The larger tilt angle might suggest a small thickness-gradient in the diamond membrane [381].

Contrary to the bare-cavity case, a simulation using a lossless model (orange curve Fig. 4.8 (b)) fails to reproduce the experimental $\mathcal{Q}$-factors: the diamond membrane introduces additional loss mechanisms. Both the simulated $\mathcal{Q}$-factor and the finesse ($\mathcal{F}_{\mathrm{perfect}}^{\mathrm{sim}} = 17\,450$) are larger than observed experimentally. We therefore need to introduce additional losses into our model. Working in a diamond-confined regime, we expect these losses to occur at the diamond-air interface.

We investigate the role of scattering at the diamond-air interface. To this end, we introduce a roughness of $\sigma_{\mathrm{q}} = 0.3\,\mathrm{nm}$ at the diamond-air interface into the simulation [389]. The choice of $\sigma_{\mathrm{q}}$ is motivated by the AFM measurement displayed in Fig. 4.3 and from previously reported measurements [77, 159, 255, 403]. The blue line in Fig. 4.8 (b) shows that scattering reduces both the $\mathcal{Q}$-factor and the finesse ($\mathcal{F}_{\mathrm{scat}}^{\mathrm{sim}} = 10\,690$). Interestingly, we now observe that the simulated finesse, $\mathcal{F}_{\mathrm{scat}}^{\mathrm{sim}}$ is in good accordance with the experimentally determined finesse $\mathcal{F}^{\mathrm{exp}}$ (equal $\frac{\Delta\mathcal{Q}}{\Delta q_{\mathrm{air}}}$ in Fig. 4.8 (b)), while the simulated $\mathcal{Q}$-factor is larger than the experimentally determined value. We rewrite Eq. 4.5

$$\mathcal{Q}^{\mathrm{exp}} = \mathcal{Q}^{\mathrm{sim}} - \Delta\mathcal{Q}_0\,. \tag{4.9}$$

This pragmatic approach gives an accurate representation of the experiment (red line in Fig. 4.8 (b)) with $\Delta\mathcal{Q}_0 = 114\,000$.

We now aim to understand the origin of the losses introduced by the diamond, in particular the origin of the rigid reduction in $\mathcal{Q}$-factor described by the $\Delta\mathcal{Q}_0$-term. By measuring successive cavity modes for fixed $\lambda$ and assuming a Gaussian cavity mode, the beam waist at the bottom mirror evolves according to [123]

$$w_{0,\mathrm{I}} = \sqrt{\frac{\lambda}{\pi}}\left(LR_{\mathrm{cav}} - L^2\right)^{1/4}\,, \tag{4.10}$$

where $L = t_{\mathrm{a}} + \frac{t_{\mathrm{d}}}{n_{\mathrm{d}}}$, thus probing a slightly larger surface area of the diamond [93]. However, the standing-wave pattern at the diamond-air interface remains unaltered. Alternatively, changing the resonant $\lambda$ changes the standing wave inside the cavity. As scattering and absorption depend on the amplitude of the electric field, tuning the field maxima across the diamond-air interface may reveal the source of surface loss [391].

To this end, we measure the dependence of the $\mathcal{Q}$-factor on excitation wavelength $\lambda$ for

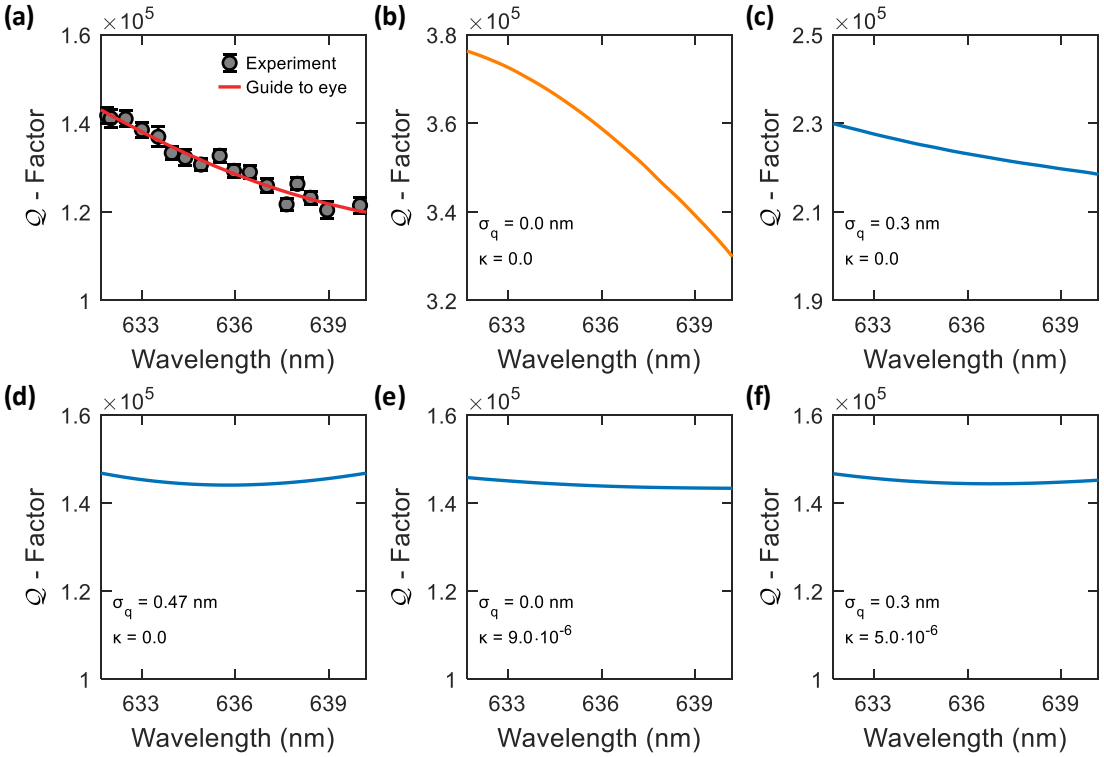


Fig. 4.10. **(a)** The measured $\mathcal{Q}$-factor as a function of wavelength for $q_{\mathrm{air}} = 4$. The $\mathcal{Q}$-factor drops for excitation wavelengths away from the stopband centre. The red line is a guide to the eye. **(b)** A calculation of the wavelength dependence of the $\mathcal{Q}$-factor for a lossless cavity. **(c)** Introducing scattering with surface roughness $\sigma_{\mathrm{q}} = 0.3\,\mathrm{nm}$ reproduces the general behaviour of the experiment, but not the absolute numbers. **(d)-(f)** Calculations of the $\mathcal{Q}$-factor with increased surface scattering ($\sigma_{\mathrm{q}}$) and absorption ($\kappa$).

mode $q_{\mathrm{air}} = 4$ (Fig. 4.10 (a)). We observe a drop in $\mathcal{Q}$-factor for wavelengths away from the stopband centre ($\lambda_{\mathrm{c}} = 625\,\mathrm{nm}$, Fig. 4.2 (b)). As before, a lossless model (Fig. 4.10 (b)) fails to reproduce the absolute value of the $\mathcal{Q}$-factor as well as the dependence on $\lambda$.

We consider enhanced diamond-related losses, surface scattering and absorption in the diamond itself, as the origin of $\Delta\mathcal{Q}_0$. In Fig. 4.10 (d) we increase the surface roughness to $\sigma_{\mathrm{q}} = 0.47\,\mathrm{nm}$. Next, in Fig. 4.10 (e) we include absorption in the diamond by varying the value of the extinction coefficient $\kappa$ [389]. Finally, in Fig. 4.10 (f) we combine surface scattering ($\sigma_{\mathrm{q}} = 0.3\,\mathrm{nm}$) with absorption ($\kappa = 5.6 \cdot 10^{-6}$). All three simulations accurately account for the $\mathcal{Q}$-factor at short $\lambda$. However, the simulations fail to reproduce the behaviour with increasing $\lambda$. The simulations predict a minimum $\mathcal{Q}$-factor for $\lambda \sim 636\,\mathrm{nm}$ beyond which an increase in $\mathcal{Q}$-factor is predicted, a feature not observed experimentally where the $\mathcal{Q}$-factor monotonically decreases for longer wavelengths. It

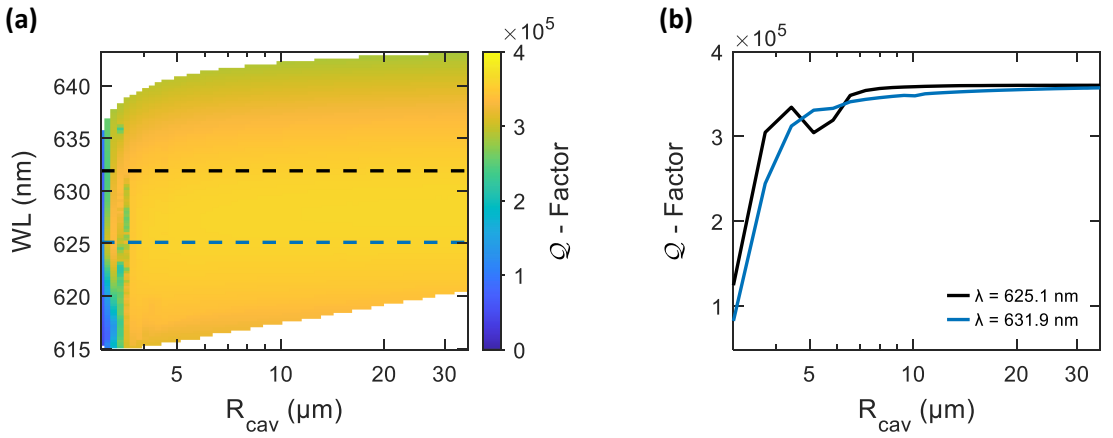


Fig. 4.11. **(a)** Calculated $\mathcal{Q}$-factor as a function of wavelength and radius of curvature $R_{\mathrm{cav}}$ for $t_{\mathrm{d}} = 733\,\mathrm{nm}$ and $q_{\mathrm{air}} = 4$. **(b)** The blue and black lines show the $\mathcal{Q}$-factor at the stopband centre ($\lambda_{\mathrm{c}} = 625\,\mathrm{nm}$) and for $\lambda = 631.9\,\mathrm{nm}$, respectively. The significant drop in $\mathcal{Q}$-factor for $R_{\mathrm{cav}} \lesssim 5-7\,\mu\mathrm{m}$ is attributed to clipping losses at the top mirror.

would appear therefore that a combination of surface roughness and absorption cannot be responsible for $\Delta\mathcal{Q}_0$. Furthermore, significant absorption in the diamond is unlikely – it results in a weak dependence of the $\mathcal{Q}$-factor on wavelength, yet in the experiments there is a strong wavelength dependence.

Another factor to consider are diffraction losses. Up until this point, only one-dimensional transfer-matrix simulations were performed; these simulations do not consider any diffraction loss at the top DBR. In addition, for tightly confined modes, the angular spread in $k$-space increases, leading to an increased loss in the DBR mirror and thus a reduction in $\mathcal{Q}$-factor [102]. To investigate this, we perform numerical simulations (COMSOL Multiphysics) of the $\mathcal{Q}$-factor as a function of $R_{\mathrm{cav}}$ and $\lambda$ (Fig. 4.11 (a)). For fixed $\lambda$ (Fig. 4.11 (b)), we observe a strong dependence of $\mathcal{Q}$-factor with radius for $R_{\mathrm{cav}} \lesssim 5-7\,\mu\mathrm{m}$. For larger radii, this dependence is weak, and the $\mathcal{Q}$-factor saturates at $\mathcal{Q} = 360\,000$ in good agreement with the one-dimensional transfer-matrix simulations. We therefore conclude that diffraction losses at the top mirror are negligible, that the one-dimensional simulations provide reliable predictions even of the behaviour of the three-dimensional cavity, and that diffraction is not responsible for $\Delta\mathcal{Q}_0$.

Based on this understanding, we simulate the cavity $\mathcal{Q}$-factor by including a scattering layer at the diamond-air interface with $\sigma_{\mathrm{q}} = 0.3\,\mathrm{nm}$ (Fig. 4.10 (c)), taking the absorption in the diamond and likewise any diffraction losses to be negligibly small. This approach reproduces the experimentally observed decrease of the $\mathcal{Q}$-factor with $\lambda$.

This analysis suggests that close to the stopband centre, scattering at the diamond-air

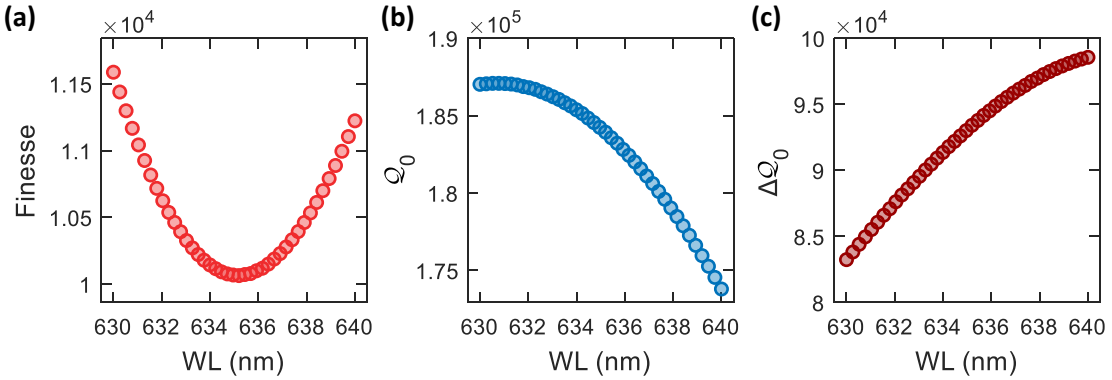


Fig. 4.12. **(a)** Simulated finesse $\mathcal{F}$ as a function wavelength $\lambda$ for $t_\mathrm{d} = 733\,\mathrm{nm}$ with $\sigma_\mathrm{q} = 0.3\,\mathrm{nm}$. The electric field anti-node across the diamond-air interface minimises the finesse for $\lambda \simeq 635\,\mathrm{nm}$. For $\lambda$ away from 635 nm, the vacuum electric field amplitude decreases, leading to less scattering and a larger finesse. **(b)** Simulated $\mathcal{Q}_0$ as a function of $\lambda$. **(c)** By assuming $\mathcal{F}_\mathrm{scat}^\mathrm{sim} \simeq \mathcal{F}^\mathrm{exp}$ for all $\lambda$ leads to a 15 % monotonic increase in $\Delta\mathcal{Q}_0$.

interface reduces the $\mathcal{Q}$-factor from an ideal value of 375 540 to 229 330. An additional loss mechanism, which results in the $\Delta\mathcal{Q}_0$-term, reduces the $\mathcal{Q}$-factor further to a value of 141 100. We note that if we assume that the experimental finesse matches the simulated finesse at all wavelengths then $\Delta\mathcal{Q}_0$ has a small wavelength dependence, increasing monotonically by about 15% from $\lambda = 630\,\mathrm{nm}$ to $\lambda = 640\,\mathrm{nm}$ (Fig. 4.12).

The microscopic origin of the $\Delta\mathcal{Q}_0$-term is not known precisely. We speculate that it arises as a consequence of the waviness in the profile of the diamond surface (Fig. 4.3). The spatial frequency of the waviness is comparable to that of the cavity mode – the waviness does not scatter in the same way as the surface roughness. Compatible with this hypothesis is the observation that the $\mathcal{Q}$-factor is position-dependent: the measured $\mathcal{Q}$-factor was rather low at certain locations of the diamond membrane. In a perturbation picture [88, 90] the waviness mixes the fundamental mode with modes at higher frequencies. The waviness has a small spatial frequency such that it may tend to ad mix lossy higher lateral modes*. It is an open question how the waviness might result in a rigid reduction of the $\mathcal{Q}$-factor according to Eq. 4.9.

## 4.4 Prediction on the Purcell Factor

Improvements in the optical properties of an NV centre in a resonant microcavity depend on the Purcell factor [86]. Based on the experimental results, we investigate the potential

*A toy model describing this mode mixing is presented in Appendix D.

Purcell factors in a cavity of this type. To do this, we make the assumptions that better fabrication can eliminate the losses implied in the $\Delta\mathcal{Q}_0$-term; that the surface roughness of $\sigma_\mathrm{q} = 0.3\,\mathrm{nm}$ is already excellent – some surface scattering is therefore inevitable; and that the absorption losses in the diamond are negligible; and that we work with the mirrors from the experiment with their slight imperfections.

We need to consider the vacuum-field standing wave inside he cavity. Fig. 4.13 (a) shows the profile of the vacuum electric-field for a diamond-confined ($t_\mathrm{d} = 2.75 \cdot \frac{\lambda_0}{n_\mathrm{d}}$) and air-confined ($t_\mathrm{d} = 3.00 \cdot \frac{\lambda_0}{n_\mathrm{d}}$) cavity, respectively. Here, $\lambda_0 = 637.7\,\mathrm{nm}$. For the diamond-confined geometry, there is a field maximum at the diamond-air interface. Surface scattering depends on the amplitude of the electric field, thus, for $\lambda = 637.7\,\mathrm{nm}$ scattering is maximised resulting in a minimum $\mathcal{Q}$-factor. For $\lambda$ away from 637 nm, the field amplitude goes down, thus the losses are reduced and the $\mathcal{Q}$-factor goes up. Fig. 4.13 (b) and (c) show the calculated behaviour of the $\mathcal{Q}$-factor over a large range of $\lambda$ for a diamond- and air-confined geometry, respectively. Introducing scattering reduces the $\mathcal{Q}$-factor significantly for the diamond-confined geometry, while for the air-confined geometry, the $\mathcal{Q}$-factor remains relatively unaltered.

We calculate the expected Purcell factor [86] for our device. To start, we simulate the vacuum electric-field distribution for a one-dimensional cavity using the same transfer-matrix algorithm used to simulate the $\mathcal{Q}$-factor (Essential Macleod). For a Gaussian cavity-mode, the vacuum electric-field is quantised according to [255]

$$\begin{aligned}\int_\mathrm{cav} \epsilon_0\epsilon_\mathrm{R}(z)|\vec{E}_\mathrm{vac}(z)|^2\mathrm{d}z \int_0^{2\pi}\mathrm{d}\phi \int_0^\infty re^{-r^2/2w_\mathrm{I}^2}\mathrm{d}r \\ = 2\pi\cdot\frac{1}{4}w_\mathrm{I}^2\int_\mathrm{cav}\epsilon_0 n^2(z)|\vec{E}_\mathrm{vac}(z)|^2\mathrm{d}z = \frac{\hbar\omega}{2}\,.\end{aligned} \tag{4.11}$$

Here, we take $\epsilon_\mathrm{R} = n_\mathrm{d}^2$ and assume a constant beam waist $w_{0,\mathrm{d}} \simeq 1.0\,\mu\mathrm{m}$ ($q_\mathrm{air} = 4$) along the length of the cavity, calculated from Eq. 4.10. Inside the diamond, we obtain a maximum $|\vec{E}_\mathrm{vac}| = 54.73\,\mathrm{kVm}^{-1}$. For an emitter located at $\vec{r} = \vec{r}_0$, the effective mode-volume is calculated according to [124, 414]

$$\begin{aligned}V_\mathrm{eff} &= \frac{\int_\mathrm{cav}\epsilon_0\epsilon_\mathrm{R}(\vec{r})|\vec{E}_\mathrm{vac}(\vec{r})|^2\mathrm{d}^3r}{\epsilon_0\epsilon_\mathrm{R}(\vec{r}_0)|\vec{E}_\mathrm{vac}(\vec{r}_0)|^2} \\ &= \frac{\hbar\omega/2}{\epsilon_0\epsilon_\mathrm{R}(\vec{r}_0)|\vec{E}_\mathrm{vac}(\vec{r}_0)|^2}\,.\end{aligned} \tag{4.12}$$

Numerically, we obtain $V_\mathrm{eff} = 54.17\cdot\left(\frac{\lambda_0}{n_\mathrm{d}}\right)^3$. For the experimental geometry,

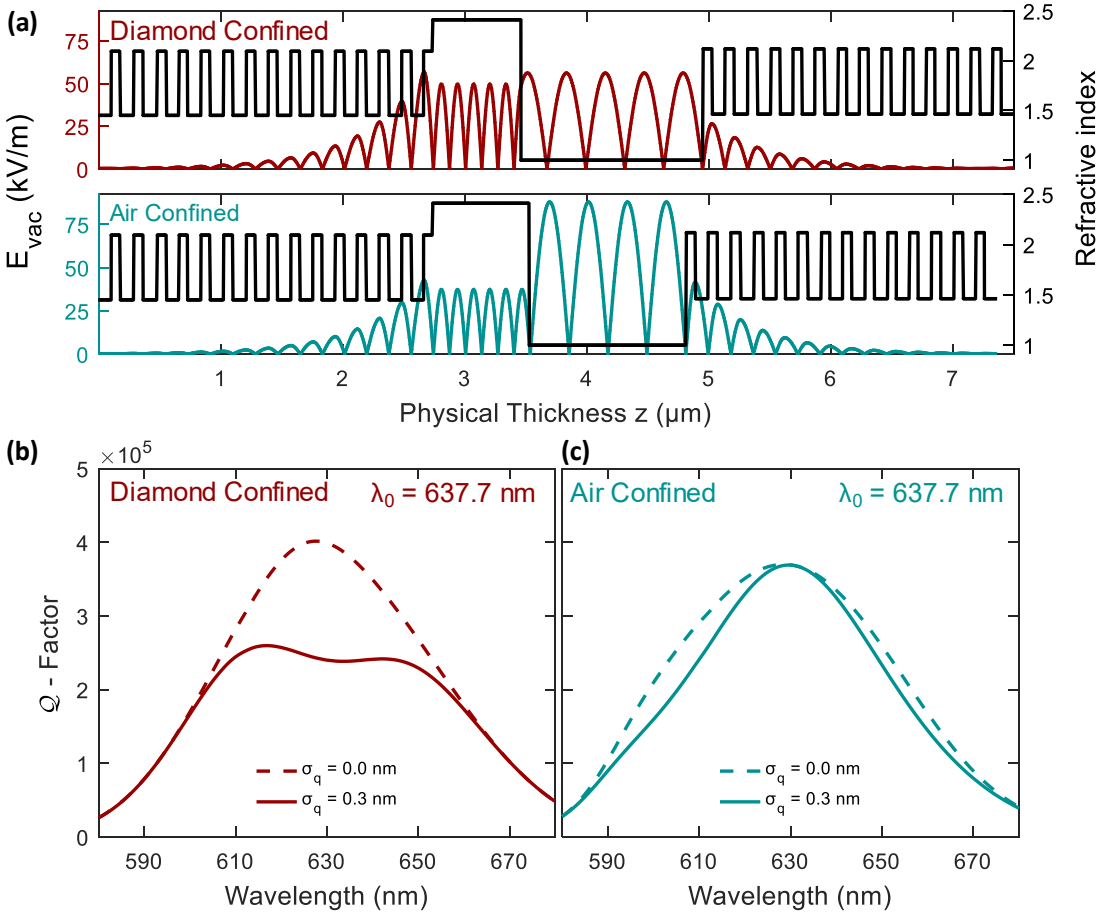


Fig. 4.13. **(a)** The vacuum electric-field distribution for a diamond-confined (top, $t_\mathrm{d} = 2.75 \cdot \frac{\lambda_0}{n_\mathrm{d}} = 727\,\mathrm{nm}$) and air-confined (bottom, $t_\mathrm{d} = 3.00 \cdot \frac{\lambda_0}{n_\mathrm{d}} = 794\,\mathrm{nm}$) geometry obtained from a one-dimensional transfer-matrix simulation using the mirror design extracted from Fig. 4.2 (b). The diamond-confined case exhibits a field anti-node at the diamond-air interface, while the air-confined geometry exhibits a field node at the diamond-air interface. **(b)-(c)** Simulation of the $\mathcal{Q}$-factor as a function of wavelength for diamond-confined (b) and air-confined (c) geometries. Introducing surface scattering with $\sigma_\mathrm{q} = 0.3\,\mathrm{nm}$ reduces the $\mathcal{Q}$-factor in the diamond-confined case, while for the air-confined geometry, the $\mathcal{Q}$-factor remains relatively unaltered.

$\mathcal{Q}^{\mathrm{sim}}_{\sigma_\mathrm{q}=0.3\,\mathrm{nm}} = 221\,000$ for $\lambda_0 = 637.7\,\mathrm{nm}$, from which we deduce

$$F_\mathrm{P} = 1 + \frac{3}{4\pi^2} \cdot \frac{\mathcal{Q}^{\mathrm{sim}}_{\sigma_\mathrm{q}=0.3\,\mathrm{nm}}}{V_\mathrm{eff}} \cdot \left(\frac{\lambda_0}{n_\mathrm{d}}\right)^3 = 309\,. \tag{4.13}$$

The probability of emission into the cavity mode for an emitter with 100 % quantum

efficiency is given by the $\beta$-factor:

$$\beta = \frac{F_\mathrm{P} - 1}{F_\mathrm{P}} = 0.9968\,. \tag{4.14}$$

We note that the Purcell factor is independent of any emitter properties: the calculation is based solely on the experimental cavity parameters [61].

### 4.4.1 Applying the Purcell Factor on an NV Centre

Next, we apply the calculated Purcell factor to an NV centre: we are interested in calculating the emission rate into the ZPL. We assume that the NV centre's optical dipole is aligned along the polarisation-axis of the cavity mode. In the absence of the cavity, the excited-state decay-rate is $\gamma_0$, consisting of radiative decay into the ZPL (rate $\xi_0\gamma_0$ where $\xi_0$ is the Debye-Waller factor) and all other decay processes (rate $(1-\xi_0)\gamma_0$). Tuning the cavity on resonance with the ZPL enhances the ZPL emission by $F_\mathrm{P}$ while the emission into the phonon-sideband remains unaltered. Therefore, in the presence of the cavity, the decay rate becomes

$$\gamma_\mathrm{cav} = F_\mathrm{P}\xi_0\gamma_0 + (1-\xi_0)\gamma_0\,, \tag{4.15}$$

where $F_\mathrm{P}$ is defined according to Eq. 4.13 [214]. Taking the ratio of the decay rate in the cavity to that of free space yields

$$\frac{\gamma_\mathrm{cav}}{\gamma_\mathrm{free}} = \frac{\tau_0}{\tau_\mathrm{cav}} = 1 + \xi_0\left(F_\mathrm{P} - 1\right)\,, \tag{4.16}$$

where $\tau_\mathrm{cav}$ is the radiative lifetime in the cavity. Taking the unperturbed lifetime $\tau_0 = 12.6\,\mathrm{ns}$ and $\xi_0 = 2.55\%$ [77] along with $F_\mathrm{P} = 309$, Eq. 4.16 predicts a reduction in lifetime to $\tau_\mathrm{cav} = 1.42\,\mathrm{ns}$. The reduction in lifetime results in a broadening of the homogeneous linewidth from $\Delta\nu_\mathrm{free} = \frac{1}{2\pi}\cdot\gamma_0 = 12.6\,\mathrm{MHz}$ to

$$\Delta\nu_\mathrm{cav}^\mathrm{ZPL} = \frac{1}{2\pi}\cdot\left[1 + \xi_0\left(F_\mathrm{P} - 1\right)\right]\cdot\gamma_0 = 112\,\mathrm{MHz}\,, \tag{4.17}$$

rendering the NV less sensitive to spectral wandering. We next calculate the efficiency, $\eta_\mathrm{ZPL}$, of emitting a photon into the ZPL [214];

$$\eta_\mathrm{ZPL} = F_\mathrm{P}\cdot\frac{\xi_0\gamma_0}{\gamma_\mathrm{cav}} = \frac{\xi_0 F_\mathrm{P}}{\xi_0\left(F_\mathrm{P} - 1\right) + 1} = 89.0\,\%\,. \tag{4.18}$$

Finally, we estimate the cooperativity of the ZPL, $\mathcal{C}_{\mathrm{ZPL}}$, for our system. Using the definition [214]

$$F_{\mathrm{P}} = 1 + \frac{\mathcal{C}_{\mathrm{ZPL}}}{\xi_0} \tag{4.19}$$

yields $\mathcal{C}_{\mathrm{ZPL}} = 7.8$. This cooperativity is larger than those achieved so far using an open microcavity. Neglecting inhomogeneous broadening, $\mathcal{C}_{\mathrm{ZPL}} = 0.90$ (D. Riedel *et al* [77]) and $\mathcal{C}_{\mathrm{ZPL}} = 0.08$ (M. Ruf *et al* [214]). We note that in practise inhomogeneous broadening (rate $\gamma^*$) reduces the value in the experiment ($\gamma_0 \rightarrow \gamma_0 + \gamma^*$ [58, 113]) to $\mathcal{C}_{\mathrm{ZPL}} = 0.011$ ($\gamma^* = 2\pi \times 1\,\mathrm{GHz}$ [77]) and $\mathcal{C}_{\mathrm{ZPL}} = 0.0067$ ($\gamma^* = 2\pi \times 190\,\mathrm{MHz}$ [214]), respectively.

Alternatively, the NV-cavity coupling can be described with the Jaynes–Cummings Hamiltonian* in terms of $\{g_{\mathrm{ZPL}}, \kappa, \gamma_0\}$: where $g_{\mathrm{ZPL}} = d_{\mathrm{NV}} E_{\mathrm{vac}}$ is the NV-cavity coupling rate, $\kappa$ is the cavity decay rate and $\gamma_0$ is, as before, the spontaneous emission rate [30, 125]. Using $d_{\mathrm{NV}}/e = \sqrt{\xi_0} 0.108\,\mathrm{nm}$ [77], we deduce

$$\begin{aligned} g_{\mathrm{ZPL}} &= 2\pi \times 228\,\mathrm{MHz} \\ \kappa &= 2\pi \times 2.13\,\mathrm{GHz} \\ \gamma_0 &= 2\pi \times 12.63\,\mathrm{MHz}\,, \end{aligned} \tag{4.20}$$

firmly placing the system in the weak-coupling regime of cavity QED. The condition ($\kappa > g > \gamma$) is favourable for photon collection [214]. This approach results in

$$\eta_{\mathrm{ZPL}} = \frac{4g_{\mathrm{ZPL}}^2/(\kappa\gamma_0)}{4g_{\mathrm{ZPL}}^2/(\kappa\gamma_0) + 1} = 88.6\,\%\,, \tag{4.21}$$

and [61]

$$\mathcal{C}_{\mathrm{ZPL}} = \frac{4g_{\mathrm{ZPL}}^2}{\kappa\gamma_0} = 7.7\,, \tag{4.22}$$

and gives the same numerical value as above (Eq. 4.18 and Eq. 4.19).

### 4.4.2 Purcell Factor for Air- and Diamond-Confined Cavity Modes

We now compare the potential Purcell factors for diamond-confined and air-confined cavities (compare Section 3.3). There is a trade-off: the diamond-confined cavity has a larger $E_{\mathrm{vac}}$ at the location of an optimally-positioned NV centre but is more sensitive to scattering at the diamond-air surface with respect to the air-confined cavity. Fig. 4.14 shows a comparison between the Purcell factor for a diamond-confined and air-confined

*See Section 2.1.2 to Section 2.1.4.

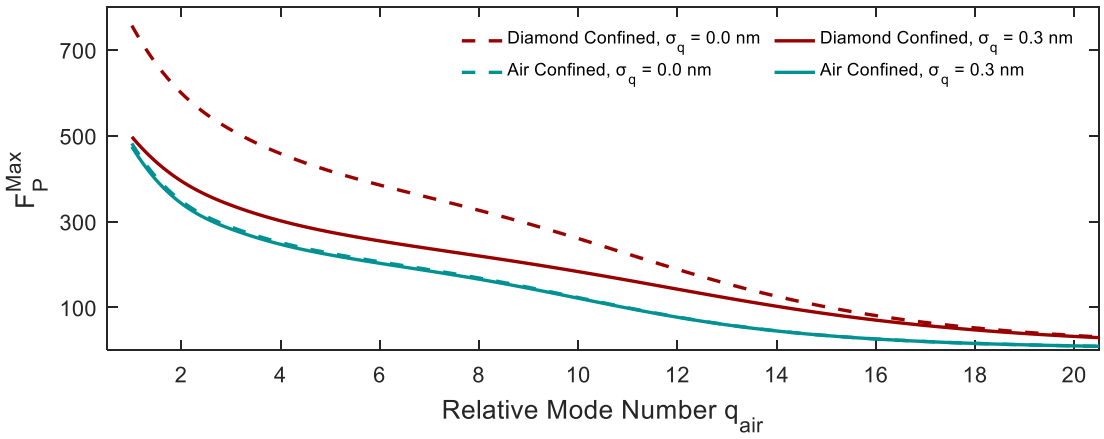


Fig. 4.14. Expected Purcell factor as a function of mode number $q_{\mathrm{air}}$ for an air- and diamond-confined geometry. The solid (dashed) lines correspond to the presence (absence) surface scattering with roughness $\sigma_{\mathrm{q}} = 0.3\,\mathrm{nm}$. Even in the presence of scattering, operating in a diamond-confined geometry is beneficial on the account of the higher Purcell factor.

cavity ($t_{\mathrm{d}} = 2.75 \cdot \lambda_0$ and $t_{\mathrm{d}} = 3.00 \cdot \lambda_0$, respectively). In the absence of any surface losses, the Purcell factor is significantly larger for the diamond-confined geometry compared to an air-confined geometry owing to two factors: the larger effective-length yields a higher $\mathcal{Q}$-factor, and the stronger confinement of the vacuum field to the diamond yields a lower effective mode volume. However, introducing surface scattering ($\sigma_{\mathrm{q}} = 0.3\,\mathrm{nm}$ as before) reduces the Purcell factor for the diamond-confined geometry, while for the air-confined geometry the Purcell factor remains roughly the same. Despite the higher losses associated with a surface roughness of $\sigma_{\mathrm{q}} = 0.3\,\mathrm{nm}$, the calculations suggest that it is beneficial to work in a diamond-confined geometry on account of the higher Purcell factor (at e.g. $q_{\mathrm{air}} = 4$, Fig. 4.14– this will result in a higher flux of coherent photons. An additional benefit of practical importance is that for the diamond-confined geometry $\frac{\mathrm{d}\lambda}{\mathrm{d}t_{\mathrm{a}}} = 0.11$ compared to $\frac{\mathrm{d}\lambda}{\mathrm{d}t_{\mathrm{a}}} = 0.27$ for the air-confined geometry with the same mode-number $q_{\mathrm{air}}$ (Fig. 4.6), thus rendering the cavity less susceptible to acoustic vibration [255].

### 4.4.3 Estimating the Cavity Outcoupling Efficiency

Following Section 3.3.5, the total cavity loss-rate $\kappa$ is given by $\kappa = \frac{2\pi c}{\lambda \mathcal{Q}}$. For a lossless cavity, a photon can only exit the cavity via the end mirrors, i.e. $\kappa = \kappa_{\mathrm{top}} + \kappa_{\mathrm{bot}}$, where

$\kappa_{\text{top (bot)}}$ is the loss-rate through the top (bottom) mirror. For the current design mirror:

$$\begin{aligned}\kappa_{\text{top}} &= \frac{\mathcal{T}_{\text{top}}}{\mathcal{T}_{\text{top}}+\mathcal{T}_{\text{bot}}}\cdot\kappa = 2\pi\times 330\,\text{MHz}\\ \kappa_{\text{bot}} &= \frac{\mathcal{T}_{\text{bot}}}{\mathcal{T}_{\text{top}}+\mathcal{T}_{\text{bot}}}\cdot\kappa = 2\pi\times 1.02\,\text{GHz}\,,\end{aligned} \tag{4.23}$$

where $\mathcal{T}_{\text{top (bot)}}$ is the transmission through the top (bottom) mirror. Here the diamond is included as part of the bottom mirror. Surface scattering increased the cavity loss-rate by amount $\kappa_{\text{loss}}$ – the total loss-rate is now given by $\kappa' = \kappa_{\text{top}}+\kappa_{\text{bot}}+\kappa_{\text{loss}}$. From the blue line Fig. 4.8 (b), we find $\kappa' = 2\pi\times 2.13\,\text{GHz}$ ($\mathcal{Q} = 221\,000$ for $q_{\text{air}} = 4$), from which we calculate the scattering loss-rate $\kappa_{\text{loss}} = \kappa_{\text{scat}}-\kappa = 2\pi\times 777\,\text{MHz}$. Finally, the probability of a ZPL photon exciting the cavity through the top mirror $\eta_{\text{tot}} = \eta_{\text{ZPL}}\cdot\frac{\kappa_{\text{top}}}{\kappa_{\text{scat}}+\gamma_0} = 0.13$.

The ultimate aim is to maximise the outcoupling efficiency, i.e. the probability of creating a photon on the outside of the top mirror following NV decay into the ZPL. The cavity should be made asymmetric, such that the loss-rate through the top mirror is larger than the loss-rate through the bottom mirror, $\kappa_{\text{top}} \gg \kappa_{\text{bot}}$. Given the high quality of the dielectric DBRs (see Fig. 4.8 (a)) this is easy to achieve. Ideally, $\kappa_{\text{top}}$ is also much larger than the unwanted scattering losses, $\kappa_{\text{loss}}$. For a given $g_{\text{ZPL}}$, $\gamma_0$ and $\kappa_{\text{loss}}$, and assuming $\kappa_{\text{top}} \gg \kappa_{\text{loss}}$, the outcoupling efficiency $\eta$ can be maximised by choosing $\kappa_{\text{top}} = \kappa_{\text{top}}^{\text{opt}}$, where [102]

$$\kappa_{\text{top}}^{\text{opt}} = \sqrt{\left(1+\frac{\kappa_{\text{loss}}}{\gamma_0}\right)\cdot\left(4g_{\text{ZPL}}^2+\kappa_{\text{loss}}\gamma_0\right)}\,. \tag{4.24}$$

For $\{g_{\text{ZPL}},\kappa_{\text{loss}},\gamma_0\} = 2\pi\times\{228\,\text{MHz},\,777\,\text{MHz},\,12.6\,\text{MHz}\}$, the values determined here, $\kappa_{\text{top}}^{\text{opt}} = 2\pi\times 3.69\,\text{GHz}$. Reassuringly, $\kappa_{\text{top}}^{\text{opt}}$ is larger than $\kappa_{\text{loss}}$. This results in a high $\eta$. With $\kappa_{\text{top}} = \kappa_{\text{top}}^{\text{opt}}$ we find $\kappa_{\text{tot}}^{\text{opt}} = 2\pi\times 5.49\,\text{GHz}$ ($\mathcal{Q}_{\text{opt}} = 85\,650$), $F_{\text{P}} = 120$ (Eq. 4.13), $\mathcal{C}_{\text{ZPL}} = 3.04$ and $\eta = \frac{4g_{\text{ZPL}}^2/(\kappa_{\text{tot}}^{\text{opt}}\gamma_0)}{4g_{\text{ZPL}}^2/(\kappa_{\text{tot}}^{\text{opt}}\gamma_0)+1}\frac{\kappa_{\text{top}}^{\text{opt}}}{\kappa_{\text{tot}}^{\text{opt}}+\gamma_0} = 50.9\,\%$.

## 4.5 Conclusions and Outlook

In this work, we have demonstrated the possibility of achieving high $\mathcal{Q}$-factors in a Fabry-Perot resonator in which the vacuum field is strongly confined to a diamond membrane. A $\mathcal{Q}$-factor of 121 700 was achieved for $\lambda \simeq 637\,\text{nm}$ for the minimum mode number, $q_{\text{air}} = 4$ of which $V_{\text{eff}} \simeq 3.9\,\lambda_0^3$. The $\mathcal{Q}$-factor is lower than the $\mathcal{Q}$-factor expected from the geometry alone. The main source of loss in this experiment is attributed to roughness

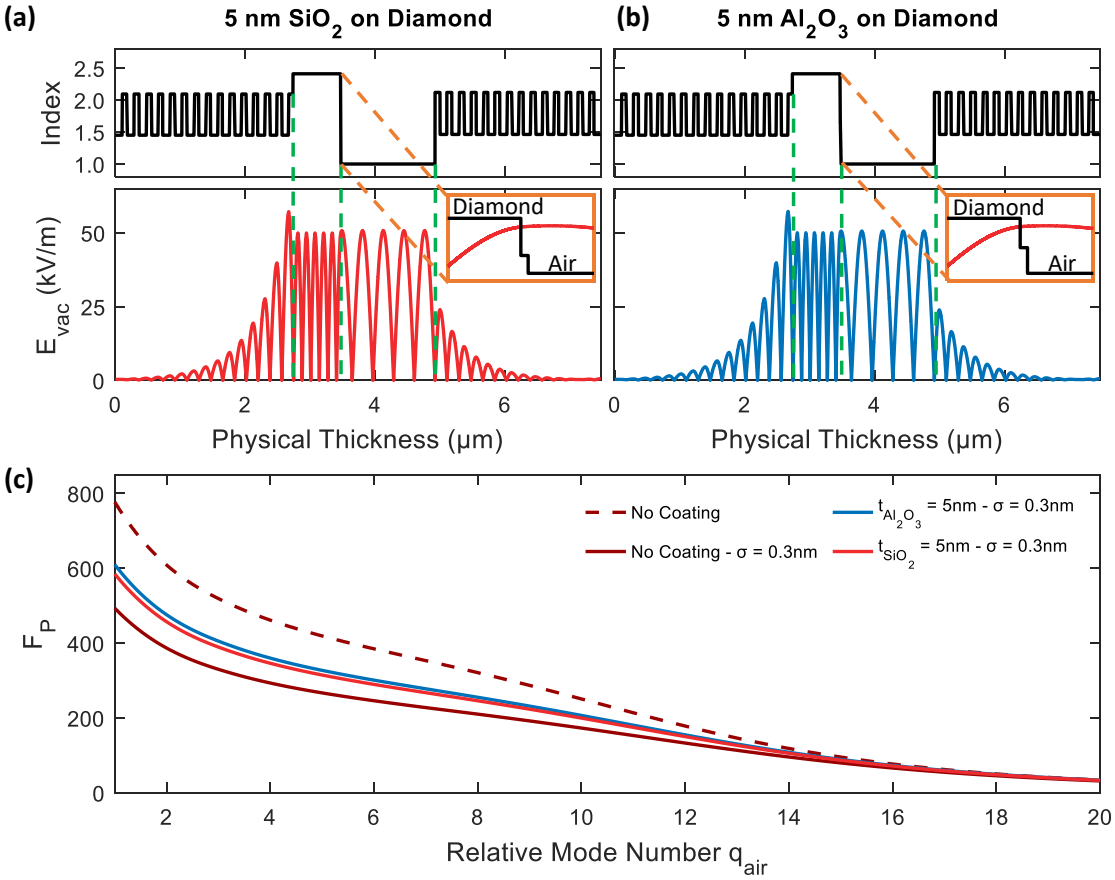


Fig. 4.15. **(a)** - **(b)** Coating the diamond with 5 nm $SiO_2$ and $Al_2O_3$. The presence of the oxide layer reduces the contrast in refractive index between the diamond and the air, thus reducing scattering. **(c)** Calculation of the Purcell factor with effective mode number $q_{\mathrm{air}}$. The reduction in scattering loss at the diamond surface is manifested by the increase in the Purcell factor.

and waviness at the diamond surface. The waviness, attributed as polishing marks, can potentially be mitigated by optimised plasma etching [159] and/or by atomic-layer deposition of a material with refractive index less than diamond [123]. Deposition of $SiO_2$ ($n = 1.47$) or $Al_2O_3$ ($n = 1.77$) will also reduce the losses due to scattering (Fig. 4.15). We note that surface passivation has previously been demonstrated to increase the $\mathcal{Q}$-factor for GaAs resonators [99, 391, 415] albeit via a different mechanism.

Despite the presence of surface-related losses, a Purcell factor $F_{\mathrm{P}} = 170$ is predicted for the current design. If the waviness can be eliminated leaving the surface roughness the same, the current design is capable of reaching $F_{\mathrm{P}} = 309$. Without the surface waviness but with the existing surface roughness, the Purcell factor is predicted to be higher for a diamond-confined cavity compared to an air-confined cavity.

The motivation behind this work is to enhance the flux of coherent photons from single NV centres in diamond [77], a step towards the realisation of an efficient spin-photon interface [34]. We note that the Purcell factor presented here is universal: $F_{\mathrm{P}}$ depends solely on the cavity parameters, not on the properties of the emitter. The versatile design of the cavity allows a wide-range of solid-state single-photon emitters to be embedded [216], for instance, other colour centres in diamond [130, 145, 257, 258, 261, 292, 300, 301], defects in SiC [316, 319, 322, 323, 416], rare-earth ions in a crystalline host [325, 332, 333, 417, 418] or emitters in 2D materials [419, 420].

CHAPTER 5

# Cavity-Enhanced Raman Scattering for *in Situ* Alignment and Characterisation of Solid-State Microcavities

**The content of this chapter is partially adapted from:**
Daniel Riedel, Sigurd Flågan, Patrick Maletinsky and Richard J. Warburton, **"Cavity-Enhanced Raman Scattering for *in Situ* Alignment and Characterization of Solid-State Microcavities"**, Physical Review Applied **13**, 014036 (2020).

**Abstract:**

We report cavity-enhanced Raman scattering from a single-crystal diamond membrane embedded in a highly miniaturised fully-tunable Fabry-Perot cavity. The Raman intensity is enhanced 58.8-fold compared to the corresponding confocal measurement. The strong signal amplification results from the Purcell effect. We show that the cavity-enhanced Raman scattering can be harnessed as a narrowband, high-intensity, internal light-source. The Raman process can be triggered in a simple way by using an optical excitation frequency outside the cavity stopband and is independent of the lateral positioning of the cavity mode with respect to the diamond membrane. The strong Raman signal emerging from the cavity output facilitates *in situ* mode-matching of the cavity mode to single-mode collection optics; it also represents a simple way of measuring the dispersion and spatial intensity-profile of the cavity modes. The optimisation of the cavity performance via the strong Raman process is extremely helpful in achieving efficient cavity-outcoupling of the relatively weak emission of single colour-centres such as the nitrogen-vacancy centre in diamond or rare-earth ions in crystalline hosts with low emitter density.

## 5.1 Introduction

The development of a quantum internet crucially relies on the scalable long-distance interconnection of quantum nodes [15]. These nodes need to combine a robust storage of quantum states and high-fidelity processing of quantum information with an efficient interface to photons mediating the network links via entanglement swapping [17]. In order to achieve high entanglement rates these photons need to exhibit transform-limited spectral linewidths, a high degree of single-photon purity and a large creation probability per laser excitation pulse. The nitrogen-vacancy (NV) centre in diamond constitutes a promising candidate for the stationary qubit due to its highly coherent, optically addressable electron spin along with coupling to multi-qubit nuclear spins in the immediate environment [72]. In seminal proof-of-principle experiments, long-distance entanglement [43] and on-demand entanglement delivery [397] between spatially separated NV centres were demonstrated. However, the entanglement rates are limited to tens of Hertz due to the small fraction ($\sim$ 3%) of coherent photons emitted into the zero-phonon line (ZPL) [77]. A promising strategy to overcome this limitation is to enhance the ZPL photon flux of NV centres via coupling to a resonant microcavity [77, 81, 82, 214, 421].

In recent years, tunable Fabry-Perot microcavities have been widely used to enhance the photon emission rate of various single emitters [77, 96–98, 100–102, 115, 126, 399–401, 422–425]. The tunability of their resonance frequency in combination with a precise lateral positioning capability allows the emitter-cavity coupling to be maximised *in situ*. A further advantage of this system is that micrometer-scale single-crystalline host materials can be integrated into the cavity while maintaining a high quality-factor to mode volume ratio ($\mathcal{Q}/V$) [77, 87]. For emitters which are highly sensitive to fluctuations of the charge environment, increasing the dimensions of a defect-free crystalline environment is clearly beneficial [158, 171]. An example of such an emitter is the NV centre in diamond. NV centres coupled to monolithic nanophotonic structures suffer from spectral fluctuations [82]; optical performance is better in a Fabry-Perot microcavity [77].

To maximise their performance, tunable Fabry-Perot microcavities require precise *in situ* mode-matching of the cavity mode to external fields. This is in principle simple for a well-constructed fibre mirror for which a concave mirror is fabricated at the exact centre of an optical fibre [402, 426]. However, this approach works well only when the mode-field diameter of the cavity is matched to that of the optical fibre. Furthermore, the mode-matching efficiency is inevitably limited by the different wavefront curvatures of the cavity mode and the fibre. Both mismatches are exacerbated for small cavity-mode volumes which require small mirror radii and mode-field diameters. Instead, the

"top" mirror can be fabricated into a silica substrate [77, 99, 115, 385, 399], and mode-matching between the cavity and a single-mode fibre can be achieved with a pair of lenses. In practice, this is a non-trivial task. Mode-matching is particularly difficult if two wavelengths are involved, for instance excitation at 532 nm and NV ZPL emission at 637 nm, on account of chromatic aberrations. In these experiments, it is also desirable to measure the dispersion of the cavity modes (dependence of the resonance frequency on mirror separation) and the electric field distribution of each mode. These are laborious tasks if a single emitter is used.

We propose here that Raman scattering from the solid-state host is a valuable resource in aligning and optimising tunable Fabry-Perot microcavities and in characterising the cavity modes. The Raman scattering is enhanced by the cavity and gives large signals, facilitating quick optimisation, and subsequently a simple way to determine the mode's dispersion and lateral intensity-profile. The Raman scattering depends at most weakly on the lateral position unlike a single emitter which benefits from cavity enhancement only once the emitter is located at the cavity antinode.

We report here experiments on diamond from which Raman scattering is well known and has been exploited for both quantum and photonic applications. In this case, the Raman process involves the inelastic scattering of a single photon and a single phonon. The creation (Stokes) or annihilation (anti-Stokes) of a phonon causes a red- or blue-shift of the wavelength of the incoming radiation [334, 427]. Correlated Stokes-anti-Stokes scattering in diamond [351] led to the development of a macroscopic phonon-based quantum memory [350, 353, 360, 361], the remote entanglement of macroscopic diamonds [357] and the development of a Raman laser in the visible wavelength regime [337, 428]. On account of the large Raman shift of diamond ($1\,332\,\mathrm{cm}^{-1}$ [138]) and the high Raman gain coefficient ($\sim 75\,\mathrm{GW}\cdot\mathrm{cm}^{-1}$ at 532 nm) [344], Stokes scattering provides an excellent narrow-linewidth, high-intensity internal light-source. We show that cavity-enhanced Raman scattering enables fast *in situ* alignment of the diamond cavity-mode with respect to external optics, a fast way of determining the dispersion of the cavity modes, and single-shot imaging of the modes' lateral profile. Additionally, a comparison of the signal with cavity-enhancement to the signal without the cavity is also an indicator of the single-emitter Purcell factor [369]. These attributes, demonstrated here on diamond, should be generic to single-crystal solid-state hosts.

## 5.2 Methodology

We create thin diamond membranes out of high-purity, single-crystal diamond (Element 6) following previously reported fabrication techniques [152, 159]. Using inductively-coupled plasma-etching and electron-beam lithography, we fabricate square-shaped membranes with a typical thickness of 1 µm and side lengths of 10 ... 50 µm (Fig. 5.1 (a)) [77, 403]. The membranes are bonded to a planar $SiO_2$ substrate coated with a highly reflective distributed Bragg-reflector (DBR, 15 layers $SiO_2/Ta_2O_5$, ECI evapcoat) using a micromanipulator. The extremely smooth surfaces of the diamond membrane (surface roughness $\lesssim 0.3\,\text{nm}$) and the DBR surface promote strong adherence due to van der Waals forces. The strong bonding is demonstrated by the possibility of bending the micromanipulator needles on attempting to displace the membrane laterally (Fig. 5.1 (a)). The bonded membranes contain NV centres which were introduced prior to nano-fabrication by nitrogen-ion implantation and subsequent annealing [77].

As a first step, we characterize the diamond membrane with a room-temperature confocal microscope (i.e. without a cavity) using an objective of high numerical aperture (Olympus, MPLFLN100x, NA = 0.9). A confocal scan under continuous-wave green excitation ($\lambda = 532\,\text{nm}$, $P = 580\,\mu\text{W}$) exhibits well-isolated bright features which we associate with individual NV centers (Fig. 5.1 (b)) [37]. Fig. 5.2 displays a photolu-

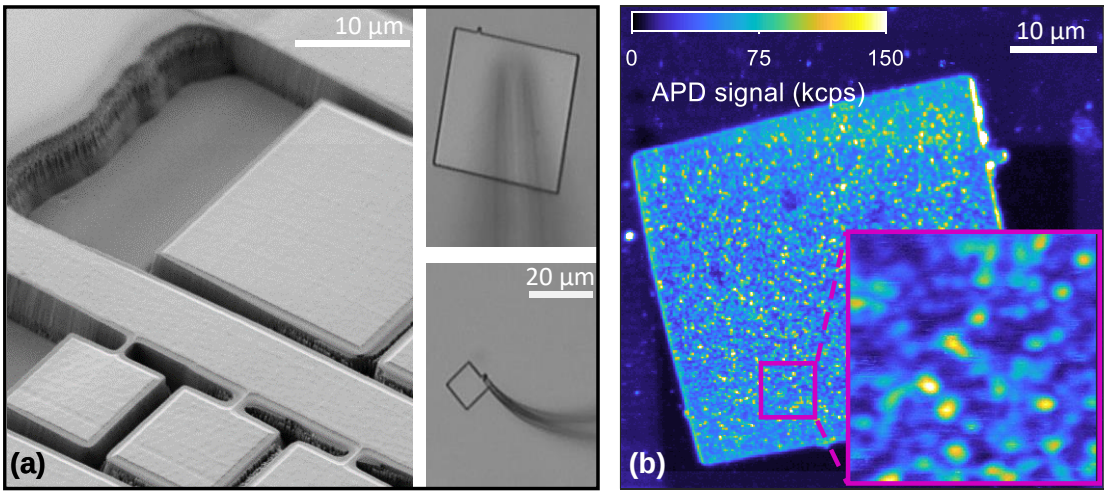


Fig. 5.1. **(a)** Fabrication and transfer of diamond membranes. *Left:* Patterning of the diamond using electron-beam lithography and inductively-coupled plasma-etching. *Right:* Transfer of a membrane using a micromanipulator. **(b)**Confocal scan of a diamond membrane under green excitation (Laser Quantum Ventus532, $\lambda = 532\,\text{nm}$, $P = 580\,\mu\text{W}$) at room temperature. The emission from single NV centres can be observed.

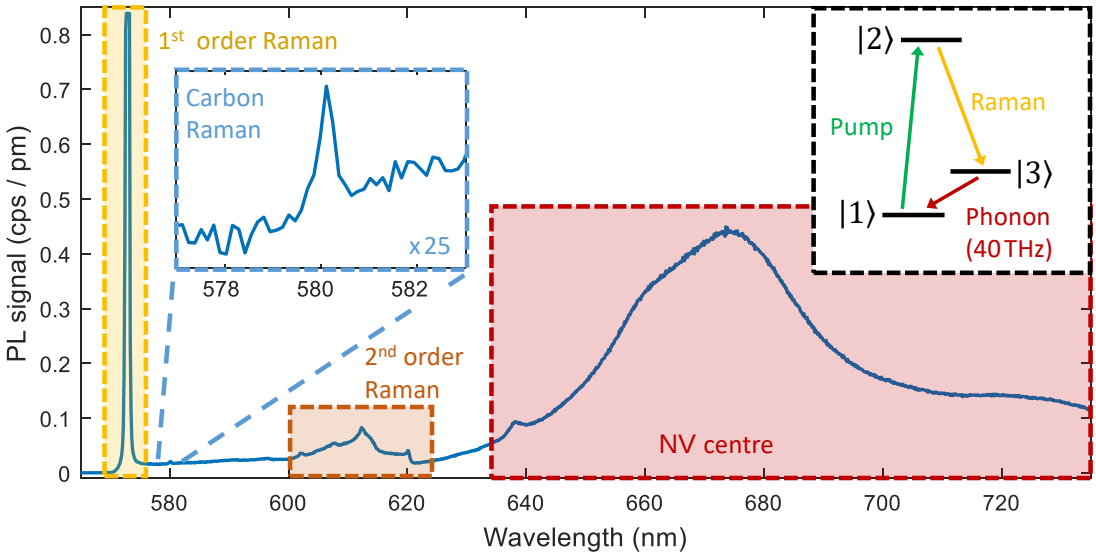


Fig. 5.2. Photoluminescence (PL) spectrum of a single NV centre at room temperature. In addition to PL, Raman features are observed: signatures of disordered carbon and first- and second-order Raman lines of the diamond lattice ($P = 3.1\,\mathrm{mW}$, integration time 600 s, for more details see text). *Inset:* Schematic of the Stokes process. A pump photon is converted into a red-shifted Stokes photon and a phonon of a fixed frequency.

minescence (PL) spectrum for a strong excitation power (532 nm, 3.1 mW) and long integration-time (600 s) recorded at one of these bright spots. The spectrum shows a temperature-broadened NV ZPL at $\sim 637\,\mathrm{nm}$ and a broad phonon-sideband whose spectral shape is slightly altered in our experiment due to the varying DBR reflectivity with wavelength and thin-film interference in the membrane. Crucially, the spectrum contains clear Raman features: the first- and second-order Stokes features at 572.67 nm and 600 . . . 620 nm, respectively [138]. In addition, we find a Raman signature of carbon $sp^2$ bonds (Raman shift $\sim 1\,560\,\mathrm{cm}^{-1}$) [429], indicating either a slight graphitic surface-contamination (which could have been created during high-temperature annealing) or the presence of organic residue.

Here, we focus on the first-order Stokes-scattering, modelled by a three-level atom-like system (inset Fig. 5.2) involving a ground state ($|1\rangle$) a virtual excited-state ($|2\rangle$) and a metastable state ($|3\rangle$) [337]. When the ground-state population is excited to state $|2\rangle$, it can de-excite via state $|3\rangle$ by emitting a red-shifted photon and an optical phonon of fixed energy. In our experiment, we determine a spectral shift of $\Delta E = hc \cdot 1\,335\,\mathrm{cm}^{-1}$ between the pump laser and the Stokes emission: this corresponds to the optical phonon energy in diamond.

### 5.2.1 The Fabry-Perot Microcavity

A schematic of our tunable microcavity is shown in Fig. 5.3 (a). A planar DBR supporting a diamond membrane ($\sim 20 \times 20 \times 0.8\,\mu m^3$) forms a cavity with a curved DBR. We fabricate an array of atomically-smooth curved microtemplates on a $SiO_2$ chip via $CO_2$-laser ablation yielding small radii of curvature ($R \sim 10\,\mu m$, Fig. 5.3 (b)) [393, 402]. Subsequently, the templates are coated with a highly reflective 14-layer $Ta_2O_5$ / $SiO_2$ DBR. The spacing between the two mirrors can be adjusted

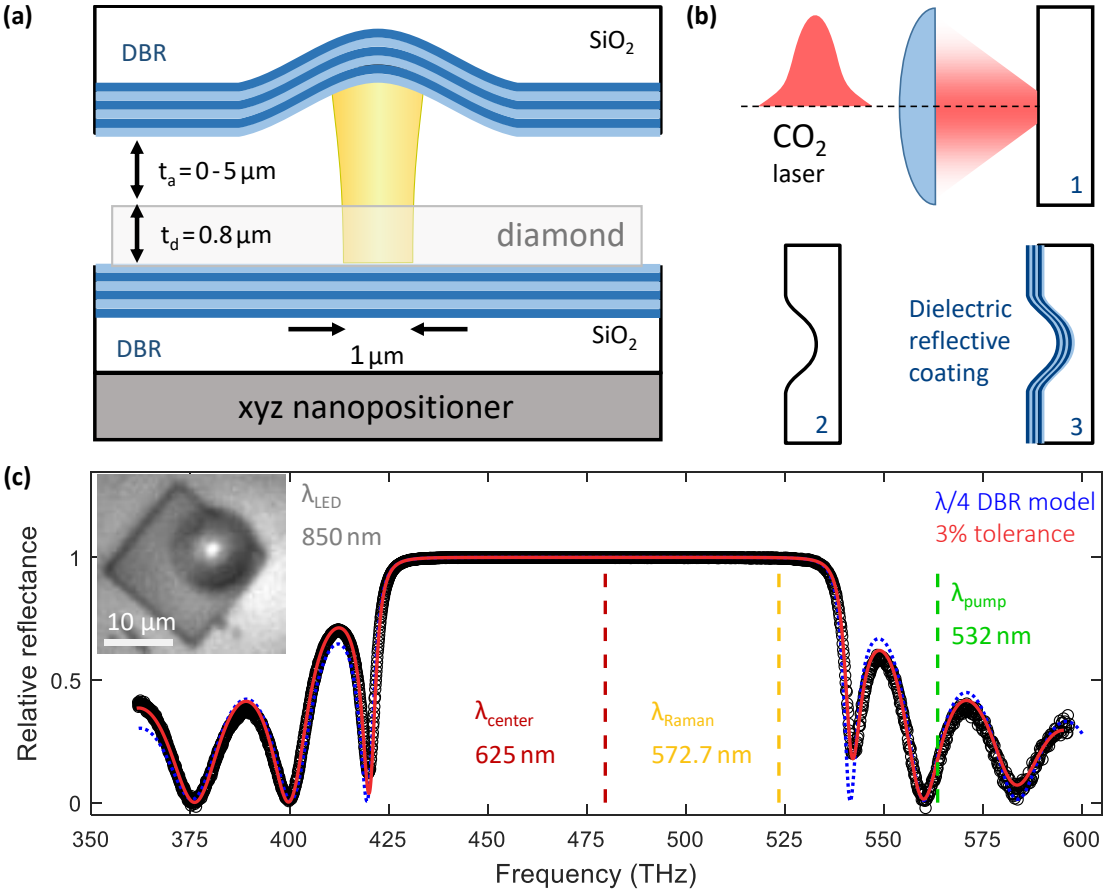


Fig. 5.3. **(a)** Schematic of a diamond membrane embedded in a tunable Fabry-Perot microcavity. Nanopositioners enable *in situ* control of both the resonance frequency and the antinode location of the microcavity mode. **(b)** Process flow of the curved micro-template fabrication. A focused $CO_2$ laser pulse creates a microindentation in a $SiO_2$ substrate via ablation. Subsequently, the template is coated with a dielectric Bragg-reflector (DBR). **(c)** Normalised white-light transmission spectrum of the DBR coating revealing the mirror stopband. The experiment is well reproduced by a model calculation. Inset: an image of the square-shaped membrane inside the cavity with the microindentation located on top. The bright feature in the centre stems from the reflection of laser excitation at wavelength $\sim 635\,nm$.

by applying a voltage to the z-nanopositioner beneath the bottom mirror; the lateral location of the cavity's antinode can be adjusted by applying a voltage to the x- and y-nanopositioners [77, 99, 115, 385, 399].

To characterise the mirrors, we measure the transmission spectrum of the planar mirror with a white-light source and quantise the data using the transmission spectrum of an uncoated quartz substrate (Fig. 5.3 (c)). With a transfer-matrix calculation, we are able to reproduce the oscillations of the reflectivity over a large frequency range. A transfer matrix-based refinement algorithm allows the reflection spectrum to be reconstructed on setting an individual layer-thickness tolerance of 3 % (Essential Macleod). For our calculation, we set a stopband centre of $\lambda_{\text{centre}} = 625\,\text{nm}$ and use 15 $\lambda/4$ layer pairs of $SiO_2$ and $Ta_2O_5$ with a refractive index of $n_{SiO_2} = 1.46$ and of $n_{Ta_2O_5} = 2.11$, respectively. For the top mirror we obtain similar results, reproducing the transmission spectrum with $\lambda_{\text{center}} = 629\,\text{nm}$ and 14 layer pairs.

To cavity-enhance the Raman process, we pump the diamond with a green laser and tune the cavity into resonance with the Stokes line. The pump laser can be coupled into the cavity independently of the mirror separation since its wavelength (532 nm) lies outside the reflection stopband of the mirror coating (Fig. 5.3 (c)). Conversely, due to the large Raman shift of diamond, the cavity supports a resonance with a finesse of $\sim 1\,000$ at the Stokes wavelength $\sim 573\,\text{nm}$.

### 5.2.2 Experimental Setup

The experimental setup used in this experiment is shown schematically in Fig. 5.4, some details are as follows. An infrared light-emitting-diode (LED*, $\lambda_{\text{LED}} = 850\,\text{nm}$ for which the DBR is transparent) is used to locate the membrane inside the cavity (inset Fig. 5.3 (c)). This visual feedback allows us to adjust the location of the diamond with respect to the top mirror. The pump laser is spectrally filtered (Semrock, LL01-532-25 and FF01-650/SP-25) and coupled into the cavity via a slightly overfilled objective of moderate numerical aperture (Microthek, 20x/0.4). The Stokes signal is collected via the same objective and coupled into a single-mode fibre (Thorlabs 630-HP); the output of this fibre is coupled into a spectrometer. A combination of a dichroic mirror (Semrock, FF560-FDi01) and long-pass/band-pass filters (Semrock, LP03-532RS-25 and FF01-572/15-25) is employed to prevent laser light from entering the collection optics. This is important to avoid exciting fluorescence and Raman scattering from the detection fibre. Using a precision mechanical-stage we can move the entire microcavity with

*Thorlabs, M850D2.

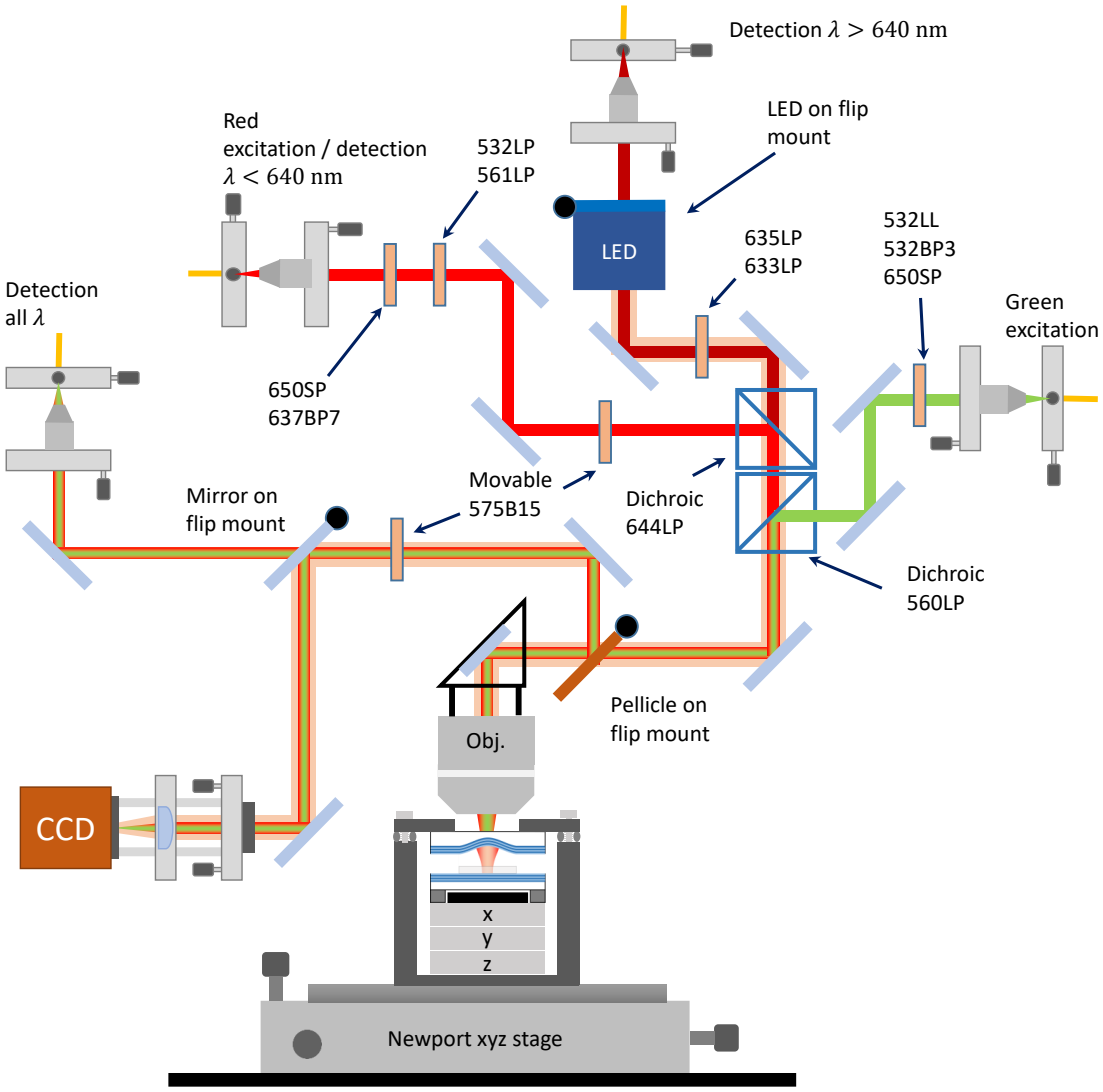


Fig. 5.4. The homebuilt fibre-based microscope used in this experiment (a generalised version of Fig. 4.4). A series of appropriate shortpass filters are used to filter fibre fluorescence caused by the green excitation laser. The PL is collected in a back-scattering geometry, and coupled into a fibre. A series of appropriate longpass filters are used to prevent laser light entering the detection fibre. For the imaging experiment in Fig. 5.6, a 50:50 pellicle beamsplitter on a flip mount was used to guide the PL to the camera.

respect to the external optics allowing the cavity output to be aligned with respect to the optical axis of the microscope.

## 5.3 Cavity-Enhanced Raman Scattering

Figure 5.5 (a) shows a spectrally resolved measurement of the cavity-enhanced Stokes emission at $\lambda_s = 572.67\,\text{nm}$ pumped at 532 nm with $P = 20\,\text{mW}$. Attaining the maximal signal strength requires careful alignment. This process is massively aided by exploiting the Raman process on account of at least three factors. First, the signal is very large. When the cavity is tuned into resonance with the Stokes photons, we detect up to $2 \times 10^6$ photon counts/s (cps) on a standard silicon single-photon avalanche-photodiode. Secondly, the signal does not depend on the $(x, y)$-alignment of the cavity: it represents a ubiquitous internal light-source. Thirdly, the Raman process couples to all the cavity modes. From the mode dispersion and the signal strengths, this allows the transverse electromagnetic (TEM) cavity mode indices (q,n,m) to be determined. In particular, the (q,0,0) modes can be identified: it is these modes whose output couples best to the single-mode fibre detection-channel.

The photon flux of the cavity-enhanced Stokes scattering is strongly enhanced with respect to the Stokes signal collected from the bare diamond membrane under equivalent experimental conditions (Fig. 5.5 (a)). Integrating over wavelength in both cases (with cavity, without cavity Fig. 5.5 (a)-(b), respectively), we find an enhancement factor of $F = 58.8$. This enhancement results from the Purcell effect [430]. At a given power, the cavity increases the Stokes photon generation rate by the Purcell factor, $F_\text{P}$. Additionally, the Stokes photons are emitted preferentially into the cavity mode – this enhances the detection efficiency by a factor $F_\text{cav}$. Overall, $F = F_\text{P} \cdot F_\text{cav} = 58.8$. The Stokes signal increases linearly with pump power (Fig. 5.5(e)): at these pump powers, there is no super-linear dependence presaging Raman lasing.

To put the cavity-enhancement into perspective we also measure the Stokes scattering intensity using a high-NA objective (NA=0.9) and find that the signal is a factor of 3.1 larger compared to the NA=0.4 objective (Fig. 5.5(c)), which corresponds to a reduction of the enhancement factor to 18.7. The signal obtained with the NA=0.9 objective is comparatively large for two reasons. First, the wide acceptance angle of the objective allows for collecting a large fraction of the generated Stokes light. Second, the tighter focusing of the pump laser increases the power density per interaction length, thus increasing the scattering probability owing to the intensity-dependent Raman gain $g_\text{Raman} = 75\,\text{GWcm}^{-1} \cdot I_\text{pump}$ [337].

We next investigate the power dependence of the Stokes signal in more detail. Using a single-photon avalanche-photodiode (SPAD), we measure the power dependence of the cavity-coupled Stokes signal and compare it to the signal collected from the bare

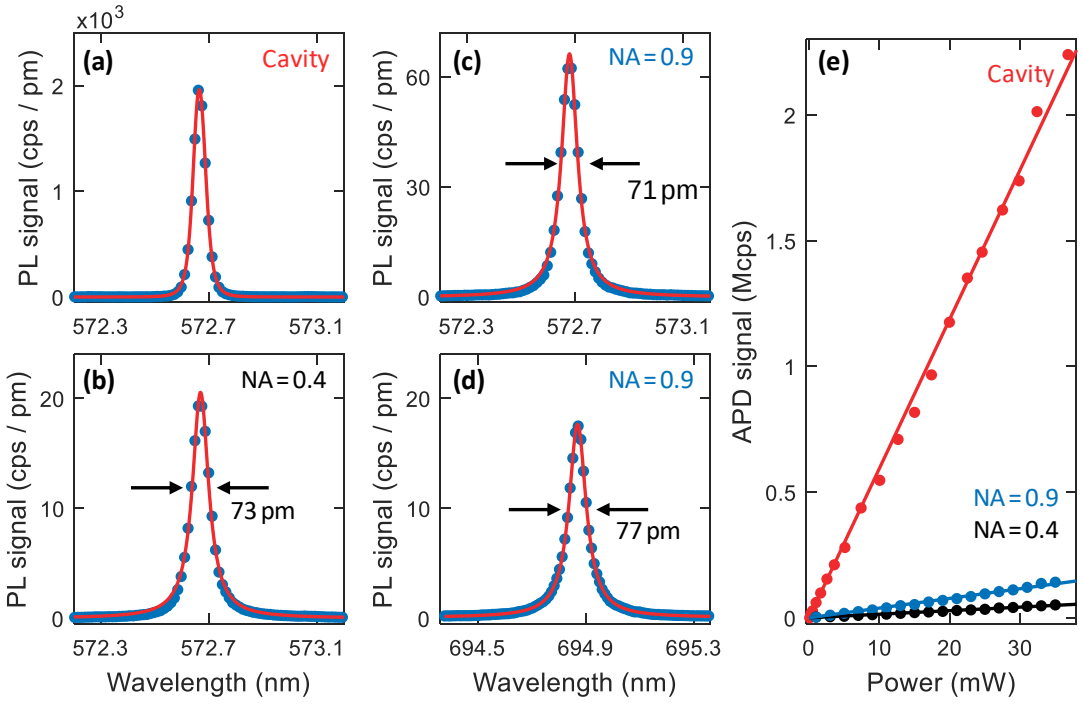


Fig. 5.5. **(a)** Typical optical spectrum of the Stokes signal in resonance with the cavity ($t_{\mathrm{int}} = 1\,\mathrm{s}$). **(b)** Typical optical spectrum of the Stokes signal for out-of-cavity detection using an objective with NA=0.4 ($t_{\mathrm{int}} = 120\,\mathrm{s}$), and **(c)** NA=0.9 ($t_{\mathrm{int}} = 30\,\mathrm{s}$). **(d)**Typical optical spectrum of the Stokes signal pumped with a narrow-band laser at $\lambda = 636\,\mathrm{nm}$ ($P = 5\,\mathrm{mW}$) without the top mirror using an objective of NA=0.9 ($t_{\mathrm{int}} = 180\,\mathrm{s}$). **(e)** Power dependence of the integrated Stokes signal for out-of-cavity detection with an objective of NA=0.4 (black), NA=0.9 (blue) along with the integrated cavity-enhanced Stokes signal (red). (a), (b) and (c): The pump wavelength is $\lambda = 532\,\mathrm{nm}$, the pump power $P = 20\,\mathrm{mW}$. The Stokes lineshape slightly deviates from a Lorentzian due to the spectral profile of the pump laser; all data were recorded at room temperature.

diamond membrane with NA=0.9 and NA=0.4 objectives. For all three cases, we find a linear increase of the signal strength with power. For the cavity-coupled signal, we fit a linear power dependence with slope $m_{\mathrm{cav}} = 59.4\,\frac{\mathrm{kcps}}{\mathrm{mW}}$. For the bare diamond membrane, we find $m_{\mathrm{NA0.9}} = 3.9\,\frac{\mathrm{kcps}}{\mathrm{mW}}$ and $m_{\mathrm{NA0.4}} = 1.4\,\frac{\mathrm{kcps}}{\mathrm{mW}}$ for the NA=0.9 and the NA=0.4 objectives, corresponding to relative enhancement factors of 15 and 42, respectively. The discrepancy in the enhancement factors can be explained by the fact that the cavity acts as a strong spectral filter. For the APD measurements on the other hand we use a narrow bandpass ($(575 \pm 8)\,\mathrm{nm}$, Semrock FF01-575/15-25). Integrating the background PL in this spectral window and comparing it to the signal obtained from the Stokes peak we find that the background PL accounts for 24.5 % (15.3 %) for the NA=0.4 (0.9) objective. The background-corrected enhancement factors of 55.6 and 18.0 for the

NA=0.4 and NA=0.9 objectives respectively are in very good agreement with what we find for the spectrally resolved measurements (Fig. 5.5 (b)).

### 5.3.1 Probing the Cavity Mode Structure

We now exploit the Raman process as a convenient way to analyze the cavity modes. To do this, we gradually increase the cavity length, monitoring the cavity emission at the Stokes wavelength. Fig. 5.6 (a) displays the spectrally resolved measurement of the cavity emission (Fig. 5.6 (b)) for different cavity length detunings $\Delta L$ recorded by adjusting the width of the air-gap $t_\mathrm{a}$. A series of cavity modes is observed. In this experiment, the linewidth of the fundamental mode $\delta t_\mathrm{a}$ is a measure of the cavity finesse $\mathcal{F} = \frac{(\lambda/2)}{\delta t_\mathrm{a}} = 350$ (Fig. 5.6 (a) top panel) [385]. Clearly, the Raman process couples to the various higher-order Gaussian modes whenever a spectral resonance with the Stokes photons is established. The collection efficiency of the higher-order modes is much lower than that of the fundamental modes due to the signal collection through a single-mode fibre but nevertheless, a number of higher-order modes are observed.

The exact locations of the cavity modes depend on the cavity geometry: an analysis of the spacings of the different modes allows the geometric parameters of the cavity to be determined. We extract the radius of curvature of the top mirror, $R_\mathrm{cav}$, from the spacings between the fundamental mode $(q, 0, 0)$ and its associated higher harmonics $(q, n, m)$. Quantitatively, we make this link with a Gaussian optics model [385]. The effective cavity length $L_\mathrm{eff}$, $R_\mathrm{cav}$ and the $(q, n, m)$ parameters are connected by

$$L_\mathrm{eff}(q, n, m) = \left[q + \frac{n + m + 1}{\pi} \cdot \cos^{-1}\left(\sqrt{g}\right)\right] \cdot \frac{\lambda}{2} \tag{5.1}$$

where $g = 1 - \frac{L_\mathrm{eff}(q,n,m)}{R_\mathrm{cav}}$ is the confocal parameter. $L_\mathrm{eff}$ is a measure of the separation of the two mirrors accounting for the penetration depth into the mirrors upon reflection [94]. From this model, we find that the modes in Fig. 5.6 (a) are well described with $R_\mathrm{cav} = 10\,\mu\mathrm{m}$ (Fig. 5.6 (a) lower panel).

The signals in these experiments are sufficiently large that the spatial intensity-distribution of the emerging cavity modes can be recorded in a single-shot imaging experiment. We directly image the modal shape of the fundamental $(q, 0, 0)$ and the first two higher-order modes $(q, 1, 0)$ and $(q, 0, 1)$ on a charge-coupled-device camera (Fig. 5.6 (a)). Using the diamond membrane (edge length $20\,\mu\mathrm{m}$) as a ruler, we can calibrate the lateral dimensions of the images. A Gaussian fit of a linecut through the fundamental mode yields a beam waist of $w_\mathrm{I} = 0.88\,\mu\mathrm{m}$ (Fig. 5.6 (a), inset).

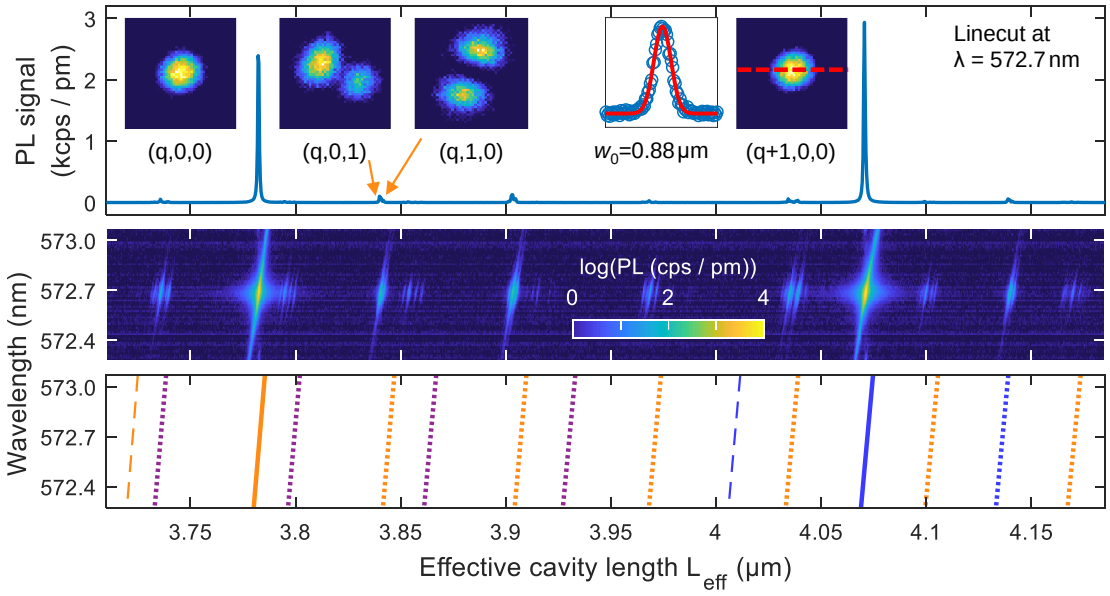


Fig. 5.6. *Center panel:* PL spectra for different relative cavity lengths $\Delta L$ about $L = 4.07\,\mu\text{m}$ under green illumination ($\lambda = 532\,\text{nm}$, $P = 20\,\text{mW}$) detected with a single-mode fibre. *Top panel:* Linecut at $\lambda = 572.67\,\text{nm}$. The Stokes light couples to the Gaussian cavity-modes $(q, n, m)$ of different mode families. Well isolated $(q, 0, 0)$, $(q, 1, 0)$ and $(q, 0, 1)$ modes can be directly imaged on a CCD camera. *Bottom panel:* Calculation of the mode dispersion using an analytic model based on Gaussian optics. The spacing of the different modes allows the geometric parameters of the cavity to be extracted (for details see text).

We now try to reproduce the beam waist using Gaussian optics. The intensity beam waist of a Gaussian beam is given by [93]

$$w_{\text{I}}(z) = w_{0,\text{I}} \cdot \left[1 + \left(\frac{z}{z_{\text{R}}}\right)^2\right]^{\frac{1}{2}}, \tag{5.2}$$

where $z_{\text{R}}$ is the Rayleigh length. The radius of curvature for a Gaussian beam is calculated from [93]

$$R(z) = z \cdot \left[1 + \left(\frac{z_{\text{R}}}{z}\right)^2\right]. \tag{5.3}$$

At the top mirror ($z = 4.07\,\mu\text{m}$), the radius of curvature of the Gaussian beam equals that of the cavity, i.e. $R(4.07\,\mu\text{m}) = R_{\text{cav}} = 10\,\mu\text{m}$, from which we extract the experimental Rayleigh length $z_{\text{R}} = 4.916\,\mu\text{m}$. Using this value for $z_{\text{R}}$, we calculate the beam waist at the top mirror from Eq. 5.2: $w_{\text{I}}(z = 4.07\,\mu\text{m}, R(z) = 10\,\mu\text{m}) = 0.87\,\mu\text{m}$, in good agreement with the measured value of $w_{\text{I}} = 0.88\,\mu\text{m}$.

The separation of the fundamental $(q, 0, 0)$ resonances, specifically the change in resonance wavelength per change in air-gap width $m = \frac{\Delta\lambda_{\mathrm{cav}}}{\Delta t_{\mathrm{a}}}$, allows the effective cavity mode number $q$ to be inferred. For the two $(q, 0, 0)$ resonances in Fig. 5.6 (a) we measure $m_1 = 87 \cdot \frac{\mathrm{pm}}{\mathrm{nm}}$ and $m_2 = 83 \cdot \frac{\mathrm{pm}}{\mathrm{nm}}$ corresponding to $q_1 = \frac{2}{m_1} = 23$ and $q_2 = \frac{2}{m_2} = 24$. To interpret these numbers, the full cavity mode-structure must be modelled including the interferences induced by the diamond membrane [399]. The Gaussian optics model of an empty cavity (Eq. 5.1) does not include these additional interferences and this underestimates the actual cavity length.

Conceptually, the cavity modes can be described using a coupled-cavity approach (compare Chapter. 3) [61, 77, 87, 123]. In this picture, there are two cavity modes, one defined by the air-gap bounded by the top DBR and the diamond-air interface; the other is defined by the diamond-air interface and the bottom DBR layer (Fig. 5.9). The two modes couple via the non-zero reflectivity of the diamond-air interface and hybridise. This hybridisation influences the dispersion, $\frac{\mathrm{d}\lambda_{\mathrm{cav}}}{\mathrm{d}t_{\mathrm{a}}}$, and results in deviations from the Gaussian model of an empty cavity.

We simulate the cavity modes with the aid of the same software we used to reconstruct the stopband of the DBR mirrors (Fig. 5.3 (c)). The exact mirror structure is included and the refractive index of diamond is assumed to be constant, $n_{\mathrm{d}} = 2.41$. $m_1$ tells us that the lowest fundamental mode is the 8th resonance (5th resonance away from contact; curved mirror depth $> 3 \cdot \frac{\lambda}{2}$). The gradients $m_{\mathrm{i}} = \frac{\mathrm{d}\lambda_{\mathrm{cav}}}{\mathrm{d}t_{\mathrm{a}}}$ of the $(q, 0, 0)$ modes depend on the exact diamond thickness $t_{\mathrm{d}}$ and the exact air-gap thickness $t_{\mathrm{a}}$. By adjusting $t_{\mathrm{d}}$ and $t_{\mathrm{a}}$ in the simulation, we match the experimental results for $m_1$ and $m_2$ with $t_{\mathrm{d}} = 0.77\,\mu\mathrm{m}$ and $t_{\mathrm{a}} = 2.60\,\mu\mathrm{m}$ (Fig. 5.7. The diamond thickness is in agreement with the value we found in our previous NV coupling experiment [77] which used the exact same membrane.

We present some details on how to extract the diamond thickness from the cavity mode-structure. To start, we calibrate the travel range of the piezo using the mode dispersion and Eq. 5.1. In the experiment, we apply a positive voltage to elongate the z-piezo, thus reducing the width of the air-gap, i.e. a larger voltage translates to a shorter cavity. To convert from voltage to travel range, we equate the free-spectral (FSR) range in voltage to FSR $\simeq \frac{\lambda}{2}$. Due to the low signal-to-noise ratio and the limited spectral width of the measurement, the piezo was calibrated by linear interpolation for $\lambda = \lambda_{\mathrm{s}}$. Next, we simulate the cavity mode structure for the same spectral range while step-wise changing $t_{\mathrm{d}}$. In Fig. 5.7, we overlap the simulated- and measured mode structure for $t_{\mathrm{d}} = 0.762\,\mu\mathrm{m}$, $t_{\mathrm{d}} = 0.772\,\mu\mathrm{m}$ and $t_{\mathrm{d}} = 0.782\,\mu\mathrm{m}$. From the line-cuts, it is apparent that $t_{\mathrm{d}} = 0.762\,\mu\mathrm{m}$ overestimates the cavity length: the simulated cavity mode occurs at a too long cavity

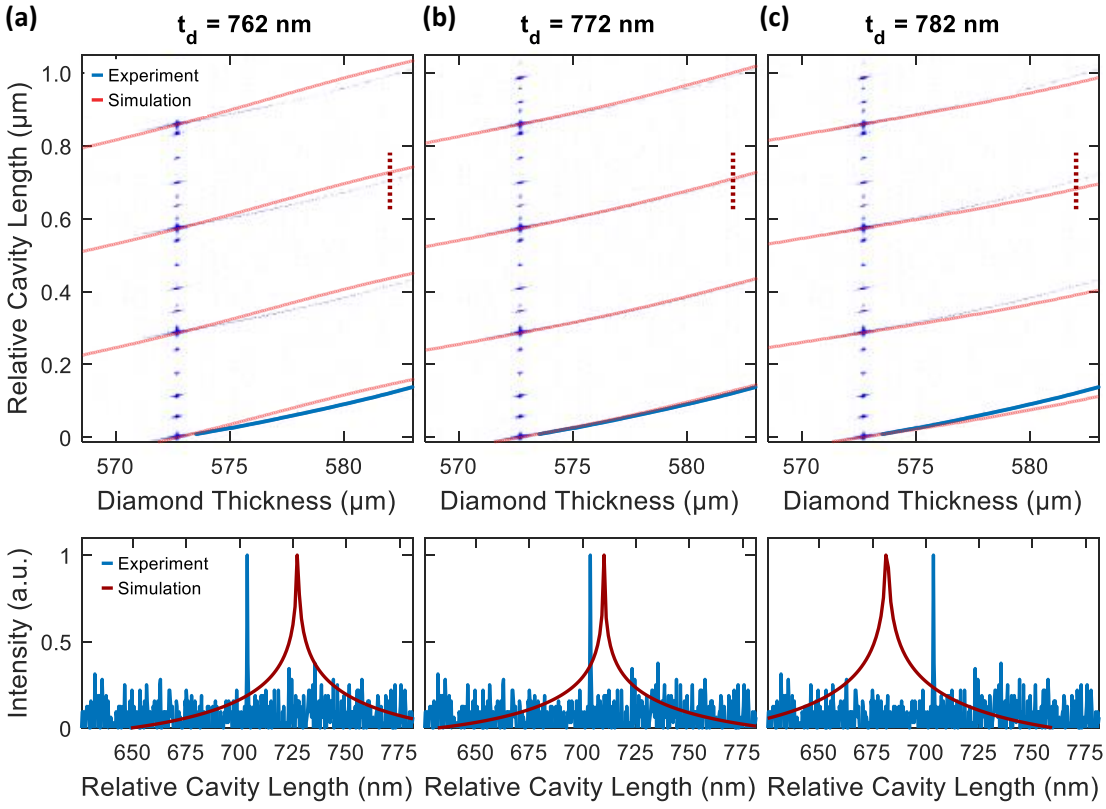


Fig. 5.7. The diamond thickness is extracted by overlapping the measured and simulated mode structure. **(a)** A diamond thickness $t_\mathrm{d} = 762\,\mathrm{nm}$ overestimates the cavity length; the simulated mode (red) occurs at a longer cavity length compared to the measured mode. **(b)** A diamond thickness $t_\mathrm{d} = 772\,\mathrm{nm}$ reproduces both the spacing and the curvature of the measured mode structure. We attribute the $\sim 7\,\mathrm{nm}$ discrepancy between the measured and simulated mode to errors in calibrating the piezo. For details, see text. **(c)** A diamond thickness $t_\mathrm{d} = 782\,\mathrm{nm}$ underestimates the cavity length; the simulated mode (red) occurs at a shorter cavity length compared to the measured mode.

length compared to the measure mode. We find the best agreement for $t_\mathrm{d} = 0.772\,\mu\mathrm{m}$. From the overlap, it is apparent that the simulation overestimates the cavity length by $\sim 7\,\mathrm{nm}$. We attribute this discrepancy to errors and uncertainties in extracting the exact peak position when calibrating the piezo. Considering both the absolute spacing and the dispersion of the modes, we find the best concordance for $t_\mathrm{d} = 0.772\,\mu\mathrm{m}$. Further increasing the diamond thickness to $t_\mathrm{d} = 0.782\,\mu\mathrm{m}$ underestimates the cavity length: the simulated cavity mode now occurs at a too short cavity length compared to the measured mode.

We now turn to analyse the $(q, n, m) = (24, 0, 0)$ mode in more detail. This particular mode is well-isolated and not perturbed by coupling to higher-order modes of

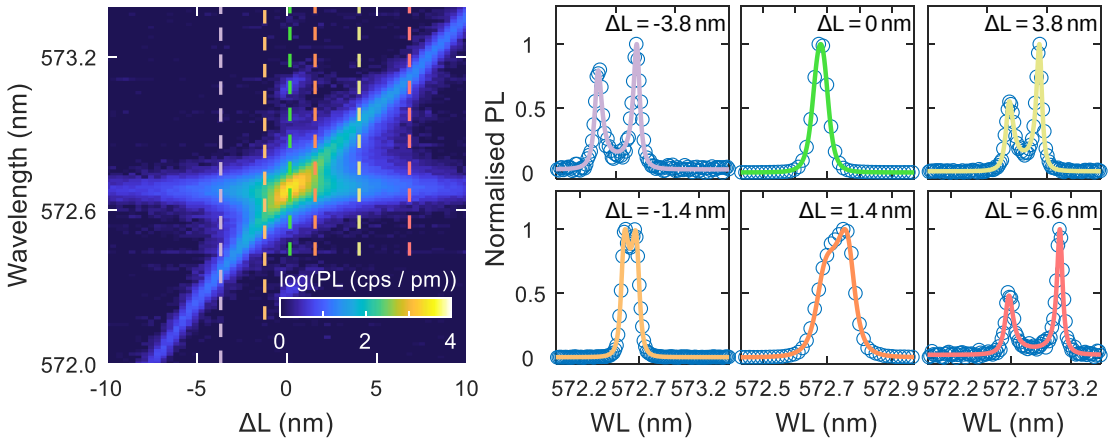


Fig. 5.8. An enlargement of the spectra in Fig. 5.6 (a) featuring linecuts at different $\Delta L$ (for mode $(q+1,0,0)$). The data can be very well fitted by fitting using two multiplied Lorentzians (Eq. 5.4). The fit allows to extract the linewidths of the Stokes and cavity, $\delta\lambda_\mathrm{s} = 71\,\mathrm{pm}$ and $\delta\lambda_\mathrm{cav} = 70\,\mathrm{pm}$ respectively.

other mode families (Fig. 5.8 (b)). Coupling between transverse modes of the cavity can be induced by a non-ideal shape of the curved mirror [88, 90] and the fact that the diamond-air interface does not conform with the curved wavefront of the Gaussian mode [87]. In particular, we focus on the spectral properties as the cavity is tuned into resonance with the Stokes process. Without the top mirror (i.e. no cavity), we find that the Stokes resonance has a Lorentzian lineshape with a full width at half maximum (FWHM) of $\delta\lambda_{\mathrm{s},532} = 71\,\mathrm{pm}$, corresponding to $\mathcal{Q}_\mathrm{s} = 8\,066$ (Fig. 5.5 (b)). This linewidth, 64.9 GHz, is determined by a convolution of the laser linewidth, $\sim 15\,\mathrm{GHz}$, with the linewidth of the Stokes scattering process, $\delta\nu_\mathrm{s} \sim 50\,\mathrm{GHz}$. We measure $\delta\nu_\mathrm{s}$ independently by pumping the Stokes process with a narrow-bandwidth laser at $\lambda = 636\,\mathrm{nm}$ and find $\delta\lambda_{\mathrm{s},636} = 77\,\mathrm{pm}$ corresponding to $\delta\nu_\mathrm{s} = 47.8\,\mathrm{GHz}$ (Fig. 5.5 (d)). In the absence of inhomogeneous strain fields, the Raman linewidth is a measure of the phonon lifetime. The measured Raman linewidth corresponds well with previously reported values, 3.6 ... 3.9 ps (40.8 ... 44.2 GHz) [350, 353], indicating low strain in our diamond membrane. Here, the main decay channel of the optical phonon involves the creation of two acoustic phonons each with lower energy [362, 431]. With the top mirror, we tune the cavity through the Stokes resonance, recording spectra at each detuning (Fig. 5.8 (b)). The experimental spectra are well fitted by the product of two Lorentzians describing the cavity and the Stokes process, $\mathcal{L}_\mathrm{cav}(\lambda_\mathrm{cav}, \delta\lambda_\mathrm{cav}) \cdot \mathcal{L}_\mathrm{s}(\lambda_\mathrm{s}, \delta\lambda_\mathrm{s})$:

$$\mathcal{L}_\mathrm{cav} \cdot \mathcal{L}_\mathrm{s} = \mathcal{A} \cdot \frac{1}{(\lambda - \lambda_\mathrm{cav})^2 + (\frac{\delta\lambda_\mathrm{cav}}{2})^2} \cdot \frac{1}{(\lambda - \lambda_\mathrm{s})^2 + (\frac{\delta\lambda_\mathrm{s}}{2})^2}\,. \tag{5.4}$$

During the experiment, we tune the resonance frequency of the cavity $\lambda_{\mathrm{cav}}$ while $\lambda_{\mathrm{s}} = 572.67\,\mathrm{nm}$ and $\delta\lambda_{\mathrm{s},532} = 71\,\mathrm{pm}$ are fixed. From our fit, we extract that the linewidth of the cavity $\delta\lambda_{\mathrm{cav}}$ decreases from 80 pm (73 GHz) to 60 pm (55 GHz) on detuning from wavelength 572 nm to 573.4 nm (corresponding to $\mathcal{Q}$-factors of 7 200 and 9 600, respectively) due to the change in mirror reflectivity (Fig. 5.3). We note that in this experiment, the bare Stokes resonance has a similar spectral width as the cavity resonance. On resonance $\lambda_{\mathrm{cav}} = \lambda_{\mathrm{s}}$, $\delta\lambda_{\mathrm{cav}} = 70\,\mathrm{pm}$ and $\mathcal{Q}_{\mathrm{cav,res}} = 8\,200$. The slight deviation of the Stokes lineshape from a Lorentzian (see Fig. 5.5) results in a $\sim 10\%$ error of the extracted linewidth.

The spectral information leads to an interpretation of the microscopic nature of the cavity-enhanced Raman process. The spectra do not mimic the behaviour of a coherent single emitter coupled to a single cavity-mode. Instead, they mimic the behaviour of an independent array of emitters (described by $\mathcal{L}_{\mathrm{s}}$) coupled to a single cavity mode (described by $\mathcal{L}_{\mathrm{cav}}$). The Lorentzian cavity mode $\mathcal{L}_{\mathrm{cav}}$ acts as a spectrally-selective booster for the Raman processes which are resonant with it.

### 5.3.2 Quantitative Analysis of the Enhancement Factor

We attempt to understand the enhancement factor $F$ quantitatively [368]. The first step is to calculate the Purcell factor. One way to describe the signal enhancement promoted by the cavity is to consider an increase of the effective Stokes scattering length. The cavity finesse is a measure of the number of times a photon bounces between the mirrors and corresponds to the factor by which the scattering length is increased. This description is formally equivalent to the Purcell formula for a cavity formed by two mirrors [30]. In our experiment, however, the cavity is more complex than a generic Fabry-Perot device. We calculate the vacuum electric-field distribution with the same software we used for the previous calculations of the mirror reflectivity and the slope of the mode dispersion (Essential Macleod). To that end, we calculate the electric field distribution of a one-dimensional cavity using the geometric parameters extracted from Fig. 5.6 (a). We then quantise the field amplitude of the Gaussian cavity mode according to (Fig. 5.9):

$$\begin{aligned}\int_{\mathrm{cav}} \epsilon_0\epsilon_{\mathrm{R}}(z)|\vec{E}_{\mathrm{vac}}(z)|^2\mathrm{d}z \int_0^{2\pi}\mathrm{d}\phi \int_0^{\infty} re^{-r^2/2w_{\mathrm{I}}^2}\mathrm{d}r \\ = 2\pi\cdot\frac{1}{4}w_{\mathrm{I}}^2\int_{\mathrm{cav}}\epsilon_0 n^2(z)|\vec{E}_{\mathrm{vac}}(z)|^2\mathrm{d}z = \hbar\omega/2\end{aligned} \tag{5.5}$$

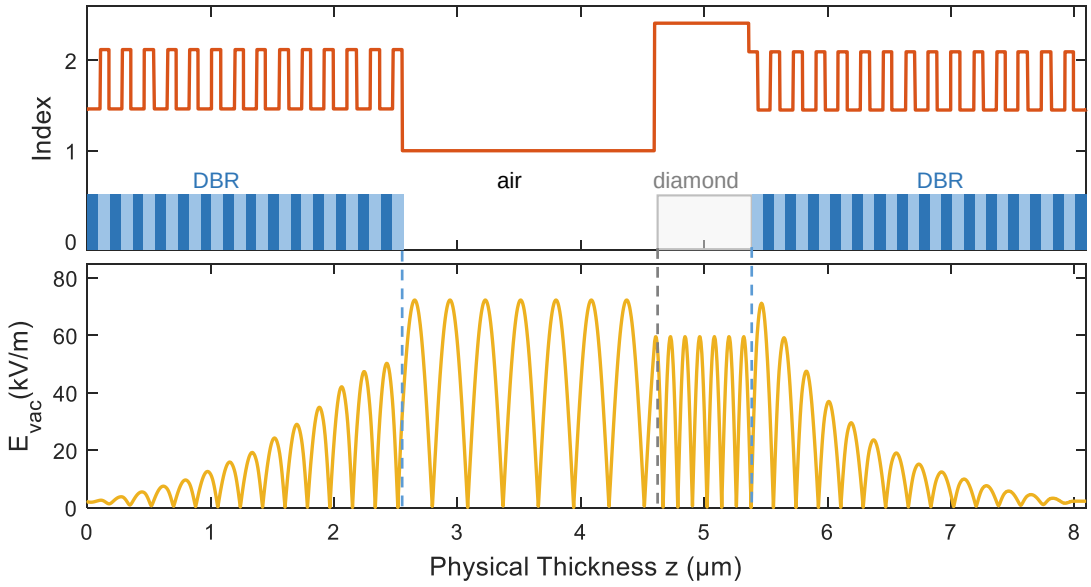


Fig. 5.9. One-dimensional transfer matrix simulation of the electric vacuum field for $t_\mathrm{a} = 2\,596\,\mathrm{nm}$ and $t_\mathrm{d} = 772\,\mathrm{nm}$. The electric-field profile possesses a field anti-node at the diamond-air interface.

We take $\epsilon_\mathrm{R} = n^2$; we assume a constant beam-waist $w_\mathrm{I}$ over the cavity length. Taking a representative value, $w_{0,\mathrm{I}} = 0.77\,\mu\mathrm{m}$ (an average of the beam-waist at the top mirror and the minimum beam-waist), we find a maximum $|\vec{E}_\mathrm{vac}(z)| = 54.4\,\frac{\mathrm{kV}}{\mathrm{m}}$ inside the diamond from which we can calculate the effective mode volume of a cubic resonator made from diamond to be $V_\mathrm{eff} = 84.9 \cdot \left(\frac{\lambda}{n}\right)^3$. With the cavity $\mathcal{Q}$-factor on resonance $\mathcal{Q}_\mathrm{cav}(\lambda_\mathrm{cav}) = 8\,200$, we calculate the Purcell factor to be

$$F_\mathrm{P}(\lambda_\mathrm{cav}) = 1 + \frac{3}{4\pi^2} \cdot \frac{\mathcal{Q}_\mathrm{cav}}{V_\mathrm{eff}} \cdot \left(\frac{\lambda}{n}\right)^3 \cdot \frac{1}{2} = 4.7\,. \tag{5.6}$$

Here, the factor $\frac{1}{2}$ takes into account averaging of the enhancement over the field profile inside the diamond. The second step is to calculate the coupling efficiencies (the derivation of this model can be found in Appendix F). Without the top mirror, we estimate the coupling efficiency $\eta_\mathrm{o}$ simply as twice the solid-angle defined by the objective lens:

$$\eta_0 \simeq 1 - \sqrt{1 - \left(\frac{\mathrm{NA}}{n_\mathrm{d}}\right)^2}\,, \tag{5.7}$$

where the factor of two accounts for reflection from the bottom DBR. From the NA = 0.4 objective, we deduce $\eta_0 = 1.4\,\%$. With the cavity, the coupling efficiency is given by

$$\eta_{\mathrm{cav}} = \frac{\kappa_{\mathrm{top}}}{\kappa_{\mathrm{top}} + \kappa_{\mathrm{bot}} + \kappa_{\mathrm{tot}}} \cdot \beta \tag{5.8}$$

where $\kappa_{\mathrm{top}}$ ($\kappa_{\mathrm{bot}}$) is the loss-rate through the top (bottom) mirror, $\kappa_{\mathrm{tot}}$ is the round-trip cavity loss-rate and

$$\beta = \frac{F_{\mathrm{P}}}{(F_{\mathrm{P}} + 1)} \tag{5.9}$$

is the probability of emission into the cavity mode. From $F_{\mathrm{P}} = 4.7$, we have $\beta = 82.46\,\%$. We determine the $\kappa_{\mathrm{top}} = 1.656 \cdot 10^{11}\,\mathrm{s}^{-1}$ and $\kappa_{\mathrm{bot}} = 9.525 \cdot 10^{10}\,\mathrm{s}^{-1}$ from the transfer-matrix simulations of the bare mirrors and $\kappa_{\mathrm{loss}} = \frac{2\pi c}{\lambda} \cdot \left(\frac{1}{\mathcal{Q}_{\mathrm{exp}}} - \frac{1}{\mathcal{Q}_{\mathrm{exp}}}\right) = 1.429 \cdot 10^{11}\,\mathrm{s}^{-1}$ (Compare Appendix F). Combining the above give $\eta_{\mathrm{cav}} = 32.5\,\%$, and consequently $\frac{\eta_{\mathrm{cav}}}{\eta_0} = 23.2$. Assuming an identical pump rate, likewise identical diamond material parameters and collection optics, the ratio of the Stokes signal with cavity enhancement to the Stokes signal without the cavity (i.e. no top mirror) is

$$\frac{S_{\mathrm{cav}}}{S_0} = F_{\mathrm{P}} \cdot \frac{\eta_{\mathrm{cav}}}{\eta_{\mathrm{o}}}\,. \tag{5.10}$$

A final factor is that the Stokes ($\mathcal{Q}_{\mathrm{s}} = 8\,066$) and cavity linewidths ($\mathcal{Q}_{\mathrm{cav}} = 8\,200$) are similar [369]: the final result is

$$\frac{S_{\mathrm{cav}}}{S_{\mathrm{o}}} \simeq F_{\mathrm{P}} \cdot \frac{\mathcal{Q}_{\mathrm{s}}}{\mathcal{Q}_{\mathrm{s}} + \mathcal{Q}_{\mathrm{cav}}} \cdot \frac{\eta_{\mathrm{cav}}}{\eta_{\mathrm{o}}} \tag{5.11}$$

Quantitatively, this result predicts that $\frac{S_{\mathrm{cac}}}{S_{\mathrm{o}}} = 56.8$, in good agreement with the experiment. (We note that the error in the experimental measurement of $\frac{S_{\mathrm{cav}}}{S_{\mathrm{o}}}$ is dominated by a systematic error of 10% arising on ensuring that the optical alignment is preserved on removing the top mirror; the error in the calculated $\frac{S_{\mathrm{cav}}}{S_{\mathrm{o}}}$ is dominated by the uncertainties of $\sim 10\%$ in the beam-waist and $\mathcal{Q}$-factor of the cavity.) It is interesting to note that $\frac{S_{\mathrm{cav}}}{S_{\mathrm{o}}}$ is much simpler to measure than the Purcell factor of a single emitter: a measurement of $\frac{S_{\mathrm{cav}}}{S_{\mathrm{o}}}$ is an indicator of the performance of a single-emitter in the same cavity structure.

## 5.4 Outlook and Conclusion

The mode-structure calculation in Fig. 5.9 shows that the cavity is in a "diamond-like" configuration at the Stokes wavelength $\lambda_{\mathrm{s}}$ (Compare Chapter 3) [87]. An advantage of

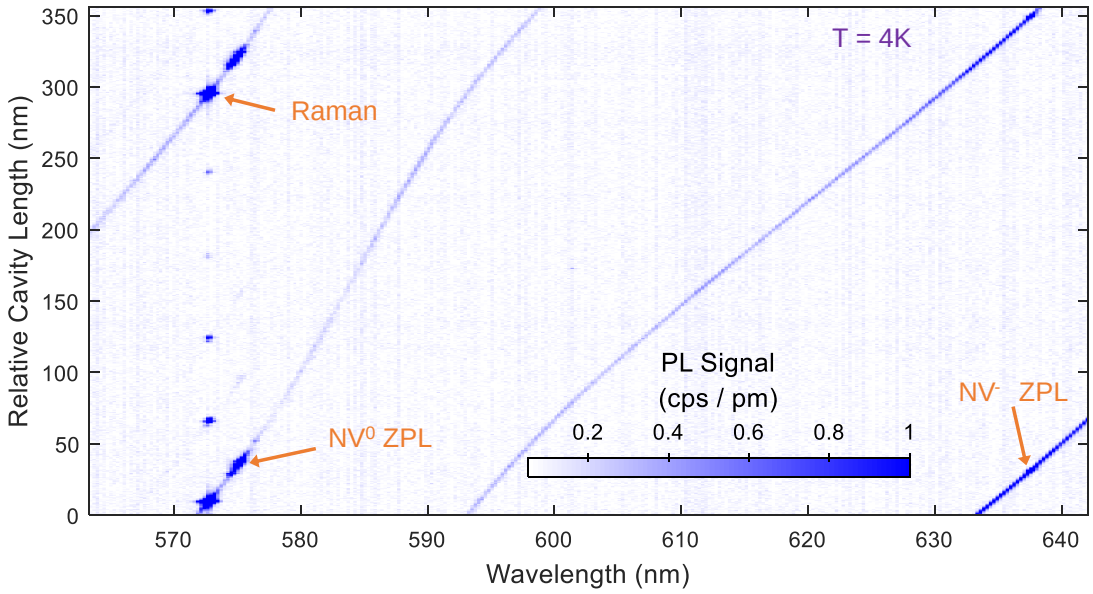


Fig. 5.10. Mode structure of the cavity recorded at a temperature of 4 K, under continuous-wave excitation at 532 nm with a power of 30 mW. In addition to the Raman transition, the ZPL of the $NV^0$ and $NV^-$ couples to the cavity.

this configuration is that the electric vacuum field is more strongly confined in the diamond layer than in the air-gap which leads to higher coupling strengths. A further advantage is that the dispersion of the mode wavelength with air-gap thickness is relatively small. This renders the cavity less susceptible to acoustic noise. However, a diamond-like cavity exhibits a vacuum field antinode at the diamond-air interface which exacerbates losses (over a configuration with a field node at the diamond-air interface) caused by scattering at this interface or absorption of the surface. In some materials, GaAs for instance, these losses can be mitigated by passivating the surface [99, 391, 415].

The results presented so far were all recorded at room temperature. For single emitters, operation at low temperature is necessary in order to eliminate phonon-related broadening of the ZPL. We therefore demonstrate that the cavity-enhanced Raman scattering works well also at cryogenic temperature. The compact cavity design facilitates low-temperature experiments in a liquid-helium bath cryostat [77, 99, 102, 115]. Fig. 5.10 shows a spectrally resolved cavity measurement where the cavity length is tuned over one free spectral range for an excitation at wavelength 532 nm. The weak background PL of the diamond allows the main cavity modes to be observed at all cavity lengths. In Fig. 5.10, the nonlinear dependence of the cavity wavelength on air-gap thickness is visible. The first-order Raman peak and the ZPLs of the two different charge states of

the NV are enhanced by the cavity and are very strong features in Fig. 5.10. The weak emission of the ZPLs is only detected efficiently once the external optical excitation and collection are properly aligned. The strong Raman signal was used to achieve the alignment: the advantage secured at room temperature therefore translates directly to operation at a cryogenic temperature.

To conclude, we show that Raman scattering provides a valuable resource in optimising and quantifying the performance of tunable microcavities. We apply this method specifically to the NV centre in diamond. More generally, the generic nature of Raman scattering renders our approach immediately applicable for improving the spin-photon interface efficiencies of a wide range of solid-state qubits. This will be particularly valuable for emitters with a weak oscillator strength: by harnessing the Stokes process as a strong, narrowband, internal light-source, the cavity performance can be optimised, facilitating the detection of signals from weak single-emitters. The modular platform improves greatly the versatility of cavity experiments and allows for creating an optimized CQED system: The different parts, bottom mirror, top mirror and optically active layer can be processed and designed individually. The possibility to combine a comparatively large pristine solid state environment ($\sim \mu m^3$) with high $\mathcal{Q}/V$ ratios is poised to facilitate combining cavity enhancement with narrow optical linewidths without the use of electric gates [99]. Examples of qubits with long spin coherence times but small optical dipole-moments include colour centres in silicon carbide [323, 416] and rare earth ions [330, 331, 417].

CHAPTER 6

# Widely-tunable, Doubly-Resonant Raman Scattering on Diamond in an Open Microcavity

**The content of this chapter is partially adapted from:**
Sigurd Flågan, Patrick Maletinsky, Richard J. Warburton and Daniel Riedel
**"Widely-tunable, doubly-resonant Raman scattering on diamond in an open microcavity"**, arXiv:2110.06242 (2021)

**Abstract:**

Raman lasers based on bulk diamond are a valuable resource for generating coherent light in wavelength regimes where no common laser diodes are available. Nevertheless, the widespread use of such lasers is limited by their high threshold power requirements on the order of several Watts. Using on-chip microresonators, a significant reduction of the lasing threshold by more than two orders of magnitude has been shown. However, these resonators lack a continuous tuning mechanism and, mainly due to fabrication limitations, their implementation in the visible remains elusive. Here, we propose a platform for a diamond Raman laser in the visible. The device is based on a miniaturised, open-access Fabry-Perot cavity. Our microcavity provides widely-tunable doubly-resonant enhancement of Raman scattering from high-quality single-crystalline diamond. We demonstrate a >THz continuous tuning range of doubly-resonant Raman scattering, a range limited only by the reflective stopband of the mirrors. Based on the experimentally determined quality factors exceeding 300 000, our theoretical analysis suggests that, with realistic improvements, a sub-mW threshold is readily within reach. Our findings pave the way to the creation of a universal low-power frequency shifter, a potentially valuable addition to the nonlinear optics toolbox.

## 6.1 Introduction

The development of new laser architectures to create coherent radiation at arbitrary wavelengths is a continuous endeavour. Solid-state based lasers have emerged as the leading platform due to their compact design, reliability, highly stable output and beam quality [432]. Several wavelength regimes, however, are not directly accessible with semiconductor lasers and require wavelength conversion in a nonlinear medium.

A promising technique relies on Raman scattering where, upon the creation of a phonon, photons are red-shifted by the fixed phonon energy. This energy shift and the efficiency of the process, quantified by the Raman gain parameter, depend on the material and in particular on the phonons involved [334]. The main advantage of this approach is that in principle any laser wavelength can be achieved if a suitable pump laser is available [372]. This gain mechanism differs from stimulated emission from excited dopants which exhibit a fixed gain frequency bandwidth [348].

Diamond is particularly well suited to the creation of a Raman-based laser due to its exceptional properties [344], notably a large Raman gain ($\sim$75 GW$\cdot$cm$^{-1}$ at 532 nm) [344] and a large Raman shift ($\sim$1 332 cm$^{-1}$) [138]. This large Raman shift enables wavelengths to be accessed for which no ideal solution exists in terms of cost, convenience and output power. Other advantages in this context are the wide bandgap of diamond, which prevents free carrier absorption minimising optical losses in the visible and the ultraviolet wavelength regimes, and diamond's high thermal conductivity, which facilitates efficient heat management [373].

Diamond Raman lasers have enabled the creation of coherent radiation in exotic wavelength regimes, e.g. the yellow band [337, 376, 428, 433, 434], where no common laser diodes are available. High-power diamond Raman lasers have been implemented across a large range of wavelengths, from the ultraviolet [374] across the visible [375, 376] and infrared [377, 378, 435–441], all the way to the mid-infrared [378]. However, current implementations are limited by their high threshold pump power requirements, typically several Watts.

Micro- and nanophotonic engineering offers the potential of reducing the threshold for lasing. Through resonant recirculation of the pump beam in a cavity with a small mode cross-section, the intensity-dependent Raman gain is significantly enhanced. In addition, simultaneous coupling of the Raman field to a second cavity mode boosts the efficiency of stimulated emission. Based on this doubly-resonant configuration, low-threshold Raman lasers in the infrared wavelength regime were demonstrated in silica microspheres [371]. Chip-integration has been implemented using silica microtoroids [380],

silicon waveguides [442, 443] and racetrack resonators [444]. Combining high quality ($\mathcal{Q}$) factors with a small mode volumes ($V$), silicon photonic crystals have enabled ultra-low threshold Raman lasing in the nanowatts regime [445]. Recently, molecules adsorbed to silica microtoroids emerged as a promising gain medium [446]. Advances in diamond nanofabrication enabled the demonstration of integrated diamond Raman lasers using ring resonators at infrared [382] and near-visible [383] wavelengths. Largely on account of nanofabrication constraints, diamond Raman microlasers at visible frequencies, however, remain elusive.

We propose to resolve this conundrum by using a different platform for the implementation of a low-threshold diamond Raman laser, namely a highly miniaturised Fabry-Perot cavity [255] (Fig. 6.1 (a)). Such microcavities, sometimes referred to as open microcavities, offer high $\mathcal{Q}/V$ ratios and thereby promote strong light-matter interactions [97, 99, 103]. Chapter 4 demonstrated that high $\mathcal{Q}$-factors at visible wavelengths can be achieved when embedding a high-quality diamond membrane into the cavity [387]. In comparison to ring resonators, there are no limitations due to bending losses and surface roughness is less detrimental.

## 6.2 Open Microcavity as a Platform for Nonlinear Optics

Our plano-concave microcavity design supports a Gaussian fundamental mode (Fig. 6.1 (a)), [104, 368, 385, 399, 447]. The microcavity is formed by two mirror-coated fused silica substrates, one of which contains an array of spherical micromirrors fabricated via laser ablation [402]enabling efficient coupling to a single free-space mode [77, 102]. The radii of curvature of these micromirrors are $\sim 10\,\mu\text{m}$ resulting in a beam waist of $\sim 1\,\mu\text{m}$. We integrate high-quality single-crystalline diamond micromembranes ($\sim 20 \times 20 \times 0.8\,\mu\text{m}^3$) into the cavity using a micromanipulator [77, 403] (see Section 6.7).

For conventional Fabry-Perot resonators, the resonance wavelength changes linearly with the mirror separation $t_\text{a}$. However, the presence of a diamond membrane with thickness $t_\text{d}$ significantly alters this linear mode structure. The hybridisation of modes confined in the air and diamond layers of the resonator manifests in avoided crossings (Fig. 6.1 (b)) [77, 87, 98, 100, 214, 405]. The cavity resonance frequencies depend on both the separation of the two mirrors and the thickness of the diamond at the location of the cavity mode (see Section 6.4.1).

One of the main advantages of our cavity platform is the *in situ* tuning capability. Both the separation of the mirrors and the lateral position of the cavity mode with respect to

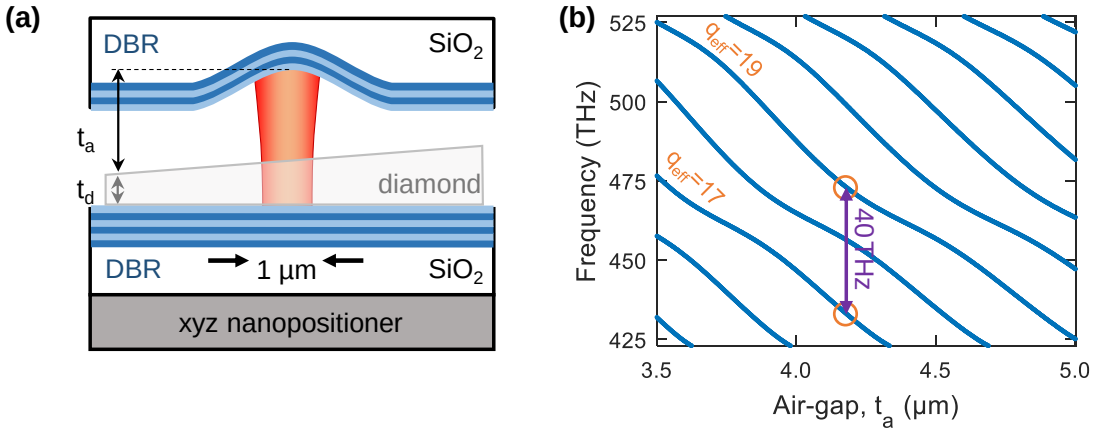


Fig. 6.1. **(a)** Schematic of the plano-concave Fabry-Perot microcavity. The cavity is formed by two fused silica ($SiO_2$) substrates coated with a distributed Bragg reflector (DBR). One of the substrates exhibits spherical microindentations resulting in a Gaussian resonator mode with a small beam waist ($\sim 1\,\mu m$). Piezoelectric nanopositioners allow for spatial and spectral tunability of the cavity mode. The wedged diamond membrane enables the diamond thickness within the cavity mode to be changed by lateral positioning. The thickness gradient of the diamond is exaggerated for enhanced visibility. **(b)** One-dimensional transfer-matrix calculation of the cavity mode-structure for a diamond thickness of $t_d = 756\,nm$. The presence of the diamond membrane leads to a nonlinear mode dispersion. At a mirror separation of $\sim 4.18\,\mu m$, the frequency spacing between modes $q_{eff} = 17$ and $q_{eff} = 19$ equals the frequency of the optical phonon in diamond ($\sim 40\,THz$, purple arrow).

the diamond membrane can be controlled via a stack of piezoelectric nano-positioners (attocube ANPx/z51, ANPz51). The cavity resonance frequencies depend on both the separation of the two mirrors and the thickness of the diamond at the location of the cavity mode. By including a slight thickness gradient into the diamond membrane, we are able to tune the exact diamond thickness of the membrane in the cavity by adjusting the relative lateral position of the mirrors. The *in situ* tuning capability allows us to control both the absolute frequency as well as the relative splitting of the resonator modes.

Excitation of the first-order Stokes process in diamond can be modelled as a three-level atom-like system (inset Fig. 6.2) involving a ground state $|1\rangle$, a virtual state $|2\rangle$ and a meta-stable state $|3\rangle$. A pump laser excites the ground-state population from $|1\rangle$ to $|2\rangle$. The system decays via state $|3\rangle$ emitting a red-shifted photon ($|2\rangle \rightarrow |3\rangle$) followed by an optical phonon of fixed frequency ($\sim 40\,THz$, $|3\rangle \rightarrow |1\rangle$).

By coupling both the pump and the Stokes photons to a cavity mode, the Stokes process can be strongly enhanced [364]. It should be noted that no population inversion is required for stimulated Raman scattering and hence the creation of a Raman laser [448].

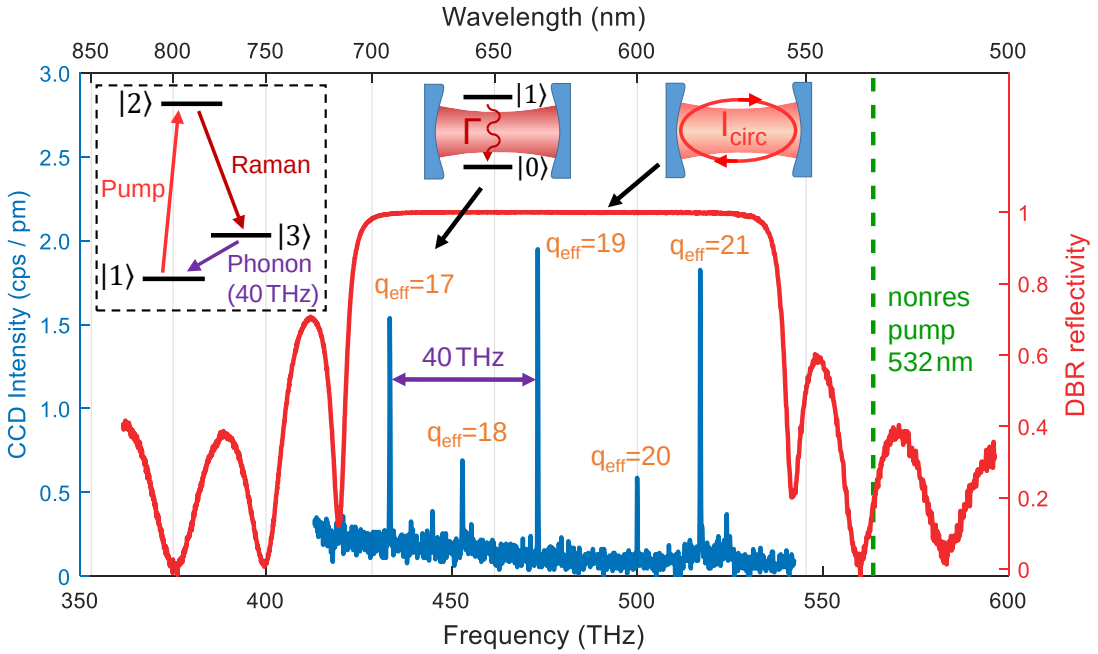


Fig. 6.2. In red: measurement of the reflectivity of the planar DBR revealing a stopband centred at 625 nm with a bandwidth of $\sim 100$ THz. In blue: experimental cavity spectrum for a fixed cavity length under 532 nm illumination. The diamond thickness and mirror separation can be inferred by comparing the spectrum with the simulated mode structure in Fig. 6.1 (b). Inset: Raman process, depicted as a three-level system. A photon is converted to a red-shifted photon and an optical phonon of fixed frequency.

Importantly, the gain of the Raman process is maximised by strong confinement of and coupling between the pump and Raman modes, which suggests the use of fundamental resonator modes. Careful tuning of the mirror separation $t_\mathrm{a}$ and the diamond thickness $t_\mathrm{d}$ allows the double-resonance condition to be established for a wide range of pump wavelengths in the visible wavelength regime. When changing the pump wavelength $t_\mathrm{d}$ and $t_\mathrm{a}$ need to be adjusted such that the cavity both remains resonant with the pump laser while another mode is red-detuned exactly by the Raman shift (see Section 6.3.2).

Importantly, the frequency of the Raman output is completely determined by the frequency of the pump laser and the fixed Raman shift. In our experiment, we focus on the visible wavelength regime. We use a continuous-wave (cw) narrow-band tunable red diode laser (Toptica DL Pro 635, $\lambda = (635 \pm 5)$ nm) as a pump source. The operation wavelength range of the cavity is given by the reflective stopband of the DBR, which we determine using a white-light transmission measurement [255]. Fig. 6.2 displays the stopband of the planar bottom mirror which is centred around $\lambda_{\mathrm{c,bot}} = 625$ nm; the

reflectivity is more than 99% over a bandwidth of $\sim$ 100 THz. The top mirror has similar properties but with a stopband centre at $\lambda_{\mathrm{c,top}} = 629\,\mathrm{nm}$.

### 6.2.1 Establishing the Double-Resonance Condition

To characterise the mode structure of the cavity, we couple a cw green laser ($\lambda_{\text{non-res}} = 532\,\mathrm{nm}$) into the cavity through the curved top mirror. We tune the mirror separation by applying a voltage to the piezo using a highly-stable voltage source (Basel Precision Instruments SP 927). Background photoluminescence (PL) from the diamond acts as an internal light source and couples to the different resonator modes [255]. Fig. 6.2 displays a PL spectrum collected through the top mirror. We set the mirror separation such that the splitting between the modes with effective mode numbers $q_{\mathrm{eff}} = 17$ and $q_{\mathrm{eff}} = 19$ corresponds to the Raman shift in diamond ($\Delta\nu_{\mathrm{R}} \sim 40\,\mathrm{THz}$). We define the effective mode number by the number of half wavelengths between the two mirrors, i.e. within the air-gap and the diamond layer, $q_{\mathrm{eff}} \cdot \frac{\lambda}{2} \approx t_{\mathrm{a}} + n_{\mathrm{d}} t_{\mathrm{d}}$. A small deviation from integer values of $q_{\mathrm{eff}}$ is caused by field penetration into the DBR mirrors [94, 406]. Using a one-dimensional transfer-matrix calculation we infer the mirror separation and diamond layer thickness to be $t_{\mathrm{a}} = 4.18\,\mu\mathrm{m}$ and $t_{\mathrm{d}} = 756\,\mathrm{nm}$, respectively (Figure 6.1 (b), and Section 6.4.1).

Next, we verify that we are able to establish the double resonance condition by coupling an additional laser resonant with mode $q_{\mathrm{eff}} = 17$ at $\lambda_{\mathrm{pump}} = 632.99\,\mathrm{nm}$ into the cavity. The resulting Raman scattered light is at a wavelength of $\lambda_{\mathrm{R}} = \left(\frac{1}{\lambda_{\mathrm{pump}}} - \frac{\Delta\nu_{\mathrm{R}}}{c}\right)^{-1} = 692.25\,\mathrm{nm}$, where $c$ is the speed of light. We then tune the mirror separation and record spectra from the cavity (Fig. 6.3 (a)). As expected, the cavity modes with effective mode numbers $q_{\mathrm{eff}} = 16...18$ and wavelengths in the range of $\lambda = 670...700\,\mathrm{nm}$ redshift with increasing mirror separation. When the pump laser at $\lambda_{\mathrm{pump}} = 632.99\,\mathrm{nm}$ is resonant with the $q_{\mathrm{eff}} = 18...20$ modes for relative mirror separations of $-316.5\,\mathrm{nm}$, $0\,\mathrm{nm}$ and $+316.5\,\mathrm{nm}$, narrow peaks appear in the spectrum at CCD pixels corresponding to $\lambda = 691.19\,\mathrm{nm}$ and $\lambda = 691.32\,\mathrm{nm}$, as highlighted in the insets of Fig. 6.3 (a).

The linecut at $\lambda = 691.19\,\mathrm{nm}$ clearly shows that the cavity resonances for $q_{\mathrm{eff}} = 16$ and $q_{\mathrm{eff}} = 18$ appear at smaller ($-345.5\,\mathrm{nm}$) and larger mirror separations ($+345.5\,\mathrm{nm}$) than the Raman peaks, respectively. Only for a mirror separation of $t_{\mathrm{a}} = 4.18\,\mu\mathrm{m}$ $\lambda_{\mathrm{pump}}$ and $\lambda_{\mathrm{R}}$ are, within the spectrometer resolution, simultaneously resonant with the cavity for $q_{\mathrm{eff}} = 19$ and $q_{\mathrm{eff}} = 17$. For this double resonance condition, the signal intensity is increased by over three orders of magnitude compared to the other peaks.

In the following we denote the wavelength of the cavity mode with $q_{\mathrm{eff}} = 17$ close

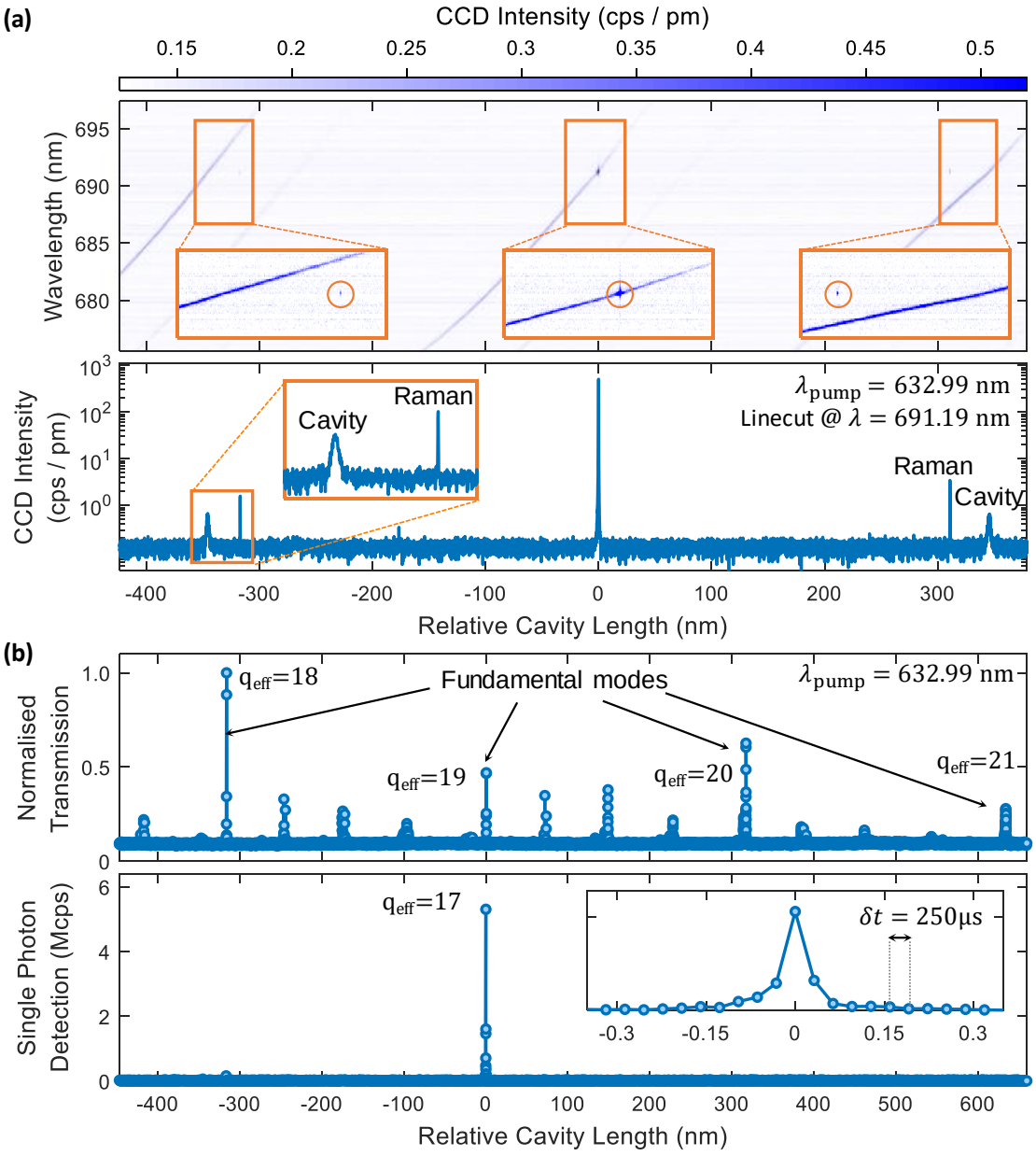


Fig. 6.3. Demonstration of cavity-enhanced doubly-resonant Raman scattering. **(a)** Top panel: Optical spectra as a function of relative cavity length reveal the cavity mode structure. Here, a laser at 532 nm excites background PL in the diamond and a narrowband diode laser at $\lambda_{\mathrm{pump}} = 632.99$ nm drives Raman scattering. For $q_{\mathrm{eff}} = 19$ and $q_{\mathrm{eff}} = 17$, the pump and Raman scattered light are resonant simultaneously, i.e. the double resonance condition is met. Bottom panel: Linecut at $\lambda = 691.19$ nm highlighting the strong signal enhancement of doubly-resonant Raman scattering. **(b)** Cavity transmission (top) and cavity emission at wavelengths $> 644$nm measured with a single photon counter (bottom) as a function of cavity length for $\lambda_{\mathrm{pump}} = 632.99$ nm. A cavity signal is only observed when the double resonance condition is satisfied. The piezo voltage is changed at a rate of $2\,\frac{\mathrm{mV}}{\mathrm{ms}}$.

in wavelength to that of the pump ($\lambda_{\text{pump}}$) as $\lambda_{\text{p}}^{\text{cav}}$; and the wavelength of the cavity mode with $q_{\text{eff}} = 19$ close in wavelength to that of the Raman photon ($\lambda_{\text{R}}$) as $\lambda_{\text{S}}^{\text{cav}}$. An analogous notation is adapted for the corresponding frequencies $\nu$.

A faster way to confirm that the double resonance condition is satisfied is displayed in Fig. 6.3 (b). Here, we only couple the diode laser at $\lambda_{\text{pump}}$ into the cavity and record the cavity transmission using a photodiode located beneath the bottom mirror. The transmission spectrum reveals several peaks at mirror separations where the pump laser is resonant with the cavity. These peaks are associated with fundamental and higher-order cavity modes. Simultaneously, we measure the cavity emission at wavelengths $> 644$nm using a single-photon counting module. A strong signal is observed only when $\lambda_{\text{pump}}$ is resonant with mode $q_{\text{eff}} = 19$, while at the same time $\lambda_{\text{R}}$ is resonant with $q_{\text{eff}} = 17$. The correlation between a peak in transmission (signifying a resonant pump laser) and a strong peak in cavity emission at longer wavelengths (signifying a resonant Raman process) is a clear demonstration that the double resonance condition is satisfied.

### 6.2.2 The $\mathcal{Q}$-Factor

Next, we determine the quality factor of the pump mode of the cavity, $\mathcal{Q}_{\text{p}}$, following the method described in Chapter 4 [387]. To extract the cavity linewidth, we keep the laser frequency $\nu_{\text{pump}}$ fixed while scanning the cavity length, monitoring the reflected light on a photodiode. An electro-optic modulator (EOM, Jenoptik PM635) is used

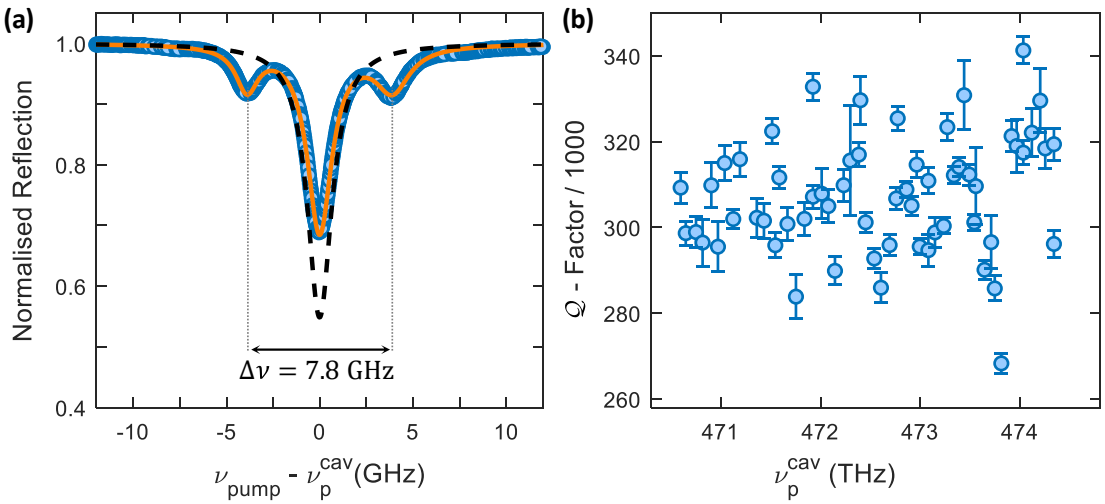


Fig. 6.4. **(a)** $\mathcal{Q}$-factor measurement for $\nu_{\text{p}}^{\text{cav}} = \frac{c}{\lambda_{\text{p}}^{\text{cav}}} = 473.233\,\text{THz}$. Sidebands created by an EOM at $\nu_{\text{pump}} \pm 3.9\,\text{GHz}$ act as a frequency ruler to extract the cavity linewidth. **(b)** $\mathcal{Q}$-factor as a function of cavity resonance frequency.

to create laser side-bands at $\nu_{\mathrm{pump}} \pm 3.9\,\mathrm{GHz}$, thereby providing a frequency ruler to extract the cavity linewidth. Fig.6.4 (a) shows the reflected signal averaged over 200 scans for $\nu_{\mathrm{pump}} = 473.233\,\mathrm{THz}$. Assuming a linear response of the piezo across the resonance, we extract a cavity mode full width at half maximum (FWHM) linewidth of $\delta\nu_{\mathrm{p}}^{\mathrm{cav}} = (1.59 \pm 0.05)\,\mathrm{GHz}$ corresponding to a quality factor of $\mathcal{Q}_{\mathrm{p}} = 297\,000 \pm 500$. Fig. 6.4 (b) shows the dependence of $\mathcal{Q}_{\mathrm{p}}$ on the cavity resonance frequency $\nu_{\mathrm{p}}^{\mathrm{cav}}$.

## 6.3 Doubly-Resonant Raman Scattering

We characterise in more detail the exact detuning dependence of the double resonance condition by tuning the pump laser. We exploit the fact that Raman signal in the cavity is only generated when a cavity-mode is resonant with the pump laser, $\nu_{\mathrm{pump}} = \nu_{\mathrm{p}}^{\mathrm{cav}}$. In this event, two signals will appear in the spectra: Raman scattering of the pump laser in the cavity at $\nu_{\mathrm{R}} = \nu_{\mathrm{pump}} + \Delta\nu_{\mathrm{R}}$, and the cavity mode nearest in frequency to this Raman signal, $\nu_{\mathrm{S}}^{\mathrm{cav}}$, which is fed by PL light that is non-resonantly generated by the pump laser. Using this technique it is not necessary to keep the cavity at one particular resonance – this circumvents any problems caused either by drift or acoustic and thermal noise.

We modulate the cavity length continuously and record the resulting cavity spectra (Fig. 6.5 (a)) varying $\nu_{\mathrm{pump}} = \nu_{\mathrm{p}}^{\mathrm{cav}}$ ($\lambda_{\mathrm{pump}} = \lambda_{\mathrm{p}}^{\mathrm{cav}}$) from 468.475 THz (639.932 nm) to 474.471 THz (631.845 nm). We find that for the pump frequency $\nu_{\mathrm{pump,dres}} = 472.434\,\mathrm{THz}$ the double resonance condition is fulfilled, $\nu_{\mathrm{R}} = \nu_{\mathrm{S}}^{\mathrm{cav}} = \nu_{\mathrm{R,dres}} = 432.520\,\mathrm{THz}$. These values are different from those in Fig. 6.3 (a) due to a slightly different lateral position of the cavity mode corresponding to a different diamond thickness. We determine a Raman shift of $\Delta\tilde{\nu}_{\mathrm{R}} = \nu_{\mathrm{pump,dres}}/c - \nu_{\mathrm{R,dres}}/c = 1\,331.4\,\mathrm{cm}^{-1}$ ($\Delta\nu_{\mathrm{R}} = c\Delta\tilde{\nu}_{\mathrm{R}} = 39.914\,\mathrm{THz}$), in good agreement with the previously reported value, $\sim 1\,332\,\mathrm{cm}^{-1}$ [339, 344, 429]. We plot the peak Raman counts for different detunings of the pump laser from the double resonance condition, $\nu_{\mathrm{pump}} - \nu_{\mathrm{pump,dres}}$ (projected blue points in Fig. 6.5 (a)). We find that these peak counts follow a Lorentzian with FWHM linewidth of 519.8 GHz [364]. The corresponding projected Raman amplitude is fitted well by a Lorentzian with FWHM linewidth of 502.9 GHz (projected red points in Fig. 6.5 (a)).

We fit the individual spectra for different detunings of the pump laser (with respect to the double-resonance frequency $\nu_{\mathrm{pump,dres}}$) to the product of two Lorentzians describing the cavity mode at $\nu_{\mathrm{S}}^{\mathrm{cav}}$ (FWHM $\delta\nu_{\mathrm{S}}^{\mathrm{cav}}$) and the gain bandwidth of the Raman scattering process at $\nu_{\mathrm{R}}$ (FWHM $\delta\nu_{\mathrm{R}}$). These fits allow the peak positions and linewidths to be extracted (Fig. 6.5 (b)) [255]. Figures 6.6 (a,b) display the results of these fits. Over

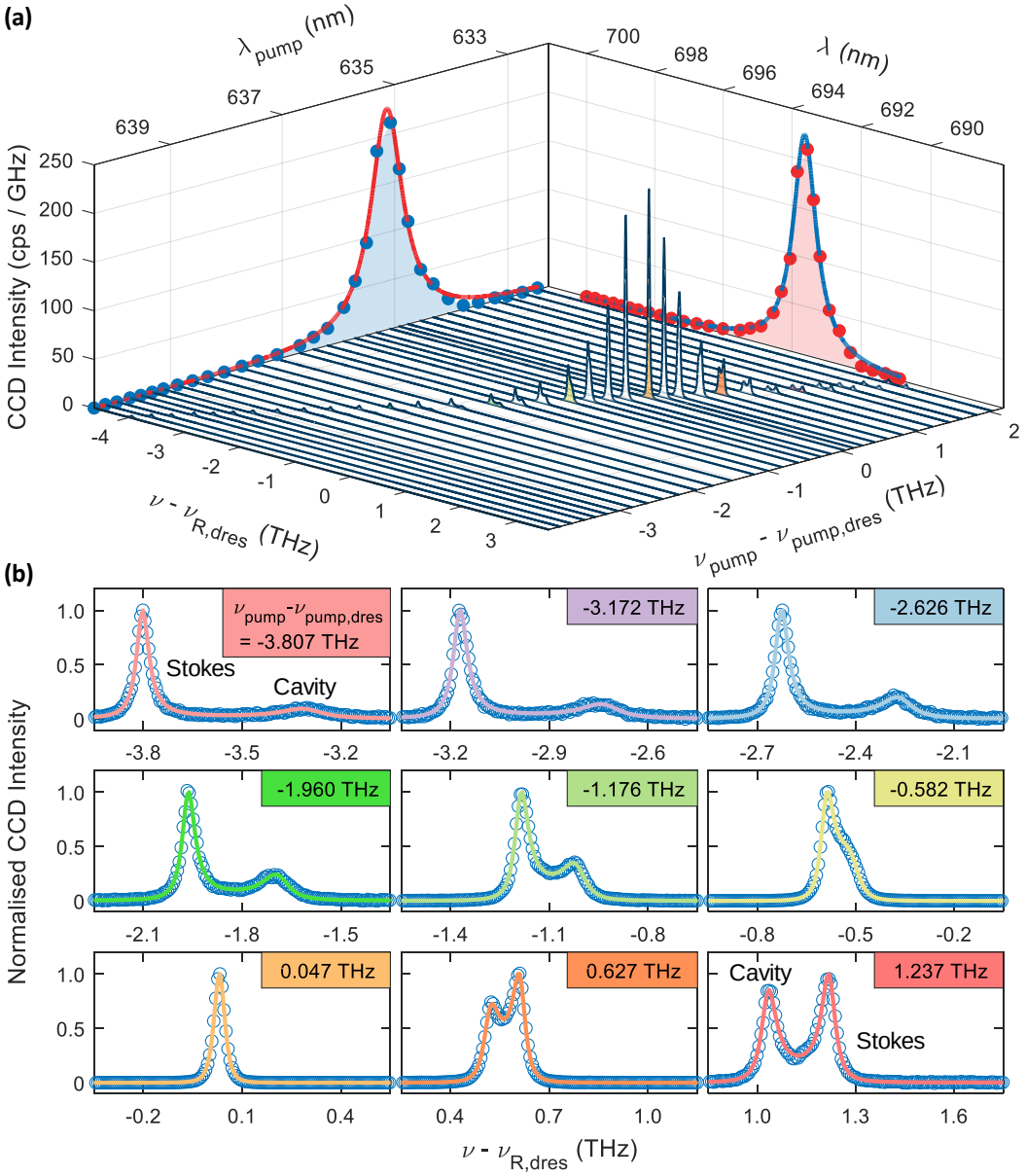


Fig. 6.5. **(a)** Series of cavity spectra for different detunings of the pump laser from the double resonance condition $\nu_{\mathrm{pump}} - \nu_{\mathrm{pump,dres}}$. We ensure that the pump laser is resonant with the cavity for every spectrum by continuously modulating the cavity length. The cavity spectra comprise the Raman signal at $\nu_{\mathrm{R}}$ and the closest cavity mode at $\nu_{\mathrm{S}}^{\mathrm{cav}}$. We fit the amplitude of the Raman signal for every value of $\nu_{\mathrm{pump}} - \nu_{\mathrm{pump,dres}}$ with a Lorentzian (projected blue points) with linewidth of 519.8 GHz. The centre frequency of the fit indicates that the double resonance condition is satisfied when $\nu_{\mathrm{R,dres}} = 432.520\,\mathrm{THz}$ for $\nu_{\mathrm{pump,dres}} = 472.434\,\mathrm{THz}$. **(b)** The individual cavity spectra can be fitted well using a model based on two multiplied Lorentzians centred at the Stokes frequency $\nu_{\mathrm{R}} - \nu_{\mathrm{R,dres}}$ and the frequency of the adjacent cavity mode $\nu_{\mathrm{S}}^{\mathrm{cav}} - \nu_{\mathrm{R,dres}}$. The inset in each panel indicates the pump frequency $\nu_{\mathrm{pump}} - \nu_{\mathrm{pump,dres}}$.

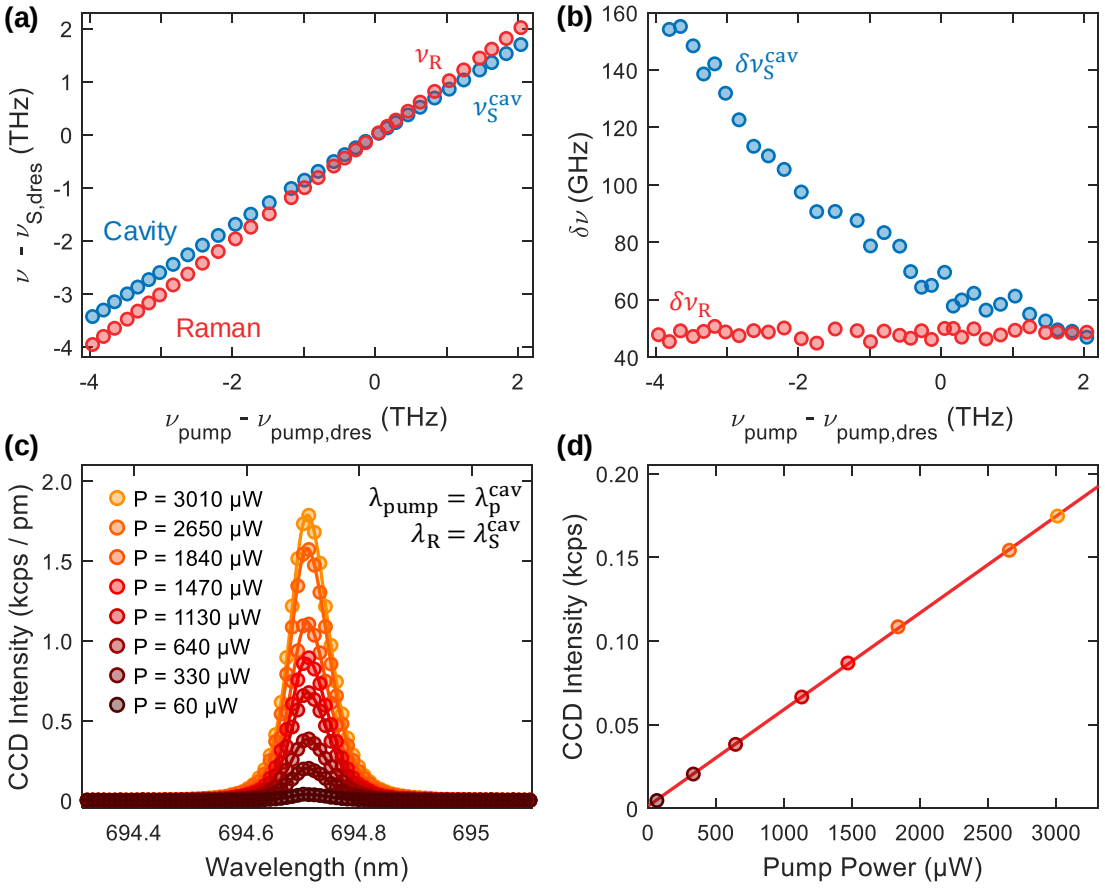


Fig. 6.6. **(a)** Peak position of the cavity ($\nu_S^{cav}$) and Raman scattered light ($\nu_R$) as a function of pump frequency $\nu_{pump}$ relative to the double resonance condition at $\nu_{pump,dres}$ and $\nu_{R,dres}$. **(b)** Linewidth of the cavity ($\delta\nu_S^{cav}$) and the Raman gain ($\delta\nu_R$) versus pump frequency $\nu_{pump} - \nu_{pump,dres}$. **(c)** Spectrally resolved cavity signal with increased pump power at the double-resonance condition. **(d)** Integrated peak intensity of peaks in (c) as a function of pump power. The linear behaviour suggests that no lasing occurs.

the tuning range of the pump laser, the detuning between $\nu_S^{cav}$ and $\nu_R$ varies from $-319.7\,\text{GHz}$ to $526.7\,\text{GHz}$. The linewidth of the Raman gain for the different fits is $\delta\nu_R = (48.3 \pm 1.6)\,\text{GHz}$ corresponding to $\mathcal{Q}_R = 8\,960 \pm 290$. This Raman linewidth agrees well with previously reported values (40.8...47.8 GHz) [255, 350, 353], indicating low strain in the diamond membrane. The linewidth of the cavity mode closest to $\nu_R$ at $\nu_S^{cav}$ decreases from $\delta\nu_S^{cav} = (167.3 \pm 0.8)\,\text{GHz}$ to $(47.0 \pm 0.4)\,\text{GHz}$ for increasing $\nu_{pump} = \nu_p^{cav}$, which is expected from the increase in reflectivity on approaching the stopband centre of the DBR mirror coatings. The corresponding $\mathcal{Q}$-factor increases from $\mathcal{Q}_p = 2\,570 \pm 90$ to $9\,250 \pm 90$. At the double-resonance condition, the $\mathcal{Q}$-factor of

the Stokes cavity mode is $\mathcal{Q}_{\mathrm{S,dres}} = 6\,650 \pm 50$.

### 6.3.1 Estimating the Lasing Threshold

Next, we perform double-resonance measurements for different pump powers $P_{\mathrm{pump}}$ (as measured before the sample objective) (Fig. 6.6 (c,d)). Up to the largest available pump power in the experiment, the intensity increases linearly: there is no superlinear dependence presaging Raman lasing.

To estimate the threshold power required to establish Raman lasing, we analyse the performance of the cavity. Raman scattering in a microcavity can be described using classical coupled mode equations [369, 384]. Lasing occurs when the round-trip gain equals the round-trip loss. Assuming that both the pump laser and the Raman light are resonant with the cavity, $\lambda_{\mathrm{pump}} = \lambda_{\mathrm{p}}^{\mathrm{cav}}$ and $\lambda_{\mathrm{R}} = \lambda_{\mathrm{S}}^{\mathrm{cav}}$, the lasing threshold $P_{\mathrm{th}}$ can be calculated via (see Appendix H):

$$P_{\mathrm{th}} = \frac{1}{\eta} \cdot \frac{2 n_{\mathrm{S}} n_{\mathrm{p}} \pi^2}{\lambda_{\mathrm{S}}^{\mathrm{cav}} \lambda_{\mathrm{p}}^{\mathrm{cav}} g_{\mathrm{R}}^{\mathrm{B}}} \cdot \frac{V_{\mathrm{R}} (Q_{\mathrm{S}} + Q_{\mathrm{R}})}{Q_{\mathrm{S}}^2 Q_{\mathrm{p}}} \,. \tag{6.1}$$

Here, $\lambda_{\mathrm{p(S)}}^{\mathrm{cav}}$, $n_{\mathrm{p(S)}}$ and $\mathcal{Q}_{\mathrm{p(S)}}$ are the wavelengths, refractive indices and $\mathcal{Q}$-factors for the cavity modes resonant with the pump laser and the Raman light, respectively. $\mathcal{Q}_{\mathrm{R}}$ is the quality factor corresponding to the bandwidth of the Raman gain. The bulk Raman gain coefficient in the employed pump wavelength range is $g_{\mathrm{R}}^{\mathrm{B}} \sim 40\,\mathrm{cm/GW}$ [449]. The power incoupling efficiency $\eta$ can be extracted from the cavity reflection measurement displayed in Fig. 6.4 (a) [93, 450]. From the dip in reflection, we infer a power incoupling efficiency of $\eta = 1 - P_{\mathrm{R}}/P_0 = 0.45$.

Modelling the cavity using a one-dimensional transfer-matrix model along with Gaussian optics, we estimate a Raman mode volume of $V_{\mathrm{R}} = 109.85\,\mu\mathrm{m}^3$ (see Section 6.4.3). Taking $n_{\mathrm{p(S)}} = n_{\mathrm{dia}} = 2.4$, we find $P_{\mathrm{th}} = 187.50\,\mathrm{mW}$. This relatively low threshold power constitutes a reduction in threshold power by more than an order of magnitude with respect to a bulk Raman laser in the visible [376, 428, 451]. With realistic improvements, we predict that our device platform could feature threshold powers in the sub-mW range (see Section 6.5).

### 6.3.2 Tuning the Double-Resonance Condition

Next, we demonstrate the possibility to tune the double resonance condition by changing the thickness of the diamond layer within the cavity mode *in situ* (Fig. 6.7 (a)). To this end, we laterally displace the cavity mode with respect to the diamond membrane,

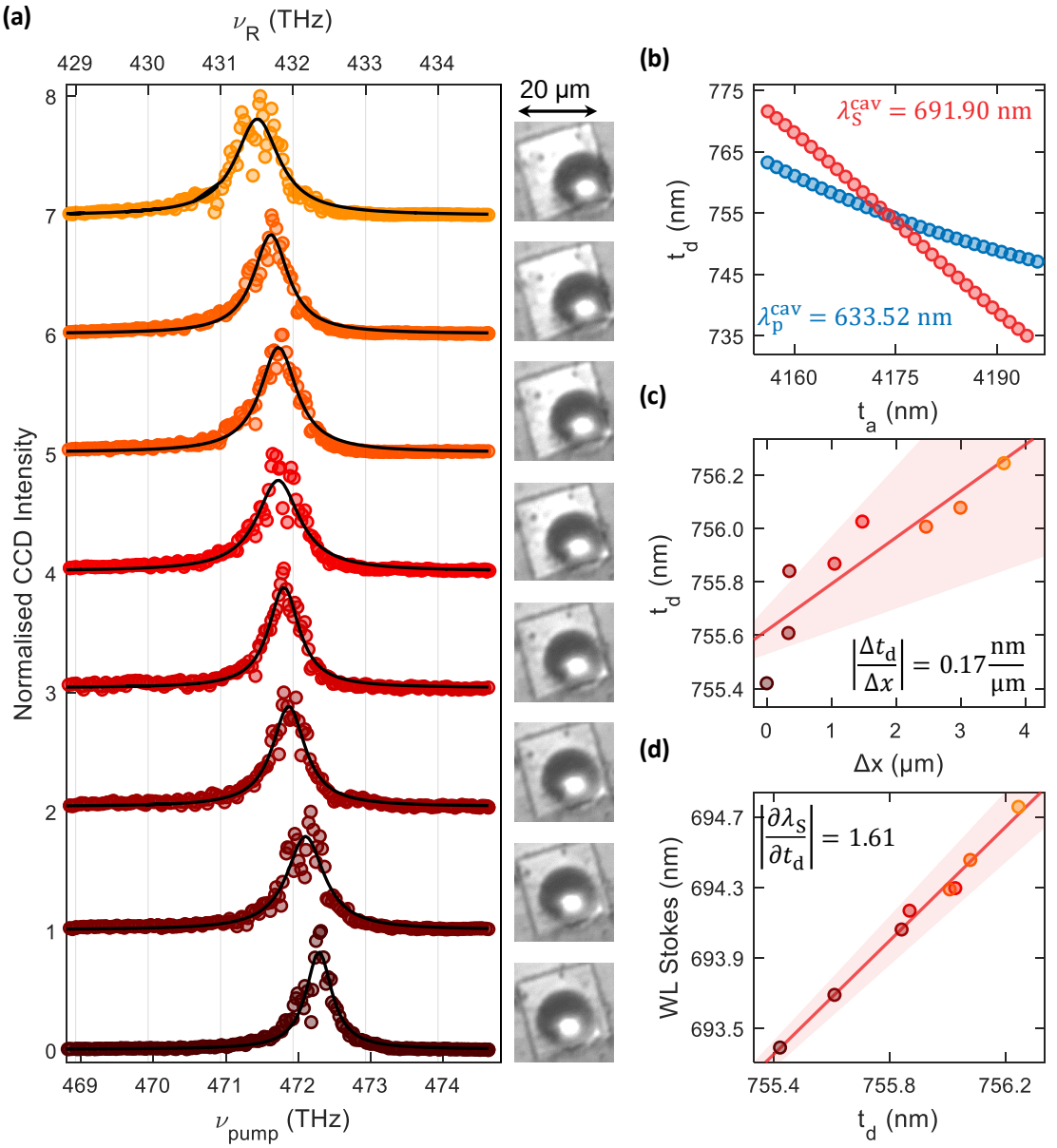


Fig. 6.7. **(a)** Demonstration of the tunability of the double resonance condition. Owing to the thickness gradient, shifting the diamond laterally changes the diamond thickness in the cavity and subsequently the condition for double resonance. **(b)** The diamond thickness and the width of the air-gap are extracted from one-dimensional transfer-matrix simulations. The double resonance is condition is satisfied when the pump mode (blue) and the Stokes mode (red) cross. For $\lambda_p^{cav} = 633.52\,nm$ and $\lambda_S^{cav} = 691.90\,nm$, we extract $t_d = 754.58\,nm$ and $t_a = 4173.98\,nm$. **(c)** Lateral displacement of the cavity mode plotted against diamond thickness $t_d$. Here, the relative position of the cavity mode is calculated with respect to the corners of the diamond. Extracting the diamond thickness from the double-resonance measurements in (a) gives a thickness gradient of $0.17\,\frac{nm}{µm}$. **(d)** Linear shift of the double-resonance condition with the diamond thickness resulting in a red-shift of the Stokes wavelength.

exploiting a small thickness gradient (Fig. 6.1 (a)). Over the lateral fine-tuning range of the nanopositioner (travel range $\sim 4\,\mu\text{m}$), the double resonance condition can be tuned from $\nu_{\text{pump,dres}} = 471.44\,\text{THz}$ to $472.29\,\text{THz}$ ($\nu_{\text{R,dres}} = 431.52\,\text{THz}$ to $432.37\,\text{THz}$), a continuous tuning range of 0.85 THz. Considering that the width of the double resonance gain profile is $> 500\,\text{GHz}$, this would enable a >THz continuous tuning range of the lasing frequency.

To extract the exact diamond thickness, we perform one-dimensional transfer-matrix-based simulations of the cavity mode structure (see Section 6.4.1). For these simulations, we use the exact mirror structure obtained from fitting the mirror stopband (Fig. 6.2 and Ref. [255, 387]), and sweep the width of the air-gap $t_\text{a}$ and the diamond thickness $t_\text{d}$ for fixed wavelengths $\lambda_\text{p}^\text{cav}$ and $\lambda_\text{S}^\text{cav}$. The double resonance condition is met whenever the modes for $\lambda_\text{p}^\text{cav}$ cross the modes for $\lambda_\text{S}^\text{cav}$. Fig. 6.7 (b) shows a transfer-matrix simulation for $\lambda_\text{p}^\text{cav} = 633.52\,\text{nm}$ and $\lambda_\text{S}^\text{cav} = 691.90\,\text{nm}$ (extracted from Fig. 6.6 (a)). Here, the two cavity modes overlap for $t_\text{a} = 4173.98\,\text{nm}$ and $t_\text{d} = 754.85\,\text{nm}$.

We extract $t_\text{d}$ for all measurements displayed in Fig. 6.7 (a) and plot $t_\text{d}$ versus lateral displacement of the cavity mode (Fig. 6.7 (c)). To calibrate the lateral displacement, we use the edges of the diamond ($\sim 18\,\mu\text{m}$) measured with a laser scanning confocal microscope (Keyence Corporation) as a reference. We find a thickness gradient $|\frac{\Delta t_\text{d}}{\Delta x}| = (0.17 \pm 0.2)\,\frac{\text{nm}}{\mu\text{m}}$. As shown in Fig. 6.7 (d), we observe a linear shift of $\lambda_\text{S}^\text{cav}$ with $t_\text{d}$. From our simulations, we find that for the right combination of $t_\text{d}$ and $t_\text{a}$, the double resonance condition can be tuned continuously across the whole mirror stopband corresponding to a continuous tuning range of tens of THz (see Section 6.4.2).

## 6.4 Discussions

### 6.4.1 Cavity Mode Structure

For conventional Fabry-Perot resonators, the resonance wavelength changes linearly with the mirror separation $t_\text{a}$. However, the presence of the diamond membrane significantly alters this linear mode structure [61, 87]. The large contrast in refractive index across the diamond-air interface leads to mode hybridisation and the emergence of avoided crossings [77, 87, 98, 405]. Conceptually, the cavity mode can be described using a coupled two-cavity model: one cavity is confined to the diamond bound by the bottom DBR and the diamond-air interface; the other cavity is confined to the air bounded by the diamond-air interface and the top DBR (compare Chapter 3) [61, 255, 387]. Figure 6.8 displays a one-dimensional transfer-matrix calculation of the cavity mode structure, using the mirror structure extracted from Fig. 6.2. These calculations confirm that the

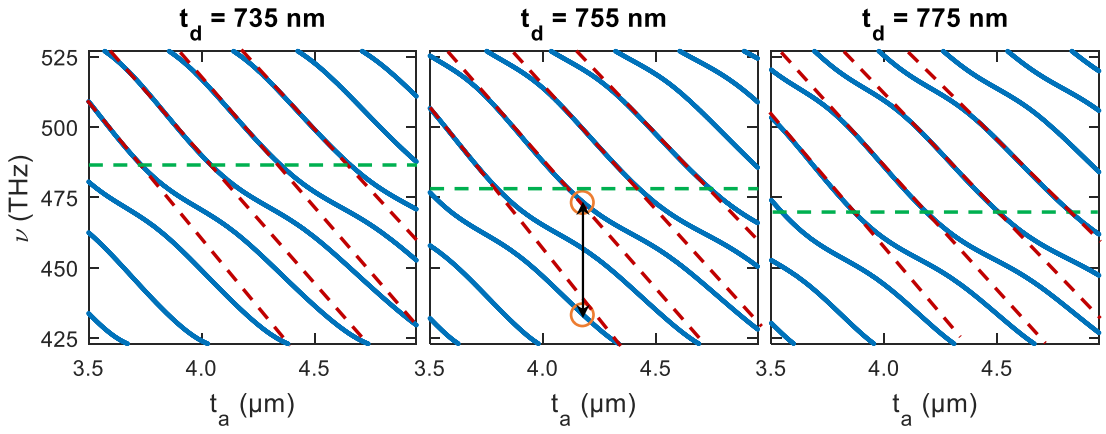


Fig. 6.8. One-dimensional transfer-matrix calculation of the cavity mode structure, i. e. resonance frequencies for different mirror separations $t_\mathrm{a}$, for different diamond thicknesses $t_\mathrm{d}$. The non-linear mode dispersion arises as a consequence of hybridisation of cavity modes resonant with the air-gap (indicated by the dashed burgundy line) and the diamond (dashed green line), respectively. The hybridisation leads to avoided crossings whose position depends on the exact diamond thickness. The central panel shows the mode-structure for the extracted diamond thickness ($t_\mathrm{d} \simeq 755\,\mathrm{nm}$) from Fig. 6.7 (b). The orange circles indicate a pair of cavity modes whose frequencies are separated by the Raman shift of $\Delta\nu_\mathrm{R} \sim 40\,\mathrm{THz}$ (black arrow).

locations of the avoided crossings in the mode structure depend on the choice of diamond thickness $t_\mathrm{d}$. We find that for $t_\mathrm{a} = 4173.98\,\mathrm{nm}$ and $t_\mathrm{d} = 754.58\,\mathrm{nm}$, the spectrum observed in Fig. 6.2 is reproduced well.

### 6.4.2 Tuning of the Double Resonance Condition

Open-access microcavities offer a convenient tuning mechanism of their resonance frequency simply by changing the separation of the two mirrors ($t_\mathrm{a}$) using a piezoelectric nanopositioner. Importantly, such cavities offer another tuning mechanism where, rather than the width of the air-gap, the thickness of the material layer is changed *in situ*. Here, a small thickness gradient in the diamond membrane converts a lateral displacement of the cavity mode into a change of the membrane thickness ($t_\mathrm{d}$). Tuning both $t_\mathrm{a}$ and $t_\mathrm{d}$ allows both the absolute wavelength and the spacing of the cavity modes to be controlled. As a consequence, a gradient in the diamond thickness $|\frac{\Delta t_\mathrm{d}}{\Delta x}|$ enables the double resonance condition to be satisfied for different pairs of wavelengths. In Fig. 6.7 (a) we demonstrate experimentally a continuous tuning range of the double resonance condition by 0.85 THz. This is achieved by changing the diamond thickness by $\sim 0.6\,\mathrm{nm}$, from 755.5 nm to 756.2 nm.

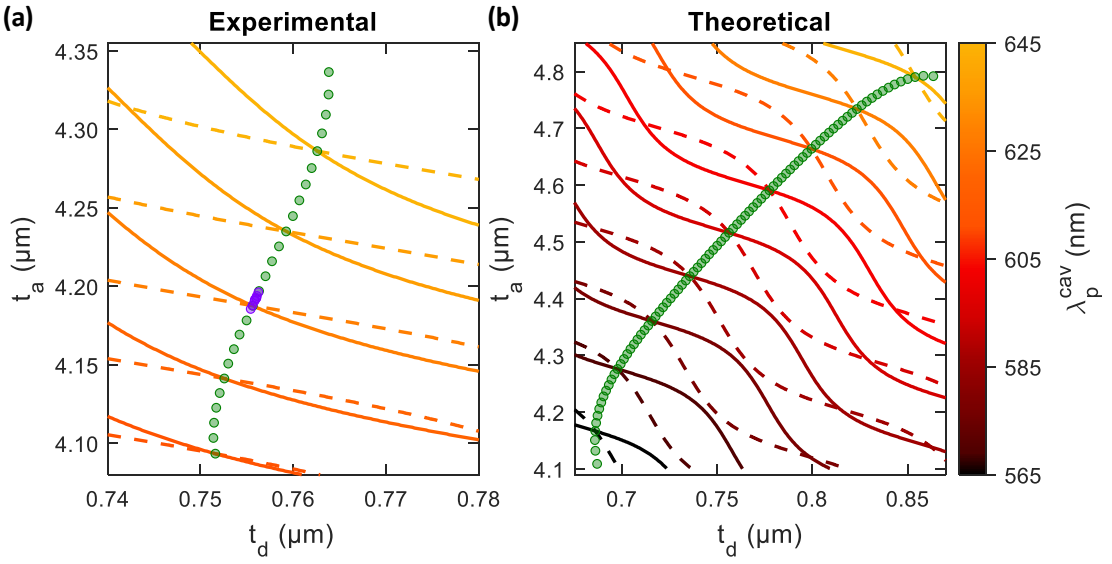


Fig. 6.9. One-dimensional transfer-matrix calculations of the cavity resonances as a function of $t_{a,d}$ for different combinations of $\lambda_p^{cav}$ (solid line) and $\lambda_S^{cav}=(1/\lambda_p^{cav} - \Delta\nu_R/c)^{-1}$ (dashed line) at specific wavelengths. The double resonance condition is satisfied when the corresponding solid and dashed lines cross (indicated by the same colour). By changing the diamond thickness, the condition for the double-resonance can be tuned continuously, as indicated by the green circles. **(a)** Calculations for pairs of $t_{a,d}$ in a range accessible with the device presented in the main text. The calculations suggest a continuous tuning range of 17.3 THz. The experimentally verified tuning is indicated by the purple circles. **(b)** Optimising the choice of $t_{a,d}$ enables continuous tuning across the entire reflective stopband, amounting to 72.2 THz. For simplicity, only cavity modes for which continuous tuning is possible are included in (b).

To explore this tuning mechanism in more detail, we perform one-dimensional transfer-matrix calculations (Essential Macleod). We calculate the combinations of air-gap width $t_a$ and diamond thickness $t_d$ at which specific wavelengths are resonant. We perform these calculations for cavity wavelengths within the tuning range of our pump laser, i.e. $\lambda_p^{cav} = 630 \cdots 640$ nm and for a range of $t_a$ and $t_d$ accessible with the device presented in the main text (solid lines Fig. 6.9 (a)). We then add calculations for the corresponding wavelengths red-shifted by the Raman shift at $\lambda_S^{cav} = \left(\frac{1}{\lambda_p^{cav}} - \frac{\Delta\nu_R}{c}\right)^{-1}$ (dashed lines Fig. 6.9 (a)). At pairs of $t_a$ and $t_d$ where the solid and dashed line cross, the double-resonance condition is satisfied.

We find that, in principle, the double resonance condition can be tuned continuously from $\lambda_{pump,dres} = 625.00$ nm ($\lambda_{R,dres} = 681.75$ nm) to $\lambda_{pump,dres} = 649.00$ nm ($\lambda_{R,dres} = 710.41$ nm) (17.3 THz) by changing the diamond thickness from 751.4 nm to 763.8 nm (green points in Fig. 6.9 (a)). The experimentally demonstrated tuning range is indicated

by the purple points in Fig. 6.9 (a).

By optimizing the choice of $t_{\mathrm{a,d}}$, we find a configuration which in principle allows the double-resonance condition to be tuned in a mode-hope free fashion harnessing the whole stopband of the mirror (72.2 THz, $\lambda_{\mathrm{pump,dres}} = 565 \cdots 645\,\mathrm{nm}$, $\lambda_{\mathrm{R,dres}} = 610.98 \cdots 705.62\,\mathrm{nm}$, see Fig. 6.9 (b)).

### 6.4.3 Calculation of the Effective Raman Mode Volume

Consider a doubly-resonant system ($\omega_{\mathrm{p}} = \omega_{\mathrm{pump}} = \omega_{\mathrm{p}}^{\mathrm{cav}}$ and $\omega_{\mathrm{S}} = \omega_{\mathrm{R}} = \omega_{\mathrm{S}}^{\mathrm{cav}}$). In the following, the "cav" superscripts will be omitted for concise notation and clarity. The effective Raman mode volume accounts for the spatial overlap of the pump (p) and Stokes (S) cavity modes and can be determined via [370, 384]

$$V_{\mathrm{R}} = \frac{\int_{\mathrm{cav}} n_{\mathrm{p}}^2(\vec{r})|\vec{E}_{\mathrm{p}}(\vec{r})|^2 \mathrm{d}^3r \times \int_{\mathrm{cav}} n_{\mathrm{S}}^2(\vec{r})|\vec{E}_{\mathrm{S}}(\vec{r})|^2 \mathrm{d}^3r}{\int_{\mathrm{dia}} n_{\mathrm{p}}^2(\vec{r})|\vec{E}_{\mathrm{p}}(\vec{r})|^2 \times n_{\mathrm{S}}^2(\vec{r})|\vec{E}_{\mathrm{S}}(\vec{r})|^2 \mathrm{d}^3r}\,, \tag{6.2}$$

where $\vec{E}_{p(S)}(\vec{r})$ is the pump (Stokes) electric field at position $\vec{r}$. Here, the integral in the numerator (subscript "cav") is evaluated across the entire cavity, while the integral in the denominator (subscript "dia") is evaluated across the diamond only. The integrals over the electric field can be calculated following the approach described in Section 5.3.2 [255]. We approximated the beam waist to be constant $w_{0,\mathrm{I}}$ and solve the integral in cylindrical coordinates:

$$\begin{aligned} &\int_{\mathrm{cav}} n^2(\vec{r})|\vec{E}(\vec{r})|^2 \mathrm{d}^3r \\ =&\int_{\mathrm{cav}} n^2(z)|\vec{E}(z)|^2 \mathrm{d}z \int_0^{2\pi} \mathrm{d}\phi \int_0^{\infty} re^{-r^2/2w_{\mathrm{I}}^2} \mathrm{d}r \\ =&2\pi\frac{1}{4}w_{\mathrm{I}}^2 \int_{\mathrm{cav}} \epsilon_0 n^2(z)|\vec{E}(z)|^2 \mathrm{d}z\,, \end{aligned} \tag{6.3}$$

where $\epsilon_{\mathrm{R}} = n^2$ and $w_{0,\mathrm{I}}$ is the intensity beam-waist given by [123, 387]

$$w_{0,\mathrm{I}} = \sqrt{\frac{\lambda}{\pi}} \left[ \left( t_{\mathrm{a}} + \frac{t_{\mathrm{d}}}{n_{\mathrm{d}}} \right) \cdot R_{\mathrm{cav}} - \left( t_{\mathrm{a}} + \frac{t_{\mathrm{d}}}{n_{\mathrm{d}}} \right)^2 \right]^{\frac{1}{4}}. \tag{6.4}$$

Calculating the respective field profiles according to Eq. 6.3 reduces Eq. 6.2 to

$$V_{\mathrm{R}} = 2\pi\frac{1}{4}\left( w_{\mathrm{p}}^2 + w_{\mathrm{S}}^2 \right) \cdot \frac{\int_{\mathrm{cav}} n_{\mathrm{p}}^2(z)|E_{\mathrm{p}}(z)|^2 \mathrm{d}z \times \int_{\mathrm{cav}} n_{\mathrm{S}}^2(z)|E_{\mathrm{S}}(z)|^2 dz}{\int_{\mathrm{dia}} n_{\mathrm{p}}^2(z)|E_{\mathrm{p}}(z)|^2 \times n_{\mathrm{S}}^2(z)|E_{\mathrm{S}}(z)|^2 \mathrm{d}z}\,. \tag{6.5}$$

To calculate the Raman mode volume, we approximate the axial vacuum electric-field

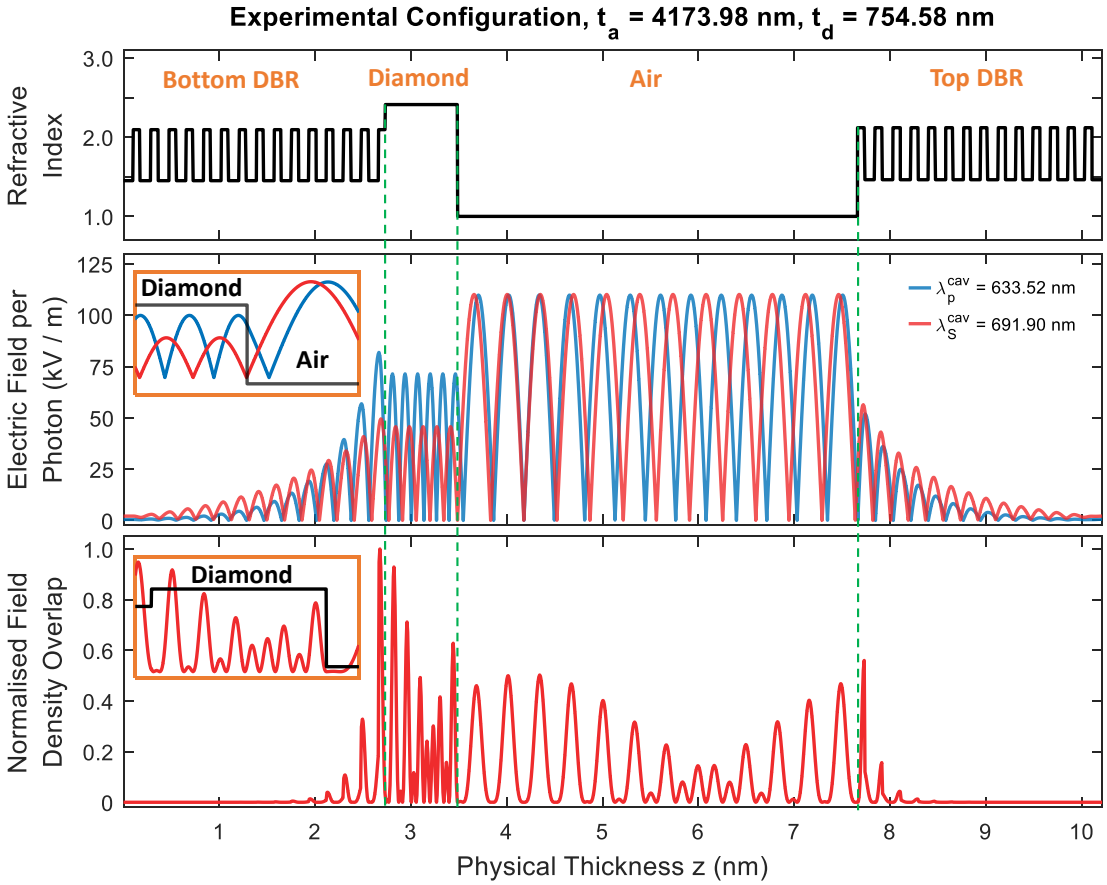


Fig. 6.10. One-dimensional transfer-matrix simulation of the cavity for $t_\mathrm{a} = 4173.98\,\mathrm{nm}$ and $t_\mathrm{d} = 754.58\,\mathrm{nm}$. The top panel shows the refractive index profile as a function of cavity length. The middle panel shows the profile of the pump (blue) and Stokes (red) electric field. The bottom panel shows the overlapped energy density calculated according to the denominator in the fraction in Eq. 6.2.

distribution with a one-dimensional cavity using a transfer-matrix calculation (Essential Macleod). We use the exact mirror structure obtained from fitting the mirror stopband (Fig. 6.2) and the combination of $t_\mathrm{a,d}$ extracted from Fig. 6.7 (b). Fig. 6.10 shows the result of our calculations. We determine the electric field profile for the pump and Stokes fields and then their product by numerical integration. Using $R_\mathrm{cav} = 11\,\mu\mathrm{m}$ and $n_\mathrm{p} \simeq n_\mathrm{S} = 2.4$, we calculate the beam waists according to Eq. 6.4, and find $w_\mathrm{p} = 1.05\,\mu\mathrm{m}$ and $w_\mathrm{S} = 1.09\,\mu\mathrm{m}$ taking the $\lambda^\mathrm{cav}_\mathrm{S,p}$ combination extracted from Fig. 6.6 (a). Finally, we arrive at $V_\mathrm{R} = 109.85\,\mu\mathrm{m}^3$, as quoted in Section 6.3.1.

## 6.5 Future Directions

We now turn to discuss some limiting factors and further possible improvements to this experiment. The double resonance condition is satisfied for the combination of $t_\mathrm{a}$ and $t_\mathrm{d}$ for which both pump and Stokes modes are resonant simultaneously. With the current top mirror design (depth of crater, $d = 1.65\,\mu\mathrm{m}$) and diamond thickness $t_\mathrm{d} = 754.58\,\mathrm{nm}$, a relatively large air-gap of $t_\mathrm{a} = 4173.98\,\mathrm{nm}$ is required to meet this condition for the range of $\lambda_\mathrm{pump}$ available (indicated by the green circle in Fig. 6.11 (a)). The large air-gap results in a large $V_\mathrm{R}$, and consequently a large lasing threshold. Establishing the double resonance condition for a shorter air-gap will reduce $V_\mathrm{R}$ and consequently $P_\mathrm{th}$.

An additional benefit of reducing $t_\mathrm{a}$ becomes apparent on simulating the behaviour of the $\mathcal{Q}$-factor with increased cavity length (Fig. 6.11 (b)). The $\mathcal{Q}$-factor and the cavity round-trip loss $\mathcal{L}_\mathrm{cav}$ are linked via $\mathcal{Q} = \frac{4\pi L_\mathrm{cav}}{\lambda \mathcal{L}_\mathrm{cav}}$, where $L_\mathrm{cav} = t_\mathrm{a} + L_0$. Here the term $L_0$ describes the diamond thickness and the field penetration into the DBR mirror coatings [94, 387]. For short cavity lengths, the $\mathcal{Q}$-factor increases linearly with $t_\mathrm{a}$. However, for large cavity lengths, the extent of the intensity mode waist at the top mirror, $w_\mathrm{I}$, becomes larger than the spherical extent of the mirror, leading to beam clipping and a subsequent drop in the $\mathcal{Q}$-factor [90, 104, 387]. For a spherical mirror with diameter $D$, the clipping losses are calculated according to $\mathcal{L}_\mathrm{clip} = e^{-D^2/2w_\mathrm{I}^2}$, where the beam waist $w_\mathrm{I}$ evolves according to [387]

$$w_\mathrm{I} = \sqrt{\frac{\lambda R_\mathrm{cav}}{\pi}} \cdot \left( \frac{R_\mathrm{cav}}{(t_\mathrm{a} + \frac{t_\mathrm{d}}{n_\mathrm{d}})} - 1 \right)^{-\frac{1}{4}} . \tag{6.6}$$

In Fig. 6.11 (b), a drop in $\mathcal{Q}$-factor is expected for $t_\mathrm{a} \gtrsim 3.5\,\mu\mathrm{m}$, a consequence of clipping losses. Therefore, a shorter $t_\mathrm{a}$ will have the added benefit of preserving a high $\mathcal{Q}$-factor. Here, the value of $R_\mathrm{cav} = 11\,\mu\mathrm{m}$ and $D = 6\,\mu\mathrm{m}$ are extracted from a scanning confocal microscope (Keyence Corporation)

### 6.5.1 Minimising $V_\mathrm{R}$

As discussed above, establishing the double-resonance condition for smaller air-gap reduces $V_\mathrm{R}$ and consequently $P_\mathrm{th}$. To this end, we simulate the cavity for a wide range of $t_\mathrm{a}$ and $t_\mathrm{d}$ using $\lambda_\mathrm{p}^\mathrm{cav} = 633.52\,\mathrm{nm}$ and $\lambda_\mathrm{S}^\mathrm{cav} = 691.10\,\mathrm{nm}$ as before (Fig. 6.11 (a)). Reducing the diamond thickness to $t_\mathrm{d} = 721.82\,\mathrm{nm}$ satisfies the double-resonance condition for $t_\mathrm{a} = 1789.75\,\mathrm{nm}$ (black circle, Fig. 6.11 (a)). For this air-gap, we calculate $V_\mathrm{R} = 20.42\,\mu\mathrm{m}^3$ (Fig. 6.12), and find a theoretical $\mathcal{Q}_\mathrm{p} = 406\,060$, $\mathcal{Q}_\mathrm{S} = 13\,550$, $\eta = 0.80$

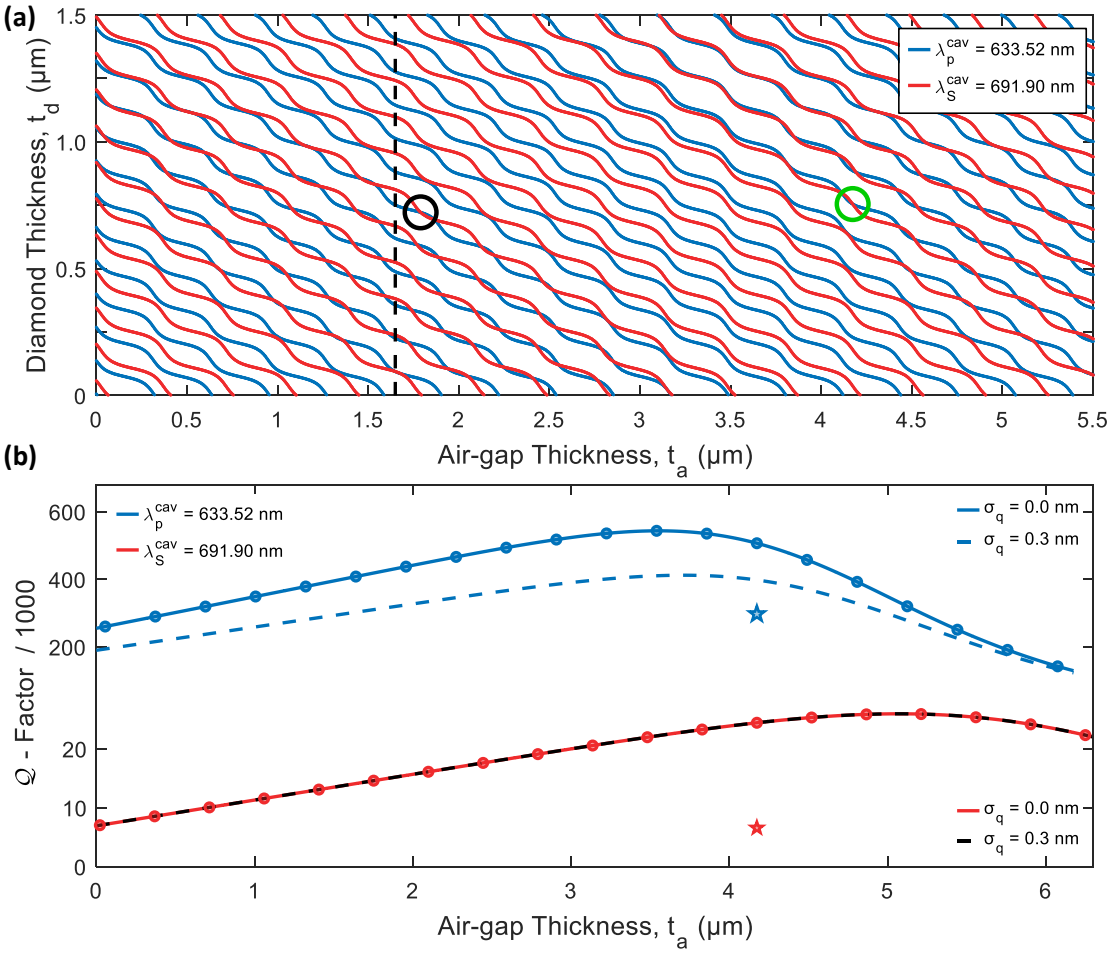


Fig. 6.11. **(a)** Simulated cavity mode structure for $\lambda_{\mathrm{p}}^{\mathrm{cav}} = 633.52\,\mathrm{nm}$ (blue) and $\lambda_{\mathrm{S}}^{\mathrm{cav}} = 691.90\,\mathrm{nm}$ (red) as a function of $t_{\mathrm{a}}$ and $t_{\mathrm{a}}$. The double resonance condition is satisfied for the pair of $t_{\mathrm{a,d}}$ where the two respective modes cross. The green circle highlights the combination $t_{\mathrm{a}} = 4173.98\,\mathrm{nm}$ and $t_{\mathrm{d}} = 754.58\,\mathrm{nm}$ used in this experiment. The black dashed line represents the depth of the crater, setting the lower limit on the possible $t_{\mathrm{a}}$ for the current cavity geometry. The pair $t_{\mathrm{d}} = 721.82\,\mathrm{nm}$ and $t_{\mathrm{a}} = 1789.75\,\mathrm{nm}$ is indicated by the black circle. **(b)** Simulated dependence of the $\mathcal{Q}$-factor with air-gap thickness for fixed $\lambda_{\mathrm{p}}^{\mathrm{cav}} = 633.52\,\mathrm{nm}$ (blue) and $\lambda_{\mathrm{S}}^{\mathrm{cav}} = 691.90\,\mathrm{nm}$ (red). The solid lines represent the $\mathcal{Q}$-factor in the absence of any losses, while the dashed lines represent the $\mathcal{Q}$-factor in the presence of surface scattering with surface roughness $\sigma_{\mathrm{q}} = 0.3\,\mathrm{nm}$. The drop in $\mathcal{Q}$-factors at large air-gap thicknesses is attributed to clipping losses at the top mirror. The experimentally measured $\mathcal{Q}$-factors are indicated by the stars.

and consequently $P_{\mathrm{th}} = 4.94\,\mathrm{mW}$.

As discussed at length in Chapter 4, the diamond surface introduces scattering losses which should be taken into account. Surface scattering can be incorporated in the transfer-matrix simulations according to Ref. [389]. Motivated by typical roughness mea-

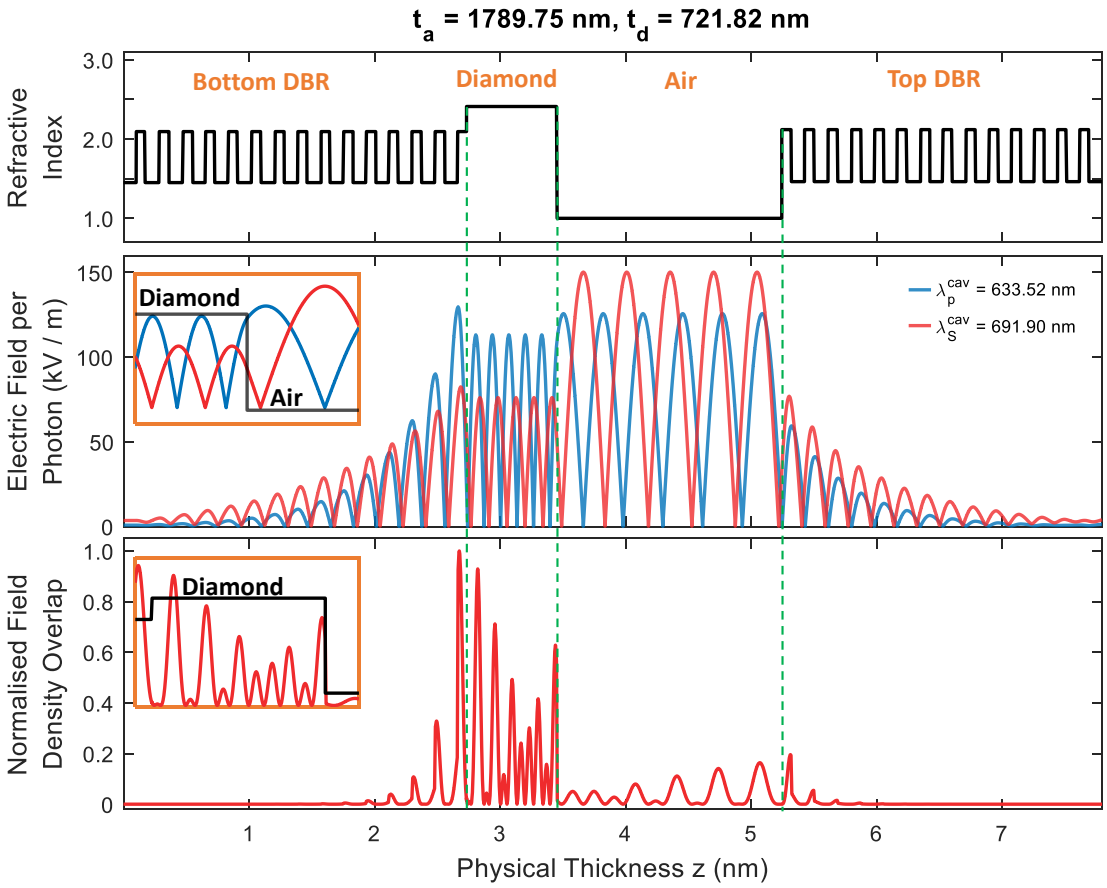


Fig. 6.12. One-dimensional transfer-matrix simulation of a double-resonance condition satisfied for $t_\mathrm{a} = 1789.75\,\mathrm{nm}$ and $t_\mathrm{d} = 721.82\,\mathrm{nm}$ (indicated by the black circle in Fig. 6.11 (a). The top panel shows the refractive index profile as a function of cavity length. The middle panel shows the profile of the pump (blue) and Stokes (red) electric field. The bottom panel shows the overlapped energy density.

surements reported by Ref. [159, 387] (Fig. 4.3), including a scattering layer with surface roughness $\sigma_\mathrm{q} = 0.3\,\mathrm{nm}$, reduces the $\mathcal{Q}$-factor to $\mathcal{Q}_\mathrm{p}^\mathrm{scat} = 257\,800$ and $\mathcal{Q}_\mathrm{S}^\mathrm{scat} = 13\,450$. Consequently, the additional loss-channel reduces $\eta^\mathrm{scat} = 0.59$. The reduction in the $\mathcal{Q}$-factor increases the lasing threshold to $P_\mathrm{th}^\mathrm{scat} = 10.71\,\mathrm{mW}$.

Finally, increasing the thickness of the diamond membrane constitutes a way to reduce further the lasing threshold on the account of larger $\mathcal{Q}$-factors offered by the longer effective cavity length. Furthermore, the larger diamond thickness leads to a larger overlap of the pump and Stokes field inside the diamond, thus minimising $V_\mathrm{R}$ (Eq. 6.2). To quantify this, we simulate the cavity for an increasingly wide range of $t_\mathrm{d}$, with $\lambda_\mathrm{p} = 633.52\,\mathrm{nm}$ and $\lambda_\mathrm{S} = 691.90\,\mathrm{nm}$ as before. As can be seen in Fig. 6.13, the double-resonance condition can be satisfied for various different combinations of $t_\mathrm{a,d}$, forming an almost hypnotic

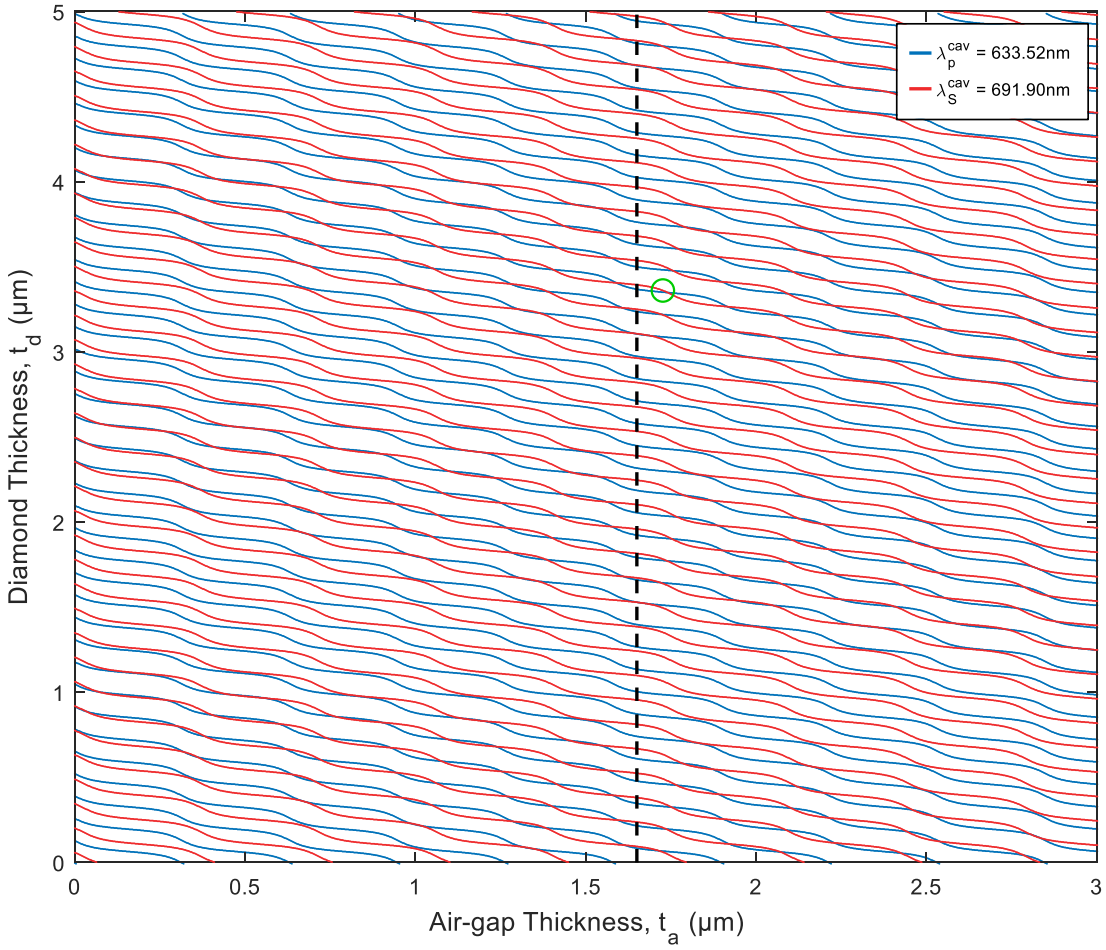


Fig. 6.13. Simulated cavity mode structure for $\lambda_p = 633.52\,\text{nm}$ (blue) and $\lambda_S = 691.90\,\text{nm}$ (red) as a function of $t_a$ and $t_d$. As before, the double-resonance condition is satisfied for the pair of $t_{a,d}$ where the two respective modes cross. The depth of the crater is represented by the dashed black line. The green circle highlights the combination $t_a = 1726\,\text{nm}$ and $t_d = 3361\,\text{nm}$ evaluated in Fig. 6.14.

pattern.

By applying the same method as discussed above, we find that the double-resonance condition can be established for $t_d = 3361\,\text{nm}$ and $t_a = 1726\,\text{nm}$ (indicated by the green circle in Fig. 6.13). Fig. 6.14 shows overlap of the pump and Stokes field for this combination of $t_a$ and $t_d$. The overlapped energy density displays periodic beating, as one would expect as the two fields go in and out of phase. Evaluating the overlap integral according to Eq. 6.5 yield $V_R = 21.2\,\mu\text{m}$, which in a loss-less cavity corresponds to $P_{th} = 0.78\,\text{mW}$. Including surface scattering increases the threshold to $P_{th} = 1.87\,\text{mW}$.

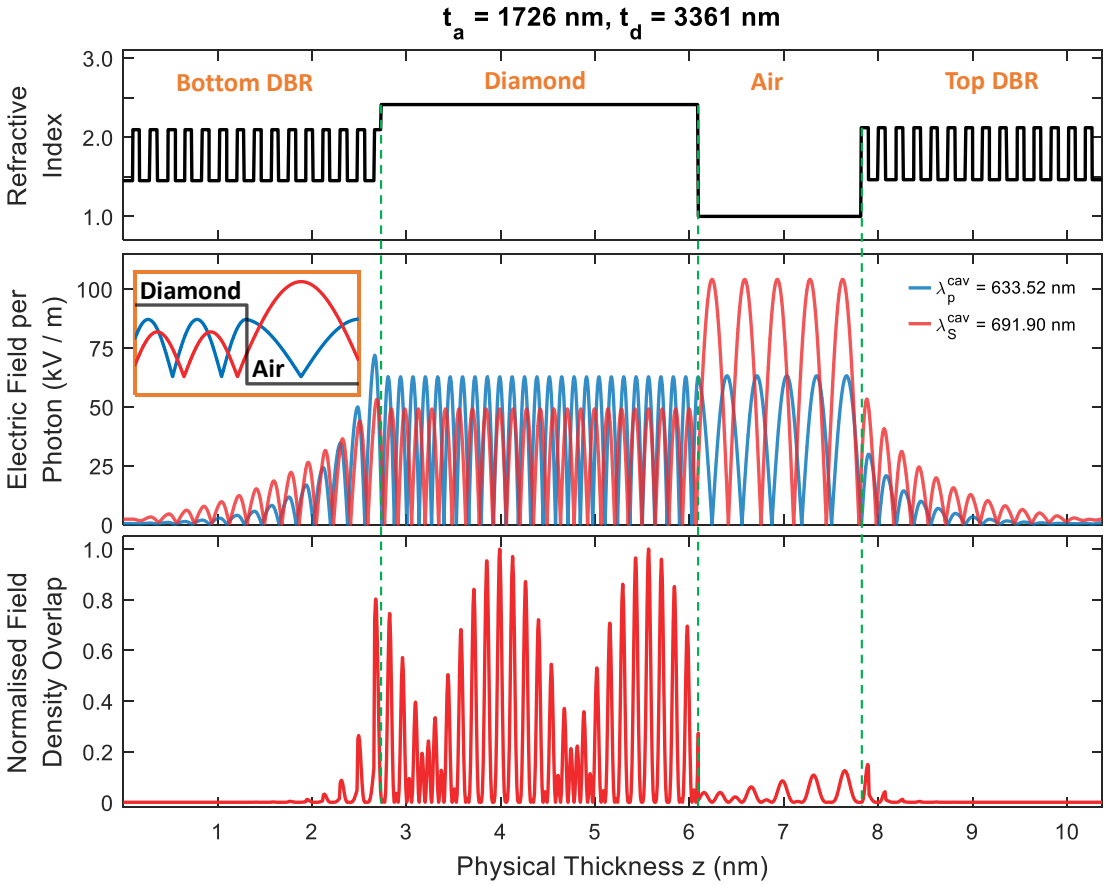


Fig. 6.14. One-dimensional transfer-matrix simulation of a double-resonance condition satisfied for $t_a = 1726\,\text{nm}$ and $t_d = 3361\,\text{nm}$, indicated by the green circle in Fig. 6.13. The top panel shows the refractive index profile as a function of cavity length. The middle panel shows the profile of the pump (blue) and Stokes (red) electric field. The bottom panel shows the overlapped energy density. The increased diamond thickness results in periodic of the overlapped energy density, as one would expect from the two fields drifting in and out of phase.

## 6.6 Conclusion

In conclusion, we demonstrate a platform for the widely-tunable doubly-resonant enhancement of Raman scattering from diamond based on a tunable open-access microcavity. The *in situ* tuning capability of our device provides a convenient way to establish a double resonance condition in which both pump and Raman wavelengths are resonant with a cavity mode. Exploiting a slight thickness gradient of the incorporated diamond membrane enables the doubly-resonant configuration to be achieved over a wide tuning range of more than 1 THz. These results, together with the high quality factors of

the cavity in the visible wavelength range, suggest that Raman lasing can be achieved with the present system. We predict a lasing threshold of 188 mW, a reduction by more than an order of magnitude compared to bulk Raman lasers [348]. We anticipate that with realistic improvements of our platform, sub-mW Raman lasing thresholds can be achieved. Importantly, we predict that there are configurations where mode-hop-free tuning of the double resonance condition over tens of THz is possible, in principle limited only by the spectral width of the reflective stopband of the mirrors. These advancements pave the way to a universal, low-power, frequency-shifter. Finally, we note that due to the generic design of our platform, other wide-bandgap Raman laser materials such as aluminium nitride [452] can readily be incorporated into our device. A wider point is that the integration of materials exhibiting a strong $\chi^{(2)}$ nonlinearity such as silicon carbide [319, 453], lithium niobate [454] or gallium phosphide [455, 456] could enable low-threshold frequency conversion using other nonlinear processes, for instance second-harmonic generation or sum- and difference-frequency mixing.

## 6.7 Appendix - Extended Methods

The core of this experiment is the tunable, planar-concave Fabry-Perot microcavity [385, 399] with an embedded diamond micromembrane, depicted schematically in Fig. 6.1 (a). The microcavity comprises two fused silica substrates exhibiting highly reflective dielectric mirror coatings (ECI evapcoat). Prior to applying the coating, we fabricate an array of spherical micro-indentations via $CO_2$ laser ablation [402] in one of the substrates. The micro-indentations feature small radii of curvature $R_{\mathrm{cav}} \sim 11\,\mu\mathrm{m}$ and depths $d \sim 1.65\,\mu\mathrm{m}$. We employ 14 (15) $\lambda_{\mathrm{c}}/4$ layers of a $SiO_2/Ta_2O_5$ distributed Bragg reflector for the curved top (planar bottom) mirrors. From a white-light transmission measurement [255, 387, 391], the centre of the stopband of the top mirror is determined to be $\lambda_{\mathrm{c}} = 625\,\mathrm{nm}$ (Fig. 6.2). Using a transfer-matrix-based refinement algorithm (Essential Macleod) we can reconstruct the reflection spectrum utilising an individual layer-thickness tolerance of 3% with $n_{SiO_2} = 1.46$ and $n_{Ta_2O_5} = 2.11$. Using the same approach we find $\lambda_{\mathrm{c}} = 629\,\mathrm{nm}$ for the top mirror.

Starting with commercially available high-purity, ⟨100⟩-cut single crystal diamond (Element Six), we fabricate membranes via inductively-coupled reactive-ion etching and electron-beam lithography [152, 159, 403]. We then transfer membranes with typical dimensions $\sim 20 \times 20 \times 0.8\,\mu\mathrm{m}^3$ to the planar mirror using a micromanipulator [77, 403]. The diamond membranes exhibit a slight thickness gradient introduced during the thinning of the diamond [305].

The bottom mirror is mounted on a stack of xyz-piezoelectric nanopositioners (attocube, 2×ANPx51 and ANPz51) and placed inside a homebuilt titanium "cage"; the top mirror is rigidly attached to the top of the cage [387]. By applying a voltage to the nanopositioners, the bottom mirror can be moved in all three dimensions with respect to the top mirror, offering both spatial and spectral tunability [77]. Finally, the titanium cage is mounted on top of a high-precision mechanical stage (Newport, M-562-XYZ) to enable the cavity output to be coupled to external detection optics (see Fig. 5.4) [255].

We use a narrow-band tunable red diode-laser as pump laser (Toptica DL Pro 635, $\lambda_{\text{pump}} = 630 \cdots 640\,\text{nm}$, $\delta\nu \leq 500\,\text{kHz}$). This pump laser is spectrally filtered (Semrock, FF01-637/7-25 and FF01-650/SP-25) and then coupled into the cavity using an objective of moderate numerical aperture (Microthek, 20×, NA=0.4) [255]. The Stokes signal is collected via the same objective in a back-scattering geometry (Fig. 6.1 (a)). A combination of a dichroic mirror (cutoff 644 nm, AHF F48-644) and a long-pass filter (Semrock, BLP02-635R-25) is used to filter the excitation laser from the signal. The Stokes signal is then coupled into a single-mode detection fibre (Thorlabs, 630-HP) and recorded with a spectrometer.

CHAPTER 7

# Photoluminescence Excitation Spectroscopy of NV centres in Microstructured Diamond

**The content of this chapter is partially adapted from:**
M. Kasperczyk, J. A. Zuber, A. Barfuss, J. Kölbl, V. Yurgens, S. Flågan, T. Jakubczyk, B. Shields, R. J. Warburton, and P. Maletinsky,
**"Statistically modeling optical linewidths of nitrogen vacancy centers in microstructures"**, Physical Review B **102**, 075312 (2020).

The NV centre has established itself as a promising building block in a large scale quantum network [61, 66, 194]. Two-photon quantum interference of single photons from spatially separated NV centres [79, 80] paved the way for spin-spin entanglement between remote NV centres [42, 43, 73, 396, 397]. Nevertheless, scalability beyond a few qubit nodes is limited by the modest entanglement rates, in turn, limited by the small flux of coherent photons. The NV centre possesses a long radiative lifetime of $\sim 12\,\mathrm{ns}$ in combination with a low branching ratio of only $\sim 3\%$ into the zero-phonon line (ZPL), thereby limiting the generation rate of coherent photons. Furthermore, local variations in strain and electric field give rise to inhomogeneous linewidth broadening [188, 216] and spectral instability [82, 230], degrading the optical coherence of the emitters [217], and consequently compromising the observable two-photon interference [213, 457]. While the generation rate of single photons can be greatly enhanced by resonant coupling to a high-quality photonic resonator via the Purcell effect [86] (compare Sec. 2.1.4), mitigating spectral diffusion has proven to be a harder nut to crack.

To date, all experiments employing coherent photons from NV centres have been performed with NV centres formed in the bulk crystal during growth [168]. These "native" NV centres are located in a close to perfect, crystalline environment, free of fabrication induced damage, and hence possess stable optical transitions. A typical high-purity

CVD grown diamond crystal exhibits nitrogen concentration below one part per billion (ppb) [458], with little to no control of the spatial location of the NV centres. However, enhancement of the emission rate of coherent photons via the Purcell effect requires careful positioning of the NV centre with respect to the cavity mode [77]. To that end, implantation of nitrogen ions [156, 167], followed by high-temperature annealing (compare Sec. 2.2.1) is a commonly used technique to create single NV centres at the desired location [157]. Despite irradiation with high-energy ions, NV centres with linewidths as low as 27 MHz have been reported in ion implanted samples [220].

Resonant enhancement of the NV ZPL has been demonstrated using photonic crystal cavities [82, 83, 165, 398], nanobeam waveguides [421, 459, 460], hybrid- [78, 84] and microring resonators [81]. While these resonators can achieve extremely small mode volumes, and hence offer a large Purcell factor, the invasive nano-fabrication deteriorates the optical coherence of the NV centres. The inhomogeneous broadening of the ZPL linewidth likely arises as a consequence of a fluctuating charge environment associated with the diamond surface [217, 461]. On the contrary, open Fabry-Perot microcavities [77, 214] facilitate the incorporation of larger, less aggressively processed diamond membranes, while still maintaining a sufficiently large $\frac{Q}{V}$-ratio. Increasing the defect-free crystalline environment around the NV centre have proven to be beneficial in order to maintain optical coherence [158, 168, 171].

## 7.1 Measurement Methodology

The overarching goal of this work is to achieve optically coherent NV centres in thin ($\sim$ µm) diamond micro-membranes. In an NV-cavity coupling experiment, thin samples are a necessity to maximise the Purcell factor. However, as mentioned above, invasive fabrication has a catastrophic impact on the NV centres' optical coherence. Therefore, a compromise between the Purcell factor and optical linewidth will have to be made. This further motivates the use of micron-sized membranes.

In this work, characterisation of the optical linewidth was performed on three different samples with different fabrication procedures and properties. For each sample, the preparation, characterisation and results will be presented in their own subsection. However, the experimental setup and the experimental procedure were the same for all the samples, and will therefore be outlined here.

The optical linewidth of the NV centre can be determined by performing photoluminescence excitation (PLE) measurements at a temperature of $T \lesssim 10\,\mathrm{K}$ [221]. In the PLE measurement, the NV centre is resonantly excited by sweeping the frequency of the

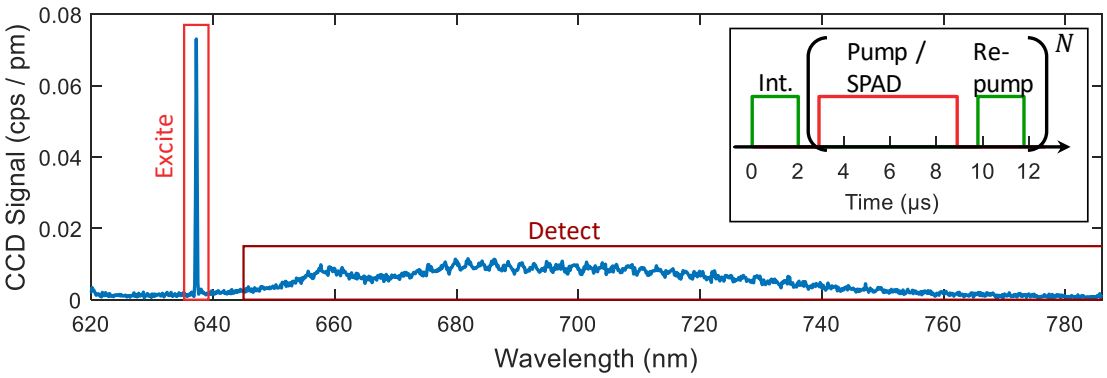


Fig. 7.1. Low-temperature PL spectrum of an NV centre. In the PLE measurements, the NV centre is resonantly excited by sweeping the laser frequency resonantly across the ZPL, while collecting the photons emitted into the PSB. The inset shows the PLE pulsing sequence used in the experiment. A short green pulse was applied to initialise the NV centre in the negative charge state, after which the resonant red laser was applied. The resonant laser was delayed by a short time to allow for the decay of fast florescence excited by the green re-pump pulse.

excitation laser $\nu$ across the ZPL, while recording the photons emitted into the phonon sideband (PSB) using a single-photon avalanche diode (SPAD) as shown in Fig 7.1.

The PLE measurements were performed in a liquid helium bath cryostat*. For improved handling, the diamond sample was glued to a silicon chip (using Crystalbond 509, SPI supplies). The silicon chip was further glued to a home-built titanium sample holder and mounted on top of two-axis piezoelectric scanning nano-positioners (attocube, ANSxy100lr). To achieve a greater travel range, the piezoelectric scanner was further mounted on top of a set of three-axis piezoelectric nano-positioners (attocube, ANPx101 and ANPz101), and placed inside a home-built titanium housing. To allow for excitation and detection of PL, a low-temperature compatible high-NA objective was attached to the top of the titanium cage†. Next, the titanium cage was fixed to a long non-magnetic steel skeleton and inserted into a steel tube (Inset Fig. 7.2). Before immersion into liquid helium, the tube was pumped to a pressure of $\sim 10^{-6}$ mbar, and subsequently filled with $\sim 30$ mbar helium exchange gas. The top of the steel tube was sealed with a laser window (Thorlabs, WL11050-C13, thickness 5 mm), allowing for optical access while acting as a barrier between the outside world and the cryogenic world.

The dynamics associated with resonant excitation were outlined in Section 2.2.4. Under resonant excitation, two-photon absorption leads to undesirable ionisation from $NV^-$

*in fact, most of the measurements were performed in a large liquid helium transport dewar with low helium consumption allowing for an uninterrupted measurement time of approximately 4 weeks.

†Two different objectives were used: Partec, 50x0.82 and Microthek, 60x0.85 with comparable results.

to $NV^0$ [222]. Therefore, a green re-pump pulse was used to restore the NV centre in the desired negative charge state. The PLE pulse sequence (inset Fig 7.1) consists of an alternating sequence of red- and green laser pulses, with duration $\tau_{\text{pump}} \sim 6\,\mu\text{s}$ and $\tau_{\text{re-pump}} \sim 2\,\mu\text{s}$, respectively. In principle, the green re-pump pulse can excite photoluminescence (PL) in the diamond. Therefore, to minimise background, the red pump pulse and the green re-pump pulse were offset by a short time ($\tau_{\text{off}} \sim 500\,\text{ns}$) to allow for the decay of fast PL. The laser pulses were created by acousto-optic modulators (Crystal Technology, 3200-146), synchronised by a dual-channel arbitrary waveform generator (Keysight, 33600A). To collect only the PL excited by the resonant laser, the gating of the single-photon avalanche diode (SPAD, Excelitas, SPCM-AQRH-15-FC) was synchronised to the resonant laser.

The excitation and detection of PL/PLE signal from the NV centre required careful overlap and alignment between the green (off-resonant excitation) and red (resonant excitation) lasers. To that end, a home-built fibre-based confocal microscope was assembled*. The microscope is displayed schematically in Fig. 7.2. The two excitation laser beams were injected via independent arms and combined on a 560 nm longpass (LP) dichroic mirror (cutoff 560 nm, Semrock, FF560-FDi01). For the detection arm, a combination of shortpass filters was used to prevent parasitic signal arising from fluorescence and Raman processes in the fibre (for the green arm: Semrock LL01-532-25, Semrock FF01-650/SP-25 and Semrock, BLP02-561R-25 and for the red arm: Semrock FF01-650/SP-25 and 2x Semrock FF01-637/7-25). All the filters were mounted in quick-release mounts (Thorlabs, QRC05A) making it easy to flip filters in and out of the beam path depending on the desired measurement. Each microscope arm contained two independent mirrors mounted in adjustable right-angled kinematic mounts to facilitate the overlap of the two beams. After the dichroic mirror, two more adjustable mirrors allowed for full angular- and lateral positioning of the combined beam, before injection through the laser window and down to the objective lens inside the cryostat.

The resulting PL was collected via the same objective in a back-scattering geometry. The signal was separated from the excitation laser by a non-polarising 90:10 beamsplitter (Thorlabs, BS025) followed by a combination of longpass filters (532LP, Semrock LP03-532RU-25, 2x635LP, Semrock BLP01-635R-25 and 594LP, Semrock, BLP01-594-R-25). To ease navigation on the sample, a red LED ($\lambda \sim 660\,\text{nm}$, Osa-Opto, OCL-440-MUR-STAR) was inserted in the detection path, where a second 90:10 beamsplitter allowed for imaging of the reflected light from the sample on a charge-coupled-device (CCD)

*The microscope head used in the PLE measurements is a modified version of a microscope inherited from Ref. [85].

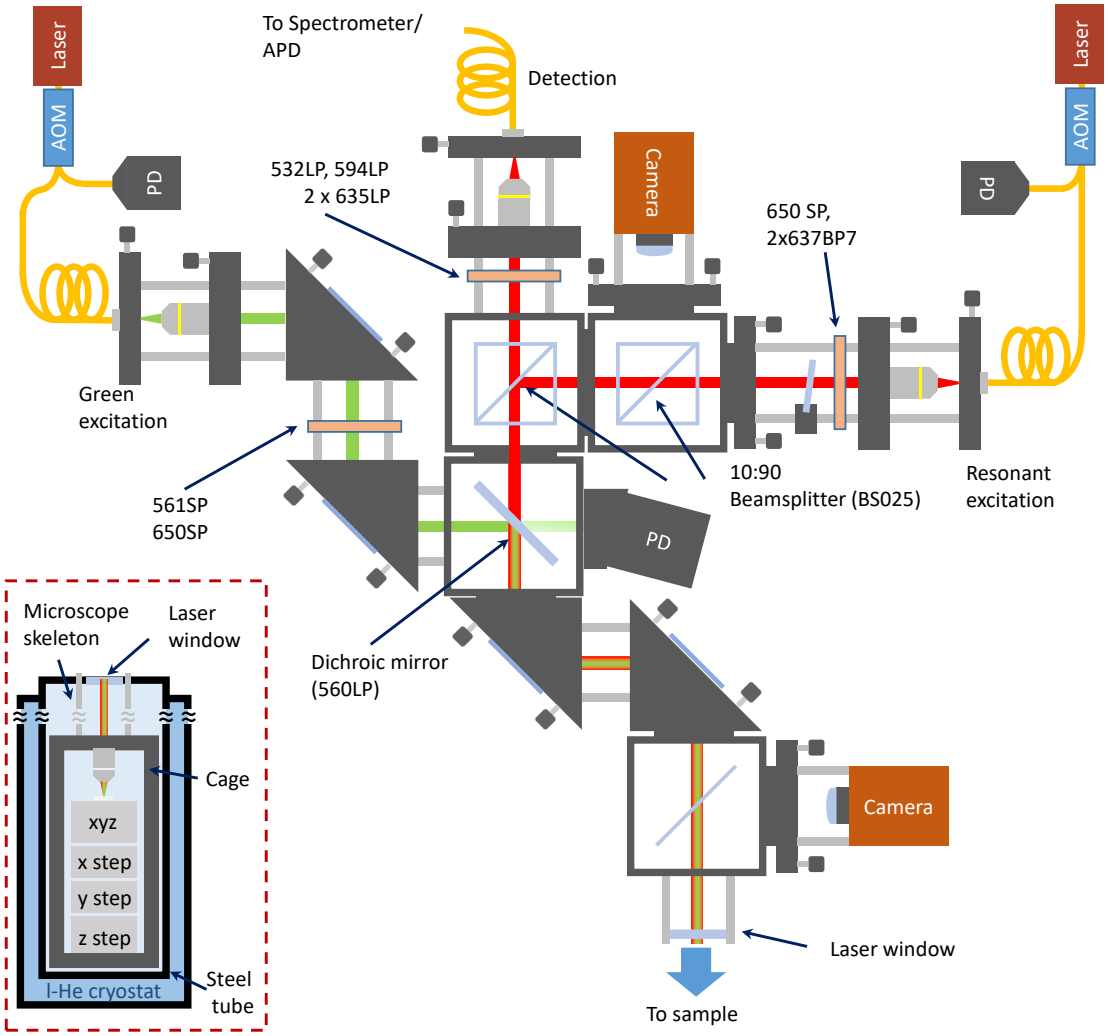


Fig. 7.2. The homebuilt confocal microscope head used for the PLE measurements. The red and green excitation lasers were injected from individual arms and combined on a 560LP dichroic mirror. A combination of shortpass filters was used to filter out florescence from the fibres. The combined laser beam was directed to the sample by two individually adjustable mirrors. The resulting PL was collected in a back-scattering geometry where the signal was filtered from the (red) excitation by a non-polarising 90:10 beam splitter followed by a set of appropriate longpass filters. A second 90:10 beam splitting cube and a CCD camera allowed for imaging of the sample. The microscope head was mounted on top of a liquid helium bath cryostat (inset). Adapted and modified from Ref. [85].

camera (Allied Vision, Guppy Pro F-503).

The PLE measurement process flow is shown schematically in Fig. 7.3 (the NV centre used in this example was located in bulk diamond, see Section 7.3.2). To start, a confocal PL map of the sample was recorded by exciting the NV centre with a green

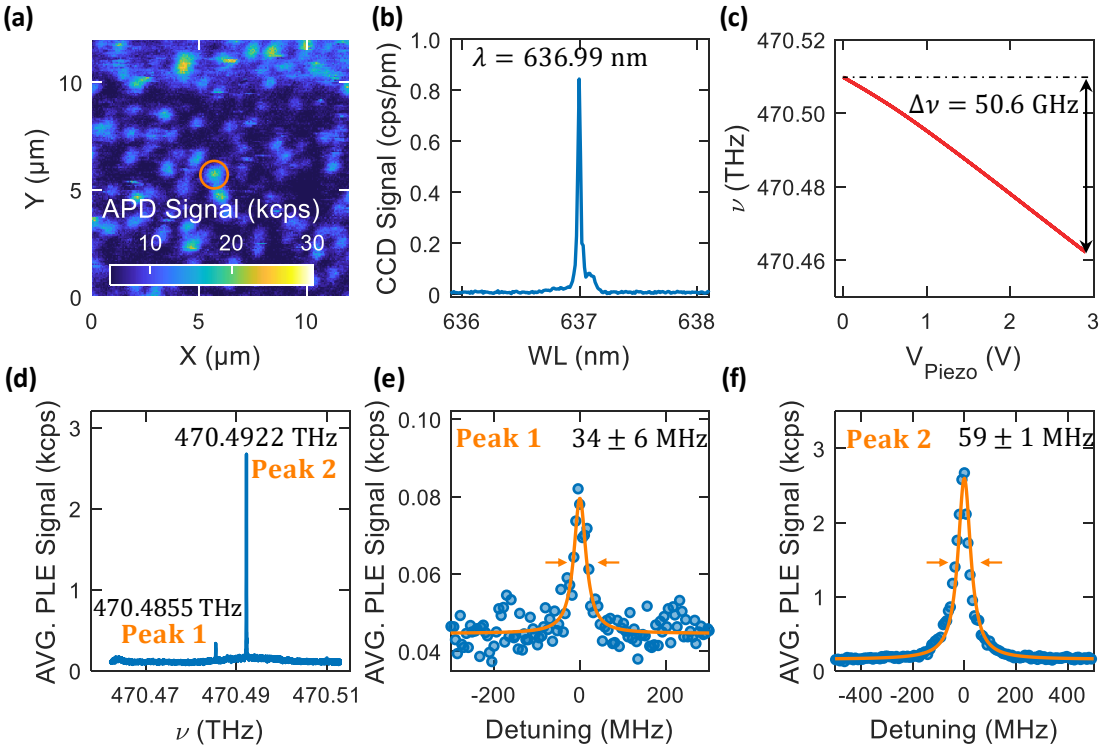


Fig. 7.3. PLE measurement procedure. All the measurements displayed here were performed in bulk. **(a)** Low-temperature confocal scan of NV centres excited by a green laser ($\lambda = 532\,\text{nm}$). The low density of NV centres allows for the characterisation of single, well-isolated centres as indicated by the orange circle. **(b)** A high-resolution PL spectrum of the highlighted NV centre in (a). The sharp ZPL gives a good indication of the exact transition frequency. **(c)** Demonstration of the $\sim 50\,\text{GHz}$ mode-hop free tuning range of the red Velocity laser utilised in this experiment. **(d)** The PLE measurement over the full 50 GHz scanning range revealed two peaks separated by 6.7 GHz. **(e)** - **(f)** High-resolution, low-power PLE scan reveals a ZPL linewidth of $34 \pm 6\,\text{MHz}$ and $59 \pm 1\,\text{MHz}$ for Peak 1 and Peak 2, respectively.

off-resonant laser (Laser Quantum, VENTUS, $\lambda = 532\,\text{nm}$, $P = 0.5 \cdots 1\,\mu\text{W}$), while collecting the resulting PL using a SPAD. An example of a PL map is displayed in Fig. 7.3 (a), showing spatially resolved NV centres. Once a well isolated NV was found, the output of the detection fibre was fed into a spectrometer (Princeton Instruments, Acton, SP2500) allowing for the acquisition of a PL spectrum (Fig. 7.3 (b)). A good indication of the ZPL transition frequency could be obtained using a high-resolution grating (2160 grooves/mm). To find the correct scanning range of the resonant laser, it was helpful to overlap the laser with the ZPL frequency on the spectrometer. To this end, the two 635LP filters in the detection arm were replaced by a 633LP filter (Semrock, LP02-633RU-25). The partial transmission of the 633LP filter allowed the laser frequency to be spectrally resolved without saturating the CCD camera provided

the laser was operated at low power. The laser was tuned to the correct frequency by applying a voltage to the laser piezo. The laser frequency was continuously monitored using a high-precision wavelength meter (High Finesse-ANGSTROM, WS/U-30U). To locate the exact ZPL transition frequency, the laser was scanned across the full tuning range ($\sim 50\,\mathrm{GHz}$) (Fig. 7.3 (c)) at high power, typically in the range $P = 5 \cdots 30\,\mu\mathrm{W}$. For these high powers, severe power broadening would be expected, leading to a strong PLE signal [462]. Fig. 7.3 (d) shows a typical PLE measurement, where two distinct peaks can be spectrally resolved. Once the ZPL transition frequency was located, both the scanning range and the laser power were reduced to minimise power broadening and thus to extract the true ZPL linewidths. A high-resolution PLE scan across the two peaks in Fig. 7.3 (d) revealed a ZPL linewidth of $34 \pm 6\,\mathrm{MHz}$ and $59 \pm 1\,\mathrm{MHz}$ for Peak 1 (Fig. 7.3 (e)) and Peak 2 (Fig. 7.3 (f)), respectively.

Initially, the resonant excitation was performed using a tunable, narrow-linewidth ($\delta\nu \lesssim 500\,\mathrm{kHz}$) laser from Toptica (DL Pro 635, $\lambda = 630 \ldots 640\,\mathrm{nm}$). However, the limited mode-hop free tuning range ($\sim 8 - 10\,\mathrm{GHz}$) made the experiment very time consuming and ever so slightly frustrating, as careful control and adjustment of the laser frequency and the diode current were needed for measurements on different NV centres. To that end, the Toptica laser was later replaced by a Velocity laser (New Focus, Velocity TLB 6704, $\lambda = 635 \ldots 638\,\mathrm{nm}$, $\delta\nu \lesssim 200\,\mathrm{kHz}$) with a mode-hop free tuning range of $\sim 50\,\mathrm{GHz}$ (Fig. 7.3 (c)). Although the Velocity laser had a better performance in terms of the achievable mode-hop free tuning range, the laser frequency was found to drift with time, attributed to creep in the laser piezo. For the first set of measurements (Section. 7.3), the laser drift was compensated for by increasing the scanning range, thus always capturing the ZPL. However, as this results in increased acquisition time, for the second set of measurements (Sec. 7.4), the laser frequency was stabilised using an in-built PID control provided by the wavelength meter. Consequently, stepwise changing the setpoint of the PID control allowed for tuning the laser frequency across the ZPL.

## 7.2 The effect of Microfabrication on the Optical Linewidth

In the seminal proof-of-principle cavity coupling experiment performed in Ref. [77, 85], an increase in the NV centre optical linewidth was observed after sample fabrication. In this experiment, diamond microplatelets were fabricated by first thinning down the diamond to a thickness of $\sim 1\,\mu\mathrm{m}$ using inductively coupled reactive ion etching (Fig 7.4 (a)). After this initial deep-etching step, the thinned-down region was microstructured using electron beam (e-beam) lithography (Fig 7.4 (b)). A final etch step was performed to

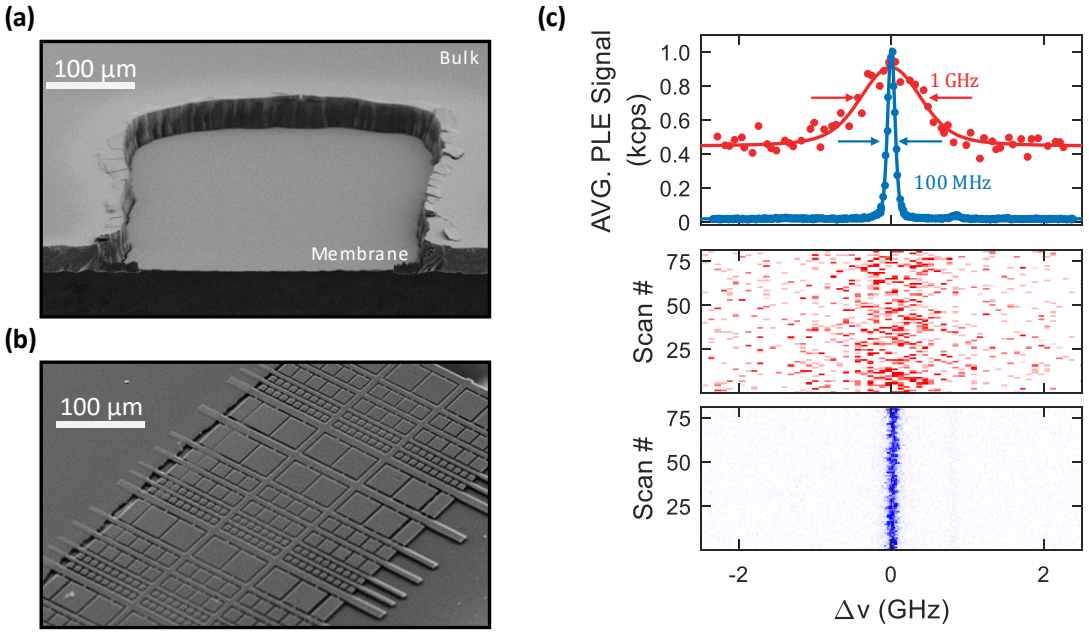


Fig. 7.4. Sample fabrication and linewidth measurements adapted from Ref. [77, 85]. **(a)** The sample was fabricated by first etching the diamond down to a thickness of $\sim 1\,\mu m$. **(b)** After the initial etching step, e-beam lithography followed by an additional etching step was performed to fabricate the microplatelets. **(c)** PLE scans of near-surface NV centres in unprocessed diamond (blue) and microstructured (red) diamond. During fabrication, the averaged ZPL linewidth increased from $\sim 100\,MHz$ to $\sim 1\,GHz$.

relieve the microplatelets. All the etching steps were performed with an alternating sequence of $Ar/Cl_2$ and $O_2$ plasmas. For more details on the sample fabrication, see Ref [77, 85] and references therein.

Fig 7.4 (c) shows photoluminescence excitation (PLE) measurements performed on near-surface NV centres (depth $\sim 70\,nm$), located in both the processed and the unprocessed part of the diamond. In the unprocessed region, NV centres with an averaged ZPL linewidth of $\sim 100\,MHz$ were observed. However, in the processed regions the average linewidth increased to $\sim 1\,GHz$. In this experiment, the green re-pump laser was applied several times for each step of the resonant laser (same protocol as in the inset of Fig. 7.1), hence randomising the local charge environment for each pixel. The large spectral diffusion induced by the re-pump laser indicates the presence of charge traps in close proximity to the NV centre, possibly generated during the fabrication [230].

## 7.3 Reversed Fabrication Order

In the aforementioned experiment (Ref. [77, 85]), the diamond material surrounding the NV centre was still relatively thick ($\sim 1\,\mu m$), and hence the fabricated surface was still several hundred nanometres away from the NV centres. Yet, the effect of fabrication significantly deteriorated the spectral stability of the NV centre. Although the linewidth broadening presumably stems from a fluctuating charge environment caused by fabrication induced surface damage, the exact mechanism causing this surface damage remains unclear. In an attempt to understand the origin of the large spectral diffusion, the optical linewidths were characterised after each fabrication step, starting with a pre-characterisation in bulk. Contrary to Ref. [77, 85], the fabrication procedure was reversed: microstructuring was performed before the deep-etching.

### 7.3.1 Sample Preparation

A commercially available, high-purity ([N] $< 5\,$ppb, [B] $< 1\,$ppb) single-crystal diamond grown via chemical vapour deposition (Element Six, (100)-oriented, "electronic grade", $4 \times 4 \times 0.5\,mm^3$) was used as starting material. The diamond was laser cut * (Almax Easy Lab) and polished down to a thickness of $\sim 50\,\mu m$. Residuals from the polishing were removed by performing a fuming tri-acid bath (nitric, sulphuric and perchloric acid, mixed 1:1:1) [463], followed by a solvent clean (deionised water, acetone, ethanol and isopropanol).

The polishing process is known to strain and damage the diamond surface. The induced stress was relieved by etching a few micrometres using inductively coupled reactive ion etching (ICP-RIE, Sentech SI 500)). The etching was performed with an alternating sequence of $ArCl_2$ and $O_2$ plasmas. Here, the $ArCl_2$ removes the damaged diamond while preserving a smooth diamond surface [152, 159, 464]. However, the $ArCl_2$ might leave $Cl_2$ residuals on the diamond surface [465, 466]. The $O_2$ plasma removes the $Cl_2$ contamination, resulting in an oxygen termination of the diamond surface [467]. For a more detailed description of the sample preparation, the reader is guided to Ref. [85, 152, 159, 305, 403] and references therein.

To aid the formation of NV centres, nitrogen ions were introduced to the top side of the sample via ion beam implantation (Ion Beam Services, $^{14}N$, $55\,keV$, $5 \cdot 10^8\,ions/cm^2$). Based on SRIM† simulations, the implantation energy corresponds to a target depth of

*The starting diamond had in-house number 10010. This diamond was cut into three pieces, where the piece labelled 00012B was used in this experiment.

†Stopping and Range of Ions in Matter.

$75 \pm 16$ nm, which is equal to $\frac{\lambda_{ZPL}}{4}$ [85]. After ion implantation, a multi-step thermal annealing process under vacuum leads to the formation of stable NV centres (compare Section 2.2.1). A tri-acid clean and a subsequent solvent clean were performed to remove any graphite formed during the annealing, thus minimising surface fluorescence [458].

### 7.3.2 Pre-Characterisation of NV Centres in Bulk Diamond

Basic room temperature characterisation was performed to verify the creation of NV centres. Fig. 7.5 (a) shows a $\sim 50 \times 50\,\mu m^2$ confocal scan obtained using a high-NA objective (Olympus, MPLFLN100x, NA=0.9). In this measurement, the NV centres were excited using a pulsed supercontinuum laser (NKT Photonics, SuperK Extreme EXW-12) operating at a repetition rate of 78 MHz with $\lambda = 530 \pm 25$ nm and $P \sim 1$ mW. The excitation laser was filtered from the PL signal using a 633 nm longpass filter. The confocal scan shows that the NV centres were distributed uniformly throughout the diamond. The inset highlights the possibility of spatially resolving single NV centres. The detection fibre was connected to a TTL controlled fibre switch, allowing the PL signal to be either directed to the spectrometer or to the SPAD. The PL spectrum displayed in Fig. 7.5 (b) shows the characteristic phonon-sideband associated with the NV centre. Unfortunately, the ZPL was spectrally filtered by the longpass filter.

Next, time-resolved PL measurements were performed to extract the radiative lifetime of the NV centres (Fig. 7.5 (c)). Fitting the data for time delay longer than 2 ns with a single exponential decay yields a lifetime of $\tau = 12.4 \pm 2$ ns. Here, the signal for the first two nanoseconds corresponds to the instrument response function (IRF) probed by fast decaying background florescence. A more accurate measure of the lifetime could be achieved by fitting the data with a single exponential decay convoluted with the IRF [77], with the IRF probed by the laser directly [300]. Nevertheless, the extracted lifetime is consistent with values reported in literature [37, 132, 194, 216].

A handful of NV centres from various regions of the diamond were characterised at room temperature, before proceeding to the low-temperature measurements. In the PLE measurement shown in Fig. 7.3 (d), two spectrally resolved lines separated by 6.7 GHz were observed. To mitigate power broadening, low-power, high-resolution PLE scans were performed across each peak independently. Fitting each peak with a single Lorentzian yield a linewidth of $\Delta\nu = 34 \pm 6$ MHz and $\Delta\nu = 50 \pm 1$ MHz (Fig. 7.3 (e) and (f), respectively). Due to the close spectral proximity combined with the similarity in linewidth, the two lines were attributed to the $E_x$ and $E_y$ transitions from the same NV centre (compare Section. 2.2.2). In total, 16 different NV centres were investigated in the bulk, with linewidths ranging from $\Delta\nu = 34$ MHz to $\Delta\nu = 5$ GHz, with a

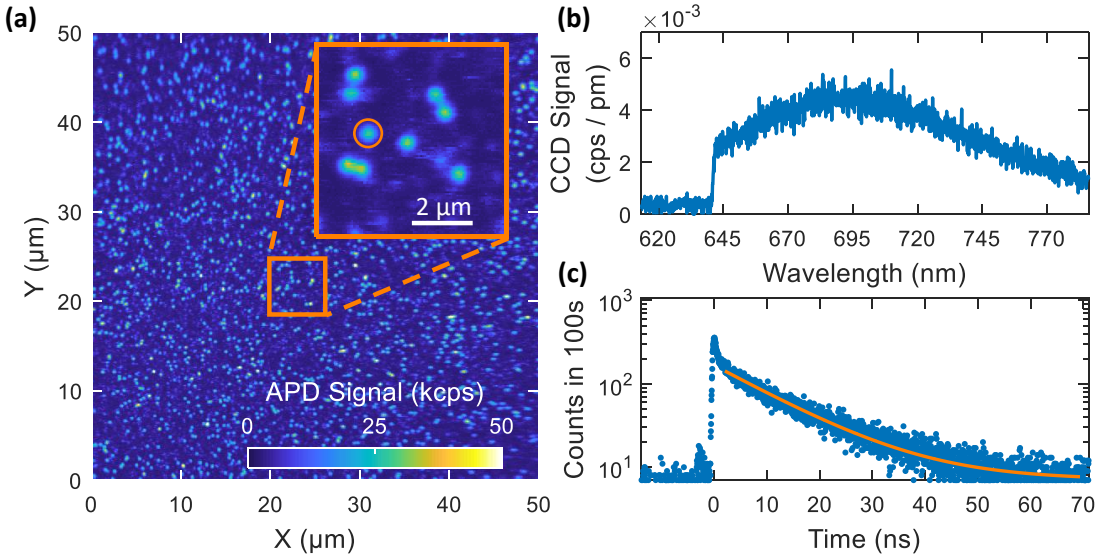


Fig. 7.5. Room temperature pre-characterisation of NV centres in bulk diamond. For all measurements, the excitation was performed using a supercontinuum laser ($\lambda = 530 \pm 25\,\text{nm}$, $P \sim 1\,\text{mW}$, 78 MHz repetition rate). The detection fibre was connected to a TTL controlled fibre switch (transmission $\sim 50\,\%$) used to direct the PL to either SPAD or spectrometer. **(a)** Long-range confocal scan revealed a uniform distribution of single NV centres. **(b)** PL spectrum of the highlighted NV centre. A shortpass filter with cutoff $\lambda \sim 640\,\text{nm}$ was used to filter the excitation laser. **(c)** Time-resolved PL measurement. Fitting a single exponential decay determines the NV centre exited state lifetime $\tau = 12.4 \pm 0.2\,\text{ns}$.

mean linewidth $\Delta\bar{\nu} = 592.4\,\text{MHz}$, median linewidth $\Delta\tilde{\nu} = 105.4\,\text{MHz}$ and standard deviation $\sigma_\nu = 1387\,\text{MHz}$. Ignoring NV centres with $\Delta\nu > 1\,\text{GHz}$ yields $\Delta\bar{\nu} = 104\,\text{MHz}$, $\Delta\tilde{\nu} = 99.9\,\text{MHz}$ and $\sigma_\nu = 56.7\,\text{MHz}$.

### 7.3.3 Microstructuring

Having characterised the NV centres in bulk, attention was turned towards microstructuring of the diamond. The goal was to create micro-membranes with typical dimensions ranging from $10 \times 10\,\mu\text{m}^2$ to $50 \times 50\,\mu\text{m}^2$. The small surface area facilitates bonding to the bottom mirrors used for cavity coupling experiments [77].

The diamond was microstructured following the method outlined in Ref. [85, 152, 159, 305, 403]. To start, the diamond was spin-coated with a hydrogen silsesquioxane (HSQ) negative electron beam resist (FOX-16, Dow Corning), and subsequently baked on a hotplate at 100°C for 10 minutes. To prevent charging during the electron beam (e-beam) exposure, the diamond was further spin-coated with a protective conducting

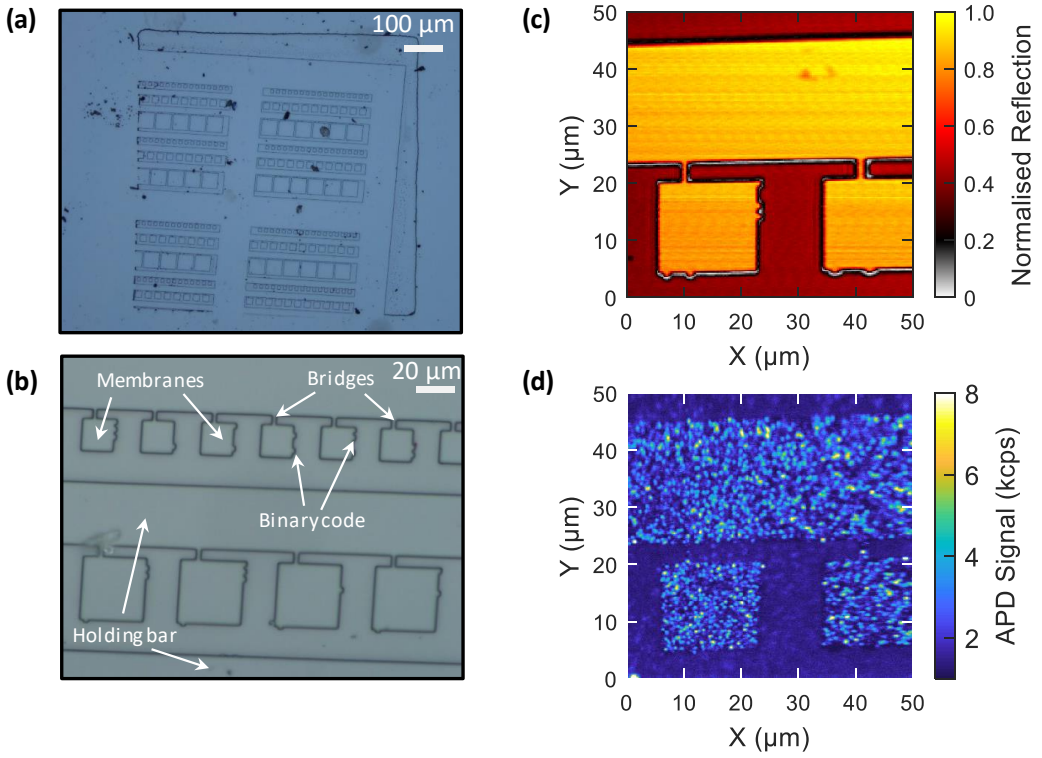


Fig. 7.6. Microstructuring of diamond using e-beam lithography and subsequent reactive ion etching. **(a)** Overview of the write-field after etching. **(b)** The membranes were attached to the holding bars via narrow bridges. The bridges were deliberately placed off-centre to aid identification of the top surface. Each membrane was assigned a unique label based on binary code allowing for easy identification of every single membrane. **(c)** Long-range confocal laser reflection scan ($\lambda = 635\,\mathrm{nm}$). The binary labels are clearly visible allowing for quick identification of the platelets. **(d)** Confocal scan excited with $\lambda = 532\,\mathrm{nm}$ shows that the NV centres survived the the fabrication process.

layer (Electra 92, Allresist). Using e-beam lithography (30 keV), a pattern consisting of square-shaped membranes (area dose $600\,\mu\mathrm{C\,cm^{-2}}$) attached to large holding bars via a small bridge (dose factor 3.0) was written (See Fig. 7.6 (a) and (b)). The bridges were deliberately written off-centre to distinguish the top from the bottom surface, should the membranes turn upside-down. Furthermore, each membrane was assigned a unique label based on binary code, which will be explained in more detail in Section 7.3.6. After exposure, the resist was developed using TMAH* for approximately 20 seconds. To protect the unprocessed region during etching, the sample was covered using a hard $SiO_2$ mask with a $\sim 1 \times 1\,\mathrm{mm^2}$ window cut out with a water jet (Microwater Jet, Switzerland). Approximately 2 µm of the unprotected diamond (i.e. not covered by e-beam resist or

*Tetramethylammonium hydroxide.

the hard mask) was removed using the ICP-RIE, creating trenches between the platelets. As before, a cycle of $ArCl_2$ plasma followed by an $O_2$ plasma was used for this etching step. After etching, the resist was removed by dipping the diamond into a buffered oxide etch (BOE) followed by a tri-acid and a solvent clean. A microscope image showing an overview of the entire write-field is shown in Fig. 7.6 (a). The bridges and unique binary label are clearly visible in the high-resolution zoom shown in Fig. 7.6 (b). To preserve the optical quality of the NV centres, no scanning electron microscope (SEM) image was recorded of the fabricated membranes. Finally, the diamond was glued to a silicon chip using crystalbond, and mounted in the experimental setup (compare Section. 7.1). Before cooling the sample down to cryogenic temperature, a room temperature confocal laser reflection scan (Fig. 7.6 (c)) and a confocal PL scan were performed (Fig. 7.6 (d)). The laser reflection scan ($\lambda = 635\,\mathrm{nm}$) was acquired by removing all the longpass filters in the detection arm and connecting the detection fibre to a photodiode. The unique binary labels are clearly visible on the sides of the membrane. The confocal PL map confirms that the NV centres survived the fabrication process.

After cooling down the sample, linewidth characterisation was performed on membranes of various size located in all four sections of the write-field (Fig. 7.6 (a)). For all membranes, a confocal laser reflection scan was recorded to identify the membrane. Fig. 7.7 summarises the results obtained on one selected membrane, where four different NV centres were characterised (Fig. 7.7 (d)-(f)). The three highlighted NV centres all exhibit linewidths $\Delta\nu < 200\,\mathrm{MHz}$, while for the fourth NV $\Delta\nu \sim 500\,\mathrm{MHz}$ (not shown). Note that NV 2 is located at the end of the bridge, and hence in close proximity to three etched surfaces. In total, 23 NV centres were characterised across all platelets, with linewidths ranging from $\Delta\nu = 105\,\mathrm{MHz}$ to $\Delta\nu = 4.48\,\mathrm{GHz}$, with mean, median and standard deviation $\Delta\bar{\nu} = 473.5\,\mathrm{MHz}$, $\Delta\tilde{\nu} = 174.8\,\mathrm{MHz}$ and $\sigma_\nu = 934.2\,\mathrm{MHz}$, respectively. Ignoring the three NV centres with $\Delta\nu > 1\,\mathrm{GHz}$ gives $\Delta\bar{\nu} = 189.0\,\mathrm{MHz}$, $\Delta\tilde{\nu} = 167.0\,\mathrm{MHz}$ and $\sigma_\nu = 72.3\,\mathrm{MHz}$.

### 7.3.4 The Effect of Microstructuring

The effect of the microfabrication was quantified by comparing the distribution of observed linewidths before and after structuring. Binning the data yields the histograms displayed Fig. 7.8 (a). Note that the histograms are binned on a logarithmic scale, and therefore bins at higher linewidth cover a broader spectral range. By looking at the histograms, two things become apparent. First, after microfabrication, the population of linewidths shifts towards broader lines. Second, the narrowest linewidth found after microstructuring ($\Delta\nu_{\mathrm{ms}} = 105\,\mathrm{MHz}$) was a factor of three broader than the narrowest

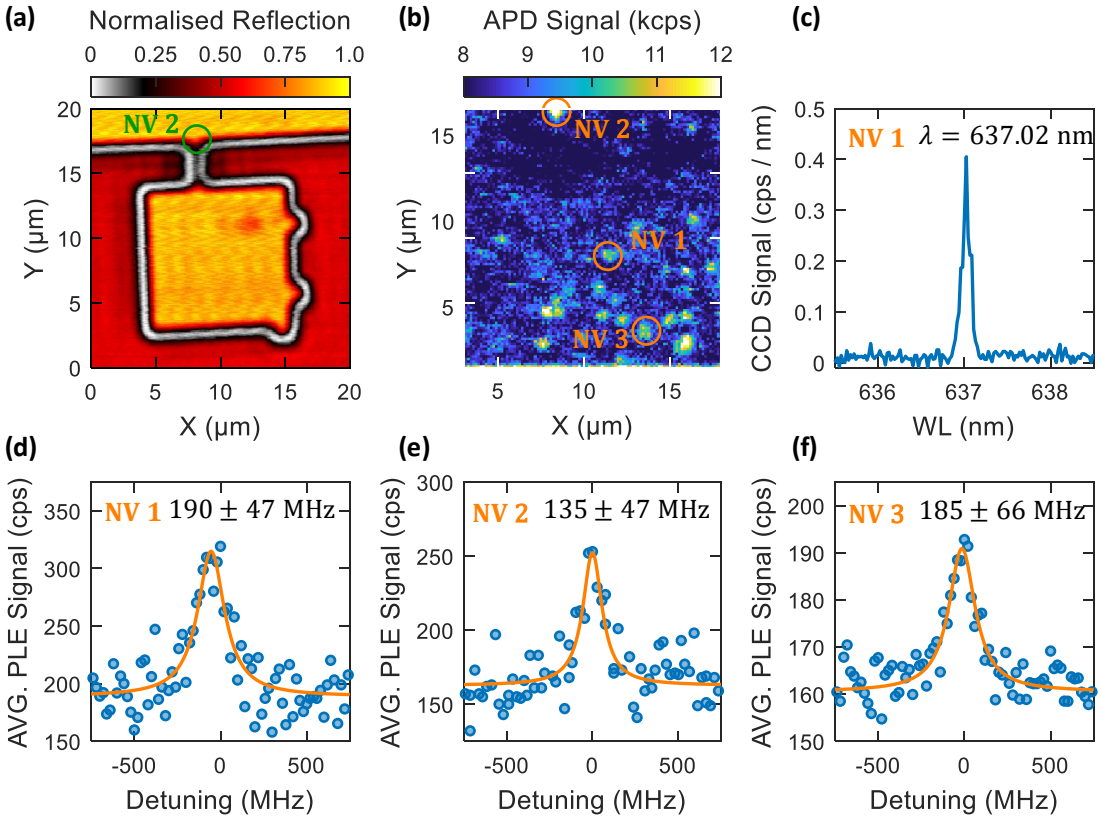


Fig. 7.7. Low temperature PLE measurement after microstructuring. **(a)** Confocal laser reflection scan to identify the membrane. **(b)** Confocal PL scan ($\lambda = 532\,\text{nm}$, $P = 0.5\,\text{mW}$) to locate the NV centres. **(c)** PL spectrum of NV 1 with $\lambda_{\text{ZPL}} = 637.02\,\text{nm}$. **(d)-(f)** PLE measurements of NV 1 ($P = 162\,\text{nW}$, $\Delta\nu = 190 \pm 47\,\text{MHz}$), NV 2 ($P = 30\,\mu\text{W}$, $\Delta\nu = 135 \pm 47\,\text{MHz}$) and NV 3 ($P = 116\,\text{nW}$, $\Delta\nu = 185 \pm 66\,\text{MHz}$), respectively. Note that NV 2 is located at the bridge, in close proximity to three etched surfaces.

linewidth found in bulk ($\Delta\nu_{\text{b}} = 34\,\text{MHz}$). The broadest linewidths found in the two ensembles, $\Delta\nu_{\text{b}} = 5.0\,\text{GHz}$ and $\Delta\nu_{\text{ms}} = 4.5\,\text{GHz}$ in the bulk and the microstructured part, respectively, both fall within the same bin.

In this comparison, only the fabrication induced effect on the narrowest linewidths are of interest, on the ground that the broad linewidths are broad for other reasons [168, 171]. To this end, the remainder of this analysis only includes NV centres with $\Delta\nu < 1\,\text{GHz}$. To start, the histograms in Fig. 7.8 (a) were fitted using a log-normal sampling distribution parameterised by the median $\mu$ and the standard deviation $\sigma$. From the fit, a population median $\mu_{\text{b}} = 90.5\,\text{MHz}$ and $\mu_{\text{ms}} = 178.9\,\text{MHz}$ were extracted, here the subscripts refer to the bulk and microstructured parts, respectively. A log-normal

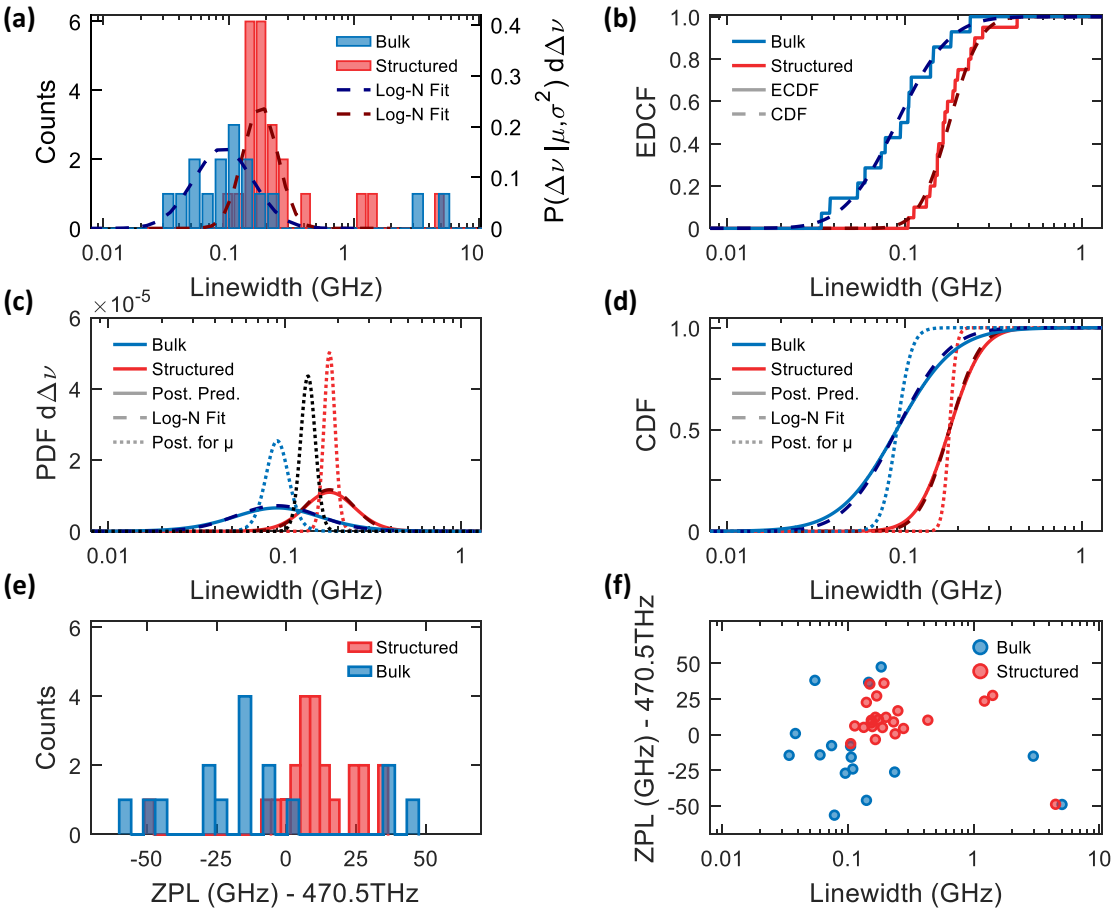


Fig. 7.8. Comparison between the optical linewidths before (blue) and after microstructuring (red). **(a)** Histogram of the measured linewidths. Fitting the histograms with a log-normal distribution yields population medians $\mu_\mathrm{b} = 90.5\,\mathrm{MHz}$ and $\mu_\mathrm{ms} = 178.9\,\mathrm{MHz}$ for the bulk and structured diamond, respectively. The two populations indicate fabrication induced deterioration of the optical linewidths. **(b)** ECDFs of the data and CDFs of the fits in (a). **(c)** Dashed lines show the log-normal fit from (a). Solid lines show the posterior predictive distribution $P(\tilde{x}|\{x_i\})$. Dotted lines are posterior distributions for the median $P(\mu|\{x_i\})$. The two medians are well separated. **(d)** CDFs of the distributions in (c). **(e)** Histogram of the ZPL transition frequency extracted from the PLE measurements. NV centres in bulk were sampled from a larger area of the diamond, thus may experience different local strain leading to a larger spread of the ZPL transition frequency. **(f)** Scatter plot of ZPL transition frequency against the ZPL linewidth revealing no obvious relationship between the ZPL frequency and the linewidth.

distribution is an appropriate distribution for any purely positive quantity affected by multiple independent sources of noise [171, 468]. In other words, external noise will only contribute to the broadening of the linewidth. Fig. 7.8 (b) shows the empirical cumulative distribution function (ECDFs) for the two datasets. Furthermore, there is

a good concordance between the computed cumulative distribution function (CDFs) for the log-normal fits and the ECDFs.

From the distributions of measured linewidths in Fig. 7.8 (a), it seems as though linewidths measured in bulk and in the structured part form two distinct distributions. Therefore, following Ref. [171], a statistical model describing the two distributions was derived. Using a Bayesian approach, the likelihood of a particular linewidth $x_i$ can be modelled using a log-normal distribution

$$P(x_i|\mu,\sigma) = \frac{1}{\sqrt{2\pi\sigma^2}}\frac{1}{x_i}e^{-\frac{(\ln(x_i)-\mu)^2}{2\sigma^2}}, \tag{7.1}$$

where $\mu$ and $\sigma$ is the median and standard deviation, respectively. Next, the posterior distributions, describing the best guess for a parameter given the data acquired and the model used, were computed. In other words, the posterior distribution allows for calculating the distribution of further linewidths $\tilde{x}$ one would expect to measure, given the data already acquired. For the derivation, the reader is guided to Ref. [171].

A graphical representation of the results is shown in Fig. 7.8 (c), where the dashed lines represent the log-normal fits acquired from Fig. 7.8 (a) and the solid lines are the posterior predictive distributions $P(\tilde{x}|\{x_i\})$. There is a close resemblance between the posterior predictive distributions $P(\tilde{x}|\{x_i\})$ and the sampling distributions $P(x_i|\mu,\sigma)$ (Eq. 7.1). However, $P(\tilde{x}|\{x_i\})$ is slightly broader on account of the uncertainty in the estimation of $\mu$ and $\sigma$. The dotted lines represent the posterior distribution for the median $P(\mu|\{x_i\})$. There is no overlap between the posterior distribution $P(\mu|\{x_i\})$ for the bulk and structured samples, indicating that the median of the two distributions is well separated. To quantify this statement, $10^8$ simulated draws from the posterior distributions revealed $P(\mu_{\mathrm{ms}} < \mu_{\mathrm{b}}|x_{\mathrm{all}}) = 0.00797$, where $\{x_{\mathrm{all}}\}$ is the combined set of all the measured linewidth.

Finally, attention is turned toward the ZPL transition frequency. Fig. 7.8 (e) shows a histogram of the ZPL transition frequency extracted from the PLE measurements. As can be seen, the spread in ZPL frequencies is larger for the bulk measurements, indicating larger variations in local strain. The NV centres characterised in bulk were sampled from a large region of the diamond (dimension $4 \times 4\,\mu\mathrm{m}^2$), hence larger variations in the crystalline environment can be expected. Fig. 7.8 (f) shows a scatter plot of the ZPL transition frequency against the ZPL linewidth. A Wilcoxon rank-sum test ($p = 0.0136$) indicates no obvious relationship between the ZPL transition frequency and the ZPL linewidth.

To summarise, this section has attempted to quantify the effect of microfabrication on

the NV centre linewidth by applying the statistical model derived in Ref. [171]. To fully capture the complete picture, a larger sample size of NV centres in bulk and structured diamond is necessary. Ideally, one would measure the same NV centres before and after fabrication, i.e. by tracking the NV centres [458].

### 7.3.5 Deep Etching

To create thin diamond micromembranes, the structured region of the diamond was thinned down by performing a long etching step from the backside of the sample. To protect the NV centres, the implanted diamond surface was coated with a titanium-gold layer (5 nm Ti, 100 nm Au) using electron beam assisted thermal evaporation. Next, the sample was flipped around, and the unprocessed parts of the diamond were protected using the same hard mask as before (Section. 7.3.3). The structured region of the sample

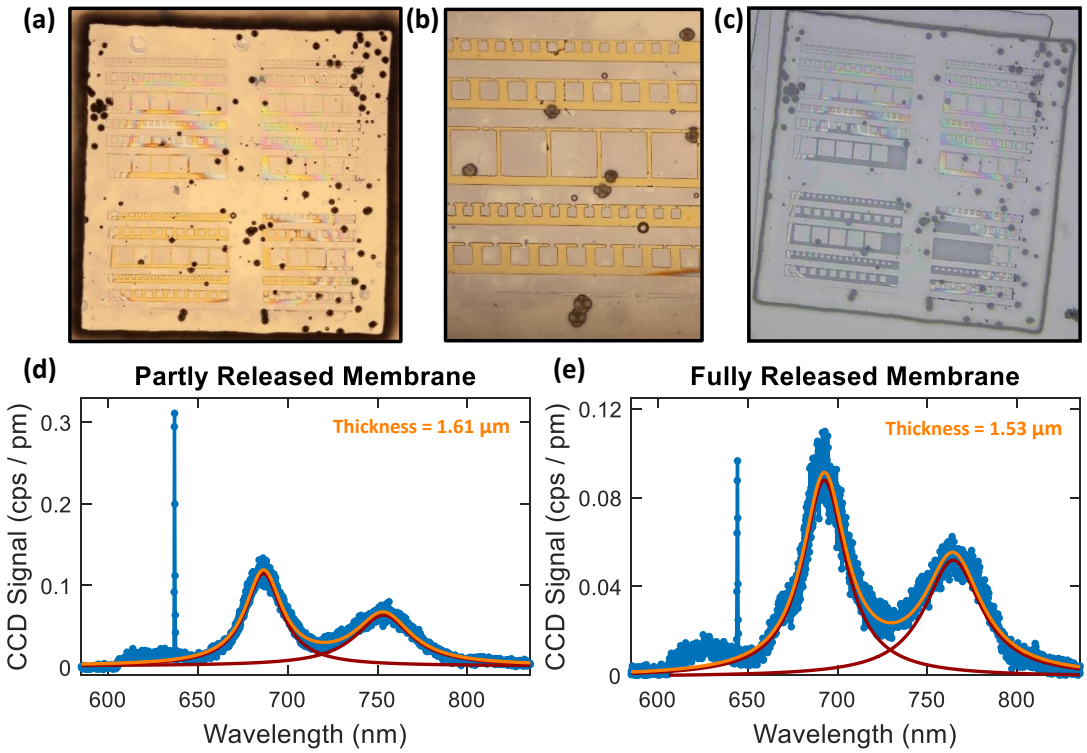


Fig. 7.9. Fabrication of thin membranes by etching. **(a)** Gold-coated write-field after etching showing fully and partially released membranes. **(b)** Zoom of fully released membranes. **(c)** Microstructured diamond after all fabrication steps. Some membranes broke out during the tri-acid clean. **(d)** - **(e)** PL spectra from NV centres located in a partially- and fully released membrane, respectively. Thin-film interference strongly alters the shape of the PSB. Fitting the fringes with a double Lorentzian yield an approximate membrane thickness of 1.61 µm and 1.53 µm, respectively.

was thinned down to a thickness of $1 - 2\,\mu m$ using an alternating sequence of $ArCl_2$ and $O_2$ plasmas. Fig. 7.9 (a) shows the still gold-coated diamond after etching. The etching process was not perfectly uniform, resulting in local thickness variations. As can be seen in Fig. 7.9 (a), only membranes in the lower-left quadrature were fully released, membranes from the two upper quadrants were only partially released. Fig. 7.9 (b) shows a zoom of the fully released membranes. Erosion from the mask or the carrier wafer redeposited on, and masked, the diamond resulting in the black pillars [158]. However, there is still a sufficient number of clean membranes.

After etching, the titanium-gold layer was removed using a gold etchant (Sigma Aldrich 651818), before a tri-acid and a subsequent solvent clean were performed. Fig. 7.9 (c) shows a microscope image after all the cleaning procedures. Unfortunately, some membranes were lost, presumably during the tri-acid clean. As before, the prepared diamond was glued to a silicon chip and mounted in the experimental setup. Fig. 7.9 (e) and (f) show PL spectra of NV centres found in the partially- and fully released membranes, respectively. Thin-film interference significantly alters the shape of the PSB. To estimate the thickness of the membranes, the fringes were fitted with two Lorentzian, yielding a thickness of 1.61 µm and 1.53 µm, respectively.

### 7.3.6 Optical Linewidths After Deep Etching

Performing the deep etch was like the opening of Pandoras's box: numerous unanticipated consequences materialised. To start, Fig. 7.10 (a) shows a low-temperature confocal PL scan after deep etching. The PL spectra acquired from the two highlighted NV centres are shown in panel (b) and (c), where the PL spectrum in Fig. 7.10 (b) shows a sharp ZPL and the characteristic PSB of an NV centre. On the contrary, the PL spectrum in Fig. 7.10 (c) shows no ZPL and arguably a differently shaped PSB. This feature was observed for different NV centres throughout the sample, but was never observed before the deep-etch. An NV centre with no ZPL is non-physical. From the PL spectrum alone, it is hard to determine if the missing ZPL arises from very large spectral diffusion, thus not capturing the ZPL at the spectrometer, or if the PL spectrum arises from a different defect altogether (e.g. the neutral vacancy GR1 [138, 469]). Note that the two highlighted spots exhibit comparable intensities in the confocal scan.

A handful of NV centres were investigated without resolving a single linewidth in PLE. The reason why becomes apparent when looking at the PL spectra in Fig. 7.10 (d). The PL spectra, recorded from the same NV centre at two different times, clearly show spectral instability. The shift in wavelength corresponds to spectral jumps of 34 pm (25 GHz). Here, the spectrometer resolution is 11 pm (8 GHz). With spectral wandering

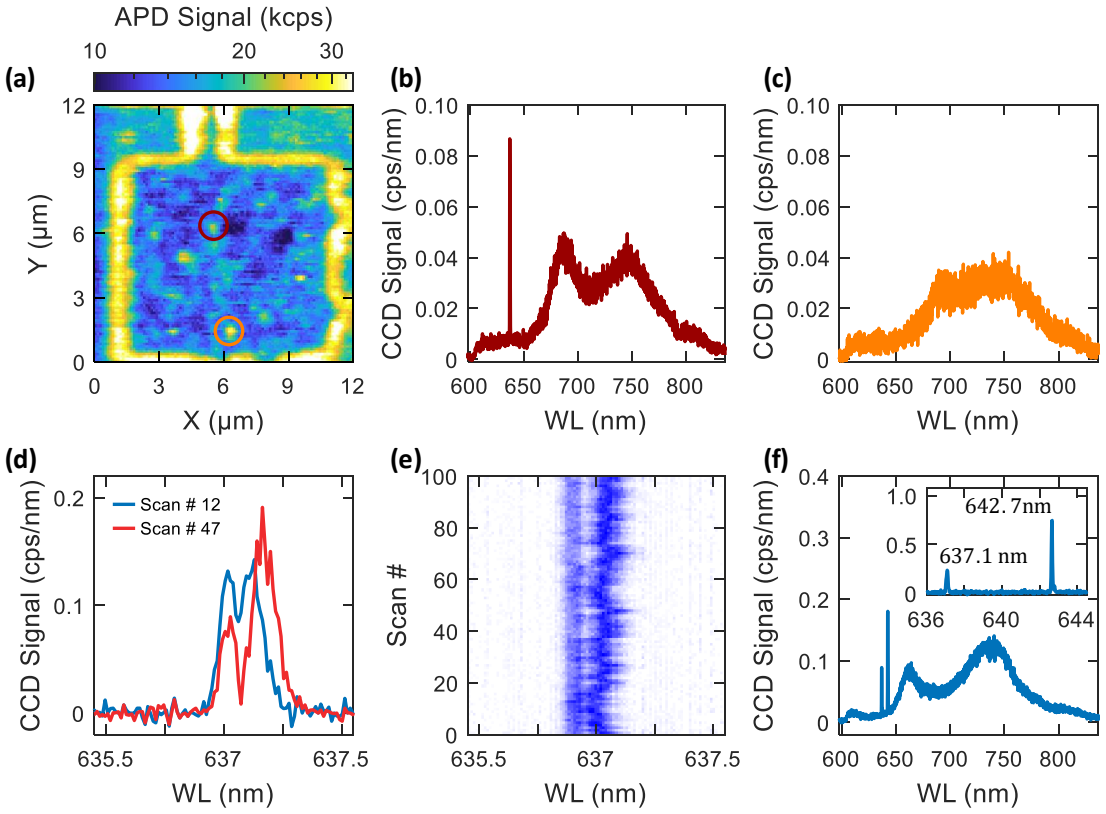


Fig. 7.10. Linewidth measurements after deep-etching. **(a)** Confocal PL scan of a membrane with two presumably identical fluorescent spots highlighted. The two spots exhibit similar countrates. **(b)** - **(c)** PL spectrum from the burgundy and orange highlighted fluorescent spot, respectively. The spectrum in (b) exhibits the sharp ZPL and PSB characteristic of an NV centre. On the other hand, the spectrum in (c) show no ZPL. From the spectrum on its own, it is hard to determine if the missing ZPL arises from very large spectral wandering or if the spectrum is from a different defect (e.g. GR1). This feature was reproducibly seen for different bright spots, across several membranes. **(d)** High-resolution PL spectra of the ZPL for a different NV centre recorded at two different times. The spectra show clear signs of spectral wandering. **(e)** PL spectra of the same NV centre as in (d), where each line is averaged over 60 seconds. **(f)** PL spectrum of yet a different NV centre showing a sharp peak at $\lambda \sim 643\,\text{nm}$. The peak position matches with a feature characteristic for pure graphite. The peak was observed for multiple NV centres.

of this magnitude, the overlap between the resonant laser and the ZPL is vanishingly small, and hence no signal is observed in PLE. To validate the functionality of the experimental setup, a control measurement was performed on the bulk part of the sample, with comparable results as obtained before the fabrication (Section 7.3.2).

Finally, Fig. 7.10 (f) shows the PL spectrum of yet another NV centre, where a striking feature was observed at $\lambda = 642.7\,\text{nm}$. Pure graphite exhibits a characteristic Raman

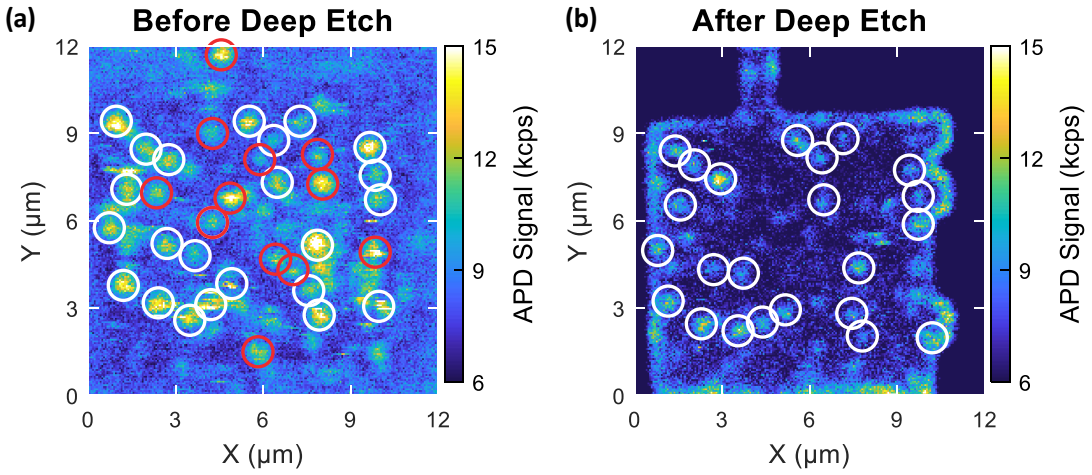


Fig. 7.11. Comparison between a confocal PL scan of the same platelet recorded **(a)** before and **(b)** after the deep etching. NV centres highlighted in white could be identified with confidence after the etching, while the NV centres highlighted in red could not. The etching resulted in the disappearance, or quenching of the PL, for a total of 12 NV centres.

feature at $3\,238\,\mathrm{cm}^{-1}$ [138]. Exciting with $\lambda = 532\,\mathrm{nm}$, corresponds to the graphite peak at $\lambda = 642.7\,\mathrm{nm}$, in good agreement with the observed spectrum. A graphitic layer could have been created during the high-temperature thermal annealing step, but should, at least in principle, have been removed by the tri-acid clean. Note, that signatures of $sp^2$ bonded carbon (Fig. 5.2) were observed in the experiment presented in Chapter 5 and in Ref. [255].

The remainder of this subsection will present a direct comparison of the optical coherence of the same NV centres as were characterised before the deep-etch. Fig. 7.11 show confocal PL scans recorded under nominally identical conditions (a) before and (b) after deep-etching. The NV centres highlighted in white could easily be identified after the etching step. On the contrary, NV centres highlighted in red could not, with confidence, be resolved after etching. Either etching resulted in quenching of the PL, or the NV centres were simply removed during the etching. The narrow lines characterised before the deep etch could stem from native NV centres deeper in the crystal, and could therefore have been etched away. However, the likelihood that all the measured NV centres prior to etching were of native origin seems highly unlikely. Quenching of the PL can be explained by surface contamination changing the Fermi level inside the diamond, thus favouring the neutral charge state.

The disappearance of NV centres, combined with the loss of membranes during the

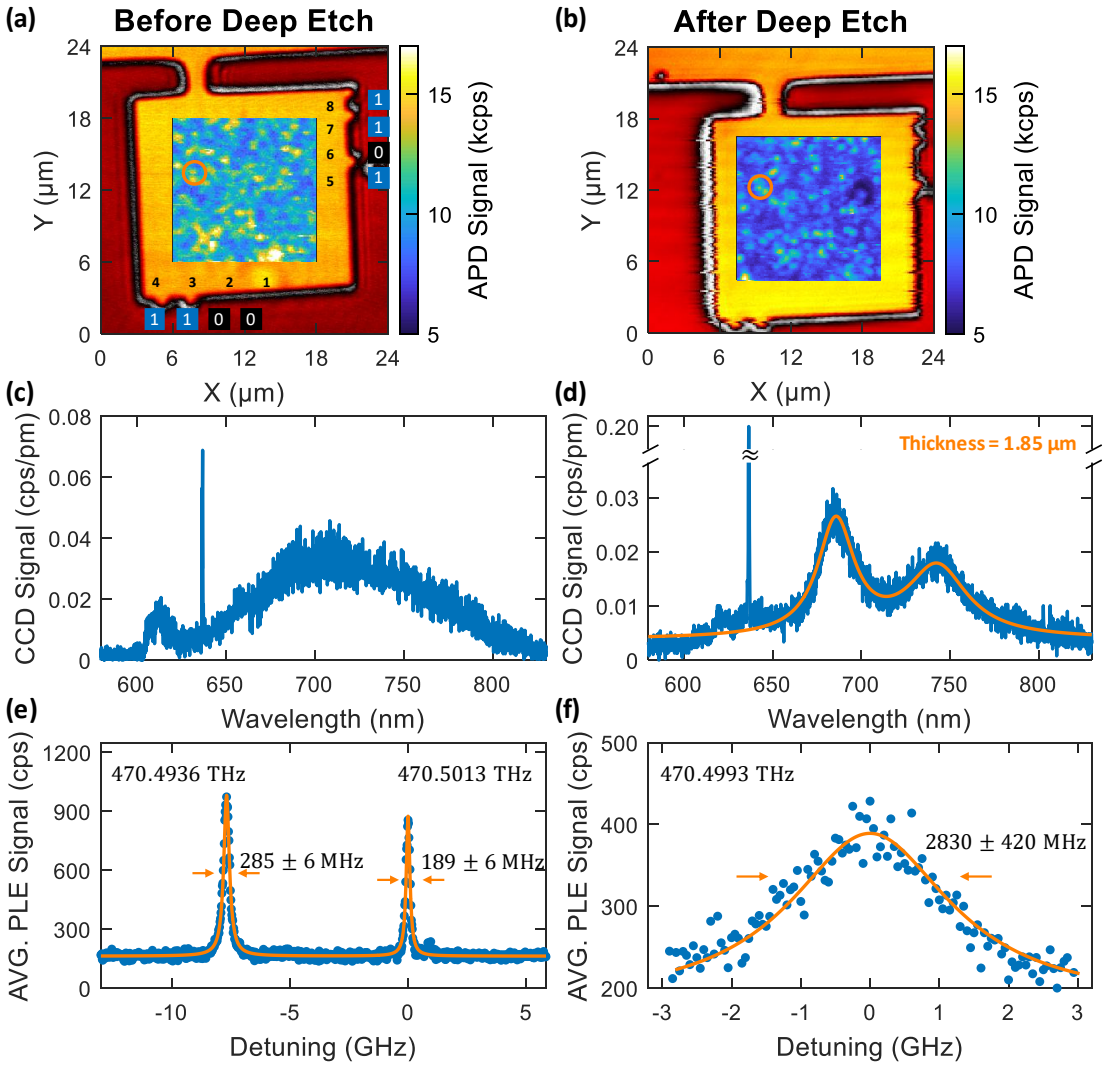


Fig. 7.12. Comparison of the same NV centre before and after deep etching. **(a)-(b)** Confocal scan before and after deep etching respectively. The targeted NV centre is highlighted by the orange circle. **(c)** Typical PL spectrum obtained before deep-etching. Note that this PL spectrum is from a different NV centre within the same membrane. **(d)** PL spectrum of the highlighted NV centre after etching. From the modulations of the PSB, the diamond thickness was estimated to be 1.85 μm. **(e)-(f)** PLE measurement before ($P_{\text{offres}} = 0.76\,\text{mW}$, $P_{\text{res}} = 2.45\,\mu\text{W}$) and after deep etching ($P_{\text{offres}} = 0.55\,\text{mW}$, $P_{\text{res}} = 1.04\,\mu\text{W}$). The etching resulted in a 15-fold increase in the linewidth.

tri-acid clean, made the tracking of NV centres a laborious task. Nevertheless, Fig. 7.12 shows the characterisation of the same NV centre before and after etching. As mentioned in Section. 7.3.3, each membrane was assigned a unique label based on binary code. The code works as follows: markers were fabricated on eight spots along two sides of the

membrane. The unique label was assigned by the presence (1) or absence (0) of a marker in each spot. For example, Fig. 7.12 (a) shows a confocal laser reflection scan performed before etching. From the markers, the label of this membrane is 00111011 (membrane 59).

Fig. 7.12 (b) shows a confocal scan of the same region performed after the deep etch. As before, the NV centre of interest is highlighted. Unfortunately, in the interest of time, no PL spectrum of this NV centre was recorded before deep etch. The PL spectrum displayed in Fig. 7.12 (c) is from a different NV centre located in the same membrane (no PLE signal was observed for this NV centre after etching). Fig. 7.12 (d) shows the PL spectrum from the highlighted NV after etching. Fitting the modulations of the PSB yields an approximate membrane thickness of 1.85 μm. The PLE measurement ($P_{\text{offres}} = 0.76\,\text{mW}$, $P_{\text{res}} = 2.45\,\mu\text{W}$) performed before deep etching (Fig. 7.12 (e)) revealed two peaks split by 7.7 GHz. Fitting each peak with a single Lorentzian yields $\Delta\nu = 286 \pm 6\,\text{MHz}$ and $\Delta\nu = 189 \pm 6\,\text{MHz}$. As before, the two peaks were attributed to the $E_{\text{x}}$ and $E_{\text{y}}$ transitions. After the deep etch (Fig. 7.12 (f)), PLE measurement ($P_{\text{offres}} = 0.55\,\text{mW}$, $P_{\text{res}} = 1.04\,\mu\text{W}$) revealed a 15-fold increase in linewidth from $\Delta\nu = 189 \pm 6\,\text{MHz}$ to $\Delta\nu = 2830 \pm 420\,\text{MHz}$. Due to the limited mode-hop free tuning range of the resonant laser, the second peak could not be resolved*.

## 7.4 Optical Linewidths in Postimplanted Microstructures

The results outlined in the previous section suggests that even minimal microfabrication deteriorates the optical coherence of the NV centre. To this end, a novel fabrication scheme was proposed, where all the fabrication steps were performed prior to nitrogen implantation. This fabrication process was christened "postimplantation" [171].

### 7.4.1 Sample Preparation

As before, the starting material was a commercially available electronic grade diamond from Element Six. Following similar fabrication procedures as described in Section 7.3.3 and Section 7.3.5, the diamond was fabricated into thin membranes with thickness $2.5 - 5\,\mu\text{m}$, and cantilevers of various dimensions. The length of the cantilever varied from $35 - 70\,\mu\text{m}$ with a width of approximately 4.5 μm and a thickness ranging from $2 - 4\,\mu\text{m}$†.

*The velocity laser (Section 7.1) was installed during the linewidth characterisation in bulk. Unfortunately, the velocity laser was not available for the last PLE measurements performed after deep etching, including the measurement in Fig. 7.12 (f).

†The in-house number of this diamond is 00013BAA. This diamond sample was the sister sample to sample A in Ref. [171].

After fabrication, the diamond was implanted with nitrogen ions followed by thermal annealing, after which NV centres were observed in bulk. However, no NV centres were observed in the cantilevers, presumably due to charging of the structured areas resulting in the deflection of the ions. Therefore, to mitigate charging, the sample was coated with a layer of 1 nm Cr and 5 nm Au, before the sample was re-implanted with nitrogen ions (Helmholtz-Zentrum Dresden-Rossendorf, $^{14}$N, 12 keV, $5 \cdot 10^{11}$ ions/cm$^2$, implanted at an angle of 7°). After annealing, NV centres were observed throughout the sample. Fig. 7.13 (a) shows an overview of the sample. For convenience, the different parts of the sample are labelled as follows: bulk, membrane, cantilever and mirror, as indicated in Fig. 7.13 (a). NV centres were sampled from all the different regions and categorised according to their location. Fig. 7.13 (b) shows a high-resolution laser scanning confocal image of the structured fabricated part.

The lateral dimensions of the cantilevers are sufficiently large to allow for implementation in a Fabry-Perot cavity without suffering from beam clipping at the edges (typical beam waist $\sim 1 - 2\,\mu$m [77, 255, 387]). Therefore, a part of the diamond (Fig. 7.13 (c)) was transferred to a DBR mirror (LaserOptik, Transmission $\simeq$ 58 ppm) using a micromanipulator system (Fig. 7.13 (d)). The transfer process was carried out as follows: first, to break the holding bars (Fig. 7.13 (e)), one needle was placed beneath said bar while the other needle gently pressed the structure down. The structure was released by breaking both the holding bars (Fig. 7.13 (f)). A combination of released tension and electrostatic forces may result in the structure flying away uncontrollably. However, due to the large size combined with electrostatic forces, the structure could be picked up and moved (Fig. 7.13 (g)). The structure was placed on a clean spot on the mirror (Fig. 7.13 (h)). For a cavity coupling experiment, it is beneficial to have the NV centre close to the bottom mirror [77]. Therefore, the structure was flipped over (Fig. 7.13 (i)). Both the diamond and the mirror exhibit very smooth surfaces: the diamond bonds efficiently to the mirror via Van der Waals forces. Strong bonding was verified by the possibility of bending and breaking the glass needles without displacing the diamond (see Fig. 5.1 (a)) [255]. Note that the observable interference fringes in Fig. 7.13 (h) is a sign of poor bonding; the rotation of the structure would not have been possible with a strongly bonded diamond.

### 7.4.2 Characterisation of the Optical Linewidths

The higher fluence of nitrogen ions used for the postimplanted sample compared to the sample described in Section 7.3, resulted in a higher concentration of NV centres. In Ref. [220], an increase in the ZPL linewidth was observed for samples with a high

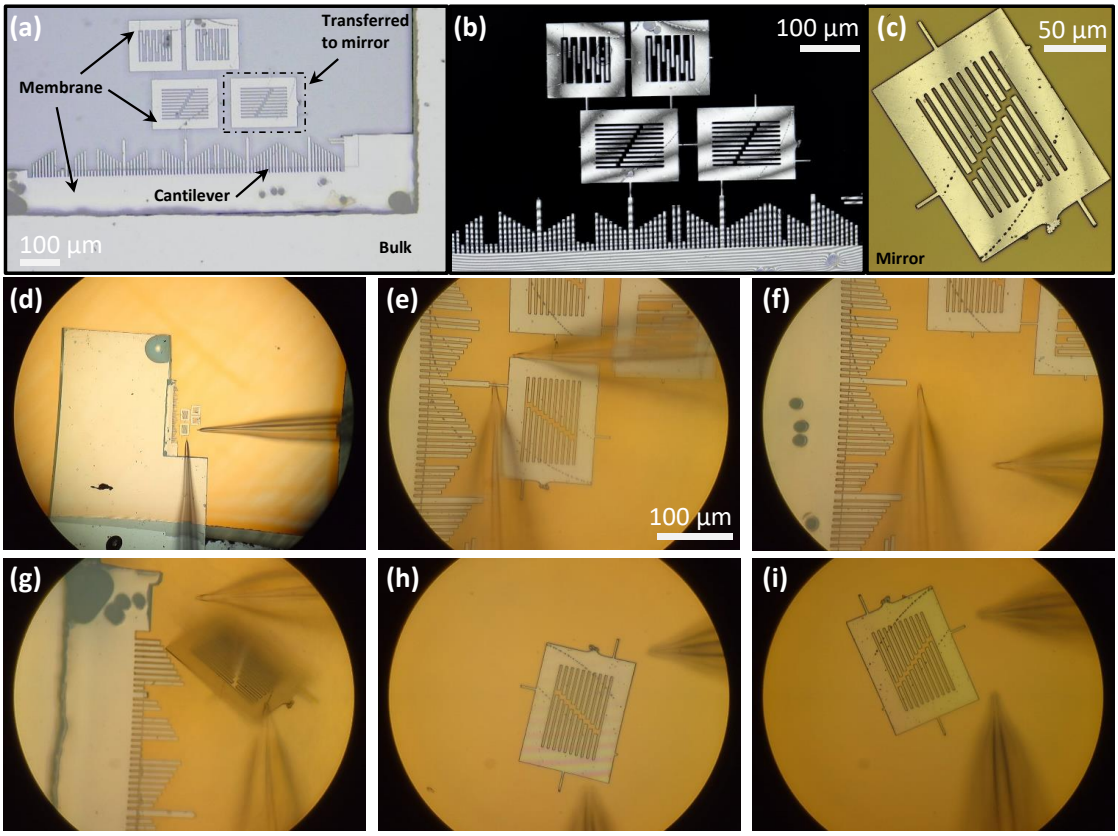


Fig. 7.13. **(a)** Microscope image of the sample. The sample consists of four different sections: bulk, thinned down membranes, cantilever and mirror. NV centres were characterised from all parts of the sample and categorised their location. The structured part inside the black rectangle was transferred to a DBR mirror. **(b)** - **(c)** Laser scanning confocal image of the whole sample and the part transferred to a mirror, respectively. **(d)** - **(i)** Process flow of transferring the diamond to the mirror using a micromanipulator system.

density of NV centres. Therefore, as a first characterisation, PLE measurements were performed on a handful of NV centres in the bulk part of the diamond. Fig 7.14 (a) shows a typical confocal scan performed in the bulk. Although the density of NV centres is higher compared to the scan in Fig. 7.5 (a), isolating single NV centres was still possible. For the highlighted NV centre, two closely spaced lines were observed in PLE, with linewidths of $\Delta\nu = 47.7 \pm 6\,\mathrm{MHz}$ and $\Delta\nu = 47.2 \pm 21\,\mathrm{MHz}$ extracted from a Lorentzian fit. These linewidths are comparable to the narrowest lines observed in the low-density sample (compare Section. 7.3.2).

Next, the optical coherence of the NV centres in the fabricated structures was investigated. Fig. 7.14 (d) shows a confocal PL scan recorded on the diamond transferred to the

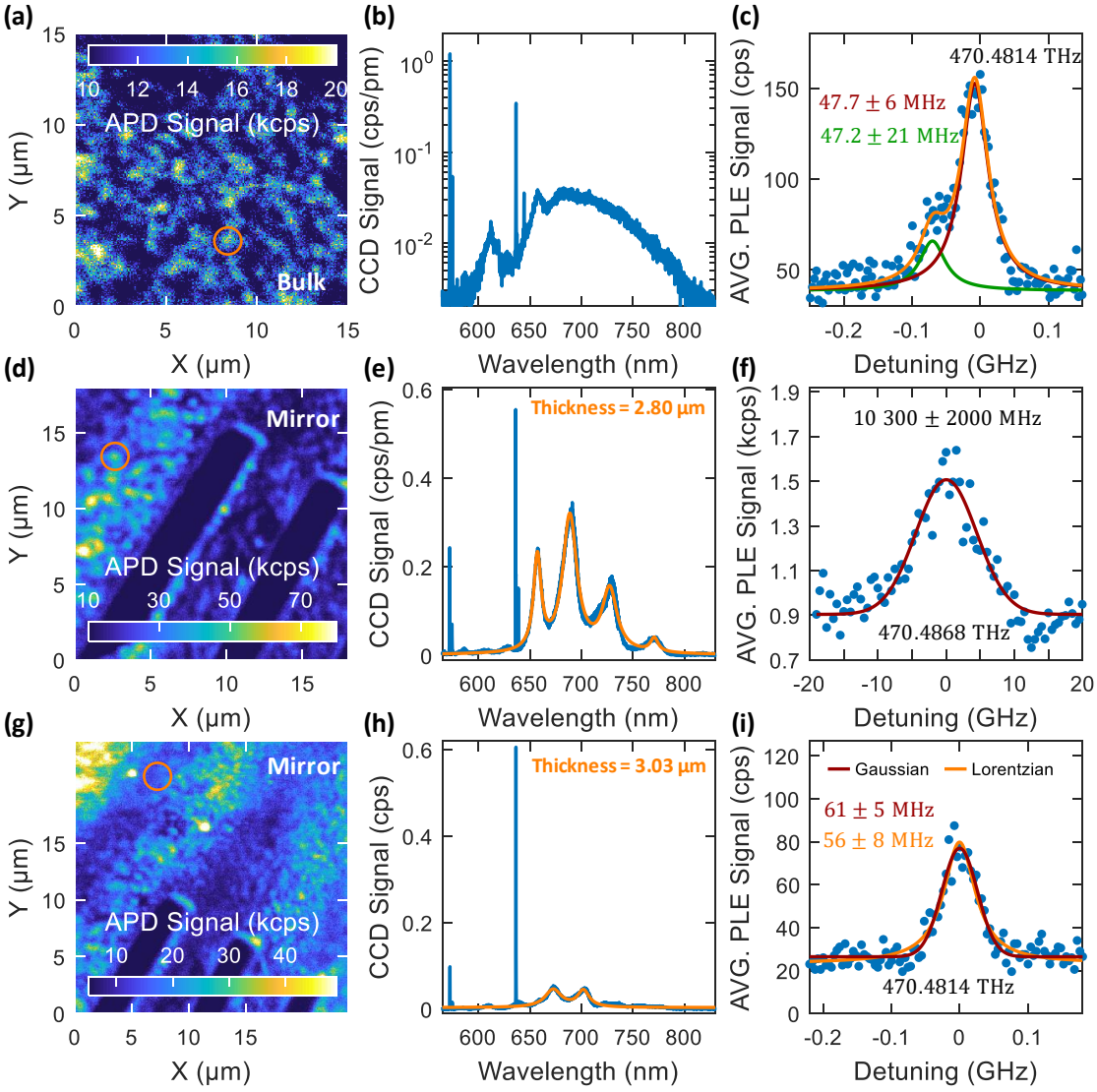


Fig. 7.14. **(a)** - **(c)** Characterisation of the optical linewidth in bulk. Despite the higher density of NV centres, narrow optical lines were observed. **(d)** - **(f)** Example of an NV centre with a broad optical linewidth ($\Delta\nu$ = 10 GHz). Fitting the modulations of the PSB yields a sample thickness of $\sim$ 2.80 µm. **(g)** - **(i)** Narrow NV centre in $\sim$ 3.03 µm thick diamond with an averaged Lorentzian linewidth 56 ± 8 MHz. For comparison, fitting the data with a Gaussian yields 61 ± 5 MHz. For details see main text.

mirror. Compared to the PL scan in bulk (Fig. 7.14 (a)), two things become apparent. First, a large increase in the PL countrate was observed, attributed to the presence of the DBR mirror beneath the sample. Second, the PL scan showed areas, or stripes, of lower PL, attributed to destructive thin-film interference caused by a slight gradient in the

diamond thickness. By fitting the fringes in the PSB for the PL spectrum in Fig. 7.14 (e) with the sum of four Lorentzians, a diamond thickness of $\sim 2.8\,\mu$m was extracted. A PLE measurement with $P_{\text{offres}} = 550\,\mu$W and $P_{\text{res}} = 0.6\,\mu$W (Fig. 7.14 (f)) revealed a broad ZPL linewidth of $10.3 \pm 2\,$GHz; as this NV centre exhibited a broad linewidth, no further PLE measurements with lower resonant power were conducted.

On the contrary, Fig. 7.14 (g) - (i) show the characterisation of a different NV centre located in a slightly different region on the mirror. Fitting the fringes in the PL spectrum (Fig. 7.5 (h)) yield a diamond thickness of $\sim 3.03\,\mu$m. However, compared to Fig. 7.5 (e), only two fringes are visible, and hence the extracted thickness carries a greater uncertainty. Performing 100 successive PLE scans over a time duration of 30 minutes with $P_{\text{res}} = 0.51\,$nW and continuous green re-pump with power $P_{\text{offres}} = 230\,\mu$W, revealed an average linewidth $\Delta\nu = 61 \pm 5\,$MHz extracted from a Lorentzian fit (Fig. 7.5 (i)). To the best of the author's knowledge, this is the narrowest reported linewidth in $\lesssim 3\,\mu$m thin diamond. For comparison, a Gaussian fit yields $\Delta\nu = 61 \pm 5\,$MHz. The smaller uncertainty implies that a Gaussian fit is a better model of the data. The motivation for a Gaussian fit is to include spectral jumps and slow spectral wandering averaged over many scans [130].

For numerous NV centres, two (or, in very few cases more than two) lines were resolved in the PLE measurements. If the two lines exhibited similar linewidths, the two lines were attributed to the $E_{\text{x}}$ and $E_{\text{y}}$ transitions from the same NV centre, on the ground that finding two NV centres with the similar ZPL frequency and similar linewidths within the same focal volume seems unlikely [171]. The $E_{\text{x}}$ and $E_{\text{y}}$ transitions have orthogonal, linear polarisation selection rules [470]. In principle, performing a polarisation resolved measurement [221] will indicate whether the two lines originate from the same NV centre or not. A study on the polarisation of the optical transitions was beyond the scope of this experiment, as the microscope head used did not allow for polarisation control. As an exception, the PLE measurement shown in Fig. 7.15 revealed 3 distinct peaks separated by $\sim 400\,$MHz. From the similarity in linewidth, the two leftmost peaks ($\nu_{\text{ZPL}} = 470.4752\,$THz and $\nu_{\text{ZPL}} = 470.4756\,$THz) were attributed to one NV centre, while the rightmost peak ($\nu_{\text{ZPL}} = 470.4759\,$THz) likely originates from a different NV centre. All three lines exhibit linewidths well below 100 MHz. Out of the totally 140 NV centres characterised in this thesis, Fig. 7.15 was the only time more than two lines were observed within a sub GHz spectral window.

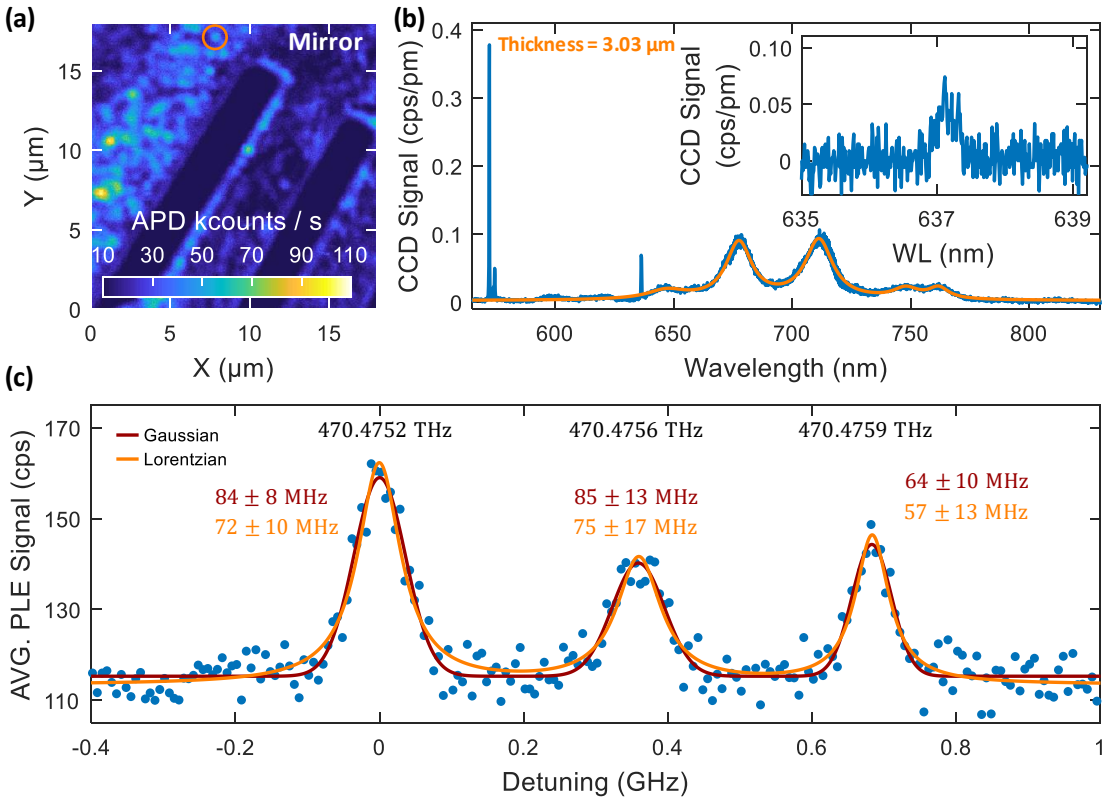


Fig. 7.15. Two narrow NV centres within the same focal volume. **(a)** Confocal PL scan ($P_{\text{offres}} = 550\,\mu\text{W}$) on the mirror. **(b)** PL Spectrum of the highlighted NV centre. The modulations of the PSB corresponds to a diamond thickness of $\sim 3.03\,\mu\text{m}$. The inset shows a high-resolution PL spectrum of the ZPL. **(c)** Three spectrally separated peaks within a spectral range $< 1\,\text{GHz}$ resolved in a low power ($P_{\text{res}} = 5.56\,\text{nW}$) PLE measurement. All three lines exhibit averaged linewidths $< 100\,\text{MHz}$. From the similarity in linewidth, the two leftmost peaks were attributed to the $E_x$ and $E_y$ transition of the same NV centre, while the rightmost peak likely originates from a different NV centre.

### 7.4.3 Spectral Stability

Spectrally stable emitters are of paramount importance for entanglement protocols relying on quantum interference of indistinguishable photons [213, 457]. To verify the spectral stability of the NV centres, successive PLE scans were performed over the timespan of several hours for two selected NV centres on the mirror with linewidths $\lesssim 100\,\text{MHz}$. Notably, a green repump pulse with power $P_{\text{offres}} = 475\,\mu\text{W}$ was applied several times for each step of the resonant laser, thus randomising the charge environment for each pixel [77]. Therefore, the measurement captures the spectral drift induced by the fluctuation charge environment.

Fig. 7.16 (a) shows the average signal after 2000 successive PLE scans, acquired over

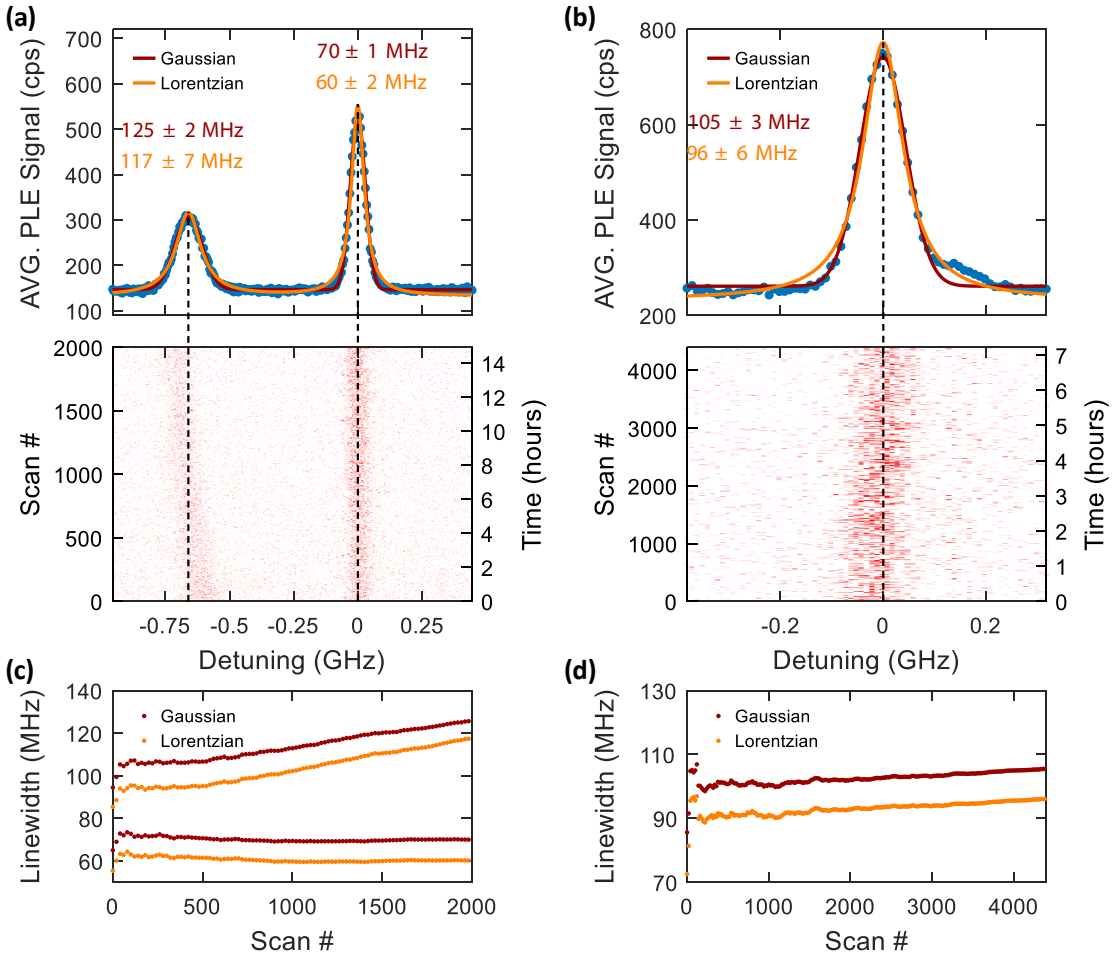


Fig. 7.16. Probing the spectral stability of two different NV centres located on the mirror by performing successive PLE scans. **(a)** Two transitions attributed to the $E_x$ and $E_y$ transition of the same NV centre. 2000 successive PLE scans ($P_{\text{offres}} = 475\,\mu\text{W}$ and $P_{\text{res}} = 9.3\,\text{nW}$, acquired over $\sim 15$ hours) resulted in an average Gaussian linewidth of $\Delta\nu = 125 \pm 2\,\text{MHz}$ and $\Delta\nu = 70 \pm 1\,\text{MHz}$ respectively. The central frequency of the transition at $-0.66\,\text{GHz}$ drifted by approximately 107 MHz, corresponding to 7.1 MHz per hour. **(b)** 4400 successive PLE scans ($P_{\text{offres}} = 475\,\mu\text{W}$ and $P_{\text{res}} = 16.3\,\text{nW}$, acquired over $\sim 7$ hours) for the second NV centre resulted in an average Gaussian linewidth of $\Delta\nu = 96 \pm 6\,\text{MHz}$. **(c)** - **(d)** Linewidth as a function of the cumulated numbers of scans for the NV centre in (a) and (b), respectively. Each data point is averaged over 20 scans.

approximately 15 hours with a scanning speed of 52.1 $\frac{\text{MHz}}{\text{s}}$ and power $P_{\text{res}} = 9.3\,\text{nW}$. For this NV centre, two peaks with an average frequency spacing of 660 MHz were observed. Fitting the peaks with a Gaussian yield an averaged linewidth of $\Delta\nu = 125 \pm 2\text{MHz}$ and $\Delta\nu = 70 \pm 1\text{MHz}$. In general, the degeneracy of the $E_x$ and $E_y$ transitions is lifted by the presence of local strain or electric field [227]. The small energy spacing combined

with the small average linewidth indicates low noise in close proximity to the NV centre. Nevertheless, a slow frequency drift was observed over the course of the measurement: the transition frequency of the leftmost peaks shifted by approximately $\sim 107\,\mathrm{MHz}$, corresponding to 7.1 MHz per hour. The slow drift can be explained by a change in the environment on the time scale of several hours, which affects one of the transitions more strongly than the other [192].

Fig. 7.16 (b) shows the spectral stability of the second NV centre investigated. Here 4400 successive PLE scans were performed over a timespan of 7 hours, with $P_{\mathrm{res}} = 16.35\,\mathrm{nW}$ and a scanning speed of $118.5\,\frac{\mathrm{MHz}}{s}$. A Gaussian fit reveals an average linewidth of $\Delta\nu = 105 \pm 3\,\mathrm{MHz}$. To further emphasise the long-time spectral stability, in Fig. 7.16 (c) and (d), the averaged linewidths are plotted as a function of the cumulated number of scans for the NV centre in Fig. 7.16 (a) and (b), respectively. In panel (c) and (d), each data point is the average of 20 scans, as the signal-to-noise ratio is inadequate to extract reliably the linewidth for a single scan.

For the sake of completeness, Fig. 7.17 (a) shows a PLE measurement performed on a different NV centre suffering from large spectral wandering. In this measurement, the NV centre was pumped with a modest pump power of $P_{\mathrm{res}} = 73\,\mathrm{nW}$ and re-pumping was done using a supercontinuum laser with $\lambda = 532 \pm 10\,\mathrm{nm}$, average power $P_{\mathrm{avg}} = 85\,\mu\mathrm{W}$ operating at a repetition rate of 78 MHz. The modest pump power resulted in a strong signal-to-noise ratio: the peak position can easily be resolved for each scan. Two sources of spectral wandering can be identified: a slow spectral drift of approximately 300 MHz, on top of which spectral jumps occurs [229], presumably induced by the re-pump laser [226, 231].

The observed spectral drift in Fig. 7.16 and Fig. 7.17 occurred over a relatively long time-scale, and can therefore be accounted for by applying an electric field via gate electrodes [161, 227] and stabilised using a feedback mechanism [42, 217, 220, 231]. The random spectral jumps induced by the re-pump laser will probably still occur, but the change in transition frequency can be accounted for quickly [231]. To illustrate, Fig. 7.17 (b) shows the overlap of the peaks obtained from the single scans in (a), resulting in an average linewidth of $\Delta\nu = 95\,\mathrm{MHz}$. Reducing the excitation power reduces power broadening at the expense of the signal-to-noise ratio for single PLE scans. Typically, NV centres characterised with excitation power $< 10\,\mathrm{nW}$ exhibit optical linewidths $\Delta\nu < 100\,\mathrm{MHz}$ averaged over several hours. However, due to the low countrate and poor signal-to-noise ratio, tracking the frequency of the ZPL cannot be easily established with the current experimental setup. Therefore, for future experiments increasing the collection efficiency using a solid-immersion lens (SIL) would be beneficial [403, 471, 472].

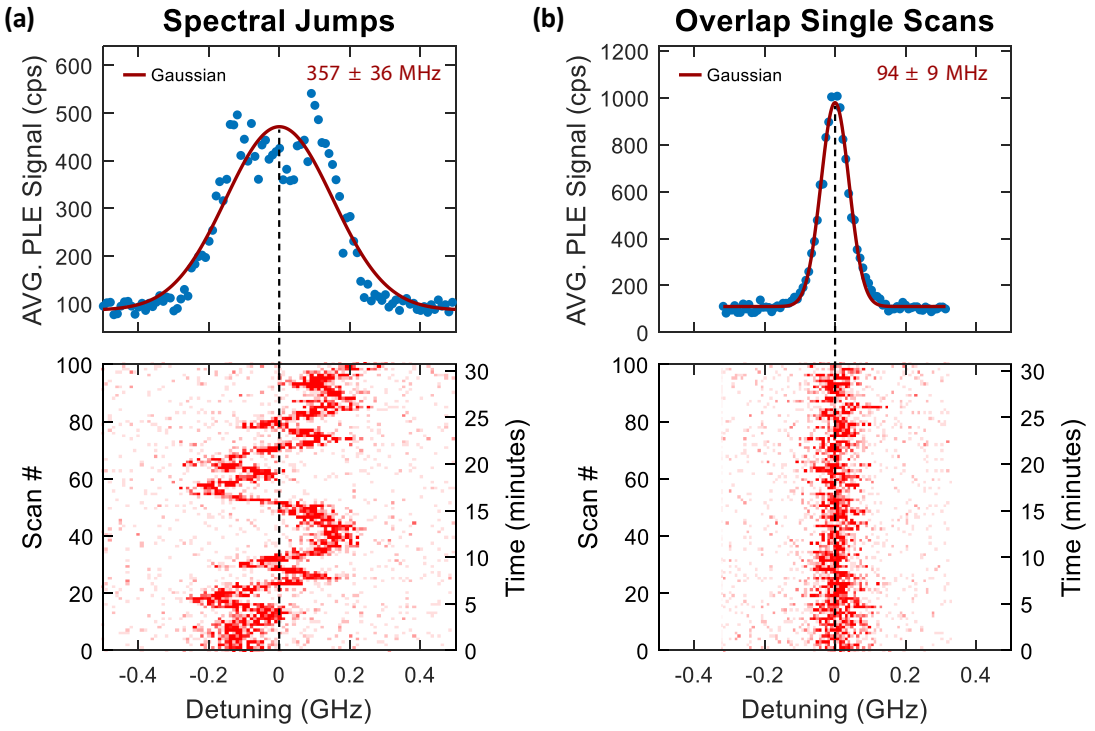


Fig. 7.17. Strong spectral wandering. **(a)** 100 PLE scans acquired over 30 minutes with $P_{\text{res}} = 73\,\text{nW}$ and re-pumped using a supercontinuum laser ($\lambda = 532 \pm 10\,\text{nm}$, $P_{\text{avg}} = 85\,\mu\text{W}$, operating at a repetition rate 78 MHz). The strong spectral wandering leads to an average linewidth of $\Delta\nu = 357 \pm 36\,\text{MHz}$. **(b)** Overlap the maxima of the single scans in (a) results in an average linewidth of $\Delta\nu = 94 \pm 9\,\text{MHz}$.

### 7.4.4 Disentangling Inhomogeneous Broadening from Power Broadening

In an attempt to disentangle inhomogeneous linewidth broadening $\Gamma_{\text{in}}$ from power broadening characterised by the Rabi coupling $\Omega$, successive PLE measurements were performed with decreasing power. This study was performed on a well isolated NV centre (Fig. 7.18 (a)) with a power broadened linewidth $\Delta\nu \simeq 100\,\text{MHz}$. As can be seen from the PL spectrum in Fig. 7.18 (b), this NV centre exhibited an unusually bright ZPL on the spectrometer under green illumination ($P_{\text{offres}} = 500\,\mu\text{W}$). The inset in Fig. 7.18 (b) shows a PL spectrum obtained by exiting the NV centre using a blue laser* ($\lambda = 450\,\text{nm}$, $P = 850\,\mu\text{W}$), predominantly exciting $\text{NV}^0$ [147]. The modulations of the PSB corresponds to a diamond thickness of $2.82\,\mu\text{m}$. Fig. 7.18 (c) shows a high-resolution PL spectrum centred at the ZPL wavelength. The four visible peaks indicate the presence of multiple NV centres within the focal volume. Indeed, in the high-power PLE measurement ($P_{\text{offres}} = 502\,\mu\text{W}$ and $P_{\text{res}} = 131\,\text{nW}$) displayed in Fig. 7.18 (d) three peaks

*The reasoning behind the blue excitation is the topic of Appendix J.

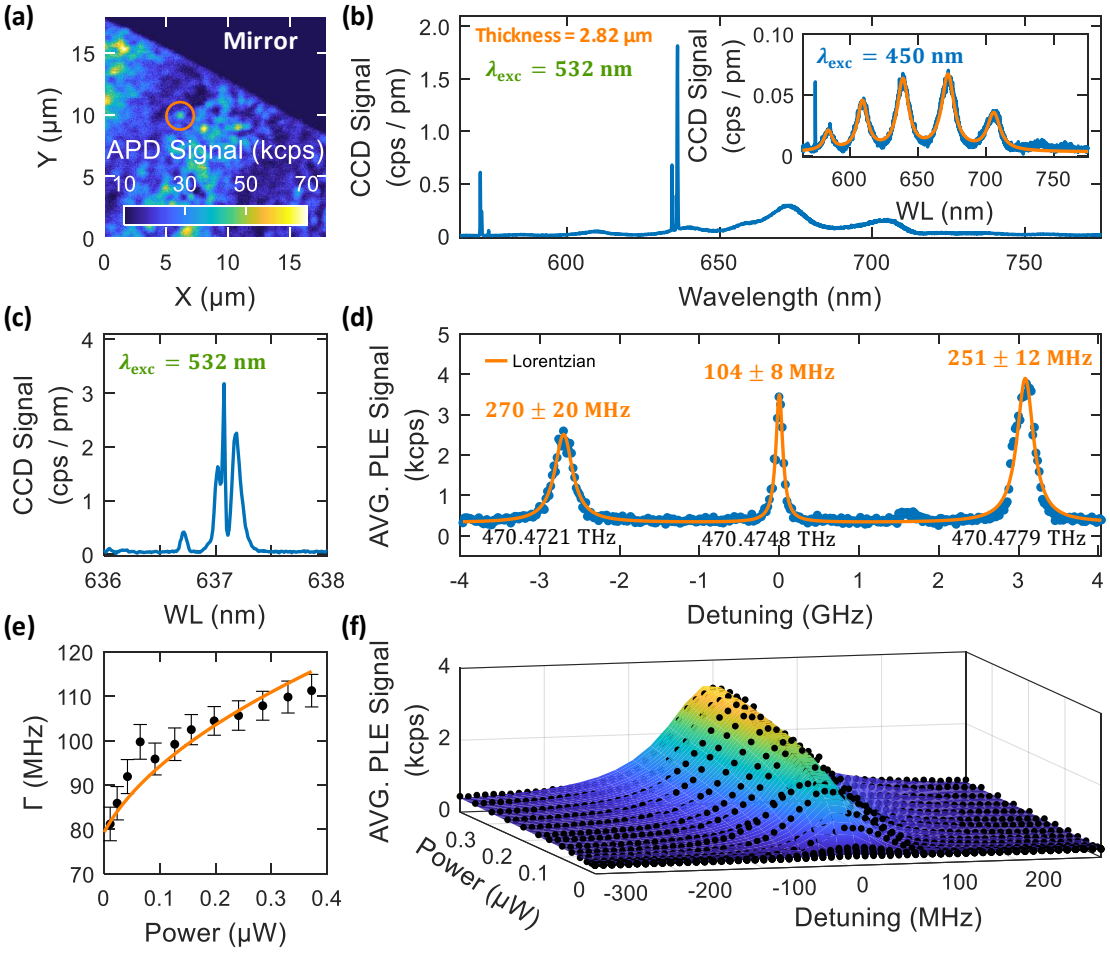


Fig. 7.18. Disentangling inhomogeneous broadening from power broadening by performing PLE scans for decreasing powers. **(a)** Confocal PL scan on the mirror ($P_{\text{offres}} = 500\,\mu\text{W}$). **(b)** PL spectrum under green illumination. Inset: PL spectrum under blue excitation ($\lambda = 450\,\text{nm}$, $P = 850\,\mu\text{W}$). The fringes in the PSB yield a diamond thickness of 2.82 µm. **(c)** High-resolution PL spectrum of the ZPL indicating the presence of multiple NV centres. **(d)** High power PLE measurement ($P_{\text{offres}} = 500\,\mu\text{W}$, $P_{\text{res}} = 131\,\text{nW}$). Left- and right-most peaks are assigned to the $E_x$ and $E_y$ transitions of the same NV centre. The central peak likely originates from a second NV centre and was the peak investigated in this power dependence. **(e)** Extracted linewidth Γ as a function of resonant excitation power. The orange line is a fit according to Eq. 7.4. **(f)** Average PLE signal as a function of resonant excitation power and detuning shows a clear indication of power broadening. Data fitted according to Eq. 7.3

are visible. Based on the linewidths, the left- and rightmost peak ($\Delta\nu = 270 \pm 20\,\text{MHz}$ and $\Delta\nu = 251 \pm 12\,\text{MHz}$, respectively) were attributed to the $E_x$ and $E_y$ transitions, and the middle peak ($\Delta\nu = 104 \pm 8\,\text{MHz}$) to a second NV centre. The remainder of this section focuses on the middle peak.

This discussion follows Ref. [178]; the full derivation can be found in Appendix I. To simplify the analysis, the spectral diffusion is assumed to follow a Lorentzian profile characterised by the full-width at half maximum $\Gamma_{\text{in}}$ (this assumption will be revisited later). The probability of the emitter frequency being equal to $f^*$ is given by the normalised Lorentzian function $L(f^* - f_0, \Gamma_{\text{in}})$, where $f_0$ is the average frequency. For a driven two-level system with radiative decay rate $\gamma$, the occupation of the excited state is given by [4]

$$\rho_{22} = \frac{\left(\frac{1}{2}\Omega\right)^2}{4\pi^2 \left(f - f^*\right)^2 + \left(\frac{1}{2}\gamma\right)^2 + \frac{1}{2}\Omega^2}\,, \tag{7.2}$$

where $\Omega = \sqrt{c \cdot P}$. Here, $P$ is the excitation power and the effective coupling strength $c$ depending on the incoupling efficiency of the laser and the orientation of the NV centre dipole moment. The experimentally measured lineshape is given by the convolution between $L(f^* - f_0, \Gamma_{\text{in}})$ and $\rho_{22}$:

$$C(f) = \frac{\mathcal{A}}{4\pi} \cdot \frac{\Omega^2}{\sqrt{\gamma^2 + 2\Omega^2}} \cdot \frac{\frac{1}{2}\Gamma}{\left(f - f_0\right)^2 + \left(\frac{1}{2}\Gamma\right)^2}\,, \tag{7.3}$$

which is a Lorentzian with full width at half maximum

$$\Gamma = \Gamma_{\text{in}} + \frac{\gamma^2 + 2\Omega^2}{2\pi}\,. \tag{7.4}$$

Here, $C(f)$ yields an expression for the countrate as a function of frequency. The factor $\mathcal{A}$ depends on the setup efficiency and the averaged emission rate of the NV centre. During the PLE measurement, the detected countrate depends on the dead-time during re-pump, time spent in the "dark" $\text{NV}^0$ [146, 147] and in the non-cyclic transitions (compare Section 2.2.4) [38]. All of these effects are incorporated into $A$.

Fig. 7.18 (e) shows a plot of the measured linewidth as a function of excitation power. By fitting the data according to Eq. 7.4 using $\gamma = \frac{1}{\tau_0} = 2\pi \times 12.6\,\text{MHz}$ revealed an inhomogeneous broadened linewidth $\Gamma_{\text{in}} = 67 \pm 3\,\text{MHz}$ and an effective coupling strength $c = (1.2 \pm 0.4) \cdot 10^5\,\frac{\text{MHz}^2}{\mu\text{W}}$. In Fig. 7.18 (f), the averaged PLE signal is plotted as a function of both excitation power and laser detuning, where power broadening is clearly observed for large powers. Fitting the full dataset according to Eq. 7.3 yields an inhomogeneous broadened linewidth $\Gamma_{\text{in}} = 48 \pm 2\,\text{MHz}$ and $c = (3.6 \pm 0.2) \cdot 10^5\,\frac{\text{MHz}^2}{\mu\text{W}}$. While Eq. 7.4 only considers the measured linewidth, the global fit (Eq. 7.3) takes spectral detuning into account and thus producing a more reliable measurement of $\Gamma_{\text{in}}$.

The above analysis assumed spectral diffusion to follow a Lorentzian lineshape. If, however, the slow spectral wandering follows a Gaussian profile, $G(f^* - f_0, \Gamma_{\text{in}})$ [130], the measured lineshape will be given by the convolution of $\rho_{22}$ with $G(f^* - f_0, \Gamma_{in})$, i.e. a Voigt profile [473]. Fig. 7.19 (a) shows a comparison between a Voigt, Gaussian and a Lorentzian fit to the same PLE measurement. Here, the signal was averaged over 550 scans (approximately three hours of acquisition time), with a scan speed of $550\,\frac{\text{MHz}}{\text{s}}$ and powers $P_{\text{offres}} = 500\,\mu\text{W}$, $P_{\text{res}} = 372\,\text{nW}$. By visual inspection, the Voigt profile reproduces the data best. In Fig. 7.19 (b), the contributions from the Gaussian and Lorentzian widths are extracted from the Voigt profile and plotted against the pump power. The Lorentzian linewidth decreases with power, approaching the natural linewidth limit of 12.6 MHz; a clear demonstration of power broadening. Note that for $P_{\text{res}} \lesssim 10\,\text{nW}$, the signal-to-noise ratio was too low to reliably distinguish the Gaussian

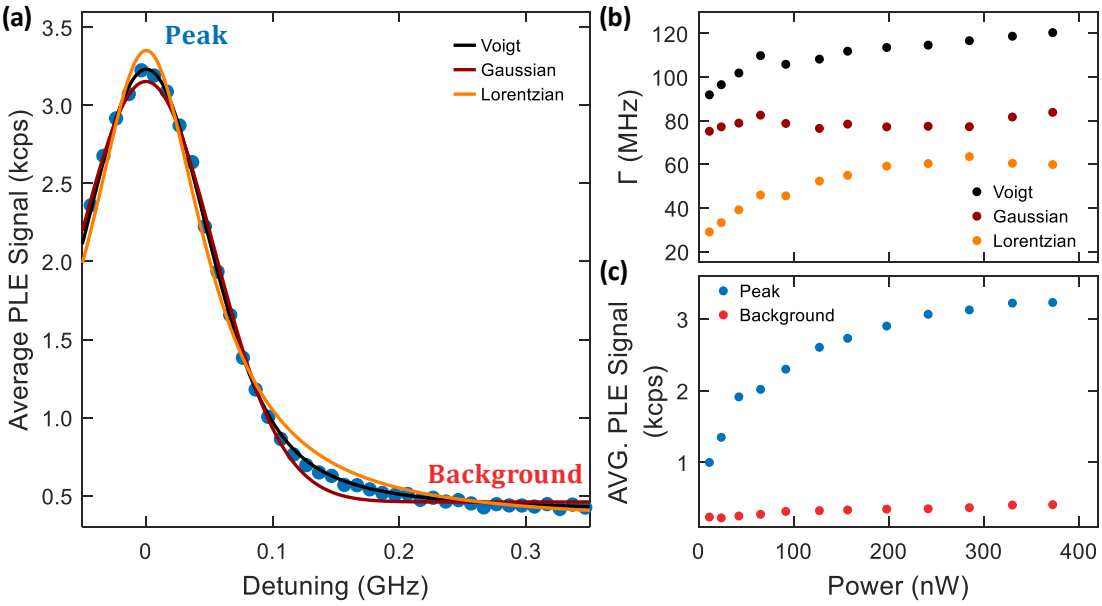


Fig. 7.19. **(a)** The blue points show a PLE measurement ($P_{\text{offres}} = 500\,\mu\text{W}$, $P_{\text{res}} = 372\,\text{nW}$) averaged over 550 scans ($\sim 3$ hours, scanning speed $550\,\frac{\text{MHz}}{\text{s}}$). The black, burgundy and orange lines show a fit to the data using a Voigt, Gaussian and Lorentzian profile, respectively. **(b)** The Voigt linewidth as a function of pump power. The burgundy and orange points represent the linewidth of the Gaussian and Lorentzian components of the Voigt profile, respectively. The Lorentzian component approaches the natural linewidth for low power. Power broadening is clearly visible for higher powers. The constant value of the Gaussian component suggests that spectral wandering is at most weakly affected by increasing pump powers for the powers accessible here. **(c)** Averaged peak (blue) and background (red) countrate extracted from the Voigt fit. The peak countrate saturates for high power, while the background increases linearly.

from the Lorentzian contribution. Measurements acquired for lower pump powers are therefore excluded from Fig. 7.19. The Gaussian linewidth, on the other hand, remains more-or-less constant with power, indicating that spectral wandering is at most weakly dependent on the resonant pump power for powers $< 0.4\,\mu\text{W}$. The dominant source of spectral wandering is therefore attributed to photoionisation processes caused by the re-pump laser [226].

### 7.4.5 Statistical Modelling of the Optical Linewidths

In this work, a total number of 101 NV centres were characterised, sampled from all different regions of the postimplanted sample (Fig. 7.13 (a)). All but 13 NV centres showed a ZPL in the PLE measurements. The motivation behind this study was to investigate whether postimplantation leads to the formation of optically coherent NV centres and to quantify the distribution of narrow linewidths. Therefore, in cases where two lines were resolved, only the narrowest line was included in the dataset [171]. As a first characterisation, Fig. 7.20 shows a plot of the ZPL transition frequency against the measured linewidth. Here, the data points are colour coded to indicate from which part of the diamond the NV centre was sampled. From Fig. 7.20, three observations can be made. First, as before (Fig. 7.8), there is no obvious connection between the ZPL transition frequency and linewidth. However, the transition frequencies are shifted by approximately 20 GHz compared to the first sample investigated (Fig. 7.8), indicating a different strain environment in the two diamonds. Secondly, the measured linewidths fall within two distinct populations with linewidth above and below 1 GHz, respectively. Thirdly, there is no obvious relationship between linewidth and the location of the NV centre. Contrary to the sample discussed in Section 7.3.6, narrow optical lines were found on all parts of the sample including in the thin membranes.

Following the procedure discussed in Section 7.3.4 and reported by Ref. [171], the distribution of measured linewidths will be investigated in more detail. To start, Fig. 7.21 (a) shows a histogram plot of the measured data, where the linewidths fall within two distinct populations: the narrow ($\Delta\nu < 1\,\text{GHz}$) and broad ($\Delta\nu > 1\,\text{GHz}$) lines, respectively. For completeness, the NV centres where no ZPL were resolved in PLE are included in the grey column. Fitting the histograms with a log-normal distribution yields population median $\mu_\text{N} = 139\,\text{MHz}$ and $\mu_\text{B} = 16045\,\text{MHz}$, where the subscript indicates the distribution of the narrow and broad lines, respectively. For completeness, the black dashed line is a log-normal fit to all the measured linewidths, excluding the NV centres where no ZPL could be resolved. Note that if the initial, high-power PLE sweep revealed a broad linewidth (several GHz), the NV centre was labelled "broad" with-

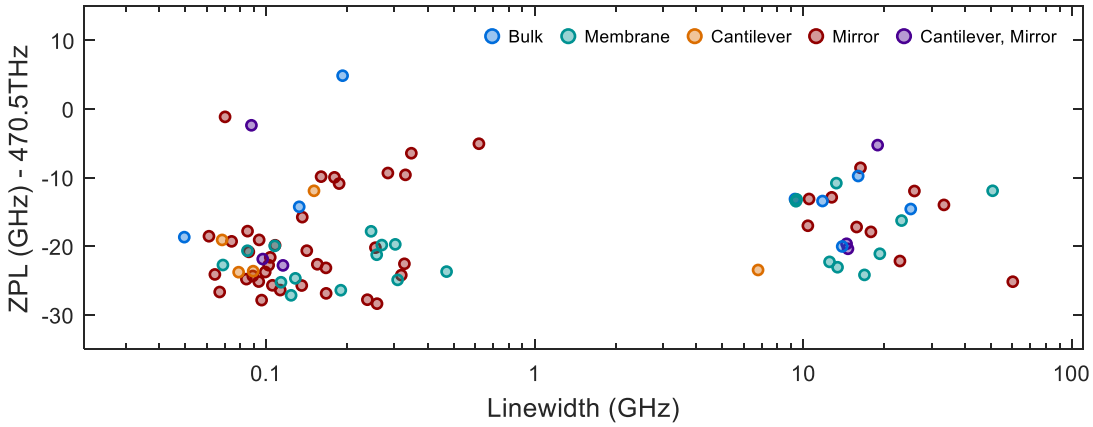


Fig. 7.20. Scatter plot of the ZPL transition frequency against linewidth. The data is colour coded to indicate from which part of the diamond the NV centres were sampled. The measured linewidths fall within two distinct populations with narrow ($< 1\,\mathrm{GHz}$) and broad ($> 1\,\mathrm{GHz}$) linewidths. There is no obvious relationship between location and linewidth; narrow lines were found in all parts of the sample.

out performing additional measurements for lower powers. Therefore, the broad lines may suffer from power broadening, thus biasing the statistics towards a broader median value. However, from the experiment reducing the power will not make a $> 10\,\mathrm{GHz}$ line narrower than 1 GHz. This is justified as the motivation of the work was to investigate the distribution of narrow lines. From the ECDFs plotted in Fig. 7.21 (b), one extracts a probability of 24 % to measure $\Delta\nu < 100\,\mathrm{MHz}$ and a 50 % to measure a linewidth narrower than 200 MHz. The dashed lines correspond to the CDFs from the log-normal fits in (a).

Following Section 7.3.4, a Bayesian approach was used to model the likelihood of measuring a particular linewidth $x_i$ based on a log-normal distribution (Eq. 7.1) [171]. Furthermore, the posterior predictive distribution $P(\tilde{x}|\{x_i\})$ was derived, allowing the distribution of future linewidths $\tilde{x}$ to be calculated. The results are shown graphically in Fig. 7.21 (c), where the solid lines are the posterior predictive distributions and the dashed lines are the log-normal fits from Fig. 7.21 (a). As before, there is a close resemblance between the posterior predictive distributions $P(\tilde{x}|\{x_i\})$ and the sampling distributions $P(\{x_i\}|\mu,\sigma)$. Computing the posterior predictive distribution for the total data set, $P(\tilde{x}|\{x_{\mathrm{all}}\})$, (not shown) yields a maximum likelihood estimation of the next linewidth $\Delta\nu = 664\,\mathrm{MHz}$. By comparison, using the distribution of narrow NV centres yields a maximum likelihood of $\Delta\nu = 139.9\,\mathrm{MHz}$, equal to the median of the sampling distribution. The narrow posterior distributions $P(\mu|\{x_i\})$ (dotted lines) show that only a small range of values $\nu_{N(B)}$ is consistent with the distribution of narrow

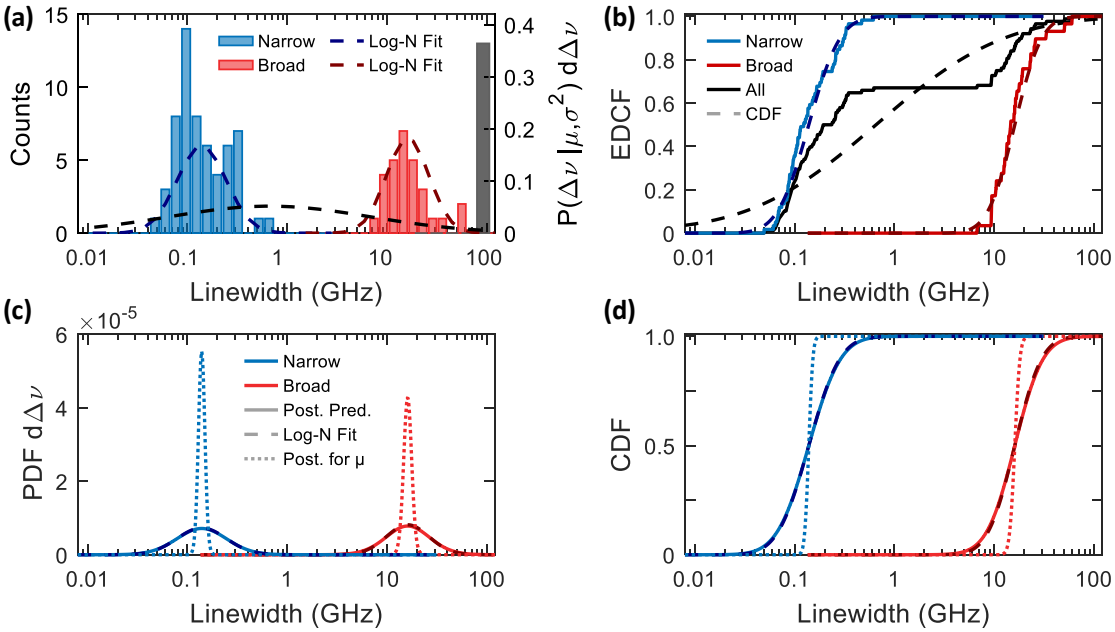


Fig. 7.21. Statistically modelling of the narrowest measurable linewidth for all the NV centres characterised. **(a)** Histogram of linewidths fitted with a log-normal distribution. The linewidths fall into two distributions, the narrow and broad lines with median $\mu_N = 139\,\text{MHz}$ and $\mu_B = 16045\,\text{MHz}$ respectively. The black dashed line is a log-normal fit to all NV centres where a ZPL could be resolved in the PLE measurements. The grey column includes the NV centres for which no ZPL were resolved. **(b)** The solid lines are the ECDF of the data in (a). The dashed lines correspond to the CDF of the log-normal fits. **(c)** Dashed lines are the log-normal fits from (a). Solid lines show the posterior predictive $P(\tilde{x}|\{x_i\})$. Dotted lines show the posterior distributions for the median $P(\mu|\{x_i\})$. The two medians are well separated, indicating sampling from two separate underlying probability distributions. **(d)** CDFs of the data in (c).

(broad) linewidths, further emphasising that the narrow and broad lines are drawn from different underlying probability distributions [171].

From the posterior predictive distributions, it is possible to calculate the probability of the next measured linewidth being narrow, i.e $P(\tilde{x} < 100\,\text{MHz}|\{x_{\text{all}}\})$ [171]. To this end, performing $10^8$ simulated draws from the posterior predictive distribution yields $P(\tilde{x} < 100\,\text{MHz}|\{x_{\text{all}}\}) \approx 0.207$. For comparison, $P(\tilde{x} < 100\,\text{MHz}|\{x_N\}) \approx 0.285$.

Next, the possible origin of the two distributions will be discussed. In Ref. [168, 171], the optical coherence of NV centres was correlated with the nitrogen isotope. In these studies, the samples were implanted with $^{15}$N (natural abundance of 0.37 % [170]). Here the implanted ions act as a mean to create vacancies and as a source of nitrogen ions (compare Section 2.2.1). During the annealing process, the vacancies diffuse and can combine and form NV centres with either the native $^{14}$N ions or the implanted $^{15}$N

ions. NV centres created from $^{14}$N ($I = 1$) and $^{15}$N ($I = \frac{1}{2}$) experience a different hyperfine interaction, and can therefore be distinguished in an ODMR measurement ($^{14}$NV show three peaks while $^{15}$NV show two peaks) [170]. In the aforementioned studies, the measured linewidth formed two distributions. Correlating the linewidth with the isotope revealed that the narrow NV centres were almost exclusively $^{14}$NV centres [168]. NV centres formed from the implanted $^{15}$N predominantly showed broad lines, with distribution median $> 1$ GHz. However, narrow $^{15}$NV centres were found in both studies, thus ruling out intrinsic effects related to the isotope. It was therefore concluded that the difference in the distributions of linewidths was a result of differences in the local environment as a consequence of the implantation process [168]. The implantation ions leave a trail of damage in the diamond, where the harm to the lattice is greatest around the stopping point of the implanted ion [169], i.e. where the $^{15}$NV centres were formed. Unfortunately, for the work presented in this section, the diamond was implanted with $^{14}$N, and hence NV centres formed from implanted nitrogen ions could not be differentiated from those formed from native nitrogen. Nevertheless, by comparing the distributions in Fig. 7.21 to the results from Ref. [168, 171], it is safe to assume that the distribution of narrow linewidth is composed of NV centres formed from native nitrogen, while the broad linewidths are formed from implanted nitrogen.

## 7.5 Overgrown NV Centres in a ⟨111⟩-oriented Diamond

The final sample investigated in this thesis was fabricated in an altogether different manner, where the NV centres were introduced during the growth of a ⟨111⟩-oriented diamond film. The structure of the sample is shown schematically in Fig. 7.22 (a). The sample consists of a $\sim 380$ µm thick ⟨111⟩-oriented high-pressure high-temperature (HPHT) diamond substrate from Element Six, to which a $\sim 35$ µm thick buffer diamond film was grown using CVD. NV centres were created by introducing $N_2$ gas during this growth step. The NV centres were subsequently overgrown with an isotopically purified $^{12}$C diamond film of thickness $\sim 15$ µm.

The ⟨111⟩-oriented diamond offers advantages over the more conventional ⟨100⟩- orientation. In the diamond, the NV centre lies along one of the four equivalent ⟨111⟩-crystal directions (Fig. 2.6 (a)), consequently at an angle of 54.7° relative to the ⟨001⟩ diamond surface [474]. As a consequence, the overlap between the NV centre optical dipole moment and an external cavity mode is compromised, thus limiting the achievable Purcell factor [475]. On the contrary, for a ⟨111⟩-oriented diamond, the dipole moment of the

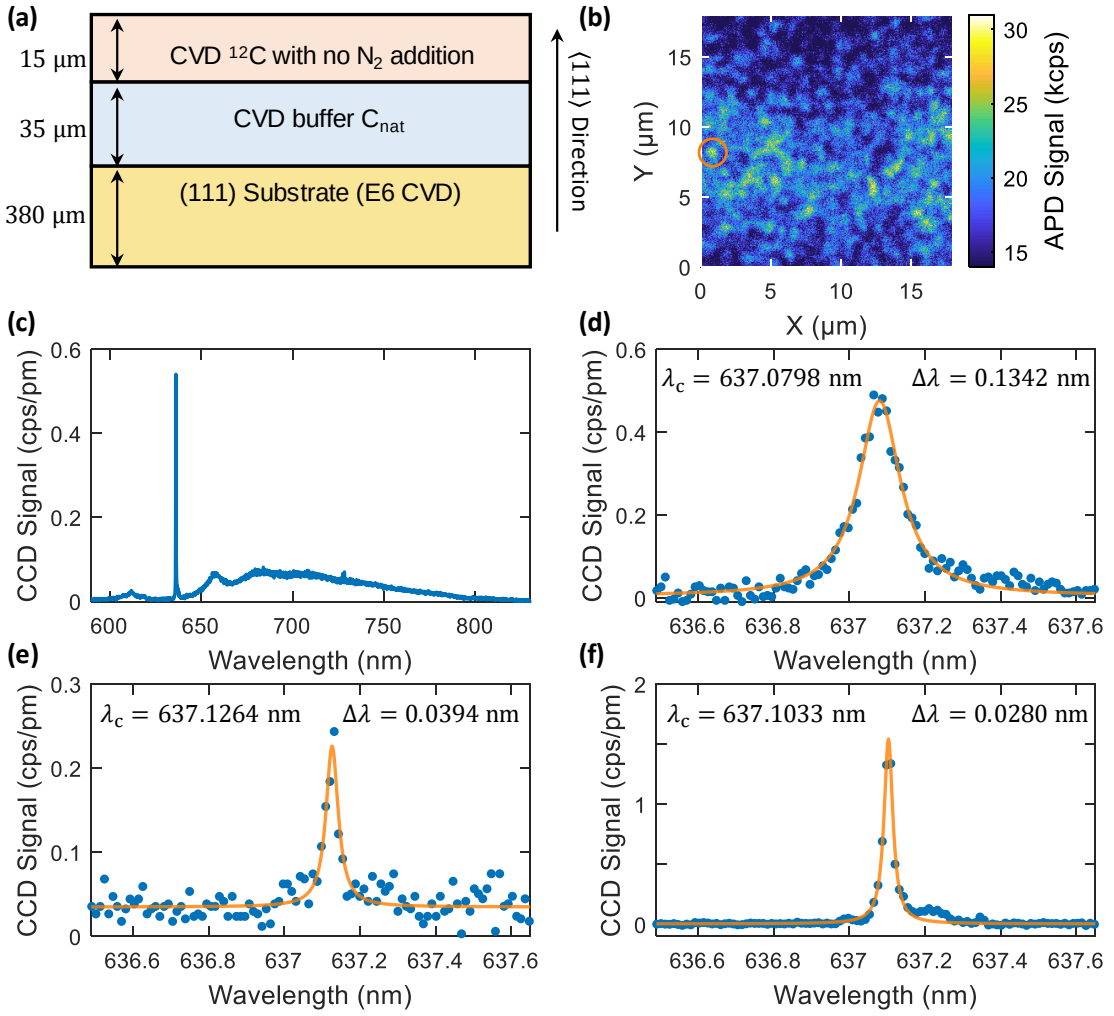


Fig. 7.22. Characterisation of the optical linewidths of overgrown NV centres in a ⟨111⟩-oriented diamond. **(a)** Sample structure. A diamond film with a thickness of $\sim$ 35 µm was grown on a ⟨111⟩-oriented diamond substrate. NV centres were introduced via $N_2$ gas during this growth step. Finally, the NV centres were overgrown with a $\sim$ 15 µm diamond film. **(b)** A typical confocal scan reveals single NV centres. **(c)** PL spectrum showing the ZPL and the PSB. **(d)** A high-resolution PL spectrum reveals a broad ZPL, with a linewidth $\Delta\lambda = 134$ pm (99 GHz). **(e)** - **(f)** For comparison, fitting a Lorentzian to the PL spectra from the postimplanted sample (Section 7.4) yields $\Delta\lambda = 39$ pm (29 GHz) and $\Delta\lambda = 28$ pm (21 GHz), respectively. Only the NV in (f) displayed a ZPL in the PLE measurement.

NV centre lies orthogonal to the diamond surface, thus maximising coupling to external cavity modes [474–476]. The orientation of the NV dipole combined with the $^{12}$C enriched surroundings constitute a promising platform for combining a large Purcell effect with long spin coherence times.

The confocal PL scan shown in Fig. 7.22 (b) demonstrates the possibility of spatially resolving single NV centres, where the PL spectrum (Fig. 7.22 (c)) show the characteristic ZPL accompanied by the broad PSB. However, the high-resolution PL spectrum in Fig. 7.22 (d) revealed a nasty surprise: the width of the ZPL is extremely broad, with a linewidth of $\Delta\lambda = 134.2\,\text{pm}$ (99 GHz) extracted from a Lorentzian fit. For comparison, Fig. 7.22 (e) and (f) show high-resolution PL spectra obtained from the postimplanted sample (Section 7.4), where a Lorentzian fit reveals a linewidth of $\Delta\lambda = 39.4\,\text{pm}$ (29 GHz) and $\Delta\lambda = 28.0\,\text{pm}$ (21 GHz), respectively. Of these two spectra, only the NV centre in Fig. 7.22 (f) revealed a line in the PLE measurement with a linewidth $\Delta\nu = 56\,\text{MHz}$ *. All the NV centres investigated on this sample showed comparably broad linewidths on the spectrometer. Naturally, no signal was observed in PLE.

The origin of the broad lines remains unclear, and little experimental effort was made towards addressing the origin of the large spectral wandering. Possible explanations include a large density of crystal defects as a result of the growth process. A candidate for such defects are impurity nitrogen ions, which can be photoionised by the green laser, causing a fluctuating charge environment (Compare Section. 2.2.4). Although the surface is far away, surface-related defects could be another potential source of noise. Performing an $O_2$ etch or another tri-acid boil would, at least in principle, oxygen terminate the surface thus quenching the surface noise.

## 7.6 Conclusion and Further Improvements

The overarching goal of this work was to achieve spectrally stable, optically coherent NV centres embedded in micro-membranes for the implementation in an open Fabry-Perot microcavity [77, 255]. In this chapter, the optical coherence of NV centres was investigated on three different samples. For the first two samples, the NV centres were formed by ion implantation and subsequent annealing. For the final sample, NV centres were introduced during the growth, and subsequently overgrown with an isotropically purified diamond film. However, as the final sample did not show any narrow lines, the sample will be omitted in the following discussion.

For the first sample, NV centres were created prior to microfabrication. In his sample the optical coherence was characterised in bulk, after microstructuring and after deep etching. Comparing the optical coherence before and after etching demonstrated that even exposing the diamond to a short etching step affects the optical coherence of the NV centres. E-beam lithography followed by etching of $1 - 2\,\mu\text{m}$ shifted the median of

*In fact, this NV centre is the same NV centre as in Fig. 7.14 (g) -(i).

the distribution of measured linewidths from $\mu_{\mathrm{b}} = 90.5\,\mathrm{MHz}$ to $\mu_{\mathrm{ms}} = 178.9\,\mathrm{MHz}$. From the posterior distributions $P(\mu|\{x_i\})$, one finds $P(\mu_{\mathrm{ms}} < \mu_{\mathrm{b}}|x_{\mathrm{all}}) = 0.00797$ indicating that the two populations are sampled from different underlying distributions. Next, a long etching step was performed from the backside of the diamond to thin the sample down to a thickness of $1 - 2\,\mu\mathrm{m}$. Characterising the same NV centre before and after this etching step revealed a 15-fold increase in the optical linewidth. These findings strongly motivated the search for a less invasive method of creating NV centres in thin microstructures.

For the second sample investigated, fabrication was performed prior to ion implantation. In this sample, NV centres with linewidths $< 100\,\mathrm{MHz}$ were routinely measured, even in $\sim 3\,\mu\mathrm{m}$ thin diamond, with the lowest measured linewidth being as low as 57 MHz. The measured linewidths fell into two separated distributions with median $\mu_{\mathrm{N}} = 139\,\mathrm{MHz}$ and $\mu_{\mathrm{B}} = 16045\,\mathrm{MHz}$ The two distributions were attributed to NV centres formed from native and implanted nitrogen, respectively, in analogy to the results from Ref. [168, 171].

By directly comparing the distribution of measured linewidths from the two samples, it is apparent that postimplantation yields NV centres with better optical coherence compared to preimplantation. Note that the two samples were implanted at different energies: 55 keV and 12 keV for the pre- and postimplantation, respectively. The larger implantation energy used for the first sample may result in more, hard to anneal lattice damage which can be further exacerbated by the etching. For a fair, direct comparison, the two samples would have to be prepared in the same manner.

It is now time to discuss possible improvements for future experiments. During resonant excitation of $\mathrm{NV}^-$, there is a probability of ionising to $\mathrm{NV}^0$ via a two-photon absorption process (compare Section 2.2.4) [223]. Restoring the charge state requires optical re-pumping. In this work, re-pump was performed using an off-resonant green laser ($\lambda = 532\,\mathrm{nm}$). However, the green re-pump pulse causes spectral wandering via the photoionisation of nearby charge traps [224–226], thus compromising the long term optical stability of the NV centres. Therefore, future efforts should be made towards reducing spectral wandering caused by re-pumping. As discussed in Section 7.4.3, slow spectral drifts and small spectral jumps can be compensated for by monitoring the ZPL transition frequency and applying a feedback mechanism utilising the Stark effect [161, 217, 227, 231].

Spectral diffusion may be suppressed by resonant ionisation of $\mathrm{NV}^0$ [220, 222], on the grounds that resonant excitation requires low laser power, and thus does not excite

nearby charge traps. Although, resonant re-pump may not help for broad lines, say $\Delta\nu >$ 500 MHz, Ref. [220] demonstrated that changing from re-pump using green ($\lambda = 532$ nm) to resonant re-pump ($\lambda = 575$ nm) reduced the averaged linewidth from 161 MHz to only 27 MHz. For comparison, the lifetime limited linewidth is 13 MHz. Resonant re-pump is compatible with the implementation in a Fabry-Perot cavity. The $NV^0$ ZPL is located at $\lambda = 575$ nm, well within the reflective stopband of the current cavity design [255]. By careful choice of cavity geometry and diamond thickness, a double resonant condition can be established [381], keeping the cavity on resonance with the ZPL of both $NV^0$ and $NV^-$ at the same cavity length, as discussed in Chapter 6.

In the absence of the green re-pump laser, weak spin non-conserving optical transitions polarise the NV centre away from the resonant cycling transitions [227, 243], and no PLE signal will be observed (compare Section 2.2.2 and Fig. 2.7 (a)). However, optical pumping into a dark state can be avoided by applying microwaves to mix continuously the spin ground-states [158]. Consequently, the implementation of microwaves will allow for a refined PLE pulsing sequence where several resonant scans can be performed before ionisation occurs, while still maintaining the cyclic resonant transitions. Furthermore, the integration of microwaves allows for individual driving of the $E_{1,2}$ and $A_{1,2}$ transitions; a key requirement for the creation of spin-photon entanglement [41–43]. Alternatively, using an EOM to create laser sidebands at a frequency equal to the zero-field splitting, i.e. $\nu_{\text{laser}} \pm 2.87$ GHz, allows for simultaneous excitation of all the ground states, thus avoiding optical pumping [461, 477].

Finally, as discussed above, postimplantation constitutes a promising method to create NV centres in thin microstructures. However, the distribution of the optical linewidths of the NV centres created by postimplantation fall within two distinct populations, with narrow ($< 1$ GHz) and broad lines ($\gtrsim 10$ GHz). Here the broad lines are associated with NV centres formed from the implanted nitrogen ions. Therefore, implanting carbon ions rather than nitrogen ions may reduce the population of broad lines, on the grounds that only the narrow distribution will fluoresce. As for nitrogen implantation, careful selection of the implantation energy may provide control of the depths of the NV centre formation. Carbon atoms may potentially reduce the number of $> 10$ GHz lines. However, it is an open question whether carbon implantation will create NV centres with narrower optical linewidths, compared to NV centres created by nitrogen implantation. Nevertheless, by reducing the population of broad lines, the probability of finding an NV centre with $\Delta\nu < 100$ MHz will increase. NV centres can also be created after fabrication via electron irradiation [158]. However, the electrons will create vacancies throughout the diamond offering little-to-no control of the formation depth.

CHAPTER 8

# Summary and Future Directions

The scalability of quantum networks using NV centres is limited by the modest entanglement rate, in turn, limited by the detection rate of coherent photons. For NV centres, the generation rate of single photons is impaired by the long radiative lifetime ($\tau_0 \simeq 12\,\mathrm{ns}$) combined with a small branching ratio of $\sim 3\,\%$ into the zero-phonon line (ZPL). Furthermore, the high refraction index of diamond, $n_\mathrm{d} = 2.41$, results in a poor photon extraction efficiency out of the host crystal, due to total internal reflection at the diamond-air interface. Finally, the permanent electric dipole moment renders the NV centre sensitive to charge fluctuations in the local environment, leading to inhomogeneous linewidth broadening and random spectral jumps [229]. When observed over time, this spectral instability renders the emitted photons distinguishable, and thus compromising the achievable two-photon quantum interference [79, 80]. Spectrally stable emitters are of paramount importance for entanglement protocols relying on quantum interference of indistinguishable photons from remote emitters.

In principle, utilising the Purcell effect [86], the first three limitations can be addressed by resonant coupling between the NV ZPL and a single-mode of a cavity [77, 81]. Resonant enhancement of the ZPL emission has been demonstrated on various nano- and microphotonic platforms [81–83, 165, 398, 421, 459, 460]. However, while these approaches offer a large Purcell factor on the ground of a minimal mode volume, the aggressive fabrication leads to the deterioration of the optical coherence, presumably due to fabrication induced surface damage.

The work done in this thesis builds on the work from Ref. [77, 85], where it was shown that a miniaturised Fabry-Perot microvcavity containing a thin ($\lesssim 1\,\mu\mathrm{m}$) diamond membrane constitutes a promising platform to combat the first three shortcomings listed above. However, in this work, the cavity coupling was limited by a modest $\mathcal{Q}$-factor of $\sim 60\,000$ in combination with a low outcoupling efficiency. Furthermore, the fabrication of the diamond micro-membranes deteriorated the optical coherence. The starting material

exhibits NV centres with long-term averaged optical linewidths $\Delta\nu \lesssim 100\,\mathrm{MHz}$, while in the finished membrane the averaged linewidths increased to $\Delta\nu \sim 1\,\mathrm{GHz}$. However, these linewidths still offer a significant improvement compared to the aforementioned work using nanophotonic platforms. Nevertheless, while a linewidth of $\sim 1\,\mathrm{GHz}$ is smaller than the ground state spin splitting of 2.7 GHz, and thus may be sufficient for applications in quantum sensing [478], it is still two orders of magnitude larger than the natural linewidth of 13 MHz.

The motivation behind the work presented in this thesis was to address and improve the shortcomings listed above. Broadly speaking, the experiments performed as part of this thesis can be divided into two groups. The first three experiments aimed at addressing the issues with the cavity, namely the modest $\mathcal{Q}$-factor and the poor photon extraction efficiency. The final chapter aimed at addressing the large inhomogeneous broadening of the NV centre's optical linewidth observed after fabrication. The following few paragraphs provide a short summary of each of the four experimental chapters.

To start, in Chapter 4, the experimental realisation of $\mathcal{Q}$-factors exceeding $10^5$ was demonstrated despite operating in a diamond-confined regime. In this regime, the vacuum electric field possesses a field anti-node at the diamond-air interface, thus maximising losses associated with the diamond surface. However, operation in a diamond-confined regime has the benefit that the electric field is strongly confined to the diamond layer, thus providing stronger coupling between the cavity mode and the NV centres [87]. In the experiment, a diamond with thickness $t_\mathrm{d} = 733\,\mathrm{nm}$ was used, resulting in a minimised mode volume. With the current design, a Purcell factor $F_\mathrm{P} \simeq 180$ can be readily achieved. A Purcell factor on this order will boost the fraction of photons emitted into the ZPL from $\sim 3\,\%$ to $\sim 80\,\%$.

The generic design of the Fabry-Perot microcavity allows for coupling to, and enhancement of various weak radiative transitions. In Chapter 5, the versatility of the cavity platform was demonstrated by enhancing the Raman transition from the crystalline diamond lattice. By comparing the signal strength inside the cavity to that of free-space under identical experimental conditions, a $\sim$ 60-fold intensity enhancement was observed. To explain this enhancement factor quantitatively, a model disentangling the contribution from the Purcell effect to that of enhanced collection efficiency was derived. The model predicts a Purcell factor $\sim$ 5 and a $\sim$ 23-fold enhancement of the detection efficiency. Furthermore, the model provides an insight into the nature of the cavity-enhanced Raman process: the cavity-enhanced Raman process consists of

an independent array of emitters $\mathcal{L}_S$ coupled to a single cavity mode $\mathcal{L}_c$, rather than a collective vibration across the waist of the cavity mode.

Next, Chapter 6 took a sharp right-hand turn onto the avenue of curiosity-driven research. Here, the possibility of establishing a double resonant Raman condition was explored, with both the pump laser and the Raman transition resonant for the same cavity length. The double-resonance condition enhances the Raman scattering process on two grounds. First, as described in Chapter 5, the Raman process experiences Purcell enhancement. Second, the resonant recirculation of the pump laser increases the power density inside the cavity. The motivation behind this work was to demonstrate a low-threshold Raman laser. For the current design, the theoretical threshold was estimated to be 187.5 mW [381], limited by the large air-gap necessary to establish the double-resonance condition for the accessible pump frequency. However, with realistic changes in the diamond, sub mW threshold pump power can be achieved. On a final note, due to a slight thickness gradient of the diamond, the double resonance condition could be continuously tuned across a $\sim 1$ THz spectral window, thereby demonstrating that the membrane-in-a-cavity constitutes a promising platform for tunable non-linear optics.

Finally, in Chapter 7, experimental effort was guided towards addressing the final issue of the large spectral wandering. The optical coherence of NV centres created by nitrogen ion implantation was investigated on two different samples*. For the first sample, the NV centres were created prior to fabrication. In the unprocessed bulk diamond, NV centres with optical linewidths as low as $\Delta\nu = 34$ MHz were found. Modelling the distribution of measured linewidths using a log-normal distribution revealed a population median $\nu_b = 90.5$ MHz for these bulk NV centres. However, after microstructuring the diamond using electron-beam lithography followed by a short etching step ($1-2$ μm), the median of the measured linewidths increased to $\nu_{ms} = 178.9$ MHz. In the final fabrication step, the diamond was etched down to a thickness of $\sim 1.5$ μm. Measuring the same NV centre before and after this etching step revealed a 15-fold increase in the optical linewidth ($\Delta\nu = 2\,800$ MHz).

The experimental result obtained from the first sample indicated that exposing the NV centres to minimal microfabrication has a devastating effect on the optical coherence. The second part of Chapter 7 explored a new technique of creating NV centres in micron thick diamond membranes. Here, all the fabrication procedures were performed prior to the ion implantation. This postimplantation technique routinely resulted in linewidths $\lesssim 100$ MHz in membranes with thickness $t_d \sim 3$ μm. As before,

*A third sample, where NV centres were introduced during the diamond growth was also investigated. However, as no narrow lines were observed, this sample will be omitted from this discussion.

the measured linewidths were modelled using a log-normal distribution. Here, the measured linewidths fell within two distinct populations, with medians $\mu_{\mathrm{N}} = 139\,\mathrm{MHz}$ and $\mu_{\mathrm{B}} = 16045\,\mathrm{MHz}$. The two distributions were attributed to NV centres created from native and implanted nitrogen ions, respectively [168, 171].

## 8.1 Towards an Efficient Spin-Photon Interface

It is now time to look towards the future. The overarching goal of this work is to enhance the flux of coherent, indistinguishable photons from NV centres by coupling to a single-mode Fabry-Perot microcavity. Utilising the Purcell effect, resonant coupling between the NV ZPL and the resonant cavity is advantageous on three grounds (Section 4.4.1). First, the Purcell effect accelerates the emission rate by reducing the excited-state lifetime according to

$$\tau_{\mathrm{cav}} = \frac{\tau_0}{1 + \xi_0 \left(F_{\mathrm{P}} - 1\right)}\,, \tag{8.1}$$

where $\xi_0$ is the Debye-Waller factor describing the branching into the ZPL, $\tau_0$ is the unperturbed lifetime and $F_{\mathrm{P}} = 1 + \frac{3}{4\pi^2} \cdot \frac{\mathcal{Q}}{V_{\mathrm{eff}}} \left(\frac{\lambda}{n}\right)^3$ is the Purcell factor*. The reduction of the lifetime broadens the transform limited linewidth to [85, 387]

$$\Delta\nu_{\mathrm{cav}}^{\mathrm{ZPL}} = \frac{1}{2\pi} \cdot \gamma_0 \left(\xi_0 \left(F_{\mathrm{P}} - 1\right) + 1\right)\,, \tag{8.2}$$

where $\gamma_0 = \frac{1}{\tau_0}$. Second, the cavity provides a well-defined output mode facilitating mode matching to external single-mode detection optics [255]. Finally, a large Purcell factor boosts the fraction of photons emitted into the ZPL, $\eta_{\mathrm{ZPL}}$ , according to [214, 387]

$$\eta_{\mathrm{ZPL}} = F_{\mathrm{P}} \cdot \frac{\xi_0 \gamma_0}{\gamma_{\mathrm{cav}}} = \frac{\xi_0 F_{\mathrm{P}}}{\xi_0 \left(F_{\mathrm{P}} - 1\right) + 1}\,. \tag{8.3}$$

A graphical representation of Eq. 8.2 and Eq. 8.3 is shown in Fig. 8.1 (a) and (b), respectively. Here, and for the remaining of this chapter, the Debye-Waller is set to $\xi_0 = 2.55\,\%$ according to Ref. [77, 85, 214]. The blue and black dashed lines in Fig. 8.1 (a) represent the median $\mu_{\mathrm{N}}$ and the narrowest linewidth measured in Chapter 7, respectively. A Purcell factor of $\sim 300$ is required for broadening of the transform-limited linewidth to $\Delta\nu_{\mathrm{cav}}^{\mathrm{ZPL}} = 100\,\mathrm{MHz}$. The remainder of this chapter will discuss potential improvements to

*With this definition, the free-space decay rate $\gamma_{\mathrm{free}} = \xi_0\gamma_0 + (1 - \xi_0)\,\gamma_0$ and the cavity-enhanced decay rate $\gamma_{\mathrm{cav}} = F_{\mathrm{P}}\xi_0\gamma_0 + (1 - \xi_0)\,\gamma_0$, i.e. $\frac{\gamma_{\mathrm{cav}}}{\gamma_{\mathrm{free}}} = 1 + \xi_0\left(F_{\mathrm{P}} - 1\right)$. For more details, see Section 4.4.1.

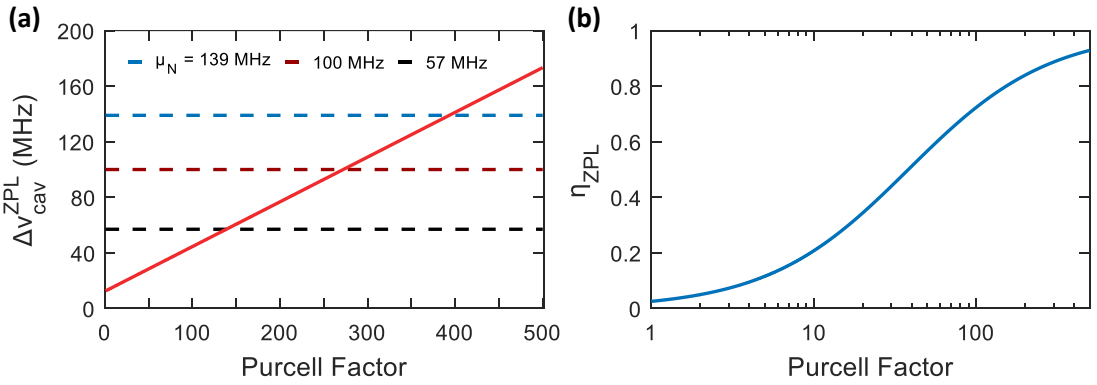


Fig. 8.1. Calculations of the modified emitter dynamics as a function of Purcell factor. **(a)** Broadening of the natural linewidth calculated from Eq. 8.2. The dashed blue line represents the median of the distribution of narrow lines, $\mu_N = 139\,\text{MHz}$ extracted from Section 7.4.5. The burgundy line indicates a linewidth of $\Delta\nu = 100\,\text{MHz}$. The smallest linewidth measured in Section. 7.4, $\Delta\nu = 57\,\text{MHz}$ is represented by the black line. **(b)** The fraction of photons emitted into the ZPL, $\eta_{\text{ZPL}}$

the existing experimental configuration to enhance further the flux of coherent photons.

Chapter 7 demonstrated that increasing the dimensions of the defect-free crystalline environment around the NV centres strongly reduces spectral wandering, and thus providing spectrally stable emitters [158, 171]. However, embedding a thicker diamond membrane into the Fabry-Perot cavity increases the mode volume $V_{\text{eff}}$, consequently reducing the achievable Purcell factor. Therefore, a compromise between spectrally stable emitters and a large Purcell factor has to be made. To this end, Fig. 8.2 shows three-dimensional numerical simulations (COMSOL Multiphysics) of the cavity resonance for increasing diamond thickness $t_{\text{d}}$. In these simulations, the cavity was constructed using a realistic top mirror with $R_{\text{cav}} = 15\,\mu\text{m}$ and depth $d = 0.5\,\mu\text{m}$*. To simplify the problem, and thus reduce the computational time, axial symmetry was assumed. All the simulations were performed for the shortest air-gap possible.

Fig. 8.2 (a) - (c) show heatmaps of the $\mathcal{Q}$-factor, effective mode volume $V_{\text{eff}}$ and Purcell factor $F_{\text{P}}$, respectively. As expected, $V_{\text{eff}}$ is minimised for the smallest $t_{\text{d}}$, thus maximising $F_{\text{P}}$. Fig. 8.2 (d) - (f) show a line-cut of (a) - (c) for $\lambda = 637.2\,\text{nm}$ indicated by the orange line. Here, the blue curve corresponds to a lossless cavity, while the red line corresponds to a scattering layer on the diamond with RMS surface roughness $\sigma_{\text{q}} = 0.3\,\text{nm}$. The value of $\sigma_{\text{q}}$ was motivated by the AFM measurement in Fig. 4.3 (c) and typical roughness measurements reported by Ref. [159, 387]. The observed oscil-

*The profile of the top mirror is described by Eq. 4.1

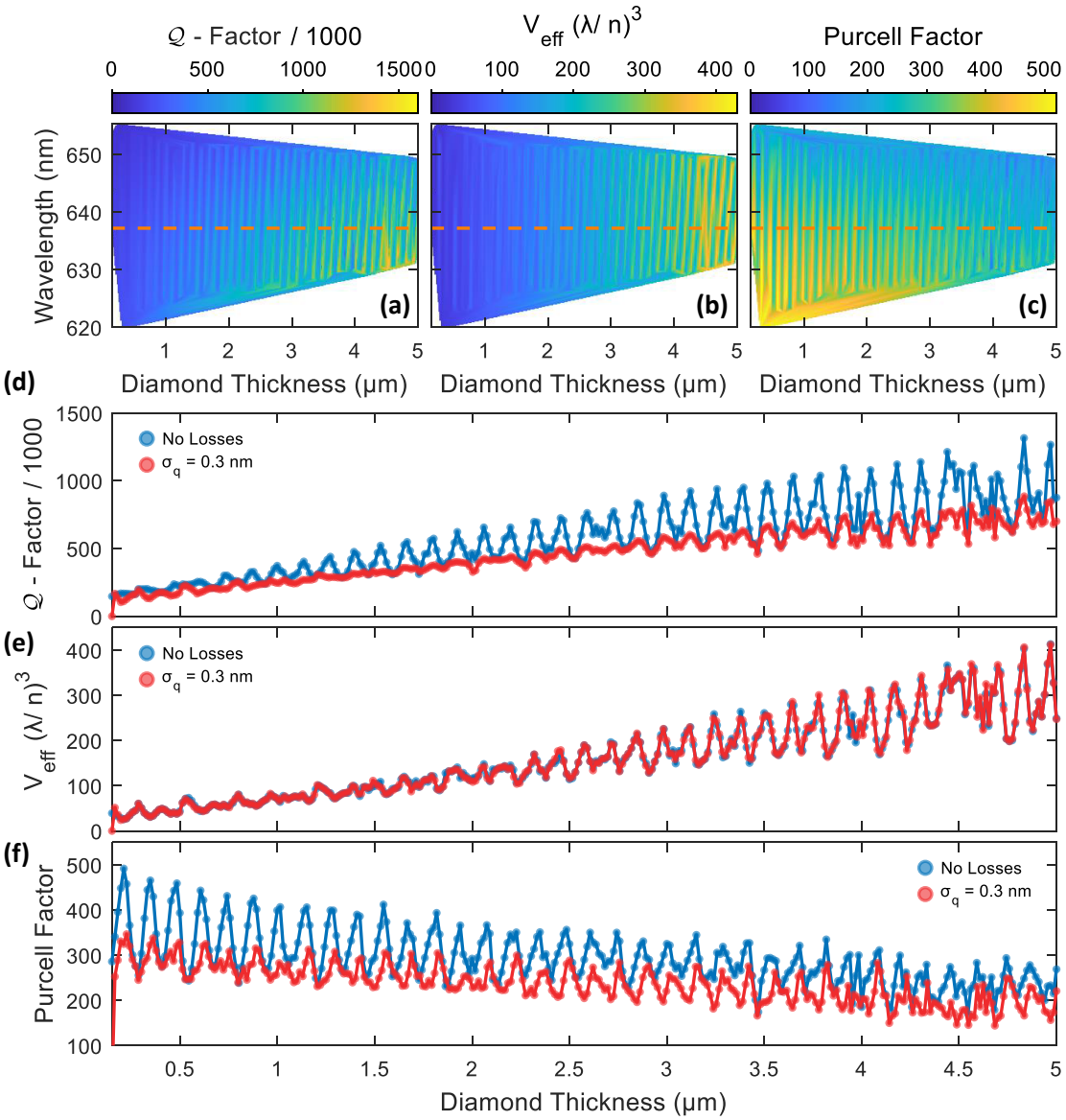


Fig. 8.2. Simulations of **(a)** $\mathcal{Q}$-factor, **(b)** mode volume $V_{\mathrm{eff}}$ and **(c)** Purcell factor, $F_{\mathrm{P}}$ as a function diamond thickness $t_{\mathrm{d}}$ for $R_{\mathrm{cav}} = 15\,\mu\mathrm{m}$. **(d)** - **(f)** Line-cut of $\mathcal{Q}$-factor, $V_{\mathrm{eff}}$ and $F_{\mathrm{P}}$ along $\lambda = 637.2\,\mathrm{nm}$ for a lossless cavity (blue) and in the presence of surface scattering with surface roughness $\sigma_{\mathrm{q}} = 0.3\,\mathrm{nm}$ (red). The oscillations arise due to the transitions between air- and diamond-confined geometries.

lations arise as a consequence of the transitions between air- and diamond-confined cavity geometries (compare Chapter 3). As expected, the envelope of the $\mathcal{Q}$-factor and $V_{\mathrm{eff}}$ exhibit a linear and superlinear increase with $t_{\mathrm{d}}$, respectively. The combination of the two results in a decrease of $F_{\mathrm{P}}$ with $t_{\mathrm{d}}$. However, the behaviour is not as

strong as one might expect: increasing the diamond thickness from $t_\mathrm{d} = 1\,\mu\mathrm{m}$ to $t_\mathrm{d} = 3\,\mu\mathrm{m}$, results in $\sim 20\,\%$ decrease in $F_\mathrm{P}$, a small price to pay for spectrally stable emitters. For comparison, in Chapter 7, the median linewidth in $\sim 3\,\mu\mathrm{m}$ thick diamond, $\mu_\mathrm{N} = 139\,\mathrm{MHz}$, is $40\,\%$ smaller than the narrowest linewidth of 250 MHz in 1.6 µm thick diamond [171].

### 8.1.1 The LaserOptik Mirrors

The following sections will evaluate different mirror designs in terms of the photon extraction efficiency and the potential improvements to quantum network nodes. A total of five different mirror designs will be discussed.

As discussed in Section 7.4, a part of the diamond sample was transferred to a planar DBR mirror prior to linewidth characterisation (Fig. 7.13). The refractive index profile of this mirror is given by $(n_\mathrm{H} \cdot n_\mathrm{L})^{14} \cdot n_\mathrm{H}$ *, with $n_\mathrm{H} = n_{\mathrm{Ta_2O_5}} = 2.120$ and $n_\mathrm{L} = n_{\mathrm{SiO_2}} = 1.481$ †, where the layer count starts at the substrate. From the modulations in the phonon sideband (PSB) caused by thin-film interference, the diamond thickness was estimated to be $t_\mathrm{d} \sim 2820 - 3030\,\mathrm{nm}$ (Fig. 7.14). For the remainder of this chapter, the upper limit ($t_\mathrm{d} = 3030\,\mathrm{nm}$) will be assumed. Fig. 8.3 (a) shows a one-dimensional transfer matrix simulation (Essential Macleod) of the mirror transmission (top) and reflected phase delay (bottom). The minimum in transmission and phase delay for $\lambda = 637.2\,\mathrm{nm}$ (dashed orange line) suggests the formation of an air-confined cavity mode (compare Chapter 3). From Fig. 8.3 (a) one finds $\mathcal{T}_\mathrm{bot}\,(\lambda = 637.2\,\mathrm{nm}) = 59\,\mathrm{ppm}$ for the diamond on the mirror. Fig. 8.3 (b) shows the resulting mode-structure for a cavity completed with a $(n_\mathrm{H} \cdot n_\mathrm{L})^{12} \cdot n_\mathrm{H}$ top mirror. The locations of the anti-crossings in combination with the steep slope ($\frac{\mathrm{d}\lambda}{\mathrm{d}t_\mathrm{a}}$) confirm the formation of an air-confined cavity mode for $\lambda = 637.2\,\mathrm{nm}$ (orange dashed line).

Next, the standing wave inside the cavity is examined. Fig. 8.4 shows a simulation of the vacuum field for a cavity constructed from the aforementioned bottom mirror and a top mirror on the form $(n_\mathrm{H} \cdot n_\mathrm{L})^j \cdot n_\mathrm{H}$, where $j = 12, 13, 14$ for (a), (b) and (c), respectively. The amplitude of the vacuum field is quantised according to Eq. 3.5 [255]. From the simulations, one finds $\mathcal{T}_{12} = 238\,\mathrm{ppm}$, $\mathcal{T}_{13} = 116\,\mathrm{ppm}$ and $\mathcal{T}_{14} = 57\,\mathrm{ppm}$ for the top mirror for $\lambda = 637.2\,\mathrm{nm}$. As expected for an air-confined geometry, all three configurations exhibit field node at the interface. Therefore, for simplicity, surface losses

*Note that this design differs from the experimental design used in Chapter 4, Chapter 5 and Chapter 6. The experimental mirrors will be considered in Section 8.1.4.

†LaserOptik, transmission = 58 ppm, using the refractive indices provided by LaserOptik.

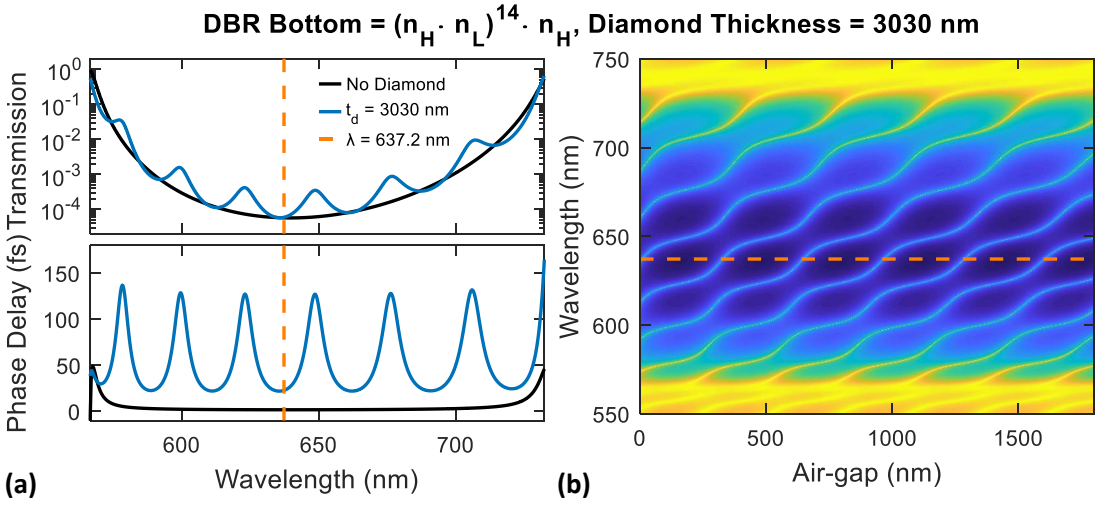


Fig. 8.3. **(a)** Effective mirror transmission (top) and reflected phase delay (bottom) for a diamond with thickness $t_\mathrm{d} = 3030\,\mathrm{nm}$ on a $(n_\mathrm{H} \cdot n_\mathrm{L})^{14} \cdot n_\mathrm{H}$ DBR mirror. The orange line indicates a transmission minimum for $\lambda = 637.2\,\mathrm{nm}$ suggesting the formation of an air-confined cavity geometry. **(b)** Resulting mode structure for the bottom mirror in (a) combined with a $(n_\mathrm{H} \cdot n_\mathrm{L})^{12} \cdot n_\mathrm{H}$ top mirror. The cavity is air-confined for $\lambda = 637.2\,\mathrm{nm}$ (dashed orange line).

will be neglected in this discussion.

Fig. 8.5 (a) simulates the $\mathcal{Q}$-factor as a function of air-gap for the cavities described above. It comes as no surprise that the more reflective top mirror ($(n_\mathrm{H} \cdot n_\mathrm{L})^{14} \cdot n_\mathrm{H}$) offers the largest $\mathcal{Q}$-factor. The thicker diamond leads to an increased effective cavity length and thus a larger beam waist at the top mirror $w_\mathrm{I}$. Therefore, for completeness,

The analysis presented here assumes no scattering or absorption losses: a cavity photon is only lost by transmission through the two mirrors. This assumption is justified on the grounds that the extracted diamond thickness ($t_\mathrm{d} = 3030\,\mathrm{nm}$) forms an air-confined cavity mode for the NV ZPL wavelength. For a diamond-confined geometry, surface losses would have to be considered, as discussed in Section 3.3.5. In the experiment, only photons exiting the top mirror will reach the detectors. For a photon already present in the cavity, the probability of transmission through the top mirror, $\eta_\mathrm{top}$, is determined by the ratio of the loss-rate through the top-mirror $\kappa_\mathrm{top}$ to the total loss-rate $\kappa_\mathrm{tot}$, i.e.

$$\eta_\mathrm{top} = \frac{\kappa_\mathrm{top}}{\kappa_\mathrm{tot}} \tag{8.4}$$

Recall from Section. 3.3.5, that for a loss-less cavity $\kappa_\mathrm{top}$ can be calculated according to

$$\kappa_\mathrm{top} = \frac{\mathcal{T}_\mathrm{top}}{\mathcal{T}_\mathrm{top} + \mathcal{T}_\mathrm{bot}} \cdot \kappa\,, \tag{8.5}$$

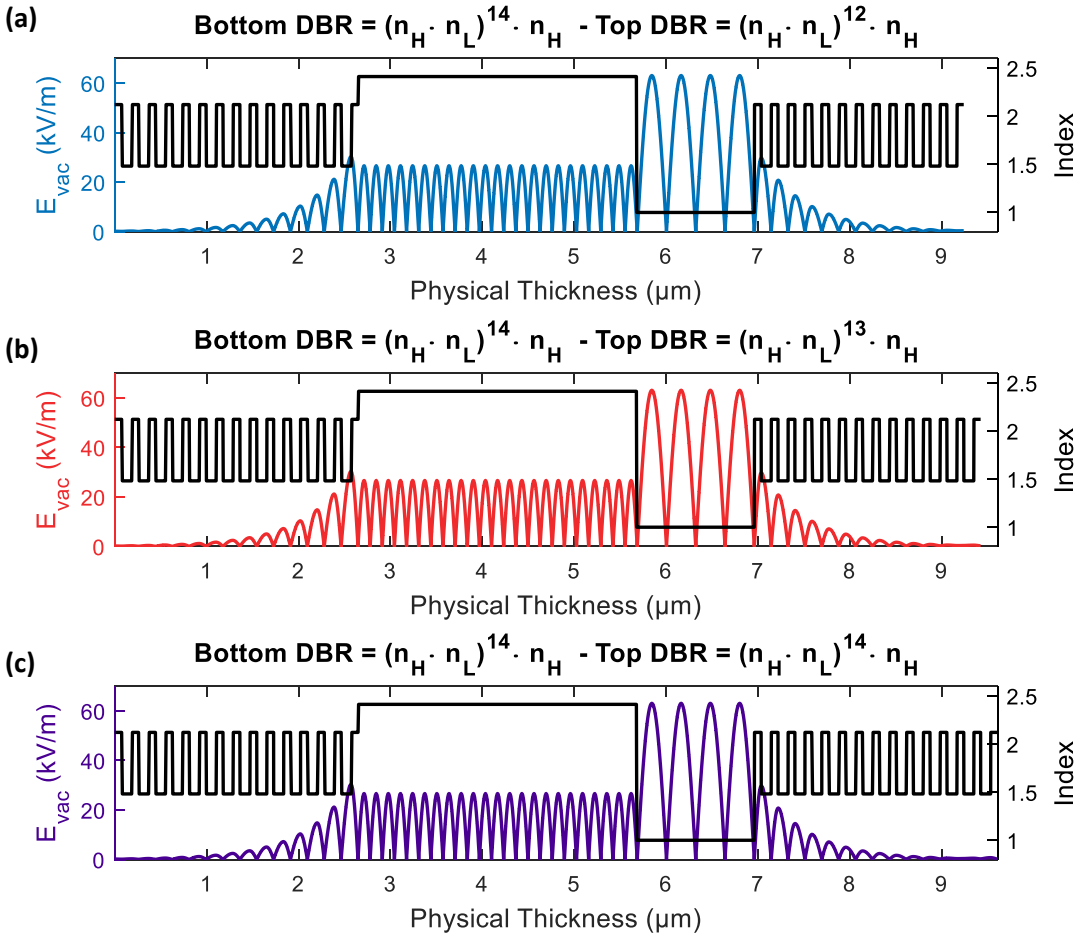


Fig. 8.4. Profile of the vacuum electric field for a cavity with $t_{\mathrm{d}} = 3030\,\mathrm{nm}$ and $t_{\mathrm{a}} = 1283\,\mathrm{nm}$ assembled from a bottom DBR made from $(n_{\mathrm{H}} \cdot n_{\mathrm{L}})^{14} \cdot n_{\mathrm{H}}$ and a top DBR made from **(a)** $(n_{\mathrm{H}} n_{\mathrm{L}})^{12} \cdot n_{\mathrm{H}}$, **(b)** $(n_{\mathrm{H}} \cdot n_{\mathrm{L}})^{13} \cdot n_{\mathrm{H}}$, **(c)** $(n_{\mathrm{H}} \cdot n_{\mathrm{L}})^{14} \cdot n_{\mathrm{H}}$ respectively. All configurations result in an air-confined cavity mode.

where $\mathcal{T}_{\mathrm{top\ (bot)}}$ is the transmission of the top (bottom) mirror and

$$\kappa = \frac{2\pi c}{\lambda \mathcal{Q}}\,. \tag{8.6}$$

Using the extracted value of $\mathcal{T}_{\mathrm{top\ (bot)}}$, Fig. 8.5 (c) evaluates $\eta_{\mathrm{top}}$ as a function of air-gap thickness. The transmission probability decreases with increasing top mirror reflectively. For a highly reflective top mirror, the large $\mathcal{Q}$-factor implies that the photon is stored in the cavity for a longer time. However, as $\mathcal{T}_{\mathrm{top}} \to \mathcal{T}_{\mathrm{bot}}$ the photons are transmitted through the top (bottom) mirror with approximately equal probability, i.e. $\eta_{\mathrm{top}} \to 0.5$.

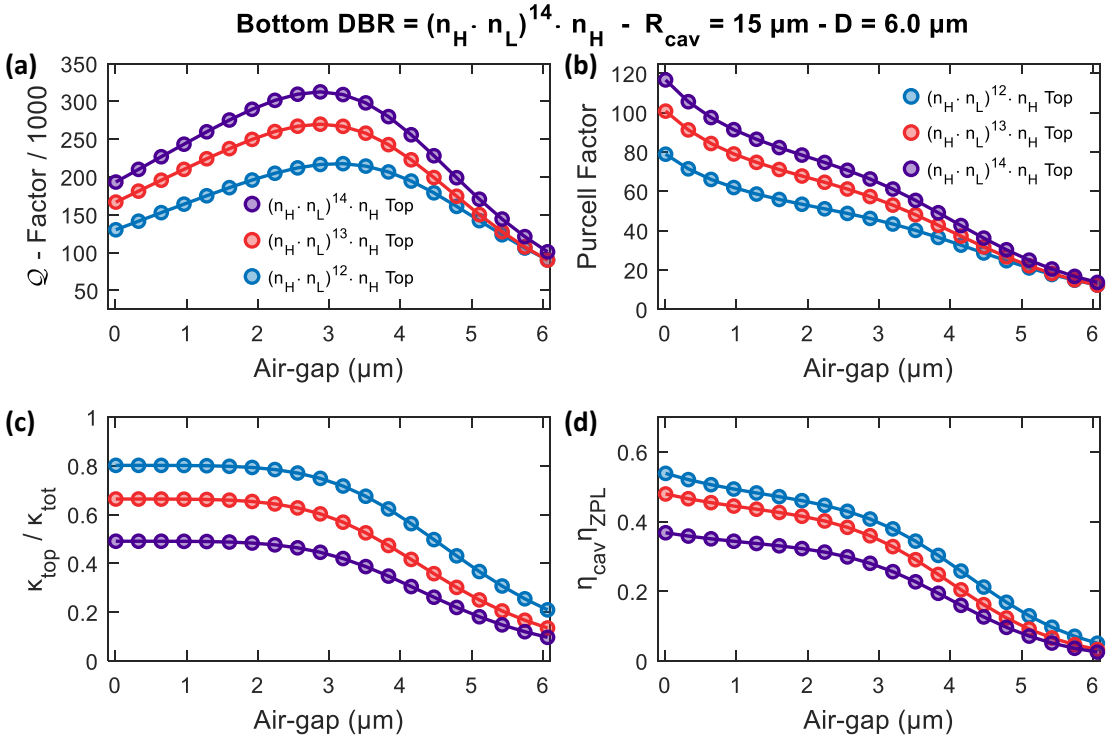


Fig. 8.5. Performance of a cavity constructed from $(n_{\mathrm{H}} \cdot n_{\mathrm{L}})^{14} \cdot n_{\mathrm{H}}$ bottom and $(n_{\mathrm{H}} \cdot n_{\mathrm{L}})^{j} \cdot n_{\mathrm{H}}$, $j = 12, 13, 14$ top mirror, with diamond thickness $t_{\mathrm{d}} = 3030\,\mathrm{nm}$, $R_{\mathrm{cav}} = 15\,\mu\mathrm{m}$ and $D = 6.0\,\mu\mathrm{m}$ as a function of increasing air-gap thickness. For simplicity, losses associated with the diamond surface have been neglected, on the grounds of the formation of an air-confined geometry for $\lambda = 637.2\,\mathrm{nm}$. **(a)** The $\mathcal{Q}$-factor increases with increasing top-mirror reflectivity. Clipping losses occur for air-gaps $> 3\,\mu\mathrm{m}$. **(b)** The maximum achievable Purcell factor is largest for the top mirror with the highest reflectivity. **(c)** With increasing top-mirror reflectivity, $\kappa_{\mathrm{top}} \to \kappa_{\mathrm{bot}} \to 0.5$. Therefore, the transmission through the top mirror, $\frac{\kappa_{\mathrm{top}}}{\kappa_{\mathrm{tot}}}$ is largest for the top mirror with the fewest layer pairs. **(d)** The total detection efficiency, and thus the achievable flux, of ZPL photons is largest for an asymmetric cavity, despite the lower Purcell factor.

The efficiency of detecting a ZPL photon $\eta_{\mathrm{out}}$ is given by

$$\eta_{\mathrm{out}} = \frac{\kappa_{\mathrm{top}}}{\kappa_{\mathrm{tot}} + \gamma_0} \cdot \eta_{\mathrm{ZPL}}\,, \tag{8.7}$$

where $\eta_{\mathrm{ZPL}}$ is given by Eq. 8.3 and $\gamma_0$ is the emission into non-cavity modes. For simplicity, Eq. 8.7 will be broken down into the "cavity part", $\eta_{\mathrm{cav}}$, and the emitter part, where $\eta_{\mathrm{cav}}$ is given by

$$\eta_{\mathrm{cav}} = \frac{\kappa_{\mathrm{top}}}{\kappa_{\mathrm{tot}} + \gamma_0}\,. \tag{8.8}$$

Fig. 8.5 (d) shows a graphical evaluation of $\eta_{\text{out}}$ as a function of air-gap thickness. Despite achieving the lowest Purcell factor, the ZPL detection efficiency is greatest for the lowest reflective top mirror, due to the favourable value of $\frac{\kappa_{\text{top}}}{\kappa_{\text{tot}}}$. From this, it becomes apparent that there is a trade-off between the highest achievable Purcell factor and the maximum photon extraction efficiency [125]. It is important to accentuate that this analysis assumes DBR mirrors without any unwanted loss; in a cavity-coupling experiment, it is of pivotal importance that the cavity loss-rate is dominated by transmission through the top mirror, as was discussed in Section 3.3.5.

### 8.1.2 Low-index Terminated Top-Mirror

Up until this point, only high-index terminated bottom DBR mirrors were examined. In the following section, the potential benefits of using a low-index terminated bottom mirror will be investigated. In this discussion, low-index termination is achieved by adding an additional $\frac{\lambda}{4}$ layer of $SiO_2$ to the bottom DBR. Consequently, the refractive index profile of the mirror becomes $(n_{\text{H}} \cdot n_{\text{L}})^{15}$. To ease the comparison, the top mirrors will be kept identical to the ones discussed above. The resulting field profile is shown in Fig. 8.6. Compared to the high-index terminated mirror (Fig. 8.4), the low-index termination results in a field anti-node at both interfaces of the diamond: the cavity is shifted from an air- to a diamond-confined regime. The added $\frac{\lambda}{4}$ layer of $SiO_2$ effectively increases the transmission of the bottom mirror from $\mathcal{T}_{\text{bot}} = 59\,\text{ppm}$ to $\mathcal{T}_{\text{bot}} = 104\,\text{ppm}$.

The performance of the low-index terminated bottom mirrors is shown graphically in Fig. 8.7. The transition from an air- to a diamond-confined configuration, alongside the added $\frac{\lambda}{4}$ layer of $SiO_2$, increases the effective cavity length, reflected by the increase in the $\mathcal{Q}$-factor for small air-gaps (compare Chapter 3). As discussed, the low-index termination results in a field anti-node across both diamond interfaces. Therefore, for completeness, a scattering layer with RMS surface roughness $\sigma_{\text{q}} = 0.3\,\text{nm}$ is introduced on both sides of the diamond (semi-transparent lines). Despite the presence of scattering, the maximum achievable Purcell factor remains larger for the low-index terminated mirror. However, the increase in the bottom-mirror transmission induced by the low-index termination reduces the value $\frac{\kappa_{\text{top}}}{\kappa_{\text{tot}}}$ according to Eq. 8.5. As a consequence, $\eta_{\text{cav}} \cdot \eta_{\text{ZPL}}$ is reduced compared to the high-index termination discussed in Fig. 8.5.

Next, the amplitude of the scattering losses, $\mathcal{L}_{\text{loss}}$ will be described, following the same procedure as in Section 3.3.5. In the presence of surface scattering, the total cavity loss-rate $\kappa'$ is given by $\kappa' = \kappa_{\text{top}} + \kappa_{\text{top}} + \kappa_{\text{loss}}$, where $\kappa_{\text{top}}$ and $\kappa_{\text{bot}}$ remain unaltered. From

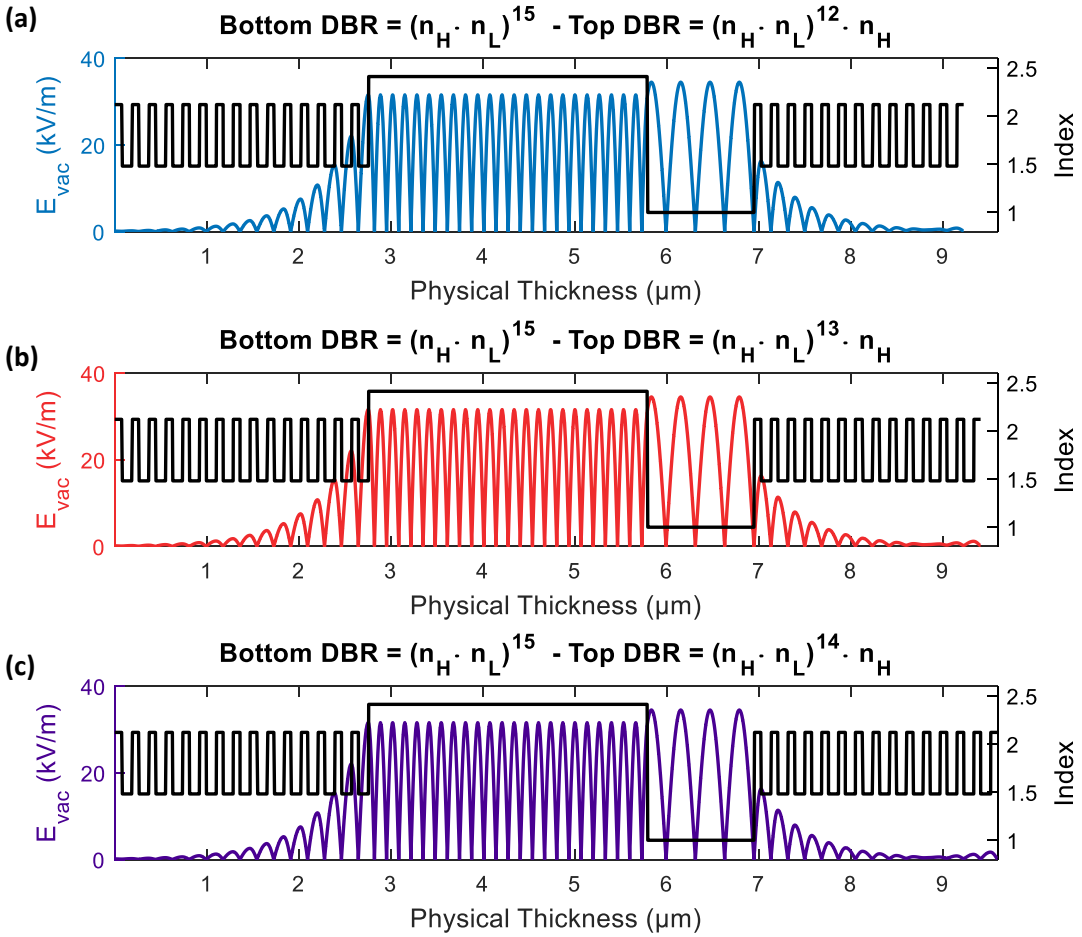


Fig. 8.6. Field profile in a cavity constructed from a low-index terminated bottom DBR with refractive index profile $(n_\mathrm{H} \cdot n_\mathrm{L})^{15}$ and diamond thickness $t_\mathrm{d} = 3030\,\mathrm{nm}$ ($\mathcal{T}_\mathrm{bot} = 104\,\mathrm{ppm}$) for top mirror **(a)** $(n_\mathrm{H} \cdot n_\mathrm{L})^{12} \cdot n_\mathrm{H}$, **(b)** $(n_\mathrm{H} \cdot n_\mathrm{L})^{13} \cdot n_\mathrm{H}$ and **(c)** $(n_\mathrm{H} \cdot n_\mathrm{L})^{14} \cdot n_\mathrm{H}$. Low-index termination results in the a field anti-node at both the diamond-mirror and the diamond-air interface.

this, the value of $\kappa_\mathrm{loss}$ can be calculated from

$$\kappa_\mathrm{loss} = \frac{2\pi c}{\lambda} \cdot \left( \frac{1}{\mathcal{Q}'} - \frac{1}{\mathcal{Q}} \right) , \tag{8.9}$$

where $\mathcal{Q}'$ and $\mathcal{Q}$ are the quality factors with and without scattering, respectively. Recall from Section. 2.1.1 that the cavity round-trip time $\tau$ is defined as $\tau = \frac{\mathcal{L}}{\kappa}$, from which a simple rearrangement yield $\mathcal{L}_\mathrm{loss} = \tau \cdot \kappa_\mathrm{loss}$. For $\sigma_\mathrm{q} = 0.3\,\mathrm{nm}$, this amounts to $\mathcal{L}_\mathrm{loss} = 33\,\mathrm{ppm}$, still considerably smaller than the mirror transmission $\mathcal{T}_\mathrm{bot} = 104\,\mathrm{ppm}$, $\mathcal{T}_{12} = 238\,\mathrm{ppm}$, $\mathcal{T}_{13} = 116\,\mathrm{ppm}$ and $\mathcal{T}_{14} = 57\,\mathrm{ppm}$. For comparison, the scattering losses are

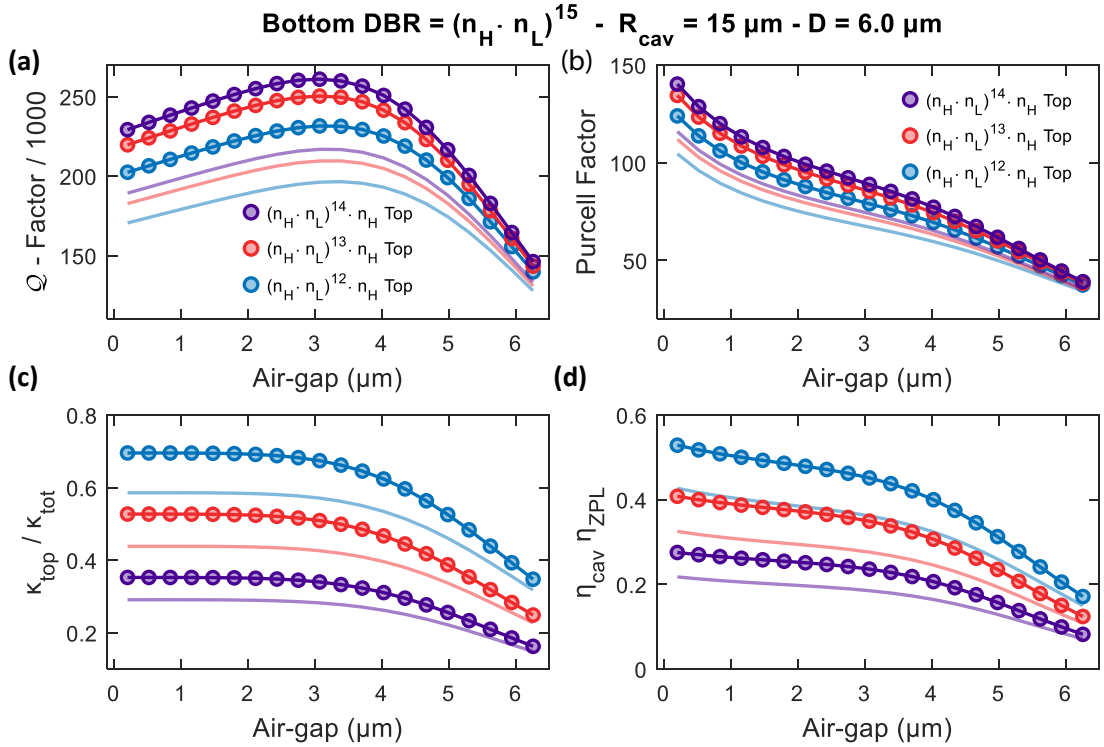


Fig. 8.7. Performance of a cavity constructed from a low-index terminated bottom DBR mirror, $(n_{\mathrm{H}} \cdot n_{\mathrm{L}})^{15}$, combined with $(n_{\mathrm{H}} \cdot n_{\mathrm{L}})^{j} \cdot n_{\mathrm{H}}$, $j = 12, 13, 14$ top mirror with $t_{\mathrm{d}} = 3030\,\mathrm{nm}$, $R_{\mathrm{cav}} = 15\mu\mathrm{m}$ and $D = 6.0\mu\mathrm{m}$. The semi-transparent lines correspond to the presence of a scattering layer with RMS surface roughness $\sigma_{\mathrm{q}} = 0.3\,\mathrm{nm}$. **(a)** $\mathcal{Q}$-factor and **(b)** Purcell factor as a function of air-gap thickness. The $\mathcal{Q}$-factor, and hence Purcell factor, increases with the reflectivity of the top mirror. **(c)** Relative loss-rate through the top mirror, $\frac{\kappa_{\mathrm{top}}}{\kappa_{\mathrm{tot}}}$ and **(d)** ZPL detection efficiency $\eta_{\mathrm{cav}} \cdot \eta_{\mathrm{ZPL}}$ as a function of air-gap. The detection efficiency is greatest for the most asymmetric cavity ($(n_{\mathrm{H}} \cdot n_{\mathrm{L}})^{12}$ top) .

estimated using $S = \left(\frac{4\pi\sigma_{\mathrm{q}}}{\lambda}\right)^2 = 35\,\mathrm{ppm}$ (Eq. 3.7) [104]. Here, the slight discrepancy can be explained by the shift in the maxima of the electric field across the diamond-air interface; the field maxima does not occur exactly at the interface (Fig. 8.6 (c)).

To conclude, for the current diamond thickness ($t_{\mathrm{d}} = 3030\,\mathrm{nm}$), a low-index terminated mirror is only beneficial in combination with a highly transmissive top mirror. Furthermore, the field anti-nodes at both of the interfaces of the diamond render the cavity sensitive to surface losses; these losses will have to be mitigated. To benefit from a low-index terminated bottom mirror, surface roughness $\sigma \ll 0.3\,\mathrm{nm}$ is a requirement. Fabrication of such a smooth diamond surface may prove to be challenging, if not impossible. Therefore, the use of low-index terminated bottom mirrors is not recommended in combination with the current design of the top mirror. Note that

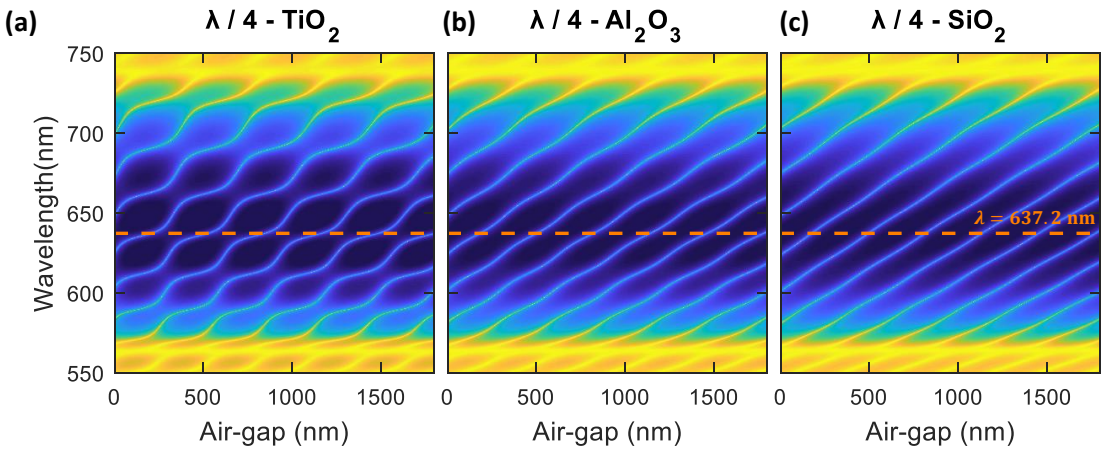


Fig. 8.8. Cavity mode structure for $\frac{\lambda}{4}$ coated diamond with **(a)** $TiO_2$ ($n = 2.58$, $t = 61.72\,\text{nm}$), **(b)** $Al_2O_3$ ($n = 1.77$, $t = 90.22\,\text{nm}$) and **(c)** $SiO_2$ ($n = 1.48$, $t = 107.56\,\text{nm}$). The presence of the oxide layer significantly changes the mode structure. The orange line indicates $\lambda = 637.2\,\text{nm}$.

this analysis was only performed with the current diamond thickness ($t_\text{d} = 3030\,\text{nm}$) in mind. A detailed theoretical study of mirror termination as a function of diamond thickness is beyond the scope of this outlook.

### 8.1.3 Depositing a $\lambda/4$-layer of Oxide on the Diamond

In Chapter 4 we proposed to use ALD to deposit a 10 nm thin layer of $SiO_2$ or $Al_2\ O_3$ on top of the diamond [123]. The motivation back then was to step-wise reduce the contrast in refractive index from the diamond to the air, and thus reducing scattering losses. Deposition of an oxide layer may have the added benefit of further reducing the surface-related losses on the grounds that ALD may smoothen the surface [479]. Therefore, this section develops the idea one step further by investigating the effect of depositing a $\frac{\lambda}{4}$ layer of $TiO_2$ ($n_{TiO_2} = 2.58$, $t_{TiO_2} = 61.72\,\text{nm}$) [480], $Al_2O_3$ ($n_{Al_2O_3} = 1.77$, $t_{Al_2O_3} = 90.22\,\text{nm}$) [481, 482] and $SiO_2$ ($n_{SiO_2} = 1.48$, $t_{SiO_2} = 107.56\,\text{nm}$) on the top surface of the diamond*. For simplicity, this analysis considers the same cavity geometry as Fig. 8.4 (a), i.e. $(n_\text{H} \cdot n_\text{L})^{12}\, n_\text{H}$ top mirror, $(n_\text{H} \cdot n_\text{L})^{14}\, n_\text{H}$ bottom mirror and $t_\text{d} = 3030\,\text{nm}$, $R_\text{cav} = 15\,\mu\text{m}$ and $D = 6\,\mu\text{m}$.

The presence of the deposited $\frac{\lambda}{4}$ oxide layer significantly alters the cavity mode-structure (Fig. 8.8) and the profile of the electric field inside the cavity (Fig. 8.9). The

*The refractive index for $TiO_2$ and $Al_2O_3$ are extracted from refractiveindex.info. Refractive index for $SiO_2$ provided by LaserOptik.

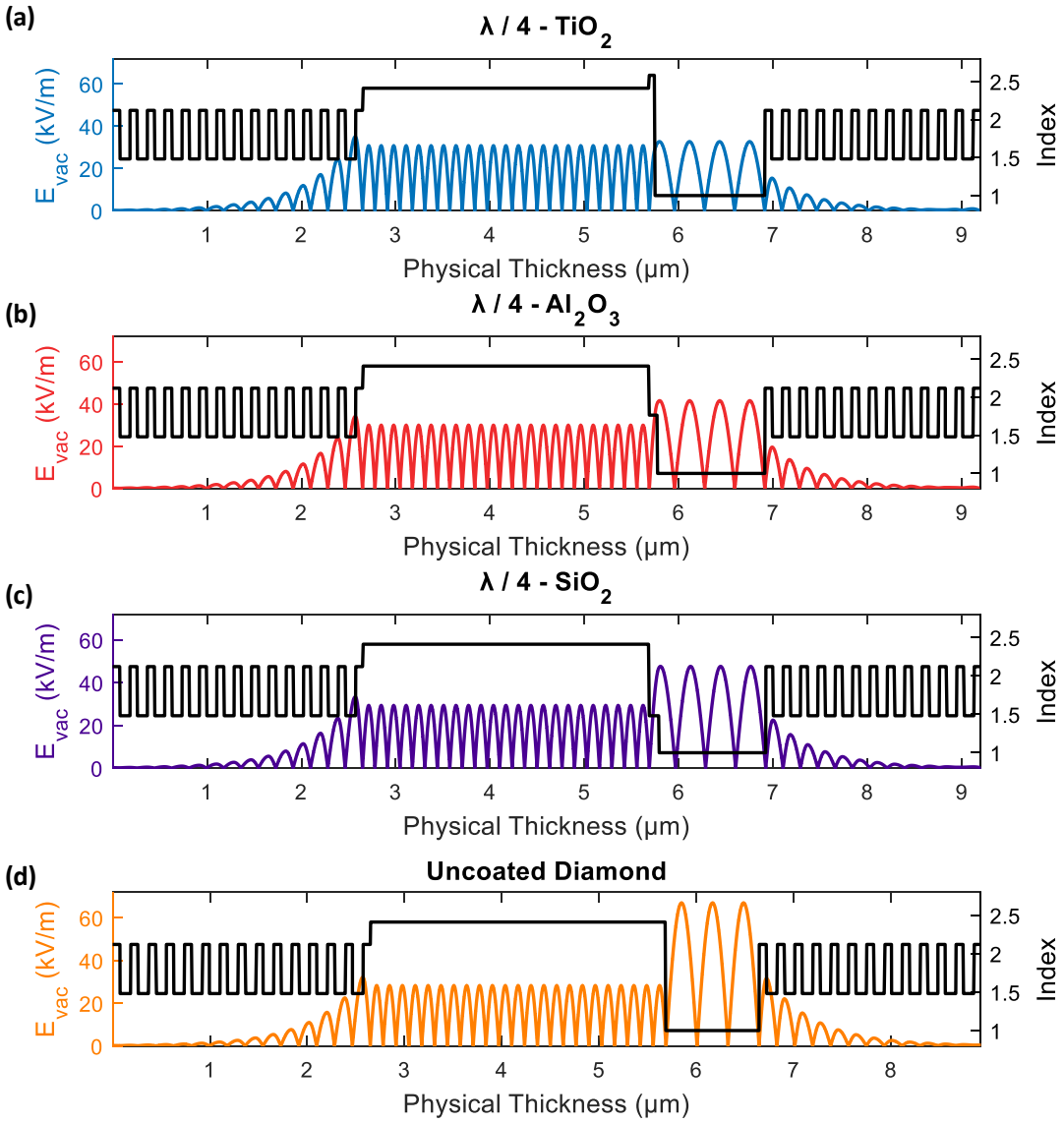


Fig. 8.9. Profile of the electric field inside the cavity with a $\frac{\lambda}{4}$ layer of **(a)** $TiO_2$, **(b)** $Al_2O_3$ and **(c)** $SiO_2$. The difference in refractive index alters the maximum field in the diamond (air); $E^{\mathrm{d(a)}}_{\mathrm{TiO_2}} = 30.85\,(32.75)\,\frac{\mathrm{kV}}{\mathrm{m}}$, $E^{\mathrm{d(a)}}_{\mathrm{Al_2O_3}} = 30.05\,(41.64)\,\frac{\mathrm{kV}}{\mathrm{m}}$ and $E^{\mathrm{d(a)}}_{\mathrm{SiO_2}} = 29.38\,(47.65)\,\frac{\mathrm{kV}}{\mathrm{m}}$. The cavity mirrors are assembled from $(n_{\mathrm{H}} \cdot n_{\mathrm{L}})^{12}\, n_{\mathrm{H}}$ top, $(n_{\mathrm{H}} \cdot n_{\mathrm{L}})^{14}\, n_{\mathrm{H}}$ bottom with $t_{\mathrm{d}} = 3030\,\mathrm{nm}$. **(d)**Field profile of an uncoated diamond for comparison.

electric field maxima in the diamond is found to increase with increasing refractive index: $E_{\mathrm{TiO_2}} = 30.85\,\frac{\mathrm{kV}}{\mathrm{m}}$, $E_{\mathrm{Al_2O_3}} = 30.05\,\frac{\mathrm{kV}}{\mathrm{m}}$ and $E_{\mathrm{SiO_2}} = 29.38\,\frac{\mathrm{kV}}{\mathrm{m}}$, respectively, compared to $E_{\mathrm{uncoat.}} = 28.32\,\frac{\mathrm{kV}}{\mathrm{m}}$ for the uncoated diamond. Furthermore, compared to an uncoated diamond, the presence of the dielectric coatings increases the relative fraction

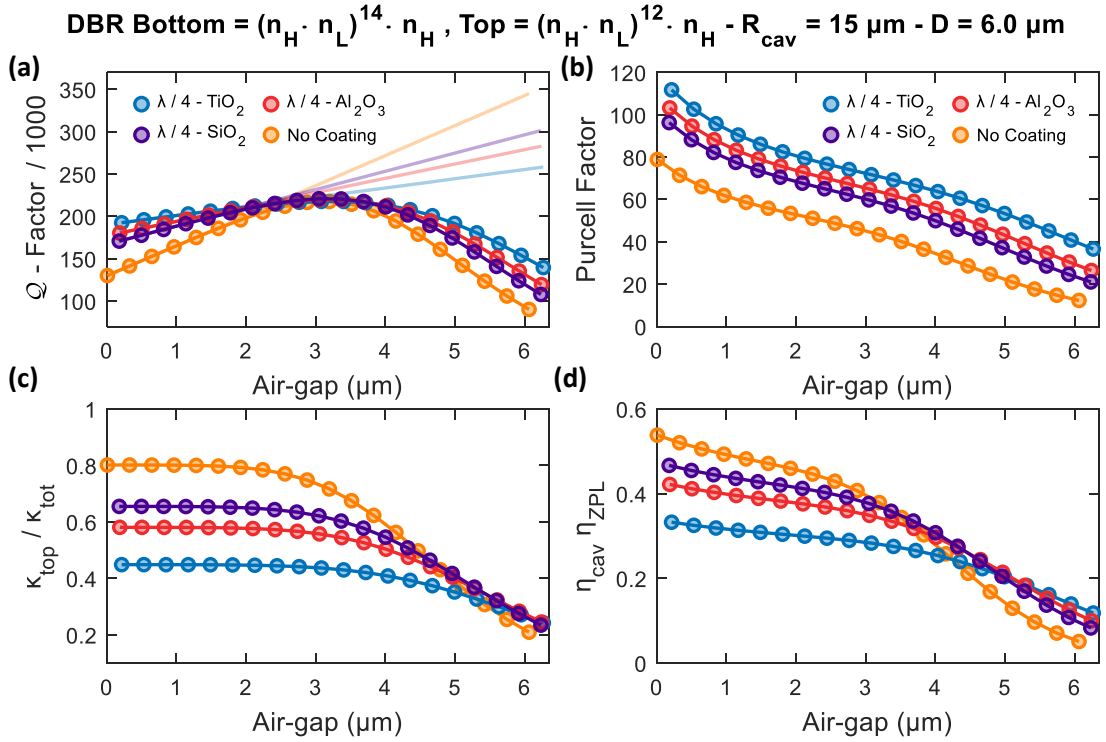


Fig. 8.10. Performance of a cavity constructed from $(n_{\mathrm{H}} \cdot n_{\mathrm{L}})^{12}\, n_{\mathrm{H}}$ top and $(n_{\mathrm{H}} \cdot n_{\mathrm{L}})^{14}\, n_{\mathrm{H}}$ bottom with a $\lambda/4$ oxide layer on the top side of the diamond, with $t_{\mathrm{d}} = 3030\,\mathrm{nm}$, $R_{\mathrm{cav}} = 15\,\mu\mathrm{m}$ and $D = 6.0\,\mu\mathrm{m}$. **(a)** The presence of the oxide layer increases the effective cavity length, thus resulting in larger $\mathcal{Q}$-factors compared to the uncoated diamond (orange). However, the transition to a diamond-confined configuration reduces the finesse for the oxide-coated diamond. The semi-transparent lines show the behaviour of the $\mathcal{Q}$-factors in the absence of beam clipping. **(b)** The larger $\mathcal{Q}$-factors combined with a smaller effective mode volume result in larger Purcell factors for the coated diamonds. The Purcell factor is largest for the highest material with the largest refractive index. **(c)** The presence of the oxide layer reduces the effective reflectivity of the bottom mirror, thus decreasing $\frac{\kappa_{\mathrm{top}}}{\kappa_{\mathrm{tot}}}$. **(d)** Detection efficiency of a ZPL photon as a function of air-gap. The larger Purcell factor for the oxide layers results in only a small reduction in the detection efficiency of 13 % and 25 % for $SiO_2$ and $Al_2O_3$ respectively. For $TiO_2$, the detection efficiency drops by 38 %.

of the field intensity confined to the diamond*, while preserving a field node across the diamond-oxide interface. As a consequence, the field profile possesses an anti-node across the oxide-air interface, thus mimicking a diamond confined geometry. In the following analysis, loss-less oxide layers are assumed – the possibility to deposit thick oxides on diamond without the formation of cracks or defects remains an open question to be

*Computing the ratio of the field maxima in the diamond to that of air yield $(|E^{\mathrm{diamond}}_{\mathrm{uncoated}}|)/(|E^{\mathrm{air}}_{\mathrm{uncoated}}|) = 0.46$ compared to $(|E^{\mathrm{diamond}}_{\mathrm{TiO_2}}|)/(|E^{\mathrm{air}}_{\mathrm{TiO_2}}|) = 0.94$.

addressed in further experiments.

Fig. 8.10 repeats the same analysis as previously done for Fig. 8.5 and Fig. 8.7. The oxide layers alter the effective transmission of the bottom mirror (here the diamond is considered to be part of the mirror). From the simulations, one finds $\mathcal{T}_{TiO_2} = 292\,\text{ppm}$, $\mathcal{T}_{Al_2O_3} = 172\,\text{ppm}$ and $\mathcal{T}_{SiO_2} = 125\,\text{ppm}$, compared to $\mathcal{T}_{bot} = 59\,\text{ppm}$ for the uncoated diamond. Fig. 8.10 (a) shows the behaviour of the $\mathcal{Q}$-factor with increasing air-gap. As predicted by the transition to a more diamond-confined geometry, the absolute value of $\mathcal{Q}$-factors is larger for the coated diamond for short cavity lengths. However, the uncoated diamond exhibits a steeper slope (larger $\frac{d\mathcal{Q}}{dt_a}$), which translates into a larger finesse (Compare Chapter. 3). Owing to the larger $\mathcal{Q}$-factors, a 20 % increase in Purcell factor can be expected for the coated samples. The magnitude of the $\mathcal{Q}$-factors, and likewise the Purcell factor, increases with the refractive index of the oxide layer. This can be understood by considering the longer effective cavity length for the higher-index materials: the photons propagate at a slower speed, and thus the overall round-trip time increases (compare Section. 2.1.1).

The increased mirror transmission induced by the oxide layers results in a decreased value of $\frac{\kappa_{top}}{\kappa_{tot}}$ (Fig. 8.10 (c)). However, as shown in Fig. 8.10 (d), the larger Purcell factor offered by the oxide layers results in only a small reduction in $\eta_{cav} \cdot \eta_{ZPL}$ of 13 % and 25 % for $SiO_2$ and $Al_2O_3$, respectively. The large refractive index of $TiO_2$ causes the output efficiency to drop by 38 %. From this analysis, it is clear that ALD deposition of $SiO_2$ and $Al_2O_3$ may provide a viable option to increase the photon flux, provided the deposition occurs without introducing additional losses.

### 8.1.4 The ECI Mirrors

The observant reader will have noticed that the mirror design used for the analysis presented so far in this chapter differs from the mirror design used in the experimental chapters (See Chapter 4, Chapter 5 and Chapter 6). The experiments presented in the aforementioned chapters were performed using a pre-existing cavity [77, 255] assembled with mirrors from an earlier fabrication run*. Therefore, for completeness, the above analysis will be repeated for the "old" cavity mirrors. Contrary to the LaserOptik mirrors discussed so far, the reflective stopband of the ECI mirrors was characterised using a white-light transmission measurement [255, 387] (for details see Fig. 5.3 (c)). Using a transfer-matrix based refinement algorithm, the mirror designs were found to

*ECI evapcoat.

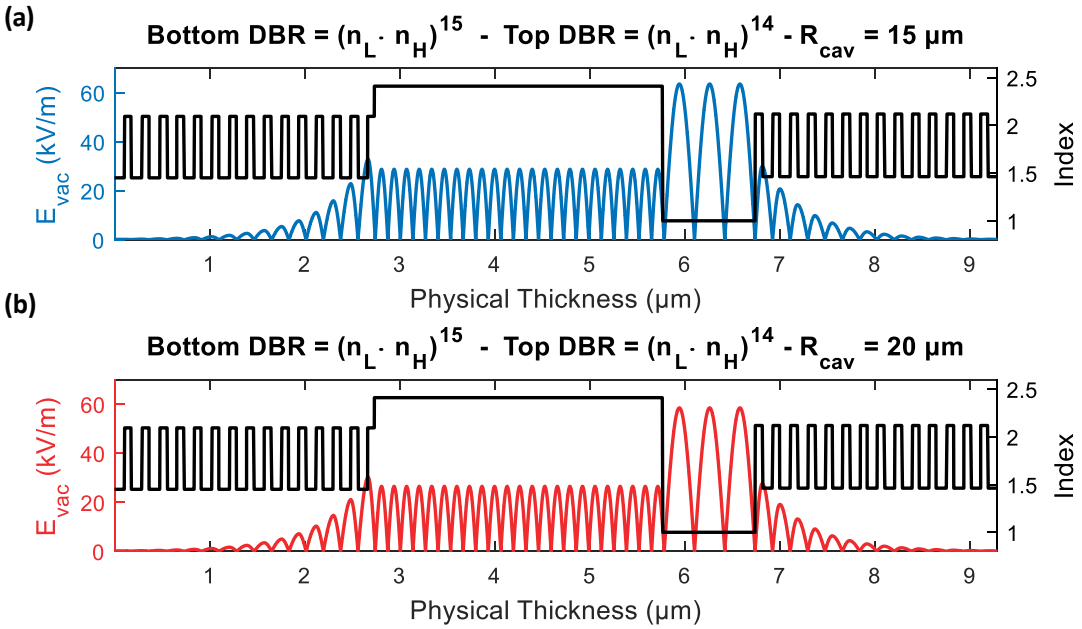


Fig. 8.11. Electric field profile for the ECI mirror; $(n_\mathrm{L} \cdot n_\mathrm{H})^{14}$ top and $(n_\mathrm{L} \cdot n_\mathrm{H})^{15}$ bottom for $D = 6.0\,\mu\mathrm{m}$ and **(a)** $R_\mathrm{cav} = 15\,\mu\mathrm{m}$ and **(b)** $R_\mathrm{cav} = 20\,\mu\mathrm{m}$. The larger radius of curvature manifests itself in a larger mode volume, and thus reduces the maximum amplitude of the vacuum field inside the diamond from $E_{R=15\,\mu\mathrm{m}} = 28.8\,\frac{\mathrm{kV}}{\mathrm{m}}$ to $E_{R=20\,\mu\mathrm{m}} = 26.5\,\frac{\mathrm{kV}}{\mathrm{m}}$.

be $(n_\mathrm{L} \cdot n_\mathrm{H})^{14}$ for the top mirror and $(n_\mathrm{L} \cdot n_\mathrm{H})^{15}$ for the bottom mirror, where $n_\mathrm{L} = n_{\mathrm{SiO_2}} = 1.46$ and $n_\mathrm{H} = n_{\mathrm{Ta_2O_5}} = 2.11$. By further allowing for a 3 % tolerance on the individual layer thickness, allowing for the reconstruction of the full reflective stopband. By simulating the bare mirrors, one finds $\mathcal{T}_\mathrm{top} = 94\,\mathrm{ppm}$ and $\mathcal{T}_\mathrm{bot} = 62\,\mathrm{ppm}$, where a diamond with thickness $t_\mathrm{d} = 3030\,\mathrm{nm}$ are included as part of the bottom mirror. Fig. 8.11 shows the profile of the electric field for (a) $R_\mathrm{cav} = 15\,\mu\mathrm{m}$ and (b) $R_\mathrm{cav} = 20\,\mu\mathrm{m}$, where $D = 6\,\mu\mathrm{m}$ for both simulations. The larger radius of curvature results in a larger mode volume, thus causing a 7 % drop in the maximum field amplitude from $E_{R=15\,\mu\mathrm{m}} = 28.8\,\frac{\mathrm{kV}}{\mathrm{m}}$ to $E_{R=20\,\mu\mathrm{m}} = 26.5\,\frac{\mathrm{kV}}{\mathrm{m}}$.

Fig 8.12 shows the performance of a cavity assembled from the ECI mirror coatings. Compared to the LaserOptik mirrors, the higher mirror reflectivity is emphasised by the increased $\mathcal{Q}$-factor and consequently larger Purcell factor. A larger radius of curvature translates to a larger beam waist at the top mirror. Therefore, beam clipping occurs for shorter cavity lengths. The close-to balanced mirror reflectivity results in a maximum detection efficiency $\frac{\kappa_\mathrm{top}}{\kappa_\mathrm{tot}} = 0.60$ and $n_\mathrm{cav} \cdot \eta_\mathrm{ZPL} = 0.53$. For short cavity lengths, the detection efficiency is more-or-less independent of the top mirror geometry.

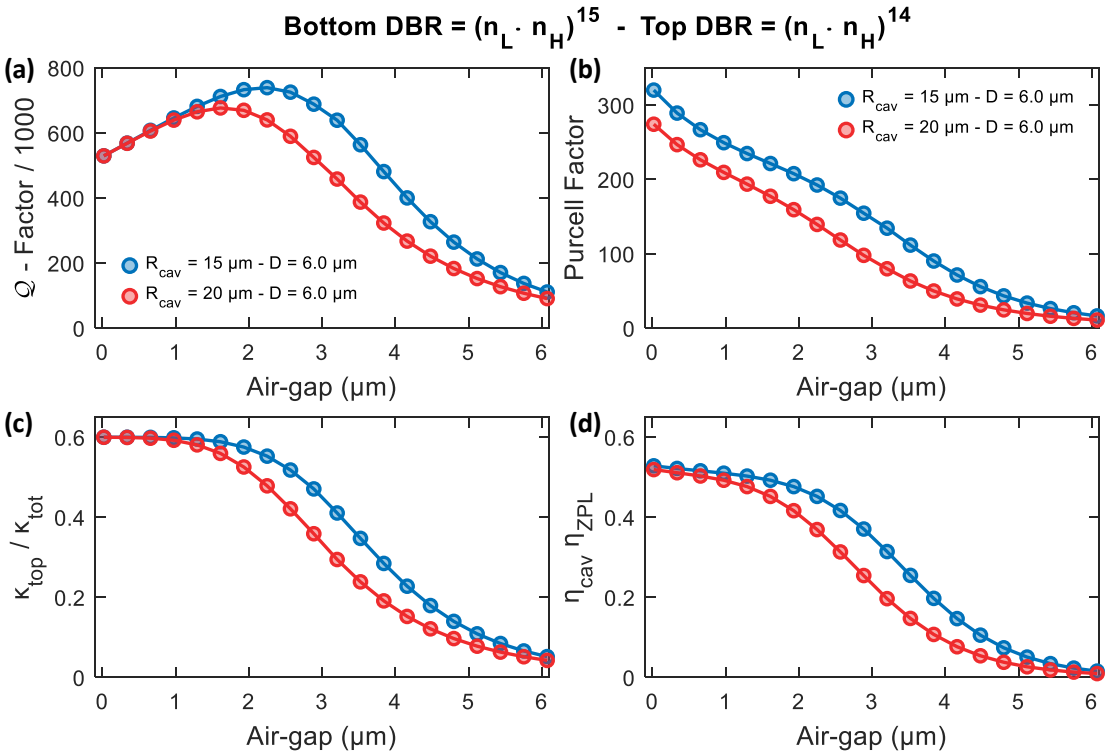


Fig. 8.12. Performance of a cavity assembled from the ECI mirrors; $(n_\mathrm{L} \cdot n_\mathrm{H})^{14}$ top and $(n_\mathrm{L} \cdot n_\mathrm{H})^{15}$ for two different top mirror geometries; $R_\mathrm{cav} = 15\,\mu\mathrm{m}$ in blue and $R_\mathrm{cav} = 20\,\mu\mathrm{m}$ in red. $D = 6\,\mu\mathrm{m}$ for both configurations. The highly reflective mirror coating manifest itself in **(a)** a large $\mathcal{Q}$-factor, and consequently **(b)** a large Purcell factor. The larger radius of curvature (red) results in a larger beam waist, and thus beam clipping occurs for shorter cavity lengths. **(c)** The close-to balanced mirror coating results in a cavity detection efficiency $\frac{\kappa_\mathrm{top}}{\kappa_\mathrm{tot}} = 0.6$, and **(c)** a ZPL detection efficiency $\eta_\mathrm{ZPL} \cdot \eta_\mathrm{cav} = 0.53$, independent of top mirror geometry for short cavity lengths.

### 8.1.5 Comparison of the Mirrors

From the above analysis, it becomes apparent that there is a trade-off between the maximum Purcell factor and the maximum detection efficiency. In this section, the aforementioned mirror configurations will be discussed and compared on the account of the achievable photon flux. The end-to-end efficiency of a photon from an NV centre in the cavity is given by $\eta_\mathrm{tot}^\mathrm{cav} = \eta_\mathrm{ex} \cdot \eta_\mathrm{ZPL} \cdot \eta_\mathrm{cav} \cdot \eta_\mathrm{ext}$, where $\eta_\mathrm{ex}$ is the excitation efficiency and $\eta_\mathrm{ext}$ is the efficiency of the external detection optics, including the quantum efficiency of the photon detectors [102, 194]. Consequentially, the detection rate of ZPL photons,

$C_{\mathrm{ZPL}}$ is calculated from $C_{\mathrm{ZPL}} = \eta_{\mathrm{tot}} \cdot \gamma_{\mathrm{cav}}$. By using Eq. 8.3, one arrives at [214]

$$\begin{aligned} C_{\mathrm{ZPL}} &= \eta_{\mathrm{ex}} \cdot \eta_{\mathrm{cav}} \cdot \eta_{\mathrm{ext}} \cdot \frac{\xi_0 F_{\mathrm{P}}}{\xi_0 \left(F_{\mathrm{P}} - 1\right) + 1} \cdot \gamma_{\mathrm{cav}} \\ &= \eta_{\mathrm{ex}} \cdot \eta_{\mathrm{cav}} \cdot \eta_{\mathrm{ext}} \cdot \xi_0 F_{\mathrm{P}} \cdot \gamma_0 \,. \end{aligned} \tag{8.10}$$

For argument's sake, assume a rather bold scenario where both $\eta_{\mathrm{ex}}$ and $\eta_{\mathrm{ext}}$ equal unity (the second assumption will be revisited below).

Fig. 8.13 shows the graphical evaluation of Eq. 8.10 for the different mirror configurations discussed above. Here, $\xi_0 = 0.025$ and $\gamma_0 = \frac{1}{\tau_0} = 2\pi \times 12.6\,\mathrm{MHz}$ as before. To start, Fig. 8.13 (a) and (b) show a comparison between the high- and low-index terminated LaserOptik mirrors, respectively. For the high-index terminated mirror, the detection rate is the largest for the intermediate reflective top mirror (red data points). Here, the reduction in the detection efficiency is counteracted by a larger Purcell factor (Fig. 8.5). On the contrary, the reduced reflectivity of the low-index terminated bottom DBR favours a lower reflectivity top mirror. For the low-index terminated mirrors, the presence of surface scattering ($\sigma_{\mathrm{q}}$, faint lines in Fig. 8.13 (b)) further reduces the detection rate. In conclusion, with the top mirrors considered here, low-terminated bottom mirrors will not improve the detection rate.

On the other hand, coating the diamond with a $\lambda/4$ layer of $SiO_2$ or $Al_2O_3$ offers a possible route to enhance the detection rate, as can be seen in Fig. 8.13 (c). In the current configuration, the deposition of higher-index $TiO_2$ offers no added benefits. To recap, here a top mirror on the form $(n_{\mathrm{H}} \cdot n_{\mathrm{L}})^{12}\, n_{\mathrm{H}}$ is considered, i.e. identical to the blue points in Fig. 8.13 (a). Note that the analysis here assumes the possibility of depositing a loss-less $\lambda/4$ layer on the diamond via ALD. Should this assumption hold, deposition using ALD could further lead to smoothing of the surface [479], and thus allowing for operating in a diamond-confined geometry with little-to-no surface scattering.

The high Purcell factor combined with a detection efficiency of $\frac{\kappa_{\mathrm{top}}}{\kappa_{\mathrm{tot}}} \sim 0.6$ renders the highly refractive ECI coating displayed in Fig. 8.13 (d) unrivalled in terms of the expected detection rate. Therefore, in the assumption of DBR mirror coatings without any unwanted losses, this mirror configuration will be the obvious choice. However, in a real-life experiment, imperfections in the mirror coating can introduce scattering and absorption with loss-rate $\kappa_{\mathrm{DBR}}$. In the presence of losses, it is of paramount importance that transmission through the top mirror constitutes the dominant loss channel, i.e. $\kappa_{\mathrm{top}} \gg \kappa_{\mathrm{DBR}}$ (compare Section 3.3.5). To verify this assumption, it is worth revisiting Chapter 4, where this exact mirror configuration was used [387]. Here, the measured finesse $\mathcal{F}^{\mathrm{exp}}_{\mathrm{bare}} = 42\,500 \pm 4\,200$ and the finesse expected from the

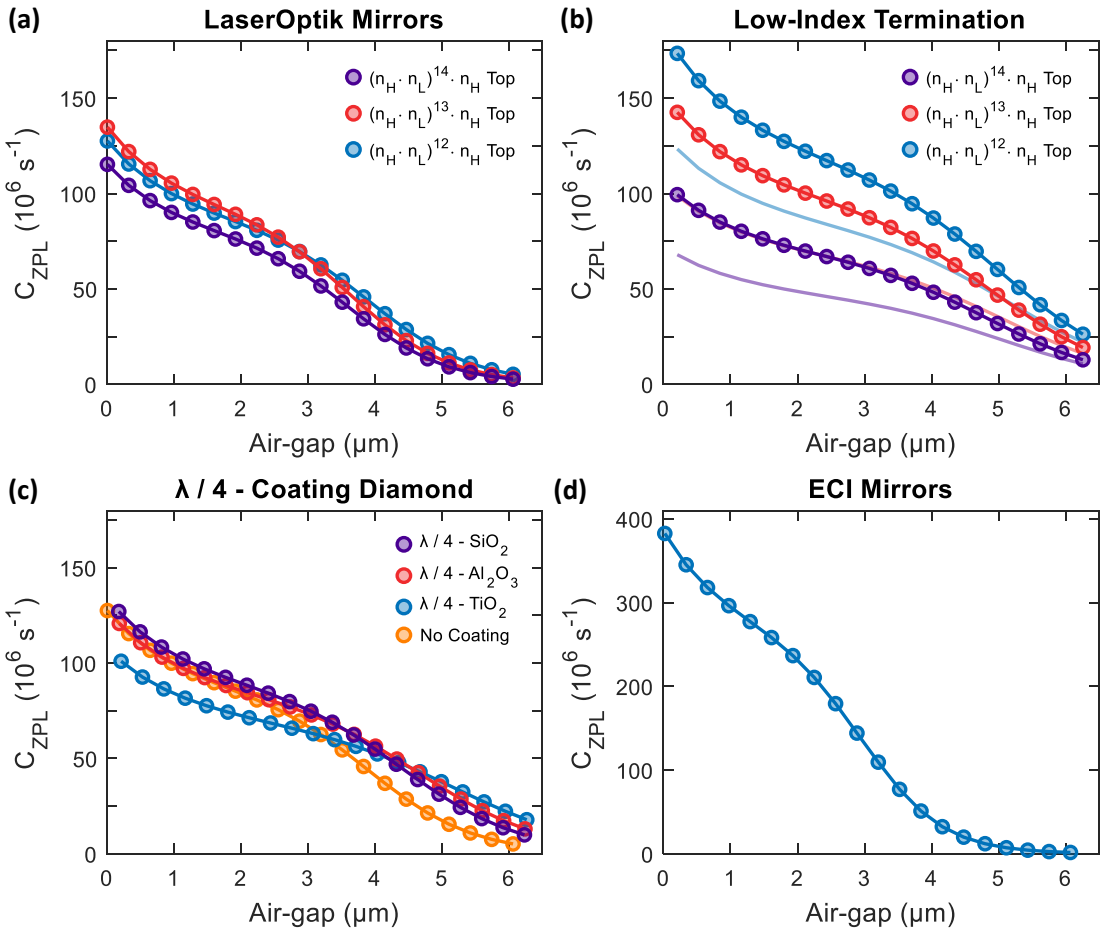


Fig. 8.13. Detection rate of ZPL photons calculated from Eq. 8.10 for different cavity configurations. Here, a top mirror with $R_{\mathrm{cav}} = 15\,\mu\mathrm{m}$ and $D = 6\,\mu\mathrm{m}$ are assumed for all cases. **(a)** Cavity constructed from the LaserOptik mirrors with bottom mirror $(n_{\mathrm{H}} \cdot n_{\mathrm{L}})^{14} \cdot n_{\mathrm{H}}$. **(b)** Low-index terminated bottom mirror, $(n_{\mathrm{H}} \cdot n_{\mathrm{L}})^{15}$. The semi-transparent lines represent scattering losses with surface roughness $\sigma_{\mathrm{q}} = 0.3\,\mathrm{nm}$. **(c)** Depositing $\lambda/4$-layer of oxide on top of the diamond surface. The cavity is constructed from DBR mirrors created from $(n_{\mathrm{H}} \cdot n_{\mathrm{L}})^{14} \cdot n_{\mathrm{H}}$ bottom and $(n_{\mathrm{H}} \cdot n_{\mathrm{L}})^{12} \cdot n_{\mathrm{H}}$ top. **(d)** Cavity constructed using the ECI coating, with $(n_{\mathrm{L}} \cdot n_{\mathrm{H}})^{14}$ top and $(n_{\mathrm{L}} \cdot n_{\mathrm{H}})^{15}$ bottom.

simulations, $\mathcal{F}_{\mathrm{bare}}^{\mathrm{sim}} = 44\,410$, was in excellent agreement, to within the errors of the experiment. The difference in finesse corresponds to $\mathcal{L}_{\mathrm{DBR}} \simeq 6\,\mathrm{ppm}$, albeit with a large errorbar. Compared to $\mathcal{T}_{\mathrm{top}} = 93.5\,\mathrm{ppm}$, it is clear that $\mathcal{L}_{\mathrm{DBR}} \ll \mathcal{T}_{\mathrm{top}}$ thus validating the assumption of loss-less mirrors.

In a cavity-coupling experiment, the parameter $\eta_{\mathrm{ext}}$ depends on the efficiency and losses of each optical component. Performing a back-of-the-envelope estimation, where

transmission through the DBR-substrate $\mathcal{T}_{\text{sub}} \simeq 97.5\,\%$, transmission through the objective $\mathcal{T}_{\text{obj}} \simeq 75\,\%$, coupling efficiency to the single-mode detection fibre $\eta_{\text{fibre}} \simeq 70\,\%$ and SPAD detection efficiency $\eta_{\text{SPAD}} \simeq 70\,\%$ [85], results in $\eta_{\text{ext}} = 35.8\,\%$. However, this number can be further improved: applying an anti-reflective coating to the DBR-substrate allow for $\mathcal{T}_{\text{sub}} \to 100\,\%$, $\mathcal{T}_{\text{obj}} \simeq 99$ for a single aspheric lens, and using superconducting nanowire detectors can increase $\eta_{\text{SPAD}} \gtrsim 90\,\%$, resulting in $\eta_{\text{ext}} \to 62.4\,\%$.

For the remainder of this chapter, consider a cavity assembled using the ECI mirror-coating and a typical crater with radius of curvature $R_{\text{cav}} = 15\,\mu\text{m}$ and depth $d \sim 0.7\mu\text{m}$ [385, 393]. From Fig. 8.12, the closest resonance to contact ($q_{\text{air}} = 4$ for $\lambda = 637.2\,\text{nm}^*$) occurs for an air-gap $t_{\text{a}} = 975\,\text{nm}$. For this mode, $\mathcal{Q} = 645\,440$, $|E_{\text{vac}}| = 28.8\,\frac{\text{kV}}{\text{m}}$ and $V_{\text{eff}} = 197.7 \cdot \left(\frac{\lambda}{n}\right)^3$. An optimally positioned NV centre will thus experience $F_{\text{P}} = 249$, $\eta_{\text{cav}} = 0.588$ and $\eta_{\text{ZPL}} = 0.867$, thus $\eta_{\text{out}} = 0.506$. By including $\eta_{\text{ext}} = 0.358$, one find $C_{\text{ZPL}} = 106.1 \cdot 10^6\,\text{s}^{-1}$ for $\gamma_0 = 2\pi \times 12.6\,\text{MHz}$ and $\xi_0 = 2.55\,\%$ [77]. With nominally the same experimental setup, Ref. [85] measured $\eta_{\text{ext}} = 0.15\,\%$, which in this analysis translates to $C_{\text{ZPL}} = 4.44 \cdot 10^5\,\text{s}^{-1}$.

State-of-the-art spin-photon entanglement schemes utilise a hemispherical solid immersion lens (SIL) [42, 43, 66, 73, 396, 397], with a typical collection efficiency of $\sim 30\,\%$ [471, 483, 484]. For $\xi_0 = 2.55\,\%$, the collection efficiency of a ZPL photon using a SIL amounts to $\eta_{\text{tot}}^{\text{SIL}} = 0.77\,\%$. Successful entanglement events are heralded by the detection of two independent ZPL photons, thus the success rate of these protocols scales with $\eta_{\text{tot}}^2$ [84, 485]. In a cavity experiment under otherwise equivalent conditions, i.e. equal $\eta_{\text{ex}}$ and $\eta_{\text{ext}}$, the spin-spin entanglement rate will be boosted by a factor [65, 85, 405]

$$\left(\frac{\eta_{\text{tot}}^{\text{cav}}}{\eta_{\text{tot}}^{\text{SIL}}}\right)^2 = \left(\frac{\eta_{\text{cav}} \cdot \eta_{\text{ZPL}}^{\text{cav}}}{\eta_{\text{SIL}} \cdot \eta_{\text{ZPL}}^{\text{SIL}}}\right)^2 \simeq 4\,440\,. \tag{8.11}$$

Deterministic light-matter interaction requires cooperativity, $\mathcal{C} = \frac{4g^2}{\kappa\gamma_0} > 1$ (compare Section 2.1.3) [30, 58, 61]. Following Ref. [61, 214], the Purcell factor of the ZPL, $F_{\text{P}}^{\text{ZPL}}$, can be calculated from

$$F_{\text{P}}^{\text{ZPL}} = 1 + \frac{\mathcal{C}_{\text{ZPL}}}{\xi_0}\,. \tag{8.12}$$

A simple rearrangement gives[†]

$$\mathcal{C}_{\text{ZPL}} = \xi_0 \cdot \left(F_{\text{P}}^{\text{ZPL}} - 1\right) = 6.3\,, \tag{8.13}$$

[*]Following the convention introduced in Chapter 4, $q_{\text{air}}$ is defined as the mode index in air starting at $q_{\text{air}} = 1$ for the first resonance, corresponding to $t_{\text{a}} = 19\,\text{nm}$.

[†]The cooperativity $\mathcal{C}_{\text{ZPL}}$ is not to be confused with $C_{\text{ZPL}}$, the detection rate of ZPL photons.

for $F_{\mathrm{P}} = 249$ and $\xi_0 = 2.55\,\%$.

Following Section 4.4.1, the NV-cavity coupling can be described using the parameters of the Jaynes–Cummings Hamiltonian. The NV-cavity coupling rate, $g_{\mathrm{ZPL}}$, is given by $g_{\mathrm{ZPL}} = d_{\mathrm{NV}} \cdot E_{\mathrm{vac}}$ (compare Section 2.1.4). Extracting $E_{\mathrm{vac}} = 28.8\,\frac{\mathrm{kV}}{\mathrm{m}}$ from Fig. 8.11 (a) and using $d_{\mathrm{NV}}/e = \sqrt{\xi_0} \cdot 0.108\,\mathrm{nm}$ [77] yields $g_{\mathrm{ZPL}} = 755 \cdot 10^6\,\mathrm{s}^{-1}$. Combining all the above, one finds

$$\begin{aligned} g_{\mathrm{ZPL}} &= 2\pi \times 120\,\mathrm{MHz} \\ \kappa &= 2\pi \times 728\,\mathrm{MHz} \\ \gamma_0 &= 2\pi \times 12.6\mathrm{MHz}\,, \end{aligned} \tag{8.14}$$

firmly placing the system in the weak coupling regime of QED. Furthermore, The condition ($\kappa > g_{\mathrm{ZPL}} > \gamma_0$) is favourable for a large photon collection efficiency [125, 214].

Finally, calculating the cooperative using the values in Eq. 8.14:

$$\mathcal{C}_{\mathrm{ZPL}} = \frac{4g_{\mathrm{ZPL}}^2}{\kappa\gamma_0} = 6.3\,, \tag{8.15}$$

giving the same numerical value as before (Eq. 8.13). Note that up to this point, spectral diffusion has been neglected in this definition of the cooperativity. Spectral diffusion can be accounted for using the coherent cooperativity $\mathcal{C}_{\mathrm{coh}}$, defined as [58, 113]

$$\mathcal{C}_{\mathrm{coh}} = \frac{4g_{\mathrm{ZPL}}^2}{\kappa\left(\gamma_{\mathrm{hom}} + \gamma^*\right)}\,, \tag{8.16}$$

where $\gamma_{\mathrm{hom}} = \gamma_{\mathrm{rad}} + \gamma_{\mathrm{nonrad}}$ and $\gamma^*$ is the spectral diffusion rate [387]. Ignoring the non-radiative decay rate $\gamma_{\mathrm{nonrad}}$ reduces $\gamma_{\mathrm{hom}} = \gamma_{\mathrm{rad}} = \gamma_0$ as used elsewhere in this chapter. Including an inhomogeneous broadened linewidth of $\gamma^* = 2\pi \times 100\,\mathrm{MHz}$ (motivated by Fig. 7.21 (a)), reduces the cooperativity to $\mathcal{C}_{\mathrm{coh}} = 0.7$.

## 8.2 Concluding Remarks

To conclude, a Fabry-Perot microcavity operating in the weak coupling regime of cavity quantum electrodynamics constitutes a promising platform to enhance significantly the flux of coherent photons from single NV centres. A careful choice of the DBR mirror coatings are required to establish a balance between a high $\mathcal{Q}$-factor and the cavity outcoupling efficiency $\eta_{\mathrm{cav}}$; it is of paramount importance that the cavity loss-rate $\kappa$ is dominated by the transmission through the top mirror $\kappa_{\mathrm{top}}$. A scenario with $\kappa_{\mathrm{loss}} > \kappa_{\mathrm{top}}$ would be detrimental to the photon detection rate, on the grounds that the cavity pho-

tons will be lost to the environment rather than by transmission through the top mirror. However, with a suitable choice of mirror coatings, a ZPL detection rate exceeding $1 \cdot 10^6\,\mathrm{s}^{-1}$, and a cooperativity $\mathcal{C}_{\mathrm{ZPL}} > 3$ are within reach, consequently allowing for a drastic increase in the spin-spin entanglement rates [42].

The overarching goal of the work presented in this thesis is to enhance the rate of coherent photons from single NV centres in diamond. With the current experimental platform, the realisation of highly efficient spin-photon [41] and spin-spin [42, 43] entanglements are within reach. However, technical hurdles, such as efficient delivery of microwaves for coherent spin control and smoothing of the diamond surface, will have to be overcome. In addition, maintaining optically coherent NV centres during the micro-fabrication is of paramount importance. Here, post-implantation constitutes a promising way to create close to the surface NV centres with narrow ($\sim 100\,\mathrm{MHz}$) linewidths [171]. Furthermore, laser-writing has proved to create NV centres in bulk diamond with outstanding optical properties [172, 178]. Vacancies are created in a highly non-linear process, thus limiting lattice damage to within the focal volume of the tightly focused laser [173]. However, due to the threshold of surface damage being lower than the threshold for vacancy creation, the creation of close-to-surface ($< 100\,\mathrm{nm}$) NV centres remains challenging. At the time of writing, it is not clear how the optical coherence of the laser-written NV centre evolves during fabrication.

On a final note, although, the work presented in this thesis is guided towards the NV centre in diamond, the versatile design of the Fabry-Perot microcavity allows for the incorporation of other defect centres in wide bandgap materials. Examples of such defect centres are the centrosymmetric group-IV defects in diamond [100, 219, 256, 257, 261, 263, 264, 269, 296, 301, 302, 486], defects in silicon carbide [318, 319, 322], rare-earth ions in crystalline hosts [101, 325, 330, 331] or emitters in 2D materials [419, 420, 487]. In other words, with a tunable Fabry-Perot microcavity, the world is your oyster!

APPENDIX A

# Introducing the Transfer-Matrix Formalism

In a nutshell, the transfer-matrix formalism describes the propagation of optical beams. In a ray optics picture, a ray is completely described by a two-element vector $\psi$ containing position $x_1$ and slope $x_1'$ with respect to the optical axes [93]

$$\psi_1 = \begin{pmatrix} x_1 \\ x_1' \end{pmatrix} . \tag{A.1}$$

The optical path through a medium with refractive index $n$ depends on the optical properties of the medium and on the input condition [91]. The corresponding output parameters, $x_2$ and $x_2'$, are linearly dependent on the input parameter, i.e.

$$\begin{pmatrix} x_2 \\ x_2' \end{pmatrix} = \mathcal{M} \cdot \begin{pmatrix} x_1 \\ x_1' \end{pmatrix} , \tag{A.2}$$

where $\mathcal{M} = \begin{pmatrix} A & B \\ C & D \end{pmatrix}$ is the transfer matrix* [91]. Depending on the various optical element, such as lenses, mirrors etc., the transfer matrix assumes different forms; for an overview the, reader is referred to Ref. [91, 93].

In this thesis, the cavity mirrors were constructed from DBR coatings, with an alternating stack of high- and low index materials. Therefore, the remaining of this section concerns the propagation of light between two different materials with different refractive indices. The forward ($E^+$) - and backward ($E^+$) propagation wave in the two different

*In the literature, this matrix is often referred to as the $ABCD$ matrix [93].

layers, labelled $j$ and $j+1$, are related via [85, 488]

$$\begin{pmatrix} E_{j+1}^{+} \\ E_{j+1}^{-} \end{pmatrix} = \mathcal{M} \cdot \begin{pmatrix} E_{j}^{+} \\ E_{j}^{-} \end{pmatrix} . \tag{A.3}$$

A plane wave exiting layer $j$ with refractive index $n_j$ is described by the following transfer matrix

$$T_j = \begin{pmatrix} 1 & 1 \\ n_j & -n_j \end{pmatrix} . \tag{A.4}$$

By symmetry, the transfer matrix for entering layer $j$ is given by the inverse $T_j^{-1}$. Consequently, the transfer from layer $j$ to layer $j+1$ is thus described by [85]

$$T_{j+1}^{-1} T_j = \begin{pmatrix} \frac{n_j + n_{j+1}}{2n_j} & \frac{n_j - n_{j+1}}{2n_j} \\ \frac{n_j - n_{j+1}}{2n_j} & \frac{n_j + n_{j+1}}{2n_j} \end{pmatrix} = \frac{1}{t_{j\to j+1}} \begin{pmatrix} 1 & r_{j\to j+1} \\ r_{j\to j+1} & 1 \end{pmatrix} , \tag{A.5}$$

where $t_{j\to j+1}$ and $r_{j\to j+1}$ are the transmission and reflection coefficients between the two layers, respectively. For a plane wave with $k = \frac{2\pi}{\lambda}$, the propagation through a layer with thickness $d_j$ and refractive index $n_j$ is described by [488]

$$\mathcal{P} = \begin{pmatrix} e^{ikn_j d_j} & 0 \\ 0 & e^{-ikn_j d_j} \end{pmatrix} . \tag{A.6}$$

By combining the above, the complete transfer through layer $j$ is described by [85]

$$\mathcal{M}_j = T_j^{-1} \mathcal{P}_j T_j = \begin{pmatrix} \cos(kn_j d_j) & \frac{i}{n_j} \cdot \sin(kn_j d_j) \\ in_j \cdot \sin(kn_j d_j) & \cos(kn_j d_j) \end{pmatrix} . \tag{A.7}$$

The transfer matrix describing the propagation through successive layers can readily be obtained by matrix multiplication, i.e.

$$\mathcal{M}_m = T_{\text{sub}}^{-1} \cdot \prod_{j}^{m} \mathcal{M}_j \cdot T_{\text{sub}} . \tag{A.8}$$

The waves entering and exiting the system is related via [85, 488]

$$\begin{pmatrix} 1 \\ r \end{pmatrix} = \begin{pmatrix} \mathcal{M}_{11} & \mathcal{M}_{12} \\ \mathcal{M}_{21} & \mathcal{M}_{22} \end{pmatrix} \cdot \begin{pmatrix} t \\ 0 \end{pmatrix} , \tag{A.9}$$

from which the transmittance $\mathcal{T}$ and reflectance $\mathcal{R}$ can be calculated from

$$\mathcal{T} = |t|^2 = \left|\frac{1}{\mathcal{M}_{11}}\right|^2 \tag{A.10a}$$

$$\mathcal{R} = |r|^2 = \left|\frac{\mathcal{M}_{21}}{\mathcal{M}_{11}}\right|^2 . \tag{A.10b}$$

Following from Eq. A.8, a DBR mirror consisting of $m$ layer pairs can be described by

$$\mathcal{M}_{\mathrm{DBR}} = T_{\mathrm{air}}^{-1} \left(\mathcal{M}_{\mathrm{Ta_2O_5}} \mathcal{M}_{\mathrm{SiO_2}}\right)^m T_{\mathrm{sub}} , \tag{A.11}$$

where $T_{\mathrm{air}}^{-1}$ and $T_{\mathrm{sub}}$ are the matrices for the air and the substrate, respectively.

For the cavity used in the experiments presented in Chapter 4, Chapter 5and Chapter 6, the structure of the top- and bottom mirror were $(n_{\mathrm{L}} \cdot n_{\mathrm{H}})^{14} \cdot n_{\mathrm{H}}$ and $(n_{\mathrm{L}} \cdot n_{\mathrm{H}})^{15} \cdot n_{\mathrm{H}}$, respectively. Here, the subscript H (L) corresponds to the high (low) refractive index material. The full description of this cavity is thus given by

$$\mathcal{M}_{\mathrm{cav}} = T_{\mathrm{sub}}^{-1} \left(\mathcal{M}_{\mathrm{Ta_2O_5}} \mathcal{M}_{\mathrm{SiO_2}}\right)^{14} \mathcal{M}_{\mathrm{air}} \mathcal{M}_{\mathrm{diamond}} \left(\mathcal{M}_{\mathrm{Ta_2O_5}} \mathcal{M}_{\mathrm{SiO_2}}\right)^{15} T_{\mathrm{sub}} . \tag{A.12}$$

Fig. A.1 shows one-dimensional transfer matrix calculations of the resonant wavelength as a function air-gap $t_{\mathrm{a}}$ for different diamond thicknesses $t_{\mathrm{d}}$. Due to the sharp nature of the cavity resonance close to the stopband centre ($\mathcal{Q} \sim 10^5$) and the discrete pixel size ($\delta t_{\mathrm{a}} = 1\,\mathrm{nm}$ and $\delta\lambda = 0.1\,\mathrm{nm}$), the cavity transmission is plotted on a logarithmic scale. The calculations of the cavity-mode structure were obtained using Essential Macleod.

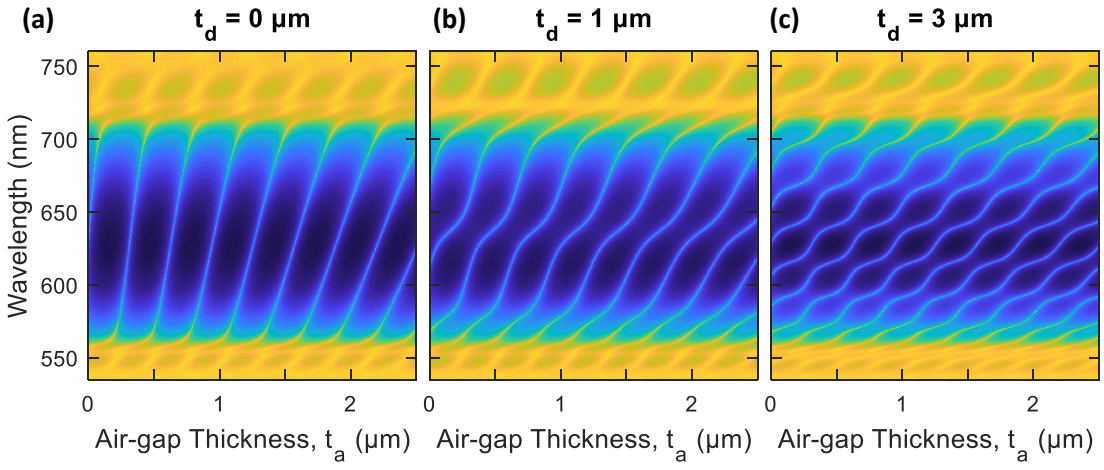


Fig. A.1. One-dimensional transfer matrix calculations of the cavity mode-structure for **(a)** $t_\mathrm{d} = 0\,\mu\mathrm{m}$, **(b)** $t_\mathrm{d} = 1\,\mu\mathrm{m}$ and **(c)** $t_\mathrm{d} = 3\,\mu\mathrm{m}$. To properly capture the cavity resonance, all panel shows the logarithm of the cavity transmission.

APPENDIX B

# Modelling Clipping Losses

In Chapter 4, a reduction in the $\mathcal{Q}$-factor was observed for air-gap $\gtrsim 2.5\mu m$, associated with clipping losses. Beam clipping occurs when the cavity beam waist at the top mirror grows larger than the spherical extend of the curvature of said mirror. In this chapter, a model describing beam clipping will be derived from a Gaussian optics approach. This model accounts for beam clipping on the side of the crater, in addition to a relative tilt angle between the two mirrors. Here, a tilt angle causes a lateral displacement of the cavity mode thereby increasing clipping losses [387].

For a Gaussian beam with beam waist $w$, the radial intensity profile is given by

$$I(r) = I_0 \cdot e^{-2r^2/w^2} \,. \tag{B.1}$$

from which the total intensity can be calculated from

$$I_{\text{total}} = I_0 \cdot \int_{r=0}^{\infty} \int_{\theta=0}^{2\pi} e^{-2r^2/w^2} \, r dr \, d\theta = I_0 \cdot 2\pi \frac{w^2}{4} \,. \tag{B.2}$$

The loss on passing through an aperture of radius $\rho < w$ is given by

$$\begin{aligned} \Delta I &= I_0 \cdot \int_{r=\rho}^{\infty} \int_{\theta=0}^{2\pi} e^{-2r^2/w^2} \, r dr \, d\theta \\ \Delta I &= I_0 \cdot 2\pi \frac{w^2}{4} e^{-2\rho^2/w^2} \,. \end{aligned} \tag{B.3}$$

The losses $\mathcal{L}$ can then be defined as [104, 390].

$$\mathcal{L} \equiv \frac{\Delta I}{I_{\text{total}}} = e^{-2\rho^2/w^2} \,, \tag{B.4}$$

In the presence of tilt, the profile of the curved mirror is described by

$$z = -\left(x^2 + R^2\right)^{\frac{1}{2}} + \theta x\,, \tag{B.5}$$

where $R$ is the radius of the mirror and $\theta$ is the tilt angle. The equation $z^2 = x^2 + R^2$ represents a circle centred at $(x, z) = (0, 0)$. However, the relative tilt displaces the beam to position $x = a$, at which the top and bottom mirrors are parallel. This $x$ position can be found from the condition

$$\left.\frac{dz}{dx}\right|_{x=a} = 0\,. \tag{B.6}$$

From Eq. B.5, one finds

$$\frac{dz}{dx} = -\frac{1}{2}\left(x^2 + R^2\right)^{-\frac{1}{2}} \cdot (2x) + \theta\,, \tag{B.7}$$

which reduces to

$$\begin{aligned}
\frac{a}{\left(a^2 + R^2\right)^{\frac{1}{2}}} &= \theta \\
\theta &= a\left(a^2 + R^2\right)^{-\frac{1}{2}} \\
\theta &= a\left[R^2 \cdot \left(1 + \left(\frac{a}{R}\right)^2\right)\right]^{-\frac{1}{2}} \\
\theta &= \frac{a}{R} \cdot \left(1 - \frac{1}{2}\left(\frac{a}{R}\right)^2 + \mathcal{O}\left[\left(\frac{a}{R}\right)^3\right]\right)\,.
\end{aligned} \tag{B.8}$$

For $a \ll R$, Eq. B.8 reduces to

$$a \simeq R \cdot \theta \tag{B.9}$$

Now, define a new Gaussian beam

$$I_0 \cdot e^{-2r^2/w^2} \rightarrow \tilde{I}(x, y) = I_0 \cdot e^{-2y^2/w^2} \cdot e^{-2(x-a)^2/w^2}\,, \tag{B.10}$$

where the $y$-dependence remain unaltered and the $x$-dependence is displaced by $a$. Expanding $\tilde{I}(x, y)$ yield

$$\tilde{I}(x, y) = I_0 \cdot e^{-2y^2/w^2} \cdot e^{-2x^2/w^2} \cdot e^{4xa/w^2} \cdot e^{-2a^2/w^2}\,, \tag{B.11}$$

which can be transformed to polar coordinates

$$\tilde{I}(r,\theta) = I_0 \cdot e^{-2a^2/w^2} \cdot e^{-2r^2/w^2} \cdot e^{4ar\cos(\theta)/w^2}\,. \tag{B.12}$$

Following from Eq. B.3, the losses on passing the aperture in the presence of tilt, $\Delta\tilde{I}$, is calculated according to

$$\begin{aligned}\Delta\tilde{I} &= \int_{r=\rho}^{\infty}\int_{\theta=0}^{2\pi} \tilde{I}(r,\theta)\, r dr\, d\theta \\ &= I_0 \cdot e^{-2a^2/w^2} \int_{r=\rho}^{\infty} r e^{-2r^2/w^2} \int_{\theta=0}^{2\pi} e^{4ar\cos(\theta)/w^2}\, d\theta\, dr\,.\end{aligned} \tag{B.13}$$

By introducing

$$\int_{\theta=0}^{2\pi} e^{b\cos(\theta)}\, d\theta = 2\pi B_0(b)\,, \tag{B.14}$$

where $B_0(b)$ is the modified Bessel functions of the first kind, Eq. B.13 becomes

$$\Delta\tilde{I} = 2\pi I_0 \cdot e^{-2a^2/w^2} \int_{r=\rho}^{\infty} r e^{-2r^2/w^2} B_0\left(4ar/w^2\right)\, dr\,. \tag{B.15}$$

There exists no analytic solution to Eq. B.15. Therefore, numerical approximations will have to be made. The integrand is largest for $r = \rho$. At this $r$,

$$\frac{4ar}{w^2} = \frac{4a\rho}{w^2} = 4 \cdot \frac{\rho}{w} \cdot \frac{a}{w}\,. \tag{B.16}$$

By using typical experimental parameters,

$$\begin{aligned} w &\simeq 1\,\mu\text{m} \\ \rho &\simeq 2.5\,\mu\text{m} \\ R &\simeq 10\mu\text{m} \\ \theta &\simeq 0.1^\circ = 1.75 \cdot 10^{-3}\ \text{radians}\,, \end{aligned} \tag{B.17}$$

one finds

$$\begin{aligned} a &\simeq 0.017\,\mu\text{m} \\ \frac{4a\rho}{w^2} &\simeq 0.17 \lesssim 1\,. \end{aligned} \tag{B.18}$$

Performing Taylor expansion of $B_0(x)$;

$$B_0(x) = 1 + \frac{x^2}{4} + \frac{x^4}{64} + \mathcal{O}(x^6)\,, \tag{B.19}$$

one finds that Eq. B.15 can be approximated to

$$\begin{aligned}\Delta\tilde{I} &\simeq 2\pi I_0 \cdot \underbrace{e^{-2a^2/w^2}}_{\approx 1} \underbrace{\int_{r=\rho}^{\infty} r e^{-2r^2/w^2} \cdot \left[1 + \frac{1}{4}\left(\frac{4ar}{w^2}\right)^2 + \frac{1}{64}\left(\frac{ar}{w^2}\right)^4\right] dr}_{=\frac{1}{4w^2}\left(w^8+2a^2\left(2\rho^2w^4+w^6\right)+2a^4\left(2\rho^4+2\rho^2w^2+w^4\right)\right)} \\ &\simeq 2\pi I_0 \cdot e^{-2\rho^2/w^2} \cdot \frac{w^2}{4} \cdot \left[1 + 4\left(\frac{a\rho}{w^2}\right)^2 + 4\left(\frac{a\rho}{w^2}\right)^4\right],\end{aligned} \tag{B.20}$$

where, for the last line, the assumption $\rho >> w$ was used. Analogously to Eq. B.4, the losses due to tilt can be calculated from

$$\begin{aligned}\tilde{\mathcal{L}} &= \frac{\Delta\tilde{I}}{I_{\text{total}}} \\ \tilde{\mathcal{L}} &= e^{-2\rho^2/w^2} \cdot \left[1 + 4\left(\frac{a\rho}{w^2}\right)^2 + \mathcal{O}\left(\left(\frac{a\rho}{w^2}\right)^4\right)\right].\end{aligned} \tag{B.21}$$

Table B.1 displays a comparison between the approximation used ($\rho \ll w$) in deriving Eq. B.21 and numerically integration of Eq. B.15 for the experimental parameters listed in Eq. B.17. Finally, defining the diameter of the crater as $D = 2\rho$, reduces Eq. B.15 to

$$\mathcal{L} = e^{-2a^2/w^2} \cdot \left[1 + \left(\frac{aD}{w^2}\right)^2\right], \tag{B.22}$$

as introduced in Section 4.3.1.

Table B.1. Calculating clipping losses from Eq. B.21 compared to numerical integration of Eq. B.15. For small angles, there is an excellent concordance between the approximation and the numerical integration.

| $\theta$ | $a\,(\mu\text{m})$ | $\tilde{\mathcal{L}}$ from Eq. B.21 | $\tilde{\mathcal{L}}$ from Eq. B.15 |
|---|---|---|---|
| 0.0° | 0 | $3.727 \cdot 10^{-6}$ | $3.727 \cdot 10^{-6}$ |
| 0.01° | $1.75 \cdot 10^{-3}$ | $3.727 \cdot 10^{-6}$ | $3.727 \cdot 10^{-6}$ |
| 0.1° | $1.75 \cdot 10^{-2}$ | $3.755 \cdot 10^{-6}$ | $3.755 \cdot 10^{-6}$ |
| 0.5° | 0.087 | $4.432 \cdot 10^{-6}$ | $4.460 \cdot 10^{-6}$ |
| 1° | 0.175 | $6.580 \cdot 10^{-6}$ | $7.065 \cdot 10^{-6}$ |

APPENDIX C

# Incorporate Clipping Losses

This chapter will discuss the incorporation of clipping losses into one-dimensional transfer-matrix simulations. In this thesis, the transfer matrix simulations were performed using Essential Macleod, where losses, such as surface scattering and absorption, can be incorporated via the complex refractive index (Compare Section. 3.3.3). However, clipping losses is an inherently three-dimensional property and can thus not be accounted for using Macleod. To this end, clipping losses have to be incorporated into the model after the one-dimensional transfer-matrix simulations.

For a cavity with finesse $\mathcal{F}$, the $\mathcal{Q}$-factor can be expressed as (Eq. 2.26)

$$\mathcal{Q} = \frac{2L_{\mathrm{cav}}\mathcal{F}}{\lambda}\,, \tag{C.1}$$

where $L_{\mathrm{cav}}$ is the length of the cavity. Introducing the phase length;

$$L_{\mathrm{cav}} = L_{\mathrm{phase}} = L_{\mathrm{air}} + L_{\mathrm{DBR}}^{\mathrm{top}} + L_{\mathrm{DBR}}^{\mathrm{bottom}}\,, \tag{C.2}$$

where $L_{\mathrm{i}} = \frac{c\tau_{\mathrm{i}}}{2}$. Here, $\tau$ is the reflected phase (group) delay, accounting for the field penetration into the DBR mirrors [94]. The phase $\tau$ can be calculated by simulating the reflectivity of each mirror individually. Recall from Section 2.1.1 the finesse is related to the cavity round-trip loss $\mathcal{L}_{\mathrm{tot}}$ via

$$\mathcal{F} = \frac{2\pi}{\mathcal{L}_{\mathrm{tot}}}\,. \tag{C.3}$$

For a perfect cavity, where $\mathcal{L}_{\mathrm{tot}} = \mathcal{T}_{\mathrm{top}} + \mathcal{T}_{\mathrm{bot}}$, combining Eq. C.1 and Eq. C.3 gives

$$\mathcal{Q}_{\mathrm{tot}} = \frac{4\pi L_{\mathrm{phase}}}{\lambda\mathcal{L}_{\mathrm{tot}}}\,. \tag{C.4}$$

Now, consider the result obtained from Macleod. For clarity, rewrite Eq. C.4 as

$$\mathcal{Q}_{\text{Macleod}} = \frac{4\pi L_{\text{phase}}}{\lambda \mathcal{L}_{\text{Macleod}}}\,, \tag{C.5}$$

where $\mathcal{Q}_{\text{Macleod}}$ is the $\mathcal{Q}$-factor obtained from Macleod for losses $\mathcal{L}_{\text{Macleod}}$. From a simple rearrangement of Eq. C.5, one finds

$$\mathcal{L}_{\text{Macleod}} = \frac{4\pi L_{\text{phase}}}{\lambda \mathcal{Q}_{\text{Macleod}}}\,. \tag{C.6}$$

In the presence of beam clipping, the total losses $\mathcal{L}_{\text{tot}} = \mathcal{L}_{\text{Macleod}} + \mathcal{L}_{\text{tilt}}$, where $\mathcal{L}_{\text{tilt}}$ is calculated from Eq. B.22. From this, Eq. C.4 becomes

$$\mathcal{Q}_{\text{tot}} = \frac{4\pi L_{\text{phase}}}{\lambda} \cdot \left( \frac{1}{\mathcal{L}_{\text{Macleod}} + \mathcal{L}_{\text{tilt}}} \right)\,, \tag{C.7}$$

which, by using Eq. C.6 reduces to

$$\mathcal{Q}_{\text{tot}} = \mathcal{Q}_{\text{Macleod}} \cdot \left( \frac{\mathcal{L}_{\text{Macleod}}}{\mathcal{L}_{\text{Macleod}} + \mathcal{L}_{\text{tilt}}} \right)\,. \tag{C.8}$$

To verify the above analysis, Fig. C.1 shows the $\mathcal{Q}$-factor as a function of increasing air-gap for a bare cavity. As expected, there is an excellent agreement between the $\mathcal{Q}$-

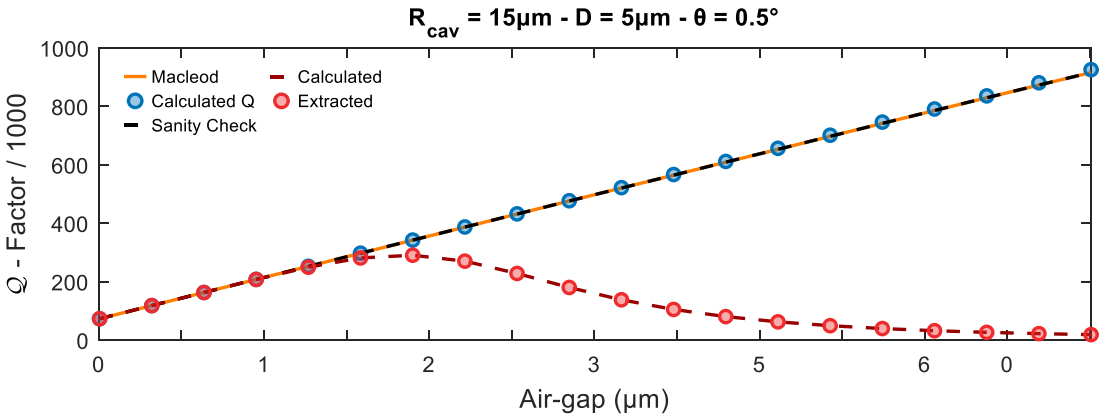


Fig. C.1. Orange line: $\mathcal{Q}$-factor obtained directly from Macleod. Blue points: $\mathcal{Q}$-factor calculated according to Eq. C.5. Black line: Sanity check of Eq. C.8. The calculated $\mathcal{Q}$-factors are in good concordance with the $\mathcal{Q}$-factor obtained directly from Macleod, as expected. Burgundy line and red points: $\mathcal{Q}$-factor in the presence of tilt of $\theta = 0.5\,^{\circ}$ for $R_{\text{cav}} = 15\,\mu\text{m}$ and $D = 5\,\mu\text{m}$ calculated from Eq. C.7 and Eq. C.8, respectively.

factor from Macleod (solid orange line) and the $\mathcal{Q}$-factor calculated from Eq. C.5 and Eq. C.8 (blue points and black dashed line, respectively). The burgundy line and red data points show the calculated $\mathcal{Q}$-factor in the presence of a tilt angle $\theta = 0.5°$ for a cavity with $R_{\mathrm{cav}} = 15\,\mu\mathrm{m}$ and $D = 5\,\mu\mathrm{m}$ calculated according to Eq. C.7 and Eq. C.8, respectively.

APPENDIX D

# A Toy Model Describing $\Delta\mathcal{Q}_0$

In the experiment presented in Chapter 4, the experimentally measured finesse was found to be in good agreement with the finesse expected from simulations [387]. However, the $\mathcal{Q}$-factor on the other hand was lower than expected. Therefore, the term $\Delta\mathcal{Q}_0$ was introduced, rigidly shifting the $\mathcal{Q}$-factor to lower values. The origin of the $\Delta\mathcal{Q}_0$ was attributed to surface waviness [387]. In this chapter, a rudimentary toy model describing the $\Delta\mathcal{Q}_0$ term will be derived. This model is inspired by Ref. [88], where imperfections lead to hybridisation and mixing of the cavity modes (compare Section 2.1.1). In this model, the imperfections and mode mixing are introduced by the waviness (see Section 4.2 and Fig. 4.3).

Consider a cavity mode at frequency $\nu_1$ with linewidth $\Gamma_1$ (Fig. D.1 (a)). The presence of waviness couples the mode to an additional mode at a larger frequency $\nu_2$ with linewidth $\Gamma_2$ as shown in Fig. D.1. Let the frequency spacing $\Delta = \nu_2 - \nu_1$ and $g$ being

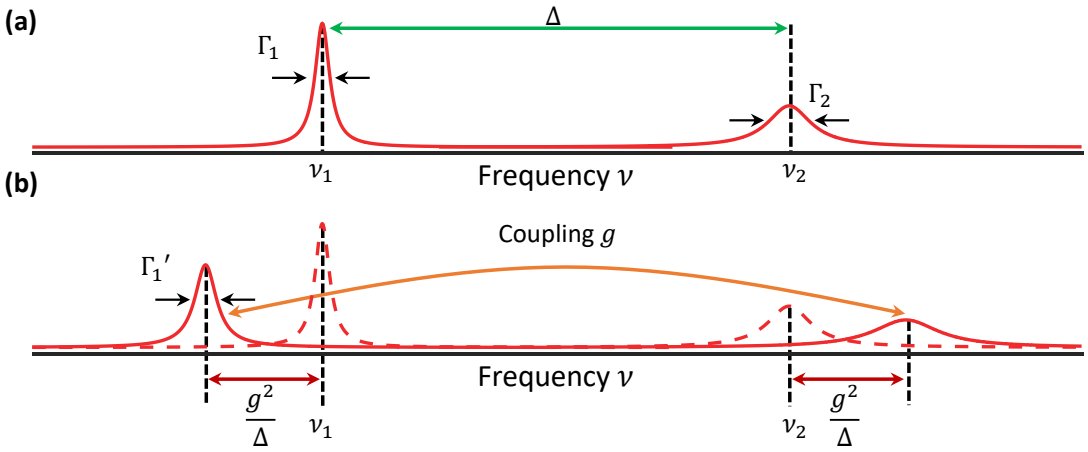


Fig. D.1. Toy model describing the hybridisation of the cavity modes. **(a)** Perfect cavity. **b** The hybridisation causes the cavity modes to repel. For details, see main text.

the coupling strength. For the unperturbed case (Fig. D.1 (a)), the finesse is given by

$$\mathcal{F} = \frac{\Delta}{\Gamma_1}\,. \tag{D.1}$$

The origin of this second mode remains unknown – for simplicity, the second mode will be treated as a fundamental mode. Assuming $g \ll \Delta$, the hybridisation causes the modes to repel, shifting the centre frequency by $\frac{g^2}{\Delta}$, i.e. the spacing of the peaks increases to $\Delta + \frac{2g^2}{\Delta}$ (Fig. D.1 (b)). The low-frequency solution of the coupled system is given by

$$\phi_- = c_1 \cdot \phi_1 + c_2 \cdot \phi_2\,, \tag{D.2}$$

where $|c_1|^2 \simeq 1 - \frac{g^2}{\Delta^2}$ and $|c_2|^2 \simeq \frac{g^2}{\Delta^2}$. As a consequence, the finesse $\mathcal{F}'$ becomes

$$\mathcal{F}' = \frac{\Delta + \frac{2g^2}{\Delta}}{|c_1|^2\Gamma_1 + |c_2|^2\Gamma_2} \tag{D.3}$$

$$= \frac{\Delta \cdot \left(1 + \frac{2g^2}{\Delta^2}\right)}{\left(1 - \frac{g^2}{\Delta^2}\right) \cdot \Gamma_1 + \frac{g^2}{\Delta^2} \cdot \Gamma_2}\,, \tag{D.4}$$

where Eq. D.2 was used. Making the dubious assumption that $\Gamma_2 = 3\Gamma_1$, reduces Eq. D.4 to

$$\mathcal{F}' = \frac{\Delta \cdot \left(1 + \frac{2g^2}{\Delta^2}\right)}{\Gamma_1 \cdot \left(1 + \frac{2g^2}{\Delta^2}\right)} = \frac{\Delta}{\Gamma_1} = \mathcal{F}\,, \tag{D.5}$$

where Eq. D.1 was used. In other words, the finesse remains unaltered.

Next, consider the $\mathcal{Q}$-factor. For the unperturbed cavity, one has

$$\mathcal{Q}_1 = \frac{\nu_1}{\Gamma_1}\,, \tag{D.6}$$

while the mode mixing leads to

$$\mathcal{Q}' = \frac{\nu_1 - \frac{g^2}{\Delta}}{\Gamma_1\left(1 + \frac{2g^2}{\Delta^2}\right)} \tag{D.7}$$

$$= \frac{\nu_1\left(1 - \frac{2g^2}{\nu_1\Delta}\right)}{\Gamma_1\left(1 + \frac{2g^2}{\Delta^2}\right)} \tag{D.8}$$

$$\simeq \frac{\nu_1}{\Gamma_1\left(1 + \frac{2g^2}{\Delta^2}\right)}\,, \tag{D.9}$$

where $\nu_1 \gg g^2$ was used in the last line. Using a Taylor expansion, $\mathcal{Q}'$ reduces to

$$\mathcal{Q}' = \frac{\nu_1}{\Gamma_1} \cdot \left(1 - \frac{2g^2}{\Delta^2}\right) = \mathcal{Q}_1 - \Delta\mathcal{Q}\,, \tag{D.10}$$

where

$$\Delta\mathcal{Q} = Q_1 \cdot \frac{2g^2}{\Delta^2}\,. \tag{D.11}$$

From Fig. 4.8, one finds $\frac{\Delta\mathcal{Q}}{\mathcal{Q}_0} \simeq \frac{1}{2}$, which, from Eq. D.11, implies $g = \frac{1}{2}\Delta$.

To summarise, this model predicts that in the presence of mode mixing under the stringent condition $\Gamma_2 = 3\Gamma_1$, the finesse remains unchanged, while the $\mathcal{Q}$-factor gets reduced by $\Delta\mathcal{Q} = Q_1 \cdot \frac{2g^2}{\Delta^2}$. Qualitatively this toy model agrees with the experimental findings presented in Chapter 4.

APPENDIX E

# Piezo-Calibration Using the Cavity Mode-Structure

In this chapter, the method of using the cavity mode-structure to calibrate the displacement of the z-piezo will be discussed. In the experiment presented in Chapter 4, the cavity length was step-wise reduced by applying an increasingly positive voltage to the z-piezo located beneath the bottom mirror (see Fig. 4.4) [387]. Fig. E.1 show the raw,

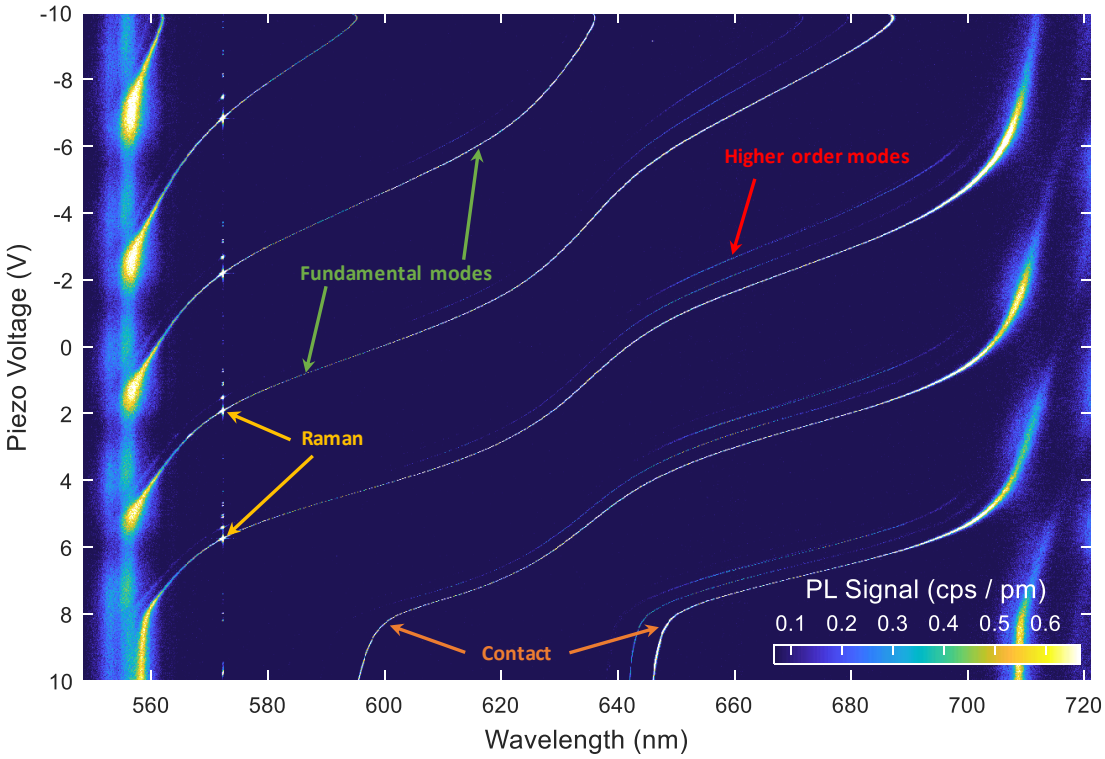


Fig. E.1. Unprocessed cavity mode-structure. In this experiment, the cavity length was made shorter and shorter until the two mirrors were in contact, at which point the resonant wavelength no longer changed with applied piezo voltage, as indicated by the orange arrows.

unprocessed mode-structure. Here, the mirror separation was decreased until the two mirrors were in contact, verified by no longer observing a change in resonant wavelength with increasing voltage. The displacement of the piezo with applied voltage is non-linear. Consequently, the resulting mode-structure exhibits non-linear features, where the relative spacing between the fundamental modes appears to increase with applied voltage.

In a nutshell, the piezo was calibrated by equating the voltage spacing between two fundamental modes to the FSR $= \frac{\lambda}{2}$ (Eq. 5.1) in nanometers. To do so, only the fundamental modes enclosed by the red box in Fig. E.2 (a) were considered, on the account of a sufficiently large signal to noise ratio to easily distinguish the cavity mode from the background in an automated fashion.

To convert from applied piezo voltage to length, the change in length per applied voltage was calculated. As previously mentioned, for a single wavelength, the cavity length changes by $\frac{\lambda}{2}$ from one fundamental mode to the next. Therefore, the conversion factor at the halfway point between the two modes was calculated according to $\frac{\text{FSR}}{\Delta V}$. For example, the two first fundamental modes for $\lambda = 630\,\text{nm}$ occurs for $V = 5.97\,\text{V}$ and $V = 1.77\,\text{V}$ respectively. At this position, a change in voltage of $\Delta V = 4.2\,\text{V}$

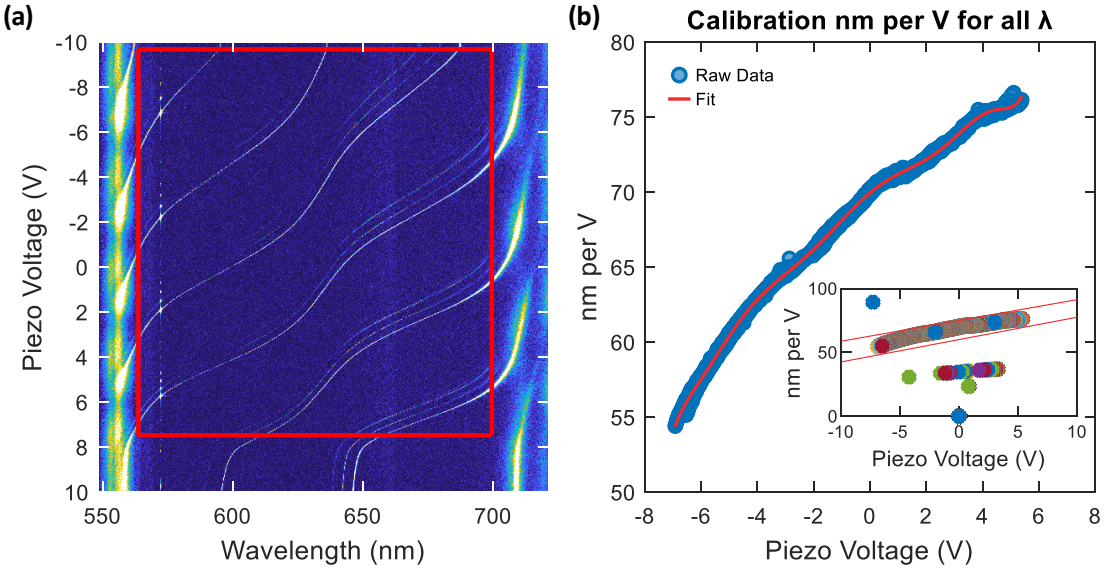


Fig. E.2. **(a)** The piezo was calibrated using the fundamental cavity modes encapsulated by the red square. **(b)** Calibration curve obtained by calculating the change in voltage required to extend the cavity length by one FSR for all wavelengths. The inset shows the few cases where the automated algorithm failed to extract the correct distance. The data were smoothed by fitting a $10^{\text{th}}$ order polynomial (red line). For details, see main text.

was required to change the cavity length by 315 nm. Hence, at the halfway point, i.e. $V = 3.87\,\mathrm{V}$, the piezo moves $75\frac{\mathrm{nm}}{\mathrm{V}}$. Repeating this procedure for each wavelength pixel ($\Delta\lambda = 0.13\,\mathrm{nm}$) for all the fundamental modes produced the curve in Fig. E.2 (b). Here, the inset highlights the few outliers, where the algorithm failed to locate the correct cavity mode. For the remainder of the procedure, only the data points located between

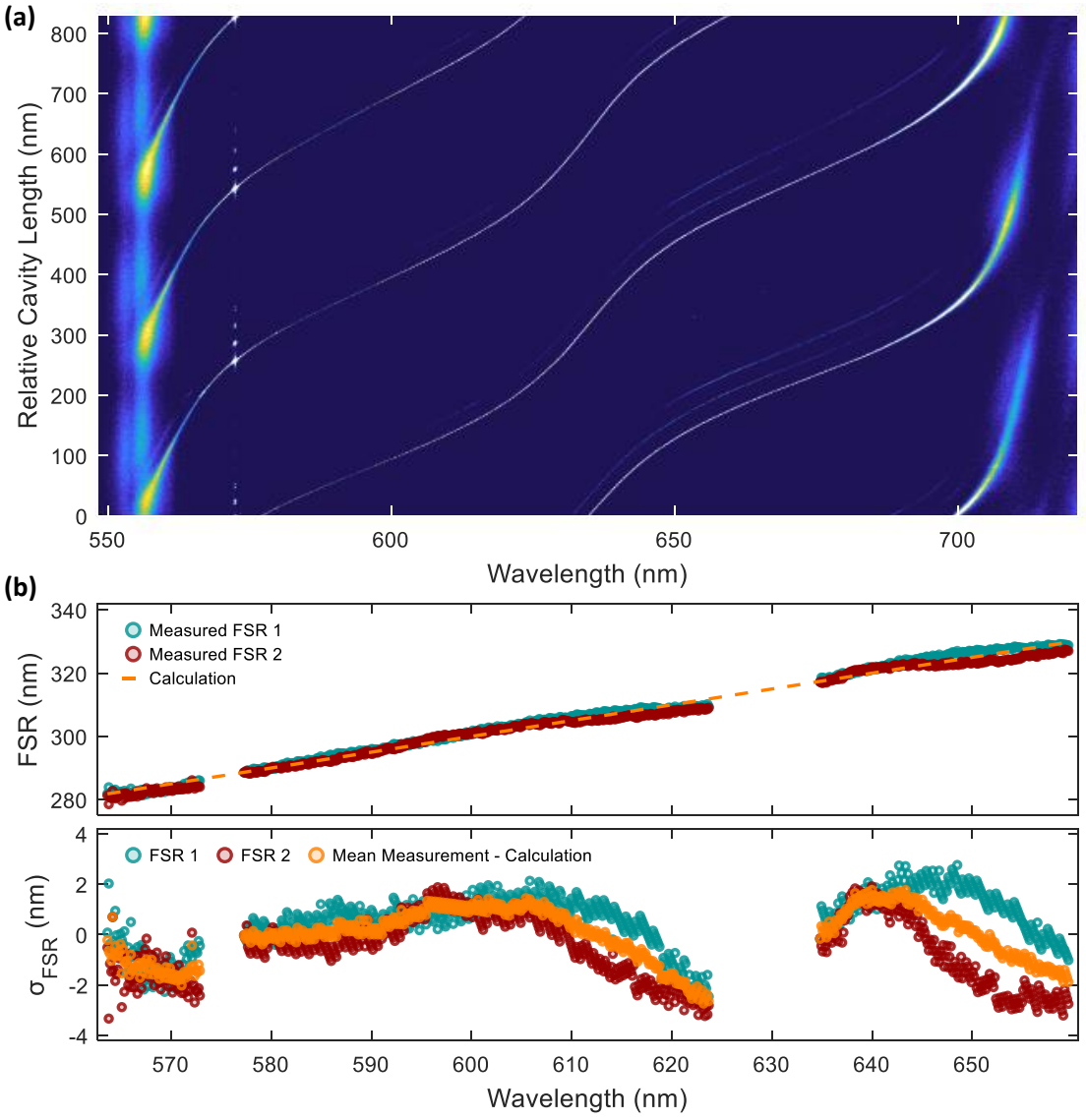


Fig. E.3. **(a)** Calibrated mode structure. **(b)** Top panel: Comparison between the calculated and extracted FSR. Bottom panel: Difference between the measured and calculated FSR, $\sigma_{\mathrm{FSR}} = L_{\mathrm{Meas}} - L_{\mathrm{Theory}}$.

the two red lines were considered. The data were smoothed by fitting a $10^{\text{th}}$ order polynomial indicated by the red line.

The calibrated mode-structure is shown in Fig. E.3 (a), where the MATLAB command *pcolor* was used to account for the non-linear pixel size. The top panel in Fig. E.3 (b) shows a comparison between the calculated (orange) and extracted FSR. The difference between the extracted and measured FSR, $\sigma_{\text{FSR}} = L_{\text{Meas}} - L_{\text{Theory}}$, is plotted in the bottom panel. The orange data points represent the average FSR calculated for the two visible modes for each wavelength. Computing the mean error of $\bar{\sigma}_{\text{FSR}} = -0.0154\,\text{nm}$ and root-mean-square error, $\text{RMS} = 1.055\,\text{nm}$ validates the calibration. The maximum error $|\sigma_{\text{FSR}}(\lambda = 623.167\,\text{nm})| = 2.7346\,\text{nm}$ underestimates the cavity length by only 3 %.

APPENDIX F

# Cavity-Enhanced Detection Efficiency

The experiment presented in Chapter 5 demonstrated cavity-enhanced Raman scattering with a 58.8-fold increase in intensity compared to free-space measurements under likewise identical conditions. The observed intensity enhancement was in good concordance with a theoretical enhancement of 56.8 based on a quantitative model, which will be derived in this chapter. Motivated by Eq. 5.4, the model assumes that the diamond is build of an array of single identical Raman scatters, all emitting at the same wavelength.

### Bare Diamond

Consider a thin diamond membrane bonded to a DBR mirror. An objective lens with numerical aperture NA = 0.4 is used for excitation and collection in a backscattering geometry (Fig. F.1 (a)). For the bare diamond, the detection efficiency, $\eta_0$, can be derived based solely on geometrical arguments; only light emitted into a cone formed by the NA of the objective will be detected:

$$\begin{aligned}\eta_0 &= \frac{1}{2}\cdot(1-\cos(\theta))\times 2 \\ &= \frac{1}{2}\cdot(1-\sqrt{1-\sin^2(\theta)})\times 2 \\ &= (1-\sqrt{1-\mathrm{NA}^2})\,,\end{aligned} \tag{F.1}$$

where the factor of 2 accounts for the light reflected by the DBR mirror and $\mathrm{NA} = n\cdot\sin(\theta)$. A ray of light emitted from inside the diamond at an angle $\theta'$ relative to the diamond surface will be diffracted according to Snell's law: (Fig. F.1 (a))

$$\sin(\theta) = n_\mathrm{d}\cdot\sin(\theta')\,, \tag{F.2}$$

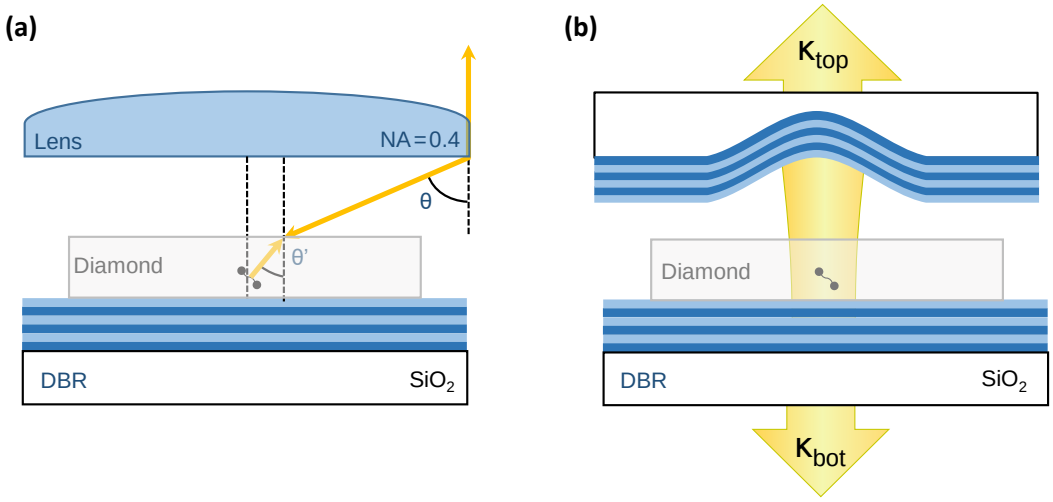


Fig. F.1. Comparison of the detection efficiency for a photon emitted in a bare diamond to a photon emitted inside the cavity. **(a)** For the bare diamond, the detection efficiency is determined by the cone spanned by the NA of the objective lens. **(b)** In a loss-less cavity, the detection efficiency is determined by the ratio of the loss-rate through the top mirror, $\kappa_{\mathrm{top}}$ to that of the bottom mirror $\kappa_{\mathrm{bot}}$.

where $n_{\mathrm{d}} = 2.4$ is the refractive index of diamond. From Eq. F.2, one finds

$$\sin(\theta') = \frac{\mathrm{NA}_0}{n_{\mathrm{d}}} \tag{F.3}$$

where $\mathrm{NA} = n_{\mathrm{d}} \cdot \sin(\theta')$ and $\mathrm{NA}_0$ indicates the NA in vacuum spanned by the objective lens. Combining Eq. F.1 and Eq. F.3, one arrives at

$$\eta_0 = 1 - \sqrt{1 - \left(\frac{\mathrm{NA}_0}{n_{\mathrm{d}}}\right)^2}\,, \tag{F.4}$$

which for $\mathrm{NA} = 0.4$ yield $\eta_0 = 1.39\,\%$.

### Diamond in the Cavity

Consider a Fabry-Perot microcavity, embedded with the same diamond membrane as before. In the cavity, the photons bounce between the mirrors with a probability $\mathcal{T}_{\mathrm{top}}$ ($\mathcal{T}_{\mathrm{bot}}$) to be transmitted through the top (bottom) mirror. Only photons transmitted through the top mirror will reach the detector. Therefore, the detection efficiency for the cavity, $\eta_{\mathrm{cav}}$ is given by

$$\eta_{\mathrm{cav}} = \frac{\kappa_{\mathrm{top}}}{\kappa_{\mathrm{top}} + \kappa_{\mathrm{bot}} + \kappa_{\mathrm{loss}}} \cdot \beta\,, \tag{F.5}$$

where $\kappa_{\mathrm{top(bot)}}$ is the loss-rate through the top (bottom) mirror, $\kappa_{\mathrm{loss}}$ is the cavity round-trip loss-rate and

$$\beta = \frac{F_{\mathrm{P}}}{F_{\mathrm{P}} + 1}\,, \tag{F.6}$$

is the probability of a photon being emitted into the cavity mode. The loss-rate through the top mirror is calculated from

$$\kappa_{\mathrm{top}} = \frac{\mathcal{T}_{\mathrm{top}}}{\mathcal{T}_{\mathrm{top}} + \mathcal{T}_{\mathrm{bot}}} \cdot \kappa_{\mathrm{tot}}\,, \tag{F.7}$$

with $\kappa_{\mathrm{tot}} = \frac{2\pi c}{\mathcal{Q}\lambda}$. From the experiment in Chapter 5, one finds $\mathcal{T}_{\mathrm{top}} = 7\,728\,\mathrm{ppm}$, $\mathcal{T}_{\mathrm{bot}} = 4\,322\,\mathrm{ppm}$ and $\mathcal{Q}_{\mathrm{sim}} = 12\,738$ for $\lambda = 572.67\,\mathrm{nm}$, $\kappa_{\mathrm{top}} = 1.656 \cdot 10^{11}\,\mathrm{s}^{-1}$, $\kappa_{\mathrm{bot}} = 9.525 \cdot 10^{10}\,\mathrm{s}^{-1}$. In the experiment, the total cavity loss rate $\kappa_{\mathrm{exp}} = \kappa_{\mathrm{top}} + \kappa_{\mathrm{bot}} + \kappa_{\mathrm{loss}}$ is extracted from the cavity linewidth

$$\begin{aligned} \kappa_{\mathrm{loss}} &= \kappa_{\mathrm{exp}} - \left(\kappa_{\mathrm{top}} + \kappa_{\mathrm{bot}}\right) \\ \kappa_{\mathrm{loss}} &= \frac{2\pi c}{\lambda} \cdot \left(\frac{1}{\mathcal{Q}_{\mathrm{exp}}} - \frac{1}{\mathcal{Q}_{\mathrm{sim}}}\right)\,, \end{aligned} \tag{F.8}$$

where $\mathcal{Q}_{\mathrm{exp}} = 8\,200$. The experimental Purcell factor were calculated to be $F_{\mathrm{P}} = 4.67$ and thus $\beta = 0.824$. Inserting the numbers yield $\kappa_{\mathrm{loss}} = 1.429 \cdot 10^{11}\,\mathrm{s}^{-1}$ and $\eta_{\mathrm{cav}} = 32.5\,\%$.

### Comparison of the Signal Strength

Assuming an identical pump rate and likewise identical diamond material and detection optics, the ratio of the cavity-enhanced Stokes emission to the free-space Stokes emission is given by

$$\frac{S_{\mathrm{cav}}}{S_0} = F_{\mathrm{P}} \cdot \frac{\eta_{\mathrm{cav}}}{\eta_0}\,. \tag{F.9}$$

Finally, the spectral overlap between the cavity mode and Stokes emission will have to be considered. In the experiment, the Stokes ($\mathcal{Q}_{\mathrm{S}} = 8\,066$) and cavity ($\mathcal{Q}_{\mathrm{cav}} = 8\,200$) exhibit similar linewidths. Only the Raman scatterers close to the resonance contributes, those in the spectral wings do not. Including the spectral dependency of $F_{\mathrm{P}}$, yield

$$\frac{S_{\mathrm{cav}}}{S_0} = F_{\mathrm{P}} \cdot \frac{Q_{\mathrm{S}}}{Q_{\mathrm{S}} + Q_{\mathrm{cav}}} \cdot \frac{\eta_{\mathrm{cav}}}{\eta_0}\,. \tag{F.10}$$

Inserting the numerical values yield $\frac{S_{\mathrm{cav}}}{S_0} = 56.78$, in excellent concordance with the measured value of 58.8.

APPENDIX G

# A Note on $\mathcal{Q}$-Factor and Mirror Parallelity

Recall from Section 4.2 and Fig. 4.4 that a thin layer of indium was used as a spacer between the cavity cage and the holder for the top mirror. Fig. G.1 shows an image of the cavity used in Chapter 5 and Chapter 6. Here, the cavity was illuminated using a LED with $\lambda_{\mathrm{LED}} \simeq 850\,\mathrm{nm}$, for which the cavity is transparent. Replacing the objective lens with a long focal length aspheric lens allows for imaging of the whole mirror. Some details; for this particular top mirror, 56 dimples were fabricated using the aforementioned $CO_2$ laser ablation technique [402]. To minimise the contact area, a circular mesa was etched into the mirror substrate prior to coating [85]. In the current configuration, the diamond was parked under the dimple with coordinates (C,3).

When minimising the separation of two, perfectly parallel mirrors, the diamond mem-

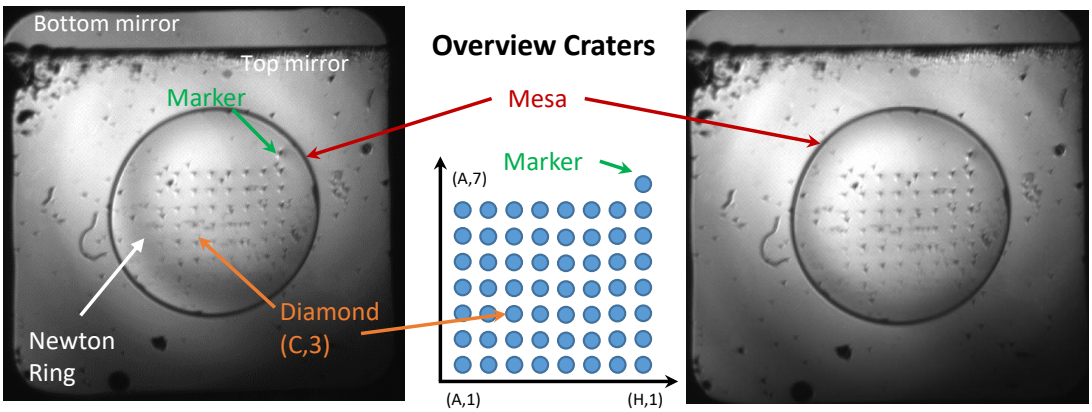


Fig. G.1. Image of the cavity used in Chapter 5 and Chapter 6 under LED illumination with wavelength $\lambda_{\mathrm{LED}} \simeq 850\,\mathrm{nm}$, to which the cavity is transparent. For the top mirror, an array of 56 craters were fabricated on top of a circular mesa. The diamond is parked under the crater with coordinates (C,3). For the left image, the asymmetric pattern of Newton fringes indicates a slight tilt angle. Adjusting the tilt between the two mirrors results in symmetric fringes (rightmost image).

brane ($t_\mathrm{d} \simeq 700\,\mathrm{nm}$) will be the point of contact, provided the mirrors are free of dust and other residuals. However, in the presence of a tilt angle, the two mirrors will go into contact at a different location. The contact point can be determined by locating the centre of the Newton fringes as can be seen in Fig. G.1. To this end, monitoring the point of contact between the two mirrors allows for minimising the tilt angle. In the experiment, this was achieved by carefully tightening the four screws mounting the top mirror to the cage, while monitoring the Newton fringes. The two mirrors are parallel when the fringes are symmetric and centred around the position of the diamond. Applying a small modulation to the cavity length facilitated the observation of the Newton fringes.

The sensitivity on the $\mathcal{Q}$-factor with tilt was first experimentally observed during

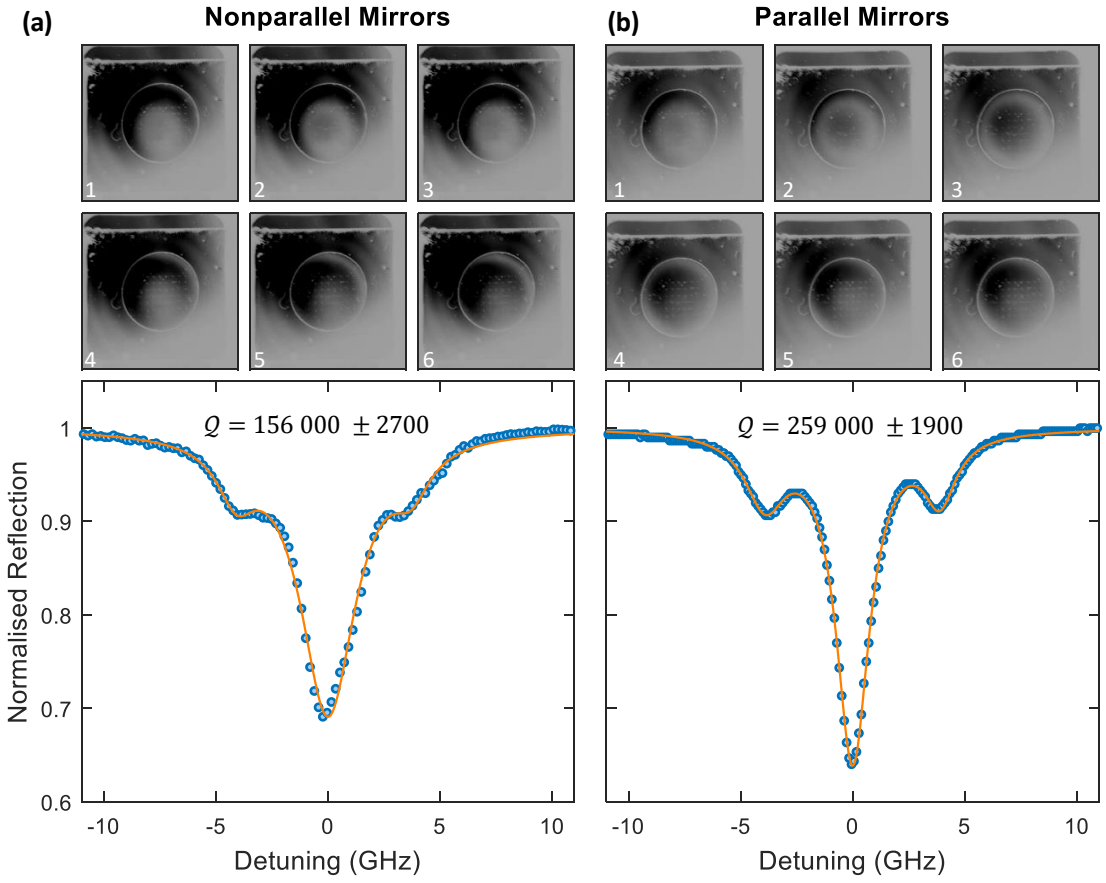


Fig. G.2. **(a)** Top panel: Snapshot of the Newton fringes while modulating the cavity length. The asymmetry and centre of the fringes hint at a small tilt angle between the mirrors. Bottom panel: using the laser sidebands at $\nu_\mathrm{laser} \pm 3.9\,\mathrm{GHz}$ as a frequency ruler yield $\mathcal{Q} = 156\,000$. **(b)** Correcting for the tilt increases the quality factor to $\mathcal{Q} = 259\,000$.

the experiments presented in Chapter 6. Here, the cavity length was large (to establish the double resonance condition), and hence sensitive to small tilt angles. Fig. G.2 shows the reflection from the cavity, where an EOM were used to create sidebands at $\nu_{\text{laser}} \pm 3.9\,\text{GHz}$. The tilt was verified by no longer being able to resolve the laser sidebands. The top panel in Fig. G.2 (a) shows snapshots of the newton fringes while modulating the cavity length. As discussed, the asymmetry and centre of the Newton fringes indicate a tilt. Extracting the cavity linewidth using the sidebands as a frequency rules yield $\mathcal{Q} = 156\,000$. Correcting for the tilt (top panel Fig. G.2 (b)) increases the quality factor to $\mathcal{Q} = 259\,000$.

APPENDIX H

# Calculation of the Raman Lasing Threshold

This chapter aims at deriving the equation for the lasing threshold presented in Chapter 6, by following the approach presented by Checoury *et al.* [370, 489]. Following the notation introduced in Chapter 6, consider a doubly-resonant system ($\omega_\mathrm{p} = \omega_\mathrm{pump} = \omega_\mathrm{p}^\mathrm{cav}$ and $\omega_\mathrm{S} = \omega_\mathrm{R} = \omega_\mathrm{S}^\mathrm{cav}$). In the following, the "cav" superscript will be omitted for concise notation and clarity. The spacing between the cavity modes is given by $\omega_\mathrm{S} = \omega_\mathrm{p} - \Delta\omega_\mathrm{R}$, where $\Delta\omega_\mathrm{R}$ is the Raman shift. The coupled mode equations linking the mean Stokes ($N_\mathrm{S}$) and pump photon numbers ($N_\mathrm{p}$) are given by:

$$\frac{\mathrm{d}N_\mathrm{p}}{\mathrm{d}t} = -\frac{N_\mathrm{p}}{\tau_\mathrm{p}} - \gamma\frac{N_\mathrm{p}}{\tau_\mathrm{R}} - (N_\mathrm{S}+1)\cdot\frac{N_\mathrm{p}}{\tau_\mathrm{R}^\mathrm{cav}} + \kappa_\mathrm{in}P_\mathrm{p} \tag{H.1}$$

$$\frac{\mathrm{d}N_\mathrm{S}}{\mathrm{d}t} = -\frac{N_\mathrm{S}}{\tau_\mathrm{S}} + (N_\mathrm{S}+1)\cdot\frac{N_\mathrm{p}}{\tau_\mathrm{R}^\mathrm{cav}}\,. \tag{H.2}$$

Here $\tau_\mathrm{S} = Q_\mathrm{S}/\omega_\mathrm{S}$ and $\tau_\mathrm{p} = Q_\mathrm{p}/\omega_\mathrm{p}$ are the Stokes and pump photon lifetimes. $\gamma$ describes the Raman scattering into modes other than the cavity mode and $\tau_\mathrm{R}$ is a measure for the spontaneous Raman scattering lifetime in bulk. Stimulated ($N_\mathrm{S}$) and spontaneous (+1) Raman scattering into the cavity mode are accelerated over the bulk scattering rate via Purcell enhancement; the corresponding lifetime becomes $\tau_\mathrm{R}^\mathrm{cav}$. The constant $\kappa_\mathrm{in}$ relates the injected pump photon-number per time to the incident pump power $P_\mathrm{p}$.

The spontaneous Raman scattering rate in bulk when the pump mode-polarisation is aligned along the $\langle 110\rangle$ crystallographic axis (Fig. H.1) can be calculated via [369]:

$$\frac{1}{\tau_\mathrm{R}} = \frac{2g_\mathrm{R}^\mathrm{B}c^2\hbar\omega_\mathrm{p}}{3n_\mathrm{p}n_\mathrm{S}V}\cdot M\,. \tag{H.3}$$

Here, $g_\mathrm{R}^\mathrm{B}$ denotes the bulk Raman gain and $V$ the mode volume of a hypothetical large

cavity. $M$ characterises the total number of Raman modes into which the system can radiate in such a large cavity with mode volume $V$ for a frequency band of width $\delta\omega_{\mathrm{R}}$ [489]:

$$M = \frac{V\omega_{\mathrm{S}}^2 n_{\mathrm{S}}^3}{2\pi c^3} \cdot \delta\omega_{\mathrm{R}} \,. \tag{H.4}$$

$\delta\omega_{\mathrm{R}}$ describes the FWHM linewidth of the gain profile of the Raman scattering process. Hence:

$$\frac{1}{\tau_{\mathrm{R}}} = \Gamma_{\mathrm{R}} = \frac{\omega_{\mathrm{S}}^2 n_{\mathrm{S}}^2 g_{\mathrm{R}}^{\mathrm{B}} \hbar\omega_{\mathrm{p}} \delta\omega_{\mathrm{R}}}{3n_{\mathrm{p}}\pi c} \,. \tag{H.5}$$

The cavity enhancement is given by a Lorentzian with amplitude $F_{\mathrm{P}}$ [399]. We approximate the Raman gain-profile with a normalised Lorentzian [369]. We assume that the cavity is resonant with the Raman scattered light $\omega_{\mathrm{S}} = \omega_{\mathrm{R}}$:

$$\frac{1}{\tau_{\mathrm{R}}^{\mathrm{cav}}} = \frac{\omega_{\mathrm{S}}^2 n_{\mathrm{S}}^2 g_{\mathrm{R}}^{\mathrm{B}} \hbar\omega_{\mathrm{p}} \delta\omega_{\mathrm{R}}}{3n_{\mathrm{p}}\pi c} \int_0^\infty \mathrm{d}\omega \times \frac{2}{\pi} \frac{\delta\omega_{\mathrm{R}}}{4(\omega-\omega_{\mathrm{S}})^2 + \delta\omega_{\mathrm{R}}^2} \times F_{\mathrm{P}} \frac{\delta\omega_{\mathrm{S}}^2}{4(\omega-\omega_{\mathrm{S}})^2 + \delta\omega_{\mathrm{S}}^2} \,. \tag{H.6}$$

For $\omega_{\mathrm{S}} \gg \delta\omega_{\mathrm{S}}$, $\delta\omega_{\mathrm{R}}$ the integrand is close to 0 for $\omega = 0$, so the lower limit of the integral can be extended to negative infinity to obtain an analytical solution:

$$\frac{1}{\tau_{\mathrm{R}}^{\mathrm{cav}}} = \Gamma_{\mathrm{R}}^{\mathrm{cav}} = \frac{\omega_{\mathrm{S}}^2 n_{\mathrm{S}}^2 g_{\mathrm{R}}^{\mathrm{B}} \hbar\omega_{\mathrm{p}} \delta\omega_{\mathrm{R}}}{3n_{\mathrm{p}}\pi c} \cdot \frac{F_{\mathrm{P}}\delta\omega_{\mathrm{S}}}{\delta\omega_{\mathrm{R}} + \delta\omega_{\mathrm{S}}} \,. \tag{H.7}$$

The Purcell enhancement of the system is given by:

$$\frac{\Gamma_{\mathrm{R}}^{\mathrm{cav}}}{\Gamma_{\mathrm{R}}} = F_{\mathrm{P}} \cdot \frac{\delta\omega_{\mathrm{S}}}{\delta\omega_{\mathrm{R}} + \delta\omega_{\mathrm{S}}}. \tag{H.8}$$

This equation resembles the expression for Purcell enhancement of a two-level emitter in a regime in which the linewidth of the cavity and a coupled emitter are comparable [126, 423, 490–492]:

$$\frac{\Gamma_{\mathrm{R}}^{\mathrm{cav}}}{\Gamma_{\mathrm{R}}} = \frac{3}{4\pi^2} \cdot \left(\frac{\lambda_{\mathrm{S}}^{\mathrm{cav}}}{n_{\mathrm{S}}}\right)^3 \cdot \frac{1}{V_{\mathrm{R}}} \frac{Q_{\mathrm{S}} Q_{\mathrm{R}}}{Q_{\mathrm{S}} + Q_{\mathrm{R}}} \,. \tag{H.9}$$

The lasing threshold power in the steady state can be calculated from:

$$\Gamma_{\mathrm{R}}^{\mathrm{cav}} N_{\mathrm{p}}(N_{\mathrm{S}}+1) = \frac{N_{\mathrm{S}}}{\tau_{\mathrm{S}}} \,. \tag{H.10}$$

Using Eq. H.1 and Eq. H.2,

$$\kappa_{\mathrm{in}} P_{\mathrm{p}} = \frac{N_{\mathrm{S}}}{\tau_{\mathrm{S}}} \cdot \left( \frac{1}{\Gamma_{\mathrm{R}}^{\mathrm{cav}}(N_{\mathrm{S}}+1)} \cdot \left( \frac{1}{\tau_{\mathrm{p}}} + \frac{\gamma}{\tau_{\mathrm{R}}} \right) + 1 \right) \,. \tag{H.11}$$

Taking into account $N_\mathrm{S} \gg 1$ and $\frac{1}{\tau_\mathrm{p}} \gg \frac{1}{\tau_\mathrm{R}}$:

$$\kappa_\mathrm{in} P_\mathrm{p} = \frac{1}{\tau_\mathrm{S}\tau_\mathrm{p}\Gamma_\mathrm{R}^\mathrm{cav}} \,. \tag{H.12}$$

With $\kappa_\mathrm{in} = \eta/(\hbar\omega_\mathrm{p})$:

$$\frac{\eta}{\hbar\omega_\mathrm{p}} \cdot P_\mathrm{p} = \frac{\omega_\mathrm{S}\omega_\mathrm{p}}{Q_\mathrm{S}Q_\mathrm{p}} \cdot \frac{n_\mathrm{S}n_\mathrm{p}V_\mathrm{R}}{2\hbar\omega_\mathrm{p}c^2 g_\mathrm{R}^\mathrm{B}} \cdot \frac{Q_\mathrm{S}+Q_\mathrm{R}}{Q_\mathrm{S}} \,, \tag{H.13}$$

one obtains the result for the lasing threshold:

$$P_\mathrm{p} = \frac{1}{\eta} \cdot \frac{2n_\mathrm{S}n_\mathrm{p}\pi^2}{\lambda_\mathrm{S}^\mathrm{cav}\lambda_\mathrm{p}^\mathrm{cav} g_\mathrm{R}^\mathrm{B}} \cdot \frac{V_\mathrm{R}(Q_\mathrm{S}+Q_\mathrm{R})}{Q_\mathrm{S}^2 Q_\mathrm{p}} \,. \tag{H.14}$$

Using the experimental values summarised in Table H.1 yield $P_\mathrm{th} = 187.5\,\mathrm{mW}$ as stated in Chapter 6. Fig. H.1 (b) evaluates the lasing threshold as a function of $g_\mathrm{R}^\mathrm{B}$.

Table H.1. Summary of experimental parameters

| | | | |
|---|---|---|---|
| $\lambda_\mathrm{p}^\mathrm{cav}$ | 634.57 nm | $\lambda_\mathrm{S}^\mathrm{cav}$ | 693.13 nm |
| $n_\mathrm{p}$ | 2.4 | $n_\mathrm{S}$ | 2.4 |
| $Q_\mathrm{p}$ | $297\,000 \pm 500$ | $Q_\mathrm{S}$ | $6\,650 \pm 50$ |
| $Q_\mathrm{R}$ | $8\,960 \pm 290$ | $g_\mathrm{R}^\mathrm{B}$ | $\sim 40\,\mathrm{cm/GW}$ [449] |
| $\eta$ | 0.45 | $V_\mathrm{R}$ | $109.85\,\mu\mathrm{m}^3$ |

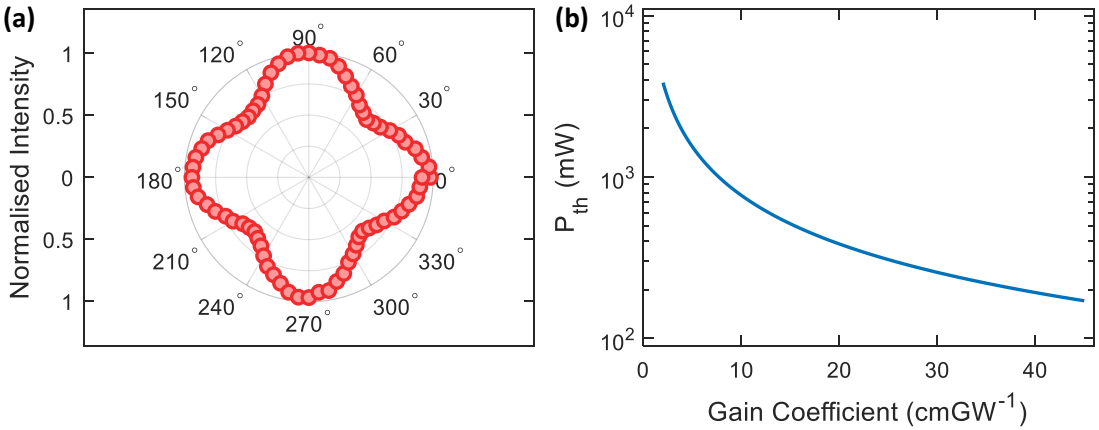


Fig. H.1. **(a)** Polarised Raman spectra obtained by rotating a $\frac{\lambda}{2}$-plate in front of the objective lens. From the angular dependence, one finds $\frac{I_\mathrm{min}}{I_\mathrm{max}} = 0.61$. **(b)** Calculation of the lasing threshold as a function of the bulk Raman gain coefficient $g_\mathrm{R}^\mathrm{B}$.

APPENDIX I

# Inhomogeneous Broadening of NV Centres under Resonant Drive

This chapter derives the model used to disentangle inhomogeneous broadening from power broadening presented in Section 7.4.4. In this model, the NV centre is simplified as a two-level system, with ground- and excited state $|1\rangle$ and $|2\rangle$, respectively (Fig. I.1). Furthermore, for simplicity, the model assumes Lorentzian spectral diffusion.

The probability of an emitter being at frequency $f_0$ is given by the normalised Lorentzian $P(f_0) = L(f_0)$:

$$L(f_0 - f_c, \Gamma) = \frac{1}{\pi} \frac{\Gamma/2}{(f_0 - f_c)^2 + \left(\Gamma/2\right)^2}\,, \tag{I.1}$$

where $\Gamma$ is the full width at half maximum (FWHM) and $\int_{-\infty}^{\infty} L(f, \Gamma)\, df = 1$.

Consider a 2-level system driven by a laser at frequency $f_\mathrm{L}$ with excited state population $\rho_{22}(\delta, \Omega)$ where $\delta = f_\mathrm{L} - f_0$ is the detuning and $\Omega = \sqrt{c \cdot P}$ is the Rabi frequency. Here $c$ is the experimentally effective coupling strength and $P$ is the laser power. For simplicity, this can be written as $\rho_{22}(\delta) = \rho_{22}(f_\mathrm{L} - f_0)$. The experimentally measured line shape $C(f_\mathrm{L})$ is given by the convolution between $L$ and $\rho_{22}$:

$$C(f_\mathrm{L}) = \int \rho_{22}(f_\mathrm{L} - f_0) \cdot P(f_0)\, df_0\,. \tag{I.2}$$

Defining

$$\begin{aligned} \tilde{f} &= f_0 - f_c \\ f &= f_L - f_c \\ d\tilde{f} &= df_0 \\ f_\mathrm{L} - f_0 &= (f + f_c) - (\tilde{f} + f_c) = f - \tilde{f} \end{aligned} \tag{I.3}$$

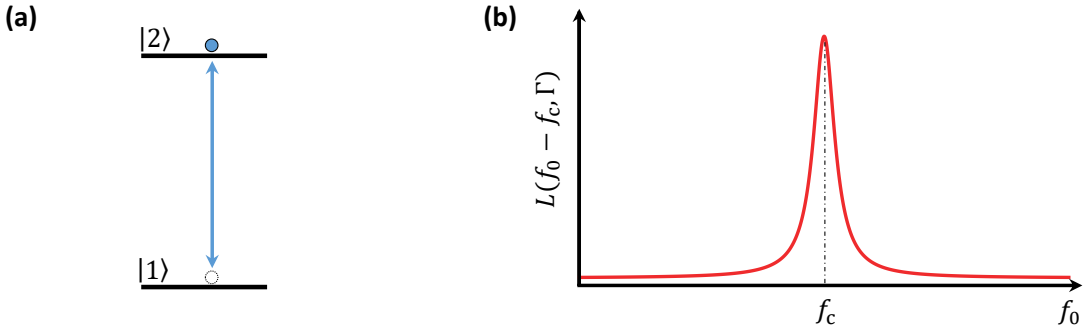


Fig. I.1. **(a)** 2-level structure in the single excitation picture, where the ground and excited state are denoted by $|1\rangle$ and $|2\rangle$, respectively. **(b)** The probability of emitter frequency being $f_0$ is given by the normalised Lorentzian function $L(f_0 - f_c, \Gamma)$, where $f_c$ is the centre frequency.

simplifies Eq. I.2 to

$$C(f) = \int_{-\infty}^{\infty} \rho_{22}(f - \tilde{f}) \cdot P(\tilde{f})\, d\tilde{f}\,, \tag{I.4}$$

where $P(\tilde{f}) = \frac{1}{\pi} \frac{\Gamma/2}{\tilde{f}^2 + (\Gamma/2)^2}$ according to Eq. I.1, i.e.

$$C(f) = \int_{-\infty}^{\infty} \rho_{22}(f - \tilde{f}) \cdot L(\tilde{f}, \Gamma)\, d\tilde{f}\,. \tag{I.5}$$

For a 2-level system, one has [4]

$$\rho_{22} = \frac{\Omega^2/4}{(\omega - \omega_0)^2 + \gamma_{\mathrm{sp}}^2 + \Omega^2/2}\,, \tag{I.6}$$

where $\omega_0 = 2\pi f_0$ and $\omega = 2\pi f$. However, in Ref. [4] the rate of spontaneous emission is defined as $2\gamma_{\mathrm{sp}}$ rather than the more familiar $\gamma$. Therefore, Eq. I.6 becomes

$$\rho_{22} = \frac{(\Omega/2)^2}{4\pi^2(f - f_0)^2 + (\gamma/2)^2 + \Omega^2/2}\,. \tag{I.7}$$

For small $\Omega$, one finds FWHM $= \gamma$. However, for large $\Omega$, one finds FWHM $= \sqrt{\gamma^2 + 2\Omega^2}$, i.e. power broadening of the linewidth.

First, consider the scenario where $\Omega$ is small:

$$\rho_{22} \simeq \frac{(\Omega/2)^2}{4\pi^2(f - f_0)^2 + (\gamma/2)^2} = \frac{(\Omega/4\pi)^2}{(f - f_0)^2 + (\gamma/4\pi)^2}\,. \tag{I.8}$$

For $f = f_0$ this reduces to $\rho_{22} \simeq (\frac{\Omega}{\gamma})^2$, i.e. $\rho_{22} \propto \Omega^2 \propto$ intensity, i.e. a linear dependence

between power and the measured countrate. In the case of small $\Omega$, substituting the expression for $\rho_{22}$ into Eq. I.5 yields

$$\begin{aligned} C(f) &= \int_{-\infty}^{\infty} \frac{(\Omega/4\pi)^2}{(f-f_0)^2 + (\gamma/4\pi)^2} \cdot L(\tilde{f}, \Gamma)\, d\tilde{f} \\ &= \left(\frac{\Omega}{4\pi}\right)^2 \frac{\pi}{\gamma/4\pi} \int_{-\infty}^{\infty} \frac{1}{\pi} \frac{\gamma/4\pi}{(f-f_0)^2 + (\gamma/4\pi)^2} \cdot L(\tilde{f}, \Gamma)\, d\tilde{f} \\ C(f) &= \frac{\Omega^2}{4\gamma} \int_{-\infty}^{\infty} L(f-\tilde{f}, \gamma/4\pi) \cdot L(\tilde{f}, \Gamma)\, d\tilde{f}\,, \end{aligned} \tag{I.9}$$

where in the last step Eq. I.2 was used. Recall that

$$\begin{aligned} \int_{-\infty}^{\infty} L(x-y, a) \cdot L(y, b)\, dy &= \frac{2(a+b)}{\pi\left(4x^2 + (a+b)^2\right)} \\ &= \frac{1}{\pi} \cdot \frac{(a+b)/2}{x^2 + \left((a+b)/2\right)^2} \\ &= L(x, a+b) \\ \therefore L(a+b) &= L(a) \otimes L(b)\,. \end{aligned} \tag{I.10}$$

For low powers,

$$C(f) = \frac{\Omega^2}{4\gamma} \cdot L(f, \gamma/2\pi + \Gamma). \tag{I.11}$$

Using $L(0, a) = \frac{2}{\pi a}$, one finds that on resonance (i.e. $f = 0$):

$$C(0) = \frac{\Omega^2}{4\gamma} \cdot \frac{2}{\pi(\gamma/2\pi + \Gamma)} = \frac{1}{2\pi} \cdot \frac{\Omega^2}{(\gamma^2/2\pi + \gamma\Gamma)}. \tag{I.12}$$

In the absence of inhomogeneous broadening ($\Gamma = 0$),

$$C(0) = \frac{1}{2\pi} \cdot \left(\frac{\Omega}{\gamma}\right)^2. \tag{I.13}$$

In the presence of inhomogeneous broadening

$$C(0) = \frac{1}{2\pi} \cdot \frac{\Omega^2}{(\gamma^2/2\pi + \gamma\Gamma)}\,, \tag{I.14}$$

which for $\Gamma \gg \gamma$ reduces to

$$C(0) = \frac{1}{2\pi} \cdot \frac{\Omega^2}{\gamma\Gamma} = \frac{\gamma}{2\pi\Gamma} \cdot \left(\frac{\Omega}{\gamma}\right)^2 . \tag{I.15}$$

By comparing Eq. I.14 to Eq. I.15, it is apparent that the presence of inhomogeneous broadening reduces the signal $C(f)$ by a factor

$$\frac{\gamma}{2\pi\Gamma} = \frac{\gamma/2\pi}{\Gamma} . \tag{I.16}$$

Next, consider a general case:

$$\rho_{22} = \left(\frac{1}{2\pi}\right)^2 \cdot \frac{\left(\frac{\Omega}{2}\right)^2}{(f-f_0)^2 + \frac{1}{4} \cdot (\gamma^2 + 2\Omega^2) \cdot \frac{1}{(2\pi)^2}} \tag{I.17}$$

$$\rho_{22} = \frac{\left(\Omega/4\pi\right)^2}{(f-f_0)^2 + \frac{1}{(4\pi)^2} \cdot \left(\gamma^2 + 2\Omega^2\right)} . \tag{I.18}$$

Expressing Eq. I.18 on the form $L(f-f_0, a)$ with $a = \frac{1}{2\pi} \cdot \sqrt{\gamma^2 + 2\Omega^2}$ gives

$$\rho_{22} = \left(\frac{\Omega}{4\pi}\right)^2 \cdot \pi \cdot \frac{4\pi}{\sqrt{\gamma^2 + 2\Omega^2}} \cdot \frac{1}{\pi} \cdot \frac{1/4\pi \cdot \sqrt{\gamma^2 + 2\Omega^2}}{(f-f_0)^2 + \left(\frac{1}{4\pi}\right)^2 \cdot (\gamma^2 + 2\Omega^2)} \tag{I.19}$$

$$\rho_{22} = \frac{\Omega^2}{4\sqrt{\gamma^2 + 2\Omega^2}} \cdot L\left(f - f_0, \frac{1}{2\pi} \cdot \sqrt{\gamma^2 + 2\Omega^2}\right) . \tag{I.20}$$

Substituting Eq. I.20 into Eq. I.5 yields

$$C(f) = \frac{\Omega^2}{4\sqrt{\gamma^2 + 2\Omega^2}} \cdot \int_{-\infty}^{\infty} L\left(f - \tilde{f}, \frac{1}{2\pi}\sqrt{\gamma^2 + 2\Omega^2}\right) L\left(\tilde{f}, \Gamma\right) \, d\tilde{f} , \tag{I.21}$$

which, by using Eq. I.10, reduces to

$$C(f) = \frac{1}{4\pi} \cdot \frac{\Omega^2}{\sqrt{\gamma^2 + 2\Omega^2}} \cdot \frac{\frac{1}{2}\left(\Gamma + \frac{1}{2\pi} \cdot \sqrt{\gamma^2 + 2\Omega^2}\right)}{f^2 + \frac{1}{4} \cdot \left(\Gamma + \frac{1}{2} \cdot \sqrt{\gamma^2 + 2\Omega^2}\right)^2} . \tag{I.22}$$

By writing (Eq. 7.4)

$$\Gamma = \Gamma_{\text{in}} + \frac{\gamma^2 + 2\Omega^2}{2\pi} \tag{I.23}$$

reduces Eq. I.22 to

$$C(f) = \frac{1}{4\pi} \cdot \frac{\Omega^2}{\sqrt{\gamma^2 + 2\Omega^2}} \cdot \frac{\frac{1}{2}\Gamma}{f^2 + \left(\frac{1}{2}\Gamma\right)^2}\,, \tag{I.24}$$

as defined in Eq. 7.3.

On resonance

$$C(0) = \frac{1}{2\pi} \cdot \frac{\Omega^2}{\sqrt{\gamma^2 + 2\Omega^2}} \cdot \frac{1}{\Gamma + \frac{1}{2\pi} \cdot \sqrt{\gamma^2 + 2\Omega^2}}\,, \tag{I.25}$$

which for $\Omega \gg \gamma, \Gamma$ reduces to

$$C(0) \to \frac{1}{2\pi} \cdot \frac{\Omega^2}{\sqrt{2}\Omega} \cdot \frac{2\pi}{\sqrt{2}\Omega} = \frac{1}{2} \tag{I.26}$$

as expected. Furthermore, for $\Gamma \ll \gamma, \Omega$ one finds

$$C(0) \to \frac{1}{2\pi} \frac{\Omega^2}{\sqrt{\gamma^2 + 2\Omega^2}} \cdot \frac{1}{\frac{1}{2\pi}\sqrt{\gamma^2 + 2\Omega^2}} = \frac{\Omega^2}{\gamma^2 + 2\Omega^2} \tag{I.27}$$

as expected. However, for low excitation power $\Omega \ll \gamma$ and $\Gamma \gg \Omega, \gamma$

$$C(0) = \frac{1}{2\pi} \cdot \frac{\Omega^2}{\gamma} \cdot \frac{1}{\Gamma}\,, \tag{I.28}$$

i.e. $C(0) \propto \Omega^2 \propto P$. For large power, $\Gamma \gg \Omega \gg \gamma$

$$\begin{aligned} C(0) &= \frac{1}{2\pi} \cdot \frac{\Omega^2}{\sqrt{2}\Omega} \cdot \frac{1}{\Gamma} \\ &= \frac{1}{2\sqrt{2}\pi} \cdot \frac{\Omega}{\Gamma}\,, \end{aligned} \tag{I.29}$$

i.e. $C(0) \propto \Omega \propto \sqrt{P}$.

To conclude, Fig. I.2 shows a graphical representation of the derived model. Motivated by the results extracted from Section 7.4.4, Fig. I.2 (a) displays the countrate on resonance ($C(0)$) in the presence of inhomogeneous broadening $\Gamma_{\text{in}} = 50\,\text{MHz}$ and an effective coupling strength $c = 2 \cdot 10^5\,\frac{\text{MHz}^2}{\mu\text{W}}$ and $\gamma = 2\pi \cdot 12.6\,\text{MHz}$. For low- and high excitation power, $C(0) \propto P$ and $C(0) \propto \sqrt{P}$ as predicted by Eq. I.28 and Eq. I.29, respectively. The inset shows the FWHM linewidth $\Gamma$ as a function of excitation power

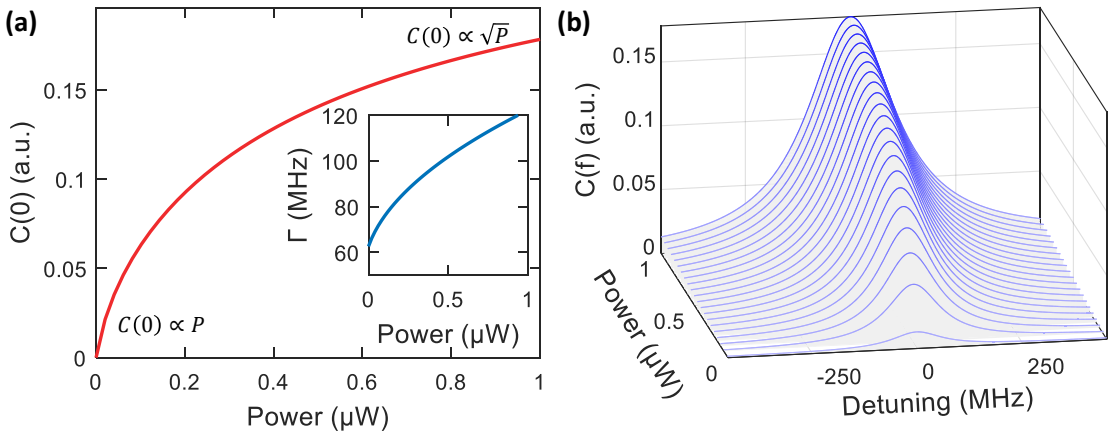


Fig. I.2. Graphical representation of Eq. I.24 for inhomogeneous broadening $\Gamma_{\text{in}} = 50\,\text{MHz}$, effective coupling strength $c = 2 \cdot 10^5\,\frac{\text{MHz}^2}{\mu\text{W}}$ and $\gamma = 2\pi \cdot 12.6\,\text{MHz}$. **(a)** Dependency of the count rate $C(f)$ with excitation power for zero detuning. The inset shows the behaviour of the FWHM linewidth $\Gamma$ with power calculated from Eq. I.23. **(b)** Dependency of the count rate as a function of detuning and power.

calculated from Eq. I.23. Finally, Fig. I.2 (b) shows the behaviour of $C(f)$ as a function of both detuning and excitation power derived from Eq. I.24.

APPENDIX J

# PLE Spectroscopy of NV Centres under Blue Illumination

As discussed in Chapter 7, spectral wandering compromises the achievable two-photon quantum interference. The spectral wandering likely arises due to fluctuating charges in the vicinity of the NV centre, excited by the green laser. This chapter discusses the possibility of illuminating the NV centre with blue light ($\lambda \sim 450\,\mathrm{nm}$) during the photoluminescence excitation (PLE) pulsing sequence. The perhaps rather naïve idea, was that the blue light saturates the charge traps in the close vicinity of the NV centre,

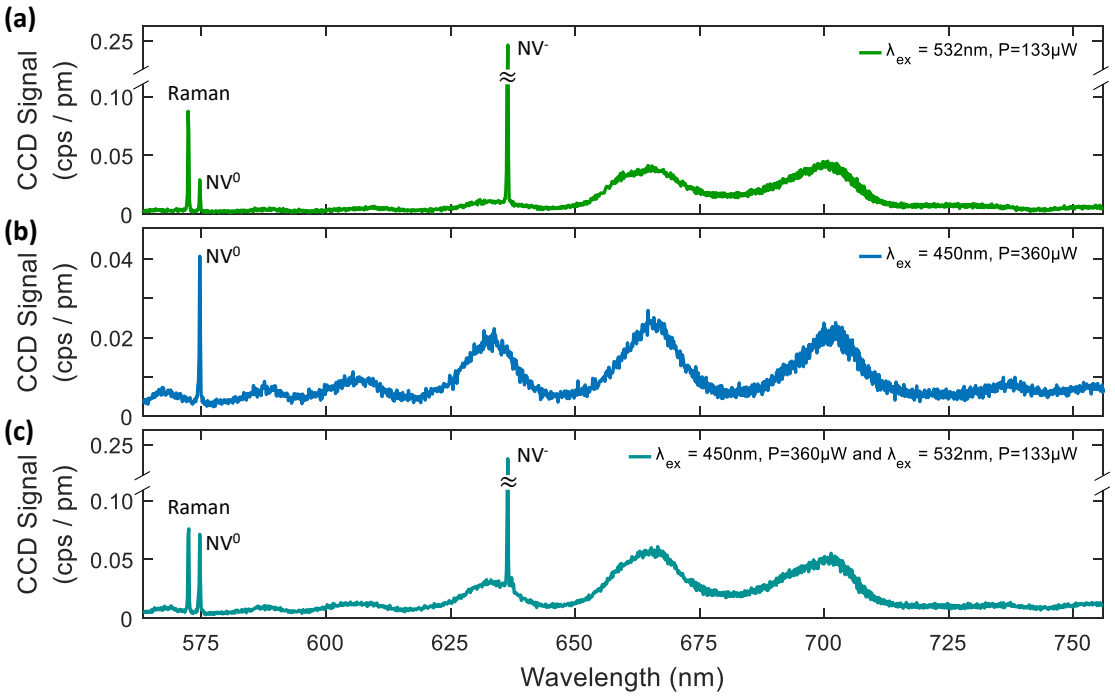


Fig. J.1. PL spectra of the same NV centre under **(a)** $P_{\mathrm{green}} = 133\,\mu\mathrm{W}$ of green light, **(b)** $P_{\mathrm{blue}} = 360\,\mu\mathrm{W}$ of blue light and **(c)** $P_{\mathrm{green}} = 133\,\mu\mathrm{W}$ of green light and $P_{\mathrm{blue}} = 360\,\mu\mathrm{W}$ blue light.

and thus hopefully result in a slower ionisation rate and minimal spectral wandering.

In this experiment, a blue laser diode (Thorlabs PL450B, $\lambda \sim 450\,\mathrm{nm}$) was injected via the same microscope arm as the green laser (Fig. 7.2). Due to the difference in wavelength, and consequently poor AOM efficiency, the blue and green laser were combined using a fibre combiner (Thorlabs RGB46HA) positioned after the green AOM. In other words, the blue laser was continuously kept on during the PLE pulsing sequence, while the green laser was pulsed according to Fig. 7.1.

As a first characterisation, PL spectra were recorded for the same NV centre under green and blue excitation. Exciting the NV centre with green light ($\lambda = 532\,\mathrm{nm}$, $P_{\mathrm{green}} = 133\,\mu\mathrm{W}$) (Fig. J.1 (a)) reveals the sharp $\mathrm{NV}^-$ ZPL at $\sim 637\,\mathrm{nm}$ and a PSB slightly altered by thin-film interference in the diamond membrane. A weak $\mathrm{NV}^0$ ZPL was observed next to the first-order Raman transition. On the contrary, when exciting the NV centre using blue light ($\lambda = 450\,\mathrm{nm}$, $P_{\mathrm{blue}} = 360\,\mu\mathrm{W}$), no $\mathrm{NV}^-$ ZPL was observed (Fig. J.1 (b)). Under blue illumination, an increase in both the $\mathrm{NV}^0$ ZPL and PSB were observed, alongside a reduction in the $\mathrm{NV}^-$ PSB. Finally, in Fig. J.1 (c) the NV centre was simultaneously excited with blue and green light, using the above-mentioned powers. An ever so slight decrease in the $\mathrm{NV}^-$ ZPL intensity was observed, while the $\mathrm{NV}^0$ ZPL intensity roughly equals the sum of the intensities in Fig. J.1 (a) and Fig. J.1 (b). Note that the small discrepancy in intensity could originate from statistical errors. Furthermore, in this experiment, the respective powers of the green and blue lasers were kept fixed, thus increasing the total power density for Fig. J.1 (c). A detailed study, with the total illuminated power kept constant, were not performed here.

From Fig. J.1 (b), it is apparent that $\lambda = 450\,\mathrm{nm}$ predominantly excites $\mathrm{NV}^0$. To characterise this dependency in more detail, PL spectra were recorded for increasing blue excitation power. In this study, the green power was kept constant at $P_{\mathrm{green}} = 133\,\mu\mathrm{W}$. As can be seen in Fig. J.2 (a), increasing the blue excitation power increases the $\mathrm{NV}^0$ ZPL, while a slight variation of the $\mathrm{NV}^-$ PSB was observed. To further quantify this behaviour, high-resolution PL spectra of the ZPL of the two charge states were recorded for each power (Fig. J.2 (b) and (c)). Here, the dashed orange lines indicate a spectral window of $\lambda_{\mathrm{ZPL}} \pm 1\,\mathrm{nm}$. The photon spectral density (SPD) was calculated by integrating the intensity across this spectral window. Fig. J.2 (d) shows the behaviour of the PSD with increasing blue power. As can be seen, the $\mathrm{NV}^0$ ZPL intensity increases with power, while the $\mathrm{NV}^-$ ZPL intensity remains roughly constant, further implying that $\lambda = 450\,\mathrm{nm}$ predominantly excites $\mathrm{NV}^0$. Finally, Fig. J.2 (e) shows the ratio of the PSD of $\mathrm{NV}^-$ ZPL to that of $\mathrm{NV}^0$ with increasing power.

A hand-wavy explanation for the predominate signature of $\mathrm{NV}^0$ under $\lambda = 450\,\mathrm{nm}$

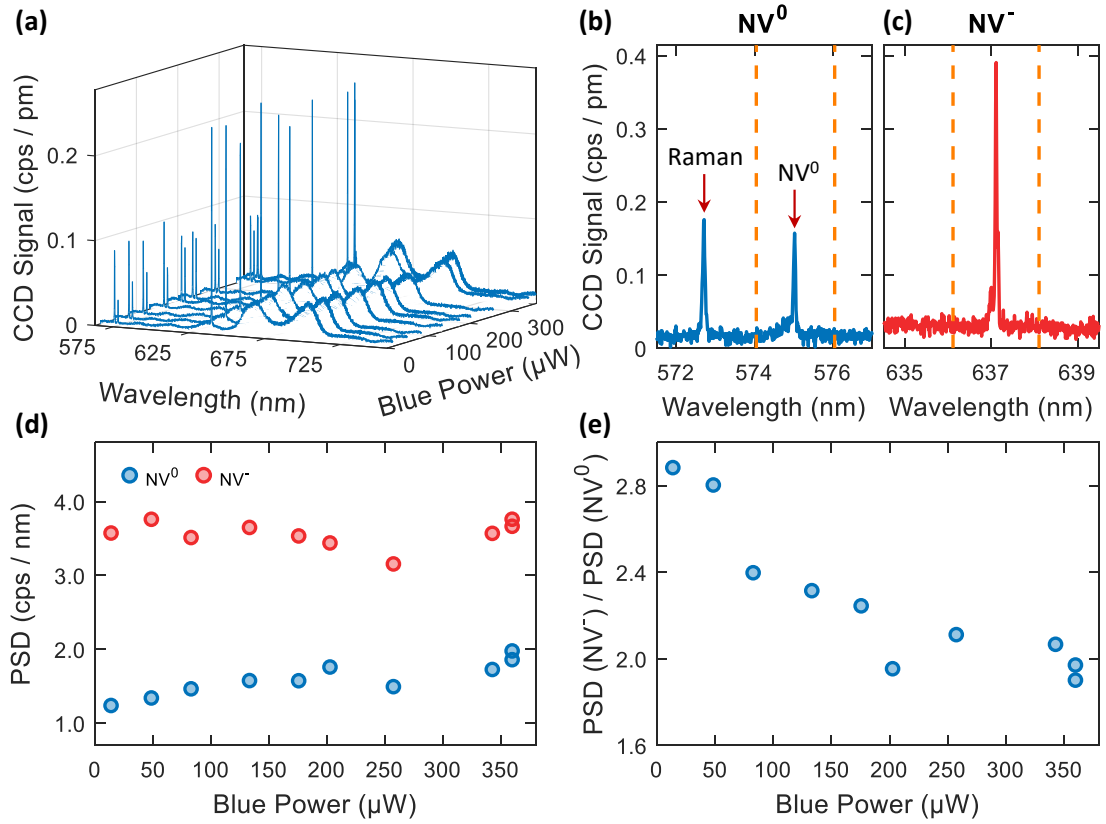


Fig. J.2. **(a)** Photoluminescence spectra under green illumination ($P_{\text{green}} = 133\,\mu\text{W}$) for increasing blue power. **(b)** - **(c)** High-resolution PL spectrum of the $NV^0$ and $NV^-$ ZPL, respectively, for $P_{\text{green}} = 133\,\mu\text{W}$ and $P_{\text{blue}} = 360\,\mu\text{W}$. The dashed orange lines indicate the spectral window $\lambda_{\text{ZPL}} \pm 1\,\text{nm}$. **(d)** Photon spectral density (PSD) of $NV^0$ ZPL (blue) and $NV^-$ ZPL (red) for increasing blue excitation power. The PSD is obtained by integrating the counts between the orange lines in (b) and (c), respectively. **(e)** Ratio of the PSD of $NV^-$ ZPL to that of $NV^0$ for increasing blue power.

illumination goes as follows. The $NV^-$ ground state lies approximately 2.6 eV beneath the conduction band minima (Compare Fig. 2.10). Therefore, under illumination with $\lambda = 450\,\text{nm}$ (2.76 eV), there is a probability of photoionisation directly from the ground state to the conduction band minima, from which the NV centre decays as $NV^0$. The continuous green laser ensures photoionisation back into the negative charge state (Compare Section 2.2.4).

Finally, the attention was guided back to the linewidth measurements. In this study, PLE measurements with increasing blue power were performed on 7 different NV centres on the part of the post-implanted sample transferred to the DBR mirror (Compare Section 7.4). Fig. J.3 summarises the results for the first NV centre. The highlighted NV

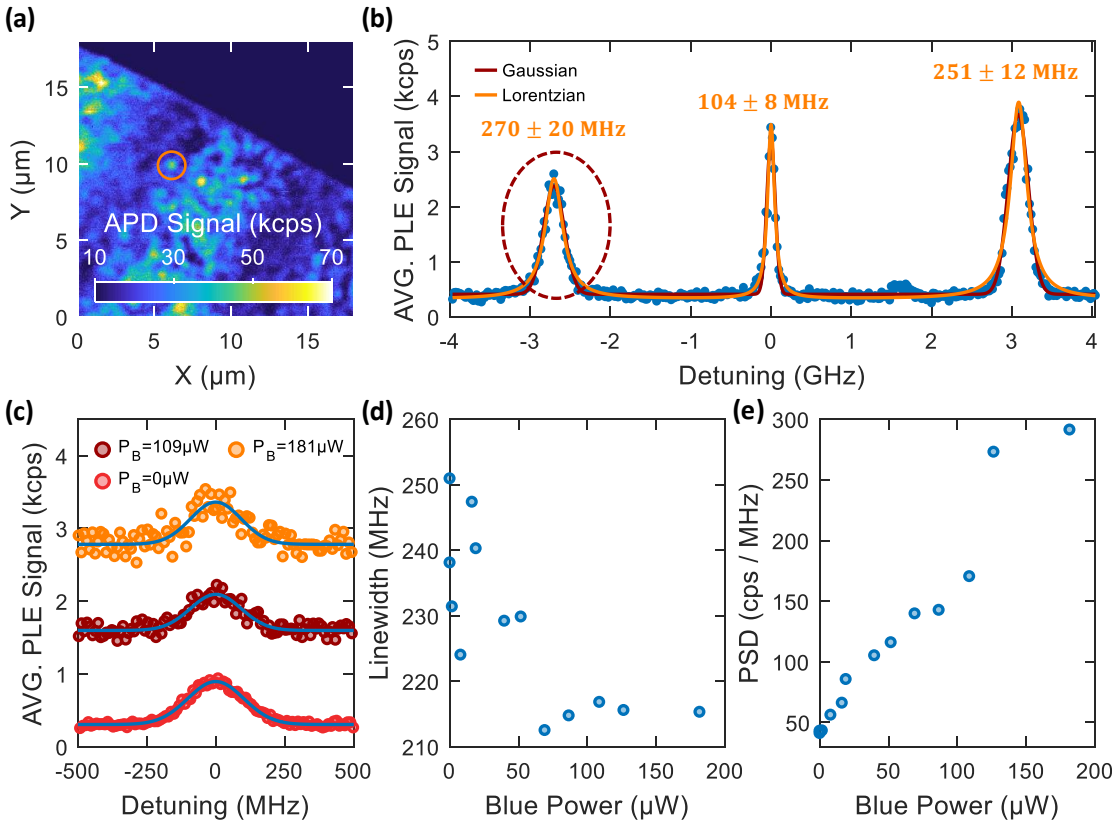


Fig. J.3. First attempt at PLE spectroscopy under blue illumination. **(a)** Confocal scan of diamond on the mirror highlighting the selected NV centre. **(b)** High-power PLE measurement ($P_{\text{green}} = 500\,\mu\text{W}$, $P_{\text{res}} = 131\text{nW}$, compare to Fig. 7.18). The left-most peak was investigated in this experiment. **(c)** PLE measurement with $P_{\text{green}} = 471\,\mu\text{W}$, $P_{\text{res}} = 11.8\text{nW}$ with increasing blue power. **(d)** Measured linewidth as a function of increasing blue power. All linewidths were averaged over 50 scans. A significant narrowing of the optical transition with power is observed. **(e)** Photon spectral density integrated over a spectral window of 1.2 GHz for increasing power. The increased PSD can be attributed to the increase in background observed in (c).

centre revealed three separate lines, where the two outermost lines were assigned to the $E_{\text{x}}$ and $E_{\text{y}}$ transitions of the same NV centre (Compare Section 7.4.4 and Fig. 7.18 *). The left-most, highlighted peak at was investigated in this study. Fig. J.3 (c) shows PLE measurement with increasing blue power, where the resonant power $P_{\text{res}} = 11.8\text{nW}$ and the green $P_{\text{green}} = 471\,\mu\text{W}$ were kept constant. For zero blue power, a Gaussian fit reveals a linewidth $\Delta\nu = 238\,\text{MHz}$. A significant rise in background fluorescence was observed with increasing blue laser power. Recall that the green and blue laser were combined after the green AOM; the blue laser is on continuously, even when collecting the photons

*The narrow central line was the subject of an extensive study with decreasing resonant laser power.

on the single-photon avalanche diode (SPAD, Compare Section 7.1). As can be seen in Fig J.3 (d), a significant linewidth narrowing were observed with increasing blue power. Here, the linewidth of each data-point was extracted from a Gaussian fit averaged over 50 scans. Due to the increase in background counts with blue power, the linewidth could not be reliably extracted for larger ($\gtrsim 181\,\mu W$) blue powers. Calculating the PSD by integrating the averaged counts in a 1.2 GHz wide spectral window further emphasised this problem. A final curiosity, the NV centre corresponding to the central peak in Fig. J.3 (b) bleached during this study. In subsequent PLE measurements, only the two outermost peaks were observed. The origin and time of bleaching remain unknown. Furthermore, this was the only NV centre observed to completely bleach.

The initial test using blue illumination during the PLE pulsing sequence revealed a promising result: a 15 % narrowing of the optical linewidth was observed. However, these results were neither consistent nor conclusive. Fig. J.4 summarises the results obtained from a different NV centre. Note that the selected NV centre exhibited an unusually strong $NV^0$ ZPL line, as can be seen in the PL spectra displayed in Fig. J.4 (b). The red data points in Fig. J.4 (c) show a PLE measurement with $P_{\text{res}} = 41.2\,\text{mW}$ and $P_{\text{green}} = 454\,\mu W$ averaged over 50 scans in the absence of the blue laser. A linewidth of $\Delta\nu = 91.6\,\text{MHz}$ was extracted from a Gaussian fit. As before, introducing the blue laser resulted increased the background fluorescence, as can be seen by the orange data-points. Now, in stark contrast to Fig. J.3 (d), the measured linewidth was found to increase with blue power (Fig. J.4 (d)). Furthermore, the PLE signal was lost in the background noise for much lower laser power, $50\,\mu W$ compared to $\simeq 180\,\mu W$ in Fig. J.3.

To conclude this chapter, the introduction of the blue laser culminated in results unintelligibly distributed over a wide spectrum. As discussed above, the blue laser leads to both narrowing (Fig. J.3 (d)) and broadening (Fig. J.4 (d)). Out of the other five NV centres characterised (not shown here), two showed a narrowing of the ZPL linewidth, while the effect on the remaining three can only be described as inconclusive. Note, that for the two NV centres included here, both the resonant and the green power differed, $P_{\text{res}} = 11.8\text{nW}$, $P_{\text{green}} = 471\,\mu W$ and $P_{\text{res}} = 41.2\,\text{mW}$ and $P_{\text{green}} = 454\,\mu W$ respectively. Furthermore, the linewidth in the absence of the blue laser greatly differed, $\Delta\nu = 238\,\text{MHz}$ compared to $\Delta\nu = 91.6\,\text{MHz}$. A systematic study of the linewidth as a function of $P_{\text{res}}$, $P_{\text{green}}$ and $P_{\text{blue}}$ was beyond the scope of this thesis. Although the sample size presented here is too small to draw a bulletproof conclusion, the initial results are promising. Nevertheless, for future experimental investigation, a laser with $\lambda \gtrsim 500\,\text{nm}$ (2.5 eV) is probably beneficial to avoid direct photoionisation from the $NV^-$ ground state. Furthermore, the observed increase in background fluorescence can be

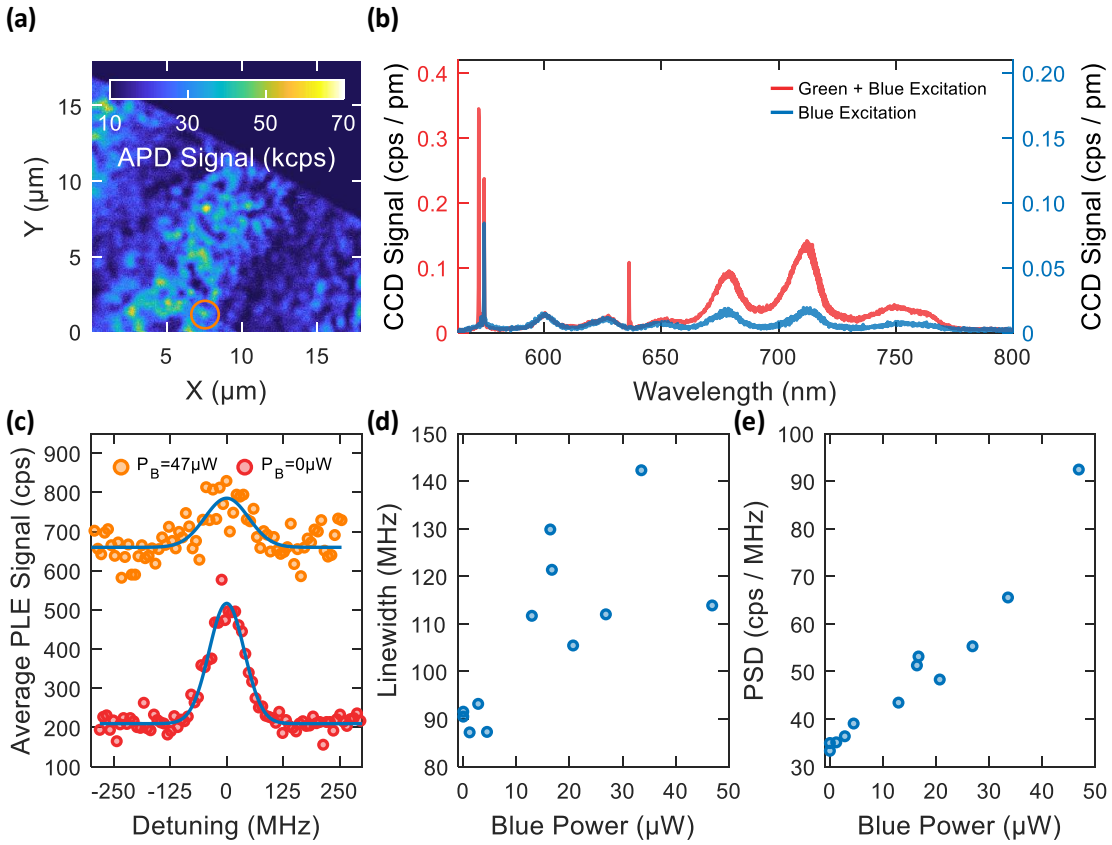


Fig. J.4. Second PLE measurement under blue illumination. **(a)** Confocal scan of diamond on the mirror highlighting the selected NV centre. **(b)** PL spectra of the highlighted NV centre excited with blue and green (red line) and blue only (blue line). The NV centre exhibits an unusually strong $NV^0$ line. **(c)** PLE measurement in the absence of the blue laser (red) and with $P_{\text{blue}} = 47\,\mu\text{W}$ for $P_{\text{res}} = 41.2\,\text{mW}$ and $P_{\text{green}} = 454\,\mu\text{W}$. A Gaussian fit revealed $\Delta\nu = 92\,\text{MHz}$ and $\Delta\nu = 114\,\text{MHz}$. **(d)** Measured linewidth as a function of blue power. Each data point was averaged over 50 scans. **(e)** PSD integrated over a spectral window of 600 MHz with increasing blue power.

mitigated by using an AOM asynchronous to the APD counting window, in a similar fashion to the current green pulse (Compare Fig. 7.1).

APPENDIX K

# Spin-Photon Entanglement

This chapter will briefly introduce spin-photon and spin-spin entanglement protocols. Starting from two spin-photon entangled pairs, remote spin-spin entanglement can be established via two-photon quantum interference of otherwise indistinguishable photons [493, 494], projecting the NV centre spin onto a joint entangled state [85, 495].

Recall from Section 2.2.2 and Section 2.2.5 that the $m_s \pm 1$ spin sub-levels of the ground-state are connected to the $A_{1,2}$ excited states via circularly polarised light. From the $A_2$ excited state, the population decays with equal probability to the $m_s \pm 1$ states, thereby creating a $\Lambda$-scheme. The decay into the two spin-states emits orthogonally polarised photons, resulting in an entangled state on the form [41]

$$|\Psi\rangle = \frac{1}{\sqrt{2}} \left( |\sigma_-\rangle |+1\rangle + |\sigma_+\rangle |-1\rangle \right) , \tag{K.1}$$

where $|\sigma_\pm\rangle$ and $|\pm 1\rangle$ corresponds to the orthogonally polarised single-photon states and the $m_s = \pm 1$ states, respectively. In Ref. [41], the state of the photon was determined by measuring in the $|\sigma_\pm\rangle$ or the $|H\rangle = \frac{1}{\sqrt{2}} \left( |\sigma_+\rangle + |\sigma_-\rangle \right)$, $|V\rangle = \frac{1}{\sqrt{2}} \left( |\sigma_+\rangle - |\sigma_-\rangle \right)$ basis. The spin state was readout using the optical techniques introduced in Section 2.2.5. Microwave fields with frequency $\omega_\pm$ were used to drive the spin from $|\pm 1\rangle$ to $|0\rangle = m_s = 0$, from which a laser pulse resonant with $|0\rangle \leftrightarrow |E_y\rangle$ allowing for resonant spin readout [242]. For more details, the reader is directed to Ref. [41, 190, 494, 496].

Spin-spin entanglement of remote NV centres has been experimentally demonstrated using the Barrett and Kok protocol [493]. In a nutshell, this protocol works by establishing spin-photon entanglement for two remote NV centres, here labelled A and B. Overlapping the photons on a 50:50 beamsplitter, project the spin onto a joint, entangled state. Following Ref. [495], the protocol goes as follows.

NV A and NV B are prepared in the $m_s = 0$ ground state by optical spin pumping (See Section 2.2.5). Applying a resonant $\frac{\pi}{2}$ microwave pulse prepares the spin in an equal

superposition state:

$$|\psi\rangle = \frac{1}{\sqrt{2}}\left(|\uparrow\rangle + |\downarrow\rangle\right) , \tag{K.2}$$

where $|\uparrow\rangle$ and $|\downarrow\rangle$ corresponds to the spin-states $m_s = 0$ and $m_s = -1$, respectively. Next, a short, resonant spin-selective optical pulse is applied, affecting only one of the spin-states, say $|\uparrow\rangle$. Subsequent emission of a resonant photon entangles the spin-state of the NV centre with the presence of a photon:

$$|\psi\rangle = \frac{1}{\sqrt{2}}\left(|\uparrow\rangle|1\rangle + |\downarrow\rangle|0\rangle\right) , \tag{K.3}$$

where $|1\rangle$ ($|0\rangle$) denotes the presence (absence) of a photon.

Applying a resonant $\pi$ pulse leads to a coherent inversion of the spin state:

$$|\psi\rangle = \frac{1}{\sqrt{2}}\left(|\downarrow\rangle|1\rangle + |\uparrow\rangle|0\rangle\right) . \tag{K.4}$$

Applying a second optical pulse resonant with $|\uparrow\rangle$ entangles the spin with the temporal mode of a photon:

$$|\psi\rangle = \frac{1}{\sqrt{2}}\left(|\downarrow\rangle|L\rangle + |\uparrow\rangle|E\rangle\right) , \tag{K.5}$$

where $|E\rangle$ and $|L\rangle$ denotes the arrival of an early or late photon, respectively. If the initial spin-state was $|\uparrow\rangle$, the NV centre was excited by the first excitation pulse, leading to the detection of an early photon $|E\rangle$. On the other hand, if the initial spin-state was $|\downarrow\rangle$, the NV centre was exited by the second pulse resulting in the detection of a late photon.

Finally, the photons from the two NV centres are overlapped on a beamsplitter. If the photons are indistinguishable, the detection of one early and one late photon projects the spins of the NV centres onto a Bell state:

$$|\Psi\rangle = \frac{1}{\sqrt{2}}\left(|\uparrow\rangle_A|\downarrow\rangle_B \pm |\downarrow\rangle_A|\uparrow\rangle_B\right) . \tag{K.6}$$

Detecting the photons in the same output port leads to a symmetric state (+), while detection in different ports leads to an anti-symmetric state (-).

In this protocol, the entanglement is heralded by the detection of a photon. The overall success probability is $\frac{1}{2}\eta^2$, where $\eta$ is the probability of detecting a single ZPL photon from the resonant excitation pulse and the factor of $\frac{1}{2}$ accounts for the need to detect two photons per successful entanglement event. As discussed extensively in Chapter 8, $\eta$ can be dramatically enhanced in a resonant cavity.

# References


[1] Jonathan P. Dowling and Gerard J. Milburn. Quantum technology: the second quantum revolution. *Philosophical Transactions of the Royal Society of London. Series A: Mathematical, Physical and Engineering Sciences*, 361(1809):1655–1674, aug 2003.

[2] M. Planck. Über eine Verbesserung der Wienschen Spektralgleichung. *Verhandlungen der Deutschen Physikalischen Gesellschaft*, 2:202–204, 1900.

[3] NobelPrize.org. The Nobel Prize in Physics 1918, 2021.

[4] Rodney Loudon. *The quantum theory of light*. Oxford University Press, 3rd edition, 2000.

[5] Gilbert N. Lewis. The Conservation of Photons. *Nature*, 118(2981):874–875, dec 1926.

[6] NobelPrize.org. The Nobel Prize in Physics 1921, 2021.

[7] William F. Koehl, Hosung Seo, Giulia Galli, and David D. Awschalom. Designing defect spins for wafer-scale quantum technologies. *MRS Bulletin*, 40(12):1146–1153, dec 2015.

[8] Ivan H. Deutsch. Harnessing the Power of the Second Quantum Revolution. *PRX Quantum*, 1(2):020101, nov 2020.

[9] Vittorio Giovannetti. Quantum-Enhanced Measurements: Beating the Standard Quantum Limit. *Science*, 306(5700):1330–1336, nov 2004.

[10] Vittorio Giovannetti, Seth Lloyd, and Lorenzo Maccone. Advances in quantum metrology. *Nature Photonics*, 5(4):222–229, apr 2011.

[11] C. L. Degen, F. Reinhard, and P. Cappellaro. Quantum sensing. *Reviews of Modern Physics*, 89(3):035002, jul 2017.

[12] Richard P. Feynman. Simulating physics with computers. *International Journal of Theoretical Physics*, 21(6-7):467–488, jun 1982.

[13] T. D. Ladd, F. Jelezko, R. Laflamme, Y. Nakamura, C. Monroe, and J. L. O'Brien. Quantum computers. *Nature*, 464(7285):45–53, mar 2010.

[14] Nicolas Gisin, Grégoire Ribordy, Wolfgang Tittel, and Hugo Zbinden. Quantum cryptography. *Reviews of Modern Physics*, 74(1):145–195, mar 2002.

[15] H J Kimble. The quantum internet. *Nature*, 453(7198):1023–1030, jun 2008.

[16] Christoph Simon. Towards a global quantum network. *Nature Photonics*, 11(11):678–680, nov 2017.

[17] Stephanie Wehner, David Elkouss, and Ronald Hanson. Quantum internet: A vision for the road ahead. *Science*, 362(6412):eaam9288, oct 2018.

[18] R. Horodecki. Quantum Information. *Acta Physica Polonica A*, 139(3):197–2018, mar 2021.

[19] G. Brassard, I. Chuang, S. Lloyd, and C. Monroe. Quantum computing. *Proceedings of the National Academy of Sciences*, 95(19):11032–11033, sep 1998.

[20] Michael A. Nielsen and Isaac L. Chuang. *Quantum Computation and Quantum Information*. Cambridge University Press, Cambridge, 10th anniv edition, 2010.

[21] D. P. DiVincenzo. Quantum Computation. *Science*, 270(5234):255–261, oct 1995.

[22] D.R. Simon. On the power of quantum computation. In A. Ekert, R. Jozsa, and R. Penrose, editors, *Proceedings 35th Annual Symposium on Foundations of Computer Science*, volume 356, pages 116–123. IEEE Comput. Soc. Press, aug 1998.

[23] P.W. Shor. Algorithms for quantum computation: discrete logarithms and factoring. In *Proceedings 35th Annual Symposium on Foundations of Computer Science*, pages 124–134. IEEE Comput. Soc. Press, 1994.

[24] Lov K. Grover. A fast quantum mechanical algorithm for database search. In *Proceedings of the twenty-eighth annual ACM symposium on Theory of computing - STOC '96*, volume 75, pages 212–219, New York, New York, USA, 1996. ACM Press.

[25] Brian C. Britt. Modeling viral diffusion using quantum computational network simulation. *Quantum Engineering*, 2(1):1–12, mar 2020.

[26] Han Sen Zhong, Hui Wang, Yu Hao Deng, Ming Cheng Chen, Li Chao Peng, Yi Han Luo, Jian Qin, Dian Wu, Xing Ding, Yi Hu, Peng Hu, Xiao Yan Yang, Wei Jun Zhang, Hao Li, Yuxuan Li, Xiao Jiang, Lin Gan, Guangwen Yang, Lixing You, Zhen Wang, Li Li, Nai Le Liu, Chao Yang Lu, and Jian Wei Pan. Quantum computational advantage using photons. *Science*, 373(6523):1460–1463, 2020.

[27] Frank Arute, Kunal Arya, Ryan Babbush, Dave Bacon, Joseph C. Bardin, Rami Barends, Rupak Biswas, Sergio Boixo, Fernando G. S. L. Brandao, David A. Buell, Brian Burkett, Yu Chen, Zijun Chen, Ben Chiaro, Roberto Collins, William Courtney, Andrew Dunsworth, Edward Farhi, Brooks Foxen, Austin Fowler, Craig Gidney, Marissa Giustina, Rob Graff, Keith Guerin, Steve Habegger, Matthew P. Harrigan, Michael J. Hartmann, Alan Ho, Markus Hoffmann, Trent Huang, Travis S. Humble, Sergei V. Isakov, Evan Jeffrey, Zhang Jiang, Dvir Kafri, Kostyantyn Kechedzhi, Julian Kelly, Paul V. Klimov, Sergey Knysh, Alexander Korotkov, Fedor Kostritsa, David Landhuis, Mike Lindmark, Erik Lucero, Dmitry Lyakh, Salvatore Mandrà, Jarrod R. McClean, Matthew McEwen, Anthony Megrant, Xiao Mi, Kristel Michielsen, Masoud Mohseni, Josh Mutus, Ofer Naaman, Matthew Neeley, Charles Neill, Murphy Yuezhen Niu, Eric Ostby, Andre Petukhov, John C. Platt, Chris Quintana, Eleanor G. Rieffel, Pedram Roushan, Nicholas C. Rubin, Daniel Sank, Kevin J. Satzinger, Vadim Smelyanskiy, Kevin J. Sung, Matthew D. Trevithick, Amit Vainsencher, Benjamin Villalonga, Theodore White, Z. Jamie Yao, Ping Yeh, Adam Zalcman, Hartmut Neven, and John M. Martinis. Quantum supremacy using a programmable superconducting processor. *Nature*, 574(7779):505–510, oct 2019.

[28] L.-M. Duan and C. Monroe. Colloquium : Quantum networks with trapped ions. *Reviews of Modern Physics*, 82(2):1209–1224, apr 2010.

[29] Stephan Ritter, Christian Nölleke, Carolin Hahn, Andreas Reiserer, Andreas Neuzner, Manuel Uphoff, Martin Mücke, Eden Figueroa, Joerg Bochmann, and Gerhard Rempe. An elementary quantum network of single atoms in optical cavities. *Nature*, 484(7393):195–200, apr 2012.

[30] Andreas Reiserer and Gerhard Rempe. Cavity-based quantum networks with single atoms and optical photons. *Reviews of Modern Physics*, 87(4):1379–1418, dec 2015.

[31] Severin Daiss, Stefan Langenfeld, Stephan Welte, Emanuele Distante, Philip Thomas, Lukas Hartung, Olivier Morin, and Gerhard Rempe. A quantum-logic gate between distant quantum-network modules. *Science*, 371(6529):614–617, feb 2021.

[32] Gang Zhang, Yuan Cheng, Jyh-Pin Chou, and Adam Gali. Material platforms for defect qubits and single-photon emitters. *Applied Physics Reviews*, 7(3):031308, sep 2020.

[33] Ronald Hanson and David D. Awschalom. Coherent manipulation of single spins in semiconductors. *Nature*, 453(7198):1043–1049, jun 2008.

[34] David D. Awschalom, Ronald Hanson, Jörg Wrachtrup, and Brian B. Zhou. Quantum technologies with optically interfaced solid-state spins. *Nature Photonics*, 12(9):516–527, sep 2018.

[35] David D. Awschalom, Lee C. Bassett, Andrew S. Dzurak, Evelyn L. Hu, and Jason R. Petta. Quantum Spintronics: Engineering and Manipulating Atom-Like Spins in Semiconductors. *Science*, 339(6124):1174–1179, mar 2013.

[36] Lilian Childress, Ronald Walsworth, and Mikhail Lukin. Atom-like crystal defects: From quantum computers to biological sensors. *Physics Today*, 67(10):38–43, oct 2014.

[37] Marcus W. Doherty, Neil B. Manson, Paul Delaney, Fedor Jelezko, Jörg Wrachtrup, and Lloyd C.L. Hollenberg. The nitrogen-vacancy colour centre in diamond. *Physics Reports*, 528(1):1–45, jul 2013.

[38] Y. Chu, M. Markham, D. J. Twitchen, and M. D. Lukin. All-optical control of a single electron spin in diamond. *Physical Review A*, 91(2):021801, feb 2015.

[39] W. B. Gao, A. Imamoglu, H. Bernien, and R. Hanson. Coherent manipulation, measurement and entanglement of individual solid-state spins using optical fields. *Nature Photonics*, 9(6):363–373, jun 2015.

[40] Prasoon K Shandilya, David P Lake, Matthew J Mitchell, Denis D Sukachev, and Paul E Barclay. Optomechanical interface between telecom photons and spin quantum memory. *Nature Physics*, oct 2021.

[41] E. Togan, Y. Chu, A. S. Trifonov, L. Jiang, J. Maze, L. Childress, M. V. G. Dutt, A. S. Sørensen, P. R. Hemmer, A. S. Zibrov, and M. D. Lukin. Quantum

entanglement between an optical photon and a solid-state spin qubit. *Nature*, 466(7307):730–734, aug 2010.

[42] H Bernien, B Hensen, W Pfaff, G Koolstra, M S Blok, L Robledo, T H Taminiau, M Markham, D J Twitchen, L Childress, and R Hanson. Heralded entanglement between solid-state qubits separated by three metres. *Nature*, 497(7447):86–90, may 2013.

[43] B. Hensen, H. Bernien, A. E. Dréau, A. Reiserer, N. Kalb, M. S. Blok, J. Ruitenberg, R. F.L. L. Vermeulen, R. N. Schouten, C. Abellán, W. Amaya, V. Pruneri, M. W. Mitchell, M. Markham, D. J. Twitchen, D. Elkouss, S. Wehner, T. H. Taminiau, and R. Hanson. Loophole-free Bell inequality violation using electron spins separated by 1.3 kilometres. *Nature*, 526(7575):682–686, oct 2015.

[44] Ryszard Horodecki, Paweł Horodecki, Michał Horodecki, and Karol Horodecki. Quantum entanglement. *Reviews of Modern Physics*, 81(2):865–942, jun 2009.

[45] Nicolas Gisin and Rob Thew. Quantum communication. *Nature Photonics*, 1(3):165–171, mar 2007.

[46] Hoi-Kwong Lo, Marcos Curty, and Kiyoshi Tamaki. Secure quantum key distribution. *Nature Photonics*, 8(8):595–604, aug 2014.

[47] Feihu Xu, Xiongfeng Ma, Qiang Zhang, Hoi-Kwong Lo, and Jian-Wei Pan. Secure quantum key distribution with realistic devices. *Reviews of Modern Physics*, 92(2):025002, may 2020.

[48] T. E. Northup and R. Blatt. Quantum information transfer using photons. *Nature Photonics*, 8(5):356–363, may 2014.

[49] Raju Valivarthi, Marcelli Grimau Puigibert, Qiang Zhou, Gabriel H. Aguilar, Varun B. Verma, Francesco Marsili, Matthew D. Shaw, Sae Woo Nam, Daniel Oblak, and Wolfgang Tittel. Quantum teleportation across a metropolitan fibre network. *Nature Photonics*, 10(10):676–680, oct 2016.

[50] J. F. Dynes, A. Wonfor, W. W. S. Tam, A. W. Sharpe, R. Takahashi, M. Lucamarini, A. Plews, Z. L. Yuan, A. R. Dixon, J. Cho, Y. Tanizawa, J. P. Elbers, H. Greißer, I. H. White, R. V. Penty, and A. J. Shields. Cambridge quantum network. *npj Quantum Information*, 5(1):101, dec 2019.

[51] Yong Yu, Fei Ma, Xi-Yu Luo, Bo Jing, Peng-Fei Sun, Ren-Zhou Fang, Chao-Wei Yang, Hui Liu, Ming-Yang Zheng, Xiu-Ping Xie, Wei-Jun Zhang, Li-Xing You, Zhen Wang, Teng-Yun Chen, Qiang Zhang, Xiao-Hui Bao, and Jian-Wei Pan. Entanglement of two quantum memories via fibres over dozens of kilometres. *Nature*, 578(7794):240–245, feb 2020.

[52] W. K. Wootters and W H Zurek. A single quantum cannot be cloned. *Nature*, 299(5886):802–803, oct 1982.

[53] Angela Sara Cacciapuoti, Marcello Caleffi, Francesco Tafuri, Francesco Saverio Cataliotti, Stefano Gherardini, and Giuseppe Bianchi. Quantum Internet: Networking Challenges in Distributed Quantum Computing. *IEEE Network*, 34(1):137–143, jan 2020.

[54] H.-J. Briegel, W. Dür, J. I. Cirac, and P. Zoller. Quantum Repeaters: The Role of Imperfect Local Operations in Quantum Communication. *Physical Review Letters*, 81(26):5932–5935, dec 1998.

[55] L.-M. Duan, M. D. Lukin, J. I. Cirac, and P. Zoller. Long-distance quantum communication with atomic ensembles and linear optics. *Nature*, 414(6862):413–418, nov 2001.

[56] Nicolas Sangouard, Christoph Simon, Hugues de Riedmatten, and Nicolas Gisin. Quantum repeaters based on atomic ensembles and linear optics. *Reviews of Modern Physics*, 83(1):33–80, mar 2011.

[57] William J. Munro, Koji Azuma, Kiyoshi Tamaki, and Kae Nemoto. Inside Quantum Repeaters. *IEEE Journal of Selected Topics in Quantum Electronics*, 21(3):78–90, may 2015.

[58] Johannes Borregaard, Anders Søndberg Sørensen, and Peter Lodahl. Quantum Networks with Deterministic Spin–Photon Interfaces. *Advanced Quantum Technologies*, 2(5-6):1800091, jun 2019.

[59] Kerry J. Vahala. Optical microcavities. *Nature*, 424(6950):839–846, aug 2003.

[60] Chun-Hsu Su, Andrew D. Greentree, and Lloyd C. L. Hollenberg. Towards a picosecond transform-limited nitrogen-vacancy based single photon source. *Optics Express*, 16(9):6240, apr 2008.

[61] Erika Janitz, Mihir K. Bhaskar, and Lilian Childress. Cavity quantum electrodynamics with color centers in diamond. *Optica*, 7(10):1232, oct 2020.

[62] N. Bar-Gill, L.M. Pham, A. Jarmola, D. Budker, and R.L. Walsworth. Solid-state electronic spin coherence time approaching one second. *Nature Communications*, 4(1):1743, jun 2013.

[63] L. Childress, J. M. Taylor, A. S. Sørensen, and M. D. Lukin. Fault-tolerant quantum repeaters with minimal physical resources and implementations based on single-photon emitters. *Physical Review A*, 72(5):052330, nov 2005.

[64] L. Childress, J. M. Taylor, A. S. Sørensen, and M. D. Lukin. Fault-Tolerant Quantum Communication Based on Solid-State Photon Emitters. *Physical Review Letters*, 96(7):070504, feb 2006.

[65] Suzanne B van Dam, Peter C. Humphreys, Filip Rozpędek, Stephanie Wehner, and Ronald Hanson. Multiplexed entanglement generation over quantum networks using multi-qubit nodes. *Quantum Science and Technology*, 2(3):034002, sep 2017.

[66] Matteo Pompili, Sophie L. N. Hermans, Simon Baier, Hans K. C. Beukers, Peter C. Humphreys, Raymond N. Schouten, Raymond F. L. Vermeulen, Marijn J. Tiggelman, L. dos Santos Martins, Bas Dirkse, Stephanie Wehner, and Ronald Hanson. Realization of a multinode quantum network of remote solid-state qubits. *Science*, 372(6539):259–264, apr 2021.

[67] L. Childress, M. V. Gurudev Dutt, J. M. Taylor, A. S. Zibrov, F. Jelezko, J. Wrachtrup, P. R. Hemmer, and M. D. Lukin. Coherent dynamics of coupled electron and nuclear spin qubits in diamond. *Science*, 314(5797):281–285, 2006.

[68] T. H. Taminiau, J. Cramer, T. van der Sar, V. V. Dobrovitski, and R. Hanson. Universal control and error correction in multi-qubit spin registers in diamond. *Nature Nanotechnology*, 9(3):171–176, mar 2014.

[69] C. E. Bradley, J. Randall, M. H. Abobeih, R. C. Berrevoets, M. J. Degen, M. A. Bakker, M. Markham, D. J. Twitchen, and T. H. Taminiau. A Ten-Qubit Solid-State Spin Register with Quantum Memory up to One Minute. *Physical Review X*, 9(3):031045, sep 2019.

[70] M. H. Abobeih, J. Randall, C. E. Bradley, H. P. Bartling, M. A. Bakker, M. J. Degen, M. Markham, D. J. Twitchen, and T. H. Taminiau. Atomic-scale imaging

of a 27-nuclear-spin cluster using a quantum sensor. *Nature*, 576(7787):411–415, 2019.

[71] H. P. Bartling, M. H. Abobeih, B. Pingault, M. J. Degen, S. J. H. Loenen, C. E. Bradley, J. Randall, M. Markham, D. J. Twitchen, and T. H. Taminiau. Coherence and entanglement of inherently long-lived spin pairs in diamond. *arXiv:2103.07961*, mar 2021.

[72] M H Abobeih, J Cramer, M A Bakker, N Kalb, M Markham, D J Twitchen, and T H Taminiau. One-second coherence for a single electron spin coupled to a multi-qubit nuclear-spin environment. *Nature Communications*, 9(1):2552, dec 2018.

[73] N. Kalb, A. A. Reiserer, P. C. Humphreys, J. J.W. W. Bakermans, S. J. Kamerling, N. H. Nickerson, S. C. Benjamin, D. J. Twitchen, M. Markham, and R. Hanson. Entanglement distillation between solid-state quantum network nodes. *Science*, 356(6341):928–932, jun 2017.

[74] P. C. Maurer, G. Kucsko, C. Latta, L. Jiang, N. Y. Yao, S. D. Bennett, F. Pastawski, D. Hunger, N. Chisholm, M. Markham, D. J. Twitchen, J. I. Cirac, and M. D. Lukin. Room-Temperature Quantum Bit Memory Exceeding One Second. *Science*, 336(6086):1283–1286, jun 2012.

[75] Anaïs Dréau, Anna Tcheborateva, Aboubakr El Mahdaoui, Cristian Bonato, and Ronald Hanson. Quantum Frequency Conversion of Single Photons from a Nitrogen-Vacancy Center in Diamond to Telecommunication Wavelengths. *Physical Review Applied*, 9(6):064031, jun 2018.

[76] Anna Tchebotareva, Sophie L.N. Hermans, Peter C. Humphreys, Dirk Voigt, Peter J. Harmsma, Lun K. Cheng, Ad L. Verlaan, Niels Dijkhuizen, Wim de Jong, Anaïs Dréau, and Ronald Hanson. Entanglement between a Diamond Spin Qubit and a Photonic Time-Bin Qubit at Telecom Wavelength. *Physical Review Letters*, 123(6):063601, aug 2019.

[77] Daniel Riedel, Immo Söllner, Brendan J. Shields, Sebastian Starosielec, Patrick Appel, Elke Neu, Patrick Maletinsky, and Richard J. Warburton. Deterministic Enhancement of Coherent Photon Generation from a Nitrogen-Vacancy Center in Ultrapure Diamond. *Physical Review X*, 7(3):031040, sep 2017.

[78] Paul E. Barclay, Kai-Mei C. Fu, Charles Santori, Andrei Faraon, and Raymond G. Beausoleil. Hybrid Nanocavity Resonant Enhancement of Color Center Emission in Diamond. *Physical Review X*, 1(1):011007, sep 2011.

[79] Hannes Bernien, Lilian Childress, Lucio Robledo, Matthew Markham, Daniel Twitchen, and Ronald Hanson. Two-photon quantum interference from separate nitrogen vacancy centers in diamond. *Physical Review Letters*, 108(4):1–5, 2012.

[80] A. Sipahigil, M. L. Goldman, E. Togan, Y. Chu, M. Markham, D. J. Twitchen, A. S. Zibrov, A. Kubanek, and M. D. Lukin. Quantum Interference of Single Photons from Remote Nitrogen-Vacancy Centers in Diamond. *Physical Review Letters*, 108(14):143601, apr 2012.

[81] Andrei Faraon, Paul E. Barclay, Charles Santori, Kai-Mei C. Fu, and Raymond G. Beausoleil. Resonant enhancement of the zero-phonon emission from a colour centre in a diamond cavity. *Nature Photonics*, 5(5):301–305, may 2011.

[82] Andrei Faraon, Charles Santori, Zhihong Huang, Victor M. Acosta, and Raymond G. Beausoleil. Coupling of Nitrogen-Vacancy Centers to Photonic Crystal Cavities in Monocrystalline Diamond. *Physical Review Letters*, 109(3):033604, jul 2012.

[83] Janine Riedrich-Möller, Sébastien Pezzagna, Jan Meijer, Christoph Pauly, Frank Mücklich, Matthew Markham, Andrew M. Edmonds, and Christoph Becher. Nanoimplantation and Purcell enhancement of single nitrogen-vacancy centers in photonic crystal cavities in diamond. *Applied Physics Letters*, 106(22):221103, jun 2015.

[84] Michael Gould, Emma R. Schmidgall, Shabnam Dadgostar, Fariba Hatami, and Kai-Mei C. Fu. Efficient Extraction of Zero-Phonon-Line Photons from Single Nitrogen-Vacancy Centers in an Integrated GaP-on-Diamond Platform. *Physical Review Applied*, 6(1):011001, jul 2016.

[85] Daniel Riedel. *Engineering of the photonic environment of single nitrogen-vacancy centers in diamond*. PhD thesis, Basel, 2017.

[86] E. M. Purcell, H. C. Torrey, and R. V. Pound. Resonance Absorption by Nuclear Magnetic Moments in a Solid. *Physical Review*, 69(1-2):37–38, jan 1946.

[87] Erika Janitz, Maximilian Ruf, Mark Dimock, Alexandre Bourassa, Jack Sankey, and Lilian Childress. Fabry-Perot microcavity for diamond-based photonics. *Physical Review A*, 92(4):043844, oct 2015.

[88] Dustin Kleckner, William T.M. M Irvine, Sumant S.R. R Oemrawsingh, and Dirk Bouwmeester. Diffraction-limited high-finesse optical cavities. *Physical Review A*, 81(4):043814, apr 2010.

[89] Nina Podoliak, Hiroki Takahashi, Matthias Keller, and Peter Horak. Harnessing the mode mixing in optical fiber-tip cavities. *Journal of Physics B: Atomic, Molecular and Optical Physics*, 50(8):085503, apr 2017.

[90] Julia Benedikter, Thomas Hümmer, Matthias Mader, Benedikt Schlederer, Jakob Reichel, Theodor W Hänsch, and David Hunger. Transverse-mode coupling and diffraction loss in tunable Fabry–Pérot microcavities. *New Journal of Physics*, 17(5):053051, may 2015.

[91] H. Kogelnik and T. Li. Laser Beams and Resonators. *Applied Optics*, 5(10):1550, oct 1966.

[92] Isidoro Kimel and L.R. Elias. Relations between Hermite and Laguerre Gaussian modes. *IEEE Journal of Quantum Electronics*, 29(9):2562–2567, 1993.

[93] Warren Nagourney. *Quantum electronics for atomic physics and telecommunication*. Oxford University Press, 2nd edition, 2014.

[94] C. Koks and M. P. van Exter. Microcavity resonance condition, quality factor, and mode volume are determined by different penetration depths. *Optics Express*, 29(5):6879, mar 2021.

[95] Aigars Atvars. Analytical description of resonances in Fabry–Perot and whispering gallery mode resonators. *Journal of the Optical Society of America B*, 38(10):3116, oct 2021.

[96] Daqing Wang, Hrishikesh Kelkar, Diego Martin-Cano, Tobias Utikal, Stephan Götzinger, and Vahid Sandoghdar. Coherent Coupling of a Single Molecule to a Scanning Fabry-Perot Microcavity. *Physical Review X*, 7(2):021014, apr 2017.

[97] Daqing Wang, Hrishikesh Kelkar, Diego Martin-Cano, Dominik Rattenbacher, Alexey Shkarin, Tobias Utikal, Stephan Götzinger, and Vahid Sandoghdar. Turning a molecule into a coherent two-level quantum system. *Nature Physics*, 15(5):483–489, may 2019.

[98] Stefan Häußler, Julia Benedikter, Kerem Bray, Blake Regan, Andreas Dietrich, Jason Twamley, Igor Aharonovich, David Hunger, and Alexander Kubanek. Diamond photonics platform based on silicon vacancy centers in a single-crystal diamond membrane and a fiber cavity. *Physical Review B*, 99(16):165310, apr 2019.

[99] Daniel Najer, Immo Söllner, Pavel Sekatski, Vincent Dolique, Matthias C. Löbl, Daniel Riedel, Rüdiger Schott, Sebastian Starosielec, Sascha R. Valentin, Andreas D. Wieck, Nicolas Sangouard, Arne Ludwig, and Richard J. Warburton. A gated quantum dot strongly coupled to an optical microcavity. *Nature*, 575(7784):622–627, nov 2019.

[100] Rasmus Høy Jensen, Erika Janitz, Yannik Fontana, Yi He, Olivier Gobron, Ilya P. Radko, Mihir Bhaskar, Ruffin Evans, César Daniel Rodríguez Rosenblueth, Lilian Childress, Alexander Huck, and Ulrik Lund Andersen. Cavity-Enhanced Photon Emission from a Single Germanium-Vacancy Center in a Diamond Membrane. *Physical Review Applied*, 13(6):064016, jun 2020.

[101] Benjamin Merkel, Alexander Ulanowski, and Andreas Reiserer. Coherent and Purcell-Enhanced Emission from Erbium Dopants in a Cryogenic High-$\mathcal{Q}$ Resonator. *Physical Review X*, 10(4):041025, nov 2020.

[102] Natasha Tomm, Alisa Javadi, Nadia Olympia Antoniadis, Daniel Najer, Matthias Christian Löbl, Alexander Rolf Korsch, Rüdiger Schott, Sascha René Valentin, Andreas Dirk Wieck, Arne Ludwig, and Richard John Warburton. A bright and fast source of coherent single photons. *Nature Nanotechnology*, 16(4):399–403, apr 2021.

[103] André Pscherer, Manuel Meierhofer, Daqing Wang, Hrishikesh Kelkar, Diego Martín-Cano, Tobias Utikal, Stephan Götzinger, and Vahid Sandoghdar. Single-Molecule Vacuum Rabi Splitting: Four-Wave Mixing and Optical Switching at the Single-Photon Level. *Physical Review Letters*, 127(13):133603, sep 2021.

[104] D. Hunger, T. Steinmetz, Y. Colombe, C. Deutsch, T. W. Hänsch, and J. Reichel. A fiber Fabry–Perot cavity with high finesse. *New Journal of Physics*, 12(6):065038, jun 2010.

[105] K. Durak, C. H. Nguyen, V. Leong, S. Straupe, and C. Kurtsiefer. Diffraction-limited Fabry–Perot cavity in the near concentric regime. *New Journal of Physics*, 16(10):103002, oct 2014.

[106] Christina J. Hood, H. J. Kimble, and Jun Ye. Characterization of high-finesse mirrors: Loss, phase shifts, and mode structure in an optical cavity. *Physical Review A*, 64(3):033804, aug 2001.

[107] E.T. Jaynes and F.W. Cummings. Comparison of quantum and semiclassical radiation theories with application to the beam maser. *Proceedings of the IEEE*, 51(1):89–109, 1963.

[108] Bruce W. Shore and Peter L. Knight. The Jaynes-Cummings Model. *Journal of Modern Optics*, 40(7):1195–1238, jul 1993.

[109] Serge Haroche Raimond and Jean-Michel. *Exploring the Quantum: Atoms, Cavities, and Photons*. Oxford University Press, 2006.

[110] Peter L.Knight Christopher C. Gerry. *Introductory Quantum Optics*. Cambridge University Press, 2004.

[111] Alexandre Blais, Steven M. Girvin, and William D. Oliver. Quantum information processing and quantum optics with circuit quantum electrodynamics. *Nature Physics*, 16(3):247–256, mar 2020.

[112] Mark Fox. *Quantum Optics, An Introduction*. Oxford University Press, 2006.

[113] Maximilian Ruf, Noel H. Wan, Hyeongrak Choi, Dirk Englund, and Ronald Hanson. Quantum networks based on color centers in diamond. *Journal of Applied Physics*, 130(7):070901, aug 2021.

[114] A. Sipahigil, R. E. Evans, D. D. Sukachev, M. J. Burek, J. Borregaard, M. K. Bhaskar, C. T. Nguyen, J. L. Pacheco, H. A. Atikian, C. Meuwly, R. M. Camacho, F. Jelezko, E. Bielejec, H. Park, M. Lončar, and M. D. Lukin. An integrated diamond nanophotonics platform for quantum-optical networks. *Science*, 354(6314):847–850, nov 2016.

[115] Lukas Greuter, Sebastian Starosielec, Andreas V Kuhlmann, and Richard J Warburton. Towards high-cooperativity strong coupling of a quantum dot in a tunable microcavity. *Physical Review B*, 92(4):045302, jul 2015.

[116] J. M. Fink, M. Göppl, M. Baur, R. Bianchetti, P. J. Leek, A. Blais, and A. Wallraff. Climbing the Jaynes-Cummings ladder and observing its $\sqrt{n}$ nonlinearity in a cavity QED system. *Nature*, 454(7202):315–318, jul 2008.

[117] Alexandre Blais, Arne L. Grimsmo, S. M. Girvin, and Andreas Wallraff. Circuit quantum electrodynamics. *Reviews of Modern Physics*, 93(2):025005, may 2021.

[118] A. Boca, R. Miller, K. M. Birnbaum, A. D. Boozer, J. McKeever, and H. J. Kimble. Observation of the Vacuum Rabi Spectrum for One Trapped Atom. *Physical Review Letters*, 93(23):233603, dec 2004.

[119] NobelPrize.org. The Nobel Prize in Physics 1952, 2021.

[120] Daniel Kleppner. Inhibited Spontaneous Emission. *Physical Review Letters*, 47(4):233–236, jul 1981.

[121] Peter Lodahl, Sahand Mahmoodian, and Søren Stobbe. Interfacing single photons and single quantum dots with photonic nanostructures. *Reviews of Modern Physics*, 87(2):347–400, may 2015.

[122] Benjamin Petrak. *Microcavity Enhanced Raman Scattering*. PhD thesis, University of South Florida, 2016.

[123] Suzanne B. van Dam, Maximilian Ruf, and Ronald Hanson. Optimal design of diamond-air microcavities for quantum networks using an analytical approach. *New Journal of Physics*, 20(11):115004, nov 2018.

[124] C. Santori, P. E. Barclay, K-M C Fu, R. G. Beausoleil, S. Spillane, and M. Fisch. Nanophotonics for quantum optics using nitrogen-vacancy centers in diamond. *Nanotechnology*, 21(27):274008, jul 2010.

[125] Thomas D. Barrett, Thomas H. Doherty, and Axel Kuhn. Pushing Purcell enhancement beyond its limits. *New Journal of Physics*, 22(6):063013, jun 2020.

[126] Hanno Kaupp, Thomas Hümmer, Matthias Mader, Benedikt Schlederer, Julia Benedikter, Philip Haeusser, Huan-Cheng Chang, Helmut Fedder, Theodor W. Hänsch, and David Hunger. Purcell-Enhanced Single-Photon Emission from Nitrogen-Vacancy Centers Coupled to a Tunable Microcavity. *Physical Review Applied*, 6(5):054010, nov 2016.

[127] H. J. Kimble. Strong Interactions of Single Atoms and Photons in Cavity QED. *Physica Scripta*, T76(1):127, 1998.

[128] Jörg Wrachtrup and Fedor Jelezko. Processing quantum information in diamond. *Journal of Physics: Condensed Matter*, 18(21):S807–S824, may 2006.

[129] Sébastien Pezzagna and Jan Meijer. Quantum computer based on color centers in diamond. *Applied Physics Reviews*, 8(1):011308, mar 2021.

[130] I. Aharonovich, S. Castelletto, D. A. Simpson, C-H Su, A. D. Greentree, and S. Prawer. Diamond-based single-photon emitters. *Reports on Progress in Physics*, 74(7):076501, jul 2011.

[131] Igor Aharonovich, Andrew D. Greentree, and Steven Prawer. Diamond photonics. *Nature Photonics*, 5(7):397–405, jul 2011.

[132] Igor Aharonovich and Elke Neu. Diamond Nanophotonics. *Advanced Optical Materials*, 2(10):911–928, oct 2014.

[133] Ronald Hanson. Mother Nature outgrown. *Nature Materials*, 8(5):368–369, may 2009.

[134] Gopalakrishnan Balasubramanian, Philipp Neumann, Daniel Twitchen, Matthew Markham, Roman Kolesov, Norikazu Mizuochi, Junichi Isoya, Jocelyn Achard, Johannes Beck, Julia Tissler, Vincent Jacques, Philip R. Hemmer, Fedor Jelezko, and Jörg Wrachtrup. Ultralong spin coherence time in isotopically engineered diamond. *Nature Materials*, 8(5):383–387, may 2009.

[135] A. Batalov, C. Zierl, T. Gaebel, P. Neumann, I.-Y. Chan, G. Balasubramanian, P. R. Hemmer, F. Jelezko, and J. Wrachtrup. Temporal Coherence of Photons Emitted by Single Nitrogen-Vacancy Defect Centers in Diamond Using Optical Rabi-Oscillations. *Physical Review Letters*, 100(7):077401, feb 2008.

[136] Kohei M. Itoh and Hideyuki Watanabe. Isotope engineering of silicon and diamond for quantum computing and sensing applications. *MRS Communications*, 4(4):143–157, dec 2014.

[137] F. Jelezko and J. Wrachtrup. Single defect centres in diamond: A review. *physica status solidi (a)*, 203(13):3207–3225, oct 2006.

[138] Alexander M Zaitsev. *Optical Properties of Diamond*. Springer, 2010.

[139] M. W. Doherty, N. B. Manson, P. Delaney, and L C L Hollenberg. The negatively charged nitrogen-vacancy centre in diamond: the electronic solution. *New Journal of Physics*, 13(2):025019, feb 2011.

[140] Justin R. Weber, W. F. Koehl, Joel B. Varley, Anderson Janotti, B. B. Buckley, Chris G. Van de Walle, and David D. Awschalom. Quantum computing with defects. *Proceedings of the National Academy of Sciences*, 107(19):8513–8518, may 2010.

[141] Kang Liu, Sen Zhang, Victor Ralchenko, Pengfei Qiao, Jiwen Zhao, Guoyang Shu, Lei Yang, Jiecai Han, Bing Dai, and Jiaqi Zhu. Tailoring of Typical Color Centers in Diamond for Photonics. *Advanced Materials*, 33(6):2000891, feb 2021.

[142] N. B. Manson, J. P. Harrison, and M. J. Sellars. Nitrogen-vacancy center in diamond: Model of the electronic structure and associated dynamics. *Physical Review B*, 74(10):104303, sep 2006.

[143] Matthias Pfender, Nabeel Aslam, Patrick Simon, Denis Antonov, Gergő Thiering, Sina Burk, Felipe Fávaro de Oliveira, Andrej Denisenko, Helmut Fedder, Jan Meijer, Jose A. Garrido, Adam Gali, Tokuyuki Teraji, Junichi Isoya, Marcus William Doherty, Audrius Alkauskas, Alejandro Gallo, Andreas Grüneis, Philipp Neumann, and Jörg Wrachtrup. Protecting a Diamond Quantum Memory by Charge State Control. *Nano Letters*, 17(10):5931–5937, oct 2017.

[144] Peter Deák, Bálint Aradi, Moloud Kaviani, Thomas Frauenheim, and Adam Gali. Formation of NV centers in diamond: A theoretical study based on calculated transitions and migration of nitrogen and vacancy related defects. *Physical Review B*, 89(7):075203, feb 2014.

[145] S. Baier, C. E. Bradley, T. Middelburg, V. V. Dobrovitski, T. H. Taminiau, and R. Hanson. Orbital and Spin Dynamics of Single Neutrally-Charged Nitrogen-Vacancy Centers in Diamond. *Physical Review Letters*, 125(19):193601, nov 2020.

[146] G. Waldherr, J. Beck, M. Steiner, P. Neumann, A. Gali, Th. Frauenheim, F. Jelezko, and J. Wrachtrup. Dark States of Single Nitrogen-Vacancy Centers in Diamond Unraveled by Single Shot NMR. *Physical Review Letters*, 106(15):157601, apr 2011.

[147] N. Aslam, G. Waldherr, P. Neumann, F. Jelezko, and J. Wrachtrup. Photo-induced ionization dynamics of the nitrogen vacancy defect in diamond investigated by single-shot charge state detection. *New Journal of Physics*, 15(1):013064, jan 2013.

[148] David A. Hopper, Joseph D. Lauigan, Tzu-Yung Huang, and Lee C. Bassett. Real-Time Charge Initialization of Diamond Nitrogen-Vacancy Centers for Enhanced Spin Readout. *Physical Review Applied*, 13(2):024016, feb 2020.

[149] Michael S.J. Barson, Elmars Krausz, Neil B. Manson, and Marcus W. Doherty. The fine structure of the neutral nitrogen-vacancy center in diamond. *Nanophotonics*, 8(11):1985–1991, jul 2019.

[150] C. L. Degen. Scanning magnetic field microscope with a diamond single-spin sensor. *Applied Physics Letters*, 92(24):243111, jun 2008.

[151] J. R. Maze, P. L. Stanwix, J. S. Hodges, S. Hong, J. M. Taylor, P. Cappellaro, L. Jiang, M. V. Gurudev Dutt, E. Togan, A. S. Zibrov, A. Yacoby, R. L. Walsworth, and M. D. Lukin. Nanoscale magnetic sensing with an individual electronic spin in diamond. *Nature*, 455(7213):644–647, oct 2008.

[152] P Maletinsky, S Hong, M S Grinolds, B Hausmann, M D Lukin, R L. Walsworth, M Loncar, and A Yacoby. A robust scanning diamond sensor for nanoscale imaging with single nitrogen-vacancy centres. *Nature Nanotechnology*, 7(5):320–324, may 2012.

[153] L. Rondin, J-P Tetienne, T. Hingant, J-F Roch, P. Maletinsky, and V. Jacques. Magnetometry with nitrogen-vacancy defects in diamond. *Reports on Progress in Physics*, 77(5):056503, may 2014.

[154] John F. Barry, Jennifer M. Schloss, Erik Bauch, Matthew J. Turner, Connor A. Hart, Linh M. Pham, and Ronald L. Walsworth. Sensitivity optimization for NV-diamond magnetometry. *Reviews of Modern Physics*, 92(1):15004, 2020.

[155] F.C. Waldermann, P. Olivero, J. Nunn, K. Surmacz, Z.Y. Wang, D. Jaksch, R.A. Taylor, I.A. Walmsley, M. Draganski, P. Reichart, A.D. Greentree, D.N. Jamieson, and S. Prawer. Creating diamond color centers for quantum optical applications. *Diamond and Related Materials*, 16(11):1887–1895, nov 2007.

[156] Sébastien Pezzagna, Detlef Rogalla, Dominik Wildanger, Jan Meijer, and Alexander Zaitsev. Creation and nature of optical centres in diamond for single-photon emission—overview and critical remarks. *New Journal of Physics*, 13(3):035024, mar 2011.

[157] J. O. Orwa, C. Santori, K. M. C. Fu, B. Gibson, D. Simpson, I. Aharonovich, A. Stacey, A. Cimmino, P. Balog, M. Markham, D. Twitchen, A. D. Greentree, R. G. Beausoleil, and S. Prawer. Engineering of nitrogen-vacancy color centers in high purity diamond by ion implantation and annealing. *Journal of Applied Physics*, 109(8):083530, apr 2011.

[158] Maximilian Ruf, Mark IJspeert, Suzanne van Dam, Nick de Jong, Hans van den Berg, Guus Evers, and Ronald Hanson. Optically Coherent Nitrogen-Vacancy Centers in Micrometer-Thin Etched Diamond Membranes. *Nano Letters*, 19(6):3987–3992, jun 2019.

[159] Patrick Appel, Elke Neu, Marc Ganzhorn, Arne Barfuss, Marietta Batzer, Micha Gratz, Andreas Tschöpe, and Patrick Maletinsky. Fabrication of all diamond scanning probes for nanoscale magnetometry. *Review of Scientific Instruments*, 87(6):063703, jun 2016.

[160] T. A. Kennedy, J. S. Colton, J. E. Butler, R. C. Linares, and P. J. Doering. Long coherence times at 300 K for nitrogen-vacancy center spins in diamond grown by chemical vapor deposition. *Applied Physics Letters*, 83(20):4190–4192, nov 2003.

[161] Philippe Tamarat, T. Gaebel, James R. Rabeau, M. Khan, Andrew D. Greentree, H. Wilson, L. C.L. L Hollenberg, Steven Prawer, Philip Hemmer, Fedor Jelezko, and Jörg Wrachtrup. Stark Shift Control of Single Optical Centers in Diamond. *Physical Review Letters*, 97(8):083002, aug 2006.

[162] David M Toyli, Lee C Bassett, Bob B Buckley, Greg Calusine, and David D Awschalom. Engineering and quantum control of single spins in semiconductors. *MRS Bulletin*, 38(2):139–143, feb 2013.

[163] Claire A. McLellan, Bryan A. Myers, Stephan Kraemer, Kenichi Ohno, David D. Awschalom, and Ania C. Bleszynski Jayich. Patterned Formation of Highly Coherent Nitrogen-Vacancy Centers Using a Focused Electron Irradiation Technique. *Nano Letters*, 16(4):2450–2454, apr 2016.

[164] Ariful Haque and Sharaf Sumaiya. An Overview on the Formation and Processing of Nitrogen-Vacancy Photonic Centers in Diamond by Ion Implantation. *Journal of Manufacturing and Materials Processing*, 1(1):6, aug 2017.

[165] T. Schröder, M. Walsh, J. Zheng, S. Mouradian, L. Li, G. Malladi, H. Bakhru, M. Lu, A. Stein, M. Heuck, and D. Englund. Scalable fabrication of coupled NV center - photonic crystal cavity systems by self-aligned N ion implantation. *Optical Materials Express*, 7(5):1514, may 2017.

[166] S. Sangtawesin, T. O. Brundage, Z. J. Atkins, and J. R. Petta. Highly tunable formation of nitrogen-vacancy centers via ion implantation. *Applied Physics Letters*, 105(6):063107, aug 2014.

[167] Jason M. Smith, Simon A. Meynell, Ania C. Bleszynski Jayich, and Jan Meijer. Colour centre generation in diamond for quantum technologies. *Nanophotonics*, 8(11):1889–1906, nov 2019.

[168] Suzanne B. van Dam, Michael Walsh, Maarten J. Degen, Eric Bersin, Sara L. Mouradian, Airat Galiullin, Maximilian Ruf, Mark IJspeert, Tim H. Taminiau, Ronald Hanson, and Dirk R. Englund. Optical coherence of diamond nitrogen-vacancy centers formed by ion implantation and annealing. *Physical Review B*, 99(16):161203, apr 2019.

[169] Felipe Fávaro de Oliveira, Denis Antonov, Ya Wang, Philipp Neumann, Seyed Ali Momenzadeh, Timo Häußermann, Alberto Pasquarelli, Andrej Denisenko, and Jörg Wrachtrup. Tailoring spin defects in diamond by lattice charging. *Nature Communications*, 8(1):15409, aug 2017.

[170] J. R. Rabeau, P. Reichart, G. Tamanyan, D. N. Jamieson, S. Prawer, F. Jelezko, T. Gaebel, I. Popa, M. Domhan, and J. Wrachtrup. Implantation of labelled single nitrogen vacancy centers in diamond using N15. *Applied Physics Letters*, 88(2):023113, jan 2006.

[171] Mark Kasperczyk, Josh A. Zuber, Arne Barfuss, Johannes Kölbl, Viktoria Yurgens, Sigurd Flågan, Tomasz Jakubczyk, Brendan Shields, Richard J. Warburton, and Patrick Maletinsky. Statistically modeling optical linewidths of nitrogen vacancy centers in microstructures. *Physical Review B*, 102(7):075312, aug 2020.

[172] Yu-Chen Chen, Patrick S. Salter, Sebastian Knauer, Laiyi Weng, Angelo C. Frangeskou, Colin J. Stephen, Shazeaa N. Ishmael, Philip R. Dolan, Sam Johnson, Ben L. Green, Gavin W. Morley, Mark E. Newton, John G. Rarity, Martin J. Booth, and Jason M. Smith. Laser writing of coherent colour centres in diamond. *Nature Photonics*, 11(2):77–80, feb 2017.

[173] Yu-Chen Chen, Benjamin Griffiths, Laiyi Weng, Shannon S. Nicley, Shazeaa N. Ishmael, Yashna Lekhai, Sam Johnson, Colin J. Stephen, Ben L. Green, Gavin W. Morley, Mark E. Newton, Martin J. Booth, Patrick S. Salter, and Jason M. Smith. Laser writing of individual nitrogen-vacancy defects in diamond with near-unity yield. *Optica*, 6(5):662, may 2019.

[174] Torataro Kurita, Nobuya Mineyuki, Yasuhiko Shimotsuma, Masanori Fujiwara, Norikazu Mizuochi, Masahiro Shimizu, and Kiyotaka Miura. Efficient generation

of nitrogen-vacancy center inside diamond with shortening of laser pulse duration. *Applied Physics Letters*, 113(21):211102, nov 2018.

[175] J. P. Hadden, V. Bharadwaj, B. Sotillo, S. Rampini, R. Osellame, J. D. Witmer, H. Jayakumar, T. T. Fernandez, A. Chiappini, C. Armellini, M. Ferrari, R. Ramponi, P. E. Barclay, and S. M. Eaton. Integrated waveguides and deterministically positioned nitrogen vacancy centers in diamond created by femtosecond laser writing. *Optics Letters*, 43(15):3586, aug 2018.

[176] C. J. Stephen, B. L. Green, Y. N. D. Lekhai, L. Weng, P. Hill, S. Johnson, A. C. Frangeskou, P. L. Diggle, Y.-C. Chen, M. J. Strain, E. Gu, M. E. Newton, J. M. Smith, P. S. Salter, and G. W. Morley. Deep Three-Dimensional Solid-State Qubit Arrays with Long-Lived Spin Coherence. *Physical Review Applied*, 12(6):064005, dec 2019.

[177] Martina Barbiero, Stefania Castelletto, and Min Gu. Multi-focal laser fabrication of nitrogen vacancy centres in a bulk diamond. *OSA Continuum*, 3(12):3416, dec 2020.

[178] Viktoria Yurgens, Josh A. Zuber, Sigurd Flågan, Marta De Luca, Brendan J. Shields, Ilaria Zardo, Patrick Maletinsky, Richard J. Warburton, and Tomasz Jakubczyk. Low-Charge-Noise Nitrogen-Vacancy Centers in Diamond Created Using Laser Writing with a Solid-Immersion Lens. *ACS Photonics*, 8(6):1726–1734, jun 2021.

[179] Torataro Kurita, Yasuhiko Shimotsuma, Masanori Fujiwara, Masahiro Fujie, Norikazu Mizuochi, Masahiro Shimizu, and Kiyotaka Miura. Direct writing of high-density nitrogen-vacancy centers inside diamond by femtosecond laser irradiation. *Applied Physics Letters*, 118(21):214001, may 2021.

[180] Yu-Chen Chen. *Laser Writing of Coherent Colour Centres in Diamond*. PhD thesis, University of Oxford, 2017.

[181] V.I. Konov. Laser in micro and nanoprocessing of diamond materials. *Laser &Photonics Reviews*, 6(6):739–766, nov 2012.

[182] Vitali V. Kononenko, Igor I. Vlasov, Viktor M. Gololobov, Taras V. Kononenko, Timur A. Semenov, Andrej A. Khomich, Vladimir A. Shershulin, Vladimir S. Krivobok, and Vitaly I. Konov. Nitrogen-vacancy defects in diamond produced by

femtosecond laser nanoablation technique. *Applied Physics Letters*, 111(8):081101, aug 2017.

[183] Faruque M. Hossain, Marcus W. Doherty, Hugh F. Wilson, and Lloyd C. L. Hollenberg. Ab Initio Electronic and Optical Properties of the N-V – Center in Diamond. *Physical Review Letters*, 101(22):226403, nov 2008.

[184] Adam Gali, Maria Fyta, and Efthimios Kaxiras. Ab initio supercell calculations on nitrogen-vacancy center in diamond: Electronic structure and hyperfine tensors. *Physical Review B*, 77(15):155206, apr 2008.

[185] Ádám Gali. Ab initio theory of the nitrogen-vacancy center in diamond. *Nanophotonics*, 8(11):1907–1943, sep 2019.

[186] J. R. Maze, A. Gali, E. Togan, Y. Chu, A. Trifonov, E. Kaxiras, and M. D. Lukin. Properties of nitrogen-vacancy centers in diamond: the group theoretic approach. *New Journal of Physics*, 13(2):025025, feb 2011.

[187] Adam Gali, Erik Janzén, Péter Deák, Georg Kresse, and Efthimios Kaxiras. Theory of Spin-Conserving Excitation of the $N - V^-$ Ceter in Diamond. *Physical Review Letters*, 103(18):186404, oct 2009.

[188] Junyi Lee, Victor Leong, Dmitry Kalashnikov, Jibo Dai, Alagappan Gandhi, and Leonid A. Krivitsky. Integrated single photon emitters. *AVS Quantum Science*, 2(3):031701, oct 2020.

[189] A. Lenef and S. C. Rand. Electronic structure of the N- V center in diamond: Theory. *Physical Review B*, 53(20):13441–13455, may 1996.

[190] Yiwen Chu and Mikhail D. Lukin. Quantum optics with nitrogen-vacancy centers in diamond. *arXiv:1504.05990*, apr 2015.

[191] V.V. Dobrovitski, G.D. Fuchs, A.L. Falk, C. Santori, and D.D. Awschalom. Quantum Control over Single Spins in Diamond. *Annual Review of Condensed Matter Physics*, 4(1):23–50, 2013.

[192] A. Batalov, V. Jacques, F. Kaiser, P. Siyushev, P. Neumann, L. J. Rogers, R. L. McMurtrie, N. B. Manson, F. Jelezko, and J. Wrachtrup. Low Temperature Studies of the Excited-State Structure of Negatively Charged Nitrogen-Vacancy Color Centers in Diamond. *Physical Review Letters*, 102(19):195506, may 2009.

[193] M. W. Doherty, F. Dolde, H. Fedder, F. Jelezko, J. Wrachtrup, N. B. Manson, and L. C. L. Hollenberg. Theory of the ground-state spin of the $NV^-$ center in diamond. *Physical Review B*, 85(20):205203, may 2012.

[194] Sam Johnson, Philip R Dolan, and Jason M Smith. Diamond photonics for distributed quantum networks. *Progress in Quantum Electronics*, 55(May):129–165, sep 2017.

[195] G. D. Fuchs, V. V. Dobrovitski, R. Hanson, A. Batra, C. D. Weis, T. Schenkel, and D. D. Awschalom. Excited-State Spectroscopy Using Single Spin Manipulation in Diamond. *Physical Review Letters*, 101(11):117601, sep 2008.

[196] Donghun Lee, Kenneth W. Lee, Jeffrey V. Cady, Preeti Ovartchaiyapong, and Ania C Bleszynski Jayich. Topical review: spins and mechanics in diamond. *Journal of Optics*, 19(3):033001, mar 2017.

[197] L. J. Rogers, S. Armstrong, M. J. Sellars, and N. B. Manson. Infrared emission of the NV centre in diamond: Zeeman and uniaxial stress studies. *New Journal of Physics*, 10(10):103024, oct 2008.

[198] V. M. Acosta, A. Jarmola, E. Bauch, and D. Budker. Optical properties of the nitrogen-vacancy singlet levels in diamond. *Physical Review B*, 82(20):201202, nov 2010.

[199] Lucio Robledo, Hannes Bernien, Toeno Van Der Sar, and Ronald Hanson. Spin dynamics in the optical cycle of single nitrogen-vacancy centres in diamond. *New Journal of Physics*, 13, 2011.

[200] M. L. Goldman, M. W. Doherty, A. Sipahigil, N. Y. Yao, S. D. Bennett, N. B. Manson, A. Kubanek, and M. D. Lukin. State-selective intersystem crossing in nitrogen-vacancy centers. *Physical Review B*, 91(16):165201, apr 2015.

[201] P. Neumann, R. Kolesov, V. Jacques, J. Beck, J. Tisler, A. Batalov, L. Rogers, N. B. Manson, G. Balasubramanian, F. Jelezko, and J. Wrachtrup. Excited-state spectroscopy of single NV defects in diamond using optically detected magnetic resonance. *New Journal of Physics*, 11(1):013017, jan 2009.

[202] M. L. Goldman, A. Sipahigil, M. W. Doherty, N. Y. Yao, S. D. Bennett, M. Markham, D. J. Twitchen, N. B. Manson, A. Kubanek, and M. D. Lukin. Phonon-Induced Population Dynamics and Intersystem Crossing in Nitrogen-Vacancy Centers. *Physical Review Letters*, 114(14):145502, apr 2015.

[203] L. J. Rogers, R. L. McMurtrie, M. J. Sellars, and N. B. Manson. Time-averaging within the excited state of the nitrogen-vacancy centre in diamond. *New Journal of Physics*, 11(6):063007, jun 2009.

[204] Lilian Childress and Ronald Hanson. Diamond NV centers for quantum computing and quantum networks. *MRS Bulletin*, 38(2):134–138, feb 2013.

[205] Kun Huang and Avril Rhys. Theory of light absorption and non-radiative transitions in F-centres. *Proc. R. Soc. Lond. A*, 204:406–423, 1950.

[206] Mark Fox. *Optical Properties of Solids*. Oxford University Press, 1st edition, 2001.

[207] G. Davies. The Jahn-Teller effect and vibronic coupling at deep levels in diamond. *Reports on Progress in Physics*, 44(7):787–830, jul 1981.

[208] Audrius Alkauskas, Bob B. Buckley, David D. Awschalom, and Chris G Van de Walle. First-principles theory of the luminescence lineshape for the triplet transition in diamond NV centres. *New Journal of Physics*, 16(7):073026, jul 2014.

[209] Lukas Razinkovas, Marcus W. Doherty, Neil B. Manson, Chris G. Van de Walle, and Audrius Alkauskas. Vibrational and vibronic structure of isolated point defects: The nitrogen-vacancy center in diamond. *Physical Review B*, 104(4):045303, jul 2021.

[210] Tetsuya Tohei, Akihide Kuwabara, Fumiyasu Oba, and Isao Tanaka. Debye temperature and stiffness of carbon and boron nitride polymorphs from first principles calculations. *Physical Review B*, 73(6):064304, feb 2006.

[211] Andreas V. Kuhlmann, Julien Houel, Daniel Brunner, Arne Ludwig, Dirk Reuter, Andreas D. Wieck, and Richard J. Warburton. A dark-field microscope for background-free detection of resonance fluorescence from single semiconductor quantum dots operating in a set-and-forget mode. *Review of Scientific Instruments*, 84(7):073905, jul 2013.

[212] Meryem Benelajla, Elena Kammann, Bernhard Urbaszek, and Khaled Karrai. Physical Origins of Extreme Cross-Polarization Extinction in Confocal Microscopy. *Physical Review X*, 11(2):021007, apr 2021.

[213] T. Legero, T. Wilk, A. Kuhn, and G. Rempe. Time-resolved two-photon quantum interference. *Applied Physics B*, 77(8):797–802, dec 2003.

[214] M. Ruf, M.J. Weaver, S.B. van Dam, and R. Hanson. Resonant Excitation and Purcell Enhancement of Coherent Nitrogen-Vacancy Centers Coupled to a Fabry-Perot Microcavity. *Physical Review Applied*, 15(2):024049, feb 2021.

[215] C. K. Hong., Z. Y. Ou, and L. Mandel. Measurement of subpicosecond time intervals between two photons by interference. *Phys. Rev. Lett*, 59:2044, 1987.

[216] Igor Aharonovich, Dirk Englund, and Milos Toth. Solid-state single-photon emitters. *Nature Photonics*, 10(10):631–641, oct 2016.

[217] Emma R. Schmidgall, Srivatsa Chakravarthi, Michael Gould, Ian R. Christen, Karine Hestroffer, Fariba Hatami, and Kai-Mei C. Fu. Frequency Control of Single Quantum Emitters in Integrated Photonic Circuits. *Nano Letters*, 18(2):1175–1179, feb 2018.

[218] Péter Udvarhelyi, Roland Nagy, Florian Kaiser, Sang-Yun Lee, Jörg Wrachtrup, and Adam Gali. Spectrally Stable Defect Qubits with no Inversion Symmetry for Robust Spin-To-Photon Interface. *Physical Review Applied*, 11(4):044022, apr 2019.

[219] Gergő Thiering and Adam Gali. Color centers in diamond for quantum applications. In Mutsuko Hatano Christoph E. Nebel, Igor Aharonovich, Norikazu Mizuochi, editor, *Semiconductors and Semimetals*, pages 1–36. 2020.

[220] Y. Chu, N.P. de Leon, B.J. Shields, B. Hausmann, R. Evans, E. Togan, M. J. Burek, M. Markham, A. Stacey, A.S. Zibrov, A. Yacoby, D.J. Twitchen, M. Loncar, H. Park, P. Maletinsky, and M.D. Lukin. Coherent Optical Transitions in Implanted Nitrogen Vacancy Centers. *Nano Letters*, 14(4):1982–1986, apr 2014.

[221] Kai-Mei C. Fu, Charles Santori, Paul E. Barclay, Lachlan J. Rogers, Neil B. Manson, and Raymond G. Beausoleil. Observation of the Dynamic Jahn-Teller Effect in the Excited States of Nitrogen-Vacancy Centers in Diamond. *Physical Review Letters*, 103(25):256404, dec 2009.

[222] P. Siyushev, H. Pinto, M. Vörös, A. Gali, F. Jelezko, and J. Wrachtrup. Optically Controlled Switching of the Charge State of a Single Nitrogen-Vacancy Center in Diamond at Cryogenic Temperatures. *Physical Review Letters*, 110(16):167402, apr 2013.

[223] K. Beha, A. Batalov, N. B. Manson, R. Bratschitsch, and A. Leitenstorfer. Optimum Photoluminescence Excitation and Recharging Cycle of Single Nitrogen-Vacancy Centers in Ultrapure Diamond. *Physical Review Letters*, 109(9):097404, aug 2012.

[224] N.B. Manson and J.P. Harrison. Photo-ionization of the nitrogen-vacancy center in diamond. *Diamond and Related Materials*, 14(10):1705–1710, oct 2005.

[225] T. Gaebel, M. Domhan, C. Wittmann, I. Popa, F. Jelezko, J. Rabeau, A. Greentree, S. Prawer, E. Trajkov, P.R. Hemmer, and J. Wrachtrup. Photochromism in single nitrogen-vacancy defect in diamond. *Applied Physics B*, 82(2):243–246, feb 2006.

[226] Janik Wolters, Nikola Sadzak, Andreas W. Schell, Tim Schröder, and Oliver Benson. Measurement of the Ultrafast Spectral Diffusion of the Optical Transition of Nitrogen Vacancy Centers in Nano-Size Diamond Using Correlation Interferometry. *Physical Review Letters*, 110(2):027401, jan 2013.

[227] L. C. Bassett, F. J. Heremans, C. G. Yale, B. B. Buckley, and D. D. Awschalom. Electrical Tuning of Single Nitrogen-Vacancy Center Optical Transitions Enhanced by Photoinduced Fields. *Physical Review Letters*, 107(26):266403, dec 2011.

[228] J. Isberg, A. Tajani, and D. J. Twitchen. Photoionization measurement of deep defects in single-crystalline CVD diamond using the transient-current technique. *Physical Review B*, 73(24):245207, jun 2006.

[229] Lucio Robledo, Hannes Bernien, Ilse van Weperen, and Ronald Hanson. Control and Coherence of the Optical Transition of Single Nitrogen Vacancy Centers in Diamond. *Physical Review Letters*, 105(17):177403, oct 2010.

[230] K.-M. C. Fu, C. Santori, P. E. Barclay, and R. G. Beausoleil. Conversion of neutral nitrogen-vacancy centers to negatively charged nitrogen-vacancy centers through selective oxidation. *Applied Physics Letters*, 96(12):121907, mar 2010.

[231] V. M. Acosta, C. Santori, A. Faraon, Z. Huang, K.-M. C. Fu, A. Stacey, D. A. Simpson, K. Ganesan, S. Tomljenovic-Hanic, A. D. Greentree, S. Prawer, and R. G. Beausoleil. Dynamic Stabilization of the Optical Resonances of Single Nitrogen-Vacancy Centers in Diamond. *Physical Review Letters*, 108(20):206401, may 2012.

[232] Andreas V. Kuhlmann, Julien Houel, Arne Ludwig, Lukas Greuter, Dirk Reuter, Andreas D. Wieck, Martino Poggio, and Richard J. Warburton. Charge noise and

spin noise in a semiconductor quantum device. *Nature Physics*, 9(9):570–575, sep 2013.

[233] Jonathan H. Prechtel, Andreas V. Kuhlmann, Julien Houel, Lukas Greuter, Arne Ludwig, Dirk Reuter, Andreas D. Wieck, and Richard J. Warburton. Frequency-Stabilized Source of Single Photons from a Solid-State Qubit. *Physical Review X*, 3(4):041006, oct 2013.

[234] Liang Zhai, Matthias C. Löbl, Giang N. Nguyen, Julian Ritzmann, Alisa Javadi, Clemens Spinnler, Andreas D. Wieck, Arne Ludwig, and Richard J. Warburton. Low-noise GaAs quantum dots for quantum photonics. *Nature Communications*, 11(1):4745, dec 2020.

[235] Petr Siyushev, Milos Nesladek, Emilie Bourgeois, Michal Gulka, Jaroslav Hruby, Takashi Yamamoto, Michael Trupke, Tokuyuki Teraji, Junichi Isoya, and Fedor Jelezko. Photoelectrical imaging and coherent spin-state readout of single nitrogen-vacancy centers in diamond. *Science*, 363(6428):728–731, feb 2019.

[236] David D. Awschalom, Ryan Epstein, and Ronald Hanson. The Diamond Age Diamond Age of Spintronics. *Scientific American*, 297(4):84–91, oct 2007.

[237] G. de Lange, Z. H. Wang, D. Riste, V. V. Dobrovitski, and R. Hanson. Universal Dynamical Decoupling of a Single Solid-State Spin from a Spin Bath. *Science*, 330(6000):60–63, oct 2010.

[238] David Hopper, Henry Shulevitz, and Lee Bassett. Spin Readout Techniques of the Nitrogen-Vacancy Center in Diamond. *Micromachines*, 9(9):437, aug 2018.

[239] G. D. Fuchs, V. V. Dobrovitski, D. M. Toyli, F. J. Heremans, C. D. Weis, T. Schenkel, and D. D. Awschalom. Excited-state spin coherence of a single nitrogen–vacancy centre in diamond. *Nature Physics*, 6(9):668–672, sep 2010.

[240] B. J. Shields, Q. P. Unterreithmeier, N. P. de Leon, H. Park, and M. D. Lukin. Efficient Readout of a Single Spin State in Diamond via Spin-to-Charge Conversion. *Physical Review Letters*, 114(13):136402, mar 2015.

[241] David A. Hopper, Richard R. Grote, Annemarie L. Exarhos, and Lee C. Bassett. Near-infrared-assisted charge control and spin readout of the nitrogen-vacancy center in diamond. *Physical Review B*, 94(24):241201, dec 2016.

[242] Lucio Robledo, Lilian Childress, Hannes Bernien, Bas Hensen, Paul F.A. A. Alkemade, and Ronald Hanson. High-fidelity projective read-out of a solid-state spin quantum register. *Nature*, 477(7366):574–578, sep 2011.

[243] Ph Tamarat, N. B. Manson, J. P. Harrison, R. L. McMurtrie, A. Nizovtsev, C. Santori, R. G. Beausoleil, P. Neumann, T. Gaebel, F. Jelezko, P. Hemmer, and J. Wrachtrup. Spin-flip and spin-conserving optical transitions of the nitrogen-vacancy centre in diamond. *New Journal of Physics*, 10(4):045004, apr 2008.

[244] Dominik M. Irber, Francesco Poggiali, Fei Kong, Michael Kieschnick, Tobias Lühmann, Damian Kwiatkowski, Jan Meijer, Jiangfeng Du, Fazhan Shi, and Friedemann Reinhard. Robust all-optical single-shot readout of nitrogen-vacancy centers in diamond. *Nature Communications*, 12(1):532, dec 2021.

[245] S. A. Wolf, I. Rosenberg, R. Rapaport, and N. Bar-Gill. Purcell-enhanced optical spin readout of nitrogen-vacancy centers in diamond. *Physical Review B*, 92(23):235410, dec 2015.

[246] Qi Zhang, Yuhang Guo, Wentao Ji, Mengqi Wang, Jun Yin, Fei Kong, Yiheng Lin, Chunming Yin, Fazhan Shi, Ya Wang, and Jiangfeng Du. High-fidelity single-shot readout of single electron spin in diamond with spin-to-charge conversion. *Nature Communications*, 12(1):1529, dec 2021.

[247] Francesco Casola, Toeno van der Sar, and Amir Yacoby. Probing condensed matter physics with magnetometry based on nitrogen-vacancy centres in diamond. *Nature Reviews Materials*, 3(1):17088, jan 2018.

[248] A Gruber. Scanning Confocal Optical Microscopy and Magnetic Resonance on Single Defect Centers. *Science*, 276(5321):2012–2014, jun 1997.

[249] Benjamin Smeltzer, Lilian Childress, and Adam Gali. 13 C hyperfine interactions in the nitrogen-vacancy centre in diamond. *New Journal of Physics*, 13(2):025021, feb 2011.

[250] M. J. Degen, S. J. H. Loenen, H. P. Bartling, C. E. Bradley, A. L. Meinsma, M. Markham, D. J. Twitchen, and T. H. Taminiau. Entanglement of dark electron-nuclear spin defects in diamond. *Nature Communications*, 12(1):3470, dec 2021.

[251] Dirk Englund, Brendan Shields, Kelley Rivoire, Fariba Hatami, Jelena Vučković, Hongkun Park, and Mikhail D. Lukin. Deterministic Coupling of a Single Nitrogen

Vacancy Center to a Photonic Crystal Cavity. *Nano Letters*, 10(10):3922–3926, oct 2010.

[252] Luke Gordon, Justin R. Weber, Joel B. Varley, Anderson Janotti, David D. Awschalom, and Chris G. Van de Walle. Quantum computing with defects. *MRS Bulletin*, 38(10):802–807, oct 2013.

[253] Victoria A. Norman, Sridhar Majety, Zhipan Wang, William H. Casey, Nicholas Curro, and Marina Radulaski. Novel color center platforms enabling fundamental scientific discovery. *InfoMat*, 3(8):869–890, aug 2021.

[254] Nathalie P. de Leon, Kohei M. Itoh, Dohun Kim, Karan K. Mehta, Tracy E. Northup, Hanhee Paik, B S Palmer, N Samarth, Sorawis Sangtawesin, and D W Steuerman. Materials challenges and opportunities for quantum computing hardware. *Science*, 372(6539):eabb2823, apr 2021.

[255] Daniel Riedel, Sigurd Flågan, Patrick Maletinsky, and Richard J. Warburton. Cavity-Enhanced Raman Scattering for In Situ Alignment and Characterization of Solid-State Microcavities. *Physical Review Applied*, 13(1):014036, jan 2020.

[256] Gergő Thiering and Adam Gali. Ab Initio Magneto-Optical Spectrum of Group-IV Vacancy Color Centers in Diamond. *Physical Review X*, 8(2):021063, jun 2018.

[257] Carlo Bradac, Weibo Gao, Jacopo Forneris, Matthew E. Trusheim, and Igor Aharonovich. Quantum nanophotonics with group IV defects in diamond. *Nature Communications*, 10(1):5625, dec 2019.

[258] Disheng Chen, Nikolay Zheludev, and Wei-bo Gao. Building Blocks for Quantum Network Based on Group-IV Split-Vacancy Centers in Diamond. *Advanced Quantum Technologies*, 3(2):1900069, feb 2020.

[259] Elke Neu, David Steinmetz, Janine Riedrich-Möller, Stefan Gsell, Martin Fischer, Matthias Schreck, and Christoph Becher. Single photon emission from silicon-vacancy colour centres in chemical vapour deposition nano-diamonds on iridium. *New Journal of Physics*, 13(2):025012, feb 2011.

[260] Johannes Görlitz, Dennis Herrmann, Gergő Thiering, Philipp Fuchs, Morgane Gandil, Takayuki Iwasaki, Takashi Taniguchi, Michael Kieschnick, Jan Meijer, Mutsuko Hatano, Adam Gali, and Christoph Becher. Spectroscopic investigations of negatively charged tin-vacancy centres in diamond. *New Journal of Physics*, 22(1):013048, jan 2020.

[261] Takayuki Iwasaki, Yoshiyuki Miyamoto, Takashi Taniguchi, Petr Siyushev, Mathias H. Metsch, Fedor Jelezko, and Mutsuko Hatano. Tin-Vacancy Quantum Emitters in Diamond. *Physical Review Letters*, 119(25):253601, dec 2017.

[262] B. Machielse, S. Bogdanovic, S. Meesala, S. Gauthier, M. J. Burek, G. Joe, M. Chalupnik, Y. I. Sohn, J. Holzgrafe, R. E. Evans, C. Chia, H. Atikian, M. K. Bhaskar, D. D. Sukachev, L. Shao, S. Maity, M. D. Lukin, and M. Lončar. Quantum Interference of Electromechanically Stabilized Emitters in Nanophotonic Devices. *Physical Review X*, 9(3):031022, aug 2019.

[263] Matthew E. Trusheim, Benjamin Pingault, Noel H. Wan, Mustafa Gündoğan, Lorenzo De Santis, Romain Debroux, Dorian Gangloff, Carola Purser, Kevin C. Chen, Michael Walsh, Joshua J. Rose, Jonas N. Becker, Benjamin Lienhard, Eric Bersin, Ioannis Paradeisanos, Gang Wang, Dominika Lyzwa, Alejandro R.P. Montblanch, Girish Malladi, Hassaram Bakhru, Andrea C. Ferrari, Ian A. Walmsley, Mete Atatüre, and Dirk Englund. Transform-Limited Photons From a Coherent Tin-Vacancy Spin in Diamond. *Physical Review Letters*, 124(2):023602, jan 2020.

[264] Alison E. Rugar, Constantin Dory, Shahriar Aghaeimeibodi, Haiyu Lu, Shuo Sun, Sattwik Deb Mishra, Zhi-Xun Shen, Nicholas A. Melosh, and Jelena Vučković. Narrow-Linewidth Tin-Vacancy Centers in a Diamond Waveguide. *ACS Photonics*, 7(9):2356–2361, sep 2020.

[265] U Wahl, J. G. Correia, R Villarreal, E Bourgeois, M Gulka, M Nesládek, A Vantomme, and L. M. C. Pereira. Direct Structural Identification and Quantification of the Split-Vacancy Configuration for Implanted Sn in Diamond. *Physical Review Letters*, 125(4):045301, jul 2020.

[266] Christian Hepp, Tina Müller, Victor Waselowski, Jonas N. Becker, Benjamin Pingault, Hadwig Sternschulte, Doris Steinmüller-Nethl, Adam Gali, Jeronimo R. Maze, Mete Atatüre, and Christoph Becher. Electronic Structure of the Silicon Vacancy Color Center in Diamond. *Physical Review Letters*, 112(3):036405, jan 2014.

[267] Lorenzo De Santis, Matthew E. Trusheim, Kevin C. Chen, and Dirk R. Englund. Investigation of the Stark Effect on a Centrosymmetric Quantum Emitter in Diamond. *Physical Review Letters*, 127(14):147402, sep 2021.

[268] Shahriar Aghaeimeibodi, Daniel Riedel, Alison E. Rugar, Constantin Dory, and

Jelena Vučković. Electrical Tuning of Tin-Vacancy Centers in Diamond. *Physical Review Applied*, 15(6):064010, jun 2021.

[269] Jonas Nils Becker and Elke Neu. The silicon vacancy center in diamond. In *Semiconductors and Semimetals*, volume 103, pages 201–235. Elsevier Inc., 1 edition, 2020.

[270] Adam Gali and Jeronimo R. Maze. Ab initio study of the split silicon-vacancy defect in diamond: Electronic structure and related properties. *Physical Review B*, 88(23):235205, dec 2013.

[271] Erika Janitz. *A Fabry-Pérot Microcavity for Quantum Optics with Atomic Defects in Diamond*. PhD thesis, McGill University, 2019.

[272] Takayuki Iwasaki. Color centers based on heavy group-IV elements. In *Semiconductors and Semimetals*, volume 103, pages 237–256. Elsevier Inc., 1 edition, 2020.

[273] Andrey Bolshakov, Victor Ralchenko, Vadim Sedov, Andrey Khomich, Igor Vlasov, Alexander Khomich, Nikolay Trofimov, Vladimir Krivobok, Sergei Nikolaev, Roman Khmelnitskii, and Vladimir Saraykin. Photoluminescence of SiV centers in single crystal CVD diamond in situ doped with Si from silane. *physica status solidi (a)*, 212(11):2525–2532, nov 2015.

[274] Youying Rong, Ke Cheng, Zhiping Ju, Chengda Pan, Qiang Ma, Shikang Liu, Si Shen, Botao Wu, Tianqing Jia, E Wu, and Heping Zeng. Bright near-surface silicon vacancy centers in diamond fabricated by femtosecond laser ablation. *Optics Letters*, 44(15):3793, aug 2019.

[275] Tim Schröder, Matthew E Trusheim, Michael Walsh, Luozhou Li, Jiabao Zheng, Marco Schukraft, Alp Sipahigil, Ruffin E Evans, Denis D Sukachev, Christian T Nguyen, Jose L Pacheco, Ryan M Camacho, Edward S Bielejec, Mikhail D Lukin, and Dirk Englund. Scalable focused ion beam creation of nearly lifetime-limited single quantum emitters in diamond nanostructures. *Nature Communications*, 8(1):15376, aug 2017.

[276] Syuto Tamura, Godai Koike, Akira Komatsubara, Tokuyuki Teraji, Shinobu Onoda, Liam P. McGuinness, Lachlan Rogers, Boris Naydenov, E. Wu, Liu Yan, Fedor Jelezko, Takeshi Ohshima, Junichi Isoya, Takahiro Shinada, and Takashi

Tanii. Array of bright silicon-vacancy centers in diamond fabricated by low-energy focused ion beam implantation. *Applied Physics Express*, 7(11):115201, nov 2014.

[277] L.J. Rogers, K.D. Jahnke, T. Teraji, L. Marseglia, C. Müller, B. Naydenov, H. Schauffert, C. Kranz, J. Isoya, L.P. McGuinness, and F. Jelezko. Multiple intrinsically identical single-photon emitters in the solid state. *Nature Communications*, 5(1):4739, dec 2014.

[278] A. Sipahigil, K. D. Jahnke, L. J. Rogers, T. Teraji, J. Isoya, A. S. Zibrov, F. Jelezko, and M. D. Lukin. Indistinguishable Photons from Separated Silicon-Vacancy Centers in Diamond. *Physical Review Letters*, 113(11):113602, sep 2014.

[279] Ruffin E Evans, Alp Sipahigil, Denis D Sukachev, Alexander S Zibrov, and Mikhail D Lukin. Narrow-Linewidth Homogeneous Optical Emitters in Diamond Nanostructures via Silicon Ion Implantation. *Physical Review Applied*, 5(4):044010, apr 2016.

[280] D. D. Sukachev, A. Sipahigil, C. T. Nguyen, M. K. Bhaskar, R. E. Evans, F. Jelezko, and M. D. Lukin. Silicon-Vacancy Spin Qubit in Diamond: A Quantum Memory Exceeding 10 ms with Single-Shot State Readout. *Physical Review Letters*, 119(22):223602, nov 2017.

[281] Jonas Nils Becker, Johannes Görlitz, Carsten Arend, Matthew Markham, and Christoph Becher. Ultrafast all-optical coherent control of single silicon vacancy colour centres in diamond. *Nature Communications*, 7(1):13512, dec 2016.

[282] Jonas Nils Becker and Christoph Becher. Coherence Properties and Quantum Control of Silicon Vacancy Color Centers in Diamond. *physica status solidi (a)*, 214(11):1700586, nov 2017.

[283] Young-Ik Sohn, Srujan Meesala, Benjamin Pingault, Haig A. Atikian, Jeffrey Holzgrafe, Mustafa Gündoğan, Camille Stavrakas, Megan J. Stanley, Alp Sipahigil, Joonhee Choi, Mian Zhang, Jose L. Pacheco, John Abraham, Edward Bielejec, Mikhail D. Lukin, Mete Atatüre, and Marko Lončar. Controlling the coherence of a diamond spin qubit through its strain environment. *Nature Communications*, 9(1):2012, dec 2018.

[284] Srujan Meesala, Young-Ik Sohn, Benjamin Pingault, Linbo Shao, Haig A. Atikian, Jeffrey Holzgrafe, Mustafa Gündoğan, Camille Stavrakas, Alp Sipahigil, Cleaven Chia, Ruffin Evans, Michael J. Burek, Mian Zhang, Lue Wu, Jose L. Pacheco, John

Abraham, Edward Bielejec, Mikhail D. Lukin, Mete Atatüre, and Marko Lončar. Strain engineering of the silicon-vacancy center in diamond. *Physical Review B*, 97(20):205444, may 2018.

[285] Jonas N. Becker, Benjamin Pingault, David Groß, Mustafa Gündoğan, Nadezhda Kukharchyk, Matthew Markham, Andrew Edmonds, Mete Atatüre, Pavel Bushev, and Christoph Becher. All-Optical Control of the Silicon-Vacancy Spin in Diamond at Millikelvin Temperatures. *Physical Review Letters*, 120(5):053603, jan 2018.

[286] Ruffin E. Evans, Mihir K. Bhaskar, Denis D. Sukachev, Christian T. Nguyen, Alp Sipahigil, Michael J. Burek, Bartholomeus Machielse, Grace H. Zhang, Alexander S. Zibrov, Edward Bielejec, Hongkun Park, Marko Lončar, and Mikhail D. Lukin. Photon-mediated interactions between quantum emitters in a diamond nanocavity. *Science*, 362(6415):662–665, nov 2018.

[287] Lachlan J. Rogers, Kay D. Jahnke, Mathias H. Metsch, Alp Sipahigil, Jan M. Binder, Tokuyuki Teraji, Hitoshi Sumiya, Junichi Isoya, Mikhail D. Lukin, Philip Hemmer, and Fedor Jelezko. All-Optical Initialization, Readout, and Coherent Preparation of Single Silicon-Vacancy Spins in Diamond. *Physical Review Letters*, 113(26):263602, dec 2014.

[288] C. T. Nguyen, D. D. Sukachev, M. K. Bhaskar, B. Machielse, D. S. Levonian, E. N. Knall, P. Stroganov, C. Chia, M. J. Burek, R. Riedinger, H. Park, M. Lončar, and M. D. Lukin. An integrated nanophotonic quantum register based on silicon-vacancy spins in diamond. *Physical Review B*, 100(16):165428, oct 2019.

[289] Mathias H. Metsch, Katharina Senkalla, Benedikt Tratzmiller, Jochen Scheuer, Michael Kern, Jocelyn Achard, Alexandre Tallaire, Martin B. Plenio, Petr Siyushev, and Fedor Jelezko. Initialization and Readout of Nuclear Spins via a Negatively Charged Silicon-Vacancy Center in Diamond. *Physical Review Letters*, 122(19):190503, may 2019.

[290] C. T. Nguyen, D. D. Sukachev, M. K. Bhaskar, B. Machielse, D. S. Levonian, E. N. Knall, P. Stroganov, R. Riedinger, H. Park, M. Lončar, and M. D. Lukin. Quantum Network Nodes Based on Diamond Qubits with an Efficient Nanophotonic Interface. *Physical Review Letters*, 123(18):183602, oct 2019.

[291] M. K. Bhaskar, R. Riedinger, B. Machielse, D. S. Levonian, C. T. Nguyen, E. N. Knall, H. Park, D. Englund, M. Lončar, D. D. Sukachev, and M. D. Lukin. Ex-

perimental demonstration of memory-enhanced quantum communication. *Nature*, 580(7801):60–64, apr 2020.

[292] Brendon C. Rose, Ding Huang, Zi-Huai Zhang, Paul Stevenson, Alexei M. Tyryshkin, Sorawis Sangtawesin, Srikanth Srinivasan, Lorne Loudin, Matthew L. Markham, Andrew M. Edmonds, Daniel J. Twitchen, Stephen A. Lyon, and Nathalie P. de Leon. Observation of an environmentally insensitive solid-state spin defect in diamond. *Science*, 361(6397):60–63, jul 2018.

[293] B. L. Green, M. W. Doherty, E. Nako, N. B. Manson, U. F. S. D'Haenens-Johansson, S. D. Williams, D. J. Twitchen, and M. E. Newton. Electronic structure of the neutral silicon-vacancy center in diamond. *Physical Review B*, 99(16):161112, apr 2019.

[294] Takayuki Iwasaki, Fumitaka Ishibashi, Yoshiyuki Miyamoto, Yuki Doi, Satoshi Kobayashi, Takehide Miyazaki, Kosuke Tahara, Kay D. Jahnke, Lachlan J. Rogers, Boris Naydenov, Fedor Jelezko, Satoshi Yamasaki, Shinji Nagamachi, Toshiro Inubushi, Norikazu Mizuochi, and Mutsuko Hatano. Germanium-Vacancy Single Color Centers in Diamond. *Scientific Reports*, 5(1):12882, oct 2015.

[295] Petr Siyushev, Mathias H. Metsch, Aroosa Ijaz, Jan M. Binder, Mihir K. Bhaskar, Denis D. Sukachev, Alp Sipahigil, Ruffin E. Evans, Christian T. Nguyen, Mikhail D. Lukin, Philip R. Hemmer, Yuri N. Palyanov, Igor N. Kupriyanov, Yuri M. Borzdov, Lachlan J. Rogers, and Fedor Jelezko. Optical and microwave control of germanium-vacancy center spins in diamond. *Physical Review B*, 96(8):1–5, 2017.

[296] M. K. Bhaskar, D. D. Sukachev, A. Sipahigil, R. E. Evans, M. J. Burek, C. T. Nguyen, L. J. Rogers, P. Siyushev, M. H. Metsch, H. Park, F. Jelezko, M. Lončar, and M. D. Lukin. Quantum Nonlinear Optics with a Germanium-Vacancy Color Center in a Nanoscale Diamond Waveguide. *Physical Review Letters*, 118(22):223603, may 2017.

[297] Disheng Chen, Zhao Mu, Yu Zhou, Johannes E. Fröch, Abdullah Rasmit, Carole Diederichs, Nikolay Zheludev, Igor Aharonovich, and Wei-bo Gao. Optical Gating of Resonance Fluorescence from a Single Germanium Vacancy Color Center in Diamond. *Physical Review Letters*, 123(3):033602, jul 2019.

[298] S. Ditalia Tchernij, T. Herzig, J. Forneris, J. Küpper, S. Pezzagna, P. Traina, E. Moreva, I. P. Degiovanni, G. Brida, N. Skukan, M. Genovese, M. Jakšić, J. Mei-

jer, and P. Olivero. Single-Photon-Emitting Optical Centers in Diamond Fabricated upon Sn Implantation. *ACS Photonics*, 4(10):2580–2586, oct 2017.

[299] Alison E. Rugar, Haiyu Lu, Constantin Dory, Shuo Sun, Patrick J. McQuade, Zhi-Xun Shen, Nicholas A. Melosh, and Jelena Vučković. Generation of Tin-Vacancy Centers in Diamond via Shallow Ion Implantation and Subsequent Diamond Overgrowth. *Nano Letters*, 20(3):1614–1619, mar 2020.

[300] Alison E. Rugar, Shahriar Aghaeimeibodi, Daniel Riedel, Constantin Dory, Haiyu Lu, Patrick J. McQuade, Zhi-Xun Shen, Nicholas A. Melosh, and Jelena Vučković. Quantum Photonic Interface for Tin-Vacancy Centers in Diamond. *Physical Review X*, 11(3):031021, jul 2021.

[301] Matthew E. Trusheim, Noel H. Wan, Kevin C. Chen, Christopher J. Ciccarino, Johannes Flick, Ravishankar Sundararaman, Girish Malladi, Eric Bersin, Michael Walsh, Benjamin Lienhard, Hassaram Bakhru, Prineha Narang, and Dirk Englund. Lead-related quantum emitters in diamond. *Physical Review B*, 99(7):075430, feb 2019.

[302] S. Ditalia Tchernij, T. Lühmann, T. Herzig, J. Küpper, A. Damin, S. Santonocito, M. Signorile, P. Traina, E. Moreva, F. Celegato, S. Pezzagna, I. P. Degiovanni, P. Olivero, M. Jakšić, J. Meijer, P. M. Genovese, and J. Forneris. Single-Photon Emitters in Lead-Implanted Single-Crystal Diamond. *ACS Photonics*, 5(12):4864–4871, dec 2018.

[303] Richard Nelz, Johannes Görlitz, Dennis Herrmann, Abdallah Slablab, Michel Challier, Mariusz Radtke, Martin Fischer, Stefan Gsell, Matthias Schreck, Christoph Becher, and Elke Neu. Toward wafer-scale diamond nano- and quantum technologies. *APL Materials*, 7(1):011108, jan 2019.

[304] Matthias Schreck, Stefan Gsell, Rosaria Brescia, and Martin Fischer. Ion bombardment induced buried lateral growth: the key mechanism for the synthesis of single crystal diamond wafers. *Scientific Reports*, 7(1):44462, apr 2017.

[305] Michel Challier, Selda Sonusen, Arne Barfuss, Dominik Rohner, Daniel Riedel, Johannes Koelbl, Marc Ganzhorn, Patrick Appel, Patrick Maletinsky, and Elke Neu. Advanced Fabrication of Single-Crystal Diamond Membranes for Quantum Technologies. *Micromachines*, 9(4):148, mar 2018.

[306] Noel H. Wan, Tsung-Ju Lu, Kevin C. Chen, Michael P. Walsh, Matthew E. Trusheim, Lorenzo De Santis, Eric A. Bersin, Isaac B. Harris, Sara L. Mouradian, Ian R. Christen, Edward S. Bielejec, and Dirk Englund. Large-scale integration of artificial atoms in hybrid photonic circuits. *Nature*, 583(7815):226–231, jul 2020.

[307] Andrew Dzurak. Diamond and silicon converge. *Nature*, 479(7371):47–48, nov 2011.

[308] Mehran Kianinia and Igor Aharonovich. Diamond photonics is scaling up. *Nature Photonics*, 14(10):599–600, oct 2020.

[309] Lee C. Bassett, Audrius Alkauskas, Annemarie L. Exarhos, and Kai-Mei C. Fu. Quantum defects by design. *Nanophotonics*, 8(11):1867–1888, oct 2019.

[310] Gary Wolfowicz, F. Joseph Heremans, Christopher P. Anderson, Shun Kanai, Hosung Seo, Adam Gali, Giulia Galli, and David D. Awschalom. Quantum guidelines for solid-state spin defects. *Nature Reviews Materials*, 6(10):906–925, oct 2021.

[311] Nguyen T. Son, Christopher P. Anderson, Alexandre Bourassa, Kevin C. Miao, Charles Babin, Matthias Widmann, Matthias Niethammer, Jawad Ul Hassan, Naoya Morioka, Ivan G. Ivanov, Florian Kaiser, Joerg Wrachtrup, and David D. Awschalom. Developing silicon carbide for quantum spintronics. *Applied Physics Letters*, 116(19):190501, may 2020.

[312] William F. Koehl, Bob B. Buckley, F. Joseph Heremans, Greg Calusine, and David D. Awschalom. Room temperature coherent control of defect spin qubits in silicon carbide. *Nature*, 479(7371):84–87, nov 2011.

[313] David J. Christle, Abram L. Falk, Paolo Andrich, Paul V. Klimov, Jawad Ul Hassan, Nguyen T. Son, Erik Janzén, Takeshi Ohshima, and David D. Awschalom. Isolated electron spins in silicon carbide with millisecond coherence times. *Nature Materials*, 14(2):160–163, feb 2015.

[314] P. Mélinon, B. Masenelli, F. Tournus, and A. Perez. Playing with carbon and silicon at the nanoscale. *Nature Materials*, 6(7):479–490, jul 2007.

[315] Mete Atatüre, Dirk Englund, Nick Vamivakas, Sang-Yun Lee, and Joerg Wrachtrup. Material platforms for spin-based photonic quantum technologies. *Nature Reviews Materials*, 3(5):38–51, may 2018.

[316] Christopher P Anderson, Alexandre Bourassa, Kevin C Miao, Gary Wolfowicz, Peter J Mintun, Alexander L Crook, Hiroshi Abe, Jawad Ul Hassan, Nguyen T Son, Takeshi Ohshima, and David D Awschalom. Electrical and optical control of single spins integrated in scalable semiconductor devices. *Science*, 366(6470):1225–1230, dec 2019.

[317] A. Lohrmann, B. C. Johnson, J. C. McCallum, and S. Castelletto. A review on single photon sources in silicon carbide. *Reports on Progress in Physics*, 80(3):034502, mar 2017.

[318] Stefania Castelletto and Alberto Boretti. Silicon carbide color centers for quantum applications. *Journal of Physics: Photonics*, 2(2):022001, mar 2020.

[319] Daniil M. Lukin, Melissa A. Guidry, and Jelena Vučković. Integrated Quantum Photonics with Silicon Carbide: Challenges and Prospects. *PRX Quantum*, 1(2):020102, dec 2020.

[320] Jun-Feng Wang, Qiang Li, Fei-Fei Yan, He Liu, Guo-Ping Guo, Wei-Ping Zhang, Xiong Zhou, Li-Ping Guo, Zhi-Hai Lin, Jin-Ming Cui, Xiao-Ye Xu, Jin-Shi Xu, Chuan-Feng Li, and Guang-Can Guo. On-Demand Generation of Single Silicon Vacancy Defects in Silicon Carbide. *ACS Photonics*, 6(7):1736–1743, jul 2019.

[321] Yu-Chen Chen, Patrick S. Salter, Matthias Niethammer, Matthias Widmann, Florian Kaiser, Roland Nagy, Naoya Morioka, Charles Babin, Jürgen Erlekampf, Patrick Berwian, Martin J. Booth, and Jörg Wrachtrup. Laser Writing of Scalable Single Color Centers in Silicon Carbide. *Nano Letters*, 19(4):2377–2383, apr 2019.

[322] Sophia E. Economou and Pratibha Dev. Spin-photon entanglement interfaces in silicon carbide defect centers. *Nanotechnology*, 27(50):504001, dec 2016.

[323] David J Christle, Paul V Klimov, Charles F de las Casas, Krisztián Szász, Viktor Ivády, Valdas Jokubavicius, Jawad Ul Hassan, Mikael Syväjärvi, William F Koehl, Takeshi Ohshima, Nguyen T Son, Erik Janzén, Ádám Gali, and David D Awschalom. Isolated Spin Qubits in SiC with a High-Fidelity Infrared Spin-to-Photon Interface. *Physical Review X*, 7(2):021046, jun 2017.

[324] Alexander L. Crook, Christopher P. Anderson, Kevin C. Miao, Alexandre Bourassa, Hope Lee, Sam L. Bayliss, David O. Bracher, Xingyu Zhang, Hiroshi Abe, Takeshi Ohshima, Evelyn L. Hu, and David D. Awschalom. Purcell Enhancement of a Single Silicon Carbide Color Center with Coherent Spin Control. *Nano Letters*, 20(5):3427–3434, may 2020.

[325] Tian Zhong and Philippe Goldner. Emerging rare-earth doped material platforms for quantum nanophotonics. *Nanophotonics*, 8(11):2003–2015, sep 2019.

[326] A. J. Freeman and R. E. Watson. Theoretical Investigation of Some Magnetic and Spectroscopic Properties of Rare-Earth Ions. *Physical Review*, 127(6):2058–2075, sep 1962.

[327] Roman Kolesov and Jörg Wrachtrup. A rare quantum leap. *Nature Physics*, 16(5):503–504, may 2020.

[328] Manjin Zhong, Morgan P. Hedges, Rose L. Ahlefeldt, John G. Bartholomew, Sarah E. Beavan, Sven M. Wittig, Jevon J. Longdell, and Matthew J. Sellars. Optically addressable nuclear spins in a solid with a six-hour coherence time. *Nature*, 517(7533):177–180, jan 2015.

[329] Mouktik Raha, Songtao Chen, Christopher M. Phenicie, Salim Ourari, Alan M. Dibos, and Jeff D. Thompson. Optical quantum nondemolition measurement of a single rare earth ion qubit. *Nature Communications*, 11(1):1605, dec 2020.

[330] A. M. Dibos, M Raha, C. M. Phenicie, and J. D. Thompson. Atomic Source of Single Photons in the Telecom Band. *Physical Review Letters*, 120(24):243601, jun 2018.

[331] Tian Zhong, Jonathan M Kindem, John G Bartholomew, Jake Rochman, Ioana Craiciu, Varun Verma, Sae Woo Nam, Francesco Marsili, Matthew D Shaw, Andrew D Beyer, and Andrei Faraon. Optically Addressing Single Rare-Earth Ions in a Nanophotonic Cavity. *Physical Review Letters*, 121(18):183603, oct 2018.

[332] Tian Zhong, Jonathan M Kindem, John G Bartholomew, Jake Rochman, Ioana Craiciu, Evan Miyazono, Marco Bettinelli, Enrico Cavalli, Varun Verma, Sae Woo Nam, Francesco Marsili, Matthew D Shaw, Andrew D Beyer, and Andrei Faraon. Nanophotonic rare-earth quantum memory with optically controlled retrieval. *Science*, 357(6358):1392–1395, sep 2017.

[333] Jonathan M. Kindem, Andrei Ruskuc, John G. Bartholomew, Jake Rochman, Yan Qi Huan, and Andrei Faraon. Control and single-shot readout of an ion embedded in a nanophotonic cavity. *Nature*, 580(7802):201–204, apr 2020.

[334] C. V. Raman and K. S. Krishnan. A New Type of Secondary Radiation. *Nature*, 121(3048):501–502, mar 1928.

[335] A. C. MENZIES. The Raman Effect. *Nature*, 125(3145):205–207, feb 1930.

[336] NobelPrize.org. The Nobel Prize in Physics 1930, 2021.

[337] Andrew D. Greentree and Steven Prawer. A little diamond goes a long way. *Nature Photonics*, 4(4):202–203, apr 2010.

[338] J. B. Cui, K. Amtmann, J. Ristein, and L. Ley. Noncontact temperature measurements of diamond by Raman scattering spectroscopy. *Journal of Applied Physics*, 83(12):7929–7933, jun 1998.

[339] Steven Prawer and Robert J. Nemanich. Raman spectroscopy of diamond and doped diamond. *Philosophical Transactions of the Royal Society of London. Series A: Mathematical, Physical and Engineering Sciences*, 362(1824):2537–2565, nov 2004.

[340] Mark Kasperczyk. *Engineering light-matter interactions: photon pair generation and magnetic dipole transitions*. PhD thesis, ETH Zürich, 2016.

[341] Mildred S. Dresselhaus, Gene Dresselhaus, and Ado Jorio. *Group theory*. Springer, 2008.

[342] Charles Kittel. Introduction to Solid State Physics, 8th edition. *Wiley & Sons, New York, NY*, 2004.

[343] N. S. Nagendra Nath. The dynamical theory of the diamond lattice. I. *Proceedings of the Indian Academy of Sciences - Section A*, 1(5):333–345, nov 1934.

[344] Richard P Mildren and James R Rabeau. *Optical Engineering of Diamond*. Wiley, 2013.

[345] Werner Weber. Adiabatic bond charge model for the phonons in diamond, Si, Ge, and $\alpha$-Sn. *Physical Review B*, 15(10):4789–4803, may 1977.

[346] V. S. Gorelik and N. S. Vasil'ev. Dispersion of optical and acoustic phonons in diamond and germanium crystals. *Inorganic Materials*, 48(5):462–468, may 2012.

[347] Nikolay V. Surovtsev and I. N. Kupriyanov. Temperature dependence of the Raman line width in diamond: Revisited. *Journal of Raman Spectroscopy*, 46(1):171–176, jan 2015.

[348] Robert J. Williams, Ondrej Kitzler, Zhenxu Bai, Soumya Sarang, Hadiya Jasbeer, Aaron McKay, Sergei Antipov, Alexander Sabella, Oliver Lux, David J. Spence, and Richard P. Mildren. High Power Diamond Raman Lasers. *IEEE Journal of Selected Topics in Quantum Electronics*, 24(5):1–14, sep 2018.

[349] Charles Santori and Raymond G. Beausoleil. Phonons in diamond crystals. *Nature Photonics*, 6(1):10–12, jan 2012.

[350] K. C. Lee, B. J. Sussman, M. R. Sprague, P. Michelberger, K. F. Reim, J. Nunn, N. K. Langford, P. J. Bustard, D. Jaksch, and I. A. Walmsley. Macroscopic non-classical states and terahertz quantum processing in room-temperature diamond. *Nature Photonics*, 6(1):41–44, jan 2012.

[351] Mark Kasperczyk, Ado Jorio, Elke Neu, Patrick Maletinsky, and Lukas Novotny. Stokes–anti-Stokes correlations in diamond. *Optics Letters*, 40(10):2393, may 2015.

[352] Duncan G. England, Kent A. G. Fisher, Jean-Philippe W. MacLean, Philip J. Bustard, Khabat Heshami, Kevin J. Resch, and Benjamin J. Sussman. Phonon-Mediated Nonclassical Interference in Diamond. *Physical Review Letters*, 117(7):073603, aug 2016.

[353] Mitchell D. Anderson, Santiago Tarrago Velez, Kilian Seibold, Hugo Flayac, Vincenzo Savona, Nicolas Sangouard, and Christophe Galland. Two-Color Pump-Probe Measurement of Photonic Quantum Correlations Mediated by a Single Phonon. *Physical Review Letters*, 120(23):233601, jun 2018.

[354] Santiago Tarrago Velez, Kilian Seibold, Nils Kipfer, Mitchell D. Anderson, Vivishek Sudhir, and Christophe Galland. Preparation and Decay of a Single Quantum of Vibration at Ambient Conditions. *Physical Review X*, 9(4):041007, oct 2019.

[355] Santiago Tarrago Velez, Vivishek Sudhir, Nicolas Sangouard, and Christophe Galland. Bell correlations between light and vibration at ambient conditions. *Science Advances*, 6(51):eabb0260, dec 2020.

[356] P.-Y. Hou, Y.-Y. Huang, X.-X. Yuan, X.-Y. Chang, C. Zu, L. He, and L.-M. Duan. Quantum teleportation from light beams to vibrational states of a macroscopic diamond. *Nature Communications*, 7(1):11736, sep 2016.

[357] K. C. Lee, M. R. Sprague, B. J. Sussman, J. Nunn, N. K. Langford, X. M. Jin, T. Champion, P. Michelberger, K. F. Reim, D. England, D. Jaksch, and I. A.

Walmsley. Entangling Macroscopic Diamonds at Room Temperature. *Science*, 334(6060):1253–1256, dec 2011.

[358] L. M. Duan. Quantum Correlation Between Distant Diamonds. *Science*, 334(6060):1213–1214, dec 2011.

[359] Khabat Heshami, Duncan G. England, Peter C. Humphreys, Philip J. Bustard, Victor M. Acosta, Joshua Nunn, and Benjamin J. Sussman. Quantum memories: emerging applications and recent advances. *Journal of Modern Optics*, 63(20):2005–2028, nov 2016.

[360] Duncan G. England, Kent A. G. Fisher, Jean-Philippe W. MacLean, Philip J. Bustard, Rune Lausten, Kevin J. Resch, and Benjamin J. Sussman. Storage and Retrieval of THz-Bandwidth Single Photons Using a Room-Temperature Diamond Quantum Memory. *Physical Review Letters*, 114(5):053602, feb 2015.

[361] D. G. England, P. J. Bustard, J. Nunn, R. Lausten, and B. J. Sussman. From Photons to Phonons and Back: A THz Optical Memory in Diamond. *Physical Review Letters*, 111(24):243601, dec 2013.

[362] P G Klemens. Anharmonic Decay of Optical Phonons. *Physical Review*, 148(2):845–848, aug 1966.

[363] A. Catellani and L. Sorba. Acoustic-wave transmission in semiconductor superlattices. *Physical Review B*, 38(11):7717–7722, oct 1988.

[364] Benjamin Petrak, Nicholas Djeu, and Andreas Muller. Purcell-enhanced Raman scattering from atmospheric gases in a high-finesse microcavity. *Physical Review A*, 89(2):023811, feb 2014.

[365] B. Petrak, J. Cooper, K. Konthasinghe, M. Peiris, N. Djeu, A. J. Hopkins, and A. Muller. Isotopic gas analysis through Purcell cavity enhanced Raman scattering. *Applied Physics Letters*, 108(9):091107, feb 2016.

[366] A. Fainstein and B. Jusserand. Phonons in semiconductor planar microcavities: A Raman scattering study. *Physical Review B*, 54(16):11505–11516, oct 1996.

[367] Hisashi Sumikura, Eiichi Kuramochi, Hideaki Taniyama, and Masaya Notomi. Cavity-enhanced Raman scattering of single-walled carbon nanotubes. *Applied Physics Letters*, 102(23):231110, jun 2013.

[368] Thomas Hümmer, Jonathan Noe, Matthias S. Hofmann, Theodor W Hänsch, Alexander Högele, and David Hunger. Cavity-enhanced Raman microscopy of individual carbon nanotubes. *Nature Communications*, 7(1):12155, nov 2016.

[369] X. Checoury, Z. Han, M. El Kurdi, and P. Boucaud. Deterministic measurement of the Purcell factor in microcavities through Raman emission. *Physical Review A*, 81(3):033832, mar 2010.

[370] X. Checoury, Z. Han, and P. Boucaud. Stimulated Raman scattering in silicon photonic crystal waveguides under continuous excitation. *Physical Review B*, 82(4):041308, jul 2010.

[371] S M Spillane, T J Kippenberg, and K J Vahala. Ultralow-threshold Raman laser using a spherical dielectric microcavity. *Nature*, 415(6872):621–623, feb 2002.

[372] H.M. Pask. The design and operation of solid-state Raman lasers. *Progress in Quantum Electronics*, 27(1):3–56, jan 2003.

[373] Richard P. Mildren, Aaron McKay, Robert J. Williams, and Ondrej Kitzler. Diamond Raman Lasers. *Optics and Photonics News*, 25(9):42, sep 2014.

[374] Eduardo Granados, David J. Spence, and Richard P. Mildren. Deep ultraviolet diamond Raman laser. *Optics Express*, 19(11):10857, may 2011.

[375] Katerina Chrysalidis, Valentin N. Fedosseev, Bruce A. Marsh, Richard P. Mildren, David J. Spence, Klaus D.A. A. Wendt, Shane G. Wilkins, and Eduardo Granados. Continuously tunable diamond Raman laser for resonance laser ionization. *Optics Letters*, 44(16):3924, aug 2019.

[376] Xuezong Yang, Ondrej Kitzler, David J. Spence, Zhenxu Bai, Yan Feng, and Richard P. Mildren. Diamond sodium guide star laser. *Optics Letters*, 45(7):1898, apr 2020.

[377] Alexander Sabella, James A. Piper, and Richard P. Mildren. Efficient conversion of a 1064 $\mu$m Nd:YAG laser to the eye-safe region using a diamond Raman laser. *Optics Express*, 19(23):23554, nov 2011.

[378] Alexander Sabella, James A. Piper, and Richard P. Mildren. 1240 nm diamond Raman laser operating near the quantum limit. *Optics Letters*, 35(23):3874, dec 2010.

[379] D. K. Armani, T. J. Kippenberg, S. M. Spillane, and K. J. Vahala. Ultra-high-Q toroid microcavity on a chip. *Nature*, 421(6926):925–928, feb 2003.

[380] T. J. Kippenberg, S. M. Spillane, D. K. Armani, and K. J. Vahala. Ultralow-threshold microcavity Raman laser on a microelectronic chip. *Optics Letters*, 29(11):1224, jun 2004.

[381] Sigurd Flågan, Patrick Maletinsky, Richard J. Warburton, and Daniel Riedel. Widely-tunable, doubly-resonant Raman scattering on diamond in an open microcavity. *arXiv:2110.06242*, oct 2021.

[382] Pawel Latawiec, Vivek Venkataraman, Michael J. Burek, Birgit J. M. Hausmann, Irfan Bulu, and Marko Lončar. On-chip diamond Raman laser. *Optica*, 2(11):924, nov 2015.

[383] Pawel Latawiec, Vivek Venkataraman, Amirhassan Shams-Ansari, Matthew Markham, and Marko Lončar. Integrated diamond Raman laser pumped in the near-visible. *Optics Letters*, 43(2):318, jan 2018.

[384] Xiaodong Yang and Chee Wei Wong. Coupled-mode theory for stimulated Raman scattering in high-$Q/V_{\mathrm{m}}$ silicon photonic band gap defect cavity lasers. *Optics Express*, 15(8):4763, 2007.

[385] Lukas Greuter, Sebastian Starosielec, Daniel Najer, Arne Ludwig, Luc Duempelmann, Dominik Rohner, and Richard J. Warburton. A small mode volume tunable microcavity: Development and characterization. *Applied Physics Letters*, 105(12):121105, sep 2014.

[386] D.I. Babic and S.W. Corzine. Analytic expressions for the reflection delay, penetration depth, and absorptance of quarter-wave dielectric mirrors. *IEEE Journal of Quantum Electronics*, 28(2):514–524, 1992.

[387] Sigurd Flågan, Daniel Riedel, Alisa Javadi, Tomasz Jakubczyk, Patrick Maletinsky, and Richard J. Warburton. High quality-factor diamond-confined open microcavity. *arXiv:2105.08736*, may 2021.

[388] Jean M. Bennett. Recent developments in surface roughness characterization. *Measurement Science and Technology*, 3(12):1119–1127, dec 1992.

[389] C. K. Carniglia and D. G. Jensen. Single-layer model for surface roughness. *Applied Optics*, 41(16):3167, jun 2002.

[390] Anthony E. Siegman. *Lasers*. Mill Valley: University Science Books, 1986.

[391] Daniel Najer, Natasha Tomm, Alisa Javadi, Alexander R. Korsch, Benjamin Petrak, Daniel Riedel, Vincent Dolique, Sascha R. Valentin, Rüdiger Schott, Andreas D. Wieck, Arne Ludwig, and Richard J. Warburton. Suppression of Surface-Related Loss in a Gated Semiconductor Microcavity. *Physical Review Applied*, 15(4):044004, apr 2021.

[392] K-M C Fu, P. E. Barclay, C. Santori, A. Faraon, and R. G. Beausoleil. Low-temperature tapered-fiber probing of diamond nitrogen-vacancy ensembles coupled to GaP microcavities. *New Journal of Physics*, 13(5):055023, may 2011.

[393] Daniel Najer, Martina Renggli, Daniel Riedel, Sebastian Starosielec, and Richard J. Warburton. Fabrication of mirror templates in silica with micron-sized radii of curvature. *Applied Physics Letters*, 110(1):011101, jan 2017.

[394] Juan Yin, Yuan Cao, Yu-Huai Li, Sheng-Kai Liao, Liang Zhang, Ji-Gang Ren, Wen-Qi Cai, Wei-Yue Liu, Bo Li, Hui Dai, Guang-Bing Li, Qi-Ming Lu, Yun-Hong Gong, Yu Xu, Shuang-Lin Li, Feng-Zhi Li, Ya-Yun Yin, Zi-Qing Jiang, Ming Li, Jian-Jun Jia, Ge Ren, Dong He, Yi-Lin Zhou, Xiao-Xiang Zhang, Na Wang, Xiang Chang, Zhen-Cai Zhu, Nai-Le Liu, Yu-Ao Chen, Chao-Yang Lu, Rong Shu, Cheng-Zhi Peng, Jian-Yu Wang, and Jian-Wei Pan. Satellite-based entanglement distribution over 1200 kilometers. *Science*, 356(6343):1140–1144, jun 2017.

[395] Sen Yang, Ya Wang, D. D. Bhaktavatsala Rao, Thai Hien Tran, Ali S. Momenzadeh, M. Markham, D. J. Twitchen, Ping Wang, Wen Yang, Rainer Stöhr, Philipp Neumann, Hideo Kosaka, and Jörg Wrachtrup. High-fidelity transfer and storage of photon states in a single nuclear spin. *Nature Photonics*, 10(8):507–511, aug 2016.

[396] W. Pfaff, B. J. Hensen, H. Bernien, S. B. van Dam, M. S. Blok, T. H. Taminiau, M. J. Tiggelman, R. N. Schouten, M. Markham, D. J. Twitchen, and R. Hanson. Unconditional quantum teleportation between distant solid-state quantum bits. *Science*, 345(6196):532–535, aug 2014.

[397] Peter C. Humphreys, Norbert Kalb, Jaco P.J. J. Morits, Raymond N. Schouten, Raymond F.L. L. Vermeulen, Daniel J. Twitchen, Matthew Markham, and Ronald Hanson. Deterministic delivery of remote entanglement on a quantum network. *Nature*, 558(7709):268–273, jun 2018.

[398] T. Jung, J. Görlitz, B. Kambs, C. Pauly, N. Raatz, R. Nelz, E. Neu, A. M. Edmonds, M. Markham, F. Mücklich, J. Meijer, and C. Becher. Spin measurements of NV centers coupled to a photonic crystal cavity. *APL Photonics*, 4(12):120803, dec 2019.

[399] Russell J. Barbour, Paul A. Dalgarno, Arran Curran, Kris M. Nowak, Howard J. Baker, Denis R. Hall, Nick G. Stoltz, Pierre M. Petroff, and Richard J. Warburton. A tunable microcavity. *Journal of Applied Physics*, 110(5):053107, sep 2011.

[400] Bernardo Casabone, Chetan Deshmukh, Shuping Liu, Diana Serrano, Alban Ferrier, Thomas Hümmer, Philippe Goldner, David Hunger, and Hugues de Riedmatten. Dynamic control of Purcell enhanced emission of erbium ions in nanoparticles. *Nature Communications*, 12(1):3570, dec 2021.

[401] Stefan Häußler, Gregor Bayer, Richard Waltrich, Noah Mendelson, Chi Li, David Hunger, Igor Aharonovich, and Alexander Kubanek. Tunable Fiber-Cavity Enhanced Photon Emission from Defect Centers in hBN. *Advanced Optical Materials*, 9(17):2002218, sep 2021.

[402] D. Hunger, C. Deutsch, R. J. Barbour, R. J. Warburton, and J. Reichel. Laser micro-fabrication of concave, low-roughness features in silica. *AIP Advances*, 2(1):012119, mar 2012.

[403] D. Riedel, D. Rohner, M. Ganzhorn, T. Kaldewey, P. Appel, E. Neu, R. J. Warburton, and P. Maletinsky. Low-Loss Broadband Antenna for Efficient Photon Collection from a Coherent Spin in Diamond. *Physical Review Applied*, 2(6):064011, dec 2014.

[404] Nadia O. Antoniadis, Natasha Tomm, Tomasz Jakubczyk, Rüdiger Schott, Sascha R. Valentin, Andreas D. Wieck, Arne Ludwig, Richard J. Warburton, and Alisa Javadi. A chiral one-dimensional atom using a quantum dot in an open microcavity. *arXiv:2110.02650*, pages 1–19, oct 2021.

[405] Stefan Bogdanović, Suzanne B. van Dam, Cristian Bonato, Lisanne C Coenen, Anne-Marije J. Zwerver, Bas Hensen, Madelaine S. Z. Liddy, Thomas Fink, Andreas Reiserer, Marko Lončar, and Ronald Hanson. Design and low-temperature characterization of a tunable microcavity for diamond-based quantum networks. *Applied Physics Letters*, 110(17):171103, apr 2017.

[406] Hrishikesh Kelkar, Daqing Wang, Diego Martín-Cano, Björn Hoffmann, Silke Christiansen, Stephan Götzinger, and Vahid Sandoghdar. Sensing Nanoparticles with a Cantilever-Based Scannable Optical Cavity of Low Finesse and Sub- ¡math display="inline"¿ ¡msup¿ ¡mi¿λ¡/mi¿ ¡mn¿3¡/mn¿ ¡/msup¿ ¡/math¿ Volume. *Physical Review Applied*, 4(5):054010, nov 2015.

[407] David H. Foster, Andrew K. Cook, and Jens U. Nöckel. Degenerate perturbation theory describing the mixing of orbital angular momentum modes in Fabry-Perot cavity resonators. *Physical Review A*, 79(1):011803, jan 2009.

[408] Manuel Uphoff, Manuel Brekenfeld, Gerhard Rempe, and Stephan Ritter. Frequency splitting of polarization eigenmodes in microscopic Fabry–Perot cavities. *New Journal of Physics*, 17(1):013053, jan 2015.

[409] John L. Hall, Jun Ye, and Long-Sheng Ma. Measurement of mirror birefringence at the sub-ppm level: Proposed application to a test of QED. *Physical Review A*, 62(1):013815, jun 2000.

[410] B. Brandstätter, A. McClung, K. Schüppert, B. Casabone, K. Friebe, A. Stute, P. O. Schmidt, C. Deutsch, J. Reichel, R. Blatt, and T. E. Northup. Integrated fiber-mirror ion trap for strong ion-cavity coupling. *Review of Scientific Instruments*, 84(12):123104, dec 2013.

[411] Johannes F. S. Brachmann, Hanno Kaupp, Theodor W. Hänsch, and David Hunger. Photothermal effects in ultra-precisely stabilized tunable microcavities. *Optics Express*, 24(18):21205, sep 2016.

[412] K. An, B. A. Sones, C. Fang-Yen, R. R. Dasari, and M. S. Feld. Optical bistability induced by mirror absorption: measurement of absorption coefficients at the sub-ppm level. *Optics Letters*, 22(18):1433, sep 1997.

[413] L.C. Flatten, A.A.P. Trichet, and J.M. Smith. Spectral engineering of coupled open-access microcavities. *Laser & Photonics Reviews*, 10(2):257–263, mar 2016.

[414] Philip Trøst Kristensen, Cole Van Vlack, and Stephen Hughes. Generalized effective mode volume for leaky optical cavities. *Optics Letters*, 37(10):1649, may 2012.

[415] Biswarup Guha, Felix Marsault, Fabian Cadiz, Laurence Morgenroth, Vladimir Ulin, Vladimir Berkovitz, Aristide Lemaître, Carmen Gomez, Alberto Amo, Sylvain Combrié, Bruno Gérard, Giuseppe Leo, and Ivan Favero. Surface-enhanced

gallium arsenide photonic resonator with quality factor of $6 \times 10^6$. *Optica*, 4(2):218, feb 2017.

[416] D Riedel, F Fuchs, H Kraus, S Väth, A Sperlich, V Dyakonov, A A Soltamova, P G Baranov, V A Ilyin, and G V Astakhov. Resonant Addressing and Manipulation of Silicon Vacancy Qubits in Silicon Carbide. *Physical Review Letters*, 109(22):226402, nov 2012.

[417] Bernardo Casabone, Julia Benedikter, Thomas Hümmer, Franziska Oehl, Karmel de Oliveira Lima, Theodor W. Hänsch, Alban Ferrier, Philippe Goldner, Hugues de Riedmatten, and David Hunger. Cavity-enhanced spectroscopy of a few-ion ensemble in Eu 3+ :Y 2 O 3. *New Journal of Physics*, 20(9):095006, sep 2018.

[418] Songtao Chen, Mouktik Raha, Christopher M. Phenicie, Salim Ourari, and Jeff D. Thompson. Parallel single-shot measurement and coherent control of solid-state spins below the diffraction limit. *Science*, 370(6516):592–595, oct 2020.

[419] Joshua D. Caldwell, Igor Aharonovich, Guillaume Cassabois, James H. Edgar, Bernard Gil, and D. N. Basov. Photonics with hexagonal boron nitride. *Nature Reviews Materials*, 4(8):552–567, aug 2019.

[420] A. Dietrich, M. W. Doherty, I. Aharonovich, and A. Kubanek. Solid-state single photon source with Fourier transform limited lines at room temperature. *Physical Review B*, 101(8):081401, feb 2020.

[421] Luozhou Li, Tim Schröder, Edward H. Chen, Michael Walsh, Igal Bayn, Jordan Goldstein, Ophir Gaathon, Matthew E. Trusheim, Ming Lu, Jacob Mower, Mircea Cotlet, Matthew L. Markham, Daniel J. Twitchen, and Dirk Englund. Coherent spin control of a nanocavity-enhanced qubit in diamond. *Nature Communications*, 6(1):6173, may 2015.

[422] Andreas Muller, Edward B Flagg, Michael Metcalfe, John Lawall, and Glenn S Solomon. Coupling an epitaxial quantum dot to a fiber-based external-mirror microcavity. *Applied Physics Letters*, 95(17):173101, oct 2009.

[423] Julia Benedikter, Hanno Kaupp, Thomas Hümmer, Yuejiang Liang, Alexander Bommer, Christoph Becher, Anke Krueger, Jason M Smith, Theodor W Hänsch, and David Hunger. Cavity-Enhanced Single-Photon Source Based on the Silicon-Vacancy Center in Diamond. *Physical Review Applied*, 7(2):024031, feb 2017.

[424] Roland Albrecht, Alexander Bommer, Christian Deutsch, Jakob Reichel, and Christoph Becher. Coupling of a Single Nitrogen-Vacancy Center in Diamond to a Fiber-Based Microcavity. *Physical Review Letters*, 110(24):243602, jun 2013.

[425] S. Johnson, P. R. Dolan, T. Grange, A. A.P. P Trichet, G. Hornecker, Y. C. Chen, L. Weng, G. M. Hughes, A. A.R. R Watt, A. Auffèves, and J. M. Smith. Tunable cavity coupling of the zero phonon line of a nitrogen-vacancy defect in diamond. *New Journal of Physics*, 17(12):122003, dec 2015.

[426] T. Steinmetz, Y. Colombe, D. Hunger, T. W. Hänsch, A. Balocchi, R. J. Warburton, and J. Reichel. Stable fiber-based Fabry-Pérot cavity. *Applied Physics Letters*, 89(11):111110, sep 2006.

[427] Chandrasekhara Venkata Raman. A new radiation. *Indian Journal of Physics*, 2(2):387–398, aug 1928.

[428] David J Spence, Eduardo Granados, and Richard P Mildren. Mode-locked picosecond diamond Raman laser. *Optics Letters*, 35(4):556, feb 2010.

[429] A C Ferrari and J Robertson. Interpretation of Raman spectra of disordered and amorphous carbon. *Physical Review B*, 61(20):14095–14107, may 2000.

[430] F Cairo, F De Martini, and D Murra. QED-vacuum confinement of inelastic quantum scattering at optical frequencies: A new perspective in Raman spectroscopy. *Physical Review Letters*, 70(10):1413–1416, mar 1993.

[431] Ming S Liu, Les A Bursill, S Prawer, and R Beserman. Temperature dependence of the first-order Raman phonon line of diamond. *Physical Review B*, 61(5):3391–3395, feb 2000.

[432] Orazio Svelto and David C Hanna. *Principles of lasers*, volume 1. Springer, 2010.

[433] Richard P. Mildren, James E. Butler, and James R. Rabeau. CVD-diamond external cavity Raman laser at 573 nm. *Optics Express*, 16(23):18950, nov 2008.

[434] R. P. Mildren and A. Sabella. Highly efficient diamond Raman laser. *Optics Letters*, 34(18):2811, sep 2009.

[435] Walter Lubeigt, Gerald M Bonner, Jennifer E Hastie, Martin D Dawson, David Burns, and Alan J Kemp. Continuous-wave diamond Raman laser. *Optics Letters*, 35(17):2994, sep 2010.

[436] Daniele C. Parrotta, Alan J. Kemp, Martin D. Dawson, and Jennifer E. Hastie. Multiwatt, Continuous-Wave, Tunable Diamond Raman Laser With Intracavity Frequency-Doubling to the Visible Region. *IEEE Journal of Selected Topics in Quantum Electronics*, 19(4):1400108–1400108, jul 2013.

[437] Ondrej Kitzler, Aaron McKay, and Richard P. Mildren. Continuous-wave wavelength conversion for high-power applications using an external cavity diamond Raman laser. *Optics Letters*, 37(14):2790, jul 2012.

[438] Jean-Philippe M. Feve, Kevin E. Shortoff, Matthew J. Bohn, and Jason K. Brasseur. High average power diamond Raman laser. *Optics Express*, 19(2):913, 2011.

[439] Robert J. Williams, Ondrej Kitzler, Aaron McKay, and Richard P. Mildren. Investigating diamond Raman lasers at the 100 W level using quasi-continuous-wave pumping. *Optics Letters*, 39(14):4152, jul 2014.

[440] Sergei Antipov, Alexander Sabella, Robert J. Williams, Ondrej Kitzler, David J. Spence, and Richard P. Mildren. 12 kW quasi-steady-state diamond Raman laser pumped by an M 2 = 15 beam . *Optics Letters*, 44(10):2506, 2019.

[441] Riccardo Casula, Jussi-Pekka Penttinen, Alan J. Kemp, Mircea Guina, and Jennifer E. Hastie. 14 µm continuous-wave diamond Raman laser. *Optics Express*, 25(25):31377, dec 2017.

[442] Haisheng Rong, Richard Jones, Ansheng Liu, Oded Cohen, Dani Hak, Alexander Fang, and Mario Paniccia. A continuous-wave Raman silicon laser. *Nature*, 433(7027):725–728, feb 2005.

[443] Haisheng Rong, Ansheng Liu, Richard Jones, Oded Cohen, Dani Hak, Remus Nicolaescu, Alexander Fang, and Mario Paniccia. An all-silicon Raman laser. *Nature*, 433(7023):292–294, jan 2005.

[444] Haisheng Rong, Shengbo Xu, Oded Cohen, Omri Raday, Mindy Lee, Vanessa Sih, and Mario Paniccia. A cascaded silicon Raman laser. *Nature Photonics*, 2(3):170–174, 2008.

[445] Yasushi Takahashi, Yoshitaka Inui, Masahiro Chihara, Takashi Asano, Ryo Terawaki, and Susumu Noda. A micrometre-scale Raman silicon laser with a microwatt threshold. *Nature*, 498(7455):470–474, jun 2013.

[446] Xiaoqin Shen, Hyungwoo Choi, Dongyu Chen, Wei Zhao, and Andrea M. Armani. Raman laser from an optical resonator with a grafted single-molecule monolayer. *Nature Photonics*, 14(2):95–101, feb 2020.

[447] Andreas Muller, Edward B Flagg, John R Lawall, and Glenn S Solomon. Ultrahigh-finesse, low-mode-volume Fabry–Perot microcavity. *Optics Letters*, 35(13):2293, jul 2010.

[448] S. G. Pavlov, N. Deßmann, B. Redlich, A. F.G. Van Der Meer, N. V. Abrosimov, H. Riemann, R. Kh Zhukavin, V. N. Shastin, and H. W. Hübers. Competing Inversion-Based Lasing and Raman Lasing in Doped Silicon. *Physical Review X*, 8(4):41003, 2018.

[449] Vasili G. Savitski, Sean Reilly, and Alan J. Kemp. Steady-State Raman Gain in Diamond as a Function of Pump Wavelength. *IEEE Journal of Quantum Electronics*, 49(2):218–223, feb 2013.

[450] J. Gallego, S. Ghosh, S. K. Alavi, W. Alt, M. Martinez-Dorantes, D. Meschede, and L. Ratschbacher. High-finesse fiber Fabry–Perot cavities: stabilization and mode matching analysis. *Applied Physics B*, 122(3):47, mar 2016.

[451] Ondrej Kitzler, Jipeng Lin, Helen M. Pask, Richard P. Mildren, Stephen C. Webster, Nils Hempler, Graeme P. A. Malcolm, and David J. Spence. Single-longitudinal-mode ring diamond Raman laser. *Optics Letters*, 42(7):1229, apr 2017.

[452] Xianwen Liu, Changzheng Sun, Bing Xiong, Lai Wang, Jian Wang, Yanjun Han, Zhibiao Hao, Hongtao Li, Yi Luo, Jianchang Yan, Tongbo Wei, Yun Zhang, and Junxi Wang. Integrated continuous-wave aluminum nitride Raman laser. *Optica*, 4(8):893, aug 2017.

[453] Melissa A. Guidry, Ki Youl Yang, Daniil M. Lukin, Ashot Markosyan, Joshua Yang, Martin M. Fejer, and Jelena Vučković. Optical parametric oscillation in silicon carbide nanophotonics. *Optica*, 7(9):1139, sep 2020.

[454] Timothy P. McKenna, Hubert S. Stokowski, Vahid Ansari, Jatadhari Mishra, Marc Jankowski, Christopher J. Sarabalis, Jason F. Herrmann, Carsten Langrock, Martin M. Fejer, and Amir H. Safavi-Naeini. Ultra-low-power second-order nonlinear optics on a chip. *arXiv: 2102.05617*, feb 2021.

[455] Alan D. Logan, Michael Gould, Emma R. Schmidgall, Karine Hestroffer, Zin Lin, Weiliang Jin, Arka Majumdar, Fariba Hatami, Alejandro W. Rodriguez, and Kai-Mei C. Fu. 400gallium phosphide-on-oxide resonators. *Optics Express*, 26(26):33687, dec 2018.

[456] Dalziel J. Wilson, Katharina Schneider, Simon Hönl, Miles Anderson, Yannick Baumgartner, Lukas Czornomaz, Tobias J. Kippenberg, and Paul Seidler. Integrated gallium phosphide nonlinear photonics. *Nature Photonics*, 14(1):57–62, jan 2020.

[457] Benjamin Kambs and Christoph Becher. Limitations on the indistinguishability of photons from remote solid state sources. *New Journal of Physics*, 20(11):115003, nov 2018.

[458] Srivatsa Chakravarthi, Chris Moore, April Opsvig, Christian Pederson, Emma Hunt, Andrew Ivanov, Ian Christen, Scott Dunham, and Kai-Mei C. Fu. Window into NV center kinetics via repeated annealing and spatial tracking of thousands of individual NV centers. *Physical Review Materials*, 4(2):023402, feb 2020.

[459] B. J. M. Hausmann, B. J. Shields, Q. Quan, Y. Chu, N. P. de Leon, R. Evans, M. J. Burek, A. S. Zibrov, M. Markham, D. J. Twitchen, H. Park, M. D. Lukin, and M. Loncăr. Coupling of NV Centers to Photonic Crystal Nanobeams in Diamond. *Nano Letters*, 13(12):5791–5796, dec 2013.

[460] Jonathan C. Lee, David O. Bracher, Shanying Cui, Kenichi Ohno, Claire A. McLellan, Xingyu Zhang, Paolo Andrich, Benjamin Alemán, Kasey J. Russell, Andrew P. Magyar, Igor Aharonovich, Ania Bleszynski Jayich, David Awschalom, and Evelyn L. Hu. Deterministic coupling of delta-doped nitrogen vacancy centers to a nanobeam photonic crystal cavity. *Applied Physics Letters*, 105(26):261101, dec 2014.

[461] Srivatsa Chakravarthi, Christian Pederson, Zeeshawn Kazi, Andrew Ivanov, and Kai-Mei C Fu. Impact of surface and laser-induced noise on the spectral stability of implanted nitrogen-vacancy centers in diamond. *Physical Review B*, 104(8):085425, aug 2021.

[462] Jonathan Levine. A simplified calculation of power-broadened linewidths, with application to resonance ionization mass spectrometry. *Spectrochimica Acta Part B: Atomic Spectroscopy*, 69:61–66, mar 2012.

[463] Kimberly Jean Brown, Elizabeth Chartier, Ellen M. Sweet, David A. Hopper, and Lee C. Bassett. Cleaning diamond surfaces using boiling acid treatment in a standard laboratory chemical hood. *Journal of Chemical Health and Safety*, 26(6):40–44, nov 2019.

[464] I. Friel, S.L. Clewes, H.K. Dhillon, N. Perkins, D.J. Twitchen, and G.A. Scarsbrook. Control of surface and bulk crystalline quality in single crystal diamond grown by chemical vapour deposition. *Diamond and Related Materials*, 18(5-8):808–815, may 2009.

[465] C.L. Lee, E. Gu, M.D. Dawson, I. Friel, and G.A. Scarsbrook. Etching and micro-optics fabrication in diamond using chlorine-based inductively-coupled plasma. *Diamond and Related Materials*, 17(7-10):1292–1296, jul 2008.

[466] Y. Tao, J. M. Boss, B. A. Moores, and C. L. Degen. Single-crystal diamond nanomechanical resonators with quality factors exceeding one million. *Nature Communications*, 5(1):3638, may 2014.

[467] Vladimíra Petráková, Andrew Taylor, Irena Kratochvílová, František Fendrych, Jiří Vacík, Jan Kučka, Jan Štursa, Petr Cígler, Miroslav Ledvina, Anna Fišerová, Peter Kneppo, and Miloš Nesládek. Luminescence of Nanodiamond Driven by Atomic Functionalization: Towards Novel Detection Principles. *Advanced Functional Materials*, 22(4):812–819, feb 2012.

[468] D. S. Silva. *Data Analysis: A Bayesian Tutorial*. Oxford University Press, 2nd edition, 2006.

[469] J. Walker C. D. Clark and Robert William Ditchburn. The neutral vacancy in diamond. *Proceedings of the Royal Society of London. A. Mathematical and Physical Sciences*, 334(1597):241–257, aug 1973.

[470] G. Davies and M.F Hamer. Optical studies of the 1.945 eV vibronic band in diamond. *Proceedings of the Royal Society of London. A. Mathematical and Physical Sciences*, 348(1653):285–298, feb 1976.

[471] J. P. Hadden, J. P. Harrison, A. C. Stanley-Clarke, L. Marseglia, Y.-L. D. Ho, B. R. Patton, J. L. O'Brien, and J. G. Rarity. Strongly enhanced photon collection from diamond defect centers under microfabricated integrated solid immersion lenses. *Applied Physics Letters*, 97(24):241901, dec 2010.

[472] K G Lee, X W Chen, H Eghlidi, P Kukura, R Lettow, A Renn, V Sandoghdar, and S. Götzinger. A planar dielectric antenna for directional single-photon emission and near-unity collection efficiency. *Nature Photonics*, 5(3):166–169, mar 2011.

[473] G. Lei, J. E. Anderson, M. I. Buchwald, B. C. Edwards, and R. I. Epstein. Determination of spectral linewidths by Voigt profiles in $Yb^{3+}$ -doped fluorozirconate glasses. *Physical Review B*, 57(13):7673–7678, apr 1998.

[474] Elke Neu, Patrick Appel, Marc Ganzhorn, Javier Miguel-Sánchez, Margarita Lesik, Vianney Mille, Vincent Jacques, Alexandre Tallaire, Jocelyn Achard, and Patrick Maletinsky. Photonic nano-structures on (111)-oriented diamond. *Applied Physics Letters*, 104(15):153108, apr 2014.

[475] Blake Regan, Sejeong Kim, Anh T. H. Ly, Aleksandra Trycz, Kerem Bray, Kumaravelu Ganesan, Milos Toth, and Igor Aharonovich. Photonic devices fabricated from (111)-oriented single crystal diamond. *InfoMat*, 2(6):1241–1246, nov 2020.

[476] D. Rohner, J. Happacher, P. Reiser, M. A. Tschudin, A. Tallaire, J. Achard, B. J. Shields, and P. Maletinsky. (111)-oriented, single crystal diamond tips for nanoscale scanning probe imaging of out-of-plane magnetic fields. *Applied Physics Letters*, 115(19):192401, nov 2019.

[477] Charles Santori, Philippe Tamarat, Philipp Neumann, Jörg Wrachtrup, David Fattal, Raymond G. Beausoleil, James Rabeau, Paolo Olivero, Andrew D. Greentree, Steven Prawer, Fedor Jelezko, and Philip Hemmer. Coherent Population Trapping of Single Spins in Diamond under Optical Excitation. *Physical Review Letters*, 97(24):247401, dec 2006.

[478] Jan Jeske, Jared H. Cole, and Andrew D. Greentree. Laser threshold magnetometry. *New Journal of Physics*, 18(1):013015, jan 2016.

[479] W. S. Lau, J. Zhang, X. Wan, J. K. Luo, Y. Xu, and H. Wong. Surface smoothing effect of an amorphous thin film deposited by atomic layer deposition on a surface with nano-sized roughness. *AIP Advances*, 4(2):027120, feb 2014.

[480] Amy Butcher, Xinghan Guo, Robert Shreiner, Nazar Delegan, Kai Hao, Peter J. Duda, David D. Awschalom, F. Joseph Heremans, and Alexander A. High. High- Q Nanophotonic Resonators on Diamond Membranes using Templated Atomic Layer Deposition of TiO 2. *Nano Letters*, 20(6):4603–4609, jun 2020.

[481] Nobuyuki Kawakami, Yoshihiro Yokota, Takeshi Tachibana, Kazushi Hayashi, and Koji Kobashi. Atomic layer deposition of Al2O3 thin films on diamond. *Diamond and Related Materials*, 14(11-12):2015–2018, nov 2005.

[482] Zeyang Ren, Dandan Lv, Jiamin Xu, Jinfeng Zhang, Jincheng Zhang, Kai Su, Chunfu Zhang, and Yue Hao. High temperature (300 °C) ALD grown Al 2 O 3 on hydrogen terminated diamond: Band offset and electrical properties of the MOSFETs. *Applied Physics Letters*, 116(1):013503, jan 2020.

[483] Thomas M. Babinec, Birgit J. M. Hausmann, Mughees Khan, Yinan Zhang, Jeronimo R. Maze, Philip R. Hemmer, and Marko Lončar. A diamond nanowire single-photon source. *Nature Nanotechnology*, 5(3):195–199, mar 2010.

[484] Marko Lončar and Andrei Faraon. Quantum photonic networks in diamond. *MRS Bulletin*, 38(2):144–148, feb 2013.

[485] Sara L. Mouradian and Dirk Englund. A tunable waveguide-coupled cavity design for scalable interfaces to solid-state quantum emitters. *APL Photonics*, 2(4):046103, apr 2017.

[486] Benjamin Pingault, David-Dominik Jarausch, Christian Hepp, Lina Klintberg, Jonas N. Becker, Matthew Markham, Christoph Becher, and Mete Atatüre. Coherent control of the silicon-vacancy spin in diamond. *Nature Communications*, 8(1):15579, aug 2017.

[487] Mehran Kianinia, Simon White, Johannes E. Fröch, Carlo Bradac, and Igor Aharonovich. Generation of Spin Defects in Hexagonal Boron Nitride. *ACS Photonics*, 7(8):2147–2152, aug 2020.

[488] S J. Byrnes. Multilayer optical calculations. *arXiv:1603.02720*, 2020.

[489] R. W. Boyd. *Nonlinear Optics*. Academic Press, New York, 1992.

[490] Bruno Romeira and Andrea Fiore. Purcell Effect in the Stimulated and Spontaneous Emission Rates of Nanoscale Semiconductor Lasers. *IEEE Journal of Quantum Electronics*, 54(2):1–12, apr 2018.

[491] A. Auffèves, D. Gerace, J.-M. Gérard, M. França Santos, L. C. Andreani, and J.-P. Poizat. Controlling the dynamics of a coupled atom-cavity system by pure dephasing. *Physical Review B*, 81(24):245419, jun 2010.

[492] A. Meldrum, P. Bianucci, and F. Marsiglio. Modification of ensemble emission rates and luminescence spectra for inhomogeneously broadened distributions of quantum dots coupled to optical microcavities. *Optics Express*, 18(10):10230, may 2010.

[493] Sean D. Barrett and Pieter Kok. Efficient high-fidelity quantum computation using matter qubits and linear optics. *Physical Review A*, 71(6):060310, jun 2005.

[494] Steven Prawer and Igor Aharonovich. *Quantum Information Processing with Diamond*. Woodhead Publishing, 1st edition, 2014.

[495] Bas Hensen. *Quantum Nonlocality with Spins in Diamond*. PhD thesis, Delft University of Technology, 2016.

[496] Emre Ismail Cengiz Togan. *Optical control of individual nitrogen-vacancy centers in diamond*. PhD thesis, Harvard University, 2011.

# Acknowledgements

Writing these words closes the door on almost a decade of physics studies. I have met many people who have supported me on my journey from high school in Norway, to my studies in Manchester to now finalising my PhD here in Basel. Therefore, I have some important people I need to thank.

First and foremost, I will like to thank Professor Richard J. Warburton for taking the gamble of hiring a nuclear physicist with little background in optics. I would also like to thank my second supervisor, Professor Patrick Maletinsky. Without their guidance, discussions and supervision, finishing this PhD would not have been possible. Next, I would like to thank Professor Stephan Götzinger from the Max Planck Institute, for his time and willingness to accept the duty as external examiner and in reading my thesis.

There is no science without funding. Therefore, I would like to thank Professor Alexander Tartakovskii and Sally Greenhough from the University of Sheffield for coordinating and administrating the Marie-Curie ITN network Spin-NANO, which funded my PhD. A big thank you to the full Spin-NANO team for fruitful and stimulating discussions during the network meetings. Looking back on my PhD, these meetings are amongst the finest memories. I would further like to thank Professor Caspar Clark, Dr. Najwa Sidqi and the rest of the team at Helia Photonics for their hospitality during my stay in Scotland.

Next, I would like to thank my former postdoc Daniel Riedel for his patience and willingness to teach me the art of optics during his time in Basel and the successive Transatlantic collaborations. The discussions in the lab or over the occasional beer certainly taught me a lot about the cavity and the NV centre. I wish you all the best for your future academic career, and I hope for more fruitful collaborations in the future.

I would now like to thank the director, editor, cameraman and sound engineer Immo Söllner. Our video* is yet to top Taylor Swift, but who knows what the future will bring? I am sure there is a job open for you in Hollywood somewhere.

I sincerely thank Nadia Antoniadis, Simon Geyer, Mark Hogg, Giang Nam Nguyen, Daniel Riedel, Clemens Spinnler, Lukas Sponfeldner, Liang Zhai and Josh Zuber for

*The video can be found here: https://www.youtube.com/watch?v=xeovlntM66U.

volunteering to carefully read and correct this thesis. Your feedback, comments and moral support has been highly appreciated and certainly added significant improvements to this manuscript. I owe you all (at least) one beer! Also thanks to the self-proclaimed colour-expert Nadia alongside Lukas and David Broadway for helpful discussions and advice on the figures, both for this thesis and for the publications. I should probably also thank Jack Barnett for having to suffer through my "around the clock" questions on British words and phrases. Consider this my payback for you dragging me into the misery that is Preston North End. Finally, thanks to Laura Cuevas for taking your time in making the artistic interpretation of me during the last couple of weeks.

A big thanks go to all past and present members of the Nano-Photonics Group and the Quantum Sensing Lab for their contributions to the enjoyable working environment. I enjoyed the discussions, be they in the corridor or during coffee breaks, Christmas dinners, summer BBQs, after-work beers or halfway up a Swiss mountain. Also thanks for all the jolly moments and occasional knees-up. I would like to list a few people. First, thanks to Immo Söllner, Guillaume Froehlicher and Alisa Javadi for their genuine interest in discussing physics and for always providing a well thought through answer to my questions, no matter how stupid they might have been. Also, Jan-Philipp Jahn deserves a pat on the back for various discussions, be they during the countless kilometres on the bike or with a beer in hand. Also thanks to Alisa for introducing me to COMSOL. On the topic of simulations, thanks to Daniel Najer for the introduction to Macleod, a tool that ended up playing a major part in this thesis. Brendan Shields, Mark Kasperczyk, Johannes Kölbl, Arne Barfuss, Josh Zuber and David Broadway for the discussions on the linewidth measurements and NV physics in general. Also thanks to Natascha Hedrich for helping with, and arguably doing the heavier lifting, our shared responsibility for the ICP. I will also like to thank all current and past members of the diamond-cavity team; Daniel Riedel, Brendan Shields, Tomasz Jakubczyk, Yannik Fontana, Andrea Corazza, Viktoria Yurgens and Marie Gruet. Finally, the realisation of the experiments would not have been possible without the excellent work of the mechanical and electronic workshops and the administrative team.

Inga Hanne Dokka, you deserve a big thanks! Without your passionate physics lessons at high school, I would never have gone on to study physics in the first place, let alone complete a PhD. And of course, a big thank you goes out to all my friends and family for the continuous support and words of encouragement during the course of my PhD.

And finally to my beloved bike, thank you for keeping me rolling through my PhD. I apologise for letting you dust over the past week, it is high time to hit the countryside roads again!

# Curriculum vitae

## Sigurd Flågan

### Personal information


| | |
|---|---|
| Email address: | sigurd.flagan@gmail.com |
| Date of birth: | 5th February 1993 |
| Place of birth: | Fredrikstad, Norway |
| Citizenship: | Norwegian |


### Education

| | |
|---|---|
| 2016 – 2021 | **PhD in Experimental Physics**<br>University of Basel, Switzerland<br>Thesis: *An open Microcavity for Diamond-based Photonics*<br>Advisors: Prof. Richard J. Warburton, Prof. Patrick Maletinsky |
| 2012 – 2016 | **MPhys Physics**<br>The University of Manchester, United Kingdom<br>Thesis: *In-Flight X-ray Emission from Fission Fragments*<br>Advisor: Dr. Alastair Smith |
| 2013 – 2016 | **High school**<br>Kongsberg Videregående Skole, Kongsberg |

# List of publications

1. S. Flågan, P. Maletinsky, R. J. Warburton, D. Riedel *Widely-tunable, doubly-resonant Raman scattering on diamond in an open microcavity*, arXiv:2110.06242 (2021).

2. S. Flågan, D. Riedel, A. Javadi, T. Jakubczyk, P. Maletinsky, R. J. Warburton, *High quality-factor diamond-confined open microcavity*, arXiv:2105.08736 (2021).

3. V. Yurgens, J. A. Zuber, S. Flågan, M. De Luca, B. J. Shields, I. Zardo, P. Maletinsky, R. J. Warburton, and T. Jakubczyk, *Low charge-noise nitrogen-vacancy centers in diamond created using laser writing with a solid-immersion lens*, ACS Photonics **8**, 1726–1734 (2021).

4. M. Kasperczyk, J. A. Zuber, A. Barfuss, J. Kölbl, V. Yurgens, S. Flågan, T. Jakubczyk, B. Shields, R. J. Warburton, and P. Maletinsky, *Statistically modeling optical linewidths of nitrogen vacancy centers in microstructures*, Physical Review B **102**, 075312 (2020).

5. D. Riedel, S. Flågan, P. Maletinsky, and R. J. Warburton, *Cavity-Enhanced Raman Scattering for In Situ Alignment and Characterization of Solid-State Microcavities*, Physical Review Applied **13**, 014036 (2020).

6. S. Flågan D. Riedel, B. J. Shields, T. Jakubczyk, P. Maletinsky, and R. J. Warburton, *A tunable Fabry-Pérot cavity for diamond-based photonics*, Symposium Latsis 2019 on Diamond Photonics - Physics, Technologies and Applications, OSA Technical Digest (Optical Society of America, 2019), paper 49 (2019).